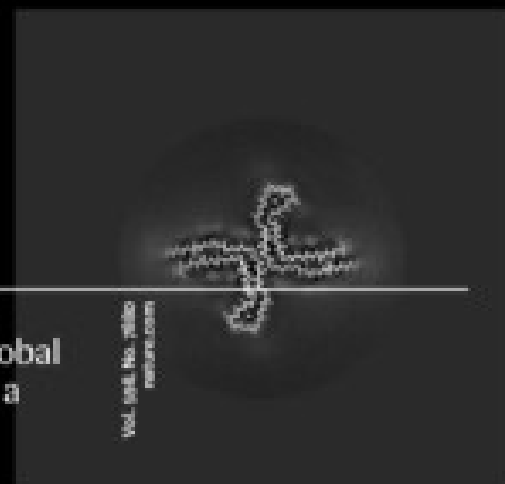
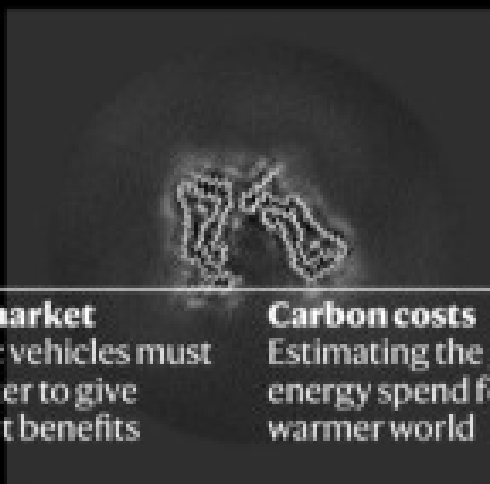
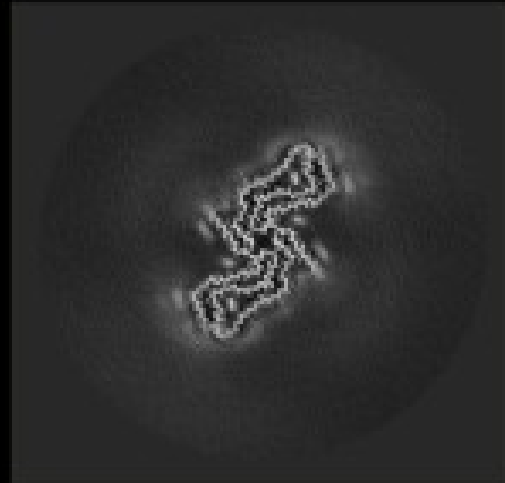
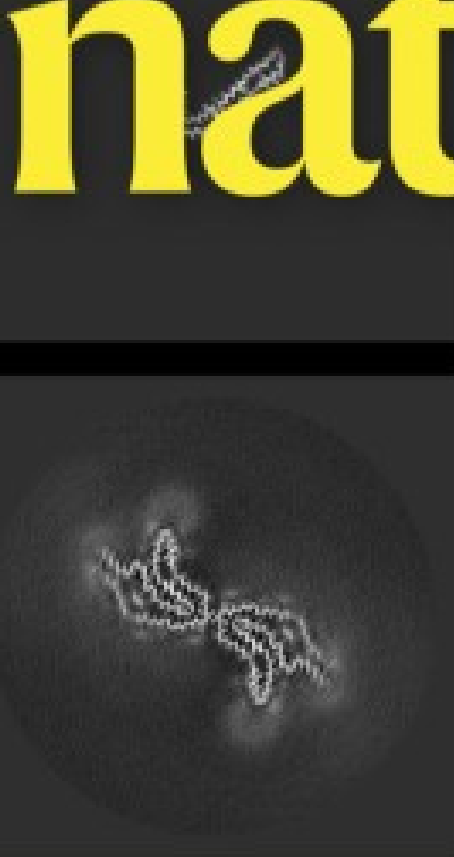


nature

PROTEIN MISFOLDS

Neurodegenerative diseases classified by shapes of tau filaments



Under fire
How scientists are harassed for speaking up about COVID-19

Mass market
Electric vehicles must be lighter to give greatest benefits

Carbon costs
Estimating the global energy spend for a warmer world

Vol. 598 No. 7416

Nature.2021.10.16

[Sat, 16 Oct 2021]

- [This Week](#)
- [News in Focus](#)
- [Opinion](#)
- [Work](#)
- [Research](#)

This Week

- **[Young people's mental health is finally getting the attention it needs](#)** [07 October 2021]
Editorial • The COVID-19 pandemic, a UNICEF report and a review of the latest research all highlight the urgent need for better prevention and treatment of youth anxiety and depression.
- **[COVID scientists in the public eye need protection from threats](#)** [13 October 2021]
Editorial • Researchers are facing harassment for speaking out during the pandemic. Their institutions must do more to support them.
- **[COVID lesson: trust the public with hard truths](#)** [12 October 2021]
World View • When governments assume that people will panic, that exacerbates the pandemic.
- **[Deal-making in the early Universe: galaxies merged to grow](#)** [05 October 2021]
Research Highlight • Galaxies were busy joining forces one billion years after the birth of the Universe.
- **[An abandoned antibiotic makes a comeback to fight a common illness](#)** [06 October 2021]
Research Highlight • Hygromycin A doesn't work well against most bacteria, but it shines as a treatment for Lyme disease.
- **[‘Rivers in the sky’ to deliver more drenchings as Earth warms](#)** [04 October 2021]
Research Highlight • Atmospheric rivers, which carry moisture towards the poles, are expected to intensify unless greenhouse-gas emissions are curbed.
- **[A toxic ‘tide’ is creeping over bountiful Arctic waters](#)** [06 October 2021]
Research Highlight • Off the Alaskan coast, scientists find dense beds of algal cysts from a species that make marine animals poisonous to eat.
- **[A ‘spirit mirror’ used in Elizabeth I’s court had Aztec roots](#)** [06 October 2021]

Research Highlight • Geochemical analysis suggests that an obsidian mirror owned by a confidant of the English Tudor queen was made in Mexico.

- **A magnetic patch on a twitchy arm makes a useful current**

[05 October 2021]

Research Highlight • Scientists have developed a material whose magnetic properties change when it's deformed — and that is also soft enough to respond to small movements.

- **Floods once lashed the Martian lake where NASA's rover roams**

[07 October 2021]

Research Highlight • Now a dusty hole, Jezero Crater hosted a lake billions of years ago.

- EDITORIAL
- 07 October 2021

Young people's mental health is finally getting the attention it needs

The COVID-19 pandemic, a UNICEF report and a review of the latest research all highlight the urgent need for better prevention and treatment of youth anxiety and depression.



A kite-flying festival in a refugee camp near Syria's border with Turkey. The event was organized in July 2020 to support the health and well-being of children fleeing violence in Syria. Credit: Muhammed Said/Anadolu Agency/Getty

Worldwide, at least 13% of people between the ages of 10 and 19 live with a diagnosed mental-health disorder, according to the latest [*State of the World's Children report*](#), published this week by the United Nations children's charity UNICEF. It's the first time in the organization's history that this flagship report has tackled the challenges in and opportunities for preventing and treating mental-health problems among young people. It reveals that adolescent mental health is highly complex, understudied — and underfunded. These findings are echoed in a parallel collection of review articles published this week in a number of Springer Nature journals.

Anxiety and depression constitute more than 40% of mental-health disorders among young people (those aged 10–19). UNICEF also reports that, worldwide, suicide is the fourth most-common cause of death (after road injuries, tuberculosis and interpersonal violence) among adolescents (aged 15–19). In eastern Europe and central Asia, suicide is the leading cause of death for young people in that age group — and it's the second-highest cause in western Europe and North America.



[Collection: Promoting youth mental health](#)

Sadly, psychological distress among young people seems to be rising. One study found that rates of depression among a nationally representative sample of US adolescents (aged 12 to 17) increased from 8.5% of young adults to 13.2% between 2005 and 2017¹. There's also initial evidence that

the coronavirus pandemic is exacerbating this trend in some countries. For example, in a nationwide study² from Iceland, adolescents (aged 13–18) reported significantly more symptoms of mental ill health during the pandemic than did their peers before it. And girls were more likely to experience these symptoms than were boys.

Although most mental-health disorders arise during adolescence, UNICEF says that only one-third of investment in mental-health research is targeted towards young people. Moreover, the research itself suffers from fragmentation — scientists involved tend to work inside some key disciplines, such as psychiatry, paediatrics, psychology and epidemiology, and the links between research and health-care services are often poor. This means that effective forms of prevention and treatment are limited, and lack a solid understanding of what works, in which context and why.

This week's [collection of review articles](#) dives deep into the state of knowledge of interventions — those that work and those that don't — for preventing and treating anxiety and depression in young people aged 14–24. In some of the projects, young people with lived experience of anxiety and depression were co-investigators, involved in both the design and implementation of the reviews, as well as in interpretation of the findings.

Quest for new therapies

Worldwide, the most common treatment for anxiety and depression is a class of drug called selective serotonin reuptake inhibitors, which increase serotonin levels in the brain and are intended to enhance emotion and mood. But their modest efficacy and substantial side effects³ have spurred the study of alternative physiological mechanisms that could be involved in youth depression and anxiety, so that new therapeutics can be developed.



Mental health: build predictive models to steer policy

For example, researchers have been investigating potential links between depression and inflammatory disorders — such as asthma, cardiovascular disease and inflammatory bowel disease. This is because, in many cases, adults with depression also experience such disorders. Moreover, there's evidence that, in mice, changes to the gut microbiota during development reduce behaviours similar to those linked to anxiety and depression in people⁴. That suggests that targeting the gut microbiome during adolescence could be a promising avenue for reducing anxiety in young people. Kathrin Cohen Kadosh at the University of Surrey in Guildford, UK, and colleagues reviewed existing reports of interventions in which diets were changed to target the gut microbiome. These were found to have had minimal effect on youth anxiety⁵. However, the authors urge caution before such a conclusion can be confirmed, citing methodological limitations (including small sample sizes) among the studies they reviewed. They say the next crop of studies will need to involve larger-scale clinical trials.

By contrast, researchers have found that improving young people's cognitive and interpersonal skills can be more effective in preventing and treating anxiety and depression under certain circumstances — although the reason for this is not known. For instance, a concept known as 'decentring' or 'psychological distancing' (that is, encouraging a person to adopt an objective perspective on negative thoughts and feelings) can help both to

prevent and to alleviate depression and anxiety, report Marc Bennett at the University of Cambridge, UK, and colleagues⁶, although the underlying neurobiological mechanisms are unclear.

In addition, Alexander Daros at the Campbell Family Mental Health Institute in Toronto, Canada, and colleagues report a meta-analysis of 90 randomized controlled trials. They found that helping young people to improve their emotion-regulation skills, which are needed to control emotional responses to difficult situations, enables them to cope better with anxiety and depression⁷. However, it is still unclear whether better regulation of emotions is the cause or the effect of these improvements.

Co-production is essential

It's uncommon — but increasingly seen as essential — that researchers working on treatments and interventions are directly involving young people who've experienced mental ill health. These young people need to be involved in all aspects of the research process, from conceptualizing to and designing a study, to conducting it and interpreting the results. Such an approach will lead to more-useful science, and will lessen the risk of developing irrelevant or inappropriate interventions.



[Science careers and mental health](#)

Two such young people are co-authors in a review from Karolin Krause at the Centre for Addiction and Mental Health in Toronto, Canada, and colleagues. The review explored whether training in problem solving helps to alleviate depressive symptoms⁸. The two youth partners, in turn, convened a panel of 12 other youth advisers, and together they provided input on shaping how the review of the evidence was carried out and on interpreting and contextualizing the findings. The study concluded that, although problem-solving training could help with personal challenges when combined with other treatments, it doesn't on its own measurably reduce depressive symptoms.

The overarching message that emerges from these reviews is that there is no ‘silver bullet’ for preventing and treating anxiety and depression in young people — rather, prevention and treatment will need to rely on a combination of interventions that take into account individual needs and circumstances. Higher-quality evidence is also needed, such as large-scale trials using established protocols.

Along with the UNICEF report, the studies underscore the transformational part that funders must urgently play, and why researchers, clinicians and communities must work together on more studies that genuinely involve young people as co-investigators. Together, we can all do better to create a brighter, healthier future for a generation of young people facing more challenges than ever before.

Nature **598**, 235-236 (2021)

doi: <https://doi.org/10.1038/d41586-021-02690-5>

References

1. 1.

Twenge, J. M., Cooper, A. B., Joiner, T. E., Duffy, M. E. & Binau, S. G. *J. Abnorm. Psychol.* **128**, 185–199 (2019).

2. 2.

Thorisdottir, I. E. *et al.* *Lancet Psychiatr.* **8**, 663–672 (2021).

3. 3.

Murphy, S. E. *et al.* *Lancet Psychiatr.* **8**, 824–835 (2021).

4. 4.

Murray, E. *et al.* *Brain Behav. Immun.* **81**, 198–212 (2019).

5. 5.

Cohen Kadosh, K. *et al.* *Transl. Psychiatr.* **11**, 352 (2021).

6. 6.

Bennett, M. P. *et al.* *Transl Psychiatr.* **11**, 288 (2021).

7. 7.

Daros, A. R. *et al.* *Nature Hum. Behav.* <https://doi.org/10.1038/s41562-021-01191-9> (2021).

8. 8.

Krause, K. R. *et al.* *BMC Psychiatr.* **21**, 397 (2021).

This article was downloaded by **calibre** from <https://www.nature.com/articles/d41586-021-02690-5>

- EDITORIAL
- 13 October 2021

COVID scientists in the public eye need protection from threats

Researchers are facing harassment for speaking out during the pandemic. Their institutions must do more to support them.



England's chief medical officer Chris Whitty is among the scientists who have experienced physical and online harassment, including death threats. Credit: Justin Tallis/AFP/Getty

The COVID-19 pandemic has seen more scientists than usual enter the public arena, many of them for the first time. Every day, researchers are interviewed in the media, advise policy-makers and write social-media

posts. They might be discussing the latest coronavirus data; explaining and interpreting new research; or commenting on government policies. Some are now as recognizable as celebrities.

Clear, accurate public communication from scientists is essential in a pandemic. But for a significant minority, the attention has had unpleasant consequences. [*Nature* has surveyed](#) a subset of researchers who have spoken to the media about COVID-19, and found that 47 people — some 15% of the 321 respondents — had received death threats and that 72 had received threats of physical or sexual violence. In response to other survey questions, the researchers who reported the highest frequency of trolling or personal attacks were more likely to say that it had affected their willingness to speak to the media in the future.



['I hope you die': how the COVID pandemic unleashed attacks on scientists](#)

The results are not a random sample: they represent those who chose to respond to *Nature*'s survey, which was based on a poll conducted by the Australian Science Media Centre, an organization that connects scientists to journalists. Other science media centres around the world sent *Nature*'s survey on to researchers in the United Kingdom, Canada, Taiwan, New Zealand and Germany, and *Nature* sent it to scientists in the United States and Brazil. Because those who have received threats might have been more

motivated to respond, the overall proportion of scientists experiencing abuse might be lower.

But the results are shocking, nonetheless. Intimidation is unacceptable on any scale, and the findings should be of concern to all those who care about scientists' well-being. Such behaviour also risks discouraging researchers from contributing to public discussion — which would be a huge loss, given their expertise, during the pandemic.

Institutions at all levels must do more to protect and defend scientists, and to condemn intimidation. Of those respondents who told their employers about death threats — and not all did — some 20% said their employers were not at all supportive. The proportion was similar for those who had experienced trolling or personal attacks online, although in these cases respondents were less likely to have notified their employer in the first place. Of those who had received death threats, more than 80% had told their employer, compared with just over half of those who had been subject to trolling or personal attacks. Respondents rightly said that scientific societies, funders and governments should talk about the problem and condemn attacks.



[Politicians must dial down the rhetoric over COVID vaccines](#)

Most of the respondents were in Europe and the United States, but threats are being made against researchers all over the world, by both individuals

and organized anti-science or anti-vaccination campaigns. The findings show the need for more support, protection and training for scientists in the public eye.

Some researchers in other high-profile fields, such as climate change and animal research, have had to deal with harassment and abuse for many years (see, for instance, *Nature* **562**, 449–450; 2018); partly as a result, their institutions have built up some level of understanding on how to support scientists. The Science Media Centre in London is among organizations that have published advice for those experiencing harassment, including when, whether and how to engage with critics, and who to turn to for support (see go.nature.com/3lyyqlj). Support and information can also be gained from many other fields, ranging from journalism to sport, in which people are targeted by toxic online threats and sometimes real-world attacks.

Taking steps to support scientists who face harassment does not mean silencing robust, open criticism and discussion. The coronavirus pandemic has seen plenty of disagreement and changing views as new data have come in, as well as differing stances on which policies to adopt. Scientists and health officials should expect their research to be questioned and challenged, and should welcome critical feedback that is given in good faith. But threats of violence and extreme online abuse do nothing to encourage debate — and risk undermining science communication at a time when it has never mattered more.

Nature **598**, 236 (2021)

doi: <https://doi.org/10.1038/d41586-021-02757-3>

This article was downloaded by **calibre** from <https://www.nature.com/articles/d41586-021-02757-3>

- WORLD VIEW
- 12 October 2021

COVID lesson: trust the public with hard truths



When governments assume that people will panic, that exacerbates the pandemic.

- [Michael Bang Petersen](#) 0

Of the many fears during the pandemic, one has been particularly pernicious: governments' fear of their people. Former US president Donald Trump admitted to playing down the risks of the coronavirus to "reduce panic". Jair Bolsonaro, president of Brazil, blamed the press for causing "hysteria". The UK government delayed its lockdown, fearing the British population would rapidly become fatigued by restrictions. And, in my home country of Denmark, the authorities tried not to draw public attention to pandemic preparations in early 2020, to avoid "unnecessary fear".

But Denmark pivoted to a strategy of trusting its citizens with hard truths. The buy-in that ensued led to low death rates and laid the groundwork for a vaccination rate of 95% for everyone aged above 50 (and 75% for the population in general). In September 2021, my country announced that COVID-19 is no longer classified as a “critical threat”.

Before the pandemic, I had studied Danes’ responses to crises, including a 2015 lethal terrorist attack in which a lone Islamist gunman attacked a free-speech event and a synagogue. My colleagues and I concluded that the majority of Danes did not lash out against Muslims or call to restrict their rights after these events, in part because of clear messaging from politicians. That is not to say that irrational, harmful behaviour does not happen, but the likelihood of mass panic in the face of crises is over-rated, especially if authorities and the media keep their heads.



[Study the role of hubris in nations’ COVID-19 response](#)

In March 2020, I began to study pandemic responses at home and abroad, and I became an adviser to the Danish government. My overall message was: don’t assume that the public will panic. That assumption is counterproductive, and not borne out by research.

During a pandemic, rapid behavioural change is crucial, so people cannot be asked to ‘keep calm and carry on’. They need clear information if they

are to take the crisis seriously enough to listen and to know how to act. In early March 2020, that was my message on social media, in the media and, ultimately, to the Danish government.

When Prime Minister Mette Frederiksen announced a lockdown on 11 March 2020, the rhetoric of the government had changed towards impressive clarity and acknowledgement of uncertainty. The #FlattenTheCurve graph (popularized by *The Economist* magazine a few days earlier) was used to show how an uncontrolled epidemic would strain hospitals. This created a sense of urgency and crisis, but not panic. And Frederiksen clearly acknowledged uncertainty. “We stand on unexplored territory in this situation,” she said. “Will we make mistakes? Yes, we will.”

One might argue that Danish authorities dared to trust their citizens only because they knew that the citizens trusted them. After all, Denmark often tops international studies of trust. But I think this experience is relevant elsewhere. Research consistently finds that in the face of disaster, people react with solidarity, not panic. For example, a study after a Chinese earthquake showed that people became more willing to share resources with strangers and do charity work ([L.-L. Rao et al. *Evol. Hum. Behav.* 32, 63–69; 2011](#)). Evidence from terrorist attacks in France and elsewhere echoes the Danish experience: if political leaders lead by example, the average citizen does not turn against the rights of people from minority ethnic groups. Even during the epitome of presumed pandemic panic — hoarding — most people waited patiently in line with their packets of toilet paper.



COVID-19 mental-health responses neglect social realities

The idea that the public is incapable of dealing effectively with the unpleasant truth stymies pandemic management. It leads authorities to communicate in self-defeating ways. My group's research shows that messages should communicate self-efficacy: people who feel that they know what to do, and how, are likely to comply ([F. Jørgensen et al. Br. J. Health Psychol. 26, 679-696; 2021](#)). Governments that underestimate their people focus on what the public cannot do.

Authorities that distrust the population also downplay negative or complicated facts. Rather than explaining emerging evidence of, say, waning immunity or new variants, paternalistic authorities resort to vague reassurances. Our research shows that vagueness inhibits vaccine acceptance and decreases trust in authorities ([M. B. Petersen et al. Proc. Natl Acad. Sci. USA 118, e2024597118; 2021](#)).

Upholding trust is key: it is the best predictor of vaccine acceptance and an antidote to misinformation. Danish health authorities talked clearly about severe, potentially fatal, side effects when they suspended the use of specific vaccines, even though the side effects are extremely rare. My research and others' shows that this decision — with explicit descriptions of trade-offs and efficacy — did not harm overall support for vaccination or

trust in health authorities ([K. M. Sønderskov et al. Dan. Med. J. 68, A03210292; 2021](#)).

In 1997, political scientist and economics Nobel laureate Elinor Ostrom warned that policymakers were creating “cynical citizens with little trust in one another” by acting without regard for people’s ability to think for themselves. Perhaps such problems persist because governments have increasingly relied on behavioural advice rooted in research on psychological biases. Although such research does not intend to promote the view that populations are irrational, it routinely highlights errors in human decision-making, which can amplify views already popular among political elites.

What can be done to ease this mutual distrust? To borrow from game theory, only the authorities can act as first mover. If authorities do not dare to trust, citizens never will.

Nature **598**, 237 (2021)

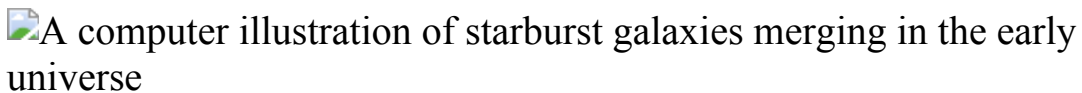
doi: <https://doi.org/10.1038/d41586-021-02758-2>

This article was downloaded by **calibre** from <https://www.nature.com/articles/d41586-021-02758-2>

- RESEARCH HIGHLIGHT
- 05 October 2021

Deal-making in the early Universe: galaxies merged to grow

Galaxies were busy joining forces one billion years after the birth of the Universe.



Two galaxies join in the early Universe (artist's impression). Such activity helped galaxies to gain mass. Credit: D. Berry, NRAO/AUI/NSF/Science Photo Library

Galaxy mergers could have played a key part in bulking up galaxies in the early Universe.

Access options

Subscribe to Journal

Get full journal access for 1 year

\$199.00

only \$3.90 per issue

[Subscribe](#)

All prices are NET prices.

VAT will be added later in the checkout.

Tax calculation will be finalised during checkout.

Rent or Buy article

Get time limited or full article access on ReadCube.

from \$8.99

[Rent or Buy](#)

All prices are NET prices.

Additional access options:

- [Log in](#)
- [Learn about institutional subscriptions](#)

Nature **598**, 238 (2021)

doi: <https://doi.org/10.1038/d41586-021-02700-6>

References

1. 1.

Romano, M. *et al. Astron. Astrophys.* <https://doi.org/10.1051/0004-6361/202141306> (2021).

This article was downloaded by **calibre** from <https://www.nature.com/articles/d41586-021-02700-6>

- RESEARCH HIGHLIGHT
- 06 October 2021

An abandoned antibiotic makes a comeback to fight a common illness

Hygromycin A doesn't work well against most bacteria, but it shines as a treatment for Lyme disease.

 Coloured scanning electron micrograph of the spirochaete bacterium *Borrelia burgdorferi*

The bacterium *Borrelia burgdorferi*, which causes Lyme disease, falters when treated with an antibiotic produced by another bacterial species.

Credit: Eye of Science/Science Photo Library

The bacterial infection called Lyme disease is difficult to treat, can inflict lasting nerve damage and affects almost 500,000 people annually in the United States alone. Now tests in mice show that an antibiotic that had been sitting on the shelf for decades blocks the bacterium that causes Lyme — without the serious side effects of current treatments¹.

Access options

Subscribe to Journal

Get full journal access for 1 year

\$199.00

only \$3.90 per issue

[Subscribe](#)

All prices are NET prices.
VAT will be added later in the checkout.
Tax calculation will be finalised during checkout.

Rent or Buy article

Get time limited or full article access on ReadCube.

from \$8.99

[Rent or Buy](#)

All prices are NET prices.

Additional access options:

- [Log in](#)
- [Learn about institutional subscriptions](#)

Nature **598**, 238 (2021)

doi: <https://doi.org/10.1038/d41586-021-02716-y>

References

1. 1.

Leimer, N. *et al.* *Cell* <https://doi.org/10.1016/j.cell.2021.09.011> (2021).

This article was downloaded by **calibre** from <https://www.nature.com/articles/d41586-021-02716-y>.

- RESEARCH HIGHLIGHT
- 04 October 2021

‘Rivers in the sky’ to deliver more drenchings as Earth warms

Atmospheric rivers, which carry moisture towards the poles, are expected to intensify unless greenhouse-gas emissions are curbed.

 Satellite image showing an arc of clouds stretching from Hawaii to the Pacific Northwest

An arc of clouds traces an atmospheric river travelling from Hawaii to the US Pacific Northwest. Such air streams are likely to transport more moisture as the climate changes. Credit: Joshua Stevens/NOAA/NESDIS/NASA GSFC

Climate change hasn’t yet had a noticeable influence on atmospheric rivers, narrow air streams that carry huge amounts of moisture towards the poles. But these ‘rivers in the sky’, which bring downpours to mid-latitude coastal regions, could become markedly more extreme if atmospheric greenhouse-gas concentrations continue to rise steeply¹.

Access options

Subscribe to Journal

Get full journal access for 1 year

\$199.00

only \$3.90 per issue

[Subscribe](#)

All prices are NET prices.
VAT will be added later in the checkout.
Tax calculation will be finalised during checkout.

Rent or Buy article

Get time limited or full article access on ReadCube.

from \$8.99

[Rent or Buy](#)

All prices are NET prices.

Additional access options:

- [Log in](#)
- [Learn about institutional subscriptions](#)

Nature **598**, 238 (2021)

doi: <https://doi.org/10.1038/d41586-021-02681-6>

References

1. 1.

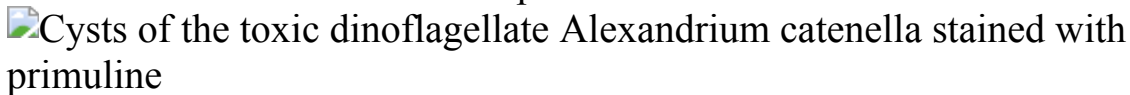
Baek, S. H. & Lora, J. M. *Nature Clim. Change*
<https://doi.org/10.1038/s41558-021-01166-8> (2021).

This article was downloaded by **calibre** from <https://www.nature.com/articles/d41586-021-02681-6>

- RESEARCH HIGHLIGHT
- 06 October 2021

A toxic ‘tide’ is creeping over bountiful Arctic waters

Off the Alaskan coast, scientists find dense beds of algal cysts from a species that make marine animals poisonous to eat.



Cysts of the toxic algae *Alexandrium catenella*, which is finding a foothold in cold Arctic waters. Credit: Evangeline Fachon

Toxic algae are likely to begin blooming more frequently in Arctic waters as the climate and the ocean warm¹.

Access options

Subscribe to Journal

Get full journal access for 1 year

\$199.00

only \$3.90 per issue

[Subscribe](#)

All prices are NET prices.

VAT will be added later in the checkout.

Tax calculation will be finalised during checkout.

Rent or Buy article

Get time limited or full article access on ReadCube.

from \$8.99

[Rent or Buy](#)

All prices are NET prices.

Additional access options:

- [Log in](#)
- [Learn about institutional subscriptions](#)

Nature **598**, 238 (2021)

doi: <https://doi.org/10.1038/d41586-021-02715-z>

References

1. 1.

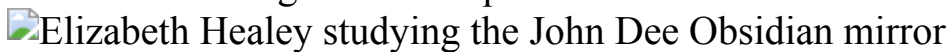
Anderson, D. M. *et al. Proc. Natl Acad. Sci. USA*
<https://doi.org/10.1073/pnas.2107387118> (2021).

This article was downloaded by **calibre** from <https://www.nature.com/articles/d41586-021-02715-z>

- RESEARCH HIGHLIGHT
- 06 October 2021

A ‘spirit mirror’ used in Elizabeth I’s court had Aztec roots

Geochemical analysis suggests that an obsidian mirror owned by a confidant of the English Tudor queen was made in Mexico.



The mirror owned by astrologer John Dee is made of stone traced to a source near Pachuca, Mexico. The Aztecs created objects of the same stone.
Credit: Stuart Campbell

To summon spirits, sixteenth-century English astrologer John Dee, a confidant of Queen Elizabeth I, gazed into a mirror made of polished stone. Now, researchers have confirmed that Dee’s mirror has Aztec origins¹.

Access options

Subscribe to Journal

Get full journal access for 1 year

\$199.00

only \$3.90 per issue

[Subscribe](#)

All prices are NET prices.

VAT will be added later in the checkout.

Tax calculation will be finalised during checkout.

Rent or Buy article

Get time limited or full article access on ReadCube.

from \$8.99

[Rent or Buy](#)

All prices are NET prices.

Additional access options:

- [Log in](#)
- [Learn about institutional subscriptions](#)

Nature **598**, 239 (2021)

doi: <https://doi.org/10.1038/d41586-021-02701-5>

References

1. 1.

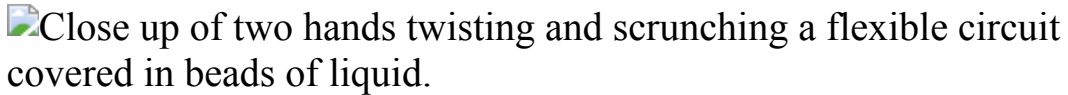
Campbell, S., Healey, E., Kuzmin, Y. & Glascock, M. D. *Antiquity*
<https://doi.org/10.15184/aqy.2021.132> (2021).

This article was downloaded by **calibre** from <https://www.nature.com/articles/d41586-021-02701-5>

- RESEARCH HIGHLIGHT
- 05 October 2021

A magnetic patch on a twitchy arm makes a useful current

Scientists have developed a material whose magnetic properties change when it's deformed — and that is also soft enough to respond to small movements.



The movement of tiny magnetic particles in this bendable patch can create an electrical current. Credit: Jun Chen/UCLA

As a hand gently taps a table-top, a soft device stuck to the elbow can generate enough electricity to power a wearable thermometer¹.

Access options

Subscribe to Journal

Get full journal access for 1 year

\$199.00

only \$3.90 per issue

[Subscribe](#)

All prices are NET prices.

VAT will be added later in the checkout.

Tax calculation will be finalised during checkout.

Rent or Buy article

Get time limited or full article access on ReadCube.

from \$8.99

[Rent or Buy](#)

All prices are NET prices.

Additional access options:

- [Log in](#)
- [Learn about institutional subscriptions](#)

Nature **598**, 239 (2021)

doi: <https://doi.org/10.1038/d41586-021-02680-7>

References

1. 1.

Zhou, Y., et al. *Nature Mater.* <https://doi.org/10.1038/s41563-021-01093-1> (2021).

This article was downloaded by **calibre** from <https://www.nature.com/articles/d41586-021-02680-7>

- RESEARCH HIGHLIGHT
- 07 October 2021

Floods once lashed the Martian lake where NASA's rover roams

Now a dusty hole, Jezero Crater hosted a lake billions of years ago.



Images snapped by NASA's Perseverance rover confirm that Jezero Crater (illustration) on Mars was filled with water eons ago. Credit: NASA/JPL-Caltech

Jezero Crater on Mars, which NASA's Perseverance rover is now exploring, was once home to a calm lake as well as powerful flash floods¹.

Access options

Subscribe to Journal

Get full journal access for 1 year

\$199.00

only \$3.90 per issue

[Subscribe](#)

All prices are NET prices.

VAT will be added later in the checkout.

Tax calculation will be finalised during checkout.

Rent or Buy article

Get time limited or full article access on ReadCube.

from \$8.99

[Rent or Buy](#)

All prices are NET prices.

Additional access options:

- [Log in](#)
- [Learn about institutional subscriptions](#)

Nature **598**, 239 (2021)

doi: <https://doi.org/10.1038/d41586-021-02745-7>

References

1. 1.

Mangold, N. *et al.* *Science* <https://doi.org/10.1126/science.abl4051> (2021).

This article was downloaded by **calibre** from <https://www.nature.com/articles/d41586-021-02745-7>

| [Section menu](#) | [Main menu](#) |

News in Focus

- **[Vaccines and Delta, Moon volcanism and an NIH departure](#)** [13 October 2021]
News Round-Up • The latest science news, in brief.
- **[Science agency on trial following deadly White Island volcano eruption](#)** [06 October 2021]
News • The rare example of a government research agency facing criminal charges after a natural disaster underlines the perils of communicating and managing risk.
- **[Head of Wellcome-funded Malawi health project investigated for bullying](#)** [06 October 2021]
News • The programme's director has resumed his post after being investigated — but some staff are not happy with the way the case was handled.
- **[Medicine Nobel goes to scientists who discovered biology of senses](#)** [04 October 2021]
News • David Julius and Ardem Patapoutian share the award for identifying receptors that allow the body's cells to sense temperature and touch.
- **[Climate modellers and theorist of complex systems share physics Nobel](#)** [05 October 2021]
News • Syukuro Manabe, Klaus Hasselmann and Giorgio Parisi split the award for their work on complex systems — including modelling Earth's climate and global warming.
- **[‘Elegant’ catalysts that tell left from right scoop chemistry Nobel](#)** [06 October 2021]
News • Benjamin List and David MacMillan share the award for developing cheap, environmentally friendly organic catalysts.
- **[Why COVID vaccines didn’t win a science Nobel this year](#)**
[07 October 2021]
News • Nobel prize insiders and observers say timing and politics meant vaccine technology was an unlikely winner — but science's most prestigious prize shouldn't be far off.
- **[NASA won’t rename James Webb telescope — and astronomers are angry](#)** [01 October 2021]

News • The agency found no evidence that the flagship observatory's namesake was involved in anti-LGBT+ activities, but some say that Webb bears responsibility.

- **'I hope you die': how the COVID pandemic unleashed attacks on scientists** [13 October 2021]

News Feature • Dozens of researchers tell Nature they have received death threats, or threats of physical or sexual violence.

- NEWS ROUND-UP
- 13 October 2021

Vaccines and Delta, Moon volcanism and an NIH departure

The latest science news, in brief.



A health worker gives a COVID-19 vaccine in Hanoi.Credit: Nhac Nguyen/AFP/Getty

Vaccines cut delta transmission risk, but not for long

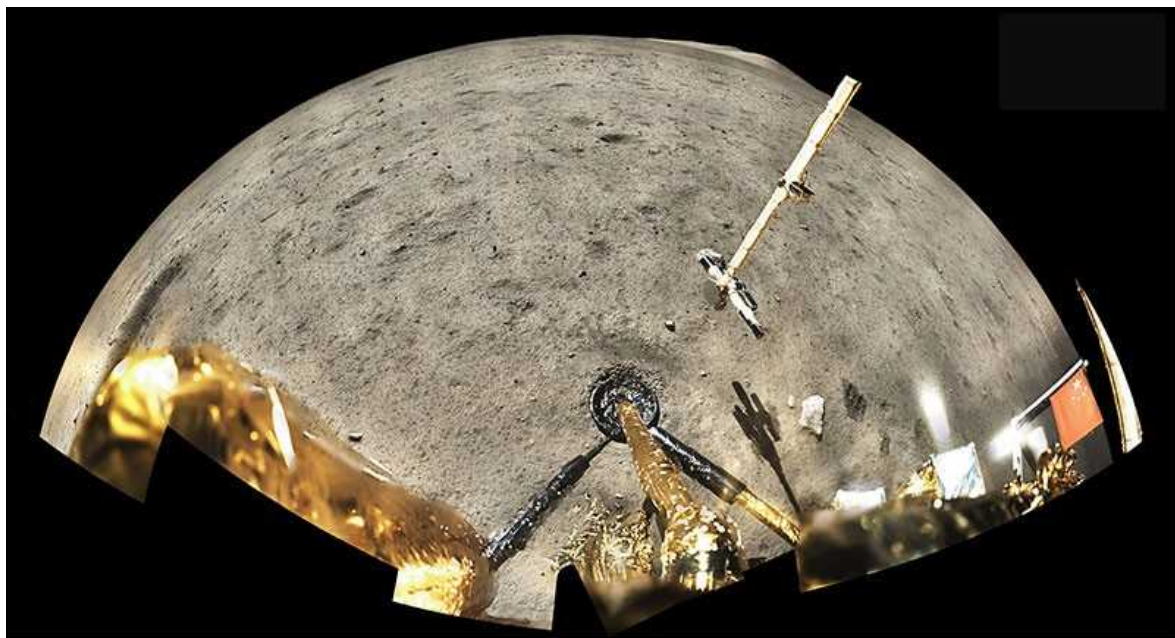
The first study to look directly at how well vaccines prevent the spread of the Delta variant of SARS-CoV-2 brings good news and bad.

It shows that people infected with Delta are less likely to pass on the virus if they have already had a COVID-19 vaccine than if they haven't (D. W. Eyre *et al.* Preprint at medRxiv <https://doi.org/gz5f>; 2021). But that protective effect is small, and dwindles alarmingly over time.

Researchers analysed testing data from 139,164 close contacts of 95,716 people infected with SARS-CoV-2 between January and August 2021 in the United Kingdom, when the Alpha and Delta variants were competing for dominance.

Although vaccines did offer some protection against infection and transmission, Delta dampened that effect. A vaccinated person who had a 'breakthrough' Delta infection was almost twice as likely to pass on the virus as was someone who was infected with Alpha. And vaccines' effect on Delta transmission waned to almost negligible levels over time.

The results "possibly explain why we've seen so much onward transmission of Delta despite widespread vaccination", says co-author David Eyre, an epidemiologist at the University of Oxford, UK.



A fish-eye view of Chang'e-5's landing site. The mission collected and shipped back to Earth 2 kilograms of lunar rock. Credit: Chinese National Space Agency's (CNSA) Lunar Exploration and Space Engineering Center

First Moon samples since 1970s reveal recent volcanism

A Chinese sample-return mission, Chang'e-5, has begun to yield results, [dating bits of lunar lava at two billion years old](#). "This is the youngest-ever lava flow dated from the Moon," says Katherine Joy, a planetary scientist at the University of Manchester, UK.

Chang'e-5 landed on the Moon on 1 December 2020, scooped up samples of the surface and lifted off again two days later. It then performed a rendezvous with its mother ship in lunar orbit, which subsequently flew back to Earth. A re-entry capsule carrying the samples landed in China's Inner Mongolia region on 16 December.

Samples returned by the US Apollo and the Soviet Luna programmes had provided evidence of volcanic eruptions on the Moon stretching back more than 4 billion years, with the majority between 3.8 billion and 3 billion years ago. But no mission had landed in an area as young as Chang'e-5's landing site, called Oceanus Procellarum.

The findings, published in *Science* on 7 October, fill a gap in the Moon's geology (X. Che *et al.* *Science* <https://doi.org/10.1126/science.abl7957>; 2021). By dating rock from the lunar surface and matching it to the number of craters in the surrounding region, scientists can infer that locations on other worlds, such as Mars, with similar numbers of craters are of a comparable age.



Francis Collins has served three US presidents as head of the National Institutes of Health. Credit: Shutterstock

Francis Collins to step down as NIH director by year's end

Renowned geneticist Francis Collins has [announced that he will step down](#) as director of the US National Institutes of Health (NIH) by December.

“This is the right time, it’s the right message, it’s the right decision,” says Collins (pictured), who has led the US\$41-billion biomedical agency through a historic and deadly pandemic. Picked for the job by then-president Barack Obama in 2009, Collins has had the role for longer than any other presidential appointee, serving under three administrations. It’s time for the agency to benefit from new leadership, he says, adding that he had considered whether his departure would upset the NIH’s response to COVID-19. “I’m not worried that if I walk away by the end of the year, that will do any serious harm to our contribution to fighting this pandemic.”

Collins has built a reputation as a savvy spokesperson for scientific research, winning supporters across party lines, even through a politically charged public-health crisis. “I think he deserves an A+ as NIH director,” says Elias Zerhouni, a radiologist who held the job for six years, before Collins. “I know how hard it is to maintain that, and frankly I think we owe him a debt of gratitude.”

Before taking the top job at the NIH, Collins made key contributions to the burgeoning field of genetics and medicine. He co-discovered the gene that causes cystic fibrosis, and his laboratory, eventually at the NIH’s National Human Genome Research Institute (NHGRI) in Bethesda, Maryland, found genes linked to conditions including Huntington’s disease. As head of the NHGRI from 1993 to 2008, he led the Human Genome Project.

“He’s a world-class scientist,” says Anthony Fauci, director of the NIH’s National Institute of Allergy and Infectious Diseases in Bethesda, who describes Collins as a close professional partner and friend.

But Collins’s time with the NIH hasn’t been without controversy. The agency has faced criticism for being slow to enact policies to protect researchers from sexual harassment, and been called on to improve funding for Black researchers.

Collins will continue to lead his laboratory at the NHGRI after he steps down. US President Joe Biden has not yet nominated a successor.

Nature **598**, 241 (2021)

doi: <https://doi.org/10.1038/d41586-021-02759-1>

This article was downloaded by **calibre** from <https://www.nature.com/articles/d41586-021-02759-1>

- NEWS
- 06 October 2021

Science agency on trial following deadly White Island volcano eruption

The rare example of a government research agency facing criminal charges after a natural disaster underlines the perils of communicating and managing risk.

- [Dyani Lewis](#) ⁰



A satellite image captures continued volcanic emissions from White Island on 13 December 2019. Credit: DigitalGlobe/ScapeWare3d/Maxar Technologies via Getty

New Zealand's Earth-science research agency, GNS Science, has pleaded not guilty to criminal charges laid in the wake of a devastating volcanic eruption at White Island in 2019 that left 22 people dead and 25 injured.

The cone-shaped volcano, 48 kilometres off the coast of the country's North Island, was the site of an [explosive eruption](#) of steam, rock and other debris on 9 December that year.

The case is unusual because government science agencies have rarely faced criminal charges following natural disasters. Some experts fear that pressing charges against a science agency in relation to the information it releases could have a chilling effect on the ability of scientific organizations to provide advice used to manage natural hazards.

But others say that the trial's outcome might clarify the roles and responsibilities of GNS Science and its co-defendants in keeping people on the island safe and informed of potential dangers.



[Why deadly New Zealand volcano eruption was hard to predict](#)

“One of the questions this case raises is how far a scientific organization has to go in terms of presenting information in a manner that is accessible to the public, and how you would assess if they have done so,” says Simon Connell, a lawyer and specialist in accident law at the University of Otago in Dunedin, New Zealand.

White Island, also known by the Māori name Whakaari, is one of New Zealand’s most active volcanoes, and was a popular tourist destination, where visitors regularly walked on the crater floor. Raymond Cas, a volcanologist at Monash University in Clayton, Australia, believes the 2019 tragedy was “a disaster waiting to happen”. He points to an eruption in April 2016 that was comparable in size, but happened to occur at night, when no one was present¹.

Last November, the country’s workplace health and safety regulator, WorkSafe New Zealand, laid two charges against GNS Science, which is based in Lower Hutt, New Zealand. The charges cover a period from April 2016 until December 2019, spanning both recent eruptions. Each carries a penalty of a fine of up to NZ\$1.5 million (US\$1 million).

‘Unexpected but not unforeseeable’

This is the first time a scientific agency has been charged under New Zealand’s Health and Safety at Work Act of 2015, which is usually applied in workplaces such as factories, says Len Andersen, a workplace health and safety lawyer in Dunedin.

WorkSafe New Zealand is not commenting on the case, but in a [statement](#) posted on 30 November 2020, chief executive Phil Parkes said that although the eruption was unexpected, it was not unforeseeable, and any organization or individual involved in getting people to the island had a duty to protect those under their care.

Co-defendants in the case — which does not cover rescue and recovery efforts — include seven tour operators and the National Emergency Management Agency (NEMA).

The first charge alleges that GNS Science — formerly known as the Institute of Geological and Nuclear Sciences Limited — failed to ensure the health and safety of helicopter pilots it hired to take its employees to the island. The second alleges that GNS Science should have consulted and coordinated with other agencies and tour operators, and reviewed “the structure, content and delivery of its volcanic alert bulletins” to ensure that they “effectively communicated the implications of volcanic activity”.

Nature approached GNS Science for comment, but the agency declined to respond while the matter is before the courts.

GNS Science issues volcanic alert bulletins for New Zealand’s 11 active volcanoes and the volcanic field that sits beneath its most populous city, Auckland, through a service called GeoNet, which disseminates them to registered media and emergency-response agencies and to the public. The bulletins contain observations about volcanic activity and include the volcanic alert level — a measure that distils the observed phenomena into a number on a scale from 0 to 5.

One common public misconception is that volcanic alert level systems — used worldwide — provide a forecast, but that’s not the case in New Zealand. “It’s simply a measure of what’s going on with a volcano at the time,” says Tom Wilson, a volcanic-risk scientist at the University of Canterbury in Christchurch, New Zealand.



New Zealand Defence Force personnel perform recovery operations at White Island in the wake of the 2019 tragedy. Credit: New Zealand Defence Force via Getty

Forecasting challenge

Predicting when an eruption might occur “is one of the most difficult things to do in a volcanic system”, says volcanologist Roberto Sulpizio at the University of Bari in Italy, especially for ‘steam-blast’ eruptions of the type that occur on White Island.

New Zealand’s volcanic alert level system does not indicate future risk, Wilson explains. And it is currently unclear where the responsibility lies for assessing risks associated with visiting or working on White Island, he says. “Ultimately, this is going to get tested in court.”

In the weeks before the 2019 tragedy — the first fatal eruption at the site since 1914, when several sulfur miners were killed — the volcanic alert

bulletins contained information about seismic activity, mud and gas emissions, and changes to water levels in the crater lake.

Charges being brought against other parties explicitly mention failures to conduct risk assessments or communicate risk. NEMA is charged with failing to communicate risk to the public. Charges against tour companies and another defendant also allege failures to conduct risk assessments.

But Wilson says that requiring tour companies to conduct volcanic risk assessments is a tall order. “Assessing volcanic risk robustly is bloody difficult,” he says. “You’re asking these relatively small companies to undertake quite sophisticated risk assessments” that very few people globally are qualified to do.

A guilty verdict for GNS Science could leave other scientific agencies that provide information about natural hazards, such as earthquakes, floods and wildfires, questioning what information they can provide without incurring liability, and how to communicate it, especially if the advice is used to make decisions about how to manage risk.

Organizations that have previously provided information “might decide not to make it available publicly any more” for fear of prosecution, says Connell.

“Everybody’s waiting to see what will happen here,” says Wilson.

L’Aquila earthquake

The unusual case brings to mind another case, brought against scientists following the 2009 L’Aquila earthquake in central Italy, which killed 309 people. Six scientists and one government official were initially [convicted of manslaughter](#). The scientists’ convictions were overturned on [appeal](#), but the case led to a reckoning in the international geoscience community over how best to communicate risk to the public.

“It dominated the conversation for a few consecutive seismological society meetings,” says Charlotte Rowe, a seismologist at the Los Alamos National Laboratory in New Mexico.

Rowe says that worldwide, the geological community is working towards communicating volcanic risks more consistently. The International Civil Aviation Organization, based in Montreal, Canada, has a globally recognized aviation alert for volcanoes, but ground-based volcanic alert levels are not standardized. “It’s an evolving system,” she says.



[Italian seismologists cleared of manslaughter](#)

In Japan — unlike the United States, New Zealand or Italy — the national meteorological agency issues volcanic warnings that explicitly link the alert to specified danger levels. The warnings also include measures, such as evacuation, that residents and others must take.

In Italy, the upshot of the L’Aquila case was that the roles and responsibilities of scientists and the Department of Civil Protection in regards to managing and communicating risk are now clearly defined, says Sulpizio.

Tours of White Island have been suspended since the 2019 eruption, and there is debate about whether they should resume. “These are difficult, massively ethically and morally charged questions. But that’s what we need to be discussing,” says Wilson.

NEMA formally pleaded not guilty in court on 3 June, followed on 26 August by all the other co-defendants. The next hearing is scheduled for the

Whakatane District Court, near White Island, on 21 October.

Nature **598**, 243-244 (2021)

doi: <https://doi.org/10.1038/d41586-021-02658-5>

References

1. 1.

Kilgour, G. *et al.* *Earth Planets Space* **71**, 36 (2019).

This article was downloaded by **calibre** from <https://www.nature.com/articles/d41586-021-02658-5>

| [Section menu](#) | [Main menu](#) |

- NEWS
- 06 October 2021

Head of Wellcome-funded Malawi health project investigated for bullying

The programme's director has resumed his post after being investigated — but some staff are not happy with the way the case was handled.

- [Linda Nordling](#) ⁹

The director of a pioneering Malawi–UK research partnership, who stepped aside from his post after being investigated for bullying, returned to the role last week on 1 October, *Nature* has learnt.

Respiratory-diseases specialist Stephen Gordon is the director of the Malawi–Liverpool–Wellcome Trust Clinical Research Programme (MLW). This is a partnership between the University of Malawi College of Medicine in Blantyre, its main funder Wellcome, based in London, and the Liverpool School of Tropical Medicine (LSTM), UK. Wellcome provided £25 million (US\$34 million) for the institute from 2018 to 2023.

When it was founded 26 years ago, the MLW was a pioneering example of research collaboration between institutions in low- and high-income countries. But in recent years, [some researchers have questioned](#) the value of these partnerships for low and middle-income countries.

The institute has conducted research into infectious diseases, including tuberculosis, HIV and, most recently, Malawi's COVID-19 response.

Gordon stepped aside from his post in April and was temporarily prevented from applying for Wellcome funding. This followed an investigation into bullying complaints from three research staff, the findings of which have not been released. LSTM, which employs Gordon and oversaw both the investigation and the disciplinary process, declined to provide details on the process or outcomes.

But according to interviews and evidence seen by *Nature*, the findings of the investigation confirmed several of the complaints — including excessive fault-finding and public shaming. Gordon declined *Nature*'s request to be interviewed for this article about the investigation and a review of MLW's institutional culture, which began in September.

MLW's handling of the accusations against Gordon has angered and upset several staff — a number of whom are now nervous about his return.

A spokesperson for LSTM confirmed that there had been a “robust investigation and disciplinary hearing” in response to grievances brought against Gordon by members of the programme’s staff. The investigation was carried out by an independent investigator with support from an external consultant.

LSTM also said that during his time away from his post as director, Gordon would remain at MLW as a senior scientist and continue his research. It added that there would be a “culture review” that “aims to ensure that all within the MLW community feel respected and can thrive”.

A Wellcome spokesperson said they were aware of the complaints and that LSTM had kept the funder "fully informed as required by our bullying and harassment policy". The spokesperson added: "We have now received a report from LSTM that demonstrates progress has been made and we have agreed the director may resume his position."

Wellcome's anti-bullying policy, updated in February this year, says the institution may withhold funding from grantees who bully or harass others. The policy says grantees who engage in such behaviour can be banned from applying for future grants, and that levies can be sanctioned for institutions that fail to disclose details of such misconduct.

Programme's divisions

One complaint about the investigation is that the academic board of the Malawi College of Medicine, which is the responsible institution for MLW under the law in Malawi, was not notified at the time of the allegations and the subsequent investigation and disciplinary hearing.

“We should have been made aware of these issues and deliberated on and been part of the solution,” says Adamson Muula, professor of epidemiology and board-member at the Malawi College of Medicine — the college was recently renamed the Kamuzu University of Health Sciences. “I think our relationship should be damaged now, and it will take time to heal,” he told *Nature*. A number of people that *Nature* spoke to echoed Muula’s concerns.

In addition, *Nature* understands that Gordon’s return is of concern to some of the staff members who contributed evidence in his investigation. *Nature* has seen e-mails addressed to some of these witnesses from Gordon directly, which several people that *Nature* spoke to on condition of anonymity, claim is evidence of a breach of confidentiality.

In one of the e-mails, which was sent to more than 20 recipients, Gordon apologizes for the pain and hurt caused and says he takes full responsibility. He also writes: “I am writing collectively so that witnesses might know who each other are, and communicate if needed.” He urges those with “private concerns” to e-mail him about them directly.

Muula says these e-mails raised concerns among witnesses about the disciplinary investigation, and the decisions made as a result. “The whole situation is a text-book treatise of how not to do an investigation,” he says.

A Wellcome spokesperson said the Trust is satisfied that whistleblowers had been sufficiently protected. They added: “We will review the conclusions of the forthcoming independent cultural review led by MLW based on feedback from staff and will take any further action necessary following it.”

The Gordon case comes after a staff workshop at the MLW in Malawi last year identified several weaknesses in the way the MLW programme is run. In a written report from the workshop, attendees describe an institution with high turnover, overworked staff and insufficient support. It quotes a “great divide” between European and African staff members.

The workshop heard that Malawian staff earn less than their international counterparts, and that the two groups are employed on different terms and conditions, with international staff having more pay and benefits, and different disciplinary processes.

The workshop report, which summarizes attendees' views, also says that the MLW programme is perceived by its stakeholders in Malawi as a “foreign institution”, and that it has not done well to shake off this image, “largely because it is still dominated by senior expatriate personnel”. The report says this legacy threatens the programme’s sustainability, undermining its reputation and relationships in Malawi and elsewhere.

One scientist not employed by MLW but who works with the programme told *Nature* that any attempt to review MLW’s institutional culture without rebalancing the uneven power relations between its international leadership and funders on the one hand, and its African staff on the other would fail. “These are the systems that the victims want dismantled,” the scientist said.

LSTM told *Nature* it was committed to “providing a safe, dignified, and inclusive working environment where every member of the community is valued and treated with respect, to ensure staff, students and partners can work towards institutional goals with shared values”.

Nature **598**, 245 (2021)

doi: <https://doi.org/10.1038/d41586-021-02662-9>

This article was downloaded by **calibre** from <https://www.nature.com/articles/d41586-021-02662-9>

- NEWS
- 04 October 2021

Medicine Nobel goes to scientists who discovered biology of senses

David Julius and Ardem Patapoutian share the award for identifying receptors that allow the body's cells to sense temperature and touch.

- [Heidi Ledford](#) &
- [Ewen Callaway](#)



Ardem Patapoutian (L) and David Julius (R), recipients of the 2021 medicine Nobel prize. Credit: Scripps Research/Noah Berger

Two researchers who discovered the molecular basis for our ability to sense temperature and touch have won this year's Nobel Prize in Physiology or Medicine.

Physiologist David Julius at the University of California, San Francisco (UCSF), used capsaicin — the compound that gives chilli peppers their gustatory kick — to track down a protein called TRPV1 that responds to painful heat. Molecular neurobiologist Ardem Patapoutian at Scripps Research in La Jolla, California, identified receptors in skin and other organs that respond to mechanical forces, such as those generated by touch and pressure.

In addition to explaining the basic biology of senses, the findings have potential medical applications: to combat chronic pain, researchers are looking for compounds that target some of the proteins Julius and Patapoutian discovered.

The prize was announced at just after 2.30 a.m. California time, and the Nobel prize committee struggled to reach both winners, said Thomas Perlmann, the committee's secretary-general. But with "the help of one father and one sister-in-law", the committee was able to track down the winners and speak quickly with them before the announcement. "They were incredibly happy," Perlmann told reporters. "And as far as I could tell, they were very surprised."

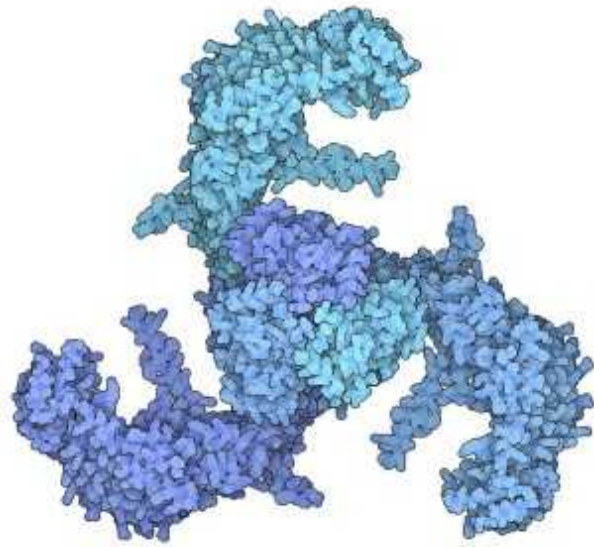
Making sense of senses

Julius's and Patapoutian's discoveries provided crucial links between external stimuli — such as temperature or touch — and the electrical signals that drive nervous-system responses.

Capsaicin, for example, was known to trigger pain responses, but it was unclear how. In the 1990s, Julius and his colleagues searched through genes that are switched on in response to pain, heat and touch to find one that would react to capsaicin. Their search led them to a gene that codes for TRPV1, a protein which forms a channel embedded in cell membranes that, when activated, allows ions to pass through¹.

Patapoutian and his collaborators, meanwhile, were looking for molecules that became activated by mechanical forces. The team identified cells that emitted an electrical signal when prodded, and then hunted for genes that

might control this response. This led to the discovery of two more ion channels, named Piezo1 and Piezo2, which are activated by pressure².



The quest to discover how the body's cells sense touch

Julius and Patapoutian also independently used menthol — a compound that creates a cooling sensation — to study how cells respond to cold. This led to the discovery of another ion channel, called TRPM8, that is activated by cold³.

“Both David and Ardem have really changed our understanding of sensory biology. I think it’s a fantastic decision to have awarded this,” says Michael Caterina, a neuroscientist at the Johns Hopkins University School of Medicine in Baltimore, Maryland, who was part of the team that identified the capsaicin-sensing TRPV1 channel in Julius’s laboratory. “It was thrilling.”

The team quickly determined that the chilli-heat sensing protein had a wider role in conveying painful sensations from heat. The identification of TRPV1 and other related pain-sensing proteins has helped researchers to understand the molecular basis for pain — and seek out new treatments. “We knew it had a chance of being medically important if it could explain some aspects of pain,” says Catarina.

“There are a lot of medical problems involving pain and [these] receptors will, for sure, be targets for drug development in the future,” medicine Nobel committee chair Nils-Göran Larsson said at the announcement ceremony.

The work carried out by Julius and Patapoutian stands out, says Caterina, because after identifying molecules responsible for sensing heat and touch, they led structural studies to better understand how the molecules work.

Julius contributed to a revolution in structural biology, brought about by cryo-electron microscopy — a technique [recognized with a chemistry Nobel in 2017](#) — when he teamed up with UCSF biophysicist Yifan Cheng to produce an extraordinarily detailed structure for the TRPV1 ion channel⁴. “That broke open the dam for understanding the details of the structure of membrane proteins,” says Caterina. “It’s not an accident that David was involved, in that I think that he just really has a knack for identifying really exciting questions, and coming up with ways of solving problems that others haven’t.”

“It’s a well-deserved award for Ardem and David, and very exciting to me,” says Bailong Xiao, a biochemist at Tsinghua University in Beijing and a former postdoctoral researcher in Patapoutian’s lab. Patapoutian’s discovery of Piezo1 and Piezo2 was especially significant, Xiao says, because the molecules had little in common with other known ion channels, opening up fresh avenues of research for labs worldwide.

The same advances in cryo-electron microscopy that helped Julius and Cheng map TRPV1 also provided key insights into how the Piezo channels work, notes Xiao, whose lab determined the structures of Piezo1 and Piezo2 using the technique. “Without a structure, it would have taken 20 to 30 years to understand how it works.”

Nature **598**, 246 (2021)

doi: <https://doi.org/10.1038/d41586-021-01283-6>

Additional reporting by Tosin Thompson.

References

1. 1.

Caterina, M. *et al.* *Nature* **389**, 816–824 (1997).

2. 2.

Coste, B. *et al.* *Science* **330**, 55–60 (2010).

3. 3.

McKemy, D. D., Neuhausser, W. M. & Julius, D. *Nature* **416**, 52–58 (2002).

4. 4.

Liao, M., Cao, E., Julius, D. & Cheng, Y. *Nature* **504**, 107–112 (2013).

This article was downloaded by **calibre** from <https://www.nature.com/articles/d41586-021-01283-6>

| [Section menu](#) | [Main menu](#) |

- NEWS
- 05 October 2021

Climate modellers and theorist of complex systems share physics Nobel

Syukuro Manabe, Klaus Hasselmann and Giorgio Parisi split the award for their work on complex systems — including modelling Earth's climate and global warming.

- [Davide Castelvecchi](#) &
- [Nisha Gaid](#)



2021 Physics Nobel laureates Klaus Hasselmann, Giorgio Parisi and Syukuro Manabe.Credit: J J Guillen/EPA/Shutterstock; Tania/Contrasto/Eyevine; Markus Marcetic, the Royal Swedish Academy of Sciences

Three researchers have won the 2021 Nobel Prize in Physics for their work on describing complex physical systems — including foundational research that created a pioneering mathematical model of Earth’s climate and predicted that increasing levels of carbon dioxide in Earth’s atmosphere would raise global temperatures.

Syukuro Manabe and Klaus Hasselmann share half of the 10-million-Swedish-kronor (US\$1.15-million) prize for this modelling. Theoretical physicist Giorgio Parisi at the Sapienza University of Rome receives the other half for his contributions to the theory of complex systems. His work has affected many areas, from neuroscience to how granular materials pack, the Nobel committee said in its announcement on 5 October.

“These are two different prizes, but there is the common theme that has to do with this order, these fluctuations together that can give rise to something that we can understand and predict,” said Thors Hans Hansson, chair of the physics Nobel committee. “We can predict what is happening with the climate in the future if we know how to code the chaotic weather.”

Climate models

Manabe, now at Princeton University in New Jersey, showed in the 1960s how increased levels of carbon dioxide in Earth’s atmosphere lead to increased temperatures at the surface, and developed early mathematical models of the planet’s climate. Around a decade later, Hasselmann, at the Max Planck Institute for Meteorology in Hamburg, Germany, built on this work to create a model linking weather and climate.

“Manabe showed us how and why increasing CO₂ leads to global warming. Hasselmann showed that it is happening,” says climate scientist Bjorn Stevens, also at the Max Planck Institute for Meteorology. He adds that the institute is “thrilled” that the pair have been awarded the “first Nobel prize for the science underpinning our understanding of climate change”.



Early climate models successfully predicted global warming

Jürgen Kurths at the Potsdam Institute for Climate Impact Research in Germany says that a “genius contribution” of Hasselmann’s was the 1970s introduction of the first ‘conceptual model’ for Earth’s climate¹ — a simple set of equations that captures global phenomena with just a few variables. This approach has given insights complementary to those from global circulation models, which are brute-force, geographically detailed calculations. “Usually you need a computer to simulate [conceptual models], but it’s much faster and easier,” Kurths says.

At the age of 89, Hasselmann continues to actively follow the field, and encourages researchers to try unconventional approaches, Kurths adds.

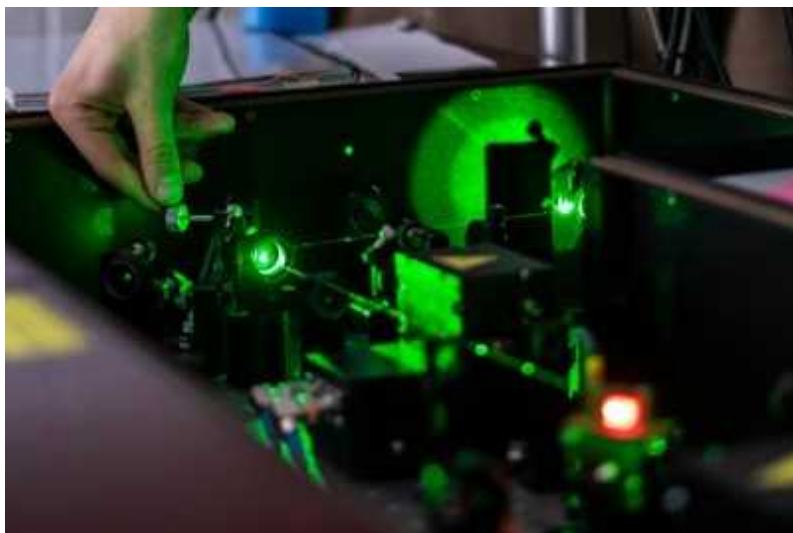
Gabriele Hegerl, a climate modeller at the University of Edinburgh, UK, who worked with Hasselmann as a postdoctoral researcher, says he was a “fantastic” mentor and supervisor, who was “full of ideas and enthusiasm”.

“I am really pleased that Suki and Klaus were chosen together, as they both contributed hugely in different ways and are two giants of climate science,” she adds. “I still use Suki’s old figures from the early papers on absorption and physics of the atmosphere in my classes, and his work is fundamental to understanding climate and, with it, climate change.”

Manabe was “gobsmacked” when he heard he had won the prize, said John Wettlaufer, an Earth and planetary scientist at Yale University in New Haven, Connecticut, and a member of the physics Nobel committee. “He said, ‘But I’m just a climatologist.’”

Hidden order

Parisi started his career in particle physics, but his research has since touched many other subfields. In the late 1970s, he switched his attention to the theory of complex systems, where he discovered a hidden and counter-intuitive type of order in the interactions of many objects². In some systems — such as magnetic materials, for example — atoms tend to align parallel to their neighbours, but complex systems are less predictable. Still, Parisi discovered that they satisfy a kind of symmetry that is noticeable only when comparing how the individual atoms arrange over different scales, says physicist Federico Ricci-Tersenghi at Sapienza.



[Giorgio Parisi: Optical system solves computational riddle](#)

“He opened up a way to see and interpret complex phenomena that until then had been missed,” says Ricci-Tersenghi, who is a former student and long-time collaborator of Parisi’s. The theory turned out to be useful even for systems that at first sight seem to be completely random, such as the structure of glass, he adds.

Parisi's research looks at underlying disorder and fluctuations and predicts emerging behaviour, said Wettlaufer. The link between his work and that of Manabe and Hasselmann is that fluctuations are key for predictability, he said. "We're recognizing that emerging phenomena sometimes require you to look at all the individual complicated physical mechanisms and knit them together to make a prediction."

Kurths is pleased that Parisi — and with him the study of complex systems, which is crucial to understanding the climate — has received recognition from the Nobel committee.

Parisi fosters a "happy environment" in his research group, Ricci-Tersenghi says, and has always encouraged his mentees to follow their curiosity and intellectual interests.

Reacting to news of his Nobel win, Parisi told reporters during the announcement: "I was very happy and I was not really expecting it." He continued: "But I knew I had some chance — so I kept the telephone near me."

The award comes before a pivotal climate meeting — the 26th United Nations Climate Change Conference, due to take place in Glasgow, UK, in November. "It's very urgent that we take a very strong decision and move at a very strong pace," said Parisi, of the climate negotiations. "For the future generations, we have to act now in a very fast way."

Asked if the Nobel committee was sending a message to world leaders with the award, Göran Hansson, secretary-general of the Royal Swedish Academy of Sciences in Stockholm, which awards the prize, said: "What we are saying is that the modelling climate is solidly based in physical theory and solid physics." He added: "Global warming is resting on solid science. That is the message."

Nature **598**, 246-247 (2021)

doi: <https://doi.org/10.1038/d41586-021-02703-3>

Additional reporting by Quirin Schiermeier, Tosin Thompson and Emma Stoye.

References

1. 1.

Hasselmann, K. *Tellus* **28**, 473–485 (1976).

2. 2.

Parisi, G. *J. Phys. A. Math. Gen.* **13**, 1101 (1980).

This article was downloaded by **calibre** from <https://www.nature.com/articles/d41586-021-02703-3>

| [Section menu](#) | [Main menu](#) |

- NEWS
- 06 October 2021

‘Elegant’ catalysts that tell left from right scoop chemistry Nobel

Benjamin List and David MacMillan share the award for developing cheap, environmentally friendly organic catalysts.

- [Davide Castelvecchi](#) &
- [Emma Stoye](#)



David MacMillan (left) and Benjamin List share the 2021 Nobel Prize in Chemistry for the development of asymmetric organocatalysis. Credit: Princeton University, Sameer A. Khan/Fotobuddy; David Ausserhofer/Max Planck Society/UPI/Shutterstock

Two researchers who developed techniques to speed up and control chemical reactions have won the 2021 Nobel Prize in Chemistry.

Benjamin List and David MacMillan separately developed a new type of catalysis in the 1990s. The technique — called asymmetric organocatalysis — is widely used today for the production of drugs and other chemicals. Crucially, the catalysts that the pair developed can distinguish left from right, synthesizing molecules that are different from their mirror image.

The pair developed “a truly elegant tool for making molecules — simpler than one could ever imagine”, said chemistry Nobel committee member Pernilla Wittung-Stafshede at the prize announcement. “Until the year 2000, we only knew about two forms of catalysts. But then everything changed. Benjamin List and David MacMillan independently reported that you can use small organic molecules to do the same job as big enzymes and metal catalysts in reactions that are precise, cheap, fast and environmentally friendly.”

“I absolutely didn’t expect this huge surprise — you really made my day today,” List told reporters at a press conference after the announcement. “When I [first] did this experiment, I didn’t know what would happen and I thought maybe it’s a stupid idea, or somebody has tried it already. When I saw it worked, I did feel that this could be something big.”

Alternative catalysts

Catalysts, substances that accelerate reactions without being used up, are fundamental tools for chemists. List, who is based at the Max Planck Institute for Coal Research in Mülheim an der Ruhr, Germany, and MacMillan, at Princeton University in New Jersey, developed catalysts that can drive asymmetric catalysis, in which a reaction produces more of the left-handed version of a molecule than the right-handed one, or vice versa.

In 2000, List showed that the amino acid proline could act as a catalyst in an aldol reaction, in which carbon atoms from two different molecules are bonded together, and that it could drive asymmetric catalysis¹. Around the

same time, MacMillan designed small organic molecules that can provide or accept electrons and therefore efficiently catalyse reactions².

Until their breakthroughs, the common wisdom among chemists was that a catalyst that synthesizes chiral molecules (those of a particular handedness) had to either be an enzyme or contain a transition metal such as iron. “It was a conceptual shift,” says chemist Cathleen Crudden at Queen’s University in Kingston, Canada. “For a long time, people thought that metals and enzymes were the only ones.”

The ‘organocatalysts’ developed by List, MacMillan and their collaborators had no metals. And unlike enzymes — typically large complexes made of proteins — they were small, organic molecules, “which, I think, is super exciting”, says chemist Claudia Felser at the Max Planck Institute for the Chemical Physics of Solids in Dresden, Germany. Organocatalysts are cheaper to produce, and more sustainable, than those containing metals, and interest in the field has exploded since their discovery.

Gift from nature

In a range of phenomena and at vastly different scales, nature often seems to prefer one handedness over another, Felser adds. This is reflected in the fact that matter predominates over antimatter in the Universe, and that life uses left-handed amino acids and right-handed sugars.

“Why in the world is biology single-handed? Why do we have this preference in nature? We don’t know,” List said. “This handedness is transferred in the catalytic reaction onto the substrates so that you get more of these handed molecules. It’s a great gift, I would say, that nature provides these molecules for us.”

“Chirality, for me, is the most interesting question in physics and chemistry and maybe even in biology,” Felser says, adding that today’s announcement could be “inspiring for the younger generations to look more for symmetry violations in nature”.

“In my opinion, the real revolution of what we have — of our discoveries — is only sort of surfacing now,” said List. He added that receiving the Nobel prize would allow him even greater freedom to pursue new ideas in his research. “I hope I live up to this recognition and continue discovering amazing things.”

Nature **598**, 247-248 (2021)

doi: <https://doi.org/10.1038/d41586-021-02704-2>

Additional reporting by Tosin Thompson.

References

1. 1.

List, B., Lerner, R. A. & Barbas, C. F. *J. Am. Chem. Soc.* **122**, 2395–2396 (2000).

2. 2.

Ahrendt, K. A., Borths, C. J. & MacMillan, D. W. C. *J. Am. Chem. Soc.* **122**, 4243–4244 (2000).

This article was downloaded by **calibre** from <https://www.nature.com/articles/d41586-021-02704-2>

| [Section menu](#) | [Main menu](#) |

- NEWS
- 07 October 2021

Why COVID vaccines didn't win a science Nobel this year

Nobel prize insiders and observers say timing and politics meant vaccine technology was an unlikely winner — but science's most prestigious prize shouldn't be far off.

- [Ewen Callaway](#)



The gap between a scientific discovery and recognition with a Nobel prize has grown over time.Credit: Jonas Ekstromer/TT News Agency/AFP/Getty

And the winner is ... not COVID-19 vaccines. Despite sky-high hopes that one of the Nobel committees would recognize research on vaccines that have been administered to billions of people and have saved countless lives, this year's science Nobels instead went to fundamental advances that had been tipped to win for years.

Some scientists expressed surprise and disappointment at the omission of COVID-19 vaccines, particularly those [developed using messenger RNA technology](#), which have launched a new class of vaccine.



['Elegant' catalysts that tell left from right scoop chemistry Nobel](#)

“The Nobel Prize folks could have done something with this year’s award to directly aid global health efforts during a 100-year pandemic. And they chose not to. This is utter dereliction. It is an indefensible decision that will cost lives,” Alexey Merz, a cell biologist at the University of Washington in Seattle, [wrote](#) on Twitter on 5 October, after research into the mechanisms behind senses won this year’s medicine or physiology prize.

But Nobel prize insiders and watchers say that timing, technical details and politics meant that a nod this year was a long shot. However, the impact of COVID-19 vaccines — and the underlying advances — indicate that it shouldn’t be long before researchers behind the work get a call from Stockholm.

“The development of mRNA vaccines is a wonderful success story that has had enormous positive consequences for humankind. And we’re all very grateful to the scientists,” says Göran Hansson, secretary-general of the Royal Swedish Academy of Sciences in Stockholm, which selects the prize winners. “This is a kind of discovery that will receive nominations. But we need to take time.”

Not mRNA’s year

The timing didn’t work in favour of a COVID-19 Nobel this year. Nominations for this year’s prizes had to be submitted by 1 February. This was more than two months after the first mRNA vaccines, and some others, [proved their mettle in clinical trials](#), but before their impact on the pandemic was fully clear, Hansson notes. “Follow-up is really still happening now.”



[Medicine Nobel goes to scientists who discovered biology of senses](#)

History was also against a nod for COVID-19 vaccines. The gap between a discovery and recognition with a scientific Nobel prize has grown over time, says Santo Fortunato, a physicist and director of the Indiana University Network Science Institute in Bloomington, and it now stands at an average of more than 30 years. The first experimental mRNA vaccines were tested in the mid-1990s, but key advances underlying the jabs developed by Moderna in Cambridge, Massachusetts, and by Pfizer in New York City and BioNTech in Mainz, Germany, didn’t come until the 2000s. And one could argue that the technology’s impact wasn’t apparent until this year.

But Fortunato says that major discoveries do tend to be recognized much more quickly. One potential parallel for mRNA vaccines is the detection of gravitational waves. The existence of gravitational waves was predicted by Albert Einstein in 1915, but it took a century for researchers to develop the tools to detect them directly. Researchers announced their discovery in February 2016, and scientists behind the observations and theoretical work won the 2017 physics prize. For COVID-19 vaccines, “I’m not surprised it didn’t happen this year. I have no doubt it will be awarded really shortly,” Fortunato says.

When it comes to COVID-19, Brian Uzzi, a computational scientist at Northwestern University in Evanston, Illinois, who studies scientific prizes, expects the Nobel committees to look more broadly than the development of vaccines. “Nobel prizes are more likely to go to scientists who teach people how to fish, rather than give them a fish,” he says. “They like to give prizes to people who do fundamental research that can go on and solve lots of different problems, not just one problem.” The committee could be waiting to gauge the impacts of mRNA vaccine technology on other infections — such as those caused by other coronaviruses, Uzzi speculates.



[Climate modellers and theorist of complex systems share physics Nobel](#)

Nobel harbingers

COVID-19 vaccines have already started hoovering up major scientific prizes: last month, [one of the US\\$3-million Breakthrough prizes](#) went to two scientists who developed modifications that silenced unwanted immune responses and were key to the Moderna and Pfizer–BioNTech vaccines. The

same researchers also won one of the Lasker Foundation's annual awards (considered by some to be predictors of Nobel prizes). The Nobel committees tend to be interested in rewarding research that has stood the test of time, rather than the latest advances, so Uzzi expects there will be more awards for COVID-19 vaccines before Stockholm comes knocking.

If the vaccines are awarded a Nobel prize, the committee will need to make some difficult decisions about whom to recognize and for what, say scientists. "I'm not surprised they held their fire," says David Naylor, a physician-scientist at the University of Toronto, Canada. He expects the committee to look past the academic and corporate teams that developed the vaccines, and instead focus on more foundational work, such as that underlying mRNA vaccines. But even there, it's not clear-cut who the recipients ought to be.

"I think the mRNA vaccines are obvious candidates," agrees Arturo Casadevall, a microbiologist at John Hopkins Bloomberg School of Public Health in Baltimore, Maryland, who notes that the vaccines' development has deep roots in several disciplines. "I can imagine the committee taking its time to sort out which contributions to recognize since many fields contributed to their deployment."

Working all this out takes time, Hansson says. "We want to give credit to the right people. And for the right discovery," he says. "So stay tuned."

Nature **598**, 248 (2021)

doi: <https://doi.org/10.1038/d41586-021-02754-6>

This article was downloaded by **calibre** from <https://www.nature.com/articles/d41586-021-02754-6>

- NEWS
- 01 October 2021

NASA won't rename James Webb telescope — and astronomers are angry

The agency found no evidence that the flagship observatory's namesake was involved in anti-LGBT+ activities, but some say that Webb bears responsibility.

- [Alexandra Witze](#)



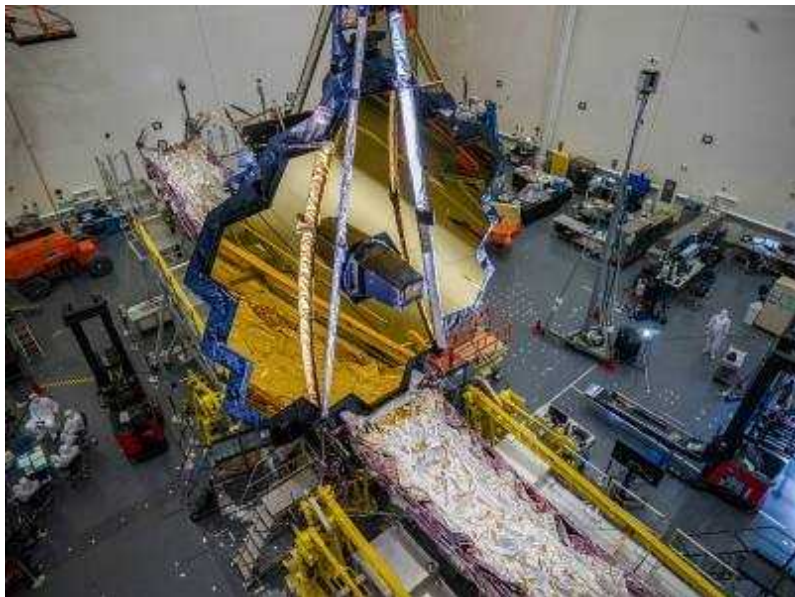
NASA's James Webb Space Telescope being prepared for shipment to its launch site. Credit: Chris Gunn/NASA

NASA has decided not to rename its soon-to-be-launched flagship observatory, the James Webb Space Telescope (JWST), [after investigating whether its namesake](#), former NASA administrator James Webb, was involved in persecuting gay and lesbian people in the 1950s and 1960s. The agency says it found no evidence to support the allegations.

The decision and the lack of transparency with which it was announced — NASA released no report about the scope of the investigation — has angered

a number of astronomers.

“I’m disappointed,” says Johanna Teske, an astronomer at the Carnegie Institution for Science in Washington DC. “Without knowing what factors were considered, it’s hard for me to respect the decision to keep the current name.”



[NASA investigates renaming James Webb telescope after anti-LGBT+ claims](#)

Since May, more than 1,200 people, including scientists who are slated to use the telescope after its planned December launch, have signed a petition calling for the JWST to be renamed. Webb held multiple leadership positions in the US government during a period in which gay and lesbian federal employees were systematically fired because of their sexual orientation. For instance, he was NASA administrator when an agency employee was fired in 1963 on suspicion of being gay.

In response to the concerns, NASA began an internal study of historical documents that might shed light on Webb’s behaviour towards gay and lesbian people. On 27 September, current agency administrator Bill Nelson released a one-sentence statement to some media outlets, including *Nature*, saying: “We have found no evidence at this time that warrants changing the name of the James Webb Space Telescope.” NASA’s acting chief historian,

Brian Odom, who led the inquiry, told *Nature* on 30 September that he considers the investigation closed.

‘Gut punch’

A NASA official had said in June that the agency would be transparent with the scientific community in its decision, but there is no final written report that could be released. Odom says that “under the circumstances of COVID, the investigation was as thorough as possible and very objective”. He says it consisted of several archivists going through NASA’s internal records, interviewing other historians who had studied Webb, and hiring an external historian to explore aspects such as Webb’s career at other government agencies. Several relevant repositories, such as the National Archives in Washington DC and the Harry S. Truman Presidential Library & Museum in Independence, Missouri, have been closed for long periods because of the COVID-19 pandemic; Odom’s team was not able to study materials from them that were not already digitized.



[Coronavirus pandemic threatens launch of world's most-expensive telescope](#)

Odom says he met Nelson several times to present the material that the investigators were able to gather. “The administrator’s participation in this

was very thoughtful and very objective,” he says. Nelson made the decision to keep the name of the telescope.

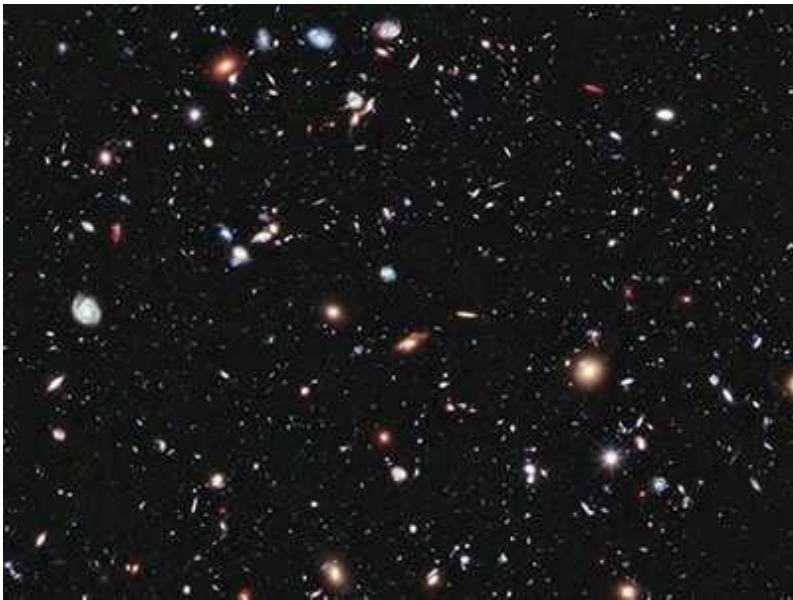
But some think NASA’s decision is the wrong one. Webb, they say, was head of the agency during a period of discrimination, and bears responsibility. “The gut punch is in the outright refusal to hear the voices of queer astronomers,” says Brian Nord, an astrophysicist at the Fermi National Accelerator Laboratory in Batavia, Illinois. “This is a refusal to confront history. If we can’t have that, how are we going to shed light on the oppression that people are facing?”

Nord is one of four astronomers who led the petition for the telescope to be renamed. The other three are Lucianne Walkowicz at the Adler Planetarium in Chicago, Illinois; Chanda Prescod-Weinstein at the University of New Hampshire in Durham; and Sarah Tuttle at the University of Washington in Seattle. In an e-mail to *Nature* about NASA’s decision, they wrote: “For all the institution’s talk of equity and diversity, they don’t seem to be particularly concerned with public accountability about sensitive issues that have impacted a historically marginalized group.”

Naming a telescope

At the heart of the controversy is what responsibility government officials bear for discriminatory actions and policies at agencies they headed. Webb ran NASA between 1961 and 1968, during the height of the exploration programmes that eventually sent astronauts to walk on the Moon. Critics point out that Webb was therefore in charge in 1963, when Clifford Norton, a suspected gay employee, was fired.

Odom says he looked closely at the Norton case for evidence of whether Webb was involved in directing the firing. “It just didn’t turn up,” he says.



US astronomers plot wish list for the next decade

But the broader context is important for assessing Webb's legacy, critics say. Webb worked in the US government system — including holding the influential position of undersecretary of state from 1949 to 1952, during Truman's administration — when firing gay people was seen as acceptable and even encouraged. Rolf Danner, an astronomer at the Jet Propulsion Laboratory in Pasadena, California, who is chair of the American Astronomical Society's committee on sexual orientation and gender minorities in astronomy, says Webb was probably an effective manager in that framework. "I just don't think that makes him the right choice for NASA's premier science project more than 60 years later."

As successor to the Hubble Space Telescope, the JWST will study cosmic phenomena including star formation, galaxy evolution and exoplanets. International partners in the mission include the European and Canadian space agencies. It was named in 2002 by former NASA administrator Sean O'Keefe, who wanted to highlight Webb's accomplishments in government. Webb "had the ability to bring together those from multiple disciplines and collectively work together to achieve something larger than themselves", says O'Keefe, who is now at Syracuse University in New York. He says that NASA would not be the same today had Webb not been administrator, and that the agency's investigation reinforces the conclusion that he and others had reached: that "indeed, this is a person of character".

Yet some say that Webb's accomplishments don't justify naming the telescope after him, given the context in which he worked. "Webb did his job, for better or worse, and will be remembered in history," says Peter Gao, a planetary scientist at the Carnegie Institution. "It's not necessary to further celebrate him given what happened under his tenure."

Astronomers who disagree with NASA's decision are now considering the future. For many, boycotting the JWST is not an option, because of its transformational capabilities. Some are talking about ways to acknowledge the controversy while still working with JWST data, perhaps by putting information about Webb's associations with anti-LGBT+ actions in the acknowledgments of papers. Others might call the telescope something else in their dealings with it. For instance, Prescod-Weinstein tweeted on 30 September: "I am personally thrilled about the Just Wonderful Space Telescope (JWST)."

Nature **598**, 249 (2021)

doi: <https://doi.org/10.1038/d41586-021-02678-1>

This article was downloaded by **calibre** from <https://www.nature.com/articles/d41586-021-02678-1>

- NEWS FEATURE
- 13 October 2021

‘I hope you die’: how the COVID pandemic unleashed attacks on scientists

Dozens of researchers tell *Nature* they have received death threats, or threats of physical or sexual violence.

- [Bianca Nogrady](#) ⁰



Public-health researcher Tara Kirk Sell (centre) experienced online and e-mail attacks after talking about COVID-19 in the media. Credit: US House of

Representatives' Committee on Science, Space, and Technology

Infectious-diseases physician Krutika Kuppalli had been in her new job for barely a week in September 2020, when someone phoned her at home and threatened to kill her.

Kuppalli, who had just moved from California to the Medical University of South Carolina in Charleston, had been dealing with online abuse for months after she'd given high-profile media interviews on COVID-19, and had recently testified to a US congressional committee on how to hold safe elections during the pandemic. But the phone call was a scary escalation. "It made me very anxious, nervous and upset," says Kuppalli, who now works at the World Health Organization (WHO) in Geneva, Switzerland.

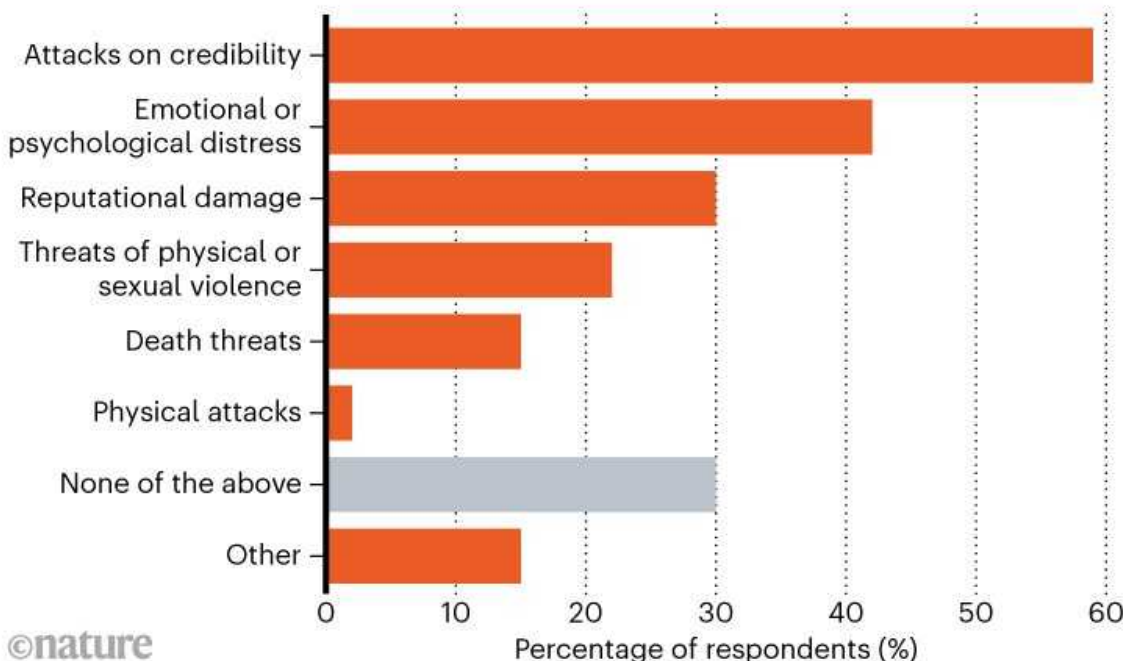
She called the police, but didn't hear that they took any action. The threatening e-mails, calls and online comments continued. The police officer who visited Kuppalli after a second death-threat call suggested she should get herself a gun.

Kuppalli's experience during the pandemic is not uncommon. A survey by *Nature* of more than 300 scientists who have given media interviews about COVID-19 — many of whom had also commented about the pandemic on social media — has found wide experience of harassment or abuse; 15% said they had received death threats (see 'Negative impacts').

NEGATIVE IMPACTS

In a *Nature* survey of scientists who have commented about COVID-19, 15% of 321 respondents said they had received death threats.

Question: Have you experienced any of the following negative impacts after speaking about COVID-19 to the media, or posting on social media? (You may select multiple options.)



Source: *Nature* analysis

Some high-profile examples of harassment have been well documented. Anthony Fauci, head of the US National Institute of Allergy and Infectious Diseases, was assigned personal security guards after he and his family received death threats; UK chief medical adviser Chris Whitty was grabbed and shoved in the street; and German virologist Christian Drosten received a parcel with a vial of liquid labelled 'positive' and a note telling him to drink it. In one extraordinary case, Belgian virologist Marc Van Ranst and his family were placed in a safe house when a military sniper went on the run after leaving a note outlining his intentions to target virologists.

These examples are extreme. But in *Nature*'s survey, more than two-thirds of researchers reported negative experiences as a result of their media appearances or their social media comments, and 22% had received threats

of physical or sexual violence. Some scientists said that their employer had received complaints about them, or that their home address had been revealed online. Six scientists said they were physically attacked (see Supplementary information for survey data tables).

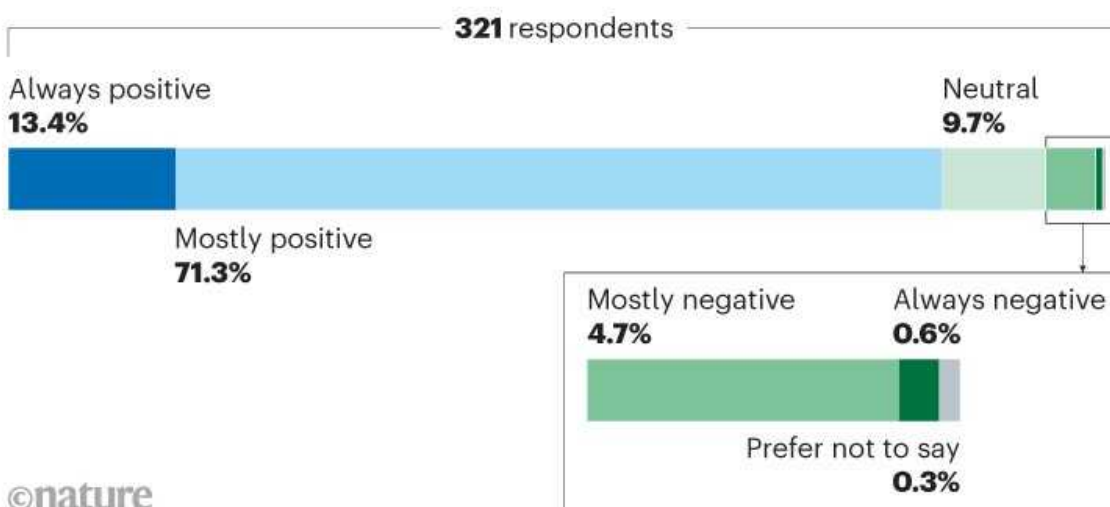
Coordinated social-media campaigns and threatening e-mails or phone calls to scientists are not new: topics such as climate change, vaccination and the effects of gun violence have drawn similar attacks in the past. But even scientists who had a high profile before COVID-19 told *Nature* that the abuse was a new and unwelcome phenomenon tied to the pandemic. Many wanted the extent of the problem discussed more openly. “I believe national governments, funding agencies and scientific societies have not done enough to publicly defend scientists,” one researcher wrote in their survey response.

Some researchers say that they have learnt to cope with the harassment, accepting it as an unpleasant but expected side effect of getting information to the public. And 85% of survey respondents said that their experiences of engaging with the media were always or mostly positive, even if they were harassed afterwards (see ‘Media experiences’). “I think scientists need training for how to engage with the media and also about what to expect from trolls — it’s just a part of digital communication,” one wrote.

MEDIA EXPERIENCES

In *Nature*'s survey, scientists mostly reported positive experiences with the media during COVID-19.

Question: How would you rate your experiences with the media during the pandemic?



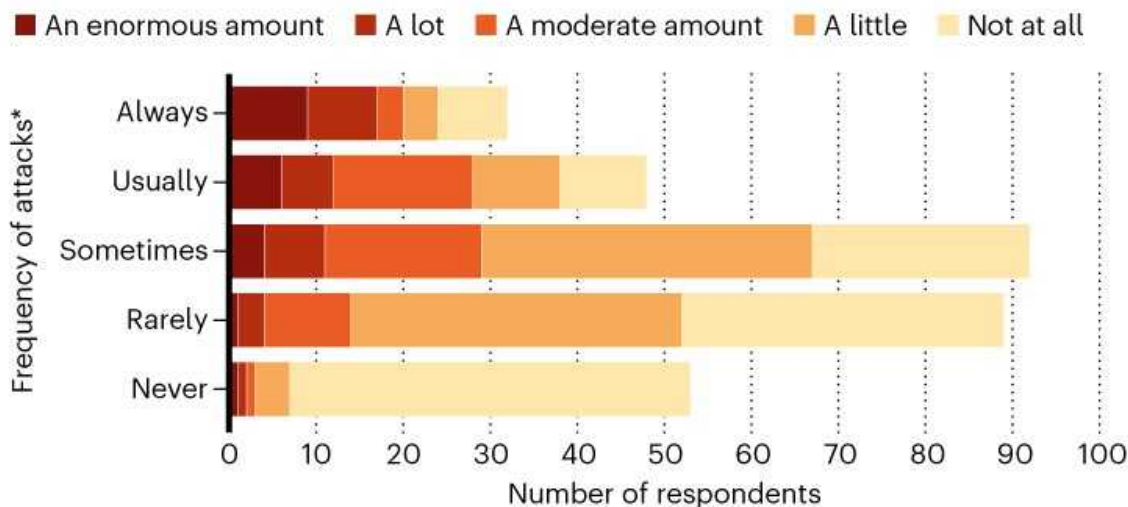
Source: *Nature* analysis

But *Nature*'s survey suggests that even though researchers try to shrug off abuse, it might already have had a chilling effect on scientific communication. Those scientists who reported higher frequencies of trolling or personal attacks were also most likely to say that their experiences had greatly affected their willingness to speak to the media in the future (see 'Chilling effect?'').

CHILLING EFFECT?

In *Nature*'s survey, scientists who reported the highest frequency of trolling or personal attacks* were also most likely to say that their experiences had greatly affected their readiness to give future media interviews.

Question: How much have your experiences with trolls and personal attacks affected your willingness to speak to the media in the future?



*Respondents who answered the question: Have you experienced trolling or personal attacks after speaking about COVID-19 in the media?

©nature

Source: *Nature* analysis

That is concerning during a global pandemic which has been accompanied by a battery of disinformation and misinformation, says Fiona Fox, chief executive of the UK Science Media Centre (SMC) in London — an organization that collates scientific comment and organizes press briefings for journalists. “It’s a great loss if a scientist who was engaging with the media, sharing their expertise, is taken out of a public debate at a time when we’ve never needed them so badly,” she says.

Tracking harassment

In June, the Australian SMC in Adelaide asked researchers on its COVID-19 media lists about their experiences. The centre had been alerted to online bullying and hate campaigns directed at scientists, and wanted to know whether it was a broader problem, says Lyndal Byford, the centre’s director of news and partnerships.

Byford shared the results with *Nature*. Fifty researchers answered the SMC's informal survey. Nearly one-third reported experiencing emotional or psychological distress after talking about COVID-19; 6 people (12%) reported receiving death threats, and 6 said they had received threats of physical or sexual violence. "I think any organization involved in helping scientists communicate would find that quite disturbing," Byford says.

To get a broader sense of the scale of harassment, *Nature* adapted the Australian SMC's survey, and asked science media centres in the United Kingdom, Canada, Taiwan, New Zealand and Germany to send it to scientists on their COVID-19 media lists. *Nature* also e-mailed researchers in the United States and Brazil who had been prominently quoted in the media.



"I had to be with bodyguards with guns" — attacks on scientists during the pandemic

The results are not a random sample of researchers who have given media interviews on COVID-19, because they represent only the experiences of the 321 scientists who chose to respond (predominantly in the United Kingdom, Germany and the United States). But the numbers reveal that researchers in many countries are facing abuse related to the pandemic, and the proportions reported were higher than in the Australian survey. More than one-quarter of respondents to the *Nature* survey said they always or usually received

comments from trolls or were personally attacked after speaking in the media about COVID-19. And more than 40% reported experiencing emotional or psychological distress after making media or social media comments.

Politicized science

To some extent, this harassment of scientists reflects their rising status as public figures. “The more prominent you are, the more abuse you’re going to get,” says historian Heidi Tworek at the University of British Columbia in Vancouver, Canada, who is studying online abuse of health communicators in the pandemic. Most US public-health departments have also received harassment directed at staff and officials, adds Beth Resnick, a public-health researcher at Johns Hopkins Bloomberg School of Public Health in Baltimore, Maryland, who has surveyed 580 departments in a study that is not yet published.

And such attacks might have little to do with the science itself and more to do with who’s talking. “If you’re a woman, or a person of colour from a marginalized group, that abuse will probably include abuse of your personal characteristics,” says Tworek. For instance, Canada’s chief public-health officer Theresa Tam is Asian Canadian, and abuse levelled against her included a layer of racism, Tworek says. Kuppalli, a female scientist of colour, says she also experienced this. Abusers told her she “needs to go back where she came from”.



Krutika Kuppalli.Credit: Kathryn Van Aernum

Both the Australian SMC and *Nature*'s survey, however, found no clear difference between the proportions of violent threats received by men and women. "We were surprised," Byford says. "We really felt women would be bearing more of a brunt in terms of the abuse that they got."

Some aspects of COVID-19 science have become so politicized that it is hard to mention them without attracting a storm of abuse. Epidemiologist Gideon Meyerowitz-Katz at the University of Wollongong in Australia, who has gained a following on Twitter for his detailed dissection of research papers, says that two major triggers are vaccines and the anti-parasite drug ivermectin — controversially promoted as a potential COVID-19 treatment without evidence it was effective. "Any time you write about vaccines — anyone in the vaccine world can tell you the same story — you get vague death threats, or even sometimes more specific death threats and endless hatred," he says. But he's found the passionate defence of ivermectin surprising. "I think I've received more death threats due to ivermectin, in

fact, than anything I've done before," he says. "It's anonymous people e-mailing me from weird accounts saying 'I hope you die' or 'if you were near me I would shoot you'."



Gideon Meyerowitz-Katz.Credit: Daniel Naidel

Andrew Hill, a pharmacologist at the University of Liverpool's Institute of Translational Medicine, received vitriolic abuse after he and his colleagues published a meta-analysis in July. It suggested ivermectin showed a benefit, but Hill and his co-authors then decided to retract and revise the analysis when one of the largest studies they included was withdrawn because of ethical concerns about its data (A. Hill et al. *Open Forum Inf. Dis.* 8, ofab394; 2021). After that, Hill was besieged with images of hanged people and coffins, with attackers saying he would be subject to 'Nuremberg trials', and that he and his children would 'burn in hell'. He has since closed his Twitter account.

In Brazil, microbiologist-turned-science-communicator Natalia Pasternak also noticed online attacks against her increasing when she spoke about the

unproven COVID-19 treatments being promoted by the Brazilian government, which include ivermectin, the antimalarial drug hydroxychloroquine and the antibiotic azithromycin. In 2018, Pasternak founded the *Instituto Questão de Ciência* — the Question of Science Institute — with the aim of promoting the use of scientific evidence in policymaking and discourse. When COVID-19 happened, Brazil “became the first country in the world to actually promote pseudoscience as a public policy, because we promote the use of unproven medications for COVID-19”, Pasternak says.

She appeared on major television stations and produced her own YouTube show, called the Plague Diary. Commenters criticized her voice and appearance, or argued that she wasn’t a real scientist. But, Pasternak says, the attacks rarely challenged what she was saying.

Some attackers have also tried to use the law to silence their targets. A group of supporters of Brazilian president Jair Bolsonaro tried to sue Pasternak for defaming him when she likened Bolsonaro to a plague on her YouTube show; the lawsuit was dismissed. And Van Ranst has been sued for defamation by a Dutch protester who opposes vaccination and public-health measures such as lockdowns in Belgium and the Netherlands.

Another topic that attracts high volumes of abuse is the question of SARS-CoV-2’s origins. Both the Australian and UK SMCs say they have struggled to find scientists who are willing to comment publicly on the issue for fear of getting attacked. Fox says the UK SMC has approached more than 20 scientists to participate in a briefing on this question, but all declined.

Virologist Danielle Anderson, now at the Peter Doherty Institute for Infection and Immunity at the University of Melbourne in Australia, received intense, coordinated online and e-mail abuse after writing a fact-checking critique in early 2020 of an article suggesting that SARS-CoV-2 might have leaked from China’s Wuhan Institute of Virology (WIV). At the time, she was based at the Duke–National University of Singapore Medical School in Singapore, but had collaborated with the WIV since the epidemic of severe acute respiratory syndrome (SARS) in 2002–04. “Eat a bat and die, bitch,” one e-mail read.



Virologist Danielle Anderson received abuse after critiquing an article on SARS-CoV-2's origins. Credit: James Bugg

Another researcher with a long-standing WIV collaboration, Peter Daszak, president of EcoHealth Alliance in New York City, has also received abuse. Daszak, who travelled to Wuhan in January [as part of a WHO-coordinated inquiry into the origins of SARS-CoV-2](#), says he's had a letter containing white powder sent to his home, had his address posted online and regularly receives death threats.

Harassment has cut both ways when it comes to SARS-CoV-2's origins. Alina Chan, a postdoctoral researcher at the Broad Institute of MIT and Harvard in Cambridge, Massachusetts, has received abuse for her work on the idea that the pandemic might have resulted from exposure to a virus at a laboratory or research site (sometimes also called the 'lab leak' hypothesis). Ultimately, she says, abusive attacks are counterproductive to the people making them. "They make the people on their own side appear unreasonable and dangerous," she says. "Second, they make it difficult to hold people

accountable because now everyone is distracted by having to address the excessively abusive attacks.”

Coping strategies

For researchers who receive online abuse, individual coping strategies include trying to ignore it; filtering and blocking e-mails and social-media trolls; or, for abuse on specific social-media platforms, deleting their accounts. But it’s not easy.

“It is very harrowing if every day, you open up your e-mails, your Twitter, you get the death threats, you get abuse every single day, undermining your work,” says Hill. It also takes time to go through messages and filter out abusers, he says. That led to his decision to delete his Twitter account.

Kuppalli has kept her social-media presence, but is more careful about how she uses it. Her rule is now not to respond to comments or posts when she is upset or angry or, in some cases, not to reply at all. “I just don’t read the comments and I don’t engage.”

Trish Greenhalgh, a health researcher and doctor at the University of Oxford, UK, said on Twitter in March that she had received “malicious abuse” from another academic and was blocking her abuser’s followers to make it harder for them to target her. She had previously tweeted that if anyone abused her PhD students, she would try to identify the abuser and report them to their employer.

But researchers shouldn’t try to cope on their own, says Tworek: there is much that institutions can do to assist scientists who are receiving abuse. Support staff can help a scientist to filter and block their e-mails and report abuse on social media, as well as remove researchers’ contact details from institutional websites and report incidents to police. “Unfortunately, it’s frequently a problem that people aren’t believed,” Tworek says — even when online threats escalate to offline ones.

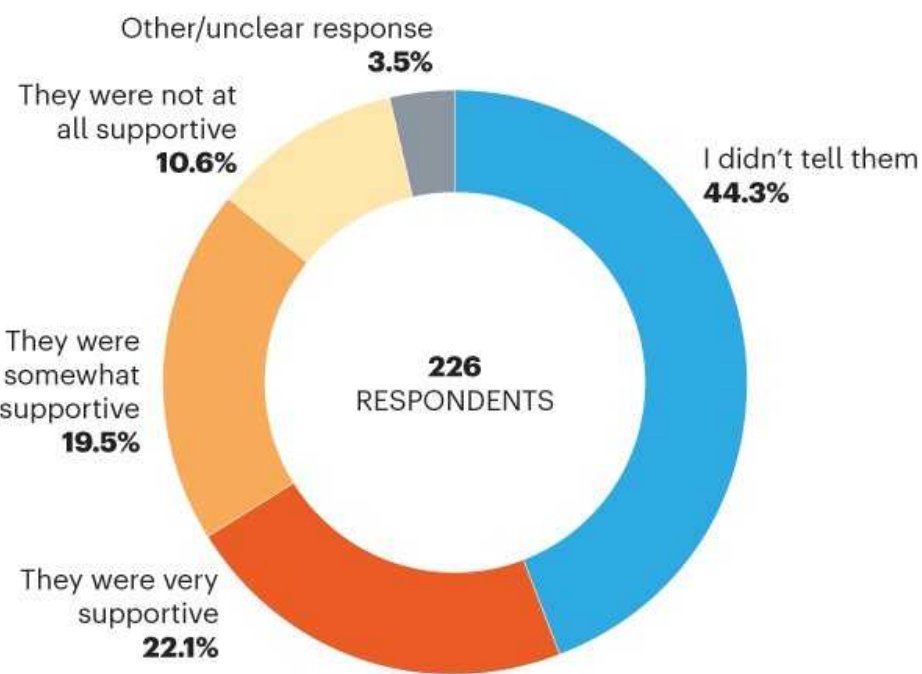
In *Nature*’s survey, 44% of scientists who said they’d been trolled or experienced personal attacks said they never told their employer. Of those who did, however, almost 80% found their employer ‘very’ or ‘somewhat’

supportive (see ‘Employer support’). When Kuppalli informed her university, for instance, she was given a car parking space much closer to her office, and the university’s IT department worked to block some of the regular abusive e-mailers.

EMPLOYER SUPPORT

Many scientists said they didn’t tell their employer about trolling or personal attacks, but those who did tended to find their employers supportive.

Question: How much support did your employer offer after you experienced trolling or personal attacks?*



*Question asked to 261 respondents who had said they received trolling comments or personal attacks. 35 respondents said this question did not apply to them or that they do not have an employer; the 226 remaining responses are shown in this chart.

©nature

Source: *Nature* analysis

Public-health researcher Tara Kirk Sell at the Johns Hopkins Center for Health Security in Baltimore has experienced online and e-mail attacks, particularly after appearing on a US conservative television network to talk about COVID-19. One e-mail suggested that Sell and her colleagues should be executed.

Sell, who'd experienced abuse as a former professional athlete, reported the e-mail to administrators, who handed it to campus security officers. They investigated, identified the sender, contacted them and warned them to stop. Sell didn't hear from them again. "I think that a lot of people don't realize that they should report their harassment to their institution," she says.

One Australian epidemiologist — who asked to remain anonymous because she didn't want more abuse — told *Nature* that she had to push her university for help after she received "vile, sexualising" e-mails in the wake of her media interviews on COVID-19. At first, her institution suggested it was her responsibility to deal with it. They only took action after she likened the online abuse to someone standing up in her lecture theatre and shouting the same words, which included a derogatory reference to her sexual anatomy. "You would march that person off the campus," she said. Eventually, her university removed her contact details from its website and put her in touch with a campus security officer.

In response to an increase in attacks on scientists and public-health officials, the Royal Society of Canada [set up a working group on 'protecting public advice'](#) in May. It is set to release a policy briefing before the end of the year. "Our fundamental concern is what do we do to make sure that expertise can still reach the public and it's not silenced by this kind of activity," says working-group chair Julia Wright, an English-literature scholar at Dalhousie University in Halifax, Canada, and president of the Academy of the Arts and Humanities at the Royal Society of Canada.

Wright says some universities have formal policies on how to handle attacks on staff, which range from ensuring that person has access to support from counselling and security services, to making public statements of support of their academics and of academic freedom. Those statements are often very helpful, Wright says, but they can also give oxygen to a harassment campaign that might otherwise have died down. "This is something that I think we're all still trying to figure out strategies for dealing with."

Social media

Much abuse happens on social media — raising the perpetual question of what responsibility social-media companies bear for what's said on their platforms. Among the scientists who responded to *Nature*'s survey, 63% used Twitter to comment on aspects of COVID-19, and around one-third of those said they were 'always' or 'usually' attacked on the platform.

Kuppalli reported abusive content to Twitter, but was told that it did not violate the platform's terms. Hill sent examples to Twitter of the abusive tweets he was receiving, featuring pictures of hanged corpses, and got the same response. A Twitter spokesperson said the company has clear rules about addressing threats of violence, abuse and harassment, and added that Twitter has introduced features to reduce abuse, including technology to detect abusive language, as well as settings that allow users to control who responds to their tweets and to hide some replies.



[COVID scientists in the public eye need protection from threats](#)

Wright, along with other researchers, says that social-media firms need to do more to combat abuse and misinformation that is spread through their networks. But the platforms are so big that the only way to deal with it is through automated algorithms, Wright says, which are easy to evade. And she worries about putting social-media companies in the position of censors.

Consequences of harassment

A positive aspect of the pandemic is the extraordinary amount of effort researchers have put into public communication about science during the crisis, says Fox. She recommends that researchers in the public eye be careful about stepping outside their own areas of expertise, and try to avoid making comments that might be perceived as political. But engaging with the media inevitably comes with the possibility of unwanted abuse that's almost impossible to stop, she adds.

Some scientists say they've learnt to temper their comments about COVID-19. Robert Booy, an infectious-diseases paediatrician at the University of Sydney says that he learnt lessons from hasty comments he made in one rushed telephone interview conducted at the side of the road. "I said, 'you can have a vaccine, or you can go to heaven early,'" he recalls. "I should not have been rushed, I should not have been glib and I should have been on home ground and calm," he says.

Whereas some scientists have put up with abuse, others have excluded themselves from commenting even on relatively uncontroversial topics. *Nature*'s survey found instances of scientists staying quiet: a few anonymous respondents wrote that they were hesitant to speak about some topics because they saw abuse being meted out to others. Anderson says her experience has changed how she communicates science, and she now declines most media interviews.

Tworek is concerned that seeing attacks and abuse levelled at senior scientists could discourage up-and-coming researchers. This applies especially to women, people of colour and individuals from minority groups. "It could be that you see anybody being abused, and you don't want to be subject to that yourself, but it may be particularly if you see somebody who is like you," she says.

Kuppalli appreciates the double-edged effect of her work being thrust into the limelight; she's been harassed, but has also had the opportunity to ensure science in the public arena is as accurate and as evidence-based as it can be. She's also aware that, as a woman of colour in a high-profile position, she

has unusual privilege and responsibility. “That’s also why I take it so seriously, because there’s all these stories and articles and things written about how women are not getting opportunities,” she says. “Every time I get that opportunity, I feel very grateful.”

Nature **598**, 250-253 (2021)

doi: <https://doi.org/10.1038/d41586-021-02741-x>

Additional reporting and survey work by Richard Van Noorden.

This article was downloaded by **calibre** from <https://www.nature.com/articles/d41586-021-02741-x>

| [Section menu](#) | [Main menu](#) |

Opinion

- **Make electric vehicles lighter to maximize climate and safety benefits** [12 October 2021]
Comment • Tax heavy cars and shrink batteries to consolidate the gains from electrifying transport.
- **Why no mention of overpopulation in talk of food systems?**
[12 October 2021]
Correspondence •
- **Recognize 727 UNESCO Biosphere Reserves for biodiversity COP15** [12 October 2021]
Correspondence •
- **Anthropocene event idea is empowering** [12 October 2021]
Correspondence •
- **Keep online option at conferences — it makes them more inclusive** [12 October 2021]
Correspondence •

- COMMENT
- 12 October 2021

Make electric vehicles lighter to maximize climate and safety benefits

Tax heavy cars and shrink batteries to consolidate the gains from electrifying transport.

- [Blake Shaffer](#) ⁰,
- [Maximilian Auffhammer](#) ¹ &
- [Constantine Samaras](#) ²



Rush hour in Times Square in New York City. Car-registration fees in New York are calculated according to the vehicle weight.Credit: Getty

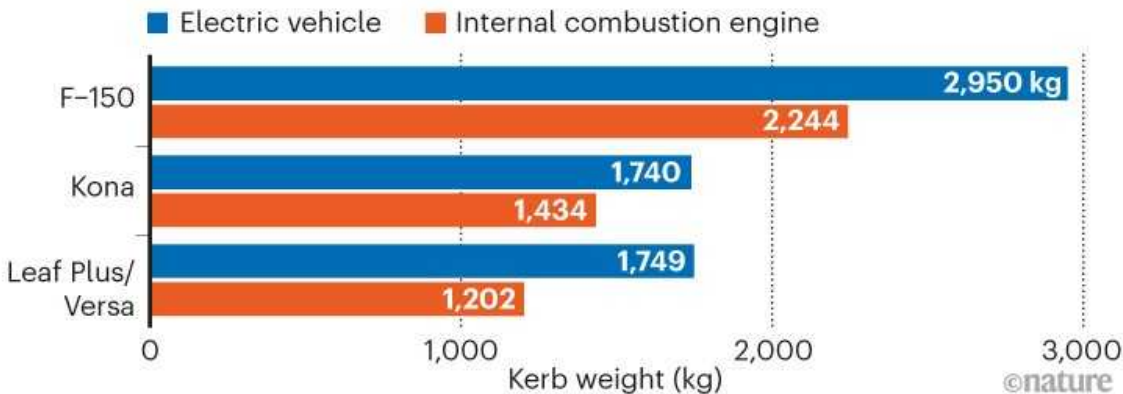
Electric vehicles are here, and they are essential for decarbonizing transport. The United Kingdom, California, the European Union, Canada and others plan to phase out the sale of fossil-fuelled vehicles as early as 2030 — Norway plans to do it sooner. Consumers are interested. In May, the Ford Motor Company unveiled an all-electric version of its best-selling pick-up truck, the F-150 Lightning. By August, so many customers had reserved one that Ford doubled its initial production target. On 27 September, the company announced that it will spend billions of dollars to build battery factories and an electric-truck plant in the United States. Other companies are expanding their production, too.

Major investments in electric vehicles are welcome news. The sector has come a long way, but many challenges lie ahead. One issue that has received too little attention, in our view, is the increasing weight of vehicles. Pick-up trucks and sport utility vehicles (SUVs) now account for 57% of US sales, compared with 30% in 1990. The mass of a new vehicle sold in the United States has also risen — cars, SUVs and pick-up trucks have gained 12% (173 kilograms), 7% (136 kg) and 32% (573 kg), respectively, since 1990. That's equivalent to hauling around a grand piano and pianist. Similar trends are seen elsewhere in the world.

Electrifying vehicles adds yet more weight. Combustible, energy-dense petroleum is replaced by bulky batteries. And the rest of the vehicle must get heavier to provide the necessary structural support¹. The electric F-150 weighs 700 kg more than its petrol-powered predecessor. Smaller electric cars are heavier than their petrol equivalents, too (see 'Heavier electric fleet').

HEAVIER ELECTRIC FLEET

Bulky batteries and their supports mean electric vehicles weigh more than petroleum predecessors.



Why does this matter? First and foremost is safety. The likelihood of passengers being killed in a collision with another vehicle increases by 12% for every 500-kg difference between vehicles². This added risk wouldn't apply if everyone drove cars of similar heft. But until they do, the number of casualties in crashes is likely to increase as heavy electric vehicles join lighter existing fleets. Pedestrians will also be at risk. If US residents who switched to SUVs over the past 20 years had stuck with smaller cars, more than 1,000 pedestrian deaths might have been averted, according to one study³.

Heavier vehicles also generate more particulate pollution from tyre wear. They require more materials and energy to build and propel them, adding to emissions and energy use.

How big a problem is this extra weight? A rough comparison between mortality costs and climate benefits shows that it is significant. Under the energy systems operating in most countries today, the cost of extra lives lost from a 700-kg increase in the weight of an electrified truck rivals the climate benefits of avoided greenhouse-gas emissions.

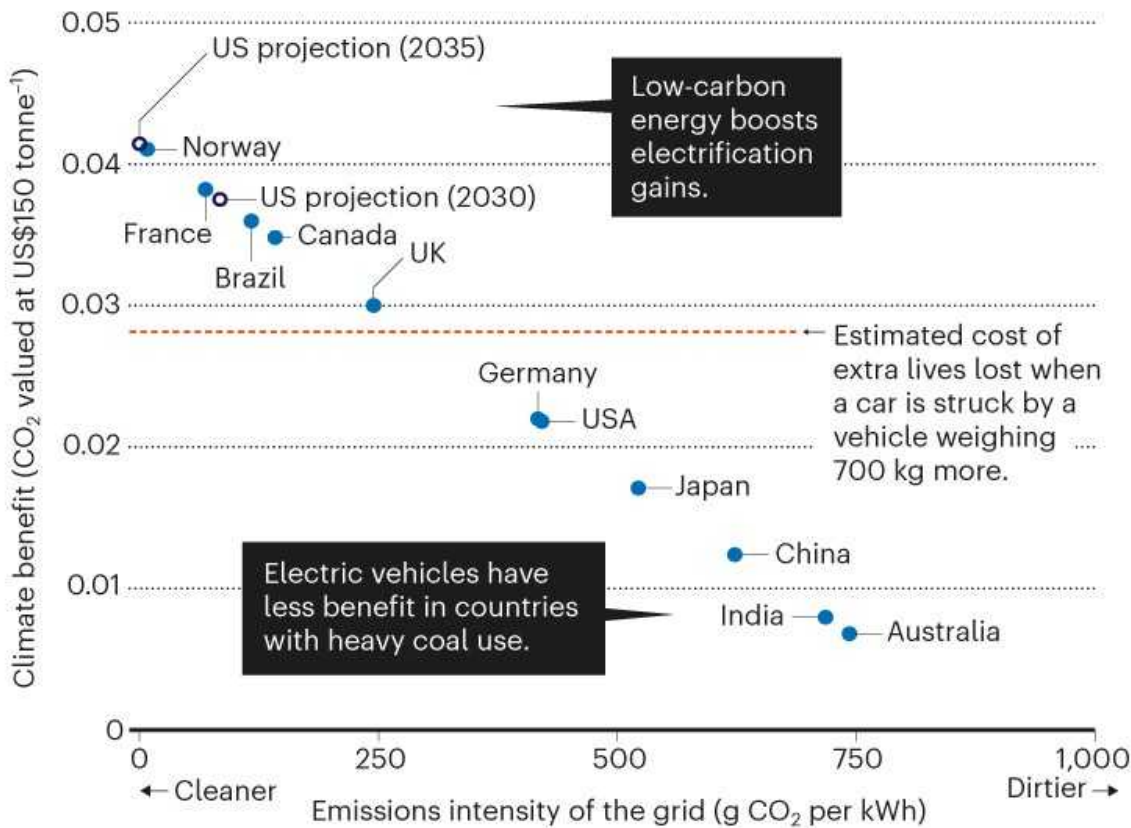
Two main factors are at play: the battery's weight and supports as well as the cleanliness of the electricity grids it is charged from. In calculating the cost of the extra weight, we used the US Department of Transport's value of US\$11.6 million per avoided fatality. The cost–benefit trade-off holds even if we assume that the social cost of emitting one tonne of carbon dioxide is

high, around \$150; lower values, such as \$50, reduce the estimates for climate benefits. Admittedly, it's an oversimplification. Realistic cost-benefit analyses for electric vehicles require the evaluation of many other factors. These include the costs from injuries in collisions, the health benefits from cleaner air and the life-cycle impacts of different car designs.

As time goes on, cleaner grids will strengthen the case for electric vehicles. Some countries with lots of clean electricity sources, such as Norway, are already at a point at which electrifying a truck has more climate benefits than safety costs. Others, including the United States, must keep on the path to net-zero electricity systems (see 'Cost-benefit calculus'). Yet without addressing the weight issue, the benefits for society of going electric will be smaller than they could be in the next decade. Here's what we think researchers, policymakers and manufacturers need to do to address the issue.

COST-BENEFIT CALCULUS

Much of the climate benefit of driving an electric vehicle instead of a petrol-fuelled one depends on what powers the grids that charge it, which varies by country. But a heavy battery increases the risk of crash deaths. In countries such as Germany and Australia, the cost of extra lives lost on the road can be as much as or more than the benefits to the climate. To make electric vehicles a win-win for both climate and safety requires lighter batteries, cleaner electricity and a wider look at other impacts.



See Supplementary information at go.nature.com/3jhk24q for assumptions and calculations used in these estimates.

©nature

Source: B. Shaffer *et al.*

Tax heavy cars

Basic economics tells us that activities that impose costs on others should be taxed. Setting registration charges on the basis of vehicle weight can discourage heavy vehicles and encourage light ones. Collecting weight-based charges also addresses another looming problem for governments — lost revenue from forgone petrol and diesel taxes as more electric vehicles hit the roads.

That's potentially a lot of money. In 2019, US federal, state and local governments collected more than \$112 billion in fuel taxes. Several states have already started levying fees on electric-vehicle owners, in the range of \$50–200 per year, to recoup some of that lost tax. It's fair, they argue, because fuel taxes cover part of the costs of road infrastructure, which electric-vehicle drivers use, too.

Varying such charges by weight would maintain revenue while incentivizing people to choose vehicles that are more energy efficient and impose fewer social costs⁴. It would also reduce other emissions from materials production and manufacturing.



[Running a car costs much more than people think — stalling the uptake of green travel](#)

A few places have such taxes. In Iowa, for example, the registration fee increases by \$0.40 for every 45 kg of vehicle weight. In New York state, the rate is \$1.50 per 45 kg for weights above 750 kg; above 1,600 kg, it rises to \$2.50. France will go even further next year, charging a whopping €10 (US\$11.60) for every kg that exceeds an 1,800 kg threshold. If that law didn't already exempt electric and hybrid vehicles, it would have added €12,000 to the price of an electric truck, such as the F-150.

Adding travel distance to the fee would also incentivize people to drive less. Oregon is piloting such a programme, giving owners the option to base their registration fees on the distance they drive in a year (at a rate of roughly 1.1 cents per kilometre) in lieu of fixed annual fees. Travel data can be collected by on-board devices; some insurance companies already offer policies that are based on total mileage and other driving habits.

Shrink batteries

Batteries now cost 90% less than they did ten years ago. And their energy density has more than tripled⁵ since lithium-ion batteries were introduced in 1991. Yet most of the gains in battery technology have gone to increase the distance an electric car can travel in a single charge, and to boost the car's power. Over the past decade, for example, Nissan has brought to market a long-range version of its flagship Leaf electrical vehicle, with triple the range (364 kilometres) and double the horsepower (214 hp). But its weight has grown, too, by 14%, to 1,749 kg.

Driving range is important for the widespread adoption of electric vehicles. Most consumers buy cars on the basis of reach because they worry about losing power or being unable to recharge on a long trip. Yet, most car journeys are short — to the shops or school. In the United States, for example, on average, drivers travel 56 kilometres per day, far short of the maximum range for electric vehicles.

Extending that reach by another 100 kilometres or so every few years will make electric vehicles more practical for people who need to travel long distances regularly, for work for example. But even now, it has diminishing returns for the average driver. Fast-charging infrastructure is being deployed more widely. Producing lightweight batteries will reap rewards immediately.



The heavy battery pack and associated support structures make the electric Hyundai Kona around 20% heavier than its petrol counterpart. Credit: Milan Jaros/Bloomberg/Getty

Ways to lighten batteries include using materials that are more energy-dense, and removing heavier components. For example, solid-state batteries that don't use liquid electrolytes and have the latest anode chemistries are more compact and could offer higher energy densities than is possible for lithium-ion cells. Lithium–silicon batteries can achieve higher energy densities if manufacturers use more silicon in anodes rather than graphite.

Improvements can also be digital — wireless battery management systems can shed up to 90% of the web of wires. Using fewer materials helps manufacturers to save money.



Electric cars and batteries: how will the world produce enough?

But cutting-edge technologies are expensive to incorporate, raising the costs of electric cars. Government support, from the laboratory to the factory to the consumer, is thus essential to spur innovation and development. Weight-based registration charges could supply some of that money. US subsidies for electric vehicles currently increase with the storage capacity of the battery. Basing electric-vehicle subsidies instead on energy storage per kg (kWh kg^{-1}) would incentivize advances in lighter batteries.

Further developments in battery technology are needed to reduce pollution from manufacturing and to consume less cobalt and other rare metals and minerals. Schemes for recycling and reusing battery and other materials need to be put in place⁶, before tens of millions of electric vehicles arrive on and then leave the roads.

Lighten frames

Tesla, Volvo, GM and other car makers are exploring using battery packaging to support part of the vehicle's chassis. On the horizon is making the vehicle frame itself the medium to store energy. Research and development is needed to improve conductivity, strength and how structural batteries handle crashes⁷.



Mapping emissions from cars and lorries

About one-third of a vehicle's mass is conventional steel, down from 44% in 1995. Vehicle structures can be made stronger and lighter by using advanced forms of steel, more aluminium and magnesium, and polymers reinforced with carbon fibre. Each material brings its own cost and technical challenges as well as emissions impacts from production and supply chains. Researchers need to assess these trade-offs to find safe, clean and affordable solutions.

Substituting aluminium for steel reduces vehicle weight and improves energy efficiency. But aluminium production can have nearly five times the embodied carbon emissions of steel⁸. Switching to recycled aluminium with a low-carbon grid can lower life-cycle emissions to below those of steel.

Reduce crashes

With heavier vehicles on the road, safety becomes even more important. Some vehicles already use cameras, radar and other sensors to avoid collisions by monitoring blind spots and driver alertness. These devices keep vehicles in lanes, adjust speeds, control headlights and apply the brakes if there's a threat of a crash. Deploying such technologies across the entire US

vehicle fleet could avoid thousands of fatalities, more than one million crashes and billions of dollars in social costs annually⁹.

Old ideas to improve street safety should still be encouraged — speed limits, traffic calming road designs and pedestrian-focused infrastructure. Paris, Brussels, Bilbao and other cities have limited speeds on most roads to 30 kilometres per hour.

Drive less

Reducing the distance driven can help in meeting climate targets as electric and, eventually, automated vehicles become widely available¹⁰. Policies should ensure that alternatives such as walking, biking and public transport are safer, more convenient, accessible, affordable and reliable.

Urban designers should consider the impacts of zoning and development on driving patterns to minimize average distances travelled and air-pollution impacts that disproportionately burden vulnerable communities. One legacy of the COVID-19 pandemic is a realization of how much work can be done remotely, with less commuting. Solving these challenges will save lives and protect the climate.

Ultimately, to manage climate change, the world needs to stop emitting greenhouse gases from vehicles and power plants. Electric vehicles powered from a clean grid are an essential step in the right direction. A focus on driving lighter, safer, cleaner and less can ensure a better future for everyone.

Nature **598**, 254–256 (2021)

doi: <https://doi.org/10.1038/d41586-021-02760-8>

References

1. 1.

Lewis, G. M. *et al.* *Environ. Sci. Technol.* **53**, 4063–4077 (2019).

2. 2.

Anderson, M. L. & Auffhammer, M. *Rev. Econ. Stud.* **81**, 535–571 (2014).

3. 3.

Tyndall, J. *Econ. Transp.* **26–27**, 100219 (2021).

4. 4.

Davis, L. W. & Sallee, J. M. *Environ. Energy Policy Econ.* **1**, 65–94 (2020).

5. 5.

Ziegler, M. S. & Trancik, J. E. *Energy Environ. Sci.* **14**, 1635–1651 (2021).

6. 6.

Baars, J., Domenech, T., Bleischwitz, R., Melin, H. E. & Heidrich, O. *Nature Sustain.* **4**, 71–79 (2021).

7. 7.

Kalnaus, S. *et al.* *J. Energy Storage* **40**, 102747 (2021).

8. 8.

Wolfram, P., Tu, Q., Heeren, N., Pauliuk, S. & Hertwich, E. G. *J. Ind. Ecol.* **25**, 494–510 (2020).

9. 9.

Khan, A., Harper, C. D., Hendrickson, C. T. & Samaras, C. *Accid. Anal. Prev.* **125**, 207–216 (2019).

10. 10.

Alarfaj, A. F., Griffin, W. M. & Samaras, C. *Environ. Res. Lett.* **15**, 0940c2 (2020).

This article was downloaded by **calibre** from <https://www.nature.com/articles/d41586-021-02760-8>

| [Section menu](#) | [Main menu](#) |

- CORRESPONDENCE
- 12 October 2021

Why no mention of overpopulation in talk of food systems?

- [Paul R. Ehrlich](#) 0

Overpopulation, one of the most important factors in the hunger nexus, is not mentioned by the Scientific Group for the UN Food Systems Summit 2021 ([J. von Braun et al. *Nature* 597, 28–30; 2021](#)).

Access options

Subscribe to Journal

Get full journal access for 1 year

\$199.00

only \$3.90 per issue

[Subscribe](#)

All prices are NET prices.

VAT will be added later in the checkout.

Tax calculation will be finalised during checkout.

Rent or Buy article

Get time limited or full article access on ReadCube.

from \$8.99

[Rent or Buy](#)

All prices are NET prices.

Additional access options:

- [Log in](#)
- [Learn about institutional subscriptions](#)

Nature **598**, 257 (2021)

doi: <https://doi.org/10.1038/d41586-021-02751-9>

This article was downloaded by **calibre** from <https://www.nature.com/articles/d41586-021-02751-9>

| [Section menu](#) | [Main menu](#) |

- CORRESPONDENCE
- 12 October 2021

Recognize 727 UNESCO Biosphere Reserves for biodiversity COP15

- [Alicia D. Barraclough](#)⁰,
- [Maureen G. Reed](#)¹,
- [Inger Elisabeth Måren](#)²,
- [Martin F. Price](#)³,
- [Andrés Moreira-Muñoz](#)⁴ &
- [Kaera Coetzer](#)⁵

The Biosphere Reserves set up by UNESCO, the United Nations scientific and cultural organization, safeguard biodiversity through a network of 727 sites in 131 countries. We argue that these reserves should be included alongside other effective area-based conservation measures (OECMs; [G. G. Gurney et al. *Nature* 595, 646–649; 2021](#)) in the Convention on Biological Diversity's agreement, due to be negotiated at the COP15 meeting in Kunming, China.

Access options

Subscribe to Journal

Get full journal access for 1 year

\$199.00

only \$3.90 per issue

[Subscribe](#)

All prices are NET prices.
VAT will be added later in the checkout.
Tax calculation will be finalised during checkout.

Rent or Buy article

Get time limited or full article access on ReadCube.

from \$8.99

[Rent or Buy](#)

All prices are NET prices.

Additional access options:

- [Log in](#)
- [Learn about institutional subscriptions](#)

Nature **598**, 257 (2021)

doi: <https://doi.org/10.1038/d41586-021-02750-w>

This article was downloaded by **calibre** from <https://www.nature.com/articles/d41586-021-02750-w>

| [Section menu](#) | [Main menu](#) |

- CORRESPONDENCE
- 12 October 2021

Anthropocene event idea is empowering

- [Jan Kunnas](#) [ORCID: http://orcid.org/0000-0002-9433-0865](http://orcid.org/0000-0002-9433-0865) 0

The proposal by Andrew Bauer and his colleagues to recognize the Anthropocene as a continuing geological event (see [Nature 597, 332; 2021](#)) could resolve some of the bitter quarrels the concept evokes. It removes the need to find a single spike, or marker, in the geological record to define the Anthropocene's start. Instead, it allows us to use the same concept — irrespective of whether it started 50,000–10,000 years ago with the extinction of the Ice Age megafauna, or with the origin of farming or any of the dozen or so suggested starting points between 1610 and 1964 ([S. L. Lewis and M. A. Maslin Nature 519, 171–180; 2015](#)).

Access options

Subscribe to Journal

Get full journal access for 1 year

\$199.00

only \$3.90 per issue

[Subscribe](#)

All prices are NET prices.

VAT will be added later in the checkout.

Tax calculation will be finalised during checkout.

Rent or Buy article

Get time limited or full article access on ReadCube.

from \$8.99

[Rent or Buy](#)

All prices are NET prices.

Additional access options:

- [Log in](#)
- [Learn about institutional subscriptions](#)

Nature **598**, 257 (2021)

doi: <https://doi.org/10.1038/d41586-021-02753-7>

This article was downloaded by **calibre** from <https://www.nature.com/articles/d41586-021-02753-7>

| [Section menu](#) | [Main menu](#) |

- CORRESPONDENCE
- 12 October 2021

Keep online option at conferences — it makes them more inclusive

- [Rocío Joo](#) 0

The COVID-19 pandemic has forced researchers to embrace online conferences (see [Nature 582, 135–136; 2020](#)), which remove some of the barriers that disproportionately affect marginalized groups. These include the cost of registration, transport and accommodation, the logistics of long-distance travel, and discriminatory visa applications ([H. J. Niner & S. N. Wassermann Front. Mar. Sci. 8, 638025; 2021](#); [Nature 569, 297–299; 2019](#)). Let's not revert to the old ways.

Access options

Subscribe to Journal

Get full journal access for 1 year

\$199.00

only \$3.90 per issue

[Subscribe](#)

All prices are NET prices.

VAT will be added later in the checkout.

Tax calculation will be finalised during checkout.

Rent or Buy article

Get time limited or full article access on ReadCube.

from \$8.99

[Rent or Buy](#)

All prices are NET prices.

Additional access options:

- [Log in](#)
- [Learn about institutional subscriptions](#)

Nature **598**, 257 (2021)

doi: <https://doi.org/10.1038/d41586-021-02752-8>

This article was downloaded by **calibre** from <https://www.nature.com/articles/d41586-021-02752-8>

| [Section menu](#) | [Main menu](#) |

Work

- **Beware survivorship bias in advice on science careers** [27

September 2021]

Career Column • For objective careers advice, talk to those who left science as well as those who stayed.

- **How Latin American researchers suffer in science** [23

September 2021]

Career Column • It's time to tackle the cumulative barriers and biases faced by scientists who aren't from wealthy countries.

- **Serving science and the Church as the Pope's astronomer**

[11 October 2021]

Where I Work • Around 100 active scientists have collaborated with the Vatican Observatory, says Brother Guy Consolmagno, its director.

- CAREER COLUMN
- 27 September 2021

Beware survivorship bias in advice on science careers

For objective careers advice, talk to those who left science as well as those who stayed.

- [Dave Hemprich-Bennett](#)⁰,
- [Dani Rabaiotti](#)¹ &
- [Emma Kennedy](#)²



If today's successful academics habitually work late in the laboratory, they're likely to advocate that the next generation does the same. Credit: Thomas Barwick/Getty

A major flaw in much scientific and academic career advice is survivorship bias. This is a common logical error, involving drawing conclusions based on those who have 'survived' a process — and are thus more visible than those who did not. In the case of science careers advice, the bias arises because those who manage to stick to their chosen career path are there to advise the next generation of researchers on how to stay in their field.

As two postdoctoral researchers in ecology (D.H.B., D.R.) and a lecturer in learning and teaching (E.K.), we have seen many examples of worthy but 'unsuccessful' colleagues who left their research field against their wishes. On the flipside, the positions we hold in our respective fields are, to some extent, the result of many chance events that we experienced.

Some of our success came from hard work, grit and good judgement. But much of it came from decisions, luck and circumstances that never make it into careers advice. For example, job opportunities for D.R. and her friends have come about through having drinks with senior scientists, and D.R. was invited to publish her first book *Does It Fart?* thanks to a completely unplanned Twitter hashtag. Chance or serendipitous experiences such as these are impossible to replicate, yet are key to many people's ability to stay in their chosen career.

Conversely, E.K. had to leave her original field, English literature, because she could not afford to stay in the insecure, low-paid teaching roles that were available. It is therefore important to know not only why some people 'succeeded', but also what pushed many more away. Assuming that all aspiring scientists and academics enjoy similar circumstances to those of their colleagues who have 'survived' can only damage the prospects of the next generation, and will lead to professions with much less diverse staff than could have been the case.



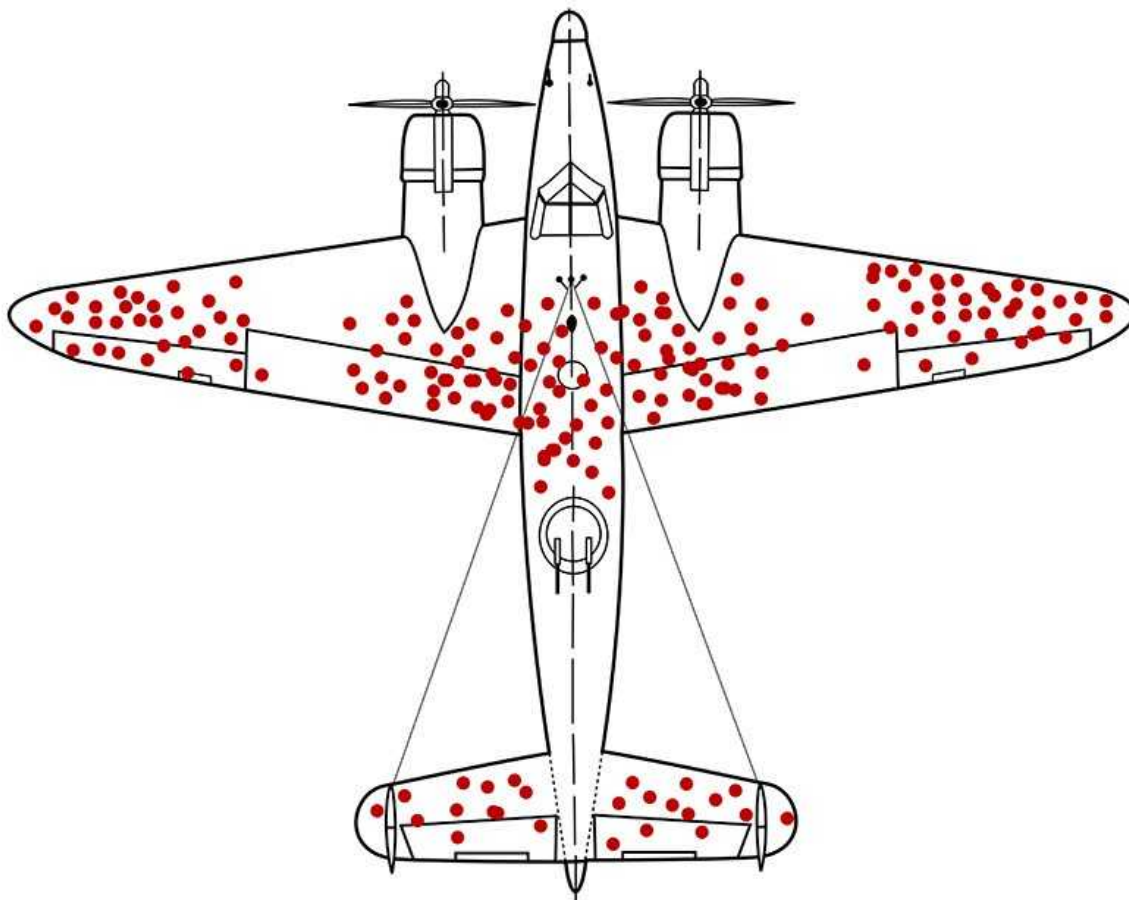
[Careers toolkit: An early career researcher's guide to the working world of science, from Nature Careers.](#)

Over the years, numerous senior researchers have assumed that we would be able to go without pay for an extended period during our research, even while living in one of the world's most expensive cities. Sometimes we've had to argue our case and explain why we couldn't afford to do so; sometimes we've simply had to find other jobs. Anyone who is able to work without pay is not only financially secure but is also unlikely to have other demands such as caring responsibilities — and those who think unpaid work is straightforward are likely to share these circumstances.

For these reasons, survivorship bias in career advice becomes self-perpetuating. Those who survived and thrived because of privilege assume that those hoping to follow in their footsteps are in similar financial and social situations; conversely, those who lack that privilege are less likely to make it to a position from which they can give less biased advice.

As the coronavirus pandemic has blurred the boundaries between 'work' and 'life', the issue of [balance has become even more prominent](#). The closest many senior researchers come to fostering work–life balance is in offering the common advice to 'take a break': perhaps between contracts, over holiday periods, or even by simply not working on weekends. Survivorship bias plays out here as well, because this advice assumes that recipients can

afford to take time off despite the pressure to publish or to keep one's head above water financially. D.R. took a six-month break between handing in her PhD and beginning her postdoc, but this was feasible only because of having savings, thanks to publishing that book about farts — a privileged position that most PhD students cannot easily replicate.



Survivorship bias: during the Second World War, the bullet holes on aircraft that returned marked out the areas that were not crucial to the planes' integrity. Credit: Martin Grandjean (vector), McGeddon (picture), Cameron Moll (concept) (CC BY-SA 4.0)

Although survivorship bias makes intuitive sense to most academics, its influence in careers advice is rarely considered. Studies that look at career outcomes of current scientists might even conclude that career setbacks are beneficial, without acknowledging that those setbacks lead many others to leave their field altogether¹. Some researchers will encounter barriers and

setbacks beyond anything we have experienced, for example active discrimination, [harassment](#) or severe financial distress, and leave their fields as a result. It is important to understand what the advice that our communities pass on is rooted in, and that none of us can be truly representative of all aspiring scientists. Every scientist has their own barriers to overcome, but let's beware of extrapolating that, because something was not an issue for us, it is therefore not seriously problematic for those around us.

During the pandemic and its aftermath, relying on conventional thinking and others' biased experience is more dangerous than ever, especially due to the documented ethnic-, class- and gender-based disparities of COVID-19 in our communities^{2,3,4}.

Those of us who are senior enough to be giving advice and setting expectations can enhance the quality and inclusivity of our working environments by asking our students and colleagues about the barriers they face, with a view to understanding the factors that might exclude people from career progression. Those around you might well have had to deal with hardships and circumstances that are different from yours: so when involved in mentoring conversations, make time to ask which ways forward would work for them, rather than just recommending your own path. The fact that you overcame a barrier does not preclude it unfairly excluding many others.

Seeking further mentorship and support from others whose background is similar to yours, and who have faced similar barriers in their career, can be particularly helpful in this regard. Frank but sensitive conversations around these issues might feel awkward, but in helping us better understand how to support one another, they could be key to reducing inequities in scientific careers.

Nature **598**, 373-374 (2021)

doi: <https://doi.org/10.1038/d41586-021-02634-z>

This is an article from the *Nature* Careers Community, a place for *Nature* readers to share their professional experiences and advice. [Guest posts are encouraged.](#)

References

1. 1.

Wang, Y., Jones, B. F. & Wang, D. *Nature Commun.* **10**, 4331 (2019).

2. 2.

Blundell, R., Dias, M. C., Joyce, R. & Xu, X. *Fiscal Stud.* **41**, 291–319 (2020).

3. 3.

Gemelas, J., Davison, J., Keltner, C. & Ing, S. *J. Racial Ethn. Health Disparities* <https://doi.org/10.1007/s40615-021-00963-3> (2021).

4. 4.

Malisch, J. L. *et al.* *Proc. Natl Acad. Sci. USA* **117**, 15378–15381 (2020).

This article was downloaded by **calibre** from <https://www.nature.com/articles/d41586-021-02634-z>

| [Section menu](#) | [Main menu](#) |

- CAREER COLUMN
- 23 September 2021

How Latin American researchers suffer in science

It's time to tackle the cumulative barriers and biases faced by scientists who aren't from wealthy countries.

- [Ana M. Valenzuela-Toro](#) ⁰ &
- [Mariana Viglino](#) ¹



Mariana Viglino uncovers a fossil of a toothed whale during fieldwork at Estancia La Redonda in Argentina. Credit: Nicolás Farroni

As female researchers from Latin American countries (one of us now works in the United States, the other in Argentina), we're used to career obstacles. These range from limited funding to language barriers and the 'tax', [in terms of time](#) and emotional energy, incurred when under-represented groups in science participate in diversity initiatives. These barriers knit together to create problems beyond the obvious.

The current focus on diversity, equity and inclusion in science is welcome, but efforts to combat biases can lack nuance. Researchers from under-represented communities often experience the intersection of sexism, racism, and colonialism. In other words, the career barriers we face have a cumulative effect.

Our academic journeys illustrate these obstacles. Many of these multidimensional and intersectional barriers are also encountered by other early-career researchers from Latin America, especially women and scientists who are LGBTQIA+, people of marginalized sexual orientations and gender identities.

Funding barriers

Latin American countries invest significantly less in science, technology, engineering and mathematics (STEM) than do high-income countries, so the continent's researchers have less access to grant opportunities and smaller budgets than they might elsewhere¹.

This has an impact on performance in the laboratory and in the field, affecting not only the scope of the research we can do, but also limiting our attendance at international conferences, which are important opportunities for networking and creating collaborations. For both of us, the first international meetings we attended, after securing funding from the conference, became a pivotal step in our academic journey, allowing us to meet people who became mentors and long-term collaborators.

In addition, we must deal with the invisible burden of the visa application. For researchers from countries without 'passport privileges', attending international conferences in the global north means coping with endless

paperwork that can be more time-consuming and emotionally overwhelming than overcoming the financial constraints.



[Collection: Careers toolkit](#)

Visa applications can be especially difficult considering that acceptance of an abstract for a paper or poster can be slow. And there is no guarantee that the application will be approved, or that a visa-holder will actually be granted entry when they arrive at their destination.

The two of us have had similar experiences with visa applications. We have been asked awkward questions, such as whether we have any intention of carrying out illicit activities, and been asked to disclose private information about our family members, personal health, social-media accounts and financial situation, ultimately to prove that we are not trying to emigrate from our own countries.

Unwritten rules

Even when you overcome these issues, the reduced exposure to meetings outside Latin America can result in feelings of unfamiliarity and discomfort when international networking and mentoring opportunities do materialize.

These events are full of hidden or unwritten norms, ranging from dress codes (what does ‘business casual’ even mean?) to how to navigate social events and pitch yourself and your work to colleagues or potential mentors. These difficulties are exacerbated by language differences, which can reduce international conferences to stressful rather than an enriching experiences. They create the feeling that we don’t belong, despite the expectation that Latin American researchers have to ‘perform’ at the same level as everyone else.



Ana Valenzuela-Toro examines a fossilized seal at the Smithsonian Institution’s National Museum of Natural History in Washington DC.Credit: Carolina S. Gutstein

Shifting to virtual conferences during the COVID-19 pandemic has alleviated some of these issues. More Latin American researchers, including ourselves, have been able to attend and present their work at international conferences, and even to organize them. In fact, we co-organized a round table on diversity, equity and inclusion in science as part of one meeting on marine tetrapods (four-legged vertebrates), earlier this year.

However, many international conferences are still expensive (the exchange rate from dollars or euros to Latin American currencies is often unfavourable). The combination of cost and all the obstacles mentioned earlier fuels the idea across the academic community that we, Latin American researchers, are passive spectators rather than active contributors in science.

Access barriers

Access to literature is usually taken for granted, but most Latin American academic and research institutions can't cover the exorbitant costs of open-access agreements with the largest academic publishers.

Journal paywalls exacerbate disparities between Latin American researchers and colleagues in the global north. Links between north and south are already weak because of the funding issues highlighted above, and become weaker still when researchers are not able to read each other's papers.

Often, the only way to access published literature is with the help of collaborators at foreign academic institutions, or through social media platforms. For example, we are both members of Facebook groups devoted to sharing papers among Latin American colleagues. Without this international social-media community, we might not have been able to complete our research.

Language barriers

Latin American researchers and others from non-English-speaking countries are expected to [publish in English](#), the standard language of science (even in this piece). Yet, it is usually not taught in many schools in our region. Many Latin American researchers cannot access English courses until they have paid positions, which, in turn, are difficult to get without a solid record of scientific publications in English, creating a chicken-and-egg situation.

During the peer-review process, editors and reviewers often make negative comments about language and request revisions by people whose first language is English. But these requests usually don't consider the

corrections already made by co-authors from English-speaking countries before submission. This compounds the impression that manuscripts with lead authors from non-English-speaking countries are somehow less professional. Moreover, paying for professional translation and editorial services imposes an extra financial burden on Latin American authors².

In our countries, these services can cost the equivalent of one month's rent, making them inaccessible. Therefore, free online translation tools, combined with the generous help of non-academic friends as well as colleagues, and countless hours of self-proofreading and editing are key to overcoming this barrier and publishing our work in English.

Gender biases

Studies show that conscious and unconscious gender biases are still prevalent in peer review³. Manuscripts authored by women are more frequently rejected and less likely to be published compared with those by men⁴, perpetuating a cycle of invisibility: one in which papers get rejected, resulting in fewer future scientific opportunities, and thus in fewer papers and perhaps more rejections in the long term.

Even when female researchers overcome these obstacles and finally publish in peer-reviewed journals, an additional barrier exists: the lack of peer recognition, including lower citation rates.

More citations means being considered more often to present work at conferences and having increased opportunities for networking, cementing the path to academic success. Contributions by women are seen as less relevant than those by male scientists, resulting in fewer citations overall, reinforcing the ‘invisibilization’ of female researchers.



The business of science

When we think about the most cited or published authors, frequent guest speakers at conferences, or most internationally distinguished scientists in our own research fields, how many Latin American female researchers come to our mind? (Un)surprisingly, nearly none. If we ask you to do the same exercise, you will probably achieve the same result. This is not explained by a lack of Latin American female researchers, but rather, by the consequences of the intersecting barriers discussed above.

Steps you can take

There is no straightforward solution to these intersectional issues; however, we suggest some starting points:

- First and foremost, listen with empathy whenever Latin American researchers — particularly women and other under-served scientists — talk about the challenges they experience.
- Use whatever platform you might have to amplify and recognize their research.
- Journals editors and reviewers should be more aware of accessibility barriers, and that English might not be an author's first language.

- When writing a paper, reflect on how representative the papers you cite are. Include articles led by colleagues from different gender identities and geographical areas, thus increasing the diversity of research cited and discussed. A similar strategy can be applied when suggesting reviewers.
- Make conferences more accessible. Promote virtual attendance and funding sources for people who have difficulties traveling, and foster equitable networking opportunities between people from diverse backgrounds and academic stages.
- Ultimately, don't forget that many Latin American researchers are starting their academic careers from an unequal position; the only way to level the playing field is if we all, as a community, take actions to dismantle these barriers.

Nature **598**, 374-375 (2021)

doi: <https://doi.org/10.1038/d41586-021-02601-8>

This is an article from the Nature Careers Community, a place for *Nature* readers to share their professional experiences and advice. [Guest posts are encouraged.](#)

References

1. 1.

Ciocca, D. R. & Delgado, G. *Cell Stress Chaperones* **22**, 847–852 (2017).

2. 2.

Ramírez-Castañeda, V. *PLoS ONE* **15**, e0238372 (2020).

3. 3.

Helmer, M., Schottdorf, M., Neef, A. & Battaglia, D. *eLife* **6**, e21718 (2017).

4. 4.

Fox, C. W. & Paine, C. E. T. *Ecol. Evol.* 9, 3599–3619 (2019).

This article was downloaded by **calibre** from <https://www.nature.com/articles/d41586-021-02601-8>

| [Section menu](#) | [Main menu](#) |

- WHERE I WORK
- 11 October 2021

Serving science and the Church as the Pope's astronomer

Around 100 active scientists have collaborated with the Vatican Observatory, says Brother Guy Consolmagno, its director.

- [Chris Woolston](#) ⁰



Brother Guy Consolmagno is director of the Vatican Observatory and president of the Vatican Observatory Foundation. Credit: Francesco Pistilli for *Nature*

I spend a lot of time looking upwards. Here, at Castel Gandolfo, outside Rome, I'm peering through the Vatican Observatory's historic 1891 telescope. It can't compete with Rome's light pollution and is mainly for fun and tourism — we're hoping to welcome visitors again soon — but it still offers views of the Moon, the rings of Saturn and other highlights of the night sky.

The observatory also does serious science, however, and we own and operate a 1.8-metre research telescope on Mount Graham in Arizona, which I've used to study minor planets beyond Neptune. I've had research roles at Harvard College Observatory and the Massachusetts Institute of Technology, in Cambridge, and Lafayette College in Easton, Pennsylvania, and spent 20 years studying the properties of meteorites collected from around the world. Many of those samples are now at the Vatican.

I usually wear a T-shirt at work. But if I'm posing for a photo, I'll always wear my Jesuit brother's attire. I took vows in 1991. The Vatican Observatory shows the world that the Church cares about science. A man of the cloth next to a piece of scientific equipment helps to tell that story.

All 12 staff astronomers at the observatory are either priests or Jesuit brothers like myself, but you don't have to be Catholic to use our facilities. We collaborate with other astronomers and graduate students from varied backgrounds. Around 100 active scientists have had their names on papers connected to the Vatican Observatory.

I was appointed in 2015 by Pope Francis, a true honour for a Catholic kid from Detroit, Michigan. Francis himself doesn't take an intense interest in astronomy, but Pope Pius XII was a real enthusiast. John XXIII had little knowledge of stars and planets, but he'd bring up a bottle of wine and hang out with the astronomers, and watch them work.

Looking at the moons of Jupiter or a distant galaxy gives me joy. To me, that joy is the presence of God.

Nature **598**, 378 (2021)

doi: <https://doi.org/10.1038/d41586-021-02761-7>

This article was downloaded by **calibre** from <https://www.nature.com/articles/d41586-021-02761-7>

Research

- **[Venus might never have been habitable](#)** [13 October 2021]
News & Views • A sophisticated climate model suggests that liquid-water oceans never formed on Venus, and that some planets outside the Solar System that were thought to be habitable might not be.
- **[A spotlight on seafood for global human nutrition](#)** [15 September 2021]
News & Views • What role might seafood have in boosting human health in diets of the future? A modelling study that assesses how a rise in seafood intake by 2030 might affect human populations worldwide offers a way to begin to answer this.
- **[The cost of changes in energy use in a warming world](#)** [13 October 2021]
News & Views • How will global energy usage change as Earth warms? Modelling now suggests that there will be a modest net decrease in energy consumption — but probably at the expense of human well-being in many regions.
- **[Structural strains of misfolded tau protein define different diseases](#)** [29 September 2021]
News & Views • In diseases called tauopathies, misfolded tau proteins form aggregates called fibrils. Fibrils from nine different tauopathies show that tau misfolds in many ways, enabling the diseases to be classified according to fibril structure.
- **[Evidence that overnight fasting could extend healthy lifespan](#)** [29 September 2021]
News & Views • A feeding schedule of prolonged overnight fasting periods extends healthy lifespan in fruit flies by promoting night-time autophagy, a process in which material in cells is degraded and recycled.
- **[A bimodal burst energy distribution of a repeating fast radio burst source](#)** [13 October 2021]
Article • For FRB 121102, 1,652 burst events are detected over 47 days, with a peak burst rate of 122 per hour, a bimodal burst rate energy distribution, and no periodicity or quasi-periodicity.
- **[A Jovian analogue orbiting a white dwarf star](#)** [13 October 2021]
Article • The authors show not only that planetary bodies around white dwarfs can survive but also that more than half of white dwarfs might have Jovian planetary companions.

- **Day-night cloud asymmetry prevents early oceans on Venus but not on Earth** [13 October 2021]
Article • Global climate model simulations of early Venus and Earth show that differences in the cloud regimes prevented ocean formation on Venus but not on Earth.
- **Fault-tolerant control of an error-corrected qubit** [04 October 2021]
Article • Fault-tolerant circuits for the control of a logical qubit encoded in 13 trapped ion qubits through a Bacon–Shor quantum error correction code are demonstrated.
- **Observation of fractional edge excitations in nanographene spin chains** [13 October 2021]
Article • Using scanning tunnelling microscopy and spectroscopy, fractional edge excitations are observed in nanographene spin chains, enabling the potential to study strongly correlated phases in purely organic materials.
- **Superior robustness of anomalous non-reciprocal topological edge states** [13 October 2021]
Article • The physics of oriented topological graphs produces anomalous non-reciprocal topological edge states that have greater robustness to disorder and defects than the best performers at present: namely, Chern states.
- **An elastic metal–organic crystal with a densely catenated backbone** [13 October 2021]
Article • A rubber-like, metal–organic crystal is reported with a mechanically interlocked catenane backbone, which could allow for easy guest molecule uptake and release.
- **Photocatalytic solar hydrogen production from water on a 100-m² scale** [25 August 2021]
Article • Carbon-neutral hydrogen can be produced through photocatalytic water splitting, as demonstrated here with a 100-m² array of panel reactors that reaches a maximum conversion efficiency of 0.76%.
- **Estimating a social cost of carbon for global energy consumption** [13 October 2021]
Article • Using global data, econometrics and climate science to estimate the damages induced by the emission of one ton of carbon dioxide, climate change is projected to increase electricity spending but reduce overall end-use energy expenditure.
- **Aquatic foods to nourish nations** [15 September 2021]
Article • Data on the nutrient content of almost 3,000 aquatic animal-source foods is combined with a food-systems model to show that an increase in aquatic-food production could reduce the inadequate intake of most nutrients.

- **Dopamine facilitates associative memory encoding in the entorhinal cortex** [22 September 2021]
Article • Cell-type-specific electrophysiological recording, fibre photometry and optogenetic manipulations in mice show that dopamine signals from the ventral tegmental area to the lateral entorhinal cortex have a key role in cue–reward associative learning.
- **Blood and immune development in human fetal bone marrow and Down syndrome** [29 September 2021]
Article • A single-cell atlas of human fetal bone marrow in healthy fetuses and fetuses with Down syndrome provides insight into developmental haematopoiesis in humans and the transcription and functional differences that occur in Down syndrome.
- **A single sulfatase is required to access colonic mucin by a gut bacterium** [06 October 2021]
Article • A single sulfatase produced by a bacterium found in the human colon is essential for degradation of sulfated O-glycans in secreted mucus.
- **Burden and characteristics of COVID-19 in the United States during 2020** [26 August 2021]
Article • Data-driven modelling including numbers of cases and population movements is used to simulate the COVID-19 pandemic in the United States in 2020, providing insights into the transmission of the disease.
- **Lectins enhance SARS-CoV-2 infection and influence neutralizing antibodies** [31 August 2021]
Article • C-type lectins and SIGLEC1 function as attachment receptors for SARS-CoV-2 and enhance ACE2-mediated infection.
- **Biologically informed deep neural network for prostate cancer discovery** [22 September 2021]
Article • A biologically informed, interpretable deep learning model has been developed to evaluate molecular drivers of resistance to cancer treatment, predict clinical outcomes and guide hypotheses on disease progression.
- **Circadian autophagy drives iTRF-mediated longevity** [29 September 2021]
Article • Circadian-regulated autophagy contributes to the health benefits of intermittent time-restricted feeding in Drosophila.
- **Structure-based classification of tauopathies** [29 September 2021]
Article • Cryo-electron microscopy structures of tau filaments from progressive supranuclear palsy and other tauopathies reveal new filament conformations, and suggest that tauopathies can be classified on several different levels according to their filament folds.

- **Structure and assembly of the mammalian mitochondrial supercomplex CIII2CIV** [06 October 2021]

Article • SCAF1 is solely required for supercomplex CIII2CIV assembly and is not involved in the formation of the respirasome (supercomplex CICIII2CIV)

- **Structural basis of human transcription–DNA repair coupling** [15 September 2021]

Article • The authors resolve the structure of five complexes containing RNA polymerase II and the CSA and CSB proteins, offering insight into how the repair of DNA lesions is coupled to transcription.

- NEWS AND VIEWS
- 13 October 2021

Venus might never have been habitable

A sophisticated climate model suggests that liquid-water oceans never formed on Venus, and that some planets outside the Solar System that were thought to be habitable might not be.

- [James F. Kasting](#) ⁰ &
- [Chester E. Harman](#) ¹

Today, Earth's sister planet Venus is more like a distant relative than a sibling. Its atmosphere is thick with carbon dioxide, its surface is hot enough to melt lead, and any water that it once had is gone — except for a tiny amount that remains as vapour in its atmosphere. But some scientists have argued that Venus might once have been habitable. [Writing in Nature](#), Turbet *et al.*¹ report a climate model that suggests the steam atmosphere produced during Venus's formation never condensed on the planet's surface to create oceans. Instead, water vapour was transported to Venus's night side (the hemisphere facing away from the Sun), where it cooled and condensed to form clouds that warmed the surface by absorbing and re-emitting the planet's outgoing infrared radiation. If the authors are correct, Venus was always a hellhole.

Access options

Subscribe to Journal

Get full journal access for 1 year

\$199.00

only \$3.90 per issue

[Subscribe](#)

All prices are NET prices.

VAT will be added later in the checkout.

Tax calculation will be finalised during checkout.

Rent or Buy article

Get time limited or full article access on ReadCube.

from \$8.99

[Rent or Buy](#)

All prices are NET prices.

Additional access options:

- [Log in](#)
- [Learn about institutional subscriptions](#)

Nature **598**, 259–260 (2021)

doi: <https://doi.org/10.1038/d41586-021-02720-2>

References

1. 1.

Turbet, M. *et al.* *Nature* **598**, 276–280 (2021).

2. 2.

Way, M. J. *et al.* *Geophys. Res. Lett.* **43**, 8376–8383 (2016).

3. 3.

Way, M. J. & Del Genio, A. D. *J. Geophys. Res. Planets* **125**, e2019JE006276 (2020).

4. 4.

Limaye, S. S. *et al. Astrobiology* **18**, 1181–1198 (2018).

5. 5.

Greaves, J. S. *et al. Nature Astron.* **5**, 655–664 (2021).

6. 6.

Snellen, I. A. G., Guzman-Ramirez, L., Hogerheijde, M. R., Hygate, A. P. S. & van der Tak, F. F. S. *Astron. Astrophys.* **644**, L2 (2020).

7. 7.

Intergovernmental Panel on Climate Change. *Climate Change 2021: The Physical Science Basis* (eds Masson-Delmotte, V. *et al.*) (Cambridge Univ. Press, 2021).

8. 8.

Hamano, K., Abe, Y. & Genda, H. *Nature* **497**, 607–610 (2013).

9. 9.

Gough, D. O. *Solar Phys.* **74**, 21–34 (1981).

10. 10.

Gaudi, B. S. *et al.* Preprint at <https://arxiv.org/abs/2001.06683> (2020).

11. 11.

Fischer, D. A. *et al.* *LUVOIR: Large UV/Optical/IR Explorer: Mission Concept Study Final Report* <https://asd.gsfc.nasa.gov/luvoir/reports> (NASA, 2019).

12. 12.

Gilmore, M. S., Mueller, N. & Helbert, J. *Icarus* **254**, 350–361 (2015).

13. 13.

Kasting, J. F., Kopparapu, R., Ramirez, R. M. & Harman, C. E. *Proc. Natl Acad. Sci. USA* **111**, 12641–12646 (2014).

This article was downloaded by **calibre** from <https://www.nature.com/articles/d41586-021-02720-2>

| [Section menu](#) | [Main menu](#) |

- NEWS AND VIEWS
- 15 September 2021

A spotlight on seafood for global human nutrition

What role might seafood have in boosting human health in diets of the future? A modelling study that assesses how a rise in seafood intake by 2030 might affect human populations worldwide offers a way to begin to answer this.

- [Lotte Lauritzen](#) [ORCID: http://orcid.org/0000-0001-7184-5949](#) 0

An adequate and sustainable supply and intake of nutritious food is essential to tackle major global health issues such as dietary deficiencies. Seafood, which in this context includes fish, shellfish and marine mammals, is rich in micronutrients (such as vitamin A, iron, vitamin B₁₂ and calcium) needed to combat the most common such deficiencies. Seafood is also the dominant source of marine omega-3 fatty acids, which have many health-promoting effects. [Writing in Nature](#), Golden *et al.*¹ present ambitious research that puts seafood centre stage.

Access options

Subscribe to Journal

Get full journal access for 1 year

\$199.00

only \$3.90 per issue

[Subscribe](#)

All prices are NET prices.
VAT will be added later in the checkout.
Tax calculation will be finalised during checkout.

Rent or Buy article

Get time limited or full article access on ReadCube.

from \$8.99

[Rent or Buy](#)

All prices are NET prices.

Additional access options:

- [Log in](#)
- [Learn about institutional subscriptions](#)

Nature **598**, 260-262 (2021)

doi: <https://doi.org/10.1038/d41586-021-02436-3>

References

1. 1.

Golden, C. *et al.* *Nature* **598**, 315–320 (2021).

2. 2.

Food and Agriculture Organization of the United Nations. *The State of World Fisheries and Aquaculture 2020. Sustainability in Action* (FAO, 2020).

3. 3.

FAO, IFAD, UNICEF, WFP & WHO. *The State of Food Security and Nutrition in the World 2021. Transforming Food Systems for Food Security, Improved Nutrition and Affordable Healthy Diets for All* (FAO, 2021).

4. 4.

Kumssa, D. B. *et al. Sci. Rep.* **5**, 10974 (2015).

5. 5.

Mithal, A. *et al. Osteoporosis Int.* **20**, 1807–1820 (2009).

6. 6.

Vuholm, S. *et al. Eur. J. Nutr.* **59**, 1205–1218 (2020).

7. 7.

Gebauer, S. K., Psota, T. L., Harris, W. S. & Kris-Etherton, P. M. *Am. J. Clin. Nutr.* **83**, 1526S–1535S (2006).

8. 8.

Djuricic, I. & Calder, P. C. *Nutrients* **13**, 2421 (2021).

This article was downloaded by **calibre** from <https://www.nature.com/articles/d41586-021-02436-3>

- NEWS AND VIEWS
- 13 October 2021

The cost of changes in energy use in a warming world

How will global energy usage change as Earth warms? Modelling now suggests that there will be a modest net decrease in energy consumption — but probably at the expense of human well-being in many regions.

- [Katrina Jessoe](#) [ORCID: http://orcid.org/0000-0002-9476-8664](http://orcid.org/0000-0002-9476-8664)⁰ &
- [Frances C. Moore](#) [ORCID: http://orcid.org/0000-0003-3866-9642](http://orcid.org/0000-0003-3866-9642)¹

Climate change affects many things: the food we grow, human health, the productivity of workers, migration decisions, conflicts and violence, ecosystem services and the amount of energy we consume^{1,2}. These disparate and diverse effects are difficult to quantify, particularly in economic terms. Nevertheless, such an evaluation is crucial for analyses of climate and energy policies. US federal agencies, for instance, are required to perform a cost–benefit analysis of all their regulations. For climate and energy policies, this requires them to put a price on carbon dioxide emissions. One measure of this is the social cost of carbon (SCC) — an evaluation of the future costs of emitting one extra tonne of CO₂ into the atmosphere, taking into account all the effects of climate change.

Access options

Subscribe to Journal

Get full journal access for 1 year

\$199.00

only \$3.90 per issue

Subscribe

All prices are NET prices.

VAT will be added later in the checkout.

Tax calculation will be finalised during checkout.

Rent or Buy article

Get time limited or full article access on ReadCube.

from \$8.99

Rent or Buy

All prices are NET prices.

Additional access options:

- [Log in](#)
- [Learn about institutional subscriptions](#)

Nature **598**, 262-263 (2021)

doi: <https://doi.org/10.1038/d41586-021-02721-1>

References

1. 1.

Dell, M., Jones, B. F. & Olken, B. A. *J. Econ. Lit.* **52**, 740–798 (2014).

2. 2.

Carleton, T. A. & Hsiang, S. M. *Science* **353**, aad9837 (2016).

3. 3.

National Academies of Sciences, Engineering, and Medicine. *Valuing Climate Damages: Updating Estimation of the Social Cost of Carbon Dioxide*. <https://doi.org/10.17226/24651> (National Academies Press, 2017).

4. 4.

Moore, F. C., Baldos, U., Hertel, T. & Diaz, D. *Nature Commun.* **8**, 1601 (2017).

5. 5.

Wagner, G. *et al.* *Nature* **590**, 548–550 (2021).

6. 6.

Rode, A. *et al.* *Nature* **598**, 308–314 (2021).

7. 7.

Davis, L. W. & Gertler, P. J. *Proc. Natl Acad. Sci. USA* **112**, 5962–5967 (2015).

8. 8.

Davis, L., Gertler, P., Jarvis, S. & Wolfram, C. *Glob. Environ. Change* **69**, 102299 (2021).

9. 9.

Diaz, D. & Moore, F. *Nature Clim. Change* **7**, 774–782 (2017).

10. 10.

Rose, S. K., Diaz, D. B. & Blanford, G. J. *Clim. Change Econ.* **8**, 1750009 (2017).

11. 11.

Buzan, J. R. & Huber, M. *Annu. Rev. Earth Planet. Sci.* **48**, 623–655 (2020).

12. 12.

Sherwood, S. C. & Huber, M. *Proc. Natl Acad. Sci. USA* **107**, 9552–9555 (2010).

13. 13.

Biddle, J. *Explor. Econ. Hist.* **45**, 402–423 (2008).

14. 14.

Auffhammer, M., Baylis, P. & Hausman, C. H. *Proc. Natl Acad. Sci. USA* **114**, 1886–1891 (2017).

This article was downloaded by **calibre** from <https://www.nature.com/articles/d41586-021-02721-1>

| [Section menu](#) | [Main menu](#) |

- NEWS AND VIEWS
- 29 September 2021

Structural strains of misfolded tau protein define different diseases

In diseases called tauopathies, misfolded tau proteins form aggregates called fibrils. Fibrils from nine different tauopathies show that tau misfolds in many ways, enabling the diseases to be classified according to fibril structure.

- [Henning Stahlberg](#) ⁰ &
- [Roland Riek](#) ¹

The protein tau contributes to the normal functioning of cells in the brain by adopting a specific structural conformation and stabilizing microtubules, which are protein filaments that act like railroads to enable various materials to be transported throughout the cell. However, in Alzheimer's disease and related diseases called tauopathies, misfolded tau molecules stack together in a manner similar to a one-dimensional crystal, and form needle-shaped fibrils around one micrometre long. Although all types of tau fibril are composed of tau molecules, these fibrils can occur in different 3D structural forms (strains), known as polymorphs. [Writing in Nature](#), Shi *et al.*¹ report the high-resolution structures of previously uncharacterized strains of tau fibril that were purified from the post-mortem brains of individuals with various neurodegenerative diseases, thereby establishing a disease classification based on tau fibril structure (Fig. 1).

Access options

Subscribe to Journal

Get full journal access for 1 year

\$199.00

only \$3.90 per issue

[Subscribe](#)

All prices are NET prices.

VAT will be added later in the checkout.

Tax calculation will be finalised during checkout.

Rent or Buy article

Get time limited or full article access on ReadCube.

from \$8.99

[Rent or Buy](#)

All prices are NET prices.

Additional access options:

- [Log in](#)
- [Learn about institutional subscriptions](#)

Nature **598**, 264-265 (2021)

doi: <https://doi.org/10.1038/d41586-021-02611-6>

References

1. 1.

Shi, Y. *et al.* *Nature* **598**, 359–363 (2021).

2. 2.

Prusiner, S. B. *Proc. Natl Acad. Sci. USA* **95**, 13363–13383 (1998).

3. 3.

Hard, J. & Selkoe, D. J. *Science* **297**, 353–356 (2002).

4. 4.

Fitzpatrick, A. W. P. *et al.* *Nature* **547**, 185–190 (2017).

5. 5.

Falcon, B. *et al.* *Acta Neuropathol.* **136**, 699–708 (2018).

6. 6.

Falcon, B. *et al.* *Nature* **561**, 137–140 (2018).

7. 7.

Falcon, B. *et al.* *Nature* **568**, 420–423 (2019).

8. 8.

Zhang, W. *et al.* *Nature* **580**, 283–287 (2020).

9. 9.

Shi, Y. *et al.* *Acta Neuropathol.* **141**, 697–708 (2021).

10. 10.

Li, J., Browning, S., Mahal, S. P., Oelschlegel, A. M. & Weissmann, C. *Science* **327**, 869–872 (2010).

11. 11.

Wang, L., Schubert, D., Sawaya, M. R., Eisenberg, D. & Riek, E. *Angew. Chem. Int. Edn* **49**, 3904–3908 (2010).

This article was downloaded by **calibre** from <https://www.nature.com/articles/d41586-021-02611-6>

| [Section menu](#) | [Main menu](#) |

- NEWS AND VIEWS
- 29 September 2021

Evidence that overnight fasting could extend healthy lifespan

A feeding schedule of prolonged overnight fasting periods extends healthy lifespan in fruit flies by promoting night-time autophagy, a process in which material in cells is degraded and recycled.

- [Stephen L. Helfand](#) ⁰ &
- [Rafael de Cabo](#) ¹

Timing is said to be the secret to comedy and to success in life, but it could also be one of the secrets to a longer, healthier life. The quest to extend healthy lifespan has been made seemingly attainable in humans through manipulations of calorie intake, such as caloric restriction^{1,2}. However, restricting calories for more than a short time is difficult because the intense hunger is hard to withstand for most. Manipulations that focus not on the number of ingested calories, but on the timing of ingestion, such as time-restricted feeding (TRF) might be much more sustainable. [Writing in Nature](#), Ulgherait *et al.*³ show that, in the fruit fly *Drosophila melanogaster*, a TRF schedule that includes prolonged periods of overnight fasting extends healthy lifespan. It does so by promoting an intracellular degradation and recycling process called autophagy, specifically at night^{4,5}.

Access options

Subscribe to Journal

Get full journal access for 1 year

\$199.00

only \$3.90 per issue

[Subscribe](#)

All prices are NET prices.

VAT will be added later in the checkout.

Tax calculation will be finalised during checkout.

Rent or Buy article

Get time limited or full article access on ReadCube.

from \$8.99

[Rent or Buy](#)

All prices are NET prices.

Additional access options:

- [Log in](#)
- [Learn about institutional subscriptions](#)

Nature **598**, 265-266 (2021)

doi: <https://doi.org/10.1038/d41586-021-01578-8>

References

1. 1.

de Cabo, R. & Mattson, M. P. *N. Engl. J. Med.* **381**, 2541–2551 (2019).

2. 2.

Mattson, M. P. *et al.* *Proc. Natl Acad. Sci. USA* **111**, 16647–16653 (2014).

3. 3.

Ulgherait, M. *et al.* *Nature* **598**, 353–358 (2021).

4. 4.

Hansen, M., Rubinsztein, D. C. & Walker, D. W. *Nature Rev. Mol. Cell Biol.* **19**, 579–593 (2018).

5. 5.

Kaushik, S. & Cuervo, A. M. *Nature Med.* **21**, 1406–1415 (2015).

6. 6.

Longo, V. D. & Panda, S. *Cell Metab.* **23**, 1048–1059 (2016).

7. 7.

Mattison, J. A. *et al.* *Nature Commun.* **8**, 14063 (2017).

8. 8.

Sutton, E. F. *et al.* *Cell Metab.* **27**, 1212–1221 (2018).

9. 9.

Mitchell, S. J. *et al.* *Cell Metab.* **29**, 221–228 (2019).

10. 10.

Finkel, T. *Nature Med.* **21**, 1416–1423 (2015).

11. 11.

Xu, K., Zheng, X. & Sehgal, A. *Cell Metab.* **8**, 289–300 (2008).

12. 12.

Stekovic, S. *et al.* *Cell Metab.* **30**, 462–476 (2019).

This article was downloaded by **calibre** from <https://www.nature.com/articles/d41586-021-01578-8>

| [Section menu](#) | [Main menu](#) |

- Article
- [Published: 13 October 2021](#)

A bimodal burst energy distribution of a repeating fast radio burst source

- [D. Li](#) ORCID: orcid.org/0000-0003-3010-7661^{1,2} na1,
- [P. Wang](#) ORCID: orcid.org/0000-0002-3386-7159¹ na1,
- [W. W. Zhu](#) ORCID: orcid.org/0000-0001-5105-4058¹ na1,
- [B. Zhang](#) ORCID: orcid.org/0000-0002-9725-2524³,
- [X. X. Zhang](#) ORCID: orcid.org/0000-0001-9587-631X¹,
- [R. Duan](#) ORCID: orcid.org/0000-0002-9260-1641¹,
- [Y. K. Zhang](#) ORCID: orcid.org/0000-0002-8744-3546^{1,2},
- [Y. Feng](#) ORCID: orcid.org/0000-0002-0475-7479^{1,2,4},
- [N. Y. Tang](#) ORCID: orcid.org/0000-0002-2169-0472^{1,5},
- [S. Chatterjee](#) ORCID: orcid.org/0000-0002-2878-1502⁶,
- [J. M. Cordes](#) ORCID: orcid.org/0000-0002-4049-1882⁶,
- [M. Cruces](#) ORCID: orcid.org/0000-0001-6804-6513⁷,
- [S. Dai](#) ORCID: orcid.org/0000-0002-9618-2499^{1,4,8},
- [V. Gajjar](#) ORCID: orcid.org/0000-0002-8604-106X⁹,
- [G. Hobbs](#) ORCID: orcid.org/0000-0003-1502-100X⁴,
- [C. Jin](#)¹,
- [M. Kramer](#) ORCID: orcid.org/0000-0002-4175-2271⁷,
- [D. R. Lorimer](#) ORCID: orcid.org/0000-0003-1301-966X^{10,11},
- [C. C. Miao](#) ORCID: orcid.org/0000-0002-9441-2190^{1,2},
- [C. H. Niu](#) ORCID: orcid.org/0000-0001-6651-7799¹,
- [J. R. Niu](#) ORCID: orcid.org/0000-0001-8065-4191^{1,2},
- [Z. C. Pan](#) ORCID: orcid.org/0000-0001-7771-2864¹,
- [L. Qian](#) ORCID: orcid.org/0000-0003-0597-0957¹,

- [L. Spitler](#) [ORCID: orcid.org/0000-0002-3775-8291⁷](#),
- [D. Werthimer⁹](#),
- [G. Q. Zhang¹²](#),
- [F. Y. Wang](#) [ORCID: orcid.org/0000-0003-4157-7714^{12,13}](#),
- [X. Y. Xie¹⁴](#),
- [Y. L. Yue](#) [ORCID: orcid.org/0000-0003-4415-2148¹](#),
- [L. Zhang](#) [ORCID: orcid.org/0000-0001-8539-4237^{1,15}](#),
- [Q. J. Zhi^{14,16}](#) &
- [Y. Zhu¹](#)

[*Nature*](#) volume **598**, pages 267–271 (2021)

- 1690 Accesses
- 530 Altmetric
- [Metrics details](#)

Subjects

- [Compact astrophysical objects](#)
- [Transient astrophysical phenomena](#)

Abstract

The event rate, energy distribution and time-domain behaviour of repeating fast radio bursts (FRBs) contain essential information regarding their physical nature and central engine, which are as yet unknown^{1,2}. As the first precisely localized source, FRB 121102 (refs. ^{3,4,5}) has been extensively observed and shows non-Poisson clustering of bursts over time and a power-law energy distribution^{6,7,8}. However, the extent of the energy distribution towards the fainter end was not known. Here we report the detection of 1,652 independent bursts with a peak burst rate of 122 h^{-1} , in 59.5 hours spanning 47 days. A peak in the isotropic equivalent energy distribution is found to be approximately $4.8 \times 10^{37}\text{ erg}$ at 1.25 GHz, below which the detection of bursts is suppressed. The burst energy distribution is

bimodal, and well characterized by a combination of a log-normal function and a generalized Cauchy function. The large number of bursts in hour-long spans allows sensitive periodicity searches between 1 ms and 1,000 s. The non-detection of any periodicity or quasi-periodicity poses challenges for models involving a single rotating compact object. The high burst rate also implies that FRBs must be generated with a high radiative efficiency, disfavouring emission mechanisms with large energy requirements or contrived triggering conditions.

Access options

Subscribe to Journal

Get full journal access for 1 year

\$199.00

only \$3.90 per issue

[Subscribe](#)

All prices are NET prices.

VAT will be added later in the checkout.

Tax calculation will be finalised during checkout.

Rent or Buy article

Get time limited or full article access on ReadCube.

from \$8.99

[Rent or Buy](#)

All prices are NET prices.

Additional access options:

- [Log in](#)

- [Access through your institution](#)
- [Learn about institutional subscriptions](#)

Fig. 1: Detected bursts and temporal energy distribution during the observation campaign.

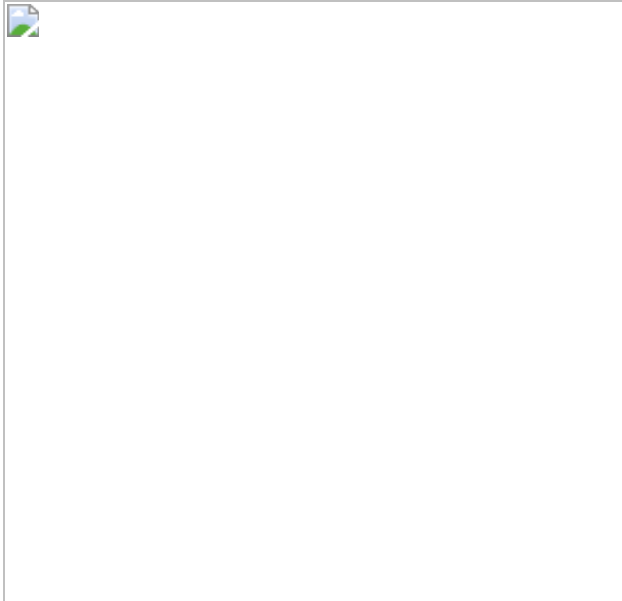


Fig. 2: Burst rate distribution of the isotropic equivalent energy at 1.25 GHz for FRB 121102 bursts.

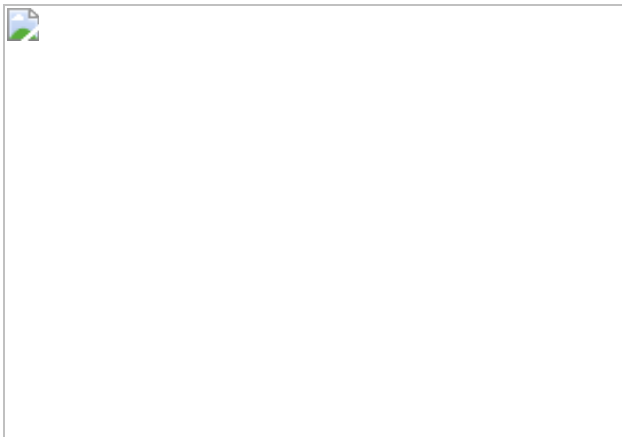


Fig. 3: Waiting time distribution of the bursts.

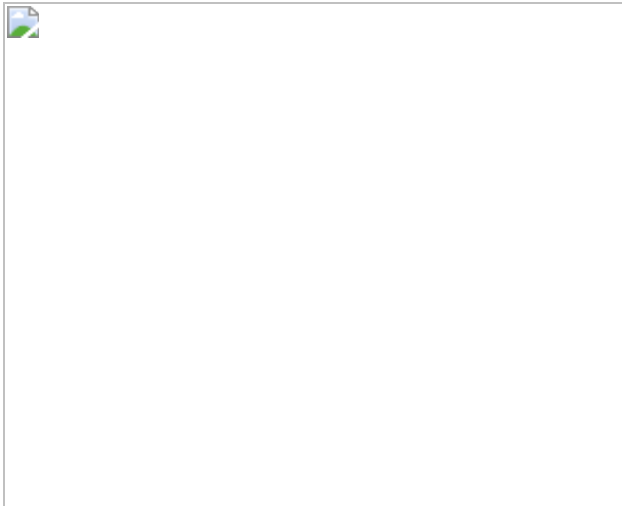
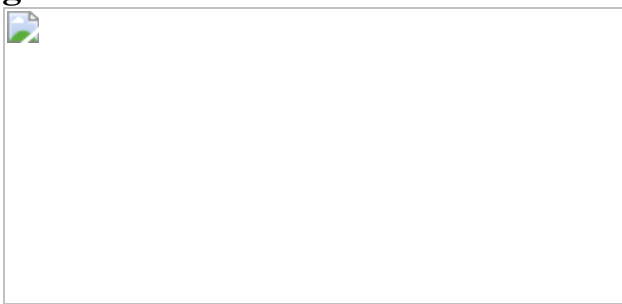


Fig. 4: DM evolution of FRB 121102.



Data availability

All relevant data for the 1,652 detected burst events are summarized in Supplementary Table 1. Observational data are available from the FAST archive (<http://fast.bao.ac.cn>) 1 year after data collection, following FAST data policy. Owing to the large data volume for these observations, interested users are encouraged to contact the corresponding author to arrange the data transfer. The data that support the findings of this study are openly available in Science Data Bank at <https://doi.org/10.11922/sciedb.01092> or <https://www.scidb.cn/en/detail?dataSetId=f172ff40142c4100855724b80a085deb>.

Code availability

Computational programs for the FRB121102 burst analysis and observations reported here are available at <https://github.com/NAOC-pulsar/PeiWang-code>. Other standard data reduction packages are available at their respective websites: PRESTO (<https://github.com/scottransom/presto>), HEIMDALL (<http://sourceforge.net/projects/heimdall-astro/>), DSPSR (<http://dpsr.sourceforge.net>), PSRCHIVE (<http://psrchive.sourceforge.net>).

References

1. 1.

Petroff, E., Hessels, J. W. T. & Lorimer, D. R. Fast radio bursts. *Astron. Astrophys. Rev.* **27**, 4 (2019).

2. 2.

Cordes, J. M. & Chatterjee, S. Fast radio bursts: an extragalactic enigma. *Ann. Rev. Astron. Astrophys.* **57**, 417–465 (2019).

3. 3.

Spitler, L. G. et al. A repeating fast radio burst. *Nature* **531**, 202–205 (2016).

4. 4.

Chatterjee, S. et al. A direct localization of a fast radio burst and its host. *Nature* **541**, 58–61 (2017).

5. 5.

Tendulkar, S. P. et al. The host galaxy and redshift of the repeating fast radio burst FRB 121102. *Astrophys. J. Lett.* **834**, L7 (2017).

6. 6.

Michilli, D. et al. An extrememagneto-ionic environment associated with the fast radio burst source FRB 121102. *Nature* **553**, 182 (2018).

7. 7.

Zhang, Y. G. et al. Fast radio burst 121102 pulse detection and periodicity: a machine learning approach. *Astrophys. J.* **866**, 149 (2018).

8. 8.

Gourdji, K. et al. A sample of low-energy bursts from FRB 121102. *Astrophys. J. Lett.* **877**, L19 (2019).

9. 9.

Li, Di. et al. FAST in space: considerations for a multibeam, multipurpose survey using China's 500-m aperture spherical radio telescope (FAST). *IEEE* **19**, 112–119 (2018).

10. 10.

Planck Collaboration et al. Planck 2015 results. XIII. Cosmological parameters. *Astron. Astrophys.* **594**, A13 (2016).

11. 11.

Shannon, R. M. et al. The dispersion-brightness relation for fast radio bursts from a wide-field survey. *Nature* **562**, 386–390 (2018).

12. 12.

Katz, J. I. Fast radio bursts. *Prog. Part. Nucl. Phys.* **103**, 1–18 (2018).

13. 13.

Palaniswamy, D., Li, Y. & Zhang, B. Are there multiple populations of fast radio bursts? *Astrophys. J. Lett.* **854**, L12 (2018).

14. 14.

Scholz, P. et al. The repeating fast radio burst FRB 121102: multi-wavelength observations and additional bursts. *Astrophys. J.* **833**, 177 (2016).

15. 15.

Petroff, E. et al. FRBCAT: rhe fast radio burst catalogue. *Publ. Astron. Soc. Aust.* **33**, e045 (2016).

16. 16.

Oostrum, L. C. et al. Repeating fast radio bursts with WSRT/Apertif. *Astron. Astrophys.* **635**, A61 (2020).

17. 17.

Hessels, J. W. T. et al. FRB 121102 bursts show complex time-frequency structure. *Astrophys. J.* **876**, L23 (2019).

18. 18.

Metzger, B. D., Berger, E. & Margalit, B. Millisecond magnetar birth connects FRB 121102 to superluminous supernovae and long-duration gamma-ray bursts. *Astrophys. J.* **841**, 14 (2017).

19. 19.

Yang, Y.-P. & Zhang, B. Dispersion measure variation of repeating fast radio burst sources. *Astrophys. J.* **847**, 22 (2017).

20. 20.

Lu, W. B., Kumar, P. & Zhang, B. A unified picture of Galactic and cosmological fast radio bursts. *Mon. Not. R. Astron. Soc.* **498**, 1397 (2020).

21. 21.

Wadiasingh, Z. et al. The fast radio burst luminosity function and death line in the low twist magnetar model. *Astrophys. J.* **891**, 82 (2020).

22. 22.

Gögüs, E. et al. Statistical properties of SGR 1806-20 bursts. *Astrophys. J. Lett.* **532**, L121–L124 (2000).

23. 23.

Wang, F. Y. & Yu, H. SGR-like behaviour of the repeating FRB 121102. *JCAP* **03**, 023 (2017).

24. 24.

Bagchi, M. A unified model for repeating and non-repeating fast radio bursts. *Astrophys. J. Lett.* **838**, L16 (2017).

25. 25.

Smallwood, J. L., Martin, R. G. & Zhang, B. Investigation of the asteroid-neutron star collision model for the repeating fast radio bursts. *Mon. Not. R. Astron. Soc.* **485**, 1367–1376 (2019).

26. 26.

Cordes, J. M. & Wasserman, I. Supergiant pulses from extragalactic neutron stars. *Mon. Not. R. Astron. Soc.* **457**, 232–257 (2016).

27. 27.

Zhang, B. Fast radio bursts from interacting binary neutron star systems. *Astrophys. J. Lett.* **890**, L24 (2020).

28. 28.

Metzger, B. D., Margalit, B. & Sironi, L. Fast radio bursts as synchrotron maser emission from decelerating relativistic blast waves. *Mon. Not. R. Astron. Soc.* **485**, 4091–4106 (2019).

29. 29.

Beloborodov, A. M. Blast waves from magnetar flares and fast radio bursts. Preprint at <https://arxiv.org/abs/1908.07743> (2019).

30. 30.

Kumar, P., Lu, W. & Bhattacharya, M. Fast radio burst source properties and curvature radiation model. *Mon. Not. R. Astron. Soc.* **468**, 2726–2739 (2017).

31. 31.

Petroff, E. et al. A real-time fast radio burst: polarization detection and multiwavelength follow-up. *Mon. Not. R. Astron. Soc.* **447**, 246 (2015).

32. 32.

Ransom, S. M. *New Search Techniques for Binary Pulsars*. PhD thesis, Harvard Univ. (2001).

33. 33.

Zhang, B. Fast radio burst energetics and detectability from high redshifts. *Astrophys. J. Lett.* **867**, L21 (2018).

34. 34.

Gupta, V. et al. Estimating fast transient detection pipeline efficiencies at UTMOST via real-time injection of mock FRBs. *Mon. Not. R. Astron. Soc.* **501**, 2316–2326 (2021).

35. 35.

Luo, R., Lee, K., Lorimer, D. R. & Zhang, B. On the normalized FRB luminosity function. *Mon. Not. R. Astron. Soc.* **481**, 2320–2337 (2018).

36. 36.

Wang, F. Y. & Zhang, G. Q. A. Universal energy distribution for FRB 121102. *Astrophys. J.* **882**, 108 (2019).

37. 37.

Lu, W. & Piro Anthony, L., Implications from ASKAP fast radio burst statistics. *Astrophys. J.* **883**, 3796–3847 (2019).

38. 38.

Luo, R. et al. On the FRB luminosity function–II. Event rate density. *Mon. Not. R. Astron. Soc.* **494**, 665–679 (2020).

39. 39.

Cordes, J. M., Bhat, N. D. E., Hankins, T. H., McLaughlin, M. A. & Kern, J. The brightest pulses in the universe: multifrequency observations of the Crab pulsar’s giant pulses. *Astrophys. J.* **612**, 375–388 (2004).

40. 40.

The CHIME/FRB Collaboration et al. CHIME/FRB detection of eight new repeating fast radio burst sources. Preprint at <https://arxiv.org/abs/1908.03507> (2019).

41. 41.

Oppermann, N., Yu, H. R. & Pen, U. L. On the non-Poissonian repetition pattern of FRB121102. *Mon. Not. R. Astron. Soc.* **475**, 5109–5115 (2018).

42. 42.

Lomb, N. R. Least-squares frequency analysis of unequally spaced data. *Astrophys. Space Sci.* **39**, 447–462 (1976).

43. 43.

Scargle, J. D. Studies in astronomical time series analysis. II. Statistical aspects of spectral analysis of unevenly spaced data. *Astrophys. J.* **263**, 835–853 (1982).

44. 44.

Rajwade, K. M. et al. Possible periodic activity in the repeating FRB 121102. *Mon. Not. R. Astron. Soc.* **495**, 3551–3558 (2020).

45. 45.

Cruces, M. et al. Repeating behaviour of FRB 121102: periodicity, waiting times and energy distribution. Preprint at <https://arxiv.org/abs/2008.03461> (2020).

46. 46.

Feng, Y. I. et al. Study of PSR J1022+1001 using the FAST radio telescope. *Astrophys. J.* **908**, 105–111 (2021).

47. 47.

Luo, R. et al. Diverse polarization angle swings from a repeating fast radio burst source. *Nature* **586**, 693–696 (2020).

48. 48.

Zhang, C. F. et al. A highly polarised radio burst detected from SGR 1935+2154 by FAST *The Astronomer's Telegram* **13699**, 1–1 (2020).

49. 49.

Hilmarsson, G. H., et al, Rotation measure evolution of the repeating fast radio burst source FRB 121102 *Astrophys. J. Lett.* **908**, 10–23 (2021).

50. 50.

Plotnikov, I. & Sironi, L. The synchrotron maser emission from relativistic shocks in fast radio bursts: 1D PIC simulations of cold pair plasmas. *Mon. Not. R. Astron. Soc.* **485**, 3816–3833 (2019).

51. 51.

Wu, Q., Zhang, G. Q., Wang, F. Y. & Dai, Z. G. Understanding FRB 200428 in the synchrotron maser shock model: consistency and possible challenge. *Astrophys. J. Lett.* **900**, L26 (2020).

Acknowledgements

This work is supported by National Natural Science Foundation of China (NSFC) programme nos. 11988101, 11725313, 11690024, 12041303, U1731238, U2031117, U1831131 and U1831207; by CAS International Partnership programme no. 114-A11KYSB20160008; by CAS Strategic Priority Research programme no. XDB23000000; the National Key R&D Program of China (no. 2017YFA0402600); and the National SKA Program of China no. 2020SKA0120200; and the Cultivation Project for FAST Scientific Payoff and Research Achievement of CAMS-CAS. S.C. and J.M.C. acknowledge support from the U.S. National Science Foundation (AAG 1815242). D.R.L. acknowledges support from the U.S. National Science Foundation awards AAG-1616042, OIA-1458952 and PHY-1430284. P.W. acknowledges support from the Youth Innovation Promotion Association CAS (ID 2021055) and CAS Project for Young Scientists in Basic Research (grant YSBR-006); P.W. and C.H.N. acknowledge support from cultivation project for FAST scientific payoff and research achievement of CAMS-CAS. Q.J.Z. is supported by the Technology Fund of Guizhou Province ((2016)-4008). L.Q. is supported by the Youth Innovation Promotion Association of CAS (ID 2018075). This work made use of data from FAST, a Chinese national mega-science facility built and operated by the National Astronomical Observatories, Chinese Academy of Sciences.

Author information

Author notes

1. These authors contributed equally: D. Li, P. Wang, W. W. Zhu

Affiliations

1. CAS Key Laboratory of FAST, NAOC, Chinese Academy of Sciences, Beijing, China

D. Li, P. Wang, W. W. Zhu, X. X. Zhang, R. Duan, Y. K. Zhang, Y. Feng, N. Y. Tang, S. Dai, C. Jin, C. C. Miao, C. H. Niu, J. R. Niu, Z. C. Pan, L. Qian, Y. L. Yue, L. Zhang & Y. Zhu

2. University of Chinese Academy of Sciences, Beijing, China

D. Li, Y. K. Zhang, Y. Feng, C. C. Miao & J. R. Niu

3. Department of Physics and Astronomy, University of Nevada, Las Vegas, Las Vegas, NV, USA

B. Zhang

4. CSIRO Astronomy and Space Science, Epping, New South Wales, Australia

Y. Feng, S. Dai & G. Hobbs

5. Department of Physics, Anhui Normal University, Wuhu, China

N. Y. Tang

6. Cornell Center for Astrophysics and Planetary Science and Department of Astronomy, Cornell University, Ithaca, NY, USA

S. Chatterjee & J. M. Cordes

7. Max-Planck-Institut für Radioastronomie, Bonn, Germany

M. Cruces, M. Kramer & L. Spitler

8. Western Sydney University, Penrith, New South Wales, Australia

S. Dai

9. Department of Astronomy, University of California Berkeley,
Berkeley, CA, USA

V. Gajjar & D. Werthimer

10. Department of Physics and Astronomy, West Virginia University,
Morgantown, WV, USA

D. R. Lorimer

11. Center for Gravitational Waves and Cosmology, West Virginia
University, Morgantown, WV, USA

D. R. Lorimer

12. School of Astronomy and Space Science, Nanjing University, Nanjing,
China

G. Q. Zhang & F. Y. Wang

13. Key Laboratory of Modern Astronomy and Astrophysics (Nanjing
University), Ministry of Education, Nanjing, China

F. Y. Wang

14. Guizhou Normal University, Guiyang, China

X. Y. Xie & Q. J. Zhi

15. School of Physics and Technology, Wuhan University, Wuhan, China

L. Zhang

16. Guizhou Provincial Key Laboratory of Radio Astronomy and Data
Processing, Guizhou Normal University, Guiyang, China

Q. J. Zhi

Contributions

D.L., R.D. and W.W.Z. launched the FAST campaign; P.W., C.H.N., Y.K.Z., Y.F., N.Y.T., J.R.N., C.C.M. and L.Z. processed the data; D.L., B.Z. and P.W. drafted the paper; R.D., X.X.Z., V.G., C.J., Y.Z., D.W. and Y.L.Y. built the FAST FRB backend; L.Q., G.H., X.Y.X., Q.J.Z. and S.D. made key contributions to the overall FAST data processing pipelines; L.S., M.C. and M.K. provided salient information on FRB 121102 from other observatories, particularly Effelsberg, and contributed to the scientific analysis; S.C., J.M.C., D.R.L. and F.Y.W. contributed to the writing and analysis, including simulations of the waiting time distribution (J.M.C.). F.Y.W. and G.Q.Z. contributed to work on the time-dependence of bimodal energy distribution.

Corresponding authors

Correspondence to D. Li or B. Zhang.

Ethics declarations

Competing interests

The authors declare no competing interests.

Additional information

Peer review information *Nature* thanks Victoria Kaspi and the other, anonymous, reviewer(s) for their contribution to the peer review of this work. Peer reviewer reports are available.

Publisher's note Springer Nature remains neutral with regard to jurisdictional claims in published maps and institutional affiliations.

Extended data figures and tables

Extended Data Fig. 1 The distribution of the instrumental gain and off-pulse brightness RMS at 1.25 GHz for observations.

The upper panel indicates the gain applied for each pulses. The red dots denote the averaged gain in each day. The bottom panel shows the off-pulse brightness RMS (mK s) of the first pulse detected each day.

Extended Data Fig. 2 Example of a dynamic spectrum of burst with RFI.

Extended Data Fig. 3 Left panel: Example of FRB simulations.

Upper panels (a and b) are injected and de-dispersed dynamic spectra respectively. The time series is shown in panel (c) with the red arrows pointing to simulated pulses that were detected, while the blue arrow indicates an undetected pulse. **Right panel: Comparison of SNR_p recovered by FRB search versus the corresponding injected values.** The SNR_p histograms separately indicate the injected FRB pulses (grey lines) and the mock FRBs detected (red lines).

Extended Data Fig. 4 The completeness fraction of the FAST survey to FRBs as a function of the observed fluence and detected width.

All FRBs lying in the integrated $\text{SNR}_f < 6$ region are below PRESTOâ€™s search threshold. The region above the integrated SNR_f of 6 shows the incompleteness of our FAST detection to broad FRBs as revealed by the injections. The map was smoothed (rebin) the map with a box of $0.05 \text{ ms} \times 0.002 \text{ Jy ms}$, which ensured the presence of at least one injected pulse in most map areas. Then for a few grid points without pulses, a simple linear

interpolation was used to improve the visual appearance. The colour bar on the right side indicates the detection recovery fraction.

Extended Data Fig. 5 Upper panel (a): The burst rate distribution of the isotropic equivalent energy.

Details as per Extended Data Fig. 2. The red line represents the recovered distribution by adding back the missing fraction based on the simulation. The grey shaded region is the uncertainty for a 95% confidence based on the Poisson statistical assumption in the “reconstructed” fitting. **Bottom panel (b): The fluence-width distribution at 1.25 GHz for FRB 121102 bursts.** The black dots indicate the 1,652 detected bursts, the colorbar is consistent with Extended Data Fig. 4. In the upper panel, the two-component lognormal (LN) distribution is separately fitted in blue dashed line and grey dot line, an overall fit for bursts is shown in green. The red line and the shaded region indicates reconstructed missing fraction of bursts detection and uncertainty.

Extended Data Fig. 6 Flux intensity and pulse width distribution of FRB 121102.

Left: Flux intensity against pulse width for the FRB 121102 bursts with peak $\text{SNR}_p > 10$ in our sample. *Right:* The equivalent pulse width histogram.

Extended Data Fig. 7 MC simulations of the waiting time distribution.

The three figures correspond to three different simulations, and the number of randomly generated pulses in each simulation are $100 \times 1652 \sim 1.6e5$, $1 \times 1652 = 1652$, and $0.2 \times 1652 \sim 330$. The peak times of the three log-normal distributions are 0.62 s, 61.89 s, and 272.04 s, respectively.

Extended Data Fig. 8 Lomb-Scargle periodograms of FRB 121102 burst arrival times (top row) along with phase

histograms for two trial periods (bottom row).

Left: Periods from 10^{-3} to 10^2 d. The four leftmost peaks in the periodogram are caused by daily sampling and its harmonics. The peak at ~ 24 d is related to the sampling window function (i.e. non-uniform sampling) over the 47 d data set, as is consistent with the broad distribution in burst phase (bottom left). Right: Periods from 1 ms to 10^3 s. The peak at 10 ms is a large multiple of the original sampling time and also yields no distinct concentration in burst phase.

Extended Data Fig. 9 Example of the DM optimization method for FRB 121102.

The complex time–frequency structures for the burst of MJD 58729.01858 was revealed with an optimal DM of 563.5 pc cm^{-3} .

Extended Data Fig. 10 Left panel: Histogram and cumulative distribution of dispersion measure for FRB 121102.

Right panel: Slope distribution of null hypothesis test.

Supplementary information

Supplementary Information

This file contains Supplementary Table 1.

Peer Review File

Supplementary Data

Supplementary Data for 1,652 burst list in Supplementary Table 1 (Supplementary Information).

Rights and permissions

Reprints and Permissions

About this article

Cite this article

Li, D., Wang, P., Zhu, W.W. *et al.* A bimodal burst energy distribution of a repeating fast radio burst source. *Nature* **598**, 267–271 (2021).
<https://doi.org/10.1038/s41586-021-03878-5>

- Received: 15 October 2020
- Accepted: 05 August 2021
- Published: 13 October 2021
- Issue Date: 14 October 2021
- DOI: <https://doi.org/10.1038/s41586-021-03878-5>

Share this article

Anyone you share the following link with will be able to read this content:

[Get shareable link](#)

Sorry, a shareable link is not currently available for this article.

[Copy to clipboard](#)

Provided by the Springer Nature SharedIt content-sharing initiative

This article was downloaded by **calibre** from <https://www.nature.com/articles/s41586-021-03878-5>

- Article
- [Published: 13 October 2021](#)

A Jovian analogue orbiting a white dwarf star

- [J. W. Blackman](#) [ORCID: orcid.org/0000-0001-5860-1157](#)^{1,2},
- [J. P. Beaulieu](#)^{1,2},
- [D. P. Bennett](#) [ORCID: orcid.org/0000-0001-8043-8413](#)^{3,4},
- [C. Danielski](#)^{2,5,6},
- [C. Alard](#)²,
- [A. A. Cole](#) [ORCID: orcid.org/0000-0003-0303-3855](#)¹,
- [A. Vandorou](#)¹,
- [C. Ranc](#)³,
- [S. K. Terry](#) [ORCID: orcid.org/0000-0002-5029-3257](#)⁷,
- [A. Bhattacharya](#)^{3,4},
- [I. Bond](#)⁸,
- [E. Bachelet](#)⁹,
- [D. Veras](#) [ORCID: orcid.org/0000-0001-8014-6162](#)^{10,11,12},
- [N. Koshimoto](#) [ORCID: orcid.org/0000-0003-2302-9562](#)^{3,13},
- [V. Batista](#)² &
- [J. B. Marquette](#)¹⁴

[Nature](#) volume **598**, pages 272–275 (2021)

- 942 Accesses
- 771 Altmetric
- [Metrics details](#)

Subjects

- [Exoplanets](#)

Abstract

Studies^{1,2} have shown that the remnants of destroyed planets and debris-disk planetesimals can survive the volatile evolution of their host stars into white dwarfs^{3,4}, but few intact planetary bodies around white dwarfs have been detected^{5,6,7,8}. Simulations predict^{9,10,11} that planets in Jupiter-like orbits around stars of $\leq 8 M_{\odot}$ (solar mass) avoid being destroyed by the strong tidal forces of their stellar host, but as yet, there has been no observational confirmation of such a survivor. Here we report the non-detection of a main-sequence lens star in the microlensing event MOA-2010-BLG-477Lb¹² using near-infrared observations from the Keck Observatory. We determine that this system contains a $0.53 \pm 0.11 M_{\odot}$ white-dwarf host orbited by a 1.4 ± 0.3 Jupiter-mass planet with a separation on the plane of the sky of 2.8 ± 0.5 astronomical units, which implies a semi-major axis larger than this. This system is evidence that planets around white dwarfs can survive the giant and asymptotic giant phases of their host's evolution, and supports the prediction that more than half of white dwarfs have Jovian planetary companions¹³. Located at approximately 2.0 kiloparsecs towards the centre of our Galaxy, it is likely to represent an analogue to the end stages of the Sun and Jupiter in our own Solar System.

Access options

Subscribe to Journal

Get full journal access for 1 year

\$199.00

only \$3.90 per issue

[Subscribe](#)

All prices are NET prices.
VAT will be added later in the checkout.
Tax calculation will be finalised during checkout.

Rent or Buy article

Get time limited or full article access on ReadCube.

from \$8.99

[Rent or Buy](#)

All prices are NET prices.

Additional access options:

- [Log in](#)
- [Access through your institution](#)
- [Learn about institutional subscriptions](#)

Fig. 1: H-band adaptive optics imaging of MOA-2010-BLG-477 from the Keck Observatory.

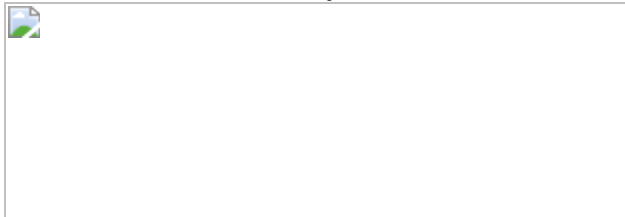


Fig. 2: H-band brightness of possible main-sequence host lenses.

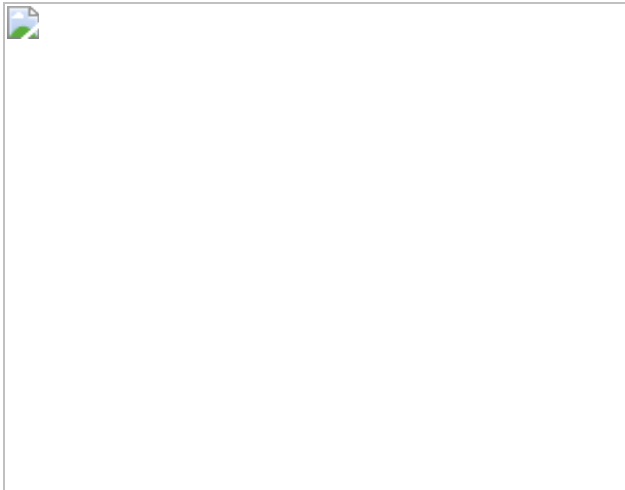


Fig. 3: Physical properties of MOA-2010-BLG-477.



Data availability

The Keck Observatory data used in this study are freely available in the Keck Observatory Archive (<https://koa.ipac.caltech.edu/cgi-bin/KOA/nph-KOALogin>). Data from the VISTA Variables in the Via Lactea (VVV) survey are available in the European Southern Observatory archive (http://archive.eso.org/wdb/wdb/adp/phase3_main/form?phase3_collection=VVV&release_tag=6). Data used to model the light curve are available from the corresponding author upon reasonable request.

Code availability

The Keck pipeline is available on GitHub (<https://github.com/blackmanjw/KeckPipeline>). The Bayesian analysis code

of D.P.B. uses routines from ref. [42](#), which are subject to restricted availability.

References

1. 1.

Vanderburg, A. et al. A disintegrating minor planet transiting a white dwarf. *Nature* **526**, 546–549 (2015).

2. 2.

Manser, C. J. et al. A planetesimal orbiting within the debris disc around a white dwarf star. *Science* **364**, 66–69 (2019).

3. 3.

Villaver, E. & Livio, M. Can planets survive stellar evolution? *Astrophys. J.* **661**, 1192–1201 (2007).

4. 4.

Duncan, M. J. & Lissauer, J. J. The effects of post-main-sequence solar mass loss on the stability of our planetary system. *Icarus* **134**, 303–310 (1998).

5. 5.

Sigurdsson, S. et al. A young white dwarf companion to pulsar B1620-26: evidence for early planet formation. *Science* **301**, 193–196 (2003).

6. 6.

Vanderburg, A. et al. A giant planet candidate transiting a white dwarf. *Nature* **585**, 363–367 (2020).

7. 7.

Luhman, K. L., Burgasser, A. J. & Bochanski, J. J. Discovery of a candidate for the coolest known brown dwarf. *Astrophys. J. Lett.* **730**, L9 (2011).

8. 8.

Gaensicke, B. T. et al. Accretion of a giant planet onto a white dwarf. *Nature* **576**, 61–64 (2019).

9. 9.

Madappatt, N., De Marco, O. & Villaver, E. The effect of tides on the population of PN from interacting binaries. *Mon. Not. R. Astron. Soc.* **463**, 1040–1056 (2016).

10. 10.

Mustill, A. J. et al. Unstable low-mass planetary systems as drivers of white dwarf pollution. *Mon. Not. R. Astron. Soc.* **476**, 3939–3955 (2018).

11. 11.

Nordhaus, J. & Spiegel, D. S. On the orbits of low-mass companions to white dwarfs and the fates of the known exoplanets. *Mon. Not. R. Astron. Soc.* **432**, 500–505 (2013).

12. 12.

Bachelet, E. et al. MOA 2010-blg-477lb: constraining the mass of a microlensing planet from microlensing parallax, orbital motion, and detection of blended light. *Astrophys. J.* **754**, 73 (2012).

13. 13.

Schreiber, M. R. et al. Cold giant planets evaporated by hot white dwarfs. *Astrophys. J. Lett.* **887**, L4 (2019).

14. 14.

Bennett, D. P. & Rie, S. H. Detecting Earth-mass planets with gravitational microlensing. *Astrophys. J.* **472**, 660–664 (1996).

15. 15.

Boyajian, T. S. et al. Stellar diameters and temperatures. III. Main sequence A, F, G, and K stars: additional high-precision measurements and empirical relations. *Astrophys. J.* **771**, 40 (2014); erratum **787**, 92 (2014).

16. 16.

Gaudi, B. S. Microlensing surveys for exoplanets. *Annu. Rev. Astron. Astr.* **50**, 411–453 (2012).

17. 17.

Bennett, D. P. et al. MOA-2011-BLG-262Lb: a sub-Earth-mass moon orbiting a gas giant primary or a high velocity planetary system in the galactic bulge. *Astrophys. J.* **785**, 155 (2014).

18. 18.

Giannicchele, N., Bergeron, P. & Dufour, P. Know your neighborhood: a detailed model atmosphere analysis of nearby white dwarfs. *Astrophys. J. Suppl. S.* **199**, 29 (2012).

19. 19.

Toonen, S., Hollands, M., Gänsicke, B. T. & Boekholt, T. The binarity of the local white dwarf population. *Astron. Astrophys.* **602**, 16 (2017).

20. 20.

Tremblay, P. E. et al. The field white dwarf mass distribution. *Mon. Not. R. Astron. Soc.* **461**, 2100–2114 (2016).

21. 21.

Veras, D. Post-main-sequence planetary system evolution. *R. Soc. Open Sci.* **3**, 150571 (2016).

22. 22.

Mustill, A. J. & Villaver, E. Foretellings of Ragnarök: world-engulfing asymptotic giants and the inheritance of white dwarfs. *Astrophys. J.* **761**, 121 (2012).

23. 23.

Ghezzi, L., Montet, B. T. & Johnson, J. A. Retired A stars revisited: an updated giant planet occurrence rate as a function of stellar metallicity and mass. *Astrophys. J.* **860**, 109 (2018).

24. 24.

Vandorou, A. et al. Revisiting MOA 2013-BLG-220L: a solar-type star with a cold super-Jupiter companion. *Astron. J.* **160**, 121 (2020).

25. 25.

OGLE Extinction Calculator. <http://ogle.astroww.edu.pl/cgi-ogle/getext.py> (2013).

26. 26.

Nataf, D. M. et al. Reddening and extinction toward the galactic bulge from OGLE-III: the Inner Milky Way's $R_V \sim 2.5$ extinction curve. *Astrophys. J.* **769**, 88 (2013).

27. 27.

Blackman, J. W. et al. Confirmation of the stellar binary microlensing event, Macho 97-BLG-28. *Astrophys. J.* **890**, 87 (2020).

28. 28.

Beaulieu, J.-P. et al. Revisiting the microlensing event Ogle 2012-BLG-0026: a solar mass star with two cold giant planets. *Astrophys. J.* **824**, 83 (2016).

29. 29.

Bertin, E. SWarp: resampling and co-adding FITS images together. *Astrophysics Source Code Library record no. ascl:1010.068* (2010).

30. 30.

Bertin, E. & Arnouts, S. SExtractor: software for source extraction. *Astron. Astrophys. Sup.* **117**, 393–404 (1996).

31. 31.

Minniti, D. et al. VISTA Variables in the Via Lactea (VVV): the public ESO near-IR variability survey of the Milky Way. *New Astron.* **15**, 433–443 (2010).

32. 32.

Bennett, D. P. et al. Planetary and other short binary microlensing events from the MOA short-event analysis. *Astrophys. J.* **757**, 119 (2012).

33. 33.

Bond, I. A. et al. The lowest mass ratio planetary microlens: OGLE 2016–BLG–1195Lb. *Mon. Not. R. Astron. Soc.* **469**, 2434–2440 (2017).

34. 34.

Bhattacharya, A. et al. WFIRST exoplanet mass-measurement method finds a planetary mass of 39 ± 8 M for OGLE-2012-BLG-0950Lb. *Astronom. J.* **156**, 289 (2018).

35. 35.

Bennett, D. P. et al. Keck observations confirm a super-Jupiter planet orbiting M dwarf OGLE-2005-BLG-071L. *Astronom. J.* **159**, 68 (2020).

36. 36.

Gaudi, B. S. et al. Discovery of a Jupiter/Saturn analog with gravitational microlensing. *Science* **319**, 927–930 (2008).

37. 37.

Bennett, D. P. et al. Masses and orbital constraints for the OGLE-2006-BLG-109Lb,c Jupiter/Saturn analog planetary system. *Astrophys. J.* **713**, 837–855 (2010).

38. 38.

Gould, A. et al. A terrestrial planet in a ~1-au orbit around one member of a ~15-au binary. *Science* **345**, 46–49 (2014).

39. 39.

Bennett, D. P. et al. The first circumbinary planet found by microlensing: OGLE-2007-BLG-349L(AB)c. *Astronom. J.* **152**, 125 (2016).

40. 40.

Zhu, W. et al. Empirical study of simulated two-planet microlensing events. *Astrophys. J.* **794**, 53 (2014).

41. 41.

Dong, S. et al. First space-based microlens parallax measurement: Spitzer observations of OGLE-2005-SMC-001. *Astrophys. J.* **664**, 862–878 (2007).

42. 42.

Press, W., Teukolsky, S., Vetterling, W. & Flannery, B. *Numerical Recipes* (Cambridge Univ. Press, 1992).

Acknowledgements

Data presented in this work were obtained at the W. M. Keck Observatory from telescope time allocated to the National Aeronautics and Space Administration through the agency's scientific partnership with the California Institute of Technology and the University of California. This work was supported by the University of Tasmania through the UTAS Foundation, ARC grant DP200101909, and the endowed Warren Chair in Astronomy. We acknowledge the support of ANR COLD WORLDS (ANR-18-CE31-0002) at the Institut d'Astrophysique de Paris and the Laboratoire d'Astrophysique de Bordeaux. D.P.B., A.B., N.K., C.R. and S.K.T. were supported by NASA through grant NASA-80NSSC18K0274 and by NASA award no. 80GSFC17M0002. E.B. acknowledges support from NASA grant 80NSSC19K0291. Work by N.K. is supported by JSPS KAKENHI grant no. JP18J00897. C.D. acknowledges financial support from the State Agency for Research of the Spanish MCIU through the 'Center of Excellence Severo Ochoa' award to the Instituto de Astrofísica de Andalucía (SEV-2017-0709), and the Group project ref. PID2019-110689RB-I00/AEI/10.13039/501100011033. D.V. gratefully acknowledges the support of the STFC via an Ernest Rutherford Fellowship (grant ST/P003850/1).

Author information

Affiliations

1. School of Natural Sciences, University of Tasmania, Hobart, Australia
J. W. Blackman, J. P. Beaulieu, A. A. Cole & A. Vandorou
2. Sorbonne Universités, UPMC Université Paris 6 et CNRS, UMR 7095, Institut d'Astrophysique de Paris, Paris, France

J. W. Blackman, J. P. Beaulieu, C. Danielski, C. Alard & V. Batista

3. Laboratory for Exoplanets and Stellar Astrophysics, NASA/Goddard Space Flight Center, Greenbelt, MD, USA

D. P. Bennett, C. Ranc, A. Bhattacharya & N. Koshimoto

4. Department of Astronomy, University of Maryland, College Park, MD, USA

D. P. Bennett & A. Bhattacharya

5. Instituto de Astrofísica de Andalucía (IAA-CSIC), Granada, Spain

C. Danielski

6. UCL Centre for Space Exochemistry Data, Didcot, UK

C. Danielski

7. Department of Astronomy, University of California Berkeley, Berkeley, CA, USA

S. K. Terry

8. Institute for Natural and Mathematical Sciences, Massey University, Auckland, New Zealand

I. Bond

9. Las Cumbres Observatory, Goleta, CA, USA

E. Bachelet

10. Centre for Exoplanets and Habitability, University of Warwick, Coventry, UK

D. Veras

11. Department of Physics, University of Warwick, Coventry, UK

D. Veras

12. Centre for Space Domain Awareness, University of Warwick,
Coventry, UK

D. Veras

13. Department of Astronomy, Graduate School of Science, The
University of Tokyo, Tokyo, Japan

N. Koshimoto

14. Laboratoire d'Astrophysique de Bordeaux, University of Bordeaux,
Pessac, France

J. B. Marquette

Contributions

J.W.B. led the photometric and formal analysis and wrote the manuscript. J.W.B., V.B. and J.P.B. took and reduced the photometric data using a pipeline written by J.W.B. and A.V. with contributions from J.B.M. for magnitude calibrations. D.P.B., J.P.B. and A.A.C. discussed the conceptual and analysis approaches. D.P.B. was the principle investigator of the Keck telescope proposal, led the planning of the observations, and conducted the light curve modelling and Bayesian analyses. C.D. provided insight into single and double white-dwarf planetary systems. I.B. processed the detrended MOA photometry. A.B. and E.B. assisted with proper motion calculations. A.B. and N.K. assisted with observing on Keck. C.R. calculated the parallax, proper motion and lens prediction contours. C.A. worked on the PSF analysis and the determining of detection limits. D.P.B., J.P.B., A.A.C., C.D., S.K.T. and D.V. contributed to the review and editing of the manuscript.

Corresponding author

Correspondence to J. W. Blackman.

Ethics declarations

Competing interests

The authors declare no competing interests.

Additional information

Peer review information *Nature* thanks Albert Zijlstra and the other, anonymous, reviewer(s) for their contribution to the peer review of this work. Peer reviewer reports are available.

Publisher's note Springer Nature remains neutral with regard to jurisdictional claims in published maps and institutional affiliations.

Extended data figures and tables

[Extended Data Fig. 1 OGLE-III and Keck imaging of MOA-2010-BLG-477Lb.](#)

(a) OGLE-III image of the OGLE-BLG176.8 field (b) H-band image of the same field taken in 2015 with Keck/NIRC2 with the narrow camera.

[Extended Data Fig. 2 Keck Point Spread Function \(PSF\) fit and residuals.](#)

(a) Keck/NIRC2 H-band image from 2018. (b) Residuals after fitting the PSF using multiple stars in the neighbourhood of the source. Both the object to the north-east (upper left in panel A) and the object at source position (lower right) are subtracted using this PSF fit. There is no structure or indication of a double star in either of the two objects. (c) The residuals from panel B normalized to the Poisson noise. (d) Panel A but subtracting the fitted PSF from the unrelated companion.

Extended Data Fig. 3 White Dwarf Mass-Luminosity distribution derived a sample of 130 white dwarfs from a homogeneous and complete sample of white dwarfs within 20pc of the Sun¹⁸.

Two unresolved double-white dwarfs (DWD), eight unresolved DWD candidates and one unresolved binary white dwarf with a main-sequence companion have been removed from this sample¹⁹. 14 stars with distances > 20 pc have also been removed. The white dots indicate the masses and V band magnitudes of the white dwarfs in this sample, and the color distribution indicates the smooth Gaussian multivariate kernel-density distribution that we have used in our analysis.

Extended Data Fig. 4 Light Curve Data and Model for microlensing event MOA-2010-BLG-477.

The solid curve is the best fit model and the dashed grey curve is the single lens model with the same single lens parameters. The different colors represent different data sets from different telescopes. One sigma error bars are shown. The data sets are explained in the discovery paper¹².

Extended Data Fig. 5 Cumulative $\Delta\chi^2$ comparing a static light curve model with that including parallax and orbital motion.

The bulk of the signal comes following the light curve peak. The parallax plus orbital motion comes primarily from the MOA data ($\Delta\chi^2 = 45$) and the SAAO data ($\Delta\chi^2 = 9.0$).

Extended Data Fig. 6 Predictions of the microlens parallax vector π_E and the corresponding predicted relative lens-source proper motion μ_{rel} for a main sequence and white dwarf lens.

Based on a Markov-Chain Monte-Carlo (MCMC) analysis using Galactic model priors as in¹⁷, the upper panels (a) and (b) show the unweighted

predicted components of (π_{EN}, π_{EE}) and $(\mu_{rel, HN}, \mu_{rel, HE})$. The middle panels (**c**) and (**d**) show the weighted predictions for a main-sequence lens. The lower panels (**e**) and (**f**) show the weighted predictions for a white-dwarf lens. The three shades of blue from dark to light denote probabilities of 0.393, 0.865, 0.989. When integrating over all parameters the limit of the 0.393 contour corresponds to the 1σ distribution of any chosen parameter.

Extended Data Fig. 7

H-band adaptive optics imaging from the KECK observatory, with contours showing the predicted position of a white dwarf lens (analogous to Fig. 1) **(a)** A crop of a narrow-camera H-band image obtained with the NIRC2 imager in 2015 centered on MOA 2010-BLG-477 with an 8 arcsec field of view. **(b)** A 0.36 arcsec zoom of the same image. The bright object in the center is the source. To the north-east (the upper left) is an unrelated $H = 18.52 \pm 0.05$ star 123 mas from the source. **(c)** The field in 2018. The contours indicate the likely positions of the white dwarf host (probability of 0.393, 0.865, 0.989 from light to dark blue) using constraints from microlensing parallax and lens-source relative proper motion.

Extended Data Table 1 Best Fit Model Parameters

Supplementary information

Peer Review File

Rights and permissions

Reprints and Permissions

About this article

Cite this article

Blackman, J.W., Beaulieu, J.P., Bennett, D.P. *et al.* A Jovian analogue orbiting a white dwarf star. *Nature* **598**, 272–275 (2021).
<https://doi.org/10.1038/s41586-021-03869-6>

- Received: 17 September 2020
- Accepted: 30 July 2021
- Published: 13 October 2021
- Issue Date: 14 October 2021
- DOI: <https://doi.org/10.1038/s41586-021-03869-6>

Share this article

Anyone you share the following link with will be able to read this content:

[Get shareable link](#)

Sorry, a shareable link is not currently available for this article.

[Copy to clipboard](#)

Provided by the Springer Nature SharedIt content-sharing initiative

This article was downloaded by **calibre** from <https://www.nature.com/articles/s41586-021-03869-6>

- Article
- [Published: 13 October 2021](#)

Day–night cloud asymmetry prevents early oceans on Venus but not on Earth

- [Martin Turbet](#) ORCID: [orcid.org/0000-0003-2260-9856¹](https://orcid.org/0000-0003-2260-9856),
- [Emeline Bolmont](#) ORCID: [orcid.org/0000-0001-5657-4503¹](https://orcid.org/0000-0001-5657-4503),
- [Guillaume Chaverot](#) ORCID: [orcid.org/0000-0003-4711-3099¹](https://orcid.org/0000-0003-4711-3099),
- [David Ehrenreich](#) ORCID: [orcid.org/0000-0001-9704-5405¹](https://orcid.org/0000-0001-9704-5405),
- [Jérémy Leconte²](#) &
- [Emmanuel Marcq](#) ORCID: [orcid.org/0000-0002-1924-641X³](https://orcid.org/0000-0002-1924-641X)

[Nature](#) volume **598**, pages 276–280 (2021)

- 1761 Accesses
- 709 Altmetric
- [Metrics details](#)

Subjects

- [Atmospheric dynamics](#)
- [Early solar system](#)
- [Palaeoclimate](#)

Abstract

Earth has had oceans for nearly four billion years¹ and Mars had lakes and rivers 3.5–3.8 billion years ago². However, it is still unknown whether water has ever condensed on the surface of Venus^{3,4} because the planet—now completely dry⁵—has undergone global resurfacing events that obscure most of its history^{6,7}. The conditions required for water to have initially condensed on the surface of Solar System terrestrial planets are highly uncertain, as they have so far only been studied with one-dimensional numerical climate models³ that cannot account for the effects of atmospheric circulation and clouds, which are key climate stabilizers. Here we show using three-dimensional global climate model simulations of early Venus and Earth that water clouds—which preferentially form on the nightside, owing to the strong subsolar water vapour absorption—have a strong net warming effect that inhibits surface water condensation even at modest insolations (down to 325 watts per square metre, that is, 0.95 times the Earth solar constant). This shows that water never condensed and that, consequently, oceans never formed on the surface of Venus. Furthermore, this shows that the formation of Earth’s oceans required much lower insolation than today, which was made possible by the faint young Sun. This also implies the existence of another stability state for present-day Earth: the ‘steam Earth’, with all the water from the oceans evaporated into the atmosphere.

Access options

Subscribe to Journal

Get full journal access for 1 year

\$199.00

only \$3.90 per issue

[Subscribe](#)

All prices are NET prices.

VAT will be added later in the checkout.

Tax calculation will be finalised during checkout.

Rent or Buy article

Get time limited or full article access on ReadCube.

from \$8.99

[Rent or Buy](#)

All prices are NET prices.

Additional access options:

- [Log in](#)
- [Access through your institution](#)
- [Learn about institutional subscriptions](#)

Fig. 1: Day and night water cloud feedbacks.

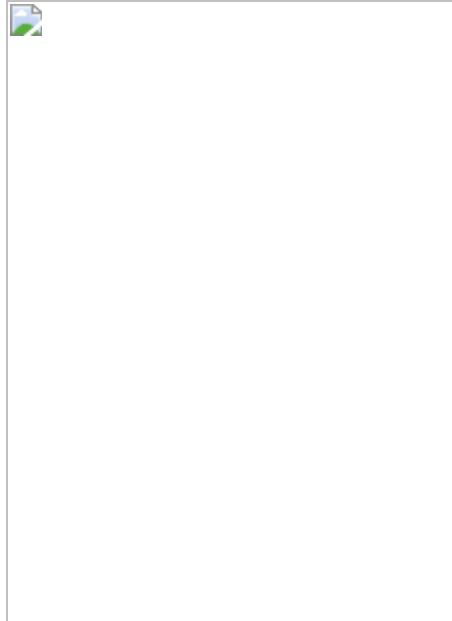


Fig. 2: Water clouds and thermal emission horizontal maps.



Fig. 3: Mechanisms of nocturnal cloud formation.

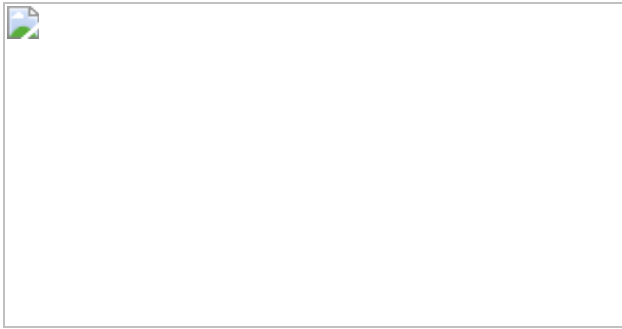
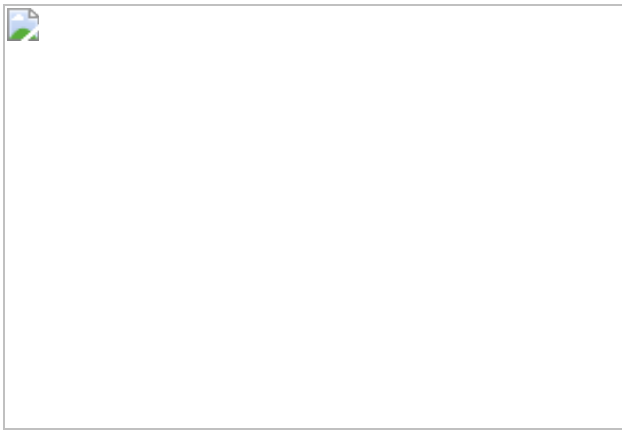


Fig. 4: Hysteresis loops and conditions of ocean formation on Earth and Venus.



Data availability

The data that support the findings of this study are available at <https://doi.org/10.5281/zenodo.4680905>. [Source data](#) are provided with this paper.

Code availability

The LMD Generic global climate model code (and documentation on how to use the model) used in this work can be downloaded from the SVN repository at <https://svn.lmd.jussieu.fr/Planeto/trunk/LMDZ.GENERIC/> (version 2528). More information and documentation are available at <http://www-planets.lmd.jussieu.fr>.

References

1. 1.

Catling, D. C. & Zahnle, K. J. The Archean atmosphere. *Sci. Adv.* **6**, eaax1420 (2020).

2. 2.

Haberle, R. M., Catling, D. C., Carr, M. H. & Zahnle, K. J. in *The Atmosphere and Climate of Mars* (eds Haberle, R. M. et al.) 526–568 (Cambridge Planetary Science, Cambridge Univ. Press, 2017).

3. 3.

Hamano, K., Abe, Y. & Genda, H. Emergence of two types of terrestrial planet on solidification of magma ocean. *Nature* **497**, 607–610 (2013).

4. 4.

Way, M. J. et al. Was Venus the first habitable world of our Solar System? *Geophys. Res. Lett.* **43**, 8376–8383 (2016).

5. 5.

Bézard, B. & de Bergh, C. Composition of the atmosphere of Venus below the clouds. *J. Geophys. Res. Planets* **112**, E04S07 (2007).

6. 6.

Phillips, R. J. et al. Impact craters and Venus resurfacing history. *J. Geophys. Res.* **97**, 15923–15948 (1992).

7. 7.

Kreslavsky, M. A., Ivanov, M. A. & Head, J. W. The resurfacing history of Venus: constraints from buffered crater densities. *Icarus* **250**, 438–450 (2015).

8. 8.

Wordsworth, R. D., Kerber, L., Pierrehumbert, R. T., Forget, F. & Head, J. W. Comparison of “warm and wet” and “cold and icy” scenarios for early Mars in a 3-D climate model. *J. Geophys. Res. Planets* **120**, 1201–1219 (2015).

9. 9.

Wordsworth, R. D. The climate of early Mars. *Annu. Rev. Earth Planet. Sci.* **44**, 381–408 (2016).

10. 10.

Kite, E. S. Geologic constraints on early Mars climate. *Space Sci. Rev.* **215**, 10 (2019).

11. 11.

Way, M. J. & Del Genio, A. D. Venusian habitable climate scenarios: modeling Venus through time and applications to slowly rotating Venus-like exoplanets. *J. Geophys. Res. Planets* **125**, e06276 (2020).

12. 12.

de Bergh, C. et al. Deuterium on Venus: observations from Earth. *Science* **251**, 547–549 (1991).

13. 13.

Marcq, E., Mills, F. P., Parkinson, C. D. & Vandaele, A. C. Composition and chemistry of the neutral atmosphere of Venus. *Space Sci. Rev.* **214**, 10 (2018).

14. 14.

Kasting, J. F. & Pollack, J. B. Loss of water from Venus. I. Hydrodynamic escape of hydrogen. *Icarus* **53**, 479–508 (1983).

15. 15.

Kasting, J. F. Runaway and moist greenhouse atmospheres and the evolution of Earth and Venus. *Icarus* **74**, 472–494 (1988).

16. 16.

Salvador, A. et al. The relative influence of H₂O and CO₂ on the primitive surface conditions and evolution of rocky planets. *J. Geophys. Res. Planets* **122**, 1458–1486 (2017).

17. 17.

Charnay, B. et al. Exploring the faint young Sun problem and the possible climates of the Archean Earth with a 3-D GCM. *J. Geophys. Res. Atmos.* **118**, 10414–10431 (2013).

18. 18.

Wolf, E. T. & Toon, E. B. Hospitable Archean climates simulated by a general circulation model. *Astrobiology* **13**, 656–673 (2013).

19. 19.

Leconte, J., Forget, F., Charnay, B., Wordsworth, R. & Pottier, A. Increased insolation threshold for runaway greenhouse processes on Earth-like planets. *Nature* **504**, 268–280 (2013).

20. 20.

Wolf, E. T. & Toon, O. B. Delayed onset of runaway and moist greenhouse climates for Earth. *Geophys. Res. Lett.* **41**, 167–172 (2014).

21. 21.

Charnay, B., Wolf, E. T., Marty, B. & Forget, F. Is the faint young Sun problem for Earth solved? *Space Sci. Rev.* **216**, 90 (2020).

22. 22.

Pierrehumbert, R. T. Thermostats, radiator fins, and the local runaway greenhouse. *J. Atmos. Sci.* **52**, 1784–1806 (1995).

23. 23.

Elkins-Tanton, L. T. Linked magma ocean solidification and atmospheric growth for Earth and Mars. *Earth Planet. Sci. Lett.* **271**, 181–191 (2008).

24. 24.

Lebrun, T. et al. Thermal evolution of an early magma ocean in interaction with the atmosphere. *J. Geophys. Res. Planets* **118**, 1155–1176 (2013).

25. 25.

Kopparapu, R. K. et al. habitable moist atmospheres on terrestrial planets near the inner edge of the habitable zone around M dwarfs. *Astrophys. J.* **845**, 5 (2017).

26. 26.

Fujii, Y., Del Genio, A. D. & Amundsen, D. S. NIR-driven moist upper atmospheres of synchronously rotating temperate terrestrial exoplanets. *Astrophys. J.* **848**, 100 (2017).

27. 27.

Kopparapu, R. K. et al. Habitable zones around main-sequence stars: new estimates. *Astrophys. J.* **765**, 131 (2013).

28. 28.

Goldblatt, C., Robinson, T. D., Zahnle, K. J. & Crisp, D. Low simulated radiation limit for runaway greenhouse climates. *Nat. Geosci.* **6**, 661–667 (2013).

29. 29.

Turbet, M., Ehrenreich, D., Lovis, C., Bolmont, E. & Fauchez, T. The runaway greenhouse radius inflation effect—an observational diagnostic to probe water on earth-sized planets and test the habitable zone concept. *Astron. Astrophys.* **628**, A12 (2019).

30. 30.

Jansen, T., Scharf, C., Way, M. & Del Genio, A. Climates of warm Earth-like planets. II. Rotational “Goldilocks” zones for fractional habitability and silicate weathering. *Astrophys. J.* **875**, 79 (2019).

31. 31.

Yang, J., Cowan, N. B. & Abbot, D. S. Stabilizing cloud feedback dramatically expands the habitable zone of tidally locked planets. *Astrophys. J. Lett.* **771**, L45 (2013).

32. 32.

Yang, J., Boué, G., Fabrycky, D. C. & Abbot, D. S. Strong dependence of the inner edge of the habitable zone on planetary rotation rate. *Astrophys. J. Lett.* **787**, L2 (2014).

33. 33.

Kopparapu, R. K. et al. The inner edge of the habitable zone for synchronously rotating planets around low-mass stars using general circulation models. *Astrophys. J.* **819**, 84 (2016).

34. 34.

Fauchez, T. J. et al. TRAPPIST Habitable Atmosphere Intercomparison (THAI) workshop report. *Planet. Sci. J.* **2**, 106 (2021).

35. 35.

Grinspoon, D. H. Was Venus wet? Deuterium reconsidered. *Science* **238**, 1702–1704 (1987).

36. 36.

Grinspoon, D. H. Implications of the high D/H ratio for the sources of water in Venus' atmosphere. *Nature* **363**, 428–431 (1993).

37. 37.

Gurwell, M. A. Evolution of deuterium on Venus. *Nature* **378**, 22–23 (1995).

38. 38.

Gillmann, C. et al. Dry late accretion inferred from Venus's coupled atmosphere and internal evolution. *Nat. Geosci.* **13**, 265–269 (2020).

39. 39.

Persson, M. et al. The Venusian atmospheric oxygen ion escape: extrapolation to the early Solar System. *J. Geophys. Res. Planets* **125**, e06336 (2020).

40. 40.

Lichtenegger, H. I. M. et al. Solar XUV and ENA-driven water loss from early Venus' steam atmosphere. *J. Geophys. Res. Space Phys.* **121**, 4718–4732 (2016).

41. 41.

Lammer, H. et al. Origin and evolution of the atmospheres of early Venus, Earth and Mars. *Astron. Astrophys. Rev.* **26**, 2 (2018).

42. 42.

Hoffman, P. F., Kaufman, A. J., Halverson, G. P. & Schrag, D. P. A Neoproterozoic snowball Earth. *Science* **281**, 1342–1346 (1998).

43. 43.

Shields, A. L., Bitz, C. M., Meadows, V. S., Joshi, M. M. & Robinson, T. D. Spectrum-driven planetary deglaciation due to increases in stellar luminosity. *Astrophys. J. Lett.* **785**, L9 (2014).

44. 44.

Hourdin, F. et al. The LMDZ4 general circulation model: climate performance and sensitivity to parametrized physics with emphasis on tropical convection. *Clim. Dyn.* **27**, 787–813 (2006).

45. 45.

Forget, F. et al. Improved general circulation models of the Martian atmosphere from the surface to above 80 km. *J. Geophys. Res.* **104**, 24155–24176 (1999).

46. 46.

Forget, F. et al. 3D modelling of the early Martian climate under a denser CO₂ atmosphere: temperatures and CO₂ ice clouds. *Icarus* **222**, 81–99 (2013).

47. 47.

Wordsworth, R. et al. Global modelling of the early Martian climate under a denser CO₂ atmosphere: water cycle and ice evolution. *Icarus* **222**, 1–19 (2013).

48. 48.

Turbet, M., Forget, F., Leconte, J., Charnay, B. & Tobie, G. CO₂ condensation is a serious limit to the deglaciation of Earth-like planets. *Earth Planet. Sci. Lett.* **476**, 11–21 (2017).

49. 49.

Turbet, M. et al. The environmental effects of very large bolide impacts on early Mars explored with a hierarchy of numerical models.

Icarus **335**, 113419 (2020).

50. 50.

Wordsworth, R. D. et al. Gliese 581d is the first discovered terrestrial-mass exoplanet in the habitable zone. *Astrophys. J. Lett.* **733**, L48 (2011).

51. 51.

Leconte, J. et al. 3D climate modeling of close-in land planets: circulation patterns, climate moist bistability, and habitability. *Astron. Astrophys.* **554**, A69 (2013).

52. 52.

Turbet, M. et al. Modeling climate diversity, tidal dynamics and the fate of volatiles on TRAPPIST-1 planets. *Astron. Astrophys.* **612**, A86 (2018).

53. 53.

Fu, Q. & Liou, K. N. On the correlated k-distribution method for radiative transfer in nonhomogeneous atmospheres. *J. Atmos. Sci.* **49**, 2139–2156 (1992).

54. 54.

Karman, T. et al. Update of the HITRAN collision-induced absorption section. *Icarus* **328**, 160–175 (2019).

55. 55.

Mlawer, E. J. et al. Development and recent evaluation of the MT CKD model of continuum absorption. *Phil. Trans. R. Soc. Lond. A* **370**, 2520–2556 (2012).

56. 56.

Rothman, L. S. et al. The HITRAN 2008 molecular spectroscopic database. *J. Quant. Spectrosc. Radiat. Transf.* **110**, 533–572 (2009).

57. 57.

Rothman, L. S. et al. HITEMP, the high-temperature molecular spectroscopic database. *J. Quant. Spectrosc. Radiat. Transf.* **111**, 2139–2150 (2010).

58. 58.

Mellor, G. L. & Yamada, T. Development of a turbulence closure model for geophysical fluid problems. *Rev. Geophys. Space Phys.* **20**, 851–875 (1982).

59. 59.

Galperin, B., Kantha, L. H., Hassid, S. & Rosati, A. A quasi-equilibrium turbulent energy model for geophysical flows. *J. Atmos. Sci.* **45**, 55–62 (1988).

60. 60.

Manabe, S. & Wetherald, R. Thermal equilibrium of the atmosphere with a given distribution of relative humidity. *J. Atmos. Sci.* **24**, 241–259 (1967).

61. 61.

Charnay, B. *Tropospheric Dynamics and Climatic Evolution of Titan and the Early Earth*. PhD thesis, Univ. Pierre et Marie Curie - Paris VI (2014); <https://tel.archives-ouvertes.fr/tel-00987546>

62. 62.

Wallace, J. M. & Hobbs, P. V. in *Atmospheric Science* 2nd edn (eds Wallace, J. M. & Hobbs, P. V.) 209–269 (Academic, 2006).

63. 63.

Charnay, B. et al. Formation and dynamics of water clouds on temperate sub-Neptunes: the example of K2-18b. *Astron. Astrophys.* **646**, A171 (2021).

64. 64.

Boucher, O., Le Treut, H. & Baker, M. B. Precipitation and radiation modeling in a general circulation model: introduction of cloud microphysical processes. *J. Geophys. Res.* **100**, 16395–16414 (1995).

65. 65.

Gregory, D. A consistent treatment of the evaporation of rain and snow for use in large-scale models. *Mon. Weather Rev.* **123**, 2716–2732 (1995).

66. 66.

Rossow, W. B. Cloud microphysics—analysis of the clouds of Earth, Venus, Mars, and Jupiter. *Icarus* **36**, 1–50 (1978).

67. 67.

Nakajima, S., Hayashi, Y.-Y. & Abe, Y. A study on the 'runaway greenhouse effect' with a one-dimensional radiative-convective equilibrium model. *J. Atmos. Sci.* **49**, 2256–2266 (1992).

68. 68.

Goldblatt, C. & Watson, A. J. The runaway greenhouse: implications for future climate change, geoengineering and planetary atmospheres. *Phil. Trans. R. Soc. Lond. A* **370**, 4197–4216 (2012).

69. 69.

Marcq, E., Salvador, A., Massol, H. & Davaille, A. Thermal radiation of magma ocean planets using a 1-D radiative-convective model of

$\text{H}_2\text{O}-\text{CO}_2$ atmospheres. *J. Geophys. Res. Planets* **122**, 1539–1553 (2017).

70. 70.

Massol, H. et al. Formation and evolution of protoatmospheres. *Space Sci. Rev.* **205**, 153–211 (2016).

71. 71.

Pluriel, W., Marcq, E. & Turbet, M. Modeling the albedo of Earth-like magma ocean planets with $\text{H}_2\text{O}-\text{CO}_2$ atmospheres. *Icarus* **317**, 583–590 (2019).

Acknowledgements

This project has received funding from the European Union’s Horizon 2020 research and innovation programme under the Marie Skłodowska-Curie grant agreement number 832738/ESCAPE. This project has received funding from the European Research Council (ERC) under the European Union’s Horizon 2020 research and innovation programme (grant agreement numbers 724427/FOUR ACES and 679030/WHIPLASH). This work has been carried out within the framework of the National Centre of Competence in Research PlanetS supported by the Swiss National Science Foundation. We acknowledge the financial support of the SNSF. M.T. thanks the Gruber Foundation for its support to this research. M.T. thanks N. Chaniaud for her help in preparing Fig. 1. We thank the LMD Generic global climate team for the teamwork development and improvement of the model. This work was performed using the high-performance computing resources of Centre Informatique National de l’Enseignement Supérieur (CINES) under the allocation A0080110391 made by Grand Équipement National de Calcul Intensif (GENCI). A total of about 600,000 CPU hours were used for this project on the OCCIGEN supercomputer, resulting in roughly one ton equivalent of CO_2 emissions.

Author information

Affiliations

1. Observatoire astronomique de l'Université de Genève, Versoix,
Switzerland

Martin Turbet, Emeline Bolmont, Guillaume Chaverot & David Ehrenreich

2. Laboratoire d'astrophysique de Bordeaux, Université de Bordeaux,
CNRS, B18N, Pessac, France

Jérémy Leconte

3. LATMOS/IPSL, UVSQ, Université Paris-Saclay, Sorbonne Université,
CNRS, Guyancourt, France

Emmanuel Marcq

Contributions

M.T. developed the core ideas of the manuscript, developed and performed the 3D GCM simulations, wrote the manuscript and prepared the figures. E.B. and G.C. provided advice on sensitivity studies. D.E., G.C. and J.L. provided advice on the structure of the figures. J.L. provided advice on the organization of the manuscript, as well as for understanding the mechanism of cloud formation. E.M. provided advice on literature selection. All authors provided guidance and comments on the manuscript.

Corresponding author

Correspondence to Martin Turbet.

Ethics declarations

Competing interests

The authors declare no competing interests.

Additional information

Peer review information *Nature* thanks Stephen Kane, James Kasting and the other, anonymous, reviewer(s) for their contribution to the peer review of this work. Peer reviewer reports are available.

Publisher's note Springer Nature remains neutral with regard to jurisdictional claims in published maps and institutional affiliations.

Extended data figures and tables

[Extended Data Fig. 1 Temporal evolution of modelled surface temperatures.](#)

Temporal evolution of the globally averaged surface temperatures in the 3-D GCM baseline simulations of (initially hot and steamy) Venus, for several insolations.

[Extended Data Fig. 2 Cloud forcings in hot and steamy early Venus and Earth simulations.](#)

Radiative balance of clouds on hot and steamy Earth (**a**) and Venus (**b**) as a function of the incident solar flux. Blue curves indicate the greenhouse effect of clouds. Red curves indicate the amount of incoming solar radiation reflected back by the clouds (the more negative the value, the greater the reflected flux.). Black curves indicate the net radiative effect of clouds (positive values mean warming). In all initially hot and steamy simulations, clouds lead to a strong atmospheric warming.

[Source data](#)

[Extended Data Fig. 3 Radiative budget comparisons between 1D and 3D models.](#)

Thermal emission to space (**a**) and bond albedo (**b**) as a function of the surface temperature for our 3-D GCM simulations of Earth (blue) and Venus (red). We have also added the results of 1-D radiative-convective cloud-free calculations²⁹ (in black), using H₂O and N₂ partial pressures of 10 and 1 bar, respectively, as in the 3-D baseline simulations. For comparison, we added the moist tropospheric radiation limits⁶⁸ for the thermal emission⁶⁷ and the bond albedo from refs. ^{27,28}.

[Source data](#)

[Extended Data Fig. 4 Impact of cloud microphysical properties on their spatial distribution.](#)

Maps of water cloud column for early Venus (at a top-of-atmosphere insolance of 500 W m⁻², i.e. the minimal insolance received on Venus, about 4 billion years ago when the Sun was 25% fainter than today), with different cloud microphysics parameterisations (10³, 10⁴, 10⁵, 10⁶ and 10⁷ cloud condensation nuclei (CCN) per kg of air, for panels **a**, **b**, **c**, **d** and **e**, respectively). The maps were calculated in the heliocentric frame (i.e., keeping the subsolar point at 0° longitude and 0° latitude), and using an average of two Venusian days. The distribution of clouds (present on the nightside, absent on the dayside) is robust to the choice of the number of CCN.

[Source data](#)

[Extended Data Fig. 5 Effects of water and carbon dioxide atmospheric contents.](#)

Impact of the water and carbon dioxide atmospheric contents on the surface temperature (a), thermal emission to space (b), bond albedo (c) and net cloud radiative forcing (d). The calculations assume a hot and steamy Venus (insolation at 500 W/m²) with 1 bar of N₂ and between 1 and 30 bar of H₂O (in blue); with 1-10 bar of CO₂ and 10 bar of H₂O (in red).

Extended Data Table 1 Summary of the main physical parameters used in the GCM for the baseline hot and steamy Earth and Venus simulations

Supplementary information

[Peer Review File](#)

Source data

[Source Data Fig. 4.](#)

[Source Data Extended Data Fig. 2.](#)

[Source Data Extended Data Fig. 3.](#)

[Source Data Extended Data Fig. 4.](#)

Rights and permissions

[Reprints and Permissions](#)

About this article

Cite this article

Turbet, M., Bolmont, E., Chaverot, G. *et al.* Day–night cloud asymmetry prevents early oceans on Venus but not on Earth. *Nature* **598**, 276–280 (2021). <https://doi.org/10.1038/s41586-021-03873-w>

- Received: 31 March 2021
- Accepted: 03 August 2021
- Published: 13 October 2021

- Issue Date: 14 October 2021
- DOI: <https://doi.org/10.1038/s41586-021-03873-w>

Share this article

Anyone you share the following link with will be able to read this content:

[Get shareable link](#)

Sorry, a shareable link is not currently available for this article.

[Copy to clipboard](#)

Provided by the Springer Nature SharedIt content-sharing initiative

Venus might never have been habitable

- James F. Kasting
- Chester E. Harman

News & Views 13 Oct 2021

This article was downloaded by **calibre** from <https://www.nature.com/articles/s41586-021-03873-w>

| [Section menu](#) | [Main menu](#) |

- Article
- [Published: 04 October 2021](#)

Fault-tolerant control of an error-corrected qubit

- [Laird Egan](#) [ORCID: orcid.org/0000-0003-2405-9106](#)^{1,2 nAff10},
- [Dipto M. Debroy](#)^{4 nAff11},
- [Crystal Noel](#)^{1,2},
- [Andrew Risinger](#)^{1,2,3},
- [Daiwei Zhu](#)^{1,2,3},
- [Debopriyo Biswas](#) [ORCID: orcid.org/0000-0003-2720-5279](#)^{1,2},
- [Michael Newman](#)^{5 nAff11},
- [Muyuan Li](#)^{6,7},
- [Kenneth R. Brown](#) [ORCID: orcid.org/0000-0001-7716-1425](#)^{4,5,6,7,8},
- [Marko Cetina](#)^{1,2} &
- [Christopher Monroe](#)^{1,2,3,4,5,9}

[Nature](#) volume **598**, pages 281–286 (2021)

- 5325 Accesses
- 231 Altmetric
- [Metrics details](#)

Subjects

- [Quantum information](#)
- [Qubits](#)

Abstract

Quantum error correction protects fragile quantum information by encoding it into a larger quantum system^{1,2}. These extra degrees of freedom enable the detection and correction of errors, but also increase the control complexity of the encoded logical qubit. Fault-tolerant circuits contain the spread of errors while controlling the logical qubit, and are essential for realizing error suppression in practice^{3,4,5,6}. Although fault-tolerant design works in principle, it has not previously been demonstrated in an error-corrected physical system with native noise characteristics. Here we experimentally demonstrate fault-tolerant circuits for the preparation, measurement, rotation and stabilizer measurement of a Bacon–Shor logical qubit using 13 trapped ion qubits. When we compare these fault-tolerant protocols to non-fault-tolerant protocols, we see significant reductions in the error rates of the logical primitives in the presence of noise. The result of fault-tolerant design is an average state preparation and measurement error of 0.6 per cent and a Clifford gate error of 0.3 per cent after offline error correction. In addition, we prepare magic states with fidelities that exceed the distillation threshold⁷, demonstrating all of the key single-qubit ingredients required for universal fault-tolerant control. These results demonstrate that fault-tolerant circuits enable highly accurate logical primitives in current quantum systems. With improved two-qubit gates and the use of intermediate measurements, a stabilized logical qubit can be achieved.

Access options

Subscribe to Journal

Get full journal access for 1 year

\$199.00

only \$3.90 per issue

[Subscribe](#)

All prices are NET prices.

VAT will be added later in the checkout.

Tax calculation will be finalised during checkout.

Rent or Buy article

Get time limited or full article access on ReadCube.

from \$8.99

[Rent or Buy](#)

All prices are NET prices.

Additional access options:

- [Log in](#)
- [Access through your institution](#)
- [Learn about institutional subscriptions](#)

Fig. 1: The Bacon–Shor subsystem code implemented on a 15-ion chain.

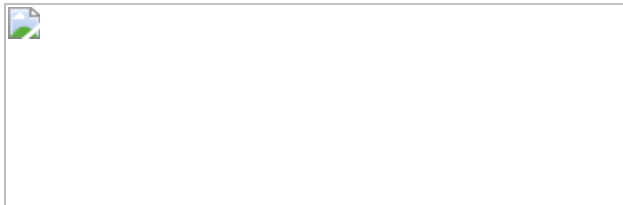


Fig. 2: Fault-tolerant logical qubit-state preparation.

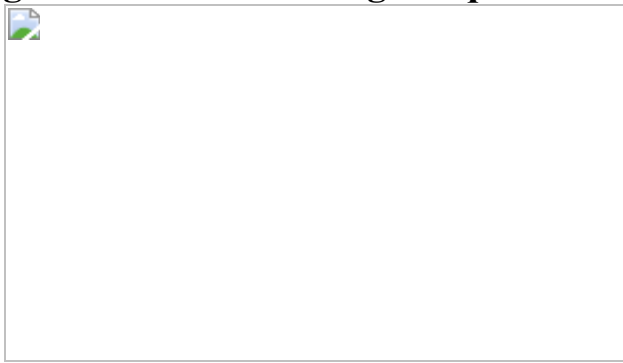


Fig. 3: Manipulating logical states.

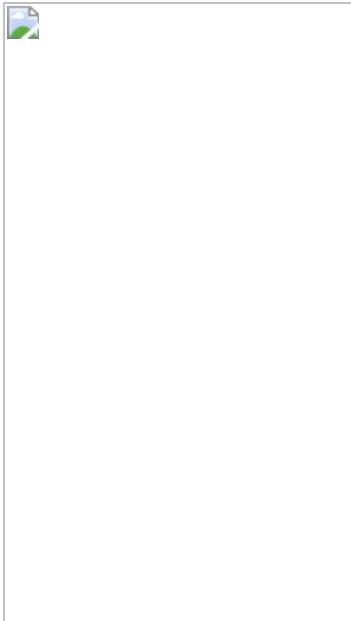
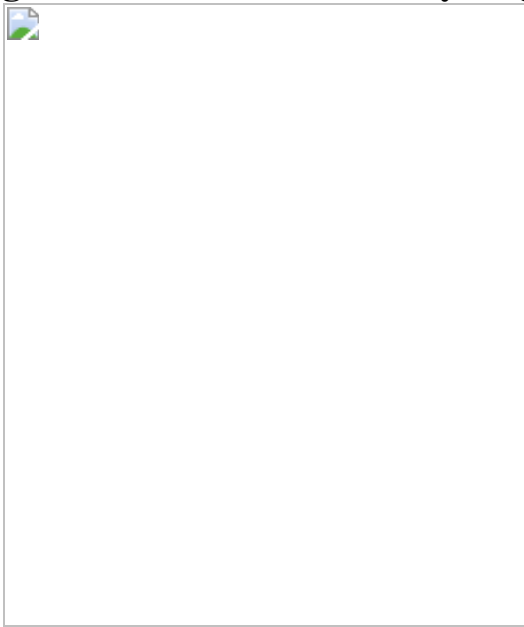


Fig. 4: Detection of arbitrary single-qubit errors.



Data availability

The data that support the findings of this study are available from the corresponding author upon request. [Source data](#) are provided with this paper.

Code availability

The code used for the analyses is available from the corresponding author upon request.

References

1. 1.
Shor, P. W. Scheme for reducing decoherence in quantum computer memory. *Phys. Rev. A* **52**, R2493 (1995).
2. 2.
Knill, E. & Laflamme, R. Theory of quantum error-correcting codes. *Phys. Rev. A* **55**, 900–911 (1997).
3. 3.
Shor, P. W. Fault-tolerant quantum computation. In *Proc. 37th Conference on Foundations of Computer Science* (1996).
4. 4.
Knill, E., Laflamme, R. & Zurek, W. Threshold accuracy for quantum computation. Preprint at <https://arxiv.org/abs/quant-ph/9610011> (1996).
5. 5.
Gottesman, D. Theory of fault-tolerant quantum computation. *Phys. Rev. A* **57**, 127–137 (1998).
6. 6.
Aharonov, D. & Ben-Or, M. Fault-tolerant quantum computation with constant error rate. *SIAM J. Comput.* (2008).
7. 7.

Bravyi, S. & Kitaev, A. Universal quantum computation with ideal Clifford gates and noisy ancillas. *Phys. Rev. A* **71**, 022316 (2005).

8. 8.

Feynman, R. P. Quantum mechanical computers. *Found. Phys.* **16**, 507–531 (1986).

9. 9.

Abrams, D. S. & Lloyd, S. Simulation of many-body Fermi systems on a universal quantum computer. *Phys. Rev. Lett.* **79**, 2586–2589 (1997).

10. 10.

Aspuru-Guzik, A., Dutoi, A. D., Love, P. J. & Head-Gordon, M. Simulated quantum computation of molecular energies. *Science* **309**, 1704–1707 (2005).

11. 11.

Reiher, M., Wiebe, N., Svore, K. M., Wecker, D. & Troyer, M. Elucidating reaction mechanisms on quantum computers. *Proc. Natl Acad. Sci. USA* **114**, 7555–7560 (2017).

12. 12.

Shor, P. W. Polynomial-time algorithms for prime factorization and discrete logarithms on a quantum computer. *SIAM Rev.* **41**, 303–332 (1999).

13. 13.

Von Burg, V. et al. Quantum computing enhanced computational catalysis. Preprint at <https://arxiv.org/abs/2007.14460> (2020).

14. 14.

Gidney, C. & Ekerå, M. How to factor 2048 bit RSA integers in 8 hours using 20 million noisy qubits. Preprint at <https://arxiv.org/abs/1905.09749> (2019).

15. 15.

Gottesman, D. E. *Stabilizer Codes and Quantum Error Correction*. PhD thesis, California Institute of Technology (1997).

16. 16.

Córcoles, A. D. et al. Demonstration of a quantum error detection code using a square lattice of four superconducting qubits. *Nat. Commun.* **6**, 6979 (2015).

17. 17.

Takita, M., Cross, A. W., Córcoles, A. D., Chow, J. M. & Gambetta, J. M. Experimental demonstration of fault-tolerant state preparation with superconducting qubits. *Phys. Rev. Lett.* **119**, 180501 (2017).

18. 18.

Linke, N. M. et al. Fault-tolerant quantum error detection. *Sci. Adv.* **3**, e1701074 (2017).

19. 19.

Harper, R. & Flammia, S. T. Fault-tolerant logical gates in the IBM quantum experience. *Phys. Rev. Lett.* **122**, 080504 (2019).

20. 20.

Andersen, C. K. et al. Repeated quantum error detection in a surface code. *Nat. Phys.* **16**, 875–880 (2020).

21. 21.

Cory, D. G. et al. Experimental quantum error correction. *Phys. Rev. Lett.* **81**, 2152–2155 (1998).

22. 22.

Chiaverini, J. et al. Realization of quantum error correction. *Nature* **432**, 602–605 (2004).

23. 23.

Schindler, P. et al. Experimental repetitive quantum error correction. *Science* **332**, 1059–1061 (2011).

24. 24.

Reed, M. D. et al. Realization of three-qubit quantum error correction with superconducting circuits. *Nature* **482**, 382–385 (2012).

25. 25.

Riste, D. et al. Detecting bit-flip errors in a logical qubit using stabilizer measurements. *Nat. Commun.* **6**, 6983 (2015).

26. 26.

Kelly, J. et al. State preservation by repetitive error detection in a superconducting quantum circuit. *Nature* **519**, 66–69 (2015).

27. 27.

Gong, M. et al. Experimental verification of five-qubit quantum error correction with superconducting qubits. Preprint at <https://arxiv.org/abs/1907.04507> (2019).

28. 28.

Nigg, D. et al. Quantum computations on a topologically encoded qubit. *Science* **345**, 302–305 (2014).

29. 29.

Luo, Y. H. et al. Quantum teleportation of physical qubits into logical code-spaces. Preprint at <https://arxiv.org/abs/2009.06242> (2020).

30. 30.

Heeres, R. W. et al. Implementing a universal gate set on a logical qubit encoded in an oscillator. *Nat. Commun.* **8**, 94 (2017).

31. 31.

Flühmann, C. et al. Encoding a qubit in a trapped-ion mechanical oscillator. *Nature* **566**, 513–517 (2019).

32. 32.

Ofek, N. et al. Extending the lifetime of a quantum bit with error correction in superconducting circuits. *Nature* **536**, 441–445 (2016).

33. 33.

Campagne-Ibarcq, P. et al. Quantum error correction of a qubit encoded in grid states of an oscillator. *Nature* **584**, 368–372 (2020).

34. 34.

de Neeve, B., Nguyen, T. L., Behrle, T. & Home, J. Error correction of a logical grid state qubit by dissipative pumping. Preprint at <https://arxiv.org/abs/2010.09681> (2020).

35. 35.

Wilhelm Maunz, P. L. *High Optical Access Trap 2.0* Report No. SAND2016-0796R (Sandia National Laboratories, 2016).

36. 36.

Debnath, S. et al. Demonstration of a small programmable quantum computer with atomic qubits. *Nature* **563**, 63–66 (2016).

37. 37.

Wright, K. et al. Benchmarking an 11-qubit quantum computer. *Nat. Commun.* **10**, 5464 (2019).

38. 38.

Bacon, D. Operator quantum error-correcting subsystems for self-correcting quantum memories. *Phys. Rev. A* **73**, 012340 (2006).

39. 39.

Aliferis, P. & Cross, A. W. Subsystem fault tolerance with the Bacon–Shor code. *Phys. Rev. Lett.* **98**, 220502 (2007).

40. 40.

Debroy, D. M., Li, M., Huang, S. & Brown, K. R. Logical performance of 9 qubit compass codes in ion traps with crosstalk errors. *Quantum Sci. Technol.* **5**, 034002 (2020).

41. 41.

Li, M., Miller, D. & Brown, K. R. Direct measurement of Bacon–Shor code stabilizers. *Phys. Rev. A* **98**, 050301 (2018).

42. 42.

Terhal, B. M. Quantum error correction for quantum memories. *Rev. Mod. Phys.* **87**, 307–346 (2015).

43. 43.

Dennis, E., Kitaev, A., Landahl, A. & Preskill, J. Topological quantum memory. *J. Math. Phys.* **43**, 4452–4505 (2002).

44. 44.

Li, M., Miller, D., Newman, M., Wu, Y. & Brown, K. R. 2D compass codes. *Phys. Rev.* **9**, 021041 (2019).

45. 45.

Reichardt, B. W. Quantum universality from magic states distillation applied to CSS codes. *Quantum Inf. Process.* **4**, 251–264 (2005).

46. 46.

Lidar, D. A., Chuang, I. L. & Whaley, K. B. Decoherence-free subspaces for quantum computation. *Phys. Rev. Lett.* **81**, 2594–2597 (1998).

47. 47.

Kielpinski, D et al. A decoherence-free quantum memory using trapped ions. *Science* **291**, 1013–1015 (2001).

48. 48.

Hu, J., Liang, Q., Rengaswamy, N. & Calderbank, R. Mitigating coherent noise by balancing weight-2z-stabilizers. Preprint at <https://arxiv.org/abs/2011.00197> (2020).

49. 49.

Eastin, B. & Knill, E. Restrictions on transversal encoded quantum gate sets. *Phys. Rev. Lett.* **102**, 110502 (2009).

50. 50.

Cetina, M. et al. Quantum gates on individually-addressed atomic qubits subject to noisy transverse motion. Preprint at <https://arxiv.org/abs/2007.06768> (2020).

51. 51.

Kielpinski, D., Monroe, C. & Wineland, D. J. Architecture for a large-scale ion-trap quantum computer. *Nature* **417**, 709–711 (2002).

52. 52.

Home, J. P. et al. Complete methods set for scalable ion trap quantum information processing. *Science* **325**, 1227–1230 (2009).

53. 53.

Pino, J. M. et al. Demonstration of the QCCD trapped-ion quantum computer architecture. Preprint at <https://arxiv.org/abs/2003.01293> (2020).

54. 54.

Brown, K. R., Harrow, A. W. & Chuang, I. L. Arbitrarily accurate composite pulse sequences. *Phys. Rev. A* **70**, 052318 (2004).

55. 55.

Mølmer, K. & Sørensen, A. Multiparticle entanglement of hot trapped ions. *Phys. Rev. Lett.* **82**, 1835–1838 (1999).

56. 56.

Maslov, D. Basic circuit compilation techniques for an ion-trap quantum machine. *New J. Phys.* **19**, 023035 (2017).

Acknowledgements

This work was performed at the University of Maryland with no material support from IonQ. We acknowledge discussions with N. M. Linke and the contributions of J. Mizrahi, K. Hudek, J. Amini, K. Beck and M. Goldman to the experimental setup. This work is supported by the ARO through the IARPA LogiQ programme, the NSF STAQ Program, the AFOSR MURIs on Dissipation Engineering in Open Quantum Systems and Quantum Interactive Protocols for Quantum Computation, and the ARO MURI on

Modular Quantum Circuits. L.E. and D.M.D. are also funded by NSF award DMR-1747426.

Author information

Author notes

1. Laird Egan

Present address: IonQ, Inc, College Park, MD, USA

2. Dripto M. Debroy & Michael Newman

Present address: Google Research, Venice, CA, USA

Affiliations

1. Joint Quantum Institute, Center for Quantum Information and Computer Science, University of Maryland, College Park, MD, USA

Laird Egan, Crystal Noel, Andrew Risinger, Daiwei Zhu, Debopriyo Biswas, Marko Cetina & Christopher Monroe

2. Department of Physics, University of Maryland, College Park, MD, USA

Laird Egan, Crystal Noel, Andrew Risinger, Daiwei Zhu, Debopriyo Biswas, Marko Cetina & Christopher Monroe

3. Department of Electrical and Computer Engineering, University of Maryland, College Park, MD, USA

Andrew Risinger, Daiwei Zhu & Christopher Monroe

4. Department of Physics, Duke University, Durham, NC, USA

Dripto M. Debroy, Kenneth R. Brown & Christopher Monroe

5. Department of Electrical and Computer Engineering, Duke University,
Durham, NC, USA

Michael Newman, Kenneth R. Brown & Christopher Monroe

6. School of Chemistry and Biochemistry, Georgia Institute of
Technology, Atlanta, GA, USA

Muyuan Li & Kenneth R. Brown

7. School of Computational Science and Engineering, Georgia Institute
of Technology, Atlanta, GA, USA

Muyuan Li & Kenneth R. Brown

8. Department of Chemistry, Duke University, Durham, NC, USA

Kenneth R. Brown

9. IonQ, Inc, College Park, MD, USA

Christopher Monroe

Contributions

L.E. collected and analysed the data. L.E., D.M.D., C.N. and M.N. wrote the manuscript and designed figures. M.C. and C.M. led construction of the experimental apparatus with contributions from L.E., C.N., A.R., D.Z. and D.B. Theory support was provided by D.M.D., M.N., M.L. and K.R.B. C.M. and K.R.B. supervised the project. All authors discussed results and contributed to the manuscript.

Corresponding author

Correspondence to Laird Egan.

Ethics declarations

Competing interests

K.R.B. is a scientific advisor for IonQ, Inc. and has a personal financial interest in the company.

Additional information

Peer review information *Nature* thanks Daniel Gottesman, Jonathan Home, Philipp Schindler and the other, anonymous, reviewer(s) for their contribution to the peer review of this work.

Publisher's note Springer Nature remains neutral with regard to jurisdictional claims in published maps and institutional affiliations.

Extended data figures and tables

Extended Data Fig. 1 Stabilizer measurement circuits.

a, b, Non-fault-tolerant (**a**, red, right) and fault-tolerant (**b**, blue, right) stabilizer measurement orderings, performed on a FT-encoded $|0\rangle$ state (**a, b**, blue, left). In both cases, a variable error $Z(\theta)$ is introduced on the ancilla qubit in the middle of the stabilizer measurement operation. These circuits were used to generate the data in Fig. [2a](#). **c**, Direct measurement of the full error syndrome. Various single-qubit ‘errors’ are introduced on any one of the data qubits to generate different ancilla measurement outcomes. This circuit was used to generate the data in Fig. [2b](#).

Supplementary information

Supplementary Information

This file contains Supplementary Information, including Supplementary Figs. 1–16, Tables 1–5 and additional references.

Source data

[Source Data Fig. 2](#)

[Source Data Fig. 3](#)

[Source Data Fig. 4](#)

Rights and permissions

[Reprints and Permissions](#)

About this article

Cite this article

Egan, L., Debroy, D.M., Noel, C. *et al.* Fault-tolerant control of an error-corrected qubit. *Nature* **598**, 281–286 (2021).
<https://doi.org/10.1038/s41586-021-03928-y>

- Received: 23 September 2020
- Accepted: 18 August 2021
- Published: 04 October 2021
- Issue Date: 14 October 2021
- DOI: <https://doi.org/10.1038/s41586-021-03928-y>

Share this article

Anyone you share the following link with will be able to read this content:

[Get shareable link](#)

Sorry, a shareable link is not currently available for this article.

[Copy to clipboard](#)

Provided by the Springer Nature SharedIt content-sharing initiative

This article was downloaded by **calibre** from <https://www.nature.com/articles/s41586-021-03928-y>.

| [Section menu](#) | [Main menu](#) |

- Article
- [Published: 13 October 2021](#)

Observation of fractional edge excitations in nanographene spin chains

- [Shantanu Mishra](#) ORCID: orcid.org/0000-0002-2900-4203^{1 na1 nAff9},
- [Gonçalo Catarina](#)^{2,3 na1},
- [Fupeng Wu](#)⁴,
- [Ricardo Ortiz](#)³,
- [David Jacob](#)^{5,6},
- [Kristjan Eimre](#) ORCID: orcid.org/0000-0002-3444-3286¹,
- [Ji Ma](#)⁴,
- [Carlo A. Pignedoli](#) ORCID: orcid.org/0000-0002-8273-6390¹,
- [Xinliang Feng](#) ORCID: orcid.org/0000-0003-3885-2703^{4,7},
- [Pascal Ruffieux](#) ORCID: orcid.org/0000-0001-5729-5354¹,
- [Joaquín Fernández-Rossier](#) ORCID: orcid.org/0000-0003-2297-0289² &
- [Roman Fasel](#) ORCID: orcid.org/0000-0002-1553-6487^{1,8}

Nature volume **598**, pages 287–292 (2021)

- 2880 Accesses
- 104 Altmetric
- [Metrics details](#)

Subjects

- [Magnetic properties and materials](#)
- [Scanning probe microscopy](#)
- [Surfaces, interfaces and thin films](#)
- [Synthesis and processing](#)

Abstract

Fractionalization is a phenomenon in which strong interactions in a quantum system drive the emergence of excitations with quantum numbers that are absent in the building blocks. Outstanding examples are excitations with charge $e/3$ in the fractional quantum Hall effect^{1,2}, solitons in one-dimensional conducting polymers^{3,4} and Majorana states in topological superconductors⁵. Fractionalization is also predicted to manifest itself in low-dimensional quantum magnets, such as one-dimensional antiferromagnetic $S=1$ chains. The fundamental features of this system are gapped excitations in the bulk⁶ and, remarkably, $S=1/2$ edge states at the chain termini^{7,8,9}, leading to a four-fold degenerate ground state that reflects the underlying symmetry-protected topological order^{10,11}. Here, we use on-surface synthesis¹² to fabricate one-dimensional spin chains that contain the $S=1$ polycyclic aromatic hydrocarbon triangulene as the building block. Using scanning tunnelling microscopy and spectroscopy at 4.5 K, we probe length-dependent magnetic excitations at the atomic scale in both open-ended and cyclic spin chains, and directly observe gapped spin excitations and fractional edge states therein. Exact diagonalization calculations provide conclusive evidence that the spin chains are described by the $S=1$ bilinear-biquadratic Hamiltonian in the Haldane symmetry-protected topological phase. Our results open a bottom-up approach to study strongly correlated phases in purely organic materials, with the potential for the realization of measurement-based quantum computation¹³.

Access options

Subscribe to Journal

Get full journal access for 1 year

\$199.00

only \$3.90 per issue

[Subscribe](#)

All prices are NET prices.

VAT will be added later in the checkout.

Tax calculation will be finalised during checkout.

Rent or Buy article

Get time limited or full article access on ReadCube.

from \$8.99

[Rent or Buy](#)

All prices are NET prices.

Additional access options:

- [Log in](#)
- [Access through your institution](#)
- [Learn about institutional subscriptions](#)

Fig. 1: On-surface synthesis of triangulene spin chains and observation of zero-energy edge excitations.

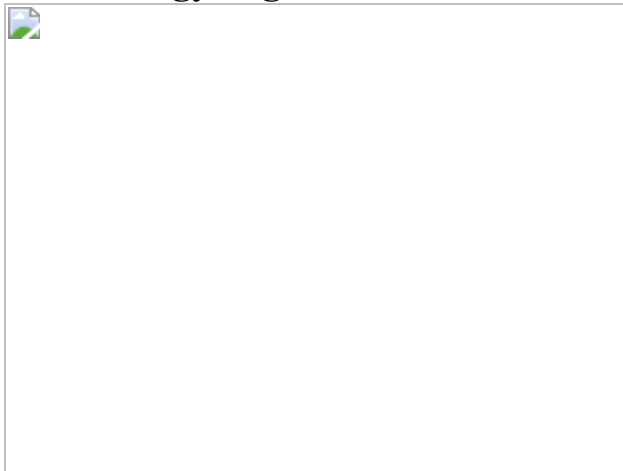


Fig. 2: The valence bond solid picture and theoretical calculations of spin excitations in open-ended triangulene spin chains.

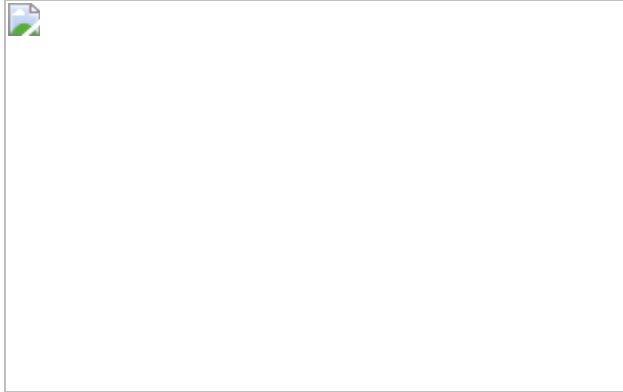


Fig. 3: Magnetic excitations in selected open-ended triangulene spin chains and comparison with the bilinear-biquadratic model.

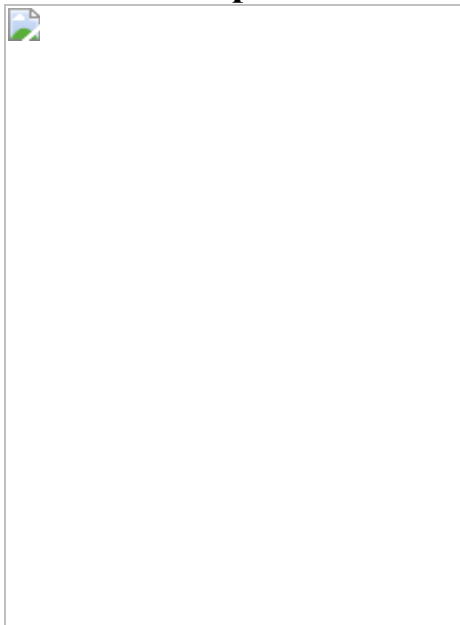
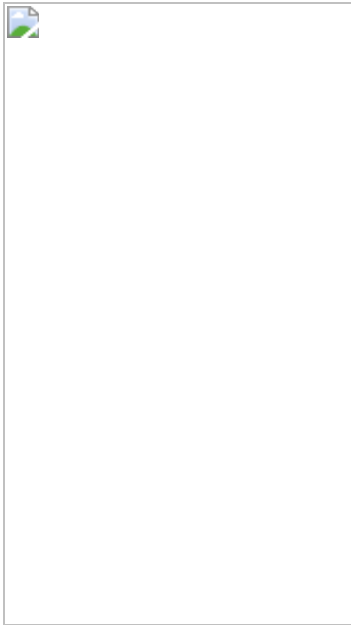


Fig. 4: Magnetic excitations in $N=6$ and 13 cyclic triangulene spin chains and comparison with the bilinear-biquadratic model.



Data availability

The data that support the findings of this study are available at the Materials Cloud platform (<https://doi.org/10.24435/materialscloud:e8-aq>).

Code availability

The custom-designed Python codes that were used for solving the bilinear-biquadratic spin Hamiltonian by exact diagonalization are available on the GitHub repository (https://github.com/GCatarina/ED_BLBQ). All other codes are available from J.F.R. (joaquin.fernandez-rossier@inl.int) upon reasonable request.

References

1. 1.

- Tsui, D. C., Stormer, H. L. & Gossard, A. C. Two-dimensional magnetotransport in the extreme quantum limit. *Phys. Rev. Lett.* **48**, 1559–1562 (1982).

2. 2.

Laughlin, R. B. Anomalous quantum hall effect: an incompressible quantum fluid with fractionally charged excitations. *Phys. Rev. Lett.* **50**, 1395–1398 (1983).

3. 3.

Jackiw, R. & Rebbi, C. Solitons with fermion number 1/2. *Phys. Rev. D* **13**, 3398–3409 (1976).

4. 4.

Su, W. P., Schrieffer, J. R. & Heeger, A. J. Solitons in Polyacetylene. *Phys. Rev. Lett.* **42**, 1698–1701 (1979).

5. 5.

Kitaev, A. Unpaired Majorana fermions in quantum wires. *Phys.-Uspekhi* **44**, 131–136 (2001).

6. 6.

Haldane, F. D. M. Nonlinear field theory of large-spin Heisenberg antiferromagnets: semiclassically quantized solitons of the one-dimensional easy-axis Néel state. *Phys. Rev. Lett.* **50**, 1153–1156 (1983).

7. 7.

Affleck, I., Kennedy, T., Lieb, E. H. & Tasaki, H. Rigorous results on valence-bond ground states in antiferromagnets. *Phys. Rev. Lett.* **59**, 799–802 (1987).

8. 8.

Kennedy, T. Exact diagonalisations of open spin-1 chains. *J. Phys. Condens. Matter* **2**, 5737–5745 (1990).

9. 9.

White, S. R. & Huse, D. A. Numerical renormalization-group study of low-lying eigenstates of the antiferromagnetic $S=1$ Heisenberg chain. *Phys. Rev. B* **48**, 3844–3852 (1993).

10. 10.

Gu, Z.-C. & Wen, X.-G. Tensor-entanglement-filtering renormalization approach and symmetry-protected topological order. *Phys. Rev. B* **80**, 155131 (2009).

11. 11.

Pollmann, F., Berg, E., Turner, A. M. & Oshikawa, M. Symmetry protection of topological phases in one-dimensional quantum spin systems. *Phys. Rev. B* **85**, 075125 (2012).

12. 12.

Clair, S. & de Oteyza, D. G. Controlling a chemical coupling reaction on a surface: tools and strategies for on-surface synthesis. *Chem. Rev.* **119**, 4717–4776 (2019).

13. 13.

Wei, T.-C., Affleck, I. & Raussendorf, R. Two-dimensional Affleck-Kennedy-Lieb-Tasaki state on the honeycomb lattice is a universal resource for quantum computation. *Phys. Rev. A* **86**, 032328 (2012).

14. 14.

Bethe, H. Zur Theorie der Metalle. *Z. Physik* **71**, 205–226 (1931).

15. 15.

Renard, J.-P., Regnault, L.-P. & Verdaguer, M. in *Magnetism: Molecules to Materials I: Models and Experiments* (eds. Miller, J. S. & Drillon, M.) 49–93 (John Wiley & Sons, 2001).

16. 16.

Soe, W.-H., Manzano, C., De Sarkar, A., Chandrasekhar, N. & Joachim, C. Direct observation of molecular orbitals of pentacene physisorbed on Au(111) by scanning tunneling microscope. *Phys. Rev. Lett.* **102**, 176102 (2009).

17. 17.

Hirjibehedin, C. F., Lutz, C. P. & Heinrich, A. J. Spin coupling in engineered atomic structures. *Science* **312**, 1021–1024 (2006).

18. 18.

Choi, D.-J. et al. Colloquium: atomic spin chains on surfaces. *Rev. Mod. Phys.* **91**, 041001 (2019).

19. 19.

Toskovic, R. et al. Atomic spin-chain realization of a model for quantum criticality. *Nat. Phys.* **12**, 656–660 (2016).

20. 20.

Yang, K. et al. Probing resonating valence bond states in artificial quantum magnets. *Nat. Commun.* **12**, 993 (2021).

21. 21.

Delgado, F., Batista, C. D. & Fernández-Rossier, J. Local probe of fractional edge states of $S = 1$ Heisenberg spin chains. *Phys. Rev. Lett.* **111**, 167201 (2013).

22. 22.

Lieb, E. H. Two theorems on the Hubbard model. *Phys. Rev. Lett.* **62**, 1201–1204 (1989).

23. 23.

Fernández-Rossier, J. & Palacios, J. J. Magnetism in graphene nanoislands. *Phys. Rev. Lett.* **99**, 177204 (2007).

24. 24.

Clar, E. & Stewart, D. G. Aromatic hydrocarbons. LXV. Triangulene derivatives¹. *J. Am. Chem. Soc.* **75**, 2667–2672 (1953).

25. 25.

Goto, K. et al. A stable neutral hydrocarbon radical: synthesis, crystal structure, and physical properties of 2,5,8-tri-*tert*-butyl-phenalenyl. *J. Am. Chem. Soc.* **121**, 1619–1620 (1999).

26. 26.

Inoue, J. et al. The first detection of a Clar's hydrocarbon, 2,6,10-tri-*tert*-butyltriangulene: a ground-state triplet of non-Kekulé polynuclear benzenoid hydrocarbon. *J. Am. Chem. Soc.* **123**, 12702–12703 (2001).

27. 27.

Pavliček, N. et al. Synthesis and characterization of triangulene. *Nat. Nanotechnol.* **12**, 308–311 (2017).

28. 28.

Mishra, S. et al. Synthesis and characterization of π-extended triangulene. *J. Am. Chem. Soc.* **141**, 10621–10625 (2019).

29. 29.

Su, J. et al. Atomically precise bottom-up synthesis of π-extended [5]triangulene. *Sci. Adv.* **5**, eaav7717 (2019).

30. 30.

Mishra, S. et al. Synthesis and characterization of [7]triangulene. *Nanoscale* **13**, 1624–1628 (2021).

31. 31.

Mishra, S. et al. Collective all-carbon magnetism in triangulene dimers. *Angew. Chem. Int. Ed.* **59**, 12041–12047 (2020).

32. 32.

Lado, J. L. & Fernández-Rossier, J. Magnetic edge anisotropy in graphenelike honeycomb crystals. *Phys. Rev. Lett.* **113**, 027203 (2014).

33. 33.

Ternes, M., Heinrich, A. J. & Schneider, W.-D. Spectroscopic manifestations of the Kondo effect on single adatoms. *J. Phys. Condens. Matter* **21**, 053001 (2008).

34. 34.

Li, J. et al. Single spin localization and manipulation in graphene open-shell nanostructures. *Nat. Commun.* **10**, 200 (2019).

35. 35.

Mishra, S. et al. Topological frustration induces unconventional magnetism in a nanographene. *Nat. Nanotechnol.* **15**, 22–28 (2020).

36. 36.

Ortiz, R. & Fernández-Rossier, J. Probing local moments in nanographenes with electron tunneling spectroscopy. *Progr. Surf. Sci.* **95**, 100595 (2020).

37. 37.

Oberg, J. C. et al. Control of single-spin magnetic anisotropy by exchange coupling. *Nat. Nanotechnol.* **9**, 64–68 (2014).

38. 38.

Jacob, D., Ortiz, R. & Fernández-Rossier, J. Renormalization of spin excitations and Kondo effect in open-shell nanographenes. *Phys. Rev. B* **104**, 075404 (2021).

39. 39.

Li, J. et al. Uncovering the triplet ground state of triangular graphene nanoflakes engineered with atomic precision on a metal surface. *Phys. Rev. Lett.* **124**, 177201 (2020).

40. 40.

Savary, L. & Balents, L. Quantum spin liquids: a review. *Rep. Prog. Phys.* **80**, 016502 (2016).

41. 41.

Georgescu, I. M., Ashhab, S. & Nori, F. Quantum simulation. *Rev. Mod. Phys.* **86**, 153–185 (2014).

42. 42.

Hieulle et al. [PLACEHOLDER]. *Angew. Chem. Int. Ed. Engl.* <https://doi.org/10.1002/anie202108301> (2021).

43. 43.

Giannozzi, P. et al. Quantum ESPRESSO toward the exascale. *J. Chem. Phys.* **152**, 154105 (2020).

44. 44.

Perdew, J. P., Burke, K. & Ernzerhof, M. Generalized gradient approximation made simple. *Phys. Rev. Lett.* **77**, 3865–3868 (1996).

45. 45.

Lejaeghere, K. et al. Reproducibility in density functional theory calculations of solids. *Science* **351**, aad3000 (2016).

46. 46.

Hutter, J., Iannuzzi, M., Schiffmann, F. & VandeVondele, J. CP2K: atomistic simulations of condensed matter systems. *Wiley Interdiscip. Rev. Comput. Mol. Sci.* **4**, 15–25 (2014).

47. 47.

Grimme, S., Antony, J., Ehrlich, S. & Krieg, H. A consistent and accurate ab initio parametrization of density functional dispersion correction (DFT-D) for the 94 elements H-Pu. *J. Chem. Phys.* **132**, 154104 (2010).

48. 48.

Goedecker, S., Teter, M. & Hutter, J. Separable dual-space Gaussian pseudopotentials. *Phys. Rev. B* **54**, 1703–1710 (1996).

49. 49.

VandeVondele, J. & Hutter, J. Gaussian basis sets for accurate calculations on molecular systems in gas and condensed phases. *J. Chem. Phys.* **127**, 114105 (2007).

50. 50.

Wilhelm, J., Del Ben, M. & Hutter, J. GW in the Gaussian and plane waves scheme with application to linear acenes. *J. Chem. Theory Comput.* **12**, 3623–3635 (2016).

51. 51.

Neaton, J. B., Hybertsen, M. S. & Louie, S. G. Renormalization of molecular electronic levels at metal-molecule interfaces. *Phys. Rev. Lett.* **97**, 216405 (2006).

52. 52.

Kharche, N. & Meunier, V. Width and crystal orientation dependent band gap renormalization in substrate-supported graphene nanoribbons. *J. Phys. Chem. Lett.* **7**, 1526–1533 (2016).

53. 53.

Yakutovich, A. V. et al. AiiDAlab – an ecosystem for developing, executing, and sharing scientific workflows. *Comput. Mater. Sci.* **188**, 110165 (2021).

54. 54.

Ortiz, R. et al. Exchange rules for diradical π -conjugated hydrocarbons. *Nano Lett.* **19**, 5991–5997 (2019).

55. 55.

Tran, V.-T., Saint-Martin, J., Dollfus, P. & Volz, S. Third nearest neighbor parameterized tight binding model for graphene nano-ribbons. *AIP Adv.* **7**, 075212 (2017).

56. 56.

Fishman, M., White, S. R. & Stoudenmire, E. M. The ITensor software library for tensor network calculations. Preprint at <https://arxiv.org/abs/2007.14822> (2020).

57. 57.

Weinberg, P. & Bukov, M. QuSpin: a Python package for dynamics and exact diagonalisation of quantum many body systems part I: spin chains. *SciPost Phys.* **2**, 003 (2017).

58. 58.

Weinberg, P. & Bukov, M. QuSpin: a Python package for dynamics and exact diagonalisation of quantum many body systems. Part II: bosons, fermions and higher spins. *SciPost Phys.* **7**, 020 (2019).

59. 59.

Fernández-Rossier, J. Theory of single-spin inelastic tunneling spectroscopy. *Phys. Rev. Lett.* **102**, 256802 (2009).

60. 60.

Spinelli, A., Bryant, B., Delgado, F., Fernández-Rossier, J. & Otte, A. F. Imaging of spin waves in atomically designed nanomagnets. *Nat. Mater.* **13**, 782–785 (2014).

61. 61.

Coleman, P. New approach to the mixed-valence problem. *Phys. Rev. B* **29**, 3035–3044 (1984).

62. 62.

Jacob, D. & Kurth, S. Many-body spectral functions from steady state density functional theory. *Nano Lett.* **18**, 2086–2090 (2018).

63. 63.

Jacob, D. Simulation of inelastic spin flip excitations and Kondo effect in STM spectroscopy of magnetic molecules on metal substrates. *J. Phys. Condens. Matter* **30**, 354003 (2018).

64. 64.

Jacob, D. & Fernández-Rossier, J. Competition between quantum spin tunneling and Kondo effect. *Eur. Phys. J. B* **89**, 210 (2016).

Acknowledgements

We thank O. Gröning and J. C. Sancho-García for fruitful discussions. This work was supported by the Swiss National Science Foundation (grant numbers 200020-182015 and IZLCZ2-170184), the NCCR MARVEL funded by the Swiss National Science Foundation (grant number 51NF40-

182892), the European Union’s Horizon 2020 research and innovation program (grant number 881603, Graphene Flagship Core 3), the Office of Naval Research (N00014-18-1-2708), ERC Consolidator grant (T2DCP, grant number 819698), the German Research Foundation within the Cluster of Excellence Center for Advancing Electronics Dresden (cfaed) and EnhanceNano (grant number 391979941), the Basque Government (grant number IT1249-19), the Generalitat Valenciana (Prometeo2017/139), the Spanish Government (grant number PID2019-109539GB-C41), and the Portuguese FCT (grant number SFRH/BD/138806/2018). Computational support from the Swiss Supercomputing Center (CSCS) under project ID s904 is gratefully acknowledged.

Author information

Author notes

1. Shantanu Mishra

Present address: IBM Research—Zurich, Rüschlikon, Switzerland

2. These authors contributed equally: Shantanu Mishra and Gonçalo Catarina

Affiliations

1. Empa—Swiss Federal Laboratories for Materials Science and Technology, Dübendorf, Switzerland

Shantanu Mishra, Kristjan Eimre, Carlo A. Pignedoli, Pascal Ruffieux & Roman Fasel

2. International Iberian Nanotechnology Laboratory, Braga, Portugal

Gonçalo Catarina & Joaquín Fernández-Rossier

3. University of Alicante, Sant Vicent del Raspeig, Spain

Gonçalo Catarina & Ricardo Ortiz

4. Technical University of Dresden, Dresden, Germany

Fupeng Wu, Ji Ma & Xinliang Feng

5. University of the Basque Country, San Sebastián, Spain

David Jacob

6. IKERBASQUE, Basque Foundation for Science, Bilbao, Spain

David Jacob

7. Max Planck Institute of Microstructure Physics, Halle, Germany

Xinliang Feng

8. University of Bern, Bern, Switzerland

Roman Fasel

Contributions

X.F., P.R. and R.F. conceived the project. F.W. and J.M. synthesized and characterized the precursor molecules. S.M. performed the on-surface synthesis, and STM and STS measurements. G.C., R.O. and J.F.R. performed the tight-binding, CAS, ED and DMRG calculations. D.J. performed the MOAM-NCA calculations. K.E. and C.A.P. performed the DFT and *GW* calculations. All authors contributed toward writing the manuscript.

Corresponding authors

Correspondence to Xinliang Feng, Pascal Ruffieux or Joaquín Fernández-Rossier.

Ethics declarations

Competing interests

The authors declare no competing interests.

Additional information

Peer review information *Nature* thanks Berthold Jäck, Yi Zhou and the anonymous reviewer(s) for their contribution to the peer review of this work. Peer reviewer reports are available.

Publisher's note Springer Nature remains neutral with regard to jurisdictional claims in published maps and institutional affiliations.

Extended data figures and tables

[Extended Data Fig. 1 Scanning tunnelling spectroscopy measurements of the frontier bands of triangulene spin chains.](#)

a, b, dI/dV spectroscopy on TSCs with *cis* (**a**) and *trans* (**b**) intertriangulene bonding configurations (open feedback parameters: $V = -1.5$ V, $I = 250$ pA; $V_{\text{rms}} = 16$ mV). Acquisition positions are marked with filled circles in **c, d**. Irrespective of the bonding configuration, TSCs exhibit an electronic band gap of 1.6 eV. **c, d**, High-resolution STM images (top panels), and constant-current dI/dV maps of the valence (middle panels) and conduction (bottom panels) bands of *cis* (**c**) and *trans* (**d**) TSCs. Scanning parameters: $V = -0.4$ V, $I = 250$ pA (top and middle panels, **c, d**) and $V = 1.1$ V, $I = 280$ pA (bottom panels, **c, d**); $V_{\text{rms}} = 30$ mV. All measurements were performed with a CO functionalized tip.

[Extended Data Fig. 2 Gas-phase density functional theory calculations on triangulene spin chains.](#)

a, e, DFT band structure and density of states (DOS) plots of TSCs with *cis* (**a**) and *trans* (**e**) intertriangulene bonding configurations in their antiferromagnetic ground state. Energies E are given with respect to the

vacuum level. A Gaussian broadening of 100 meV has been applied to the DOS plots. Note that spin up and spin down bands are energetically degenerate. **b**, **f**, Corresponding band structure plots around the frontier bands. k denotes the reciprocal lattice vector. The unit cells for the band structure calculations contain four and two triangulene units for *cis* and *trans* TSCs, respectively, with the lattice periodicities $a = 30.0 \text{ \AA}$ (*cis* TSC) and 17.4 \AA (*trans* TSC). The dashed lines indicate the middle of the band gap. The calculations reveal nearly dispersionless frontier bands due to a weak intertriangulene electronic hybridization. In addition, TSCs exhibit a band gap of 0.68 eV irrespective of the intertriangulene bonding configuration. **c**, **g**, Ground state spin density distributions for *cis* (**c**) and *trans* (**g**) TSCs. Spin up and spin down densities are denoted in blue and red, respectively. **d**, **h**, Local DOS maps of the valence (VB) and conduction (CB) bands of *cis* (**d**) and *trans* (**h**) TSCs. Spin density distributions and local DOS maps were calculated at a height of 3 \AA above the TSCs.

Extended Data Fig. 3 Derivation of the bilinear-biquadratic model.

a, **b**, Schematic energy level diagram of $N=2$ (**a**) and 3 (**b**) oTSCs for the Heisenberg, Hubbard and BLBQ models. Analytical expressions for the spin models are provided in the [Supplementary Information](#) (Supplementary Note 2). The Hubbard model is defined such that each triangulene unit is represented by a four-site lattice (**c**) and the many-body energy levels are computed with DMRG, taking $t = -1.11 \text{ eV}$, $t' = -0.20 \text{ eV}$ and $U = 1.45|t|$. The parameters of the BLBQ model ($\langle J \rangle = 18 \text{ meV}$ and $\langle \beta \rangle = 0.09$) are obtained by matching its excitation energies to those of the Hubbard model for the $N=2$ TSC. **c**, Description of the four-site toy model with the intra- and intertriangulene hopping, t and t' , respectively, indicated. The coloured filled circles denote the two sublattices. **d**, **e**, Comparison of the excitation energies for an $N=3$ oTSC computed with CAS(6,6) for the complete Hubbard model with $t_1 = -2.70 \text{ eV}$, $t_2 = 0 \text{ eV}$ and $t_3 = -0.35 \text{ eV}$ (**d**), and with DMRG for the four-site Hubbard model (**e**), as the atomic Hubbard U is varied. Dashed lines indicate the experimental spin excitation energies of 14 meV for $N=2$ TSC (**a**) and, 11 and 35 meV for N

$= 3$ oTSC (**b**, **d**, **e**). Note that the Heisenberg model fails to capture both the experimental spin excitation energies for the $N = 3$ oTSC (**b**), and the Hubbard model results for the $N = 2$ (**a**) and $N = 3$ (**b**) oTSCs.

Extended Data Fig. 4 Experimental and theoretical spectroscopic signatures of spin excitations in an $N = 4$ open-ended triangulene spin chain.

Comparison between experimental and theoretical (using the four-site Hubbard and BLBQ models) d^2I/dV^2 spectra of an $N = 4$ oTSC shows a good agreement in both the energies and the modulation of the spin spectral weight across the different units in the TSC. Numerals along the abscissa denote the unit number of the TSC. BLBQ model calculations are performed with two different T_{eff} values for the tunnelling quasiparticle, which determine the linewidth of the d^2I/dV^2 profile. Model parameters are the same as in Extended Data Fig. 3.

Extended Data Fig. 5 Average magnetization for the first three $S_z = +1$ states of an $N = 16$ open-ended triangulene spin chain, obtained with the bilinear-biquadratic model.

Calculations were performed with $\langle J \rangle = 18$ meV and $\langle \beta \rangle = 0.09$. Orange filled circles denote the magnetization profile of the state with the lowest excitation energy $E = 0.4$ meV, much smaller than the theoretical Haldane gap (9 meV), and $\langle |S_z\rangle \rangle = |1, +1\rangle$. The average magnetization is clearly the largest at the terminal units, and is strongly depleted at the central units, as expected for an edge state. Blue and green filled circles denote spin excitations with energies larger than the theoretical Haldane gap. Blue filled circles correspond to a state with $E = 12.1$ meV and $\langle |S_z\rangle \rangle = |1, +1\rangle$, where the magnetization profile forms a nodeless standing wave with maximum average magnetization at the central units. This can be identified as a spin wave state, except for the minor upturn at the terminal units. Green filled circles are associated to a state with $E = 11.6$ meV and $\langle |S_z\rangle \rangle = |2, +1\rangle$, where the average magnetization shares similarities with both the edge and nodeless spin wave states.

Extended Data Fig. 6 Theoretical and experimental spin excitation energies of open-ended and cyclic triangulene spin chains.

a, Spin excitation energies calculated by ED of the BLBQ model ($\langle J \rangle = 18$ meV and $\langle \beta \rangle = 0.09$) for oTSCs with $N = 2\text{--}16$ (circles) and cTSCs with $N = 5, 6, 12, 13, 14, 15$ and 16 (crosses) up to 50 meV. The size of the symbols accounts for the spin spectral weight of the corresponding spin excitation. The lowest energy bulk excitation, as indicated for the $N = 16$ cTSC, converges to the Haldane gap (9 meV) with increasing N . **b**, Experimental spin excitation energies up to 50 meV for seventeen oTSCs with N between 2 and 20, and eight cTSCs with $N = 5, 6, 12, 13, 14, 15, 16$ and 47. The lowest energy bulk excitation, indicated for the $N = 47$ cTSC, converges to the Haldane gap (14 meV) with increasing N . Experimentally, starting from both $N = 16$ oTSC and cTSC, convergence to the Haldane gap is observed. Note the odd–even effect observed for the lowest energy excitation of cTSCs, seen both in theory and experiments.

Extended Data Fig. 7 Non-crossing approximation results for the multi-orbital Anderson model of an $N = 3$ open-ended triangulene spin chain ($t_1 = -2.70$ eV, $t_2 = 0$ eV, $t_3 = -0.35$ eV and $U = 1.90|t_1|$) coupled to the surface ($\Gamma/\pi = 13$ meV).

a, Total spectral function of CAS(6,6) at different temperatures T for the case of particle–hole symmetry. **b**, Orbital-resolved spectral function of CAS(6,6) for $T = 4.64$ K and for the particle–hole symmetric case. **c**, Detuning from particle–hole symmetry: total spectral function of CAS(6,6) for different values of $\delta\varepsilon$ and $T = 4.64$ K. **d**, Local spectral functions at $T = 4.64$ K for carbon sites of one of the outer triangulene units and the central triangulene unit ($\delta\varepsilon = 200$ meV). The inset shows a sketch of the $N = 3$ oTSC with the two carbon sites marked with the corresponding coloured filled circles. The spectral functions in individual panels are offset vertically for visual clarity.

Supplementary information

Supplementary Information

Supplementary Figs. 1–49 and Supplementary Notes 1 and 2: additional STM and STS data, effect of extrinsic spin-orbit coupling on triangulenes, analytical solutions of the Heisenberg and BLBQ models, materials and methods in solution synthesis and characterization, solution synthetic procedures, and NMR spectroscopy and high-resolution mass spectrometry of chemical compounds.

Peer Review File

Rights and permissions

Reprints and Permissions

About this article

Cite this article

Mishra, S., Catarina, G., Wu, F. *et al.* Observation of fractional edge excitations in nanographene spin chains. *Nature* **598**, 287–292 (2021). <https://doi.org/10.1038/s41586-021-03842-3>

- Received: 30 April 2021
- Accepted: 20 July 2021
- Published: 13 October 2021
- Issue Date: 14 October 2021
- DOI: <https://doi.org/10.1038/s41586-021-03842-3>

Share this article

Anyone you share the following link with will be able to read this content:

[Get shareable link](#)

Sorry, a shareable link is not currently available for this article.

[Copy to clipboard](#)

Provided by the Springer Nature SharedIt content-sharing initiative

This article was downloaded by **calibre** from <https://www.nature.com/articles/s41586-021-03842-3>

| [Section menu](#) | [Main menu](#) |

- Article
- Open Access
- [Published: 13 October 2021](#)

Superior robustness of anomalous non-reciprocal topological edge states

- [Zhe Zhang ORCID: orcid.org/0000-0003-2063-5217¹](#),
- [Pierre Delplace ORCID: orcid.org/0000-0002-7474-1798²](#) &
- [Romain Fleury ORCID: orcid.org/0000-0002-9486-6854¹](#)

Nature volume **598**, pages 293–297 (2021)

- 2461 Accesses
- 48 Altmetric
- [Metrics details](#)

Subjects

- [Electronics, photonics and device physics](#)
- [Topological insulators](#)

Abstract

Robustness against disorder and defects is a pivotal advantage of topological systems¹, manifested by the absence of electronic backscattering in the quantum-Hall² and spin-Hall effects³, and by unidirectional waveguiding in their classical analogues^{4,5}. Two-dimensional (2D) topological insulators^{4,5,6,7,8,9,10,11,12,13}, in particular, provide unprecedented opportunities in a variety of fields owing to their compact planar geometries, which are compatible with the fabrication technologies used in modern electronics and photonics. Among all 2D topological phases, Chern insulators^{14,15,16,17,18,19,20,21,22,23,24,25} are currently the most reliable designs owing to the genuine backscattering immunity of their non-reciprocal edge modes, brought via time-reversal symmetry breaking. Yet such resistance to fabrication tolerances is limited to fluctuations of the same order of magnitude as their bandgap, limiting their

resilience to small perturbations only. Here we investigate the robustness problem in a system where edge transmission can survive disorder levels with strengths arbitrarily larger than the bandgap—an anomalous non-reciprocal topological network. We explore the general conditions needed to obtain such an unusual effect in systems made of unitary three-port non-reciprocal scatterers connected by phase links, and establish the superior robustness of anomalous edge transmission modes over Chern ones to phase-link disorder of arbitrarily large values. We confirm experimentally the exceptional resilience of the anomalous phase, and demonstrate its operation in various arbitrarily shaped disordered multi-port prototypes. Our results pave the way to efficient, arbitrary planar energy transport on 2D substrates for wave devices with full protection against large fabrication flaws or imperfections.

[Download PDF](#)

Main

Among the unique and counter-intuitive attributes of topological systems, topological robustness¹ against disorder and flaws is undoubtedly one of the most remarkable.

This property shows substantial application potential by relaxing the tight constraints imparted by fabrication tolerances, and provides a way to route energy and information in a wide variety of 2D

platforms^{4,5,6,7,8,9,10,11,12,13,14,15,16,17,18,19,20,21,22,23,24,25,26,27}, ranging from quantum electronics²³ to classical photonic^{4,5} and phononic devices^{25,26,27}. Topological edge states were found in systems with broken time-reversal symmetry, such as Chern insulators^{14,28}, and then extended to time-reversal invariant scenarios, including the Z2 (ref. ³) and other symmetry-protected schemes²⁹, simultaneously stimulating study of their classical analogues^{6,10,17}. So far, Chern topological edge modes^{14,15,16,17,18,19,20,21,22,23,24,25} undeniably represent the most reliable solution for point-to-point energy guiding, as they provide truly unidirectional, backscattering-immune wave transport at their boundaries. They have been reported in non-reciprocal artificial wave media, such as externally biased magneto-photonic crystals¹⁶ or mechanical systems¹³ with moving^{17,19,20,25} or time-dependent^{8,24} elements. Albeit protected from the presence of local defects by the Chern number, the edge modes cannot survive the presence of distributed disorder of sufficiently large magnitude^{1,4,5,14}, especially when the average amplitude of frequency fluctuations gets larger than the bandgap size. This behaviour inherently confines the topological protection of Chern phases to small distributed disorder levels.

Here we demonstrate an anomalous non-reciprocal topological phase in which edge transmission is quantitatively stronger than for the Chern phase, surviving parametric fluctuations arbitrarily larger than the bandgap size. We find such anomalous

robustness in unitary scattering networks made of interconnected non-reciprocal resonant scatterers coupled by non-directed phase links. We compare quantitatively the robustness of transmission through the anomalous and Chern channels to phase-link and scattering disorder, by statistical averaging over many disorder realizations. Our experiments at microwave frequencies confirm the superior resilience of the anomalous transmission channel over the Chern one. We apply our findings to the design of ideally robust networks with arbitrarily located ports and irregular shapes, including a perfect six-port circulator.

A non-reciprocal scattering network

Consider the non-reciprocal unitary scattering network of Fig. 1a, which consists of general three-port non-reciprocal scatterers connected by bidirectional links in a honeycomb periodic structure. The scattering elements exhibit threefold (C_3) rotational symmetry, while the links impart a phase delay of φ , as represented in the zoomed-in view of the unit cell (Fig. 1b). The scattering process is described by a unitary 3×3 asymmetric scattering matrix S_0 whose general parametrization involves only two angles, ζ and η , in the interval $(-\pi/2, \pi/2)$ (see [Supplementary Information](#) and Extended Data Fig. 1). The wave propagation in the infinite network can be described by a Bloch eigenproblem, which considers the scattering at the nodes, described by a 6×6 unitary matrix $S(\mathbf{k})$, and also involves the bidirectional phase delay φ induced by the links:

$$\$\$S(\{\backslash\text{bf}\{\mathbf{k}\}\})|\psi(\{\backslash\text{bf}\{\mathbf{k}\}\})\rangle = \{\{\backslash\text{rm}\{e\}\}\}^{\wedge\{-i\{\backslash\text{rm}\{\varphi\}\}\}}|\psi(\{\backslash\text{bf}\{\mathbf{k}\}\})\rangle \\ (1)$$

Fig. 1: Topological non-reciprocal wave network and its bulk band structure.

 **figure1**

a, We consider a unitary scattering network made of three-port non-reciprocal elements, described by asymmetric unitary scattering matrices. **b**, Unit cell of the honeycomb lattice, highlighting the signals entering the non-reciprocal elements, their 120° rotational symmetry, and the reciprocal phase delay φ imparted by the links. The network is described by a unitary unit-cell scattering operator $S(\mathbf{k})$ defining a Floquet unitary mapping with quasi-energy φ . **c**, Evolution of the Floquet band structure on increasing the level of reflection of the non-reciprocal elements from $|R| = 0.16$ (leftmost panel, with angular parameter values $\xi = -\eta = 2.5\pi/12$) to $|R| = 0.51$ (rightmost panel, $\xi = -\eta = 3.5\pi/12$). While the type 1 bandgaps do not change much, at $|R| = 1/3$ (centre panel, $\xi = -\eta = \pi/4$), the type 2 bandgap closes, symptomatic of a topological phase transition.

So far, topological unitary scattering wave networks^{6,30,31,32,33,34} have only been implemented in reciprocal systems^{7,35,36,37} exploiting two time-reversed subspaces that are never genuinely decoupled. On the contrary, our non-reciprocal scattering network is formally analogous to a rigorously oriented kagome graph (see [Supplementary Information](#)), described by a unitary matrix³³ $S(\mathbf{k})$, which can be mapped³⁸ onto the Floquet eigenproblem of a periodically driven lattice^{39,40,41,42,43,44,45}, with the angle variable φ taking the role of the quasi-energy.

Therefore, we can truly benefit from both the advantages of non-reciprocity⁴⁶, and the potentially richer topological physics of Floquet systems⁴⁴.

Chern and anomalous phases

We used the model of equation (1) to explore the parameters influencing potential topological phase transitions in the network. We found the individual reflection coefficient $|R|$ of the non-reciprocal scatterers to be the main ‘control knob’ for the closing of the quasi-energy bandgaps. The evolution of the bulk band structure with increasing values of $|R|$ is shown in Fig. 1c. Our semi-analytical model shows a systematic closing of two of the bandgaps at $|R| = 1/3$ (denoted type 2, in red) while the others (type 1, in blue) do not change much. This suggests that topological phase transitions may be controlled by the individual scatterer reflectance.

To confirm this intuition, we probe the existence of edge modes for each of these situations by numerically calculating the band structure of a ribbon terminated by full-reflection boundary conditions at top and bottom. As depicted in Fig. 2a, both the low- and high-reflection cases (respectively the leftmost and rightmost panels) exhibit chiral edge modes located at the walls either at the top (red line) or bottom (blue line), with profiles represented in Fig. 2b. The main difference is that the low-reflection case has edge modes in every quasi-energy bandgap, whereas at high reflection, they are found only in bandgaps of type 1. This low- $|R|$ behaviour is the hallmark of anomalous Floquet insulators^{33,35,42,45} (AFI), which possess topological edge states despite the Chern number of all surrounding bands being zero. In contrast, the high-reflection case corresponds to the Chern insulator (CI). We map out in Fig. 2c the complete topological phase diagram for every possible realization of the scattering matrix S_0 , represented by the angle parameters ξ and η . The CI and AFI regimes are shaded in red and blue, respectively. To connect this phase diagram with physically meaningful quantities, we plot it twice in the same parameter space, together with contour lines depicting the reflectance (Fig. 2c, left) and non-reciprocal isolation (Fig. 2c, right). Remarkably, the phase diagram unambiguously demonstrates the coincidence between the $1/3$ reflection contours with the topological phase transition. Its centre corresponds to a semi-metallic phase, with all bandgaps closed, whereas the green point is the perfect circulator case with $|R| = 0$ and infinite isolation, for which the bulk bands are flat and the edge modes are dispersionless (see Extended Data Fig. 2). Such a critical condition corresponds to a phase rotation symmetric point³³, which can only occur in the anomalous (or trivial) phases.

Fig. 2: Anomalous and Chern topological phases in non-reciprocal wave networks.

 **figure2**

a, Band structure of a supercell with periodic boundary conditions along x and unitary reflection at the top and bottom. The parameters are the same as in Fig. 1c. The low-reflection case is the anomalous topological phase (an anomalous Floquet insulator, AFI), which features an edge mode in every quasi-energy gap. Conversely, the high-reflection case supports edge modes only inside the type 1 bandgaps, consistent with the Chern insulator (CI) phase. Edge modes localized to the top and bottom are shown in red and blue, respectively. The phase transition is depicted in the middle panel. **b**, Supercell with examples of the profiles of Chern and anomalous topological edge modes, corresponding to the markers in **a**. **c**, Topological phase diagrams in the (ξ, η) plane. The blue-shaded areas correspond to the anomalous phase, and the red-shaded areas to the Chern phase. Left, comparison with the iso-reflection contours of the individual scatterers, demonstrating the coincidence between the topological phase transition and the $|R| = 1/3$ contour. Right, comparison with the non-reciprocal isolation level of the individual scatterers $|S_{21}/S_{12}|$. On the thick grey diagonals in panel **c**, the scatterers are reciprocal and the type 1 bandgaps close. At the centre red point, all bandgaps close. The two green points represent the perfect circulator cases, either with right-handed circulation (upper-left point) or left-handed circulation (lower-right point).

Robustness comparison

From the band structures of Fig. 2a, we can already intuitively expect the AFI edge transmission to be much more robust than the CI one to quasi-energy fluctuations, even those much larger than the bandgap size. Indeed, the AFI phase occurs in the ballistic regime, in which reflections at nodes are low, yielding relatively flat (slow) bulk bands and large bandgaps. An abrupt jump of φ within the lattice is very likely to land in a bandgap, which necessarily carries an edge mode. Conversely, in the CI phase, the probability of an edge mode being destroyed by fluctuations larger than the bandgap is much higher, owing to the increased width of the bulk bands³³ and the occurrence of trivial bandgaps. As an example of such a situation, let us consider the transport properties of edge modes in a finite non-reciprocal network with an abrupt quasi-energy jump in the middle (Fig. 3a, right). As a reference, we also include the case of a uniform sample (Fig. 3a, left). The two hexagonal-shaped networks have three input/output ports, as shown in the top row of Fig. 3a. Network 1 (N1) consists of uniformly distributed phase links $\varphi = \pi/8$, while for network 2 (N2), a quasi-energy jump is introduced by changing all phase links in the bottom part to $\pi/2$. With numerical simulations, we then compare the propagation of the anomalous and Chern edge modes, when exciting from port 1. The anomalous phase finds itself in topological bandgaps at both $\varphi = \pi/8$ and $\pi/2$ (Fig. 2a, left), whereas the Chern phase possesses a nontrivial bandgap only at $\varphi = \pi/8$ (Fig. 2a, right). As shown in Fig. 3a, the anomalous edge mode crosses the interface completely unperturbed. In stark contrast, the Chern edge mode is unable to transmit to port 2 in the presence of the interface, and all the energy is guided to port 3.

Fig. 3: Superior robustness of anomalous non-reciprocal topological edge transmission.



a, Numerical simulation of the steady-state energy propagation in finite non-reciprocal networks with different phase-link distributions. The signal is incident from port 1 (see top panel for positions of ports 1–3). The parameters used to generate the anomalous (centre panel) and Chern (bottom panel) phases are the same as in Figs. 1 and 2. Left column (network 1, N1), the phase-link distribution is uniform, with $\varphi = \pi/8$, and the energy can be transmitted to port 2 in both the anomalous and Chern phases. Right column (network 2, N2), we introduce an interface and abruptly change the value of φ to $\pi/2$ for the bottom part of the network. Only the anomalous phase is robust to this change, and keeps transmitting to port 2. In the Chern phase, the edge mode travels along the interface and reaches port 3. **b**, Experimental validation using microwaves in a network made of ferrite circulators. The colourmap represents the measured field amplitude distribution, where brighter colours correspond to a large field amplitude, and darker colours a low field amplitude. **c**, Top panel, transmission between ports 1 and 2 in a disordered system with randomly generated phase delays. The phases are uniformly drawn in an interval $[-\delta_\varphi/2, \delta_\varphi/2]$ around $\varphi = \pi/8$. Solid lines represent the value of transmission averaged over 1,000 realizations of disorder, and the dashed lines are the first and last quartiles (Q1 and Q3). The anomalous edge transmission channel can survive disorder strengths up to a full 2π rotation. Bottom panel, same but for the case of scattering matrix disorder within a given topological phase ($\varphi = \pi/8$). Transmission in the anomalous channel is also more resilient to this disorder type. See [Supplementary Information](#) for particular field maps and other Chern cases.

We validate experimentally this fundamental distinction between the anomalous and Chern phases by designing a non-reciprocal network operating at microwave frequencies. The scatterers are ferrite circulators connected with microstrip lines. Our experimental design, which takes into account both the frequency dispersion of the scatterers and delay lines, finds itself in the anomalous and Chern phases at 4.9 GHz and 3.6 GHz, respectively. Modification of the phase delays of the links is induced by changing the total lengths of the microstrip lines with serpentine paths. As shown in Fig. 3b, the measured field amplitude profiles confirm the resilience of the anomalous edge mode to the phase jump, in perfect agreement with the numerical predictions. Further evidence is provided by the measured changes in scattering parameters and field maps upon exciting ports 2 and 3 (Extended Data Figs. 3, 4d, e, 5 and 6).

The resilience of the anomalous edge transport in these interface scenarios, involving two periodic networks, raises the question of its generalization to non-periodic quasi-energy perturbations. To answer quantitatively, we consider the same hexagonal network as in the left of Fig. 3a, and impose site-dependent disorder on the phase links, with fluctuations of strength δ_φ randomly drawn with uniform probability in the interval $\pi/8 + [-\delta_\varphi/2, \delta_\varphi/2]$. We then numerically extract the transmission from ports 1 to 2 for 1,000 realizations of disorder, and plot its magnitude versus δ_φ in the top panel of Fig. 3c. The solid lines represent the ensemble average, and the dashed lines are the

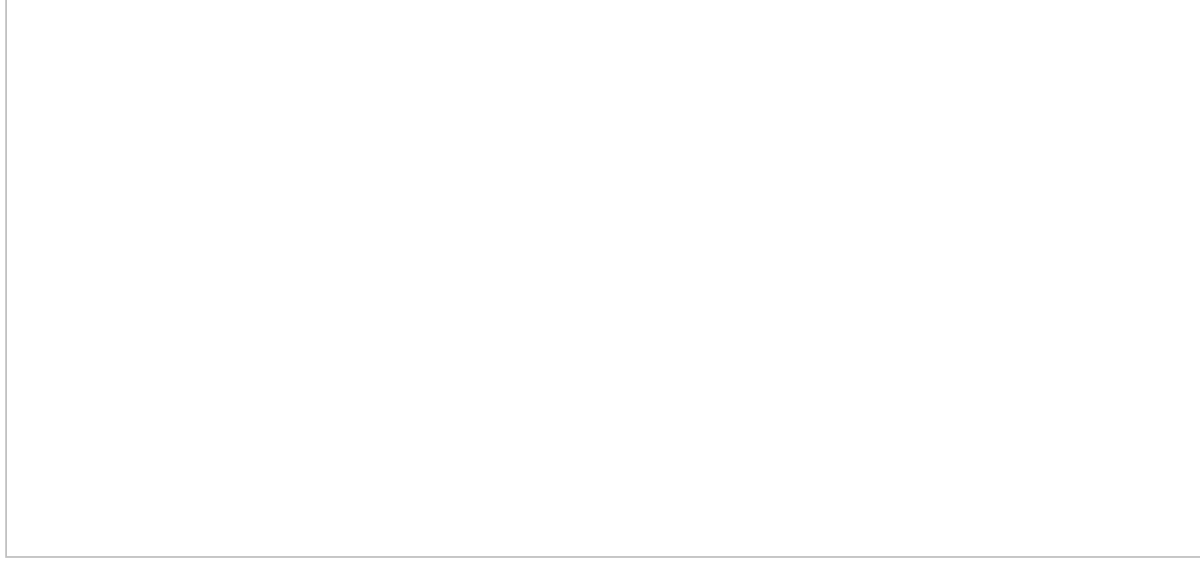
first and last quartiles (Q1 and Q3). In the clean limit ($\delta_\varphi = 0$), both AFI and CI phases show high transmission, since the edge states exist in both cases and are unperturbed. We now turn on the disorder, up to the maximal possible strength, which corresponds to randomly drawn values in the entire 2π quasi-energy range, much larger than the bandgap size of both AFI and CI phases (roughly $\pi/4$). Upon increasing δ_φ , the average transmission in the Chern case quickly drops to low values. Remarkably, the AFI transmission shows a markedly different behaviour, remaining near 90% even when δ_φ reaches 2π (fully random case). Note that this exceptional robustness does not require the critical condition $|R| = 0$ to be reached, since the figure is generated for $|R| = 16\%$. Such statistically stable transmission constitutes solid evidence of the superiority of anomalous non-reciprocal topological networks, which survive phase disorder levels arbitrarily larger than their bandgap size. We also consider the other possible source of disorder, namely the scattering matrices of the nodes, which we pick randomly within the Chern or anomalous phases, fixing $\varphi = \pi/8$. The transmission statistics are shown in the bottom panel of Fig. 3c. We see that the anomalous transmission can tolerate 100% disorder in the choice of scattering matrices, whereas the Chern one falls after 25%. The reason for this surprising behaviour is that in a disordered Chern phase (random $|R| > 1/3$), transmission is mediated by both bulk and edge modes, but is blocked by trivial gaps, whereas in the anomalous case (random $|R| < 1/3$), those trivial gaps are absent (see Supplementary Fig. 8). This shows that the superior robustness of the anomalous phase is not restricted to phase-link disorder, but also to the other possible source of disorder: fluctuations of the scattering matrices.

We validate the resilience of the anomalous transmission by performing experiments on irregularly shaped disordered networks. First, we demonstrate the use of anomalous phases in a practical scenario, where an anomalous non-reciprocal topological network is used to create a robust six-port circulator with arbitrary shape and port locations. The prototype is shaped like Switzerland, and we place six ports at the locations of six boundary cities (Fig. 4a). We aim at connecting each city to its clockwise closest neighbour, with strong non-reciprocal isolation to any other city. A picture of the fabricated prototype is shown in Fig. 4b. We sequentially excite each input of this six-port non-reciprocal network, and report the measured experimental field maps in the AFI band (Fig. 4c). Despite the presence of finite fabrication tolerances, such as the inaccuracy in the surface mounting process of the elements, and shrinking effects due to the employed reflow oven method, and regardless of the tortuous shape of the border, we observe the expected clockwise non-reciprocal circulation of the energy, consistent with simulations (Extended Data Fig. 7c). Such robustness is also observed in longer-range transmission tests between ports 1 and 4 (Extended Data Fig. 7a and b). Second, we provide an experimental validation of the superiority of the anomalous transmission in the presence of fully random phase delays. We built five different prototypes, one of them shown in Fig. 4d, with phase fluctuations in a 2π range implemented via serpentine links. The measured field maps in the AFI and CI phases

show that only the anomalous channel survives such strong distributed perturbations, consistent with our statistical studies.

Fig. 4: Experiments on irregularly shaped and disordered networks.

 figure4



a, We consider a network shaped like the map of Switzerland, and placed six ports on the external boundary at six city locations. **b**, Photograph of the associated prototype, showing ports 1–6. **c**, Experimental field maps upon sequential excitation of this six-port system. The network behaves as a six-port circulator despite its irregular shape, the random port locations and the high number of ports. **d**, Experimental validation of robust anomalous transmission in a two-port system with randomly disordered phase links under the largest possible disorder strength ($\delta_\phi = 2\pi$). Top, photograph of one of our prototypes. Bottom, measured field maps in the AFI and CI cases. The AFI edge mode reaches port 2, while the Chern one is blocked. The other four results are shown in Extended Data Fig. 9.

Conclusion and outlook

We envision that such anomalous wave platforms may be used in a new generation of multiple-input multiple-output devices, capable of reaching an unprecedented level of robustness. Since individual reflection is the sole ‘control knob’ for the transition from the CI to the AFI phase, one could foresee very practical ways to reconfigure a domain wall between the two phases—for example, by simply changing the matching of the scatterers—without the need for flipping a magnetic field. Our table-top experiment, compatible with standard printed circuit board microwave technologies and off-the-shelf surface mount components, provides genuine non-reciprocity and large robustness, not only to local defects, but also to distributed imperfections. This opens

an avenue to a new generation of wave systems⁴⁷ that can provide reconfigurable point-to-point unidirectional energy guiding, with arbitrary control over the imparted phase delays and full immunity against backscattering. Finally, exploration of the interplay between anomalous non-reciprocal networks and non-Hermitian perturbations (such as radiation losses occurring when coupling the edge mode to the free-space continuum) represents a promising future opportunity for topologically controlled radiation patterns in applications such as multiple beam antennas for 5G communications.

Methods

Network topology

The Chern number does not fully account for the topology of unitary operators, such as the scattering matrix in equation (1). For unitary evolutions, the eigenvalue (quasi-energy) spectrum being defined on a circle, each (quasi-energy) band is now allowed to be connected to the next one by an edge state⁴². Because of the cyclicity of the spectrum, and because the Chern number of a band counts the number of edge states that merge into that band, it follows that the Chern numbers of each band vanish. Since all the gaps are filled by a chiral edge state, this regime is called anomalous.

Actually, the topology of unitaries, such as evolution operators or our scattering matrix, is better described by the homotopy group $\pi_3(U(N)) = \mathbb{Z}$, whose elements are the topological numbers

$$\text{\$}\$\{W\}_{\psi}=\{(24\{\rm{\pi}}\})^2\}^{-1}\int \rm{tr}\{\{V\}_{\psi}\}^3.\text{\$}\$ \\ (2)$$

The power 3 must be understood in the language of differential forms, and the integral runs over a 3-torus, spanned by the quasi-momentum $\mathbf{k} = (k_x, k_y)$ and time t (over a time period T). Time is not explicit in scattering networks. However, the cyclicity of the network makes possible a direct mapping with a Floquet (that is, T -periodic in time) evolution operator $U(t, \mathbf{k})$, such that an interpolation parameter that formally plays the role of time can be introduced³³. Finally, the operator V_ψ is a periodized (in time) evolution operator. For Floquet systems, it reads as⁴².

$$\text{\$}\$\{V\}_{\psi}(t,\mathbf{k})=U(t,\mathbf{k})\exp(itH_{\rm eff}(\mathbf{k}))\text{\$}\$ \\ (3)$$

with

$$\$ \$ \{H\}_{\{\mathrm{rm}\{\mathrm{eff}\}\}}(\{\mathbf{k}\}) = i/T \{\mathrm{ln}\}_{-\psi} U(t=T, \{\mathbf{k}\}), \$ \$$$

(4)

where $-\psi$ denotes the branch-cut of the logarithm. The procedure to define such an operator V_ψ and thus the invariant W_ψ for discrete-time evolutions (that is, when the dynamics is given by a succession of scattering events and where time therefore does not appear explicitly), as in our model, was developed in a previous detailed study³³ (in particular in sections V.A. and V.B.).

Importantly, the branch-cut ψ must be chosen in a spectral gap of $U(T, \mathbf{k})$, or $S(\mathbf{k})$ in our case. For this reason, W_ψ is said to be a gap invariant, and indeed directly gives the number of chiral edge states in a given quasi-energy gap ψ . In contrast, Chern numbers are band invariants. They are inferred from the eigenstates of $H_{\mathrm{eff}}(\mathbf{k})$ expressed in equation (4) and thus cannot capture the full unitary evolution. Finally, the details for the calculation of the invariants W_ψ in oriented kagome graphs can be found in Delplace et al.³³. Their values for the band structures of Fig. 1c are 1,1,1,1,1,1 in the anomalous case and 1,0,1,1,0,1 for the Chern case. For completeness, we provide the bandgap map of the network together with the values of the homotopy invariant in Supplementary Fig. 8.

Simulations

The simulation method of arbitrary finite non-reciprocal honeycomb networks is based on the scattering matrix method. For a finite non-reciprocal network with N_r input/output ports, once we have the information of the scattering matrix of each non-reciprocal element and the distribution of the phase delays of the links, this method can provide (i) the scattering matrix S_{Nr} regarding the N_r port system, and (ii) the field map across the network knowing the excitations at the N_r ports (see details in [Supplementary Information part II](#)).

We exemplify this method by calculating the transmission between ‘Geneva’ and ‘Davos’ through the Switzerland-shaped network (the network used in Fig. 4 of the main text) as a function of φ , and compare the transmission results with the ribbon band structures (see [Supplementary Fig. 2](#)). We assume a uniform distribution for the phase delay φ and the same non-reciprocal elements (in anomalous or Chern phase) in the Switzerland-shaped network. When both anomalous and Chern phases fall in a topological bandgap, the transmission is near unity. When both phases fall in a bulk band, the transmission undergoes sharp variations with φ , depending on the excited bulk mode. Only the Chern phase exhibits bands of blocked transmission, owing to the trivial bandgaps.

Design

The non-reciprocal networks are designed and fabricated on 0.508 mm thick Rogers RT/duroid 5880 substrate (dielectric loss $\tan\delta = 0.0009$ at 10 GHz) with 35 μm thick copper on each side. Here, the non-reciprocal element is a surface mount microwave circulator (UIYSC9B55T6, UIY Co.), designed from a ‘Y’-shaped strip line on a printed circuit board⁴⁸. The three ports are placed 120° apart from each other such that they are iso-spaced. The printed circuit board is sandwiched between two pieces of ferrite. Without magnetic fields, the ‘Y’-junction strip line supports two degenerate modes at ω_0 : right-handed and left-handed. To bias it, two magnets are fixed outside, providing the required magnetic field of $50 \text{ kA m}^{-1} = 628 \text{ Oe}$, normal to the printed circuit board and polarizing the ferrite, therefore lifting the initial degeneracy, with chiral modes at ω_+ and ω_- . In our experiment, we first measure an individual circulator and retrieve its scattering matrix S_0 . The measured reflection of an individual circulator is shown in Extended Data Fig. 4a, and sets the frequency bands for CI and AFI operations.

Microstrip lines serve as phase delay links, with a width of 1.65 mm, corresponding to a standard 50 ohm characteristic impedance. The phase delay φ induced by a microstrip line with length L operating at frequency f is expressed as $\varphi = (2\pi/Lf)\varepsilon_{\text{eff}}^{1/2}$, where ε_{eff} is the effective permittivity of the microstrip line, and can be determined by an empirical formula⁴⁹. Taking into account the frequency dispersion of the lines and circulators, we construct a more practical topological bandgap map, shown in Extended Data Fig. 4b, as a function of the effective length of the microstrip lines L and the operating frequency f . With the aid of the map, we select $L_1 = 26.5 \text{ mm}$ and $L_2 = 37.5 \text{ mm}$, which produce the conditions $\varphi = \pi/8$ and $\varphi = \pi/2$, respectively, in the simulations (Fig. 3a, Extended Data Figs. 5a, 6a). As exhibited in Extended Data Fig. 4c, the fabricated networks show the microstrip lines of L_1 (blue dashed region) and L_2 (red dashed region).

Measurements

The scattering parameters and field maps of three fabricated networks (network 1, network 2 and the Switzerland-shaped network) are measured by a vector network analyser (VNA; ZNB20, R&S), as demonstrated in Extended Data Fig. 8. For the scattering parameter measurements (Extended Data Fig. 4), as the networks are multiport, we connect the two ports of the VNA to two ports of the measured network, with the other network ports perfectly matched with 50-ohm terminations (no reflection). For the longer-range transport measurement shown in Extended Data Fig. 7, we connect ports 1 and 4 to the two VNA ports, while letting ports 2 and 3 be open

(full reflection) and perfectly matching ports 5 and 6. For the field map measurements, we connect the signal input port of the measured network to VNA port 1, while perfectly matching the other ports of the network. We manually probe the field at the middle of the microstrip lines by using a coaxial probe, which is connected to VNA port 2, as shown in Extended Data Fig. [8b](#).

Validation of the model assumptions

The model is the one of a unitary scattering network, namely, lossless scatterers connected by links imparting phase delays. Microstrip transmission lines are known to behave as pure phase delays in this frequency range, since the propagation losses over so short distances are negligible (we indeed measured them to be $0.0167 \text{ dB cm}^{-1}$). We are therefore left with checking that Supplementary equations (1)–(3) (see details in [Supplementary Information](#) part II) are a good model for the scatterers.

We start by checking the validity of the assumptions behind Supplementary equations (1)–(3), namely, that the scatterers have three-fold rotational symmetry (C_3 symmetry), and that they are unitary. To do this, we measured the scattering matrix S^M of our scatterers. We start with checking C_3 symmetry, which implies that $S_{12} = S_{23} = S_{31}$, as well as $S_{11} = S_{22} = S_{33}$. Extended Data Fig. [3a](#) plots the moduli and arguments of all these quantities in the considered frequency range. From these plots, we see that although some small deviations from C_3 symmetry are observed in the reflection coefficients, they correspond to fluctuations of reflection below -20 dB . We conclude that C_3 symmetry is a valid assumption.

Next, we check unitarity. Extended Data Fig. [3b](#) plots the eigenvalues of the measured scattering matrix versus frequency, in the complex plane. We can see that they are always very close to the unit circle, meaning that unitarity is also a very reasonable assumption. This is expected since we used a substrate with a small loss tangent of 10^{-4} and circulators with low insertion losses of 0.2 dB . Absorption is therefore not expected to alter the prediction of the unitary theory, but simply to add an exponential decay which shows itself especially for large samples. For example, while long range transport from Geneva to Davos in the circulator network of Fig. [4b](#) is associated with 20 dB of signal attenuation, the presence of the edge mode predicted by the unitary theory is not affected (see Extended Data Fig. [7](#)).

Now, we estimate the error that we make by modelling the real matrix S^M with Supplementary equations (1)–(3). To do this, we find the C_3 -symmetric unitary scattering matrix S^U that is the closest to S^M . We get S^U by rescaling the eigenvalues of S^M to make them exactly unitary, keeping their arguments. We then determine the parameters ξ and η of S^U , which we plot against frequency in Extended Data Fig. [3c](#). We then define an S-parameter error metric as

$$\begin{aligned} \text{\$}\$\varepsilon = & \left\{ \frac{1}{3} \left(\left| S_{11}^M - S_{11}^U \right|^2 + \left| S_{12}^M - S_{12}^U \right|^2 + \left| S_{21}^M - S_{21}^U \right|^2 \right) \right\}^{1/2}. \end{aligned} \quad (5)$$

This quantity represents the error that we make by using Supplementary equations (1)–(3). It is plotted in Extended Data Fig. 3d. We see that this error is below 5% at all frequencies, which unambiguously validates the relevance of Supplementary equation (3).

Data availability

The data that support the findings of this study are available at <https://doi.org/10.5281/zenodo.5101825>.

Code availability

The codes that support the findings of this study are available at <https://doi.org/10.5281/zenodo.5101825>.

References

1. 1. Hasan, M. Z. & Kane, C. L. Topological insulators. *Rev. Mod. Phys.* **82**, 3045–3067 (2010).
2. 2. Thouless, D. J., Kohmoto, M., Nightingale, M. P. & den Nijs, M. Quantized Hall conductance in a two-dimensional periodic potential. *Phys. Rev. Lett.* **49**, 405–408 (1982).
3. 3. Kane, C. L. & Mele, E. J. Z_2 topological order and the quantum spin Hall effect. *Phys. Rev. Lett.* **95**, 146802 (2005).
4. 4. Lu, L., Joannopoulos, J. D. & Soljačić, M. Topological photonics. *Nat. Photon.* **8**, 821–829 (2014).

5. 5.

Ozawa, T. et al. Topological photonics. *Rev. Mod. Phys.* **91**, 015006 (2019).

6. 6.

Hafezi, M., Demler, E. A., Lukin, M. D. & Taylor, J. M. Robust optical delay lines with topological protection. *Nat. Phys.* **7**, 907–912 (2011).

7. 7.

Hafezi, M., Mittal, S., Fan, J., Migdall, A. & Taylor, J. M. Imaging topological edge states in silicon photonics. *Nat. Photon.* **7**, 1001–1005 (2013).

8. 8.

Fleury, R., Khanikaev, A. B. & Alù, A. Floquet topological insulators for sound. *Nat. Commun.* **7**, 11744 (2016).

9. 9.

Khanikaev, A. B. & Shvets, G. Two-dimensional topological photonics. *Nat. Photon.* **11**, 763–773 (2017).

10. 10.

Cha, J., Kim, K. W. & Daraio, C. Experimental realization of on-chip topological nanoelectromechanical metamaterials. *Nature* **564**, 229–233 (2018).

11. 11.

Zeng, Y. et al. Electrically pumped topological laser with valley edge modes. *Nature* **578**, 246–250 (2020).

12. 12.

Zangeneh-Nejad, F., Sounas, D. L., Alù, A. & Fleury, R. Analogue computing with metamaterials. *Nat. Rev. Mater.* **6**, 207–225 (2021).

13. 13.

Nassar, H. et al. Nonreciprocity in acoustic and elastic materials. *Nat. Rev. Mater.* **5**, 667–685 (2020).

14. 14.

Haldane, F. D. M. Model for a quantum Hall effect without Landau levels: condensed-matter realization of the ‘parity anomaly’. *Phys. Rev. Lett.* **61**, 2015–2018 (1988).

15. 15.

Haldane, F. D. M. & Raghu, S. Possible realization of directional optical waveguides in photonic crystals with broken time-reversal symmetry. *Phys. Rev. Lett.* **100**, 013904 (2008).

16. 16.

Wang, Z., Chong, Y., Joannopoulos, J. D. & Soljačić, M. Observation of unidirectional backscattering-immune topological electromagnetic states. *Nature* **461**, 772–775 (2009).

17. 17.

Khanikaev, A. B., Fleury, R., Mousavi, S. H. & Alù, A. Topologically robust sound propagation in an angular-momentum-biased graphene-like resonator lattice. *Nat. Commun.* **6**, 8260 (2015).

18. 18.

Bahari, B. et al. Nonreciprocal lasing in topological cavities of arbitrary geometries. *Science* **358**, 636–640 (2017).

19. 19.

Banerjee, D., Souslov, A., Abanov, A. G. & Vitelli, V. Odd viscosity in chiral active fluids. *Nat. Commun.* **8**, 1573 (2017).

20. 20.

Souslov, A., van Zuiden, B. C., Bartolo, D. & Vitelli, V. Topological sound in active-liquid metamaterials. *Nat. Phys.* **13**, 1091–1094 (2017).

21. 21.

Mitchell, N. P., Nash, L. M., Hexner, D., Turner, A. M. & Irvine, W. T. M. Amorphous topological insulators constructed from random point sets. *Nat. Phys.* **14**, 380–385 (2018).

22. 22.

Hofmann, T., Helbig, T., Lee, C. H., Greiter, M. & Thomale, R. Chiral voltage propagation and calibration in a topoelectrical Chern circuit. *Phys. Rev. Lett.* **122**, 247702 (2019).

23. 23.

Nuckolls, K. P. et al. Strongly correlated Chern insulators in magic-angle twisted bilayer graphene. *Nature* **588**, 610–615 (2020).

24. 24.

Darabi, A., Ni, X., Leamy, M. & Alù, A. Reconfigurable Floquet elastodynamic topological insulator based on synthetic angular momentum bias. *Sci. Adv.* **6**, eaba8656 (2020).

25. 25.

Ding, Y. et al. Experimental demonstration of acoustic Chern insulators. *Phys. Rev. Lett.* **122**, 014302 (2019).

26. 26.

Süsstrunk, R. & Huber, S. D. Observation of phononic helical edge states in a mechanical topological insulator. *Science* **349**, 47–50 (2015).

27. 27.

Peri, V. et al. Experimental characterization of fragile topology in an acoustic metamaterial. *Science* **367**, 797–800 (2020).

28. 28.

Chen, G. et al. Tunable correlated Chern insulator and ferromagnetism in a moiré superlattice. *Nature* **579**, 56–61 (2020); correction **581**, E3 (2020).

29. 29.

Wu, L.-H. & Hu, X. Scheme for achieving a topological photonic crystal by using dielectric material. *Phys. Rev. Lett.* **114**, 223901 (2015).

30. 30.

Chalker, J. T. & Coddington, P. D. Percolation, quantum tunnelling and the integer Hall effect. *J. Phys. C* **21**, 2665–2679 (1988).

31. 31.

Liang, G. Q. & Chong, Y. D. Optical resonator analog of a two-dimensional topological insulator. *Phys. Rev. Lett.* **110**, 203904 (2013).

32. 32.

Pasek, M. & Chong, Y. D. Network models of photonic Floquet topological insulators. *Phys. Rev. B* **89**, 075113 (2014).

33. 33.

Delplace, P., Fruchart, M. & Tauber, C. Phase rotation symmetry and the topology of oriented scattering networks. *Phys. Rev. B* **95**, 205413 (2017).

34. 34.

Upreti, L. K. et al. Topological swing of Bloch oscillations in quantum walks. *Phys. Rev. Lett.* **125**, 186804 (2020).

35. 35.

Afzal, S., Zimmerling, T. J., Ren, Y., Perron, D. & Van, V. Realization of anomalous Floquet insulators in strongly coupled nanophotonic lattices. *Phys. Rev. Lett.* **124**, 253601 (2020).

36. 36.

Gao, F. et al. Probing topological protection using a designer surface plasmon structure. *Nat. Commun.* **7**, 11619 (2016).

37. 37.

Peng, Y.-G. et al. Experimental demonstration of anomalous Floquet topological insulator for sound. *Nat. Commun.* **7**, 13368 (2016).

38. 38.

Delplace, P. Topological chiral modes in random scattering networks. *SciPost Phys.* **8**, 081 (2020).

39. 39.

Kitagawa, T., Berg, E., Rudner, M. & Demler, E. Topological characterization of periodically driven quantum systems. *Phys. Rev. B* **82**, 235114 (2010).

40. 40.

Lindner, N. H., Refael, G. & Galitski, V. Floquet topological insulator in semiconductor quantum wells. *Nat. Phys.* **7**, 490–495 (2011).

41. 41.

Rechtsman, M. C. et al. Photonic Floquet topological insulators. *Nature* **496**, 196–200 (2013).

42. 42.

Rudner, M. S., Lindner, N. H., Berg, E. & Levin, M. Anomalous edge states and the bulk-edge correspondence for periodically driven two-dimensional systems. *Phys. Rev. X* **3**, 031005 (2013).

43. 43.

Maczewsky, L. J., Zeuner, J. M., Nolte, S. & Szameit, A. Observation of photonic anomalous Floquet topological insulators. *Nat. Commun.* **8**, 13756 (2017).

44. 44.

Rudner, M. S. & Lindner, N. H. Band structure engineering and non-equilibrium dynamics in Floquet topological insulators. *Nat. Rev. Phys.* **2**, 229–244 (2020).

45. 45.

Wintersperger, K. Realization of an anomalous Floquet topological system with ultracold atoms. *Nat. Phys.* **16**, 1058–1063 (2020).

46. 46.

Fruchart, M., Hanai, R., Littlewood, P. B. & Vitelli, V. Non-reciprocal phase transitions. *Nature* **592**, 363–369 (2021).

47. 47.

Bogaerts, W. et al. Programmable photonic circuits. *Nature* **586**, 207–216 (2020).

48. 48.

Kord, A., Sounas, D. L. & Alu, A. Microwave nonreciprocity. *Proc. IEEE* **108**, 1728–1758 (2020).

49. 49.

Pozar, D. M. *Microwave Engineering* (Wiley, 1998).

Acknowledgements

Z.Z. and R.F. acknowledge funding from the Swiss National Science Foundation under the Eccellenza award number 181232. P.D. acknowledges support from the IDEX Lyon Breakthrough programme ToRe (contract no.ANR-16-IDEX-0005).

Author information

Affiliations

1. Laboratory of Wave Engineering, School of Electrical Engineering, EPFL, Lausanne, Switzerland

Zhe Zhang & Romain Fleury

2. Univ Lyon, ENS de Lyon, Univ Claude Bernard, CNRS, Laboratoire de Physique, Lyon, France

Pierre Delplace

Contributions

Z.Z. performed the numerical simulations and experiments, under the supervision of R.F. P.D. and R.F. conceived the project. All authors participated in writing and revising the manuscript.

Corresponding author

Correspondence to Romain Fleury.

Ethics declarations

Competing interests

The authors declare no competing interests.

Additional information

Peer review information *Nature* thanks Ching Hua Lee, Xue-Feng Zhu and Rui Yu for their contribution to the peer review of this work. Peer reviewer reports are available.

Publisher's note Springer Nature remains neutral with regard to jurisdictional claims in published maps and institutional affiliations.

Extended data figures and tables

[Extended Data Fig. 1 Detailed schematic of the unit cell of the non-reciprocal network and signal labelling convention.](#)

We define three state vectors: $|a\rangle$, $|b\rangle$, and $|c\rangle$, which represent scattering wave amplitudes propagating out, between and into the non-reciprocal elements, respectively. The total phase delay between two scatterers is φ .

[Extended Data Fig. 2 Floquet band structures at two special points of the topological phase diagram.](#)

a, b, Bulk band structures at the green (**a**) and centre (**b**) points of the phase diagram of Fig. [2c](#) in the main text. The green point corresponds to a phase-rotation symmetric network of perfect matched circulators, thus in AFI phase. The red centre point represents a network of reciprocal resonant scatterers, with all bandgaps closed. **c, d**, Ribbon band structures corresponding to panel **a** and **b**, respectively. The perfect circulator network features flat bulk band with dispersionless edge modes regardless of the value of the quasi-energy φ , which can only occur in the AFI phase.

[Extended Data Fig. 3 Experimental validation of the model assumptions.](#)

a, C3 symmetry holds when $S_{12} = S_{23} = S_{31}$ as well as $S_{11} = S_{22} = S_{33}$, which is very well satisfied in the considered frequency range. **b**, Eigenvalues of the measured scattering matrix, with nearly-unitary behaviour over the entire experimental bandwidth. **c**, ξ and η parameters used to approximate the real scattering matrix with a C3-symmetric unitary matrix. The red area is the Chern phase, and the blue area the anomalous one. **d**, Error in % made by approximating the real scattering matrix with equation (4) over the entire bandwidth.

Extended Data Fig. 4 Experimental network design and measured scattering parameters.

a, Measured reflection spectrum of an individual ferrite circulator. The blue-shaded area represents the bandwidth of the anomalous phase, corresponding to low reflection ($|R| < -9.5 \text{ dB} = 20 \cdot \log_{10}(1/3)$). By contrast, the red-shaded area shows the Chern phase with high reflection ($|R| > -9.5 \text{ dB}$). Topological phase transitions happen at around 3.9 GHz and 7 GHz. **b**, Topological bandgap map predicted from the individual scattering data, when varying the length of the microstrip connections and the operating frequency. The blue and red regions correspond to bandgaps with and without topological edge modes, respectively. The white regions represent bulk bands. **c**, Design details of the experimental networks probed in Fig. 3b of the main text. Network 1 (N1) has a uniform length distribution of microstrip lines with $L = L_1$. For network 2 (N2), we introduce an interface and replace the bottom part with lines of different length L_2 . **d**, Measured amplitudes of the scattering parameters S_{21} (left), S_{31} (middle) and S_{22} (right) in the Chern-phase frequency band (green dashed box in panel b). **e**, Measured scattering parameters in the anomalous-phase frequency band (yellow dashed box in panel b).

Extended Data Fig. 5 Numerical and experimental field maps for excitation at port 2.

a, Numerical predictions for excitation at port 2 for the same system as in Fig. 3 of the main text. While the anomalous phase supports transmission to port 3 regardless of the phase link distribution, the Chern phase possesses a trivial bandgap at $\varphi = \pi/2$, and reflects all the energy incident from port 2, see bottom right plot (the field distribution exhibits exponential decay). **b**, Corresponding experimental data.

Extended Data Fig. 6 Numerical and experimental field maps for excitation at port 3.

a, Numerical predictions for excitation at port 3 for the same system as in Fig. 3 of the main text. Both the anomalous and Chern phases fall in topological bandgap at $\varphi = \pi/2$, leading to transmission to port 1. **b**, Corresponding experimental data.

Extended Data Fig. 7 Additional field maps for the anomalous topological Switzerland-shaped network.

We plot simulated (**a**) and experimental (**b**) transmissions from Geneva (port 1) to Davos (port 4) for the same network in Fig. 4 of the main text, leaving all other ports

open. **c**, Numerical prediction corresponding to the experimental data shown in Fig. 4c of the main text.

[Extended Data Fig. 8 Experimental setups for scattering parameter and field distribution measurements.](#)

a, The setup consists of a vector network analyser (VNA) and three microwave non-reciprocal networks: the Switzerland-shaped network (left), N1 (middle), and N2 (right). **b**, Field map measurement with a coaxial probe for measuring fields on the microstrip lines.

[Extended Data Fig. 9 Experimental validation of anomalous phase disorder robustness in four other prototypes with distinct disorder realizations.](#)

a, Pictures of the prototypes, having the same irregular shape but different phase delay distributions implemented by varying the geometry of the serpentine links. **b**, Measured field maps in the AFI phase. **c**, Measured field maps in the CI phase.

Supplementary information

[Supplementary Information](#)

This file contains six Supplementary Discussion sections I–VI, Supplementary Figures 1–11 and Supplementary References. The six Supplementary Discussion Sections include: I. Theoretical modelling; II. Simulation method of arbitrary finite non-reciprocal networks; III. Examples of disorder realisations for phase-link delays and scattering matrices; IV. Discussion of the measured amplitudes of the scattering parameters in Extended Data Fig. 4; V. Mapping of the honeycomb lattice to an oriented graph and VI. Robustness comparisons with other Chern phases.

[Peer Review File](#)

Rights and permissions

Open Access This article is licensed under a Creative Commons Attribution 4.0 International License, which permits use, sharing, adaptation, distribution and reproduction in any medium or format, as long as you give appropriate credit to the original author(s) and the source, provide a link to the Creative Commons license, and indicate if changes were made. The images or other third party material in this article

are included in the article's Creative Commons license, unless indicated otherwise in a credit line to the material. If material is not included in the article's Creative Commons license and your intended use is not permitted by statutory regulation or exceeds the permitted use, you will need to obtain permission directly from the copyright holder. To view a copy of this license, visit <http://creativecommons.org/licenses/by/4.0/>.

[Reprints and Permissions](#)

About this article

Cite this article

Zhang, Z., Delplace, P. & Fleury, R. Superior robustness of anomalous non-reciprocal topological edge states. *Nature* **598**, 293–297 (2021). <https://doi.org/10.1038/s41586-021-03868-7>

- Received: 03 March 2021
- Accepted: 29 July 2021
- Published: 13 October 2021
- Issue Date: 14 October 2021
- DOI: <https://doi.org/10.1038/s41586-021-03868-7>

Share this article

Anyone you share the following link with will be able to read this content:

[Get shareable link](#)

Sorry, a shareable link is not currently available for this article.

[Copy to clipboard](#)

Provided by the Springer Nature SharedIt content-sharing initiative

This article was downloaded by **calibre** from <https://www.nature.com/articles/s41586-021-03868-7>

- Article
- [Published: 13 October 2021](#)

An elastic metal–organic crystal with a densely catenated backbone

- [Wenjing Meng](#)¹ na1 nAff8,
- [Shun Kondo](#)² na1,
- [Takuji Ito](#)³,
- [Kazuki Komatsu](#) [ORCID: orcid.org/0000-0003-3573-9174](#)⁴,
- [Jenny Pirillo](#)⁵,
- [Yuh Hijikata](#) [ORCID: orcid.org/0000-0003-4883-5085](#)⁵,
- [Yuichi Ikuhara](#)²,
- [Takuzo Aida](#) [ORCID: orcid.org/0000-0002-0002-8017](#)^{1,6} &
- [Hiroshi Sato](#) [ORCID: orcid.org/0000-0002-5899-1340](#)^{1,6,7}

[Nature](#) volume **598**, pages 298–303 (2021)

- 3300 Accesses
- 34 Altmetric
- [Metrics details](#)

Subjects

- [Crystal engineering](#)
- [Interlocked molecules](#)
- [Mechanical properties](#)

Abstract

What particular mechanical properties can be expected for materials composed of interlocked backbones has been a long-standing issue in materials science since the first reports on polycatenane and polyrotaxane in the 1970s^{1,2,3}. Here we report a three-dimensional porous metal–organic crystal, which is exceptional in that its warps and wefts are connected only by catenation. This porous crystal is composed of a tetragonal lattice and dynamically changes its geometry upon guest molecule release, uptake and exchange, and also upon temperature variation even in a low temperature range. We indented⁴ the crystal along its *a/b* axes and obtained the Young's moduli of 1.77 ± 0.16 GPa in *N,N*-dimethylformamide and 1.63 ± 0.13 GPa in tetrahydrofuran, which are the lowest among those reported so far for porous metal–organic crystals⁵. To our surprise, hydrostatic compression showed that this elastic porous crystal was the most deformable along its *c* axis, where 5% contraction occurred without structural deterioration upon compression up to 0.88 GPa. The crystal structure obtained at 0.46 GPa showed that the catenated macrocycles move translationally upon contraction. We anticipate our mechanically interlocked molecule-based design to be a starting point for the development of porous materials with exotic mechanical properties. For example, squeezable porous crystals that may address an essential difficulty in realizing both high abilities of guest uptake and release are on the horizon.

Access options

Subscribe to Journal

Get full journal access for 1 year

\$199.00

only \$3.90 per issue

[Subscribe](#)

All prices are NET prices.

VAT will be added later in the checkout.

Tax calculation will be finalised during checkout.

Rent or Buy article

Get time limited or full article access on ReadCube.

from \$8.99

[Rent or Buy](#)

All prices are NET prices.

Additional access options:

- [Log in](#)
- [Access through your institution](#)
- [Learn about institutional subscriptions](#)

Fig. 1: Crystal structure of CTN MOF at 25°C with a space group of $P4_122$.

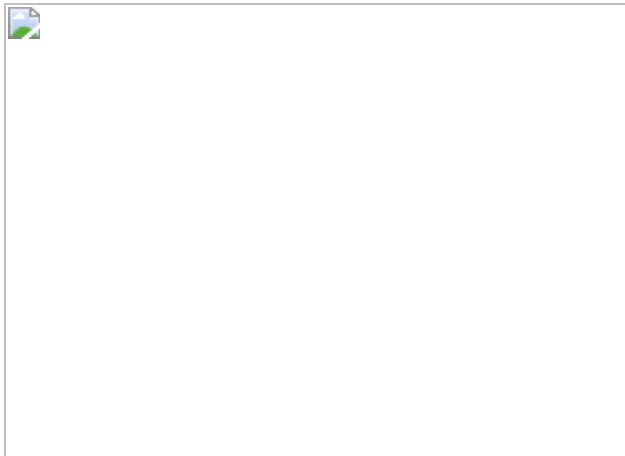


Fig. 2: Guest-responsive properties of CTN MOF.

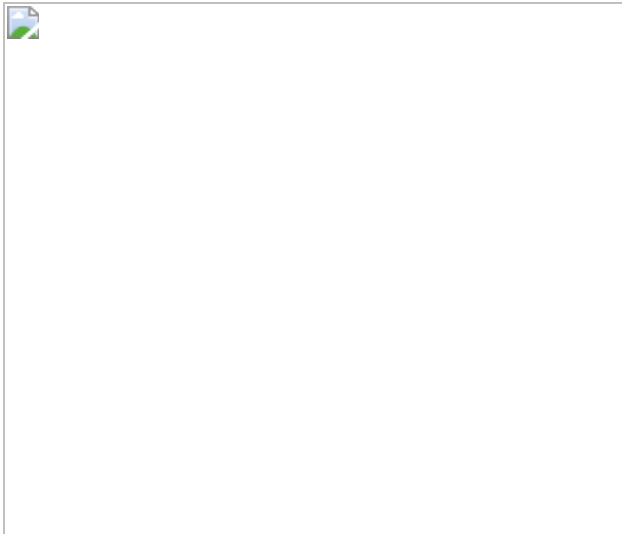


Fig. 3: Temperature- and guest-dependent structural transformations of CTNMOF .

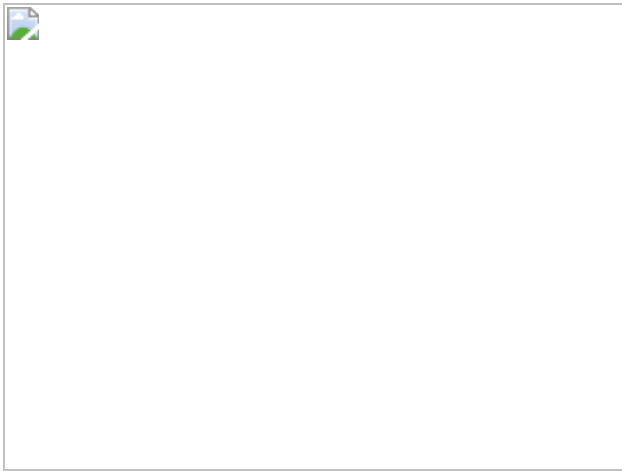
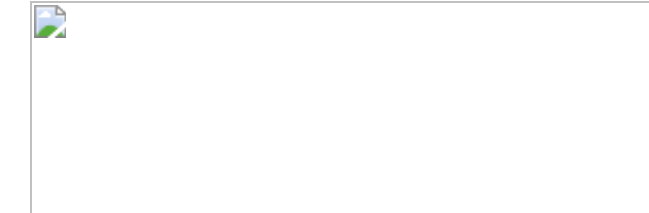


Fig. 4: Elastic properties of CTNMOF .



Data availability

All data are available in the Article or its [Supplementary Information](#).

References

1. 1.

Agam, G., Graiver, D. & Zilkha, A. Studies on the formation of topological isomers by statistical methods. *J. Am. Chem. Soc.* **98**, 5206–5214 (1976).

2. 2.

Ogata, N., Sanui, K. & Wada, J. Novel synthesis of inclusion polyamides. *J. Polym. Sci. Polym. Lett. Ed.* **14**, 459–462 (1976).

3. 3.

Raymo, F. M. & Stoddart, J. F. Interlocked macromolecules. *Chem. Rev.* **99**, 1643–1663 (1999).

4. 4.

Bhushan, B. & Li, X. A review of nanoindentation continuous stiffness measurement technique and its applications. *Mater. Charact.* **48**, 11–36 (2002).

5. 5.

Tan, J. C. & Cheetham, A. K. Mechanical properties of hybrid inorganic–organic framework materials: establishing fundamental structure–property relationships. *Chem. Soc. Rev.* **40**, 1059–1080 (2011).

6. 6.

Bruns, C. J. & Stoddart, J. F. *The Nature of the Mechanical Bond: From Molecules to Machines* Ch. 1 (John Wiley & Sons, 2017).

7. 7.

Frisch, H. L. & Wasserman, E. Chemical topology. *J. Am. Chem. Soc.* **83**, 3789–3795 (1961).

8. 8.

Evans, N. H. & Beer, P. D. Progress in the synthesis and exploitation of catenanes since the millennium. *Chem. Soc. Rev.* **43**, 4658–4683 (2014).

9. 9.

Gil-Ramírez, G., Leigh, D. A. & Stephens, A. J. Catenanes: fifty years of molecular links. *Angew. Chem. Int. Ed.* **54**, 6110–6150 (2015).

10. 10.

Xue, M., Yang, Y., Chi, X., Yan, X. & Huang, F. Development of pseudorotaxanes and rotaxanes: from synthesis to stimuli-responsive motions to applications. *Chem. Rev.* **115**, 7398–7501 (2015).

11. 11.

Sauvage, J.-P. EurJOC—50 years of rotaxanes. *Eur. J. Org. Chem.* **2019**, 3287–3288 (2019).

12. 12.

Amabilino, D. B. & Stoddart, J. F. Interlocked and intertwined structures and superstructures. *Chem. Rev.* **95**, 2725–2828 (1995).

13. 13.

Sauvage, J.-P. & Dietrich-Buchecker, C. *Molecular Catenanes, Rotaxanes and Knots: a Journey Through the World of Molecular Topology* (Wiley-VCH, 1999).

14. 14.

Kassem, S. et al. Artificial molecular motors. *Chem. Soc. Rev.* **46**, 2592–2621 (2017).

15. 15.

Erbas-Cakmak, S., Leigh, D. A., McTernan, C. T. & Nussbaumer, A. L. Artificial molecular machines. *Chem. Rev.* **115**, 10081–10206 (2015).

16. 16.

Niu, Z. & Gibson, H. W. Polycatenanes. *Chem. Rev.* **109**, 6024–6046 (2009).

17. 17.

Takata, T. Polyrotaxane and polyrotaxane network: supramolecular architectures based on the concept of dynamic covalent bond chemistry. *Polym. J.* **38**, 1–20 (2006).

18. 18.

Harada, A., Hashidzume, A., Yamaguchi, H. & Takashima, Y. Polymeric rotaxanes. *Chem. Rev.* **109**, 5974–6023 (2009).

19. 19.

Wu, Q. et al. Poly[*n*]catenanes: synthesis of molecular interlocked chains. *Science* **358**, 1434–1439 (2017).

20. 20.

Mena-Hernando, S. & Pérez, E. M. Mechanically interlocked materials. Rotaxanes and catenanes beyond the small molecule. *Chem. Soc. Rev.* **48**, 5016–5032 (2019).

21. 21.

Qiu, Y. et al. A precise polyrotaxane synthesizer. *Science* **368**, 1247–1253 (2020).

22. 22.

Okumura, Y. & Ito, K. The polyrotaxane gel: a topological gel by figure-of-eight cross-links. *Adv. Mater.* **13**, 485–487 (2001).

23. 23.

Choi, S., Kwon, T.-W., Coskun, A. & Choi, J. W. Highly elastic binders integrating polyrotaxanes for silicon microparticle anodes in lithium ion batteries. *Science*, **357**, 279–283 (2017).

24. 24.

<http://www-materials.eng.cam.ac.uk/mpsite/properties/non-IE/stiffness.html>

25. 25.

Charitidis, C. A., Koumoulos, E. P., Nikolakis, V. & Dragatogiannis, D. A. Structural and nanomechanical properties of a zeolite membrane measured using nanoindentation. *Thin Solid Films* **526**, 168–175 (2012).

26. 26.

Kitagawa, S., Kitaura, R. & Noro, S. Functional porous coordination polymers. *Angew. Chem. Int. Ed.* **43**, 2334–2375 (2004).

27. 27.

Yaghi, O. M. et al. Reticular synthesis and the design of new materials. *Nature* **423**, 705–714 (2003).

28. 28.

Loeb, S. J. Metal–organic rotaxane frameworks; MORFs. *Chem. Commun.* 1511–1518 (2005).

29. 29.

Li, Q. et al. A catenated strut in a catenated metal–organic framework. *Angew. Chem. Int. Ed.* **49**, 6751–6755 (2010).

30. 30.

Li, Q. et al. A metal–organic framework replete with ordered donor–acceptor catenanes. *Chem. Commun.* **46**, 380–382 (2010).

31. 31.

Zhao, Y.-L. et al. Rigid-strut-containing crown ethers and [2]catenanes for incorporation into metal–organic frameworks. *Chem. Eur. J.* **15**, 13356–13380 (2009).

32. 32.

Vukotic, V. N., Harris, K. J., Zhu, K., Schurko, R. W. & Loeb, S. J. Metal–organic frameworks with dynamic interlocked components. *Nat. Chem.* **4**, 456–460 (2012).

33. 33.

Zhu, K., Vukotic, V. N., O’Keefe, C. A., Schurko, R. W. & Loeb, S. J. Metal–organic frameworks with mechanically interlocked pillars: controlling ring dynamics in the solid-state via a reversible phase change. *J. Am. Chem. Soc.* **136**, 7403–7409 (2014).

34. 34.

Zhu, K., O’Keefe, C. A., Vukotic, V. N., Schurko, R. W. & Loeb, S. J. A molecular shuttle that operates inside a metal–organic framework. *Nat. Chem.* **7**, 514–519 (2015).

35. 35.

Chen, Q. et al. A redox-active bistable molecular switch mounted inside a metal–organic framework. *J. Am. Chem. Soc.* **138**, 14242–14245 (2016).

36. 36.

Frank, N. C., Mercer, D. J. & Loeb, S. J. An interwoven metal-organic framework combining mechanically interlocked linkers and interpenetrated networks. *Chem. Eur. J.* **19**, 14076–14080 (2013).

37. 37.

Gholami, G., Zhu, K., Ward, J. S., Kruger, P. E. & Loeb, S. J. Formation of a polythreaded, metal–organic framework utilizing an interlocked hexadentate, carboxylate linker. *Eur. J. Inorg. Chem.* 4524–4529 (2016).

38. 38.

Gholami, G., Baggi, G., Zhu, K. & Loeb, S. J. Metal–organic frameworks utilising an interlocked, hexadentate linker containing a tetra-carboxylate axle and a bis(pyridine) wheel. *Dalton Trans.* **46**, 2462–2470 (2017).

39. 39.

Lewis, J. E. M. Self-templated synthesis of amide catenanes and formation of a catenane coordination polymer. *Org. Biomol. Chem.* **17**, 2442–2447 (2019).

40. 40.

Johnston, A. G., Leigh, D. A., Pritchard, R. J. & Deegan, M. D. Facile synthesis and solid-state structure of a benzylic amide [2]catenane. *Angew. Chem. Int. Ed. Engl.* **34**, 1209–1212 (1995).

41. 41.

Spek, A. L. Single-crystal structure validation with the program PLATON. *J. Appl. Cryst.* **36**, 7–13 (2003).

42. 42.

Schneemann, A. et al. Flexible metal–organic frameworks. *Chem. Soc. Rev.* **43**, 6062–6096 (2014).

43. 43.

Chui, S. S.-Y., Lo, S. M.-F., Charmant, J. P. H., Orpen, A. G. & Williams, I. D. A chemically functionalizable nanoporous material $[\text{Cu}_3(\text{TMA})_2(\text{H}_2\text{O})_3]_n$. *Science* **283**, 1148–1150 (1999).

44. 44.

Bundschuh, S. et al. Mechanical properties of metal–organic frameworks: an indentation study on epitaxial thin films. *Appl. Phys. Lett.* **101**, 101910 (2012).

45. 45.

Henke, S., Li, W. & Cheetham, A. K. Guest-dependent mechanical anisotropy in pillared-layered soft porous crystals—a nanoindentation study. *Chem. Sci.* **5**, 2392–2397 (2014).

46. 46.

Engineering ToolBox. Young’s modulus—tensile and yield strength for common materials, https://www.engineeringtoolbox.com/young-modulus-d_417.html (2003).

47. 47.

Boehler, R. New diamond cell for single-crystal X-ray diffraction. *Rev. Sci. Instrum.* **77**, 115103 (2006).

48. 48.

Ratajczyk, P., Sobczak, S. & Katrusiak, A. High-pressure structure and properties of *N,N*-dimethylformamide. *Cryst. Growth Des.* **19**, 896–901 (2019).

49. 49.

CrystalClear v.1.3.6 (Rigaku, 2015).

50. 50.

CrysAlis v.40.84a (Rigaku, 2015).

51. 51.

Burla, M. C. et al. SIR2011: a new package for crystal structure determination and refinement. *J. Appl. Cryst.* **45**, 357–361 (2012).

52. 52.

Burla, M. C. et al. IL MILIONE: a suite of computer programs for crystal structure solution of proteins. *J. Appl. Cryst.* **40**, 609–613 (2007).

53. 53.

Creagh, D. C. & McAuley, W. J. in *International Tables for Crystallography* Vol. C (ed. Wilson, A. J. C.) 572 (Kluwer Academic, 1992).

54. 54.

Ibers, J. A. & Hamilton, W. C. Dispersion corrections and crystal structure refinements. *Acta Crystallogr.* **17**, 781–782 (1964).

55. 55.

Creagh, D. C. & McAuley, W. J. in *International Tables for Crystallography* Vol. C (ed. Wilson, A. J. C.) 219–222 (Kluwer Academic, 1992).

56. 56.

Creagh, D. C. & Hubbell, J. H. in *International Tables for Crystallography*, Vol. C (ed. Wilson, A. J. C.) 200–206 (Kluwer Academic, 1992).

57. 57.

CrystalStructure v.4.2.5 (Rigaku, 2017).

58. 58.

Sheldrick, G. A. A short history of SHELX. *Acta Crystallogr. A* **64**, 112–122 (2008).

59. 59.

Oliver, W. C. & Pharr, G. M. Measurement of hardness and elastic modulus by instrumented indentation: advances in understanding and refinements to methodology. *J. Mater. Res.* **19**, 3–20 (2004).

60. 60.

Piermarini, G. J., Block, S. J., Barnett, D. & Forman, R. A. Calibration of the pressure dependence of the R_1 ruby fluorescence line to 195 kbar. *J. Appl. Phys.* **46**, 2774–2780 (1975).

Acknowledgements

A part of this work was conducted at the Advanced Characterization Nanotechnology Platform of the University of Tokyo, supported by ‘Nanotechnology Platform’ of the Ministry of Education, Culture, Sports, Science and Technology (MEXT), Japan. We thank K. Okitsu and K. Fukawa for technical assistance with SCXRD and PXRD, respectively; D. Hamane for discussions on high-pressure experiments; T. Uemura, N. Hosono and H. Taketomi for help with thermogravimetry/mass spectrometry measurements; S. Suginome for help with NMR spectral measurements and J.-S. M. Lee and K. Morishita for discussion on preparing the manuscript. T.A. acknowledges the Japan Society for the Promotion of Science (JSPS) for a JSPS Grant-In-Aid for Scientific Research (S) (18H05260) on ‘Innovative Functional Materials based on Multi-Scale Interfacial Molecular Science’. This work was also supported by JST, PRESTO (grant number JPMJPR20A5), Japan. H.S. is grateful for

JSPS KAKENHI grant numbers 17H05357 (Coordination Asymmetry), 18H04501 (Soft Crystal) and 20H02705 (Scientific Research (B)). W.M. acknowledges the receipt of a JSPS Postdoctoral Fellowship for Research in Japan and JSPS KAKENHI grant number 20K15251.

Author information

Author notes

1. Wenjing Meng

Present address: Research Center for Functional Materials, National Institute for Materials Science, Ibaraki, Japan

2. These authors contributed equally: Wenjing Meng, Shun Kondo

Affiliations

1. Department of Chemistry and Biotechnology, School of Engineering, The University of Tokyo, Tokyo, Japan

Wenjing Meng, Takuzo Aida & Hiroshi Sato

2. Institute of Engineering Innovation, School of Engineering, The University of Tokyo, Tokyo, Japan

Shun Kondo & Yuichi Ikuhara

3. ELIONIX INC., Tokyo, Japan

Takuji Ito

4. Geochemical Research Center, Graduate School of Science, The University of Tokyo, Tokyo, Japan

Kazuki Komatsu

5. Institute for Chemical Reaction Design and Discovery (WPI-ICReDD), Hokkaido University, Sapporo, Japan

Jenny Pirillo & Yuh Hijikata

6. RIKEN Center for Emergent Matter Science, Saitama, Japan

Takuzo Aida & Hiroshi Sato

7. Japan Science and Technology Agency (JST), Precursory Research for Embryonic Science and Technology (PRESTO), Saitama, Japan

Hiroshi Sato

Contributions

W.M., H.S. and T.A. conceived the project, designed experiments and directed the research. W.M. performed and interpreted all of the experiments associated with molecular synthesis, crystal growth and structural characterization. H.S. performed the sorption experiments. S.K., W.M. and Y.I. designed nanoindentation experiments. S.K., T.I. and W.M. conducted nanoindentation experiments. K.K., W.M. and H.S. performed high-pressure experiments. J.P. and Y.H. conducted the computational studies. All authors contributed to the writing and editing of the manuscript.

Corresponding authors

Correspondence to Takuzo Aida or Hiroshi Sato.

Ethics declarations

Competing interests

The authors declare no competing interests.

Additional information

Peer review information *Nature* thanks the anonymous reviewers for their contribution to the peer review of this work. Peer reviewer reports are available.

Publisher's note Springer Nature remains neutral with regard to jurisdictional claims in published maps and institutional affiliations.

Supplementary information

Supplementary Information

This file contains Supplementary text, figs. 1–47, tables 1–23 and references.

Peer Review File

Rights and permissions

Reprints and Permissions

About this article

Cite this article

Meng, W., Kondo, S., Ito, T. *et al.* An elastic metal–organic crystal with a densely catenated backbone. *Nature* **598**, 298–303 (2021).
<https://doi.org/10.1038/s41586-021-03880-x>

- Received: 25 February 2021
- Accepted: 06 August 2021
- Published: 13 October 2021
- Issue Date: 14 October 2021

- DOI: <https://doi.org/10.1038/s41586-021-03880-x>

Share this article

Anyone you share the following link with will be able to read this content:

[Get shareable link](#)

Sorry, a shareable link is not currently available for this article.

[Copy to clipboard](#)

Provided by the Springer Nature SharedIt content-sharing initiative

This article was downloaded by **calibre** from <https://www.nature.com/articles/s41586-021-03880-x>

| [Section menu](#) | [Main menu](#) |

- Article
- [Published: 25 August 2021](#)

Photocatalytic solar hydrogen production from water on a 100-m² scale

- [Hiroshi Nishiyama](#) ORCID: orcid.org/0000-0003-2065-3773^{1 na1},
- [Taro Yamada](#)^{1 na1},
- [Mamiko Nakabayashi](#) ORCID: orcid.org/0000-0001-6101-0382²,
- [Yoshiki Maehara](#)^{3,4},
- [Masaharu Yamaguchi](#)¹,
- [Yasuko Kuromiya](#)¹,
- [Yoshie Nagatsuma](#)¹,
- [Hiromasa Tokudome](#) ORCID: orcid.org/0000-0001-6624-0515^{3,5},
- [Seiji Akiyama](#)^{3,6},
- [Tomoaki Watanabe](#)⁷,
- [Ryoichi Narushima](#)¹,
- [Sayuri Okunaka](#) ORCID: orcid.org/0000-0003-3888-7201^{3,5 nAff9},
- [Naoya Shibata](#) ORCID: orcid.org/0000-0003-3548-5952²,
- [Tsuyoshi Takata](#)⁸,
- [Takashi Hisatomi](#) ORCID: orcid.org/0000-0002-5009-2383⁸ &
- [Kazunari Domen](#) ORCID: orcid.org/0000-0001-7995-4832^{1,8}

[Nature](#) volume 598, pages 304–307 (2021)

- 13k Accesses
- 72 Altmetric

- [Metrics details](#)

Subjects

- [Devices for energy harvesting](#)
- [Photocatalysis](#)
- [Solar fuels](#)

Abstract

The unprecedented impact of human activity on Earth's climate and the ongoing increase in global energy demand have made the development of carbon-neutral energy sources ever more important. Hydrogen is an attractive and versatile energy carrier (and important and widely used chemical) obtainable from water through photocatalysis using sunlight, and through electrolysis driven by solar or wind energy^{1,2}. The most efficient solar hydrogen production schemes, which couple solar cells to electrolysis systems, reach solar-to-hydrogen (STH) energy conversion efficiencies of 30% at a laboratory scale³. Photocatalytic water splitting reaches notably lower conversion efficiencies of only around 1%, but the system design is much simpler and cheaper and more amenable to scale-up^{1,2}—provided the moist, stoichiometric hydrogen and oxygen product mixture can be handled safely in a field environment and the hydrogen recovered. Extending our earlier demonstration of a 1-m² panel reactor system based on a modified, aluminium-doped strontium titanate particulate photocatalyst⁴, we here report safe operation of a 100-m² array of panel reactors over several months with autonomous recovery of hydrogen from the moist gas product mixture using a commercial polyimide membrane⁵. The system, optimized for safety and durability, and remaining undamaged on intentional ignition of recovered hydrogen, reaches a maximum STH of 0.76%. While the hydrogen production is inefficient and energy negative overall, our findings demonstrate that safe, large-scale photocatalytic water splitting, and gas collection and separation are possible. To make the technology economically viable and practically useful, essential next steps are reactor and process optimization to substantially reduce costs and improve STH efficiency, photocatalyst stability and gas separation efficiency.

Access options

Subscribe to Journal

Get full journal access for 1 year

\$199.00

only \$3.90 per issue

[Subscribe](#)

All prices are NET prices.

VAT will be added later in the checkout.

Tax calculation will be finalised during checkout.

Rent or Buy article

Get time limited or full article access on ReadCube.

from \$8.99

[Rent or Buy](#)

All prices are NET prices.

Additional access options:

- [Log in](#)
- [Access through your institution](#)
- [Learn about institutional subscriptions](#)

Fig. 1: The 100-m² water splitting photocatalyst panel reactor.

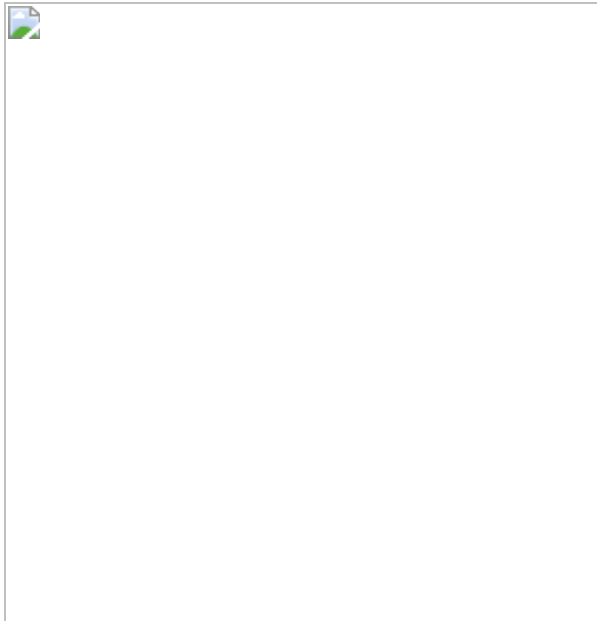


Fig. 2: Electron microscopy images of photocatalyst sheets.

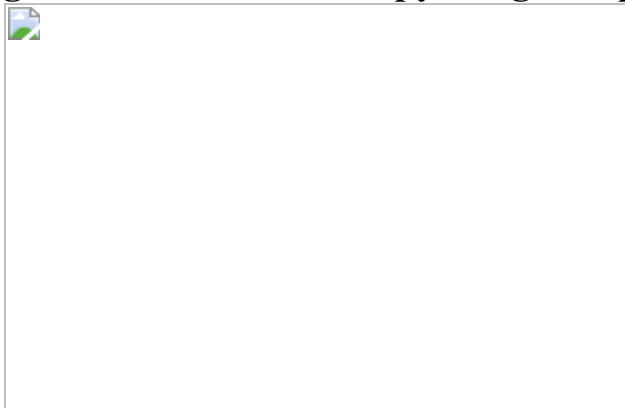
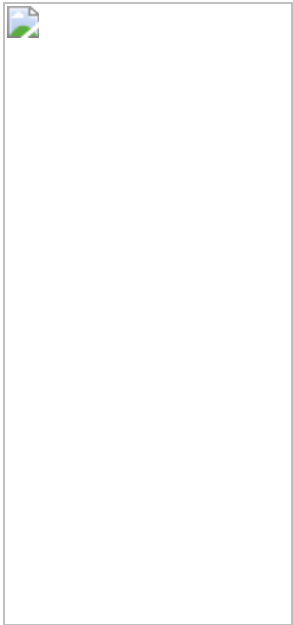


Fig. 3: Performance of the gas separation unit connected to the 100-m² water splitting photocatalyst panel reactor on 2 October 2020 at the Kakioka Research Facility.



Data availability

The authors declare that the data supporting the findings of this study are available within the paper and its Supplementary Information. [Source data](#) are provided with this paper.

References

1. 1.

Hisatomi, T. & Domen, K. Reaction systems for solar hydrogen production via water splitting with particulate semiconductor. *Nat. Catal.* **2**, 387–399 (2019).

2. 2.

Kim, J. H., Hansora, D., Sharma, P., Jang, J.-W. & Lee, J. Toward practical solar hydrogen production – an artificial photosynthetic leaf-to-farm challenge. *Chem. Soc. Rev.* **48**, 1908–1971 (2019).

3. 3.

Jia, J. et al. Solar water splitting by photovoltaic-electrolysis with a solar-to-hydrogen efficiency over 30%. *Nat. Commun.* **7**, 13237 (2016).

4. 4.

Goto, Y. et al. A particulate photocatalyst water-splitting panel for large-scale solar hydrogen production. *Joule* **2**, 509–520 (2018).

5. 5.

Tanahara, N., Nakanishi, S. & Yoshinaga, T. Gas and vapor separation through polyimide membranes. *J. Jpn. Petrol. Inst.* **59**, 276–282 (2016).

6. 6.

Pagliaro, M. Preparing for the future: solar energy and bioeconomy in the United Arab Emirates. *Energy Sci. Eng.* **7**, 1451–1457 (2019).

7. 7.

Boretti, A., Castelletto, S. & Al-Zubaidy, S. Concentrating solar power tower technology: present status and outlook. *Nonlinear Eng.* **8**, 10–31 (2019).

8. 8.

Wang, Q. et al. Scalable water splitting on particulate photocatalyst sheets with a solar-to-hydrogen energy conversion efficiency exceeding 1%. *Nat. Mater.* **15**, 611–615 (2016).

9. 9.

Takata, T. et al. Photocatalytic water splitting with quantum efficiency of almost unity. *Nature* **581**, 411–414 (2020).

10. 10.

Wang, Z. et al. Overall water splitting by Ta₃N₅ nanorod single crystals grown on the edges of KTaO₃ particles. *Nat. Catal.* **1**, 756–763 (2018).

11. 11.

Wang, Q. et al. Oxysulfide photocatalyst for visible-light-driven overall water splitting. *Nat. Mater.* **18**, 827–832 (2019).

12. 12.

Lyu, H. et al. An Al-doped SrTiO₃ photocatalyst maintaining sunlight-driven overall water splitting activity over 1000 h of constant illumination. *Chem. Sci.* **10**, 3196–3201 (2019).

13. 13.

Yamada, T. & Domen, K. Development of sunlight driven water splitting devices towards future artificial photosynthetic industry. *ChemEngineering* **2**, 36 (2018).

14. 14.

Maeda, K. et al. Characterization of Rh-Cr mixed-oxide nanoparticles dispersed on (Ga_{1-x}Zn_x)(N_{1-x}O_x) as a cocatalyst for visible-light-driven overall water splitting. *J. Phys. Chem. B* **110**, 13753–13758 (2006).

15. 15.

Peñas, P. et al. Decoupling gas evolution from water-splitting electrodes. *J. Electrochem. Soc.* **166**, H769–H776 (2019).

16. 16.

Kemppainen, E. et al. Effect of the ambient conditions on the operation of a large-area integrated photovoltaic-electrolyser. *Sustain. Energy Fuel* **4**, 4831–4847 (2020).

17. 17.

Wang, Q. et al. Particulate photocatalyst sheets based on carbon conductor layer for efficient Z-scheme pure-water splitting at ambient pressure. *J. Am. Chem. Soc.* **139**, 1675–1683 (2017).

18. 18.

Sayama, K. & Miseki, Y. Research and development of solar hydrogen production – toward the realization of ingenious photocatalysis-electrolysis hybrid system. *Synthesiology (Eng. edn)* **7**, 79–91 (2014).

19. 19.

Schroeder, V. & Holtappels K. Explosion characteristics of hydrogen-air and hydrogen-oxygen mixtures at elevated pressures. In *Proc. International Conference on Hydrogen Safety* 120001 (ICHS, 2005).

Acknowledgements

This work was funded by the New Energy and Industrial Technology Development Organization (NEDO), Japan. A part of this work was supported by the Nanotechnology Platform project by the Ministry of Education, Culture, Sports, Science and Technology of Japan (grant number JPMXP09A20UT0004). We are grateful to R. Dobashi and T. Mogi of the University of Tokyo for their advice with regard to gas explosion experiments and safety procedures. We are also grateful to H. Kita of Yamaguchi University and N. Tanihara of Ube Industries, Ltd for providing advice concerning polyimide separation membranes. We thank H. Ito of ARPChem for his support on the construction of the arrayed panel reactor. Finally, we thank all of the technical staff that participated in the fabrication and construction of the complete system.

Author information

Author notes

1. Sayuri Okunaka

Present address: Global Zero Emission Research Center (GZR),
National Institution of Advanced Industrial Science and Technology
(AIST), Tsukuba, Ibaraki, Japan

2. These authors contributed equally: Hiroshi Nishiyama, Taro Yamada

Affiliations

1. Office of University Professors, The University of Tokyo, Tokyo, Japan

Hiroshi Nishiyama, Taro Yamada, Masaharu Yamaguchi, Yasuko Kuromiya, Yoshie Nagatsuma, Ryoichi Narushima & Kazunari Domen

2. Institute of Engineering Innovation, School of Engineering, The University of Tokyo, Tokyo, Japan

Mamiko Nakabayashi & Naoya Shibata

3. Japan Technological Research Association of Artificial Photosynthetic Chemical Process (ARPChem), Tokyo, Japan

Yoshiki Maehara, Hiromasa Tokudome, Seiji Akiyama & Sayuri Okunaka

4. FUJIFILM Corporation, Ashigarakami-gun, Kanagawa, Japan

Yoshiki Maehara

5. Research Institute, TOTO Ltd., Chigasaki, Kanagawa, Japan

Hiromasa Tokudome & Sayuri Okunaka

6. Mitsubishi Chemical Corporation, Science & Innovation Center, Yokohama-shi, Kanagawa, Japan

Seiji Akiyama

7. Department of Applied Chemistry, School of Science and Technology,
Meiji University, Kawasaki-shi, Kanagawa, Japan

Tomoaki Watanabe

8. Research Initiative for Supra-Materials, Interdisciplinary Cluster for
Cutting Edge Research, Shinshu University, Nagano-shi, Nagano,
Japan

Tsuyoshi Takata, Takashi Hisatomi & Kazunari Domen

Contributions

K.D. planned and supervised this project. H.N. and T.Y. were responsible for the basic design, on-site design, construction and supervision of the plant. H.N. and T.T. investigated the cocatalyst deposition process, and designed, tested, fabricated and supervised the mass production of the photocatalytic reactors. S.O. and H.T. prepared the SrTiO₃:Al photocatalyst on a large scale. M.Y., Y.K., Y.N., R.N. and T.H. prepared the modified photocatalyst. M.N. and N.S. performed electron microscopy. Y.M. examined in situ gas evolution. T.Y. designed and constructed the gas filtration apparatus. T.Y. and H.N. performed the field testing of the entire solar hydrogen production system. H.N., T.Y., S.A, T.W. and K.D. examined the safety issues. T.Y., H.N., T.H. and K.D. discussed the results and wrote the manuscript.

Corresponding author

Correspondence to Kazunari Domen.

Ethics declarations

Competing interests

H.N., T.Y. and K.D. of the University of Tokyo hold patents related to this work (Japanese Unexamined Patent Application publication no. 2021-

75,319).

Additional information

Peer review information *Nature* thanks Frank Osterloh and the other, anonymous, reviewer(s) for their contribution to the peer review of this work. Peer reviewer reports are available.

Publisher's note Springer Nature remains neutral with regard to jurisdictional claims in published maps and institutional affiliations.

Extended data figures and tables

Extended Data Fig. 1 The photocatalyst panel reactors.

a, The design of a panel reactor unit (625 cm^2). **b**, A diagram showing the structure. **c**, **d**, Photographic images of the 3-m^2 module consisting of 48 panel reactor units viewed from the front (**c**) and rear (**d**).

Extended Data Fig. 2 Photocatalyst sheet microstructures.

a, **b**, Cross-sectional backscattered electron images acquired by scanning electron microscopy of photocatalyst sheets prepared using a manual sprayer on a flat, clear glass sheet (**a**) or a program-controlled sprayer on a frosted glass sheet (**b**). **c**, **d**, Cross-sectional images of a photocatalyst deposited by manual spraying on a flat, clear glass sheet, acquired by transmission electron microscopy before (**c**) and after (**d**) a field test lasting approximately six months.

Extended Data Fig. 3 The dependence of the water splitting rate of the photocatalyst sheet on the loading amount of the photocatalyst layer.

Small photocatalyst sheets ($5\text{ cm} \times 5\text{ cm}$) prepared on the flat, clear glass were irradiated with the ultraviolet light emitting diode array. The loading

amount of the photocatalyst layer is expressed as a relative value to the case where the modified $\text{SrTiO}_3:\text{Al}$ loading is 0.89 mg cm^{-2} .

[Source data](#)

Extended Data Fig. 4 Durability of photocatalyst sheets.

a, b, The STH values of small photocatalyst sheets (25 cm^2) prepared using manual spraying with flat, clear glass (**a**) and a program-controlled sprayer with frosted glass (**b**) during the overall water splitting reaction under continuous irradiation with simulated standard sunlight.

[Source data](#)

Extended Data Fig. 5 Long-term records of the field test of the 100-m² photocatalyst panel reactor at Kakioka Research Facility from 22 September to 21 December 2020.

a–f, Solar radiation (**a**), ultraviolet power (**b**), oxyhydrogen gas production rate (**c**), ambient temperature (**d**), daily STH value (**e**) and proportion of ultraviolet energy (**f**). The oxyhydrogen gas was not produced in late December 2020, because of the cold weather freezing the panel reactor units and other equipment. On 2, 6 and 30 October, the gas was directed to the gas separation equipment, without delivery to the gas flowmeter. On 9 and 10 October, the daily STH values were abnormally high. These values are not reliable because of bad weather and the low solar radiation. On 9 and 10 October, the daily STH values were abnormally high. These values are not reliable because of bad weather and the low solar radiation. The data on 18 November and 8 December were not reliable either, owing to malfunction of the soap-film flowmeter.

[Source data](#)

Extended Data Fig. 6 Structure of the gas separating facility.

a, Schematic of the gas filtration cartridge. **b**, Schematic of the oxyhydrogen gas separation apparatus. The routes for the incoming oxyhydrogen gas, hydrogen-enriched filtrate gas and oxygen-enriched residual gas are shown in purple, red and black, respectively.

Extended Data Fig. 7 Performance of the gas separation unit connected to the 100-m² water splitting photocatalyst panel reactor.

The hydrogen concentration in the filtrate gas and the oxygen concentration in the residue gas are intermittently notated along the curves. **a**, **b**, The data were acquired on a day with mixed sun and cloud (6 February 2020; **a**) and a consistently sunny day (1 May 2020; **b**) at the Kakioka Research Facility. Note that the throttle valve was partially closed at 10:00 am on 1 May 2020 to reduce the gas feed rate.

[Source data](#)

Extended Data Fig. 8 Ignition test of the panel reactor.

The gas in the area indicated within the red square, with a light receiving area of 70 m², was ignited by a spark. The spark gap was an assembly of two needle electrodes facing each other within a tube. The distance between the electrodes was adjusted at approximately 0.5 mm. The ignition voltage was 15-kV a.c. and pulsed for approximately 1 s.

Supplementary information

[Supplementary Video 1](#)

| Nucleation of moist oxyhydrogen bubbles on a photocatalyst sheet under irradiation from a Xe lamp, played at ten times the original speed.

[Supplementary Video 2](#)

| A reactor unit evolving and expelling oxyhydrogen gas bubbles at approximately 13 ml min^{-1} under a diode array emitting ultraviolet light.

Supplementary Video 3

| Moist oxyhydrogen gas bubbles generated at a rate of 3.71 min^{-1} by the 100-m^2 photocatalyst panel reactor under natural sunlight on 30 September 2020, played at the original speed.

Supplementary Video 4

| Intentional ignition of the oxyhydrogen gas in polyurethane gas collection and carrying tubes with an inner diameter of 8 mm connected to the water splitting panel reactor with a 70-m^2 light receiving area during water splitting under natural sunlight at 10:00 am on 20 August 2020, played in slow motion (1/240 of the original speed). Reactor internal pressure = 101 kPa, temperature = 30°C . This experiment was conducted twice without damaging the setup.

Supplementary Video 5

| Intentional ignition of a mixed gas of hydrogen and oxygen ($\text{H}_2/\text{O}_2 = 2$) saturated with water vapour, filled in the soft polyvinyl chloride tube with an inner diameter of 10 mm and a length of 100 m with the end bobbed in a water tub, played in the original speed. Internal pressure = 101 kPa, temperature = 20°C . This experiment was conducted five times without any damage.

Supplementary Video 6

| The same experiment with Supplementary Video 5 but recorded from a different angle and played in slow motion (1/132 of the original speed).

Source data

Source Data Fig. 3

Source Data Extended Data Fig. 3

Source Data Extended Data Fig. 4

Source Data Extended Data Fig. 5

Source Data Extended Data Fig. 7

Peer Review File

Rights and permissions

Reprints and Permissions

About this article

Cite this article

Nishiyama, H., Yamada, T., Nakabayashi, M. *et al.* Photocatalytic solar hydrogen production from water on a 100-m² scale. *Nature* **598**, 304–307 (2021). <https://doi.org/10.1038/s41586-021-03907-3>

- Received: 23 October 2020
- Accepted: 12 August 2021
- Published: 25 August 2021
- Issue Date: 14 October 2021
- DOI: <https://doi.org/10.1038/s41586-021-03907-3>

Share this article

Anyone you share the following link with will be able to read this content:

[Get shareable link](#)

Sorry, a shareable link is not currently available for this article.

[Copy to clipboard](#)

Provided by the Springer Nature SharedIt content-sharing initiative

This article was downloaded by **calibre** from <https://www.nature.com/articles/s41586-021-03907-3>

| [Section menu](#) | [Main menu](#) |

- Article
- [Published: 13 October 2021](#)

Estimating a social cost of carbon for global energy consumption

- [Ashwin Rode](#) [ORCID: orcid.org/0000-0003-1369-4331¹](#),
- [Tamma Carleton](#) [ORCID: orcid.org/0000-0002-5518-0550^{2,3}](#),
- [Michael Delgado⁴](#),
- [Michael Greenstone](#) [ORCID: orcid.org/0000-0002-2364-2810^{3,5}](#),
- [Trevor Houser⁴](#),
- [Solomon Hsiang](#) [ORCID: orcid.org/0000-0002-2074-0829^{3,6}](#),
- [Andrew Hultgren](#) [ORCID: orcid.org/0000-0002-6720-6252^{1,5}](#),
- [Amir Jina](#) [ORCID: orcid.org/0000-0003-3446-7883^{3,7}](#),
- [Robert E. Kopp](#) [ORCID: orcid.org/0000-0003-4016-9428^{8,9}](#),
- [Kelly E. McCusker⁴](#),
- [Ishan Nath¹⁰](#),
- [James Rising](#) [ORCID: orcid.org/0000-0001-8514-4748¹¹](#) &
- [Jiacan Yuan^{12,13,14,15}](#)

[Nature](#) volume 598, pages 308–314 (2021)

- 1753 Accesses
- 140 Altmetric
- [Metrics details](#)

Subjects

- [Climate-change impacts](#)
- [Energy economics](#)

- [Environmental economics](#)

Abstract

Estimates of global economic damage caused by carbon dioxide (CO₂) emissions can inform climate policy^{1,2,3}. The social cost of carbon (SCC) quantifies these damages by characterizing how additional CO₂ emissions today impact future economic outcomes through altering the climate^{4,5,6}. Previous estimates have suggested that large, warming-driven increases in energy expenditures could dominate the SCC^{7,8}, but they rely on models^{9,10,11} that are spatially coarse and not tightly linked to data^{2,3,6,7,12,13}. Here we show that the release of one ton of CO₂ today is projected to reduce total future energy expenditures, with most estimates valued between –US\$3 and –US\$1, depending on discount rates. Our results are based on an architecture that integrates global data, econometrics and climate science to estimate local damages worldwide. Notably, we project that emerging economies in the tropics will dramatically increase electricity consumption owing to warming, which requires critical infrastructure planning. However, heating reductions in colder countries offset this increase globally. We estimate that 2099 annual global electricity consumption increases by about 4.5 exajoules (7 per cent of current global consumption) per one-degree-Celsius increase in global mean surface temperature (GMST), whereas direct consumption of other fuels declines by about 11.3 exajoules (7 per cent of current global consumption) per one-degree-Celsius increase in GMST. Our finding of net savings contradicts previous research^{7,8}, because global data indicate that many populations will remain too poor for most of the twenty-first century to substantially increase energy consumption in response to warming. Importantly, damage estimates would differ if poorer populations were given greater weight¹⁴.

Access options

Subscribe to Journal

Get full journal access for 1 year

\$199.00

only \$3.90 per issue

[Subscribe](#)

All prices are NET prices.

VAT will be added later in the checkout.

Tax calculation will be finalised during checkout.

Rent or Buy article

Get time limited or full article access on ReadCube.

from \$8.99

[Rent or Buy](#)

All prices are NET prices.

Additional access options:

- [Log in](#)
- [Access through your institution](#)
- [Learn about institutional subscriptions](#)

Fig. 1: Estimated effect of temperature on energy consumption is mediated by income and climate.

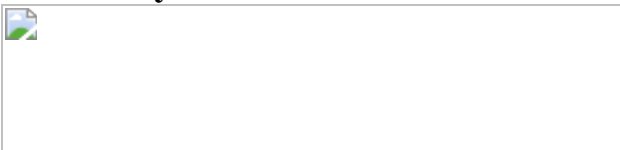


Fig. 2: Projected impact of climate change on energy consumption in the twenty-first century.

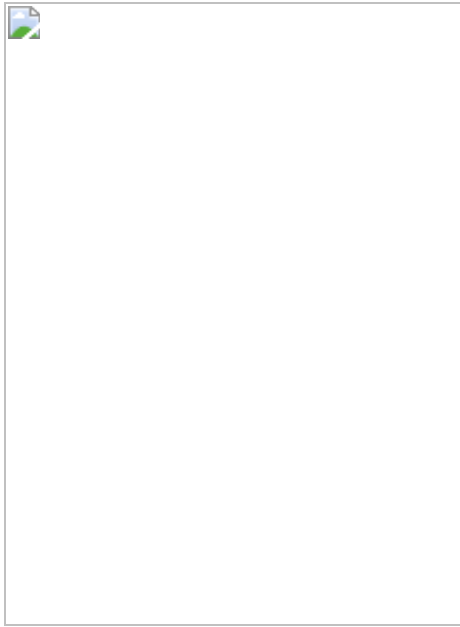


Fig. 3: Economic costs from energy consumption impact of climate change.

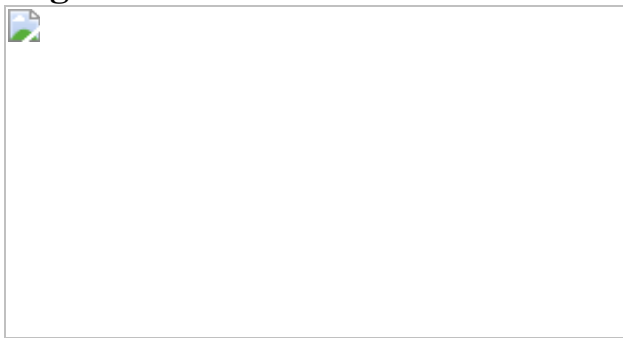
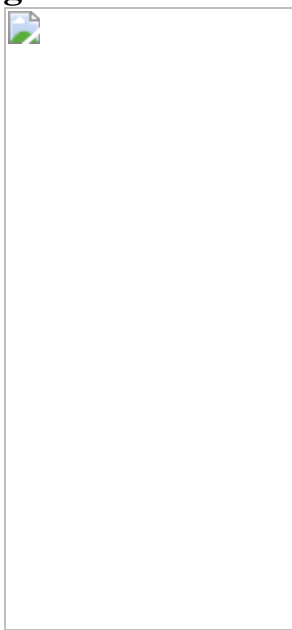


Fig. 4: Social cost of carbon for global energy consumption.



Data availability

The data for replicating the findings of this study are available on Zenodo at <https://doi.org/10.5281/zenodo.5099834>.

Code availability

The code for replicating the findings of this study is available on GitHub at <https://github.com/ClimateImpactLab/energy-code-release-2020/>.

References

1. 1.

Interagency Working Group on Socal Cost of Carbon *Social Cost of Carbon for Regulatory Impact Analysis—under Executive Order 12866 Technical Report* (United States Government, 2010).

2. 2.

Revesz, R. L. et al. Global warming: improve economic models of climate change. *Nature* **508**, 173–175 (2014).

3. 3.

Pizer, W. et al. Using and improving the social cost of carbon. *Science* **346**, 1189–1190 (2014).

4. 4.

Nordhaus, W. D. An optimal transition path for controlling greenhouse gases. *Science* **258**, 1315–1319 (1992).

5. 5.

Greenstone, M., Kopits, E. & Wolverton, A. Developing a social cost of carbon for US regulatory analysis: a methodology and

interpretation. *Rev. Environ. Econ. Policy* **7**, 23–46 (2013).

6. 6.

National Academies of Sciences, Engineering, and Medicine *Valuing Climate Damages: Updating Estimation of the Social Cost of Carbon Dioxide* (The National Academies Press, 2017).

7. 7.

Diaz, D. & Moore, F. Quantifying the economic risks of climate change. *Nat. Clim. Change* **7**, 774–782 (2017).

8. 8.

Anthoff, D. & Tol, R. S. The uncertainty about the social cost of carbon: a decomposition analysis using FUND. *Climatic Change* **117**, 515–530 (2013).

9. 9.

Stern, N. *Stern Review Report on the Economics of Climate Change* (HM Treasury, 2006).

10. 10.

Waldhoff, S., Anthoff, D., Rose, S. & Tol, R. S. The marginal damage costs of different greenhouse gases: an application of FUND. *Economics* **8**, 1–33 (2014).

11. 11.

Nordhaus, W. D. *Estimates of the Social Cost of Carbon: Background and Results from the Rice-2011 Model Technical Report* (National Bureau of Economic Research, 2011).

12. 12.

Pindyck, R. S. Climate change policy: what do the models tell us? *J. Econ. Lit.* **51**, 860–872 (2013).

13. 13.

Burke, M. et al. Opportunities for advances in climate change economics. *Science* **352**, 292–293 (2016).

14. 14.

Adler, M. et al. Priority for the worse-off and the social cost of carbon. *Nat. Clim. Change* **7**, 443–449 (2017).

15. 15.

Moore, F. C., Baldos, U., Hertel, T. & Diaz, D. New science of climate change impacts on agriculture implies higher social cost of carbon. *Nat. Commun.* **8**, 1607 (2017).

16. 16.

Diaz, D. B. *Evaluating the Key Drivers of the US Government's Social Cost of Carbon: A Model Diagnostic and Inter-Comparison Study of Climate Impacts in DICE, FUND, and PAGE* (Stanford University Policy and Economics Research Roundtable, 2014).

17. 17.

Carleton, T. A. et al. *Valuing the Global Mortality Consequences of Climate Change Accounting for Adaptation Costs and Benefits* Working Paper 27599 (National Bureau of Economic Research, 2020); <http://www.nber.org/papers/w27599>

18. 18.

Hsiang, S. et al. Estimating economic damage from climate change in the United States. *Science* **356**, 1362–1369 (2017).

19. 19.

Taylor, K. E., Stouffer, R. J. & Meehl, G. A. An overview of CMIP5 and the experiment design. *Bull. Am. Meteorol. Soc.* **93**, 485–498 (2012).

20. 20.

Auffhammer, M., Hsiang, S. M., Schlenker, W. & Sobel, A. Using weather data and climate model output in economic analyses of climate change. *Rev. Environ. Econ. Policy* **7**, 181–198 (2013).

21. 21.

Kopp, R., Hsiang, S. & Oppenheimer, M. Empirically calibrating damage functions and considering stochasticity when integrated assessment models are used as decision tools. In *Impacts World 2013 Conference Proc.* 834–843 (Potsdam Institute for Climate Impact Research, 2013).

22. 22.

O'Neill, B. C. et al. A new scenario framework for climate change research: the concept of shared socioeconomic pathways. *Climatic Change* **122**, 387–400 (2014).

23. 23.

Rasmussen, D. J. & Kopp, R. E. in *Economic Risks of Climate Change: An American Prospectus* 219–248 (Columbia Univ. Press, 2015); <https://cup.columbia.edu/book/economic-risks-of-climate-change/9780231174565>

24. 24.

Hsiang, S. Climate econometrics. *Annu. Rev. Resour. Econ.* **8**, 43–75 (2016).

25. 25.

Smith, C. J. et al. FAIR v1. 3: a simple emissions-based impulse response and carbon cycle model. *Geosci. Model Dev.* **11**, 2273–2297 (2018).

26. 26.

Dell, M., Jones, B. F. & Olken, B. A. Temperature shocks and economic growth: evidence from the last half century. *Am. Econ. J. Macroecon.* **4**, 66–95 (2012).

27. 27.

Burke, M., Hsiang, S. M. & Miguel, E. Global non-linear effect of temperature on economic production. *Nature* **527**, 235–239 (2015).

28. 28.

Moore, F. C. & Diaz, D. B. Temperature impacts on economic growth warrant stringent mitigation policy. *Nat. Clim. Change* **5**, 127–131 (2015).

29. 29.

Ricke, K., Drouet, L., Caldeira, K. & Tavoni, M. Country-level social cost of carbon. *Nat. Clim. Change* **8**, 895–900 (2018).

30. 30.

Deschênes, O. & Greenstone, M. Climate change, mortality, and adaptation: evidence from annual fluctuations in weather in the US. *Am. Econ. J. Appl. Econ.* **3**, 152–185 (2011).

31. 31.

Davis, L. W. & Gertler, P. J. Contribution of air conditioning adoption to future energy use under global warming. *Proc. Natl Acad. Sci. USA* **112**, 5962–5967 (2015).

32. 32.

Auffhammer, M., Baylis, P. & Hausman, C. H. Climate change is projected to have severe impacts on the frequency and intensity of peak electricity demand across the United States. *Proc. Natl Acad. Sci. USA* **114**, 1886–1891 (2017).

33. 33.

Wenz, L., Levermann, A. & Auffhammer, M. North–south polarization of European electricity consumption under future warming. *Proc. Natl Acad. Sci. USA* **114**, E7910–E7918 (2017).

34. 34.

Auffhammer, M. *Climate Adaptive Response Estimation: Short and Long Run Impacts of Climate Change on Residential Electricity and Natural Gas Consumption using Big Data Technical Report* (National Bureau of Economic Research, 2018).

35. 35.

Hadley, S. W., Erickson, D. J., Hernandez, J. L., Broniak, C. T. & Blasing, T. Responses of energy use to climate change: a climate modeling study. *Geophys. Res. Lett.* **33**, L17703 (2006).

36. 36.

Zhou, Y., Eom, J. & Clarke, L. The effect of global climate change, population distribution, and climate mitigation on building energy use in the US and China. *Climatic Change* **119**, 979–992 (2013).

37. 37.

Isaac, M. & Van Vuuren, D. P. Modeling global residential sector energy demand for heating and air conditioning in the context of climate change. *Energy Policy* **37**, 507–521 (2009).

38. 38.

Clarke, L. et al. Effects of long-term climate change on global building energy expenditures. *Energy Econ.* **72**, 667–677 (2018).

39. 39.

Gollier, C. & Hammitt, J. K. The long-run discount rate controversy. *Annu. Rev. Resour. Econ.* **6**, 273–295 (2014).

40. 40.

Bauer, M. & Rudebusch, G. D. *The Rising Cost of Climate Change: Evidence from the Bond Market* (Federal Reserve Bank of San Francisco, 2020).

41. 41.

Sheffield, J., Goteti, G. & Wood, E. F. Development of a 50-year high-resolution global dataset of meteorological forcings for land surface modeling. *J. Clim.* **19**, 3088–3111 (2006).

42. 42.

World Energy Balances (Edition 2017) International Energy Agency, 2018); <https://www.oecd-ilibrary.org/content/data/9ddec1c1-en>

43. 43.

Rasmussen, D. J., Meinshausen, M. & Kopp, R. E. Probability-weighted ensembles of US county-level climate projections for climate risk analysis. *J. Appl. Meteorol. Climatol.* **55**, 2301–2322 (2016).

44. 44.

McNeil, M. A. & Letschert, V. E. Modeling diffusion of electrical appliances in the residential sector. *Energy Build.* **42**, 783–790 (2010).

45. 45.

Legros, G. et al. *The Energy Access Situation in Developing Countries: A Review Focusing on the Least Developed Countries and Sub-Saharan Africa* (World Health Organization, 2009).

46. 46.

Almond, D., Chen, Y., Greenstone, M. & Li, H. Winter heating or clean air? Unintended impacts of China's Huai River policy. *Am. Econ. Rev.* **99**, 184–190 (2009).

47. 47.

Ramsey, F. P. A mathematical theory of saving. *Econ. J.* **38**, 543–559 (1928).

48. 48.

Tong, D. et al. Committed emissions from existing energy infrastructure jeopardize 1.5 °C climate target. *Nature* **572**, 373–377 (2019).

49. 49.

Woodard, D. L., Davis, S. J. & Randerson, J. T. Economic carbon cycle feedbacks may offset additional warming from natural feedbacks. *Proc. Natl Acad. Sci. USA* **116**, 759–764 (2019).

50. 50.

Global Administrative Areas *GADM Database of Global Administrative Areas, Version 2.0* (University of California, Berkeley, Museum of Vertebrate Zoology, International Rice Research Institute, University of California, Davis, 2012); www.gadm.org/data.html

51. 51.

Thrasher, B., Maurer, E. P., McKellar, C. & Duffy, P. Technical note: Bias correcting climate model simulated daily temperature extremes with quantile mapping. *Hydrol. Earth Syst. Sci.* **16**, 3309–3314 (2012).

52. 52.

Riahi, K. et al. RCP 8.5—a scenario of comparatively high greenhouse gas emissions. *Climatic Change* **109**, 33–57 (2011).

53. 53.

Thomson, A. M. et al. RCP 4.5: a pathway for stabilization of radiative forcing by 2100. *Climatic Change* **109**, 77 (2011).

54. 54.

Van Vuuren, D. P. et al. The representative concentration pathways: an overview. *Climatic Change* **109**, 5 (2011).

55. 55.

Tebaldi, C. & Knutti, R. The use of the multi-model ensemble in probabilistic climate projections. *Phil. Trans. R. Soc. Lond. A* **365**, 2053–2075 (2007).

56. 56.

Riahi, K. et al. The shared socioeconomic pathways and their energy, land use, and greenhouse gas emissions implications: an overview. *Glob. Environ. Change* **42**, 153–168 (2017).

57. 57.

Samir, K. & Lutz, W. The human core of the shared socioeconomic pathways: population scenarios by age, sex and level of education for all countries to 2100. *Glob. Environ. Change* **42**, 181–192 (2017).

58. 58.

Cuaresma, J. C. Income projections for climate change research: a framework based on human capital dynamics. *Glob. Environ. Change* **42**, 226–236 (2017).

59. 59.

Dellink, R., Chateau, J., Lanzi, E. & Magné, B. Long-term economic growth projections in the shared socioeconomic pathways. *Glob. Environ. Change* **42**, 200–214 (2017).

60. 60.

IIASA Energy Program *SSP Database, Version 1.1 Data set Technical Report* (National Bureau of Economic Research, 2016);
<https://tntcat.iiasa.ac.at/SspDb>

61. 61.

Bright, E. A., Coleman, P. R., Rose, A. N. & Urban, M. L. *LandScan 2011* (2012); <https://web.ornl.gov/sci/landscan/index.shtml>

62. 62.

Jiang, L. & O'Neill, B. C. Global urbanization projections for the shared socioeconomic pathways. *Glob. Environ. Change* **42**, 193–199 (2017).

63. 63.

Jones, B. & O'Neill, B. C. Spatially explicit global population scenarios consistent with the shared socioeconomic pathways. *Environ. Res. Lett.* **11**, 084003 (2016).

64. 64.

Huppmann, D. et al. *IAMC 1.5 °C Scenario Explorer and Data hosted by IIASA*. (Integrated Assessment Modeling Consortium & International Institute for Applied Systems Analysis, 2018).

65. 65.

Carleton, T. A. & Hsiang, S. M. Social and economic impacts of climate. *Science* **353**, aad9837 (2016).

66. 66.

Auffhammer, M. & Aroonruengsawat, A. Simulating the impacts of climate change, prices and population on California's residential electricity consumption. *Climatic Change* **109**, 191–210 (2011).

67. 67.

Graff Zivin, J. & Neidell, M. Temperature and the allocation of time: implications for climate change. *J. Labor Econ.* **32**, 1–26 (2014).

68. 68.

Schlenker, W. & Roberts, M. J. Nonlinear temperature effects indicate severe damages to US crop yields under climate change. *Proc. Natl Acad. Sci. USA* **106**, 15594–15598 (2009).

69. 69.

Wooldridge, J. M. *Econometric Analysis of Cross Section and Panel Data* (MIT Press, 2002).

70. 70.

Millar, R. J., Nicholls, Z. R., Friedlingstein, P. & Allen, M. R. A modified impulse-response representation of the global near-surface air temperature and atmospheric concentration response to carbon dioxide emissions. *Atmos. Chem. Phys.* **17**, 7213–7228 (2017).

71. 71.

Board of Governors of the US Federal Reserve System *10-year Treasury Inflation-indexed Security, Constant Maturity (DFII10) Technical Report* (FRED, Federal Reserve Bank of St. Louis, 2020); <https://fred.stlouisfed.org/series/DFII10>

72. 72.

Carleton, T. & Greenstone, M. *Updating the United States Government's Social Cost of Carbon Working Paper* (Univ. Chicago, Becker Friedman Institute for Economics, 2021).

73. 73.

Nordhaus, W. *A Question of Balance: Weighing the Options on Global Warming Policies* (Yale Univ. Press, 2014).

74. 74.

Arrow, K. J. Global climate change: a challenge to policy. *The Economists' Voice* **4**, 1–5 (2007).

75. 75.

Dasgupta, P. The Stern review's economics of climate change. *Natl Inst. Econ. Rev.* **199**, 4–7 (2007).

76. 76.

Dasgupta, P. Discounting climate change. *J. Risk Uncertain.* **37**, 141–169 (2008).

77. 77.

Hall, R. E. Reconciling cyclical movements in the marginal value of time and the marginal product of labor. *J. Polit. Econ.* **117**, 281–323 (2009).

78. 78.

Weitzman, M. L. A review of the Stern review on the economics of climate change. *J. Econ. Lit.* **45**, 703–724 (2007).

79. 79.

Weitzman, M. L. On modeling and interpreting the economics of catastrophic climate change. *Rev. Econ. Stat.* **91**, 1–19 (2009).

80. 80.

McGrath, G. Natural gas-fired electricity conversion efficiency grows as coal remains stable. *Today in Energy* <https://www.eia.gov/todayinenergy/detail.php?id=32572> (2017).

81. 81.

Emission factors for greenhouse gas inventories. *US Environmental Protection Agency* https://www.epa.gov/sites/production/files/2018-03/documents/emission-factors_mar_2018_0.pdf (2018).

82. 82.

IPCC *Climate Change 2014: Synthesis Report* (eds Core Writing Team, Pachauri, R. K. & Meyer L. A.) (IPCC, 2014).

Acknowledgements

This project is an output of the Climate Impact Lab consortium that gratefully acknowledges funding from the Carnegie Corporation, Energy Policy Institute of Chicago (EPIC), the International Growth Centre, the National Science Foundation (SES1463644), the Sloan Foundation and the Tata Center for Development. T.C. acknowledges funding from the US Environmental Protection Agency Science To Achieve Results Fellowship (FP91780401). J.R. acknowledges funding from the H2020-MSCA-RISE project GEMCLIME-2020 GA number 681228. We thank L. Alcocer, T. Bearpark, T. Chong, Z. Delgerjargal, G. Dobbels, D. Gergel, R. Goyal, S. Greenhill, I. Higuera-Mendieta, D. Hogan, A. Hussain, T. Kulczycki, R. Li, B. Malevich, M. Norman, O. Nwabuikwu, S. Annan-Phan, C. Schwarz, N. Sharma, J. Simcock, Y. Song, E. Tenezakis, J. Wang and J. Yang for research assistance during all stages of this project, and we thank S. Anderson, J. Chang, M. Landín and T. Mayer for project management. We acknowledge the World Climate Research Programme's Working Group on Coupled Modeling, which is responsible for the CMIP, and we thank the climate modelling groups (listed in Extended Data Fig. 2b) for producing and making available their model output. For CMIP, the US Department of

Energy's Program for Climate Model Diagnosis and Intercomparison provides coordinating support and led development of software infrastructure in partnership with the Global Organization for Earth System Science Portals. We thank seminar participants at the UC Berkeley Energy Camp, the University of Chicago EPIC Lunch Series and the Mansueto Institute Lunch Colloquium, LSE Workshop in Environmental Economics, International Energy Workshop, International Workshop on Empirical Methods in Energy Economics, the University of Michigan Sustainability and Development Conference, the Berkeley/Harvard/Yale Environmental and Energy Economics Seminar, the NBER EEE Summer Institute, the UCLA Luskin Center for Innovation Climate Adaptation Research Symposium and the Federal Reserve Bank of Richmond Climate Change Economics Workshop for helpful comments.

Author information

Affiliations

1. Energy Policy Institute, University of Chicago, Chicago, IL, USA
Ashwin Rode & Andrew Hultgren
2. Bren School of Environmental Science and Management, University of California, Santa Barbara, Santa Barbara, CA, USA
Tamma Carleton
3. National Bureau of Economic Research, Cambridge, MA, USA
Tamma Carleton, Michael Greenstone, Solomon Hsiang & Amir Jina
4. Rhodium Group, New York, NY, USA
Michael Delgado, Trevor Houser & Kelly E. McCusker
5. Department of Economics, University of Chicago, Chicago, IL, USA
Michael Greenstone & Andrew Hultgren

6. Global Policy Laboratory, Goldman School of Public Policy,
University of California, Berkeley, Berkeley, CA, USA

Solomon Hsiang

7. Harris School of Public Policy, University of Chicago, Chicago, IL,
USA

Amir Jina

8. Department of Earth & Planetary Sciences, Rutgers University, New
Brunswick, NJ, USA

Robert E. Kopp

9. Rutgers Institute of Earth, Ocean, and Atmospheric Sciences, Rutgers
University, New Brunswick, NJ, USA

Robert E. Kopp

10. Department of Economics, Princeton University, Princeton, NJ, USA

Ishan Nath

11. School of Marine Science and Policy, University of Delaware,
Newark, DE, USA

James Rising

12. Department of Atmospheric and Oceanic Sciences, Fudan University,
Shanghai, China

Jiacan Yuan

13. Institute of Atmospheric Sciences, Fudan University, Shanghai, China

Jiacan Yuan

14. IRDR ICoE-RIG-WECEIPHE, Fudan University, Shanghai, China

Jiacan Yuan

15. Big Data Institute for Carbon Emission and Environmental Pollution,
Fudan University, Shanghai, China

Jiacan Yuan

Contributions

A.R., S.H., M.G., R.K., T.H., A.J., J.R., M.D. and T.C. conceived and planned the study. J.Y., K.E.M., M.D., R.K., A.R., A.J. and T.C. prepared the historical climate data. J.Y., K.E.M., M.D. and R.K. created and prepared the climate projection data. A.R., T.C., A.H., M.D., I.N. and T.H. prepared the energy data. A.R., T.C., A.H., I.N., A.J., J.R., S.H. and MG estimated energy–climate response functions. J.R. and A.R. computed projected impacts of future climate change. A.R., M.D., T.C., K.E.M., A.H., I.N., A.J., J.R., S.H. and M.G. constructed damage functions and computed partial social cost of carbon. A.R., S.H. and M.G. wrote the main text, A.R., T.C., A.J., M.D., J.R., J.Y. and K.M. wrote the supplementary materials, and all authors edited.

Corresponding authors

Correspondence to Ashwin Rode or Solomon Hsiang.

Ethics declarations

Competing interests

A.R., T.C., A.H., A.J., R.K., I.N., J.R. and J.Y. declare no competing interests. M.D., T.H., K.E.M.: The Rhodium Group provides independent research and analysis on a range of global economic topics to clients in the public and private sectors. This includes analysis of global energy market trends. Although some of those clients could potentially be impacted by the results of this research, both positively and negatively, Rhodium staff contributions to this research were conducted completely independently.

M.G., S.H. and R.K.: we received no financial or in-kind support for the research conducted in this paper, nor have we received funding or in-kind support from any ‘interested’ parties. As part of a diversified portfolio, we each hold more than US\$10,000 in stocks and bonds of various companies including those within the energy sector. No other parties have the right to review the paper before its circulation. M.G. holds the position of director at the Energy Policy Institute at the University of Chicago and the Environment and Energy Lab at University of Chicago Labs, and is faculty director at the E2e Lab. From July 2015 to January 2017, M.G. was a member of the US Department of Energy’s Secretary of Energy Advisory Board. S.H. is the director of the Global Policy Laboratory at the University of California, Berkeley. R.K. previously served as a consultant to Rhodium Group, which provides independent research and analysis on a range of global economic topics to clients in the public and private sectors, including analysis of global energy market trends. R.K. currently serves as director of the Rutgers Institute of Earth, Ocean, and Atmospheric Sciences. R.K. provided technical support to and M.G. was a co-chair of the US Federal Government Interagency Working Group on Social Cost of Carbon between September 2009 and March 2010. R.K. was an author of the National Academies of Sciences, Engineering, and Medicine report Valuing Climate Damages Updating Estimation of the Social Cost of Carbon Dioxide published in 2017.

Additional information

Peer review information *Nature* thanks Katrina Jessoe, William Pizer and the other, anonymous, reviewer(s) for their contribution to the peer review of this work. Peer reviewer reports are available.

Publisher’s note Springer Nature remains neutral with regard to jurisdictional claims in published maps and institutional affiliations.

Extended data figures and tables

[Extended Data Fig. 1 Map of the 24,378 “impact regions” for which location-specific projections are calculated.](#)

Map is produced with R software, ggplot2 package, using Global Administrative Region dataset (GADM) basemap⁵⁰. A clustering algorithm¹⁷ is used to form these impact regions from the full set of GADM administrative regions⁵⁰, such that they are roughly similar in total population, and so that they are approximately internally homogenous with respect to mean temperature, diurnal temperature range, and mean precipitation.

Extended Data Fig. 2 Future climate projections used in generating probabilistic, empirically-based climate change impact projections.

Panel (a) shows local climate distributions under the 21 climate models (outlined maps) and 12 model surrogates (dimmed maps) ('Data assembly' in Methods, Supplementary Sections [A.2.2](#), [A.2.3](#)) that are weighted in climate change impact projections so that the weighted distribution of the 2080 to 2099 global mean surface temperature anomaly (ΔGMST) exhibited by the 33 total models matches the probability distribution of estimated ΔGMST responses (blue-grey line) under a high (RCP8.5) emissions scenario. For this construction, the anomaly is relative to values in 1986–2005. Maps are produced with Python programming language, using data from ref. [43](#) and Global Administrative Region dataset (GADM) basemap⁷⁹. Panel (b) lists all 33 models and model surrogates, and their corresponding model weights for both high (RCP8.5) and moderate (RCP4.5) emissions scenarios⁴³. These are used to capture climate model uncertainty when generating climate change impact projections under a given emissions scenario (Supplementary Section [B.5](#)).

Extended Data Fig. 3 Sample overlap between present and future.

The density plots demonstrate the overlap in the joint income \times long-run climate distributions at 2010 and 2090. Long-run climate is measured by heating degree days (**a**) and cooling degree days (**b**). Distributions are for 24,378 impact regions, in 2010 (grey-black) and 2090 under the RCP8.5 emissions scenario and SSP3 socioeconomic scenario (red-orange). All

impact regions within a country are assigned the national per capita income. Although the future distribution is shifted towards higher incomes, greater cooling degree days, and fewer heating degree days, the substantial overlap in the two distributions allows for credible extrapolation of energy-temperature responses into the future ('Projecting the impacts of climate change' in Methods).

Extended Data Fig. 4 Climate-change induced changes in total energy expenditures at end-of-century, by present-day income deciles.

The bar chart above depicts annual climate-change induced changes in total energy expenditures at 2099 under a high emissions scenario (RCP8.5) and the SSP3 socioeconomic scenario, separately for each decile of 2012 national per capita income. Income deciles are calculated across all countries at 2012; representative countries in selected deciles are indicated. Expenditures are calculated under a 1.4% annual price growth scenario and are expressed in 2019 USD per capita based on each decile's projected 2099 population. Bars represent mean estimates across an ensemble of 33 climate models. Intervals indicate 5th–95th percentiles of projected distributions, accounting for climate model and econometric uncertainty (Supplementary Section [B.5](#)). The chart demonstrates that heterogeneity in expenditure changes at end-of-century (Fig. [2a](#)) is systematically correlated with present-day national income per capita. Over the upper half of the present-day income distribution, we find that countries with higher incomes today are generally projected to experience larger overall net savings at end-of-century. This partly reflects the fact that today's richest countries tend to be in temperate climates, where energy savings from fewer cold days will more than offset increases in costs from more hot days. The smallest savings at end-of-century are projected to occur in middle deciles of the present-day income distribution, which is consistent with many of these countries being situated in the tropics and also attaining sufficiently high income levels at end-of-century to increase electricity consumption due to more hot days. The positive correlation between present-day income and net savings at end-of-century does not hold in the lower ranges of today's income distribution. Net savings in today's poorest deciles (i.e. first and second) are actually higher than in the third and fourth deciles, as many of

the poorest countries are projected to remain too poor at end-of-century to increase electricity consumption on hot days.

Extended Data Fig. 5 The impacts of climate change on energy expenditures.

Time series of changes in total global energy expenditures under the SSP3 socioeconomic scenario for moderate (RCP4.5; Panel **a**) and high (RCP8.5; Panel **b**) emissions scenarios, assuming various energy price trajectories. Three of these trajectories are based on direct extrapolation of present-day price statistics at either moderate (1.4%), stagnant (0%), or high (3%) annual growth rates (Supplementary Section [C.1](#)), while five are based on price projections from integrated assessment models (Supplementary Section [C.2](#)) named in the legend. Expenditure changes in a given year are expressed as a percent of global GDP in that year. Aggregate global expenditure changes are obtained by monetizing and summing over the spatially disaggregated impacts across both electricity and other fuels. Regardless of the emissions scenario or assumed price trajectory, end-of-century changes (i.e. net savings) represent a minute fraction of the US \$ 353 trillion end-of-century global GDP projected under SSP3.

Extended Data Fig. 6 Recovering local temperature-energy consumption relationships using aggregate energy consumption data.

An illustration demonstrating how the effect of local temperature on local per capita energy consumption can be recovered from observations of local temperatures and national per capita energy consumption. **a:** Let a hypothetical, linear response of daily temperature and energy consumption exist at a local (i.e. grid cell) level, depicted by the diagonal grey line. Let E denote baseline daily energy consumption on a 20 °C day. Average per capita energy consumption is observed on day d in countries i (blue circle) and j (pink circle), respectively consisting of 8 and 5 equally populated grid cells experiencing different temperatures. While the temperature is observed in each grid cell, only the national average per capita energy consumption is observed. **b:** Height of each bar represents unobserved

energy consumption on day d within each grid cell. Pink bars are grid cells in country j and blue bars are grid cells in country i . Energy consumption within each grid cell responds to temperature within that grid cell.

Averaging temperature and per capita energy consumption across grid cells within each country produces the country-level observations in Panel **a**. A regression using these observations recovers the grid cell-level response.

Note that this illustration depicts a linear energy-temperature response for illustrative purposes, however a nonlinear temperature-energy consumption response can be recovered as well, if nonlinear transformations of temperature are computed at the grid-cell-level before being aggregated to the national level ('Econometric estimation of energy-temperature responses' in Methods, Equation 2).

Extended Data Table 1 Social cost of energy consumption due to climate change under alternative future price scenarios

Extended Data Table 2 Social cost of energy consumption due to climate change under alternative future price scenarios

Extended Data Table 3 Feedback effects of climate change-induced energy consumption on CO₂ emissions

Supplementary information

[Supplementary Information](#)

This file contains raw datasets, numerical methods, intermediate results and further supplementary information. See page 1 for list of contents.

[Peer Review File](#)

Rights and permissions

[Reprints and Permissions](#)

About this article

Cite this article

Rode, A., Carleton, T., Delgado, M. *et al.* Estimating a social cost of carbon for global energy consumption. *Nature* **598**, 308–314 (2021).
<https://doi.org/10.1038/s41586-021-03883-8>

- Received: 25 February 2020
- Accepted: 06 August 2021
- Published: 13 October 2021
- Issue Date: 14 October 2021
- DOI: <https://doi.org/10.1038/s41586-021-03883-8>

Share this article

Anyone you share the following link with will be able to read this content:

[Get shareable link](#)

Sorry, a shareable link is not currently available for this article.

[Copy to clipboard](#)

Provided by the Springer Nature SharedIt content-sharing initiative

[The cost of changes in energy use in a warming world](#)

- Katrina Jessie
- Frances C. Moore

News & Views 13 Oct 2021

This article was downloaded by **calibre** from <https://www.nature.com/articles/s41586-021-03883-8>

- Article
- [Published: 15 September 2021](#)

Aquatic foods to nourish nations

- [Christopher D. Golden](#) ORCID: [orcid.org/0000-0002-2258-7493](#)^{1,2,3 na1},
- [J. Zachary Koehn](#) ORCID: [orcid.org/0000-0002-2668-6093](#)^{4 na1},
- [Alon Shepon](#) ORCID: [orcid.org/0000-0002-4345-8957](#)^{1,5,6 na1},
- [Simone Passarelli](#) ORCID: [orcid.org/0000-0003-1044-3393](#)^{1 na1},
- [Christopher M. Free](#) ORCID: [orcid.org/0000-0002-2557-8920](#)^{7,8 na1},
- [Daniel F. Viana](#)^{1,9 na1},
- [Holger Matthey](#)¹⁰,
- [Jacob G. Eurich](#) ORCID: [orcid.org/0000-0003-1764-7524](#)^{8,11},
- [Jessica A. Gephart](#) ORCID: [orcid.org/0000-0001-6836-9291](#)¹²,
- [Etienne Fluet-Chouinard](#) ORCID: [orcid.org/0000-0003-4380-2153](#)¹³,
- [Elizabeth A. Nyboer](#) ORCID: [orcid.org/0000-0003-3004-009X](#)¹⁴,
- [Abigail J. Lynch](#) ORCID: [orcid.org/0000-0001-8449-8392](#)¹⁵,
- [Marian Kjellevold](#) ORCID: [orcid.org/0000-0001-7070-5784](#)¹⁶,
- [Sabri Bromage](#) ORCID: [orcid.org/0000-0002-6552-4871](#)¹,
- [Pierre Charlebois](#)¹⁷,
- [Manuel Barange](#)¹⁷,
- [Stefania Vannuccini](#)¹⁷,
- [Ling Cao](#)¹⁸,
- [Kristin M. Kleisner](#)¹⁹,
- [Eric B. Rimm](#)¹,
- [Goodarz Danaei](#)^{3,20},
- [Camille DeSisto](#) ORCID: [orcid.org/0000-0002-8828-2334](#)²¹,
- [Heather Kelahan](#) ORCID: [orcid.org/0000-0003-4162-9668](#)¹,
- [Kathryn J. Fiorella](#) ORCID: [orcid.org/0000-0002-8625-2473](#)²²,
- [David C. Little](#)²³,
- [Edward H. Allison](#) ORCID: [orcid.org/0000-0003-4663-1396](#)²⁴,
- [Jessica Fanzo](#) ORCID: [orcid.org/0000-0002-6760-1359](#)²⁵ &
- [Shakuntala H. Thilsted](#)²⁴

[Nature](#) volume **598**, pages 315–320 (2021)

- 14k Accesses

- 382 Altmetric
- [Metrics details](#)

Subjects

- [Risk factors](#)
- [Sustainability](#)

Abstract

Despite contributing to healthy diets for billions of people, aquatic foods are often undervalued as a nutritional solution because their diversity is often reduced to the protein and energy value of a single food type ('seafood' or 'fish')^{1,2,3,4}. Here we create a cohesive model that unites terrestrial foods with nearly 3,000 taxa of aquatic foods to understand the future impact of aquatic foods on human nutrition. We project two plausible futures to 2030: a baseline scenario with moderate growth in aquatic animal-source food (AASF) production, and a high-production scenario with a 15-million-tonne increased supply of AASFs over the business-as-usual scenario in 2030, driven largely by investment and innovation in aquaculture production. By comparing changes in AASF consumption between the scenarios, we elucidate geographic and demographic vulnerabilities and estimate health impacts from diet-related causes. Globally, we find that a high-production scenario will decrease AASF prices by 26% and increase their consumption, thereby reducing the consumption of red and processed meats that can lead to diet-related non-communicable diseases^{5,6} while also preventing approximately 166 million cases of inadequate micronutrient intake. This finding provides a broad evidentiary basis for policy makers and development stakeholders to capitalize on the potential of aquatic foods to reduce food and nutrition insecurity and tackle malnutrition in all its forms.

[Download PDF](#)

Main

Globally, multiple forms of malnutrition continue to be important and universal. Among children under the age of five, 149 million (22%) are affected by stunting and 45 million by wasting⁷. Among adults globally, 2.1 billion are overweight or obese⁸. Sparse data suggest that vitamin A deficiency is prevalent among children in Africa and South Asia, and zinc deficiency affects half of all children in regions for which information exists⁹. Dietary inadequacies could be the leading reason that people experience multiple nutrient deficiencies and subsequent morbidity and mortality¹⁰.

Cardiovascular diseases, which are largely driven by diet-related factors, are the greatest contributor to global mortality, causing 17.8 million deaths in 2017¹¹—greater than the approximately 2 million deaths that were caused by COVID-19 in 2020.

To address these multiple forms of malnutrition, contemporary food policy discourses centre on the role of sustainable and healthy diets in improving human nutrition. The EAT–Lancet Commission report detailed a strategy to transform the global food system into one that could nourish the world without exceeding planetary boundaries¹². The report, however, focused predominantly on terrestrial food production, even as it noted that it would be difficult for many populations to obtain adequate quantities of micronutrients from plant-source foods alone. Yet the treatment of AASFs as a homogenous group ('seafood' or 'fish') has limited the potential for their inclusion and recognition in global diets.

Nutrition from aquatic food diversity

Here we reframe the role of aquatic foods in global food systems as a highly diverse food group, which can supply critical nutrients^{1,2,3,13} and improve overall health¹⁴. Aquatic foods are defined as animals, plants and microorganisms, as well as cell- and plant-based foods of aquatic origin emerging from new technologies¹⁵. They include finfish, crustaceans (such as crabs and shrimp), cephalopods (octopus and squids), other molluscs (clams, cockles and sea snails), aquatic plants (water spinach; *Ipomoea aquatica*), algae (seaweed) and other aquatic animals (mammals, insects and sea cucumbers). Aquatic foods can be farmed or wild-caught, and are sourced from inland (for example, lakes, rivers and wetlands), coastal (estuaries, mangroves and near-shore) and marine waters, producing a diversity of foods across all seasons and geographic regions. Here we focus on AASFs, which constitute the majority of aquatic foods.

Relative to the limited variation in domesticated terrestrial animal-source foods (for example beef, poultry, pork), AASFs present myriad options for supplying nutrients (Fig. 1). Currently, wild fisheries harvest more than 2,370 taxa and aquaculture growers farm approximately 624 species or species-types¹⁶. To provide evidence of the variability in nutrient composition across this diverse array of aquatic foods, we created the Aquatic Foods Composition Database¹⁷ (AFCD) ([Methods](#)), a comprehensive global database that comprises hundreds of nutrients, including minerals (for example, calcium, iron and zinc), vitamins and fatty acids from 3,753 aquatic food taxa. Our analysis indicates that the top 7 categories of nutrient-rich animal-source foods are all aquatic foods, including pelagic fish, bivalves and salmonids (Fig. 1).

Fig. 1: Nutrient diversity of aquatic animal-source foods in relation to terrestrial animal-source foods.

 figure1

Aquatic (blue) and terrestrial (green) food richness assessed as a ratio of concentrations of each nutrient per 100 g to the daily recommended nutrient intake.

Each shaded box represents the median value of each nutrient in a muscle tissue across all species within each taxonomic group. Food groups were ordered vertically by their mean nutrient richness with higher values meeting a higher percentage of the daily recommended intake. See [Supplementary Table 4](#) for the recommended nutrient intake values and their citations.

Aquatic foods to benefit human health

AASFs improve human health through at least three pathways: by reducing micronutrient (for example, vitamin A, calcium and iron) deficiencies that can lead to subsequent disease; by providing the dominant source of the omega-3 long-chain polyunsaturated fatty acids docosahexaenoic acid (DHA) and eicosapentaenoic acid (EPA) (hereafter referred to jointly as DHA+EPA), which may reduce the risk of heart disease and promote brain and eye health; and by displacing the consumption of less-healthy red and processed meats that can cause adverse health outcomes¹⁴. Any of these three pathways may overlap in an individual, or predominantly target consumers of particular geographies or age–sex groups. The third pathway, specifically, is characteristic of the nutrition transition—the process by which demographic and economic shifts lead to concomitant dietary and epidemiological shifts that often accompany the Westernization of food systems¹⁸. To better understand these pathways, we examine how aquatic food policy initiatives and investments could improve diets and public health through increasing access to the diversity of aquatic foods and the nutrients that they provide.

We explicitly integrated aquatic and terrestrial food-systems models to evaluate the potential health impacts of increasing global AASF production. This integration enables a more realistic portrayal of the trade-offs made within our global terrestrial and aquatic food systems. To understand the health impacts of increased AASF consumption, we modelled future food systems to 2030. We used an integrated version of the FISH model¹⁹ from the United Nations Food and Agriculture Organization (FAO), and the Aglink–Cosimo model²⁰, which is jointly maintained by the Organization for Economic Cooperation and Development (OECD) and the FAO. The embedded budgeting framework and price elasticities across foods enabled the addition of AASFs and the substitution of aquatic for terrestrial foods within national diets. This affects the supply and demand of a broad range of related food items, particularly terrestrial animal-source foods (such as poultry, pork, beef, eggs and dairy).

We used the integrated model to produce two scenarios: first, a baseline scenario with projections of moderate growth trends in AASF production and expert consensus regarding macroeconomic conditions, agriculture and trade policy settings, long-term productivity, international market developments and average weather conditions; and

second, a high-AASF-production scenario that assumes higher growth rates in production as a result of increased financial investment and innovation in aquaculture and improved and effective management in capture fisheries²¹ ([Methods](#)). The projections are not forecasts about the future, but rather plausible scenarios based on a set of internally consistent assumptions. Increases in aquaculture and capture fisheries in the high-production scenario led to a 26% decrease in the international reference price of AASFs, and an increase in their production by 15.5 million tonnes (an approximate 8% increase in annual global production) in 2030 as compared to the baseline scenario. In each scenario, we calculated the nutrients supplied to 191 countries from the projected composition of the food-system models by assigning nutrient composition values to the suite of foods being consumed within 22 food commodity categories, using the Global Nutrient Database (GND)²² and the AFCD. For 21 of the 22 food commodity categories (all terrestrially produced foods), the GND was used as the source of nutrient composition data. For the one commodity category containing aquatic foods, the AFCD nutrient composition values were used. A set of refuse factors is applied to all foods, highly specific to individual foods and their respective forms of preparation. Within the food group of fish and seafood, these refuse factors vary from 55% for fresh crustaceans to 10% for fresh cephalopods.

To assess the role of diversity in the aquatic food system, we compared estimated nutrient outputs with and without species diversity fully disaggregated at national levels. The GND uses relatively similar nutrient composition values across all aquatic foods, varying only for the 12 categories explicitly modelled in the GND (for example, demersal fish, pelagic fish and so on). We disaggregated national consumption to the species level in proportion to species-specific aquaculture and capture-fisheries production reported by the FAO, and linked these disaggregated species to the AFCD ([Methods](#)). Instead of 12 GND categories for aquatic foods, we used supply and nutrient composition values for 2,143 taxa. This comparison enabled us to determine whether incorporating species diversity, as opposed to relying on common commercial species, shifted the levels of nutrients supplied by aquatic foods. The disaggregated model outputs in the baseline scenario resulted in a higher supply of calcium (8% higher; median across countries), iron (4%), DHA+EPA (186%), zinc (4%) and vitamin B₁₂ (13%), with a 1% decline in vitamin A (Extended Data Fig. 1). This result provides evidence that narrowly focusing on the nutrient contributions of commercially important species underestimates the nutritional benefits of aquatic foods, especially from diverse small-scale fisheries.

Aquatic foods can reduce meat intake

In addition to the key role of AASFs in providing essential micronutrients, DHA+EPA and protein, AASFs can also prevent diet-related non-communicable diseases. These health benefits are delivered through two mechanisms. First, AASFs directly provide

DHA+EPA, which may improve brain function and reduce the incidence of heart disease and certain types of cancer^{5,6}. Second, AASFs displace the consumption of more harmful animal-source foods—such as red and processed meats (Fig. 2, Extended Data Figs. 2–4, Supplementary Data 1)—particularly in the global north, or can attenuate their increased consumption in the global south^{23,24}, in both cases reducing the risk of diet-related non-communicable disease²⁵.

Fig. 2: Shifts in fish and red meat consumption resulting from an increase in aquatic animal-source foods.

 figure2

a–f, The percentage difference in consumption of mean aquatic animal-source food (**a**), red meat (bovine, ovine and pork) (**b**), poultry (**c**), egg (**d**), dairy (milk, butter and other dairy products) (**e**) and all non-aquatic animal-source food (**f**) in 2030 under the high-production and baseline-production scenarios. Values greater than zero indicate greater consumption under the high-production scenario. Countries smaller than 25,000 km² are illustrated as points (small European countries excluded). All European Union member countries have the same value because they are modelled as a single unit in the Aglink–Cosimo model.

In much of the global north, an increase in AASF consumption was associated either with reductions in the consumption of red meat, poultry, eggs and dairy, or with no notable impact (that is, no discernible increases; Fig. 2). In the global south, an

increase in AASF consumption was not associated with declines in the consumption of red meat, poultry, eggs and dairy. The combined dietary effect of increasing AASFs and reducing red and processed meats may lead to a reduced risk of hypertension, stroke, heart disease, diabetes, colorectal cancer and breast cancer. Countries that are rapidly undergoing the nutrition transition (such as China, India, Philippines, Malaysia, Indonesia, Vietnam, South Korea, Mexico, Brazil, Peru, Chile, Nigeria, Russia, USA and Canada) are most likely to benefit from increases in AASF production, which could avert the trajectory of their populations towards harmful levels of meat consumption (Fig. 2).

Aquatic foods can fill the nutrient gap

Deficiencies in key micronutrients—such as iron, zinc, calcium, iodine, folate, vitamins A, B₁₂ and D—have led to 1 million premature deaths annually⁸. Further, an estimated 30% of the global population (around 2.3 billion people) have diets that are deficient in at least one micronutrient⁸. Inadequate nutrient intakes can arise from various factors: the formulation of food systems, including the availability and accessibility of foods; ecological or environmental conditions—such as soil nutrient loss, drought or fishery declines—that decrease availability; reduced access to markets and natural resources through tariffs, fisheries governance, or other economic incentives; and/or taste preferences, consumer behaviour or other individualized factors^{8,26,27}. AASFs have the capability to reduce or fill this nutrient gap with bioavailable forms of micronutrients, particularly in geographies where AASF reliance and nutritional deficiencies are high, such as equatorial regions¹.

Here we focus on nutrient supply to estimate the contribution of AASFs to overall nutrient intake. In the high-production scenario by 2030, AASFs may contribute a global average of 2.2% of energy, 13.7% of protein, 8.6% of iron, 8.2% of zinc, 16.8% of calcium, 1.1% of vitamin A, 27.8% of vitamin B₁₂ and 98–100% of DHA+EPA, an approximate 0–10% increase for each nutrient above 2020 reference values (Extended Data Fig. 5, Supplementary Data 2). For each of the AASF taxa included in the analysis, we used standardized nutrient composition values for muscle tissue because the species coverage was higher than for other parts (such as liver, bones and eyes). Because these other parts are often more nutrient-rich than muscle tissue, our estimates are likely to be conservative, underestimating the true value of AASFs in human diets.

We calculated summary exposure values (SEVs) to assess the excess risk that each country experiences because of inadequate nutrient supply in their overall food systems, comparing the total amount of nutrition derived from apparent consumption against age- and sex-specific nutrient demands ([Methods](#)). SEVs range from 0% to

100% and should be viewed as a risk-weighted prevalence, with higher SEVs representing higher risk of inadequate micronutrient intake²⁸. The difference in SEVs represents the change in potential risk of inadequate nutritional intake between the two AASF production scenarios in 2030 (Fig. 3, Supplementary Data 3). With overall trends in increasing AASF consumption and concomitant reductions in poultry, eggs, dairy, and red and processed meats (Fig. 2), there are large gains in micronutrient and DHA+EPA consumption (Fig. 3). Globally, the high-production scenario will lead to reductions in inadequate intake across most assessed nutrients (reduction of 8.1 million iron, 5.5 million zinc, 49.3 million calcium, 36.0 million vitamin B₁₂, and 76.8 million DHA+EPA inadequate intakes), while potentially increasing 10.1 million vitamin A inadequate intakes (Extended Data Fig. 6). Particular geographies will also experience small declines in calcium, iron, vitamin A and zinc supply. This phenomenon probably arises from modest reductions in the consumption of iron- and zinc-rich red meat (as shown in historical trends), and large reductions in the consumption of calcium- and vitamin-A-rich dairy, egg and poultry. Notably, certain regions that are characterized by food and nutrition insecurity (for example, sub-Saharan Africa and Southeast Asia) experience increases in intake for all measured nutrients. However, some populations will face increasing risk of inadequate micronutrient intake if consumption of AASFs displaces other foods, as evidenced by reduced calcium intake in Turkey, zinc intake in Azerbaijan, and vitamin A intake in Indonesia and Mexico, among others (Fig. 3). Yet, globally, there is a pattern in which increasing the diversity of aquatic animal-source food consumption leads to reduced micronutrient-inadequate intakes (Extended Data Fig. 7).

Fig. 3: Shifts in micronutrient intake resulting from an increase of aquatic animal-source foods.

 **figure3**

The maps show the difference in SEVs in 2030 under the high-production and baseline-production scenarios by country. Values less than zero indicate reduced risk (lower SEVs) of inadequate intake under the high-production scenarios. The bottom panels show the difference in the number of people with inadequate micronutrient intakes, by age–sex group. Values less than zero indicate fewer inadequate intakes under the high-production scenario. Countries smaller than 25,000 km² are illustrated as points (small European countries excluded).

Recognition of the diversity of AASFs and their nutrient composition could be harnessed to direct their production and consumption across a range of deficient minerals, fatty acids and vitamins. For instance, if calcium deficiency is an issue in Turkey, one prudent option might be to increase the consumption of pelagic small fish (such as herrings and sardines)²⁹. Similarly, if vitamin A deficiency is an issue in

Brazil, then efforts to promote the production of oysters or the consumption of sardines might be appropriate³⁰. These types of food-system solutions will require sub-national targeting of vulnerable populations and will rely on efforts to increase both production and consumption.

Aquatic foods support the vulnerable

Diets are shaped by the structure of food systems. Access to the foods produced by these systems can vary by age, sex, culture, socio-economic status and geography, as does a given population's reliance on AASFs. AASFs are important for both sexes and all ages, but particularly so for young children, pregnant women and women of childbearing age, due to the critical role of micronutrients and DHA+EPA in fetal and child growth and development³⁰.

Because different age–sex groups have different vulnerabilities to certain health outcomes, a disproportionate benefit is associated with consuming AASFs for particular groups. The function of reducing micronutrient deficiencies is more important for children and women of reproductive age, and the function of attenuating morbidity and mortality as a result of chronic disease is more important for adults. For example, older people in Tunisia, Algeria, St Lucia, Iran and Moldova would experience large benefits in reduced inadequate intake of DHA+EPA (ΔSEV of at least -10.0 percentage points) and reduced inadequate intake in iron in Kiribati and the Republic of the Congo ($\Delta\text{SEV} = -3.6$ percentage points). In several countries, children would experience large benefits in reduced inadequate calcium intake due to increased AASF consumption (ΔSEV percentage points for 5–9-year-olds = -6.0 for girls and -5.5 for boys in Myanmar; -5.9 for girls in Vietnam and Cambodia; -5.1 for girls in Morocco; and -4.5 for boys and girls in Gabon; and ΔSEV percentage points for 0–4 year-olds = -4.9 for girls and -4.4 for boys in Maldives and -4.7 for boys and -4.3 for girls in Kiribati). In Panama, Iran, Moldova, Dominica and Egypt, a segment of reproductive-aged women (25–49 years) would receive a large health benefit from increased DHA+EPA consumption ($\Delta\text{SEV} = -6.7$ to -8.6 percentage points). Across all measured nutrients, there were significant sex differences in benefits between the base and the high-production scenario ($n = 73$ of a total 115 age–nutrient groups), in which increased AASF production and consumption disproportionately improved the intakes of women and girls (average of 51.4% of countries) over men and boys (average of 18.2% of countries; Supplementary Data 4). Thus, there is an almost three times greater likelihood of increased AASF consumption benefitting female nutrition, providing a potential pathway for nutritional equity ([Supplementary Methods](#)).

Discussion

We illustrate the role of AASFs in improving the future of human health, focusing on supplying critical micronutrients and attenuating morbidity and mortality from chronic disease that is characteristic of the nutrition transition. Our analyses demonstrate that an increase in production of the rich diversity of AASFs (and the nutrients contained therein) can improve the diets of many nations. Notably, our analysis focuses on the consumption of muscle tissue from AASFs and therefore must be viewed as a probable underestimate of the potential contribution to micronutrient supplies. Our projection of declines in global vitamin A supply may be incorrect, given the high levels of this nutrient in certain fish parts (such as liver) that are not included because of our focus on muscle tissue.

The diversity of aquatic foods highlighted here evidences the limitations of treating them as a homogenous group. The EAT–Lancet Commission Report¹² undervalues the importance of aquatic foods; key food policy dialogues (such as the UN Sustainable Development Goal 2: Zero Hunger) ignore aquatic foods completely; and funding for the aquatic foods sector from the World Bank and Regional Development Banks lack targeted support³¹. Two main issues seem to be pervasive in misunderstanding the importance of aquatic foods. First, a very narrow view of the diversity of fish and seafood is often taken, with a focus on a set of commercially grown or wild-harvested finfish and bivalves. This classification ignores the vast diversity of other species, forms of culture production, and wild harvest by small-scale fisheries³². Second, the nutritional contribution of aquatic foods has traditionally focused on its low contribution to global energy (that is, calories) and protein intake, failing to consider the contribution of aquatic foods to nutrition via highly bioavailable essential micronutrients and fatty acids. The AFCD presented here enables future studies to move beyond this limited view of nutrition from aquatic foods. However, there are still limitations in our current presentation (for example, a lack of focus on vitamin D due to variable intake requirements and a lack of recognition of the nutritional value of small fish and non-muscle fish parts in human nutrition). Vitamin D deficiency is a major health issue in some countries, and an increase in fatty fish intake could reduce this.

It is critical to consider where and how aquatic foods are produced, because environmental, social and economic impacts can vary widely across both the wild-capture and aquaculture sectors ([Supplementary Methods](#)). Despite the variability in environmental impacts across animal-source food-production sectors, aquaculture and wild-capture fisheries nearly always produce fewer greenhouse gas emissions and use less land than the farming of red meats, and many AASFs outperform poultry³³. Sustainably and equitably achieving the human health benefits of expanded aquatic food production will require policies and technologies that mitigate impacts on adjacent ecosystems, industries and communities²¹.

Policy translation

Our findings suggest the following strategic research and policy opportunities:

First, in countries in which there are high burdens of micronutrient deficiencies, the supply chains and availability of aquatic foods may be strengthened by improving fisheries management; enhancing sustainable aquaculture; and building more equitable national and regional trade networks.

Second, the promotion of a diversity of nutrient-rich aquatic foods in sustainable aquaculture systems, in designing national food-based dietary guidelines, and for public-health interventions targeting particular nutritional deficiencies among vulnerable populations living in particular geographies.

Third, incentivizing access and affordability of aquatic foods in countries experiencing a rapid nutrition transition.

Fourth, prioritizing aquatic foods in social protection programs, including food assistance, school meal programmes, and safety nets for the most nutritionally vulnerable, including pregnant and lactating women, young children in the first 1,000 days of life, and older people.

In line with the Voluntary Guidelines on Food Systems and Nutrition³⁴ of the Committee on World Food Security, national food and nutrition policy is needed to transform food systems by prioritizing aquatic foods where culturally and socially appropriate. Also, policy may ensure that the governance of and investment in aquatic food systems aims to preserve, support and improve aquatic species diversity; production and harvest methods and practices; and efficient and safe distribution channels. With more than 1.5 billion people unable to afford a healthy and sustainable diet³⁵, our model results showcase the importance of price and economic policies in creating nutritious diets that are affordable for consumers. These measures should enable aquatic foods to have an important role in nourishing the global population and improving global nutrition and health.

Methods

Food system modelling approach

The FAO FISH¹⁹ and Aglink–Cosimo²⁰ models are recursive-dynamic, partial equilibrium models used to simulate developments of annual market balances and prices for the main agricultural commodities produced, consumed and traded worldwide. Aglink–Cosimo and FAO FISH are managed by the Secretariats of the

OECD and FAO, and used to generate the annual OECD–FAO Agricultural Outlook²⁰ and other peer-reviewed scenario analyses³⁶. The references cited provide full model descriptions.

The FAO FISH model contains 2,019 equations and covers 47 country and/or region endogenous modules. Three products are covered with complete supply-disposition variables and prices: an aggregate of all aquatic animals except mammals; fishmeal; and fish oil. For the aggregate aquatic animals, the model supplies functions for both capture and aquaculture depending on the country or regional aggregate. On the demand side, the model produces one aggregate aquatic animal demand function, but includes 3 different types of use: food; processed into fishmeal and oil; and other uses.

To reflect the fact that fisheries are a renewable natural resource that are fully exploited and regulated or over-exploited, capture fisheries are kept exogenous in most modules of the model as they are controlled under strict fishing quotas and subject to regulations preventing economically driven supply. Therefore, the supply of only 11% of world capture fisheries respond to price for those countries and regions with insufficiently strict regulations. However, it is assumed that their capture production will always stay below the maximum sustainable yield. Conversely, in the model, 99% of world aquaculture production is endogenous and responsive to the price of the output, and 75% of aquaculture is additionally responsive to feed prices. In terms of aquaculture supply, the model contains 115 functions that cover the combination of countries and species. Each species has its specific feed rations (different mix of feed ingredients), production lags driven by the species biology, and elasticities (the level of responsiveness of production to price changes). Ninety seven per cent of the global reduction of fish into fishmeal and oil is endogenous in the model. In 63% of the modules, fishmeal and oil is controlled by a simple technical parameter, whereas in the remaining modules it is price-responsive.

The Aglink–Cosimo model, described as a structural sector model, provides a mathematical representation of the decision processes of producers and consumers of agricultural commodities. The equations relate exogenously provided projections of the macroeconomic environment, such as population growth and gross domestic product (GDP) developments, through commodity- and country-specific parameters to agricultural supply and demand variables. These variables are projected forward in a dynamic-recursive way using prices at domestic and global levels to clear markets at all stages. The demand for food is a function of income, own and cross prices, in which the respective elasticities control the relative strength of each variable. Because Aglink–Cosimo and the FAO FISH model are ‘partial-equilibrium’ sector models, income does not change in the scenario. The substitution between the various food items is caused by shifts in relative prices.

The FAO FISH model was integrated into Aglink–Cosimo to represent the aquatic foods component of the overall global food and agriculture system. Once integrated, the fish, fishmeal and fish oil of the FISH model become fully integrated into the merged model and the full set of commodities is simulated simultaneously. Per capita food demand of aquatic products is determined by their retail price, retail price of substitutes (mostly beef, pork and poultry), and by real per capita GDP. Typically, consumers from wealthier countries respond less to a change in the retail price of fish expressed in real terms (that is, deflated by the overall consumer price index) than consumers who spend a higher share of their income on food. The retail price of aquatic products is determined by the price of traded products (which can be considered a wholesale price) and the GDP deflator to capture movement in the other costs along the supply chain. The higher the GDP of a country, the smaller the influence of the wholesale price in the calculation of the retail price. Imports and exports are a function of the ratio between the domestic (adjusted by tariff and exchange rate) and world price of aquatic products with different levels of responsiveness depending on the openness of the different countries' aquatic product markets. Finally, the price of traded aquatic products is the market clearing variable of each country component.

Scenario development

Two alternative outlook projections, a baseline and high-production scenario (Supplementary Table 1; Supplementary Fig. 1), were used to represent food production, consumption, and trade to 2030 for 22 food groups. The baseline scenario is driven by the results of the FAO FISH model included in the OECD–FAO Agricultural Outlook 2020–2029, with 2030 data reflecting the UN FAO's best understanding of likely fisheries and aquaculture growth (Supplementary Fig. 2) based on anticipated macroeconomic conditions, agriculture and trade policy settings, fisheries management outcomes, long-term productivity, international market developments and average weather conditions³⁷. Aquaculture will be the main driver of the growth up to 2030, while fisheries production is expected to slightly decline. The high-production scenario is not a prediction but represents the UN FAO's specific estimation of the upper limits of aquatic foods growth potential³⁷, reflecting an imposed change to AASF production. This could be obtained by applying innovative technologies, capacity building, increased and cost-effective financial investment in aquaculture and improved and effective management in fisheries production constrained by estimates of global maximum sustainable yield. Also in the high-production scenario, major growth in production is expected to originate mainly from aquaculture, but fisheries production will slightly grow. The improved and effective management will support the sustainable growth in fisheries production through increased catches in areas recovering from previous overexploitation patterns, as well

as underfished resources, and improved utilization of the harvest, including reduced onboard discards, waste and losses.

Although the high-production scenario is optimistic, it is within the realm of possible futures, and is used to explicitly highlight the potential nutritional and health gains that could arise from targeted interventions. Species composition of broad commodity categories and feed composition (which could affect nutrient composition of products) were left unchanged between the present and 2030. We estimated country-level AASF consumption corresponding to marine and freshwater capture and aquaculture production projections in 2030 based on the joint Aglink–Cosimo FISH baseline and high-production outputs.

As the supply of fish is increased relative to the baseline, under the assumption that demand does not shift, a new equilibrium price is found along the demand curve. This new price of fish influences the consumption and production of other agricultural commodities through links on the production and consumption side. The shift in the international reference price of fish, which represents the aggregate behavior of all consumers, leads to changes in individual decisions that are determined by the relative changes in their domestic prices. They, in turn, are determined by the integration of each commodity market into the global trade system and the respective shift of the fish supply in the scenario. Consumers in a fish-producing or importing country will take advantage of the lower fish price and consume more fish and less terrestrial meats, depressing terrestrial meat prices. These prices are also transmitted through trade to countries that do not produce or import a substantial volume of fish. Thus, consumers take advantage of the lower meat prices and increase their meat consumption.

On the production side, similar effects are simulated. As demand for meat declines globally owing to its substitution with cheaper fish, demand for feed also declines, lowering its price. Depending on the production technology, certain producers take advantage of the cheaper feed and increase production of livestock products. As cereals are used as feed and food, the consumption of staples also increases. The relative size of all of these responses culminates in the trade flows. They shift relative to the baseline and a new global market equilibrium is found. A full description of the high-production scenario parameters and assumptions can be found in the [Supplementary Methods](#).

Global Nutrient Database

The GND matched over 400 food and agricultural commodities from the FAO's Supply and Utilization Accounts to food items in the United States Department of Agriculture Food Composition Database and obtained data on nutrient composition of the Supply and Utilization Accounts food items²². After adjusting for the inedible

portion of each food item, the GND can estimate the national availability of macronutrients and micronutrients in a given year. On the basis of this, the 22 food group model outputs from the Aglink–Cosimo model were cross-walked to the GND, and nutrient supply was estimated for each scenario (Supplementary Table 1).

Species disaggregation

Aquatic foods in the GND are based on FAO FishStat production data and currently include the following categories: demersal fish; pelagic fish; fish oils; crustaceans; cephalopods; other marine fish; freshwater fish; other molluscs; aquatic mammals; other aquatic animals; and aquatic plants. To derive more resolved consumption estimates, we first assigned fish consumption estimates to freshwater and marine species on the basis of historical shares. Within these broad categories, consumption was then assigned to capture and aquaculture sources to allow for future projections to reflect increased share (for some key species) in aquaculture production. Next, we used FAO FishStat production data to predict which species are actually being consumed in each country, adjusting for trade flows. We assumed that future diets preserved the current taxonomic make-up within each of these categories.

For marine species disaggregation, we used country-specific FAO FishStat historical catch and production data from 2014 to proportionally assign consumption projections to the Aglink–Cosimo outputs. Freshwater species, with the exception of salmon (calculated separately using FAO trade data), and any fish destined to fishmeal, fish oil or discards were removed. National apparent consumption of marine seafood by species from all producing sectors and sources (aquaculture, capture and import) was calculated by subtracting exports from production, using FAO food balance sheets (according to the proportion of species within each seafood commodity category), and adding imports (assuming a species mix within trade codes proportional to trade partner production). Negative apparent consumption was assumed to be zero. Finally, we scaled total harvest by the edible portion of each species.

Consumption of freshwater taxa was generated by matching FAO FishStat production and trade labels nested in the same commodity group ([Supplementary Methods](#); [Supplementary Figs. 3, 4](#)). All commodities were converted to live weights using freshwater conversion factors³⁸. The proportion of freshwater species consumed was further disaggregated with household survey data³⁸, and recreational fishery consumption ([Supplementary Methods](#)). Household surveys were used to adjust the volume of capture fishery relative to aquaculture in 31 countries and disaggregated unidentified commodity groups for five countries³⁸. Recreational fisheries data from ancillary sources were included for 11 countries that have high but potentially under-reported recreational participation. Finally, we estimated consumable harvest by scaling total harvest by edible proportion ([Supplementary Methods](#)).

Aquatic Foods Composition Database

The AFCD synthesizes information from international and national food composition tables and peer-reviewed literature. Food composition tables were assumed to be correct and directly integrated. Data were sourced from international food composition databases from the United States Department of Agriculture (USDA), FAO INFOODS and the EU SMILING project in Southeast Asia, as well as individual food composition tables from Australia, New Zealand, Pacific Islands, South Korea, India, Bangladesh, West Africa, Canada, Norway and Hawaii, and previous reviews of peer-reviewed literature².

The search strategy focused on studies between 1990 and 2020, and prioritized specific journals known to include food composition data (for example, *Food Chemistry*, *Journal of Food Composition and Analysis*). A broader search was also conducted using Web of Science including 20 aquatic and 15 nutritional search terms, with elimination hedges to avoid irrelevant studies (see [Supplementary Methods](#) for full terms). Peer-reviewed data were collected from 1,063 individual studies. In total, the AFCD contains 29,912 lines of data representing 3,753 unique taxa.

We estimated the likely mix of species consumed as described above and then matched these individual species identities with the AFCD. To link disaggregated species to the AFCD, we used a hierarchical approach to assign the nutritional value for all 7 nutrients to all species consumed globally (Supplementary Fig. 5). When multiple entries were present for a single species, we took the mean of all entries. We built this hierarchy according to the following order: scientific name, average of species genus, average of species family, common name, average of species order, and average of GND category. In the disaggregation effort, we found 2,143 different aquatic species being consumed globally. We matched nutrient composition values from muscle tissue for protein, iron, zinc, calcium, vitamin A, vitamin B₁₂ and DHA+EPA. After this matching process, we updated the estimates of nutrient intake at national levels.

Sub-national intake distributions

To evaluate the health impacts of AASF consumption, we first modelled the distribution of habitual dietary intake across age–sex groups and geographies. Using SPADE (Statistical Program to Assess Habitual Dietary Exposure), an R-base package that uses 24-hour recall data to remove within-person variability and estimate habitual intake distributions³⁹, we estimated usual intakes of iron, zinc, calcium, vitamin A, vitamin B₁₂, DHA+EPA and red meat. These distributions relied on the availability of individual dietary intake data with variable days of 24-hour recalls, which were available in 13 datasets to which we had access, including: United States, Zambia, Mexico, China, Lao PDR, Philippines, Uganda, Burkina Faso, Bulgaria, Romania,

Italy, Bangladesh and Bolivia. A summary of the datasets used to estimate the sub-national intake distributions is available in [Supplementary Table 7](#).

We fit gamma and log-normal distributions to the habitual intake distributions for all available age–sex groups using the `fitdistrplus` package⁴⁰. We selected the distribution with the best Kolmogorov–Smirnov (KS) goodness-of-fit statistic (0.002–0.373) as the final distribution for each group. The parameters of this best fitting distribution describe the shape of habitual intake distribution for each age–sex group and can be shifted along the x axis in response to changing diets.

Assigning national intake distributions

We disaggregated country-level intakes into sub-national distributions of intake in three steps. First, we disaggregated the European Union, which is modelled as a single entity in the integrated model, into its 27 constituent countries ([Supplementary Table 5](#)). Second, we disaggregated country-level mean intakes into age–sex-level mean intakes using the Global Expanded Nutrient Supply (GENuS) database⁴¹ for all nutrients except DHA+EPA and vitamin B₁₂, which are not included in the GENuS database. We used the SPADE habitual intake output to derive age–sex-level mean intakes for these two nutrients. Finally, we used the SPADE habitual intake output to describe the shape of intake distribution for each age–sex group.

The GENuS database uses historical national dietary trend data to estimate the availability of 23 individual nutrients across 225 food categories for 34 age–sex groups in nearly all countries in 2011⁴¹. We used these estimates to calculate scalars for relating country-level availability to age-group-level availability as:

$$\$ \$ \{ \mathrm{Scalar} \} _{c,n,a,s} = \{ \mathrm{availability} \} _{c,n,a,s} / \mathrm{mean} \{ \mathrm{availability} \} _{c,n} \$ \$$$

where the scalar for country c , nutrient n , age group a and sex s is calculated by dividing the nutrient availability for each age–sex group by the mean nutrient availability for all age–sex groups. We assume these ratios of nutrient availability are proportional to ratios of nutrient intake and scale the country-level mean nutrient intakes as follows:

$$\$ \$ \{ \mathrm{Intake} \} _{c,n,a,s} = \{ \mathrm{intake} \} _{c,n} \times \{ \mathrm{scalar} \} _{c,n,a,s} \$ \$$$

We used the same process to disaggregate intakes for DHA+EPA and vitamin B₁₂ but used the country-level and age-sex-level means derived from SPADE habitual intakes

described above. See [Supplementary Table 6](#) for details on crosswalking the Aglink–Cosimo and GENuS outputs.

We then used the SPADE habitual intake outputs to characterize the distribution of nutrient intakes within each age–sex group. The habitual intake data and associated statistical probability distributions are incomplete across all country–nutrient–age–sex combinations (Supplementary Fig. [6](#)) so we filled gaps by imputing data from the nearest neighbour (37% of age–sex groups). First, we filled within-country gaps by borrowing intake distributions, in order of preference, from the nearest age group within a sex and country; the opposite sex from within a country; and the nearest country geographically and/or socioeconomically (Supplementary Fig. [7](#)). We then mapped these to the rest of the world, based on UN sub-regions, with a few expert-identified modifications (Supplementary Fig. [8](#)).

Health impact modelling approach

SEVs integrate relative risks of sub-optimal diets with actual intake distributions^{[28](#)}. They estimate the population-level risk related to diets and compare it to a population in which everyone is at a maximal risk level, giving values ranging from 0% (no risk) to full population-level risk (100%). For DHA+EPA, we used the updated Institute for Health Metrics and Evaluation relative risk curves that are associated only with ischaemic heart disease and have different values for adolescent and adult subpopulations (with no risk for children). These relative risk curves capture mild risk associated with consumption of omega-3 long-chain polyunsaturated fatty acids under 0.4 g per day^{[28](#)}. For inadequate micronutrient intake risk assessment, we derived continuous relative risk curves for iron, zinc, calcium and vitamin A, based on the probability approach for calculating inadequate intake, often a precursor to micronutrient deficiencies^{[42](#)}. To evaluate the risk of inadequate micronutrient intake, distributions of intake are compared against requirements. The latter is defined as a continuous risk curve that has a value of 1 at low intakes, 0.5 at the relevant estimated average requirement (EAR) and zero at large intakes. These absolute risk curves are based on the cumulative normal distribution function of requirements^{[43](#)} with a mean at the EAR and a coefficient of variation of 10%. The latter value is used when more information on exact nutrient requirement is unavailable^{[42,44](#)}. The prevalence of risk at the population level is derived by computing the expected micronutrient deficiency across the entire population^{[43](#)}, by applying an integral of the intake distribution per age–sex–location–nutrient multiplied by its specific relative risk. The values derived range from 0 to 1, and evaluates the risk of inadequate intake, as SEV, on a population level from no risk (0) to maximal (1; everyone is at risk). Estimated average requirements were derived from several sources^{[45,46,47](#)}. Because zinc and iron requirements depend on other dietary factors (for example, inhibitors such as phytate), we used three levels for each nutrient, based on overall diets, which crudely divide

between diets based on their cereals and animal-source food intakes^{48,49}. We then assigned each country to their proxy zinc and iron values, based on its social development index⁵⁰. For vitamin B₁₂, we used the values used by the Institute of Medicine⁵¹ but acknowledge that uncertainties regarding recommended intakes exist, and used a coefficient of variation of 25% instead of the default 10% in constructing our risk curves⁵².

Reporting summary

Further information on research design is available in the [Nature Research Reporting Summary](#) linked to this paper.

Data availability

The AFCD is open access and can be found at:

<https://dataverse.harvard.edu/dataverse/afcd>. All other nutrient data were sourced from the USDA FoodData Central (<https://fdc.nal.usda.gov/>) or the GND as described in Methods. For sub-national data evaluation, data was sourced from the following locations: FAO/GIFT: <http://www.fao.org/gift-individual-food-consumption/data-and-indicator/en/>; NHANES: <https://wwwn.cdc.gov/nchs/nhanes/continuousnhanes/default.aspx?BeginYear=2017>; ENSANUT: <https://ensanut.insp.mx/encuestas/ensanut2016/descargas.php>; China Health and Nutrition Survey: <https://www.cpc.unc.edu/projects/china/data/datasets>; Uganda: <https://doi.org/10.7910/DVN/FOYZBL>; Burkina Faso: <https://doi.org/10.7910/DVN/5CXCLX>. Proprietary input datasets protected by data-sharing agreements (that is, the GND) are not posted in these repositories. All processed outputs and non-proprietary raw inputs are available on GitHub. The data associated with the diversity disaggregation is available at <https://github.com/cg0lden/Fisheries-Nutrition-Modeling>. The data associated with the SPADE analysis is available at https://github.com/cg0lden/subnational_distributions_BFA. The data associated with the health impacts analysis is available at <https://github.com/alonsheron/Health-Benefit-Calculation-BFA>.

Code availability

The code associated with the diversity disaggregation is available at <https://github.com/cg0lden/Fisheries-Nutrition-Modeling>. The code associated with the SPADE analysis is available at https://github.com/cg0lden/subnational_distributions_BFA. The code associated with

the health impacts analysis is available at <https://github.com/alonshepon/Health-Benefit-Calculation-BFA>.

References

1. 1.

Golden, C. D. et al. Nutrition: fall in fish catch threatens human health. *Nature* **534**, 317–320 (2016).

2. 2.

Byrd, K. A., Thilsted, S. H. & Fiorella, K. J. Fish nutrient composition: a review of global data from poorly assessed inland and marine species. *Public Health Nutr.* **24**, 476–486 (2021).

3. 3.

Hicks, C. C. et al. Harnessing global fisheries to tackle micronutrient deficiencies. *Nature* **574**, 95–98 (2019).

4. 4.

Bernhardt, J. R., & O'Connor, M. I. Aquatic biodiversity enhances multiple nutritional benefits to humans. *Proc. Natl Acad. Sci.* **118**, e1917487118 (2021).

5. 5.

Manson, J. E. et al. Marine n-3 fatty acids and prevention of cardiovascular disease and cancer. *N. Engl. J. Med.* **380**, 23–32 (2019).

6. 6.

Meat, Fish and Dairy Products and the Risk of Cancer. Continuous Update Project Expert Report 2018 (World Cancer Research Fund/American Institute for Cancer Research, 2018).

7. 7.

UNICEF, WHO & The World Bank Group. *Levels and Trends in Child Malnutrition*. (WHO, 2021).

8. 8.

Global Nutrition Report: Action on Equity to End Malnutrition (Development Initiatives Poverty Research, 2020).

9. 9.

Victora, C. G. et al. Revisiting maternal and child undernutrition in low-income and middle-income countries: variable progress towards an unfinished agenda. *Lancet* **397**, 1388–1399 (2021).

10. 10.

Afshin, A. et al. Health effects of dietary risks in 195 countries, 1990–2017: a systematic analysis for the Global Burden of Disease Study 2017. *Lancet* **393**, 1958–1972 (2019).

11. 11.

Mensah, G. A., Roth, G. A. & Fuster, V. The global burden of cardiovascular diseases and risk factors: 2020 and beyond. *J. Am. Coll. Cardiol.* **74**, 2529–2532 (2019).

12. 12.

Willett, W. et al. Food in the Anthropocene: the EAT–Lancet Commission on healthy diets from sustainable food systems. *Lancet* **393**, 447–492 (2019).

13. 13.

Youn, S. J. et al. Inland capture fishery contributions to global food security and threats to their future. *Glob. Food Sec.* **3**, 142–148 (2014).

14. 14.

Rimm, E. B. et al. Seafood long-chain n-3 polyunsaturated fatty acids and cardiovascular disease: a science advisory from the American Heart Association. *Circulation* **138**, e35–e47 (2018).

15. 15.

WorldFish. *2030 Research and Innovation Strategy: Aquatic Foods for Healthy People and Planet* (eds Lala-Pritchard, T. & Johnstone, G) (WorldFish, 2020).

16. 16.

Global Production by Production Source 1950–2019. *FishStatJ* (FAO, 2021).

17. 17.

Golden, C. D. et al. *Aquatic Food Composition Database*
<https://doi.org/10.7910/DVN/KI0NYM> (Harvard Dataverse, 2021).

18. 18.

Popkin, B. M. & Gordon-Larsen, P. The nutrition transition: worldwide obesity dynamics and their determinants. *Int. J. Obes.* **28**, S2–S9 (2004).

19. 19.

The State of World Fisheries and Aquaculture 2020. 186–193 (FAO, 2020).

20. 20.

OECD/FAO. *OECD-FAO Agricultural Outlook 2021–2030.*
<https://doi.org/10.1787/19428846-en> (OECD Publishing, 2020).

21. 21.

Costello, C. et al. The future of food from the sea. *Nature* **588**, 95–100 (2020).

22. 22.

Schmidhuber, J. et al. The Global Nutrient Database: availability of macronutrients and micronutrients in 195 countries from 1980 to 2013. *Lancet Planet. Health* **2**, e353–e368 (2018).

23. 23.

Dey, M. M. et al. Demand for fish in Asia: a cross-country analysis. *Aust. J. Agric. Resour. Econ.* **52**, 321–338 (2008).

24. 24.

Gallet, C. A. The demand for fish: a meta-analysis of the own-price elasticity. *Aquac. Econ. Manag.* **13**, 235–245 (2009).

25. 25.

Zhao, L. G. et al. Fish consumption and all-cause mortality: a meta-analysis of cohort studies. *Eur. J. Clin. Nutr.* **70**, 155–161 (2015).

26. 26.

Vermeulen, S. J., Park, T., Khoury, C. K. & Béné, C. Changing diets and the transformation of the global food system. *Ann. NY Acad. Sci.* **1478**, 3–17 (2020).

27. 27.

Naylor, R. L., et al. The demand for blue foods across geographic and temporal scales. *Nat. Commun.* (in the press).

28. 28.

Murray, C. J. L. et al. Global burden of 87 risk factors in 204 countries and territories, 1990–2019: a systematic analysis for the Global Burden of Disease Study 2019. *Lancet* **396**, 1223–1249 (2020).

29. 29.

Isaacs, M. The humble sardine (small pelagics): fish as food or fodder. *Agric. Food Secur.* **5**, 27 (2016).

30. 30.

Bernstein, A. S., Oken, E. & de Ferranti, S. Fish, shellfish, and children's health: an assessment of benefits, risks, and sustainability. *Pediatrics* **143**, e20190999 (2019).

31. 31.

Bennett, A. et al. Recognize fish as food in policy discourse and development funding. *Ambio* **50**, 981–989 (2021).

32. 32.

Gelcich, S. et al. Challenges and opportunities for small-scale actors in aquatic food systems. *Nature Food* (in the press).

33. 33.

Gephart, J. A. et al. Environmental performance of blue foods. *Nature* <https://doi.org/10.1038/s41586-021-03889-2> (2021).

34. 34.

Hirvonen, K., Bai, Y., Headey, D. & Masters, W. A. Affordability of the EAT–Lancet reference diet: a global analysis. *Lancet Glob. Health* **8**, e59–e66 (2020).

35. 35.

Committee on World Food Security. *The CFS Voluntary Guidelines on Food Systems and Nutrition (VGFSyN)* CFS 2021/47/7/Rev.1 (FAO, 2021).

36. 36.

Pieralli, S., Pérez Domínguez, I., Elleby, C. & Chatzopoulos, T. Budgetary impacts of adding agricultural risk management programmes to the CAP. *J. Agric. Econ.* **72**, 370–387 (2021).

37. 37.

Ahern, M., Thilsted, S. H. & Oenema, S. *The Role of Aquatic Foods in Sustainable Healthy Diets*. Discussion Paper (UN Nutrition, 2021).

38. 38.

Fluet-Chouinard, E., Funge-Smith, S. & McIntyre, P. B. Global hidden harvest of freshwater fish revealed by household surveys. *Proc. Natl Acad. Sci. USA* **115**, 7623–7628 (2018).

39. 39.

Dekkers, A. L., Verkaik-Kloosterman, J., van Rossum, C. T. & Ocké, M. C. SPADE, a new statistical program to estimate habitual dietary intake from multiple food sources and dietary supplements. *J. Nutr.* **144**, 2083–2091 (2014).

40. 40.

Delignette-Muller, M. L. & Dutang, C. fitdistrplus: an R package for fitting distributions. *J. Stat. Softw.* **64**, 1–34 (2015).

41. 41.

Smith, M. R., Micha, R., Golden, C. D., Mozaffarian, D. & Myers, S. S. Global Expanded Nutrient Supply (GENuS) Model: a new method for estimating the global dietary supply of nutrients. *PLoS ONE* **11**, e0146976 (2016).

42. 42.

Institute of Medicine (US) Subcommittee on Interpretation and Uses of Dietary Reference Intakes; Institute of Medicine (US) Standing Committee on the Scientific Evaluation of Dietary Reference Intakes. *DRI Dietary Reference Intakes: Applications in Dietary Assessment* (National Academies Press, 2000).

43. 43.

Carriquiry, A. L. Assessing the prevalence of nutrient inadequacy. *Public Health Nutr.* **2**, 23–34 (1999).

44. 44.

Román-Viñas, B. et al. Overview of methods used to evaluate the adequacy of nutrient intakes for individuals and populations. *Br. J. Nutr.* **101**, S6–S11 (2009).

45. 45.

FAO/WHO. *Vitamin and Mineral Requirements in Human Nutrition* (World Health Organization, 2004).

46. 46.

FAO/WHO. *Guidelines on Food Fortification with Micronutrients* (eds Allen, L., de Benoist, B., Dary, O. & Hurrell, R.) (World Health Organization, 2006).

47. 47.

Institute of Medicine. *Dietary Reference Intakes: The Essential Guide to Nutrient Requirements* (eds Otten, J. J., Hellwig, J. P. & Meyers, L. D.) (National Academies Press, 2006).

48. 48.

Gibson, R. S., King, J. C. & Lowe, N. A review of dietary zinc recommendations. *Food Nutr. Bull.* **37**, 443–460 (2016).

49. 49.

Smith, M. R. & Myers, S. S. Impact of anthropogenic CO₂ emissions on global human nutrition. *Nat. Clim. Change* **8**, 834–839 (2018).

50. 50.

Chua, H.-W., Wong, A., & Shek, Daniel T. L. In *Encyclopedia of Quality of Life and Well-Being Research* (ed. Michalos, A. C.) 6047–6051 (Springer, 2014).

51. 51.

Institute of Medicine. *Dietary Reference Intakes for Thiamin, Riboflavin, Niacin, Vitamin B6, Folate, Vitamin B12, Pantothenic Acid, Biotin, and Choline* (National Academies Press, 1998).

52. 52.

Doets, E. L. et al. Systematic review on daily vitamin B12 losses and bioavailability for deriving recommendations on vitamin B12 intake with the factorial approach. *Ann. Nutr. Metab.* **62**, 311–322 (2013).

Acknowledgements

This paper is part of the Blue Food Assessment (BFA) (<https://www.bluefood.earth/>), a comprehensive examination of the role of aquatic foods in building healthy, sustainable and equitable food systems. The BFA was supported financially by the Builders Initiative, the MAVA Foundation, the Oak Foundation and the Walton Family Foundation, and has benefitted from the intellectual input of the wider group of scientists leading other components of the BFA. We are also grateful for the financial support of the National Science Foundation (CNH 1826668 to C.D.G., J.A.G. and J.G.E.) and the John and Katie Hansen Family Foundation (C.D.G. and D.F.V.). Support was provided to SP and HK by a National Institutes of Health Departmental Training Grant in Academic Nutrition (2T32DK007703-26). This work was also undertaken as part of the CGIAR Research Program (CRP) on Fish Agri-Food Systems (FISH), led by WorldFish and contributing to the WorldFish 2030 Research and Innovation Strategy: Aquatic Foods for Healthy People and Planet and the One CGIAR. This work is a product of the new Planetary Health laboratory at the Harvard T. H. Chan School of Public Health. For data sharing, visualization support and comments on study design, analysis and early drafts of writing, we thank J. Schmidhuber, H. Lescinsky, A. Afshin, T. Beal, S. Pires, L. Jakobsen, C. Costello, S. Funge-Smith, A. Castellanos, C. Batis, J. Rivera, Y. Li, W. Willett, A. Dekkers, M. Moursi, H. Embke, A. Robertson, J. J. Hallo and K. Manning. Any use of trade, firm, or product names is for descriptive purposes only and does not imply endorsement by the US Government.

Author information

Author notes

1. These authors contributed equally: Christopher D. Golden, J. Zachary Koehn, Alon Shepon, Simone Passarelli, Christopher M. Free, Daniel F. Viana

Affiliations

1. Department of Nutrition, Harvard T. H. Chan School of Public Health, Boston, MA, USA

Christopher D. Golden, Alon Shepon, Simone Passarelli, Daniel F. Viana, Sabri Bromage, Eric B. Rimm & Heather Kelahan

2. Department of Environmental Health, Harvard T. H. Chan School of Public Health, Boston, MA, USA

Christopher D. Golden

3. Department of Global Health and Population, Harvard T. H. Chan School of Public Health, Boston, MA, USA

Christopher D. Golden & Goodarz Danaei

4. Center for Ocean Solutions, Stanford University, Stanford, CA, USA

J. Zachary Koehn

5. Department of Environmental Studies, The Porter School of the Environment and Earth Sciences, Tel Aviv University, Tel Aviv, Israel

Alon Shepon

6. The Steinhardt Museum of Natural History, Tel Aviv University, Tel Aviv, Israel

Alon Shepon

7. Bren School of Environmental Science and Management, University of California, Santa Barbara, Santa Barbara, CA, USA

Christopher M. Free

8. Marine Sciences Institute, University of California, Santa Barbara, CA, USA

Christopher M. Free & Jacob G. Eurich

9. Betty and Gordon Moore Center for Science, Conservation International,
Arlington, VA, USA

Daniel F. Viana
10. Markets and Trade Division, Food and Agriculture Organization of the United
Nations (FAO), Rome, Italy

Holger Matthey
11. Department of Ecology, Evolution and Marine Biology, University of California,
Santa Barbara, Santa Barbara, CA, USA

Jacob G. Eurich
12. Department of Environmental Science, American University, Washington, DC,
USA

Jessica A. Gephart
13. Department of Earth System Science, Stanford University, Stanford, CA, USA

Etienne Fluet-Chouinard
14. Department of Biology, Carleton University, Ottawa, Ontario, Canada

Elizabeth A. Nyboer
15. U.S. Geological Survey, National Climate Adaptation Science Center, Reston,
VA, USA

Abigail J. Lynch
16. Institute of Marine Research, Bergen, Norway

Marian Kjellevold
17. Fisheries and Aquaculture Division, Food and Agriculture Organization of the
United Nations (FAO), Rome, Italy

Pierre Charlebois, Manuel Barange & Stefania Vannuccini
18. School of Oceanography, Shanghai Jiao Tong University, Shanghai, China

Ling Cao

19. Environmental Defense Fund, New York, NY, USA

Kristin M. Kleisner

20. Department of Epidemiology, Harvard T. H. Chan School of Public Health, Boston, MA, USA

Goodarz Danaei

21. Nicholas School of the Environment, Duke University, Durham, NC, USA

Camille DeSisto

22. Department of Population Medicine and Diagnostic Sciences and Master of Public Health Program, Cornell University, Ithaca, NY, USA

Kathryn J. Fiorella

23. Institute of Aquaculture, University of Stirling, Stirling, UK

David C. Little

24. WorldFish, Bayan Lepas, Malaysia

Edward H. Allison & Shakuntala H. Thilsted

25. Bloomberg School of Public Health and Nitze School of Advanced International Studies, Johns Hopkins University, Washington, DC, USA

Jessica Fanzo

Contributions

C.D.G. and S.H.T. conceptualized the research idea, with substantial methodological and design input from J.Z.K., A.S., C.M.F., D.F.V. and H.M. Data acquisition and compilation was conducted by subgroups for the Aquatic Foods Composition Database (C.D.G., J.Z.K., C.D., H.K., K.J.F., M.K. and D.F.V.), Global Nutrient Database (H.M.), Aglink–Cosimo model (H.M.), FAO Fish model (P.C., S.V. and M.B.), species disaggregation models (E.F.-C., E.A.N., J.A.G., A.J.L., D.F.V., J.G.E. and C.D.G.), sub-national distribution model (S.P., C.D.G., L.C. and S.B.), and health impact models (A.S., C.D.G., G.D. and E.B.R.). The food systems modelling was led by H.M. and P.C.; sub-national distributions modelling was led by S.P. and S.B.; and the health impact modelling was led by A.S., C.M.F. and G.D. C.D.G. drafted the original manuscript, and all co-authors edited and revised the writing.

Corresponding author

Correspondence to Christopher D. Golden.

Ethics declarations

Competing interests

The authors declare no competing interests.

Additional information

Peer review information *Nature* thanks Lotte Lauritzen, Max Nielsen and Albert Tacon for their contribution to the peer review of this work.

Publisher's note Springer Nature remains neutral with regard to jurisdictional claims in published maps and institutional affiliations.

Extended data figures and tables

[Extended Data Fig. 1 Difference in daily per capita intake of various nutrients from increasing aquatic animal-source food production and fully accounting for species diversity.](#)

The maps show the difference in mean nutrient intakes in 2030 under the high and baseline production scenarios when fully accounting for species diversity. Values greater than zero indicate higher nutrient intake under the high production scenario. Values less than zero indicate lower nutrient intake under the high production scenario. The boxplots show the difference in mean nutrient intakes in 2030 under both production scenarios, with and without fully accounting for species diversity. In the boxplots, the solid line indicates the median, the box indicates the interquartile range (IQR; 25th and 75th percentiles), the whiskers indicate 1.5 times the IQR, and the points beyond the whiskers indicate outliers. Countries smaller than 25,000 km² are illustrated as points (small European countries excluded). All European Union (EU) member countries have the same value because they are modelled as a single economic unit in the Aglink-Cosimo model (n=164 independent countries remain for comparison).

[Extended Data Fig. 2 Difference in 2030 food consumption under the base and high production scenarios \(part 1\).](#)

Mean daily per capita food consumption in 2030 under the (A) base and (B) high production scenarios and (C) the difference in consumption between the high production and base scenarios.

Extended Data Fig. 3 Difference in 2030 food consumption under the base and high production scenarios (part 2).

Mean daily per capita food consumption in 2030 under the (A) base and (B) high production scenarios and (C) the difference in consumption between the high production and base scenarios.

Extended Data Fig. 4 Difference in 2030 food consumption under the base and high production scenarios (part 3).

Mean daily per capita food consumption in 2030 under the (A) base and (B) high production scenarios and (C) the difference in consumption between the high production and base scenarios.

Extended Data Fig. 5 Difference in 2030 nutrient intakes under the base and high production scenarios accounting for the full diversity of nutrient compositions in seafood.

The mean daily per capita nutrient intake in 2030 when accounting for the full diversity of nutrient compositions in seafood under the (A) base and (B) high production scenarios and (C) the difference in intakes between the high production and base scenarios.

Extended Data Fig. 6 The relationship between the difference in 2030 health outcomes under the high and base production scenarios and base scenario status.

Each point represents a country where point color indicates the difference in national micronutrient deficiency averages between the scenarios (blue=reduced deficiencies; red=increased deficiencies) and point size indicates the scale of nutrient deficiencies in the base scenario (small=few deficiencies; large=many deficiencies). The vertical line indicates zero difference in nutrient intakes between the high and base scenarios; positive values indicate increased nutrient intake under the high production scenario and negative values indicate reduced intake. The dashed horizontal line indicates the average Estimated Average Requirement (EAR) for all age-sex groups. Countries falling below this line often have more room for health improvements than countries falling above this line. Counter-clockwise from the top-left, the quadrants of each plot

indicate countries with mean 2030 intakes in the base scenario that are: (1) higher than the mean EAR and higher than the high production scenario; (2) higher than the mean EAR but lower than the high production scenario; (3) lower than the mean EAR and lower than the high production scenario; and (4) lower than the EAR but higher than the high production scenario.

Extended Data Fig. 7 Summary exposure values (SEVs) in the high production scenario with and without the diversity disaggregation.

Summary exposure values (SEVs) for each country-age-sex group in the high production scenario with and without the diversity disaggregation. The diagonal line indicates the 1:1 line. Points below this line indicate country-age-sex groups with lower SEVs with the diversity disaggregation. Points above this line indicate country-age-sex groups with higher SEVs with the diversity disaggregation.

Supplementary information

Supplementary Information

This file contains Supplementary Methods, Supplementary References, Supplementary Figures 1-8 and Supplementary Tables 1-7.

Reporting Summary

Supplementary Data 1

Mean national per capita food consumption in 2030 under the base and high production scenarios.

Supplementary Data 2

Mean national per capita nutrient intakes in 2030 under the base and high production scenarios.

Supplementary Data 3

Mean national per capita inadequate nutrient intakes (SEVs) in 2030 under the base and high production scenarios.

Supplementary Data 4

Two-tailed t-test comparison by sex of changes in age-group inadequate nutrient intakes (SEVs) in response to increased production of aquatic foods.

Rights and permissions

Reprints and Permissions

About this article

Cite this article

Golden, C.D., Koehn, J.Z., Shepon, A. *et al.* Aquatic foods to nourish nations. *Nature* **598**, 315–320 (2021). <https://doi.org/10.1038/s41586-021-03917-1>

- Received: 18 January 2021
- Accepted: 16 August 2021
- Published: 15 September 2021
- Issue Date: 14 October 2021
- DOI: <https://doi.org/10.1038/s41586-021-03917-1>

Share this article

Anyone you share the following link with will be able to read this content:

[Get shareable link](#)

Sorry, a shareable link is not currently available for this article.

[Copy to clipboard](#)

Provided by the Springer Nature SharedIt content-sharing initiative

A spotlight on seafood for global human nutrition

- Lotte Lauritzen

News & Views 15 Sept 2021

| [Section menu](#) | [Main menu](#) |

- Article
- [Published: 22 September 2021](#)

Dopamine facilitates associative memory encoding in the entorhinal cortex

- [Jason Y. Lee](#) [ORCID: orcid.org/0000-0002-5670-7211](#)¹ na1,
- [Heechul Jun](#) [ORCID: orcid.org/0000-0002-5905-2716](#)¹ na1,
- [Shogo Soma](#) [ORCID: orcid.org/0000-0002-7381-9477](#)¹ na1 nAff3,
- [Tomoaki Nakazono](#)¹ na1 nAff4,
- [Kaori Shiraiwa](#)¹,
- [Ananya Dasgupta](#)¹,
- [Tatsuki Nakagawa](#)¹,
- [Jiayun L. Xie](#)¹,
- [Jasmine Chavez](#)¹,
- [Rodrigo Romo](#)¹,
- [Sandra Yungblut](#) [ORCID: orcid.org/0000-0003-2549-5065](#)¹,
- [Meiko Hagiwara](#)²,
- [Koshi Murata](#)² &
- [Kei M. Igarashi](#) [ORCID: orcid.org/0000-0002-5635-169X](#)¹

[Nature](#) volume **598**, pages 321–326 (2021)

- 9790 Accesses
- 488 Altmetric
- [Metrics details](#)

Subjects

- [Cortex](#)
- [Hippocampus](#)

Abstract

Mounting evidence shows that dopamine in the striatum is critically involved in reward-based reinforcement learning^{1,2}. However, it remains unclear how dopamine reward signals influence the entorhinal–hippocampal circuit, another brain network that is crucial for learning and memory^{3,4,5}. Here, using cell-type-specific electrophysiological recording⁶, we show that dopamine signals from the ventral tegmental area and substantia nigra control the encoding of cue–reward association rules in layer 2a fan cells of the lateral entorhinal cortex (LEC). When mice learned novel olfactory cue–reward associations using a pre-learned association rule, spike representations of LEC fan cells grouped newly learned rewarded cues with a pre-learned rewarded cue, but separated them from a pre-learned unrewarded cue. Optogenetic inhibition of fan cells impaired the learning of new associations while sparing the retrieval of pre-learned memory. Using fibre photometry, we found that dopamine sends novelty-induced reward expectation signals to the LEC. Inhibition of LEC dopamine signals disrupted the associative encoding of fan cells and impaired learning performance. These results suggest that LEC fan cells represent a cognitive map of abstract task rules, and that LEC dopamine facilitates the incorporation of new memories into this map.

Access options

Subscribe to Journal

Get full journal access for 1 year

\$199.00

only \$3.90 per issue

[Subscribe](#)

All prices are NET prices.
VAT will be added later in the checkout.
Tax calculation will be finalised during checkout.

Rent or Buy article

Get time limited or full article access on ReadCube.

from \$8.99

[Rent or Buy](#)

All prices are NET prices.

Additional access options:

- [Log in](#)
- [Access through your institution](#)
- [Learn about institutional subscriptions](#)

Fig. 1: LEC fan cells, but not pyramidal cells, are necessary for associative learning.

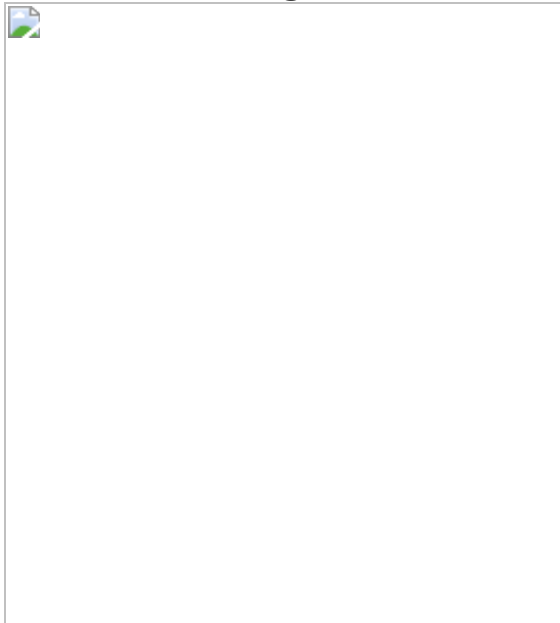


Fig. 2: LEC fan cells encode cue–reward association during learning.

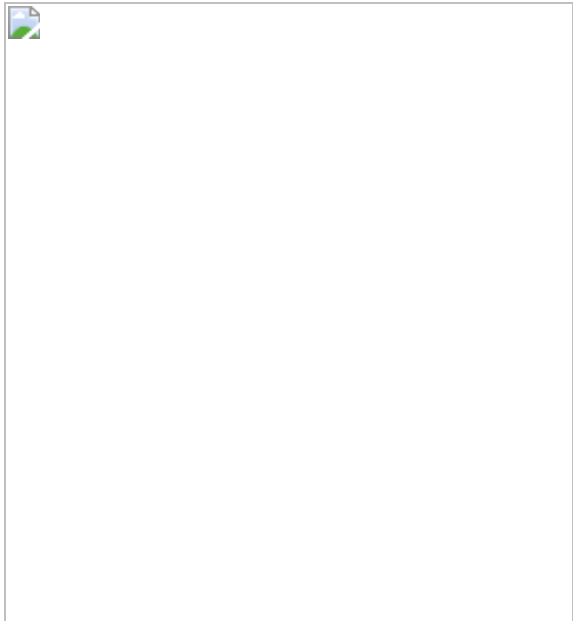


Fig. 3: LEC dopamine fibres send novelty-induced reward expectation signals.

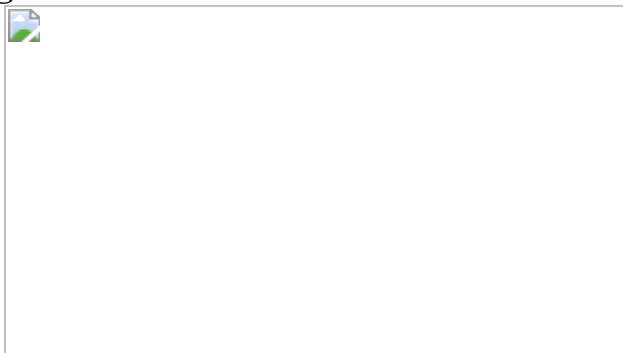
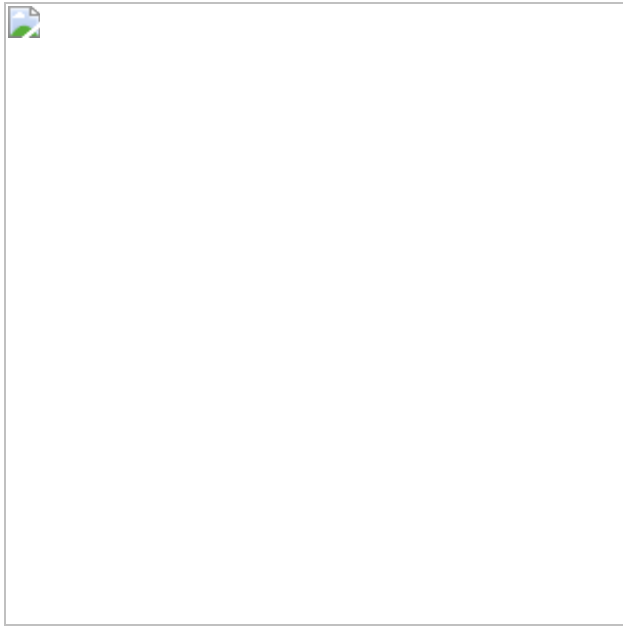


Fig. 4: Inhibition of dopamine inputs impairs the cue–reward encoding of LEC fan cells.



Data availability

Neurophysiological data generated in this study are available upon request, and will be deposited with a subsequent protocol paper.

References

1. 1.

Schultz, W., Dayan, P. & Montague, P. R. A neural substrate of prediction and reward. *Science* **275**, 1593–1599 (1997).

2. 2.

Watabe-Uchida, M., Eshel, N. & Uchida, N. Neural circuitry of reward prediction error. *Annu. Rev. Neurosci.* **40**, 373–394 (2017).

3. 3.

Scoville, W. B. & Milner, B. Loss of recent memory after bilateral hippocampal lesions. *J. Neurol. Neurosurg. Psychiatry* **20**, 11–21 (1957).

4. 4.

Squire, L. R. Memory and the hippocampus: a synthesis from findings with rats, monkeys, and humans. *Psychol. Rev.* **99**, 195–231 (1992).

5. 5.

Buzsaki, G. & Moser, E. I. Memory, navigation and theta rhythm in the hippocampal-entorhinal system. *Nat. Neurosci.* **16**, 130–138 (2013).

6. 6.

Cohen, J. Y., Haesler, S., Vong, L., Lowell, B. B. & Uchida, N. Neuron-type-specific signals for reward and punishment in the ventral tegmental area. *Nature* **482**, 85–88 (2012).

7. 7.

Witter, M. P. & Amaral, D. G. in *The Rat Nervous System* 3rd edn (ed. Paxinos, G.) Ch. 21 (Elsevier, 2004).

8. 8.

Moser, E. I. et al. Grid cells and cortical representation. *Nat. Rev. Neurosci.* **15**, 466–481 (2014).

9. 9.

Igarashi, K. M., Lu, L., Colgin, L. L., Moser, M. B. & Moser, E. I. Coordination of entorhinal–hippocampal ensemble activity during associative learning. *Nature* **510**, 143–147 (2014).

10. 10.

Kitamura, T. et al. Island cells control temporal association memory. *Science* **343**, 896–901 (2014).

11. 11.

Surmeli, G. et al. Molecularly defined circuitry reveals input–output segregation in deep layers of the medial entorhinal cortex. *Neuron* **88**, 1040–1053 (2015).

12. 12.

Vandrey, B. et al. Fan cells in layer 2 of the lateral entorhinal cortex are critical for episodic-like memory. *Curr. Biol.* **30**, 169–175 (2020).

13. 13.

Leitner, F. C. et al. Spatially segregated feedforward and feedback neurons support differential odor processing in the lateral entorhinal cortex. *Nat. Neurosci.* **19**, 935–944 (2016).

14. 14.

Ohara, S. et al. Entorhinal layer II calbindin-expressing neurons originate widespread telencephalic and intrinsic projections. *Front. Syst. Neurosci.* **13**, 54 (2019).

15. 15.

Chuong, A. S. et al. Noninvasive optical inhibition with a red-shifted microbial rhodopsin. *Nat. Neurosci.* **17**, 1123–1129 (2014).

16. 16.

Hokfelt, T., Ljungdahl, A., Fuxe, K. & Johansson, O. Dopamine nerve terminals in the rat limbic cortex: aspects of the dopamine hypothesis of schizophrenia. *Science* **184**, 177–179 (1974).

17. 17.

Fallon, J. H., Koziell, D. A. & Moore, R. Y. Catecholamine innervation of the basal forebrain. II. Amygdala, suprarhinal cortex and entorhinal cortex. *J. Comp. Neurol.* **180**, 509–532 (1978).

18. 18.

Swanson, L. W., Köhler, C. & Björklund, A. in *Handbook of Chemical Neuroanatomy* Vol. 5, Part I (eds Björklund, A., Hökfelt, T. & Swanson, L. W.) 125–227 (Elsevier, 1987).

19. 19.

Kudo, Y. et al. A single optical fiber fluorometric device for measurement of intracellular Ca^{2+} concentration: its application to hippocampal neurons in vitro and in vivo. *Neuroscience* **50**, 619–625 (1992).

20. 20.

Menegas, W., Babayan, B. M., Uchida, N. & Watabe-Uchida, M. Opposite initialization to novel cues in dopamine signaling in ventral and posterior striatum in mice. *Elife* **6**, e21886 (2017).

21. 21.

Igarashi, K. M. et al. Parallel mitral and tufted cell pathways route distinct odor information to different targets in the olfactory cortex. *J. Neurosci.* **32**, 7970–7985 (2012).

22. 22.

Nilssen, E. S. et al. Inhibitory connectivity dominates the fan cell network in layer II of lateral entorhinal cortex. *J. Neurosci.* **38**, 9712–9727 (2018).

23. 23.

Yagishita, S. et al. A critical time window for dopamine actions on the structural plasticity of dendritic spines. *Science* **345**, 1616–1620 (2014).

24. 24.

Tse, D. et al. Schemas and memory consolidation. *Science* **316**, 76–82 (2007).

25. 25.

Tolman, E. C. Cognitive maps in rats and men. *Psychol. Rev.* **55**, 189–208 (1948).

26. 26.

Behrens, T. E. J. et al. What is a cognitive map? organizing knowledge for flexible behavior. *Neuron* **100**, 490–509 (2018).

27. 27.

McNaughton, B. L., Battaglia, F. P., Jensen, O., Moser, E. I. & Moser, M. B. Path integration and the neural basis of the ‘cognitive map’. *Nat. Rev. Neurosci.* **7**, 663–678 (2006).

28. 28.

Kakade, S. & Dayan, P. Dopamine: generalization and bonuses. *Neural Netw.* **15**, 549–559 (2002).

29. 29.

Lisman, J. E. & Grace, A. A. The hippocampal–VTA loop: controlling the entry of information into long-term memory. *Neuron* **46**, 703–713 (2005).

30. 30.

Takeuchi, T. et al. Locus coeruleus and dopaminergic consolidation of everyday memory. *Nature* **537**, 357–362 (2016).

31. 31.

Mori, K., Takahashi, Y. K., Igarashi, K. M. & Yamaguchi, M. Maps of odorant molecular features in the mammalian olfactory bulb. *Physiol. Rev.* **86**, 409–433 (2006).

32. 32.

Uchida, N. & Mainen, Z. F. Speed and accuracy of olfactory discrimination in the rat. *Nat. Neurosci.* **6**, 1224–1229 (2003).

33. 33.

Li, Y. et al. (2017). A distinct entorhinal cortex to hippocampal CA1 direct circuit for olfactory associative learning. *Nat. Neurosci.* **20**, 559–570.

34. 34.

Kvitsiani, D. et al. Distinct behavioural and network correlates of two interneuron types in prefrontal cortex. *Nature* **20**, 363–366 (2013).

35. 35.

Cunningham, J. P. & Byron, M. Y. Dimensionality reduction for large-scale neural recordings. *Nat. Neurosci.* **17**, 1500–1509 (2014).

36. 36.

Russo, A. A. et al. Neural trajectories in the supplementary motor area and motor cortex exhibit distinct geometries, compatible with different classes of computation. *Neuron* **107**, 745–758 (2020).

37. 37.

Sano, H. et al. (2003). Conditional ablation of striatal neuronal types containing dopamine D2 receptor disturbs coordination of basal ganglia function. *J. Neurosci.* **23**, 9078–9088.

Acknowledgements

We thank N. Uchida and M. Watabe-Uchida for their mentorship, including support in setting up optogenetic recording and photometry experiments and providing discussions throughout the course of this project; R. Amo and H. Matsumoto in the Uchida laboratory for their help with setting up the behaviour and photometry experiments; T. Viaclovsky, A. Bramian and

M. Savadkohighodjanaki in the Igarashi laboratory for technical assistance; and M. P. Witter, A. Treves, H. T. Ito, B. McNaughton, C. Gall and G. Lynch for providing comments on the work. The work was supported by NIH R01 grants (R01MH121736, R01AG063864, R01AG066806), a PRESTO grant from Japan Science and Technology Agency (JPMJPR1681), a Brain Research Foundation Fay-Frank Seed Grant (BRFSG-2017-04), a Whitehall Foundation Research Grant (2017-08-01), a BrightFocus Foundation Research grant (A2019380S), an Alzheimer's Association Research Grant (AARG-17-532932) and a New Vision Research Investigator Award (CCAD201902) to K.M.I. H.J. was supported by the University of California, Irvine Medical Scientist Training Program (MSTP) (T32GM008620) and an NIH F31 grant (1F31AG069500).

Author information

Author notes

1. Shogo Soma

Present address: Department of Molecular Cell Physiology, Kyoto Prefectural University of Medicine, Kyoto, Japan

2. Tomoaki Nakazono

Present address: Department of Systems Neuroscience, Fukushima Medical University, Fukushima, Japan

3. These authors contributed equally: Jason Y. Lee, Heechul Jun, Shogo Soma, Tomoaki Nakazono

Affiliations

1. Department of Anatomy and Neurobiology, School of Medicine, University of California, Irvine, Irvine, USA

Jason Y. Lee, Heechul Jun, Shogo Soma, Tomoaki Nakazono, Kaori Shiraiwa, Ananya Dasgupta, Tatsuki Nakagawa, Jiayun L.

Xie, Jasmine Chavez, Rodrigo Romo, Sandra Yungblut & Kei M. Igarashi

2. Division of Brain Structure and Function, Faculty of Medical Sciences, University of Fukui, Fukui, Japan

Meiko Hagihara & Koshi Murata

Contributions

K.M.I. conceived the project and designed the experiments. J.Y.L., H.J., S.S., K.M.I., T. Nakazono, K.S., T. Nakagawa, J.L.X., J.C., R.R. and S.Y. performed the behaviour experiments. J.Y.L., H.J., S.S., K.M.I. and T. Nakazono performed the electrophysiology experiments. K.M.I. performed the pharmacology experiment. K.M.I. and A.D. performed the photometry experiment. J.Y.L., H.J. and S.S. performed the histology experiments. M.H. and K.M. performed *in situ* hybridization experiments. K.M.I., S.S., J.Y.L. and H.J. performed the analyses. K.M.I wrote the paper with input from all authors.

Corresponding author

Correspondence to Kei M. Igarashi.

Ethics declarations

Competing interests

The authors declare no competing interests.

Additional information

Peer review information *Nature* thanks the anonymous reviewers for their contribution to the peer review of this work.

Publisher's note Springer Nature remains neutral with regard to jurisdictional claims in published maps and institutional affiliations.

Extended data figures and tables

Extended Data Fig. 1 Histological validation of implanted sites.

(a). Optic fibre positions in the LEC of Sim1-Cre mice injected with AAV-flex-Jaws-GFP for inhibition experiments. Arrowhead, the tip of optic fibres. D, dorsal, V, ventral, M, medial, L, lateral. (b). Optic fibre positions in the LEC of Wfs1-Cre mice for inhibition experiment of Wfs1-expressing pyramidal cells. (c). Recording position in the superficial layer of LEC from Sim1-Cre mice for opt-tagging experiment. Note large lesions because of the electrical lesioning. (d). Optic fibre positions in the LEC of DAT-Cre mice injected with AAV-flex-Jaws-GFP in the VTA/SNc for inhibition experiment. (e). Optic fibre positions in the LEC of DAT-Cre x Ai14 mice for photometry experiment. Two mice received unilateral implantations and four mice received bilateral implantations. (f). Recording position in the superficial layer of LEC from Sim1-Cre x DAT-Cre mice for opt-tagging + inhibition experiment. (g). Optic fibre positions in the LEC of Sim1-Cre mice injected with AAV-flex-GFP for control inhibition experiment. (h). Optic fibre positions in the LEC of Wfs1-Cre mice injected with AAV-flex-GFP for control inhibition experiment. (i). Optic fibre positions in the LEC of DAT-Cre mice injected with AAV-flex-GFP at VTA and SNc for control inhibition experiment. (j). Recording position in the superficial layer of LEC from Sim1-Cre x DAT-Cre mice for opt-tagging (ChR2-mCherry) + control inhibition (GFP) experiment.

Extended Data Fig. 2 Performance of mice during associative learning.

(a). A model for LEC dopamine and fan cells in associative learning. When novel cues are presented, LEC dopamine functions as a “detonator” of fan cell activity. Dopamine gradually supplies reward expectation signals only during rewarded Odour A and Odour 1 trials, serving as a supervising signal so that Odour A and Odour 1 are represented in the same fan cell

population. Odour B is represented by a fan cell population distinct from Odours-A/1, resulting in A-B separation. Novel unrewarded Odour 2 was not clearly represented in our recorded population. Two types of errors were observed in our study: The spontaneous error where A-B separation and A-1 overlap were both abolished (Fig. 2g), and the error observed in the unilateral dopamine inhibition sessions where A-B separation was spared but A-1 overlap was abolished (Fig. 4c). (b). SIM1 and WFS1 population counts in the LEC. (Top) Reelin immunohistochemistry in Sim1-Cre mice injected with AAV-DIO-mCherry. D, dorsal, V, ventral, M, medial, L, lateral. (Middle) Calbindin immunohistochemistry in Wfs1-Cre mice injected with AAV-DIO-mCherry. (Bottom) From left, density of mCherry-positive neurons in Sim1-Cre and Wfs1-Cre mice, Reelin and Calbindin positive cells, and percentage of mCherry-labelled neurons. ($p > 0.05$, Wilcoxon rank sum test; $n = 16$ sections obtained from $n = 2$ mice for each group). (c). We performed an additional experiment to inhibit fan cells during the whole period of pre-learning with Odour A and Odour B (these mice are not included in the data in the main figures). After injecting Jaws in Sim1-Cre mice, A/B training was repeated ($n = 6$ GFP control mice and $n = 6$ Jaws inhibition mice). Days until mice reached criterion (three consecutive days of reaching 80%) were compared ($p = 0.012$, Wilcoxon rank sum test). (d). Detailed performance of mice during fan cell inhibition. (d1) Learning curves during control (left) and fan cell inhibition (middle) sessions. In these plots, the data shown in Fig. 1d were plotted for percent correct trials in each odour trial type as a function of trial number for each odour type. (Right) Performance of mice in the last 10 trials ($p = 6.1e-19$, ANOVA; $p = 6.0e-8$, post-hoc Tukey test; $n = 10$ mice). (d2) Performance of mice in trials 121-160 as in Fig. 1d, but assessed with discriminability index (D-prime) ($p=3.1e-3$, ANOVA; $p = 1.2e-5$ or better, post-hoc Tukey test; $n = 10$ mice). (d3) We performed control experiment using Sim1-Cre mice injected with AAV-flex-GFP with laser ($n = 5$ mice). The GFP control experiment showed same result as no-laser control in Fig. 1d ($p = 0.0028$, ANOVA; $p = 3.1e-5$ or better, post-hoc Tukey test; $n = 5$ GFP control mice; $n = 10$ Jaws inhibition mice). (e). Same as (d), but for pyramidal cell inhibition in Wfs1-Cre mice in Fig. 2e ($p > 0.05$, ANOVA; $n = 5$ GFP control mice; $n = 9$ Jaws inhibition mice). (g). Same as (d), but for bilateral dopamine inhibition in DAT-Cre mice in Fig. 3e ($p=0.0017$, ANOVA; $p = 2.0e-5$ or better, post-hoc Tukey test; $n = 4$ GFP control mice; $n = 9$ Jaws

inhibition mice). **(f)**. Difference of percent correct sessions between control and inhibition as in Fig. [1f](#), but plotted for discriminability index (D-prime) ($p = 0.019$, ANOVA; $p = 0.0021$ or better, post-hoc Tukey test).

Extended Data Fig. 3 Performance and spikes in Sim1-Cre mice.

a, Behavioural performance of mice used for fan cell opt-tag recording (Fig. [2](#)). **(a1)** Learning curves for Odour A/Odour B (blue) and Odour 1/Odour 2 (red) during correct sessions where mice acquired the association of Odours1/2 (Correct sessions, top left), and during error sessions where mice did not acquire the new association (Error sessions, top right). (Bottom left) Percent correct trials averaged for trials 121-160 for Odour A/B trials and Odour 1/2 trials during correct and error sessions ($p=6.5e-5$, ANOVA; $p = 1.7e-6$ or better, post-hoc Tukey test; $n = 10$ mice). (Bottom right) Percent of correct and error sessions. **(a2)**. Learning curves during correct (left) and error (middle) sessions. In these plots, the data shown in **(a1)** were plotted for percent correct trials in each odour trial type as a function of trial number for each odour type. (Right) Performance of mice in the last 10 trials ($p=3.3e-8$, ANOVA; $p = 0.001$ or better, post-hoc Tukey test; $n = 10$ mice). **(a3)**. Performance of mice in trials 121-160 as in **(a1)**, but assessed with discriminability index (D-prime) ($p=1.5e-4$, ANOVA; $p = 6.4e-6$ or better, post-hoc Tukey test; $n = 10$ mice). **b**, A representative fan cell shown in Fig. [2b](#). (Right) Firing frequency in Trials 1 – 10 was plotted. Mean firing frequencies during 0.5 – 1.5 s after cue onset in each trial are shown in the bar graph. **c-e**, Three additional example fan cells that fired to Odour 1. These cells showed high firing frequency to Odour 1 within 10 trials. **f**, Mean firing frequency to each odour in trials 1 – 10 in T1. Fan cells showed larger firing frequency to Odour 1 than to other odours starting from trial 2 ($n = 213$ cells, $p = 4.1e-30$, ANOVA; $p < 0.05$ or better, post-hoc Tukey test).

Extended Data Fig. 4 Spike properties of fan cells in Sim1-Cre mice.

(a)-(c), spike properties of fan cells. Fan cells were recorded in a session with Odour A and Odour B (AB session). After ~20 trials in AB session,

associative learning (AB12) session was tested (T1-T5). T5 in error sessions is also shown. **(a)** Spike firing of 213 fan cells. Mean spike activity was averaged in 50 ms bins and shown in z-score compared with $-1 - 0$ s before odour onset. In this panel, cells were sorted using a cluster analysis of firing property in T5. **(b)**. Mean firing rate of 213 fan cells shown in z-score. **(c)** Percent responsive cells in periods of 0.5-1.5 s (odour), 2-3 s (delay) and 3-4 s (choice) after odour onset. Neurons with significant firing during each period were counted (Wilcoxon signed-rank test, $p < 0.05$). **(d)** Percent responsive cells in correct T5 (top) and error T5 (bottom). Neurons with significant firing during 0.5-1.5 s after odour onset were counted (Wilcoxon signed-rank test, $p < 0.05$). Asterisk denotes lower percentage of A-1 responsive cells in error T5 than that in correct T5 ($p < 0.05$, chi-square test; $p < 0.05$ for A-1 cells, post-hoc residual test with false discovery rate correction for multiple comparisons). **(e)** Trajectories of neural firing of fan cell population (top), Euclidian distance between odour trial types (middle) and mean Euclidian distance and similarity index during 0.5-1.5 s after odour onset (cue period) for timepoints T1 – T5 of correct sessions (bottom). Ninety-fifth percentile distance obtained from shuffled data denotes significant distance (red line). Data during 2-3 s (delay) and 3-4 s (choice) after odour onset were also plotted. **(f)**. Same as **(e)**, but for error sessions where mice did not learn new associations. **(g)**. Example trajectories obtained from shuffling analysis. Trajectories of neuronal data obtained from three shuffled data in correct T5 sessions are shown. **(h)**. Distribution of mean Euclidian distance obtained from shuffle data in correct T5. Distance obtained from six possible odour pairs were averaged and plotted. A 95th percentile of the distribution (red) was used for the cut-off indicating significant distance.

Extended Data Fig. 5 Bootstrapping test for spike similarity index.

The change of similarity index (SI) during associative learning was compared using the bootstrapping method. PCA was performed from a resampled neuronal population, and this procedure was repeated 1,000 times to make 1,000 bootstraps. SI was calculated for each bootstrap, then SIs in T2 – T5 were subtracted by that in T1, to test if there was a significant distribution above or below zero. **(a)**. (Top) In correct sessions in

Fig. 2, SI for Odours A-B showed significant decrease in T5 compared to T1 ($p = 0.039$) whereas SI for Odours A-1 increased ($p = 1.2\text{e-}10$), confirming A-B separation and A-1 overlap. (Middle) In the error sessions, no A-B separation was observed ($p > 0.05$). Although A-1 distance decreased during the session ($p < 0.05$), SIAB stayed in negative values. (Bottom) The subtraction of bootstraps in error session from correct sessions confirms the difference in A-1 overlap ($p < 0.05$ in T3 and T5, right). * $p < 0.05$, ** $p < 0.01$, *** $p < 0.001$; n = 1,000, bootstrapping test.

(b). (Top) In dopamine control sessions, SI for Odours A-B showed significant decrease in T5 compared to T1 ($p = 0.044$) whereas SI for Odours A-1 increased ($p = 0.0082$), confirming A-B separation and A-1 overlap. (Middle) In the unilateral inhibition sessions, although A-B separation was observed ($p < 0.05$), no A-1 overlap was observed ($p > 0.05$). (Bottom) The subtraction of bootstraps in inhibition session from control sessions confirms the effect of inhibition on A-1 overlap ($p < 0.05$ in T3 – T5, right). These data suggest that dopamine plays a critical role in establishing A-1 overlapped representations. * $p < 0.05$, ** $p < 0.01$, *** $p < 0.001$; n = 1,000, bootstrapping test.

Extended Data Fig. 6 Additional principal component analyses.

(a). Trajectories of neural firing of fan cell population using only correct (hit) trials for Odour A and Odour 1 and correct rejection (CR) trials for Odour B and Odour 2. The separation and overlap of fan cells were again observed when the incorrect trials were removed from the PC analysis. **(b).** Trajectories of neural firing of fan cell population using only hit trials for Odour A and Odour 1 and error lick (false alarm, FA) trials for Odour B and Odour 2. Although all of them are trials in which mice made lick responses, similar overlapped representations between Odours-A and 1, and their separation from Odour B were observed, suggesting that fan cells do not simply represent lick-related motor information. **(c).** Principal component analysis (PCA) for 213 fan cells as in Fig. 2d, but using conjunctive PCA with data from all timepoints (AB-only, T1 – T5). The results show similar A-1 overlap and A-B separation as in Fig. 2d.

Extended Data Fig. 7 Repeated associative learning using the same odour cues.

(a). To test the effect of repeated exposure to the same odour pair during associative learning, sessions with Odour A, -B, -C and -D were repeated for 10 days in Sim1xDAT mice injected with AAV-flex-GFP ($n = 4$ mice, without laser). **(b)**. Learning curves between Day 1 – Day 4 and Day 5 – Day 10. In Day 1 – Day 4, mice gradually learned Odour C and Odour D as in the regular new association experiment with novel odour pairs. However, after Day 5, mice showed better performance for Odour C and Odour D from the initial trials. This was confirmed with increased correct rate for Odour C/D on trials 1 – 20 in Day 5 – 10 compared to that in Day 1 – 4 (bottom left, $p = 3.5e-4$, ANOVA with post-hoc Tukey test, $p = 0.0025$). **(c)**. Fan cell trajectories for Odour A, -B, -C and -D in T5 during Day 1 – Day 4 (left, $n = 101$ cells) and during Day 5 – 10 (right, $n = 93$ cells). **(d)**. Fan cells showed A-B separation and A-1 overlap in Day 1-4, but this representation disappeared after mice were overtrained. These results further support the idea that fan cells were needed only when new associative memory is formed.

Extended Data Fig. 8 Properties of LEC dopamine inputs.

a-d, Pharmacological blockade experiments during associative learning. We performed a supplementary pharmacological experiment to validate the optogenetic inhibition experiments using dopamine D1 receptor antagonist SCH23390, or GABA_A receptor agonist muscimol. SCH23390 bilateral injection abolished new learning of Odour 1 and Odour 2, while sparing the pre-learned association, replicating the result obtained from the optogenetic inhibition of dopamine fibres (Fig. 3e). Injection of muscimol impaired both the pre-learned association and acquisition of new association, implying an involvement of LEC neurons other than fan cells in the retrieval of pre-learned association. **(a)**. Learning curves during saline, SCH23390 and muscimol infusions. **(b)**. Percent correct sessions during trials 121 – 160 where mice correctly learned new association ($p=6.1e-4$, ANOVA; 0.0032 or better, post-hoc Tukey test; $n = 5$ mice). **(c)**. Example histology from cannula implantations. **(d)**. Learning curves during saline (left), SCH23390 (middle) and muscimol (right) sessions. In these plots, the data shown in (a) were plotted for percent correct trials in each odour trial type as a function of trial number for each odour type. (Right) Performance of mice in the last 10 trials ($p=1.3e-15$, ANOVA; $p = 2.2e-7$, post-hoc

Tukey test; $n = 5$ mice). **e-h**, Retrograde tracing of LEC dopaminergic fibres from VTA and SNc. **(e)**. Coronal section of the right hemisphere including LEC, where the retrograde tracer cholera toxin B (CTB, red) was injected. **(f)**. Coronal section of the right hemisphere midbrain including VTA and SNc. Anti-tyrosine hydroxylase (TH, green) immunostaining reveals dopaminergic cells. **(g)**. Magnified windows from **(f)**. Yellow arrows point to example cells expressing both TH and CTB, which are further magnified in the rightmost panels. **(h)**. From left, density of TH-expressing neurons in VTA and SNc, TH⁺CTB⁺ population between VTA and SNc, percentage of double-positive neurons among TH+ neurons. Although VTA has more cells for both TH+ and TH+CTB+ neurons ($p < 0.001$, Wilcoxon rank sum test), the percentage of CTB+ neurons did not differ between VTA and SNc ($p=0.50$, Wilcoxon rank sum test; $n = 22$ sections obtained from $n = 3$ mice). **i-k**, Calcium imaging of dopamine inputs. **(i)**. Calcium signals from individual hemisphere ($n = 10$) during first 10 trials (T1, top) and last 10 trials (middle, T5) in correct sessions. Mean traces are shown at the bottom for T1 (black) and T5 (red). * $p < 0.05$ and ** $p < 0.01$, Wilcoxon signed-rank test during 0.5 – 3 s after cue onset compared with 1-s pre-cue period. **(j)**. Same as **(b)**, but for error sessions. **(k)**. Plot of GCaMP calcium signal as a function of trial number after starting AB12 session ($n = 10$ hemispheres).

Extended Data Fig. 9 Dopamine unilateral inhibition during fan cell recording.

(a) Performance of mice during unilateral dopamine inhibition. (Left) Performance of mice in trials 121-160 as in Fig. [4a](#), but assessed with discriminability index (D-prime) ($p=5.1\text{e-}4$, ANOVA; $p = 9.6\text{e-}3$ or better, post-hoc Tukey test; $n = 8$ mice). (Middle) Learning curves during control (left) and unilateral dopamine inhibition (right) sessions. In these plots, the data shown in Fig. [4a](#) were plotted for percent correct trials in each odour trial type as a function of trial number for each odour type. Plot using 2-trial moving window is also shown for control sessions. (Right) Performance of mice in the last 10 trials ($p=6.5\text{e-}6$, ANOVA; $p = 0.046$ or better, post-hoc Tukey test; $n = 10$ mice). In the unilateral dopamine inhibition experiments, each mouse ($n = 8$) had 10 – 16 inhibition sessions. Of them, percentage of correct sessions (i.e. #correct sessions/(#correct sessions + #error sessions))

were 46.6%, 55.6%, 43.3%, 50.0%, 54.7%, 53.6%, 53.6%, and 42.8%. (b). We performed control experiments using DAT-Cre mice injected with AAV-DIO-ChR2 and AAV-flex-GFP for unilateral opt-tagging and laser control ($n = 4$ mice). The GFP control experiment showed same result as no-laser control in Fig. 4a ($p=0.035$, ANOVA; $p = 0.044$ or better, post-hoc Tukey test; $n = 4$ GFP control mice; $n = 8$ Jaws inhibition mice).

Extended Data Fig. 10 Firing property of fan cells during dopamine unilateral inhibition.

(a). Firing property of fan cells in the no-laser control sessions obtained from Sim1xDAT mice ($n = 148$ cells). (Top to bottom) Z-scored firing rates, mean firing rate, percent cells for each response type, PCA trajectories, Euclidian distance and mean Euclidian distance are shown as in Fig. 2d. (b). Same as (a), but for fan cells during unilateral dopamine inhibition ($n = 134$ cells). Mean firing rates for Odour A and Odour 1 were lower than control in T1 ($p < 0.05$, Wilcoxon rank sum test). No difference was observed for the distribution of responsive type in T5 between control and inhibition ($p=0.24$, chi-square test). (c). Trajectories, mean Euclidian distance and similarity index of fan cells as in Fig. 4b, but from GFP control mice ($n = 130$ cells).

Supplementary information

Supplementary Information

This file contains Supplementary Tables 1–4.

Reporting Summary

Rights and permissions

Reprints and Permissions

About this article

Cite this article

Lee, J.Y., Jun, H., Soma, S. *et al.* Dopamine facilitates associative memory encoding in the entorhinal cortex. *Nature* **598**, 321–326 (2021).
<https://doi.org/10.1038/s41586-021-03948-8>

- Received: 13 November 2020
- Accepted: 23 August 2021
- Published: 22 September 2021
- Issue Date: 14 October 2021
- DOI: <https://doi.org/10.1038/s41586-021-03948-8>

Share this article

Anyone you share the following link with will be able to read this content:

[Get shareable link](#)

Sorry, a shareable link is not currently available for this article.

[Copy to clipboard](#)

Provided by the Springer Nature SharedIt content-sharing initiative

This article was downloaded by **calibre** from <https://www.nature.com/articles/s41586-021-03948-8>

- Article
- [Published: 29 September 2021](#)

Blood and immune development in human fetal bone marrow and Down syndrome

- [Laura Jardine^{1,2}](#) na1,
- [Simone Webb](#) [ORCID: orcid.org/0000-0003-3058-8952](#)¹ na1,
- [Issac Goh](#) [ORCID: orcid.org/0000-0002-6397-3518](#)¹,
- [Mariana Quiroga Londoño](#) [ORCID: orcid.org/0000-0003-2352-0773](#)³,
- [Gary Reynolds](#)¹,
- [Michael Mather](#) [ORCID: orcid.org/0000-0001-7972-7111](#)¹,
- [Bayanne Olabi](#)¹,
- [Emily Stephenson](#)¹,
- [Rachel A. Botting](#) [ORCID: orcid.org/0000-0001-9595-4605](#)¹,
- [Dave Horsfall](#) [ORCID: orcid.org/0000-0002-8086-812X](#)¹,
- [Justin Engelbert](#)¹,
- [Daniel Maunder](#)¹,
- [Nicole Mende](#) [ORCID: orcid.org/0000-0002-5078-2333](#)³,
- [Caitlin Murnane](#)⁴,
- [Emma Dann](#) [ORCID: orcid.org/0000-0002-7400-7438](#)⁵,
- [Jim McGrath](#)¹,
- [Hamish King](#) [ORCID: orcid.org/0000-0001-5972-8926](#)⁶,
- [Iwo Kucinski](#) [ORCID: orcid.org/0000-0002-9385-0359](#)³,
- [Rachel Queen](#)¹,
- [Christopher D. Carey](#)⁷,
- [Caroline Shrubsole](#)²,
- [Elizabeth Poyner](#)¹,
- [Meghan Acres](#)¹,

- [Claire Jones⁸](#),
- [Thomas Ness⁸](#),
- [Rowen Coulthard⁸](#),
- [Natalina Elliott⁴](#),
- [Sorcha O'Byrne⁴](#),
- [Myriam L. R. Haltalli](#) ORCID: [orcid.org/0000-0002-0886-4466³](http://orcid.org/0000-0002-0886-4466),
- [John E. Lawrence⁵](#),
- [Steven Lisgo¹](#),
- [Petra Balogh⁵](#),
- [Kerstin B. Meyer](#) ORCID: [orcid.org/0000-0001-5906-1498⁵](http://orcid.org/0000-0001-5906-1498),
- [Elena Prigmore⁵](#),
- [Kirsty Ambridge⁵](#),
- [Mika Sarkin Jain⁵](#),
- [Mirjana Efremova](#) ORCID: [orcid.org/0000-0002-8107-9974⁹](http://orcid.org/0000-0002-8107-9974),
- [Keir Pickard²](#),
- [Thomas Creasey](#) ORCID: [orcid.org/0000-0001-8536-5428^{2,10}](http://orcid.org/0000-0001-8536-5428),
- [Jaume Bacardit](#) ORCID: [orcid.org/0000-0002-2692-7205¹¹](http://orcid.org/0000-0002-2692-7205),
- [Deborah Henderson¹](#),
- [Jonathan Coxhead](#) ORCID: [orcid.org/0000-0002-6128-9560¹](http://orcid.org/0000-0002-6128-9560),
- [Andrew Filby¹](#),
- [Rafiqul Hussain¹](#),
- [David Dixon¹](#),
- [David McDonald¹](#),
- [Dorin-Mirel Popescu¹](#),
- [Monika S. Kowalczyk¹²](#),
- [Bo Li¹²](#),
- [Orr Ashenberg^{12,13}](#),
- [Marcin Tabaka¹²](#),
- [Danielle Dionne¹²](#),
- [Timothy L. Tickle](#) ORCID: [orcid.org/0000-0002-6592-6272^{12,14}](http://orcid.org/0000-0002-6592-6272),
- [Michal Slyper¹²](#),
- [Orit Rozenblatt-Rosen](#) ORCID: [orcid.org/0000-0001-6313-3570¹²](http://orcid.org/0000-0001-6313-3570),
- [Aviv Regev](#) ORCID: [orcid.org/0000-0003-3293-3158¹²](http://orcid.org/0000-0003-3293-3158),
- [Sam Behjati](#) ORCID: [orcid.org/0000-0002-6600-7665^{5,15}](http://orcid.org/0000-0002-6600-7665),

- [Elisa Laurenti](#) [ORCID: orcid.org/0000-0002-9917-9092³](#),
- [Nicola K. Wilson](#) [ORCID: orcid.org/0000-0003-0865-7333^{3 na2}](#),
- [Anindita Roy](#) [ORCID: orcid.org/0000-0001-8607-5748^{4,16,17,18 na2}](#),
- [Berthold Göttgens](#) [ORCID: orcid.org/0000-0001-6302-5705^{3 na2}](#),
- [Irene Roberts^{4,16,17,18 na2}](#),
- [Sarah A. Teichmann](#) [ORCID: orcid.org/0000-0002-6294-6366^{5,19 na2}](#)
&
- [Muzlifah Haniffa](#) [ORCID: orcid.org/0000-0002-3927-2084^{1,5,20 na2}](#)

Nature volume **598**, pages 327–331 (2021)

- 5674 Accesses
- 102 Altmetric
- [Metrics details](#)

Subjects

- [Haematological diseases](#)
- [Haematopoiesis](#)

Abstract

Haematopoiesis in the bone marrow (BM) maintains blood and immune cell production throughout postnatal life. Haematopoiesis first emerges in human BM at 11–12 weeks after conception^{1,2}, yet almost nothing is known about how fetal BM (FBM) evolves to meet the highly specialized needs of the fetus and newborn. Here we detail the development of FBM, including stroma, using multi-omic assessment of mRNA and multiplexed protein epitope expression. We find that the full blood and immune cell repertoire is established in FBM in a short time window of 6–7 weeks early in the second trimester. FBM promotes rapid and extensive diversification of myeloid cells, with granulocytes, eosinophils and dendritic cell subsets emerging for the first time. The substantial expansion of B lymphocytes in FBM contrasts with fetal liver at the same gestational age. Haematopoietic

progenitors from fetal liver, FBM and cord blood exhibit transcriptional and functional differences that contribute to tissue-specific identity and cellular diversification. Endothelial cell types form distinct vascular structures that we show are regionally compartmentalized within FBM. Finally, we reveal selective disruption of B lymphocyte, erythroid and myeloid development owing to a cell-intrinsic differentiation bias as well as extrinsic regulation through an altered microenvironment in Down syndrome (trisomy 21).

Access options

Subscribe to Journal

Get full journal access for 1 year

\$199.00

only \$3.90 per issue

[Subscribe](#)

All prices are NET prices.

VAT will be added later in the checkout.

Tax calculation will be finalised during checkout.

Rent or Buy article

Get time limited or full article access on ReadCube.

from \$8.99

[Rent or Buy](#)

All prices are NET prices.

Additional access options:

- [Log in](#)
- [Access through your institution](#)

- [Learn about institutional subscriptions](#)

Fig. 1: A single-cell atlas of human FBM.

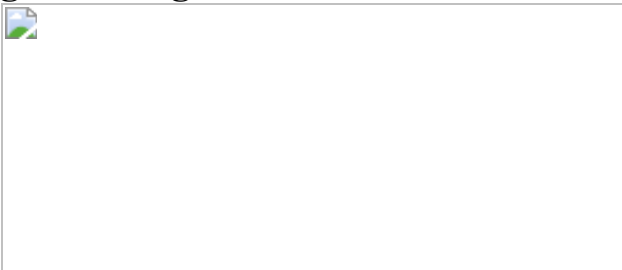


Fig. 2: Myeloid diversification, B-lineage expansion and tissue-specific properties of HSC/MPPs.

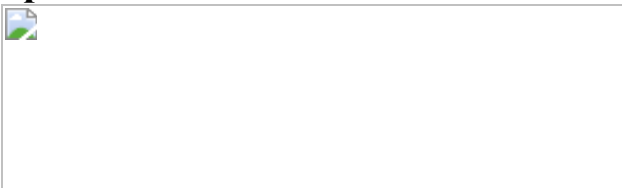
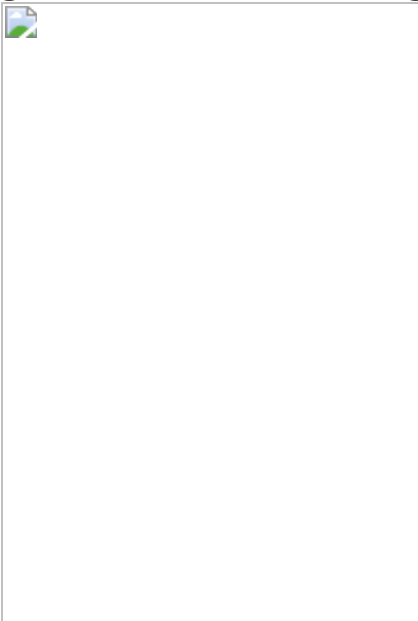


Fig. 3: Stromal cell heterogeneity in FBM.



Data availability

There are no restrictions on data availability for new data presented in this study. FASTQ and raw count matrices for droplet-based scRNA-seq data for FBM from fetuses with Down syndrome and fetuses without Down syndrome have been deposited at EMBL-EBI ArrayExpress and at the

European Nucleotide Archive (ENA), with accession codes as follows: [E-MTAB-9389](#) (FBM from fetuses with Down syndrome and FBM from fetuses without Down syndrome), [E-MTAB-10042](#) (FBM from fetuses with Down syndrome) and [ERP125305](#) (FBM from fetuses without Down syndrome). FASTQ and raw count matrices for all other new data in this study have been deposited at EMBL-EBI ArrayExpress and at the Gene Expression Omnibus (GEO) with accession codes [E-MTAB-9801](#) (FBM Smart-seq2 scRNA-seq); [E-MTAB-9389](#) (BCR- or TCR-enriched VDJ FBM scRNA-seq; FASTQs only); [GSE166895](#) (CD34⁺ FBM, fetal liver and cord blood CITE-seq) and [GSE166895](#) (FBM total CITE-seq). The following data are also available to download as Scanpy h5ad objects with transformed counts through our interactive webportal:

<https://fbm.cellatlas.io/>: (i) FBM scRNA-seq (fetuses with Down syndrome); (ii) FBM scRNA-seq (fetuses without Down syndrome); (iii) CD34⁺ FBM, fetal liver and cord blood CITE-seq; and (iv) FBM total CITE-seq. All source data are available in the accompanying source data file, unless manuscript or figure legend refers to a Supplementary Table. External datasets incorporated into this study include: (i) human fetal liver and yolk sac scRNA-seq data⁴ ([E-MTAB-7407](#)); (ii) human blood monocyte–DC scRNA-seq data¹⁰ ([GSE94820](#)); (iii) mouse BM scRNA-seq data¹⁹ ([GSE122467](#)); (iv) fetal and paediatric thymus scRNA-seq data³ ([E-MTAB-8581](#)); and (v) adult BM and cord blood scRNA-seq data from the Human Cell Atlas Data Coordination Portal ‘Census of Immune Cells’ project (<https://data.humancellatlas.org/explore/projects/cc95ff89-2e68-4a08-a234-480eca21ce79>). At the time of submission, there are no known accessibility restrictions on these external datasets. [Source data](#) are provided with this paper.

Code availability

Single-cell sequencing data were processed and analysed using publicly available software packages. Python and R code and notebooks for reproducing single-cell analyses are available at https://github.com/haniffalab/FCA_bone_marrow.

References

1. 1.

O'Byrne, S. et al. Discovery of a CD10-negative B-progenitor in human fetal life identifies unique ontogeny-related developmental programs. *Blood* **134**, 1059–1071 (2019).

2. 2.

Charbord, P., Tavian, M., Humeau, L. & Péault, B. Early ontogeny of the human marrow from long bones: an immunohistochemical study of hematopoiesis and its microenvironment. *Blood* **87**, 4109–4119 (1996).

3. 3.

Park, J.-E. et al. A cell atlas of human thymic development defines T cell repertoire formation. *Science* **367**, eaay3224 (2020).

4. 4.

Popescu, D.-M. et al. Decoding human fetal liver haematopoiesis. *Nature* **574**, 365–371 (2019).

5. 5.

Wiemels, J. L. et al. Prenatal origin of acute lymphoblastic leukaemia in children. *Lancet* **354**, 1499–1503 (1999).

6. 6.

Muntean, A. G., Ge, Y., Taub, J. W. & Crispino, J. D. Transcription factor GATA-1 and Down syndrome leukemogenesis. *Leuk. Lymphoma* **47**, 986–997 (2006).

7. 7.

Roy, A. et al. Perturbation of fetal liver hematopoietic stem and progenitor cell development by trisomy 21. *Proc. Natl Acad. Sci. USA* **109**, 17579–17584 (2012).

8. 8.

Olsson, A. et al. Single-cell analysis of mixed-lineage states leading to a binary cell fate choice. *Exp. Hematol.* **44**, S24 (2016).

9. 9.

Dahl, R. et al. Regulation of macrophage and neutrophil cell fates by the PU.1:C/EBP α ratio and granulocyte colony-stimulating factor. *Nat. Immunol.* **4**, 1029–1036 (2003).

10. 10.

Villani, A.-C. et al. Single-cell RNA-seq reveals new types of human blood dendritic cells, monocytes, and progenitors. *Science* **356**, eaah4573 (2017).

11. 11.

Mullighan, C. G. et al. Genome-wide analysis of genetic alterations in acute lymphoblastic leukaemia. *Nature* **446**, 758–764 (2007).

12. 12.

Summers, Y. J., Heyworth, C. M., de Wynter, E. A., Chang, J. & Testa, N. G. Cord blood G₀ CD34⁺ cells have a thousand-fold higher capacity for generating progenitors in vitro than G₁ CD34⁺ cells. *Stem Cells* **19**, 505–513 (2001).

13. 13.

Pimanda, J. E. et al. Gata2, Fli1, and Scl form a recursively wired gene-regulatory circuit during early hematopoietic development. *Proc. Natl Acad. Sci. USA* **104**, 17692–17697 (2007).

14. 14.

Iwasaki, H. et al. Distinctive and indispensable roles of PU.1 in maintenance of hematopoietic stem cells and their differentiation. *Blood* **106**, 1590–1600 (2005).

15. 15.

Palii, C. G. et al. Single-cell proteomics reveal that quantitative changes in co-expressed lineage-specific transcription factors determine cell fate. *Cell Stem Cell* **24**, 812–820 (2019).

16. 16.

Muskens, I. S. et al. The genome-wide impact of trisomy 21 on DNA methylation and its implications for hematopoiesis. *Nat. Commun.* **12**, 821 (2021).

17. 17.

Yu, S. et al. GABP controls a critical transcription regulatory module that is essential for maintenance and differentiation of hematopoietic stem/progenitor cells. *Blood* **117**, 2166–2178 (2011).

18. 18.

Sullivan, K. D. et al. Trisomy 21 causes changes in the circulating proteome indicative of chronic autoinflammation. *Sci. Rep.* **7**, 14818 (2017).

19. 19.

Baccin, C. et al. Combined single-cell and spatial transcriptomics reveal the molecular, cellular and spatial bone marrow niche organization. *Nat. Cell Biol.* **22**, 38–48 (2020).

20. 20.

Suchting, S. et al. The Notch ligand Delta-like 4 negatively regulates endothelial tip cell formation and vessel branching. *Proc. Natl Acad. Sci. USA* **104**, 3225–3230 (2007).

21. 21.

Kusumbe, A. P., Ramasamy, S. K. & Adams, R. H. Coupling of angiogenesis and osteogenesis by a specific vessel subtype in bone. *Nature* **507**, 323–328 (2014).

22. 22.

Itkin, T. et al. Distinct bone marrow blood vessels differentially regulate haematopoiesis. *Nature* **532**, 323–328 (2016).

23. 23.

Long, M. W., Briddell, R., Walter, A. W., Bruno, E. & Hoffman, R. Human hematopoietic stem cell adherence to cytokines and matrix molecules. *J. Clin. Invest.* **90**, 251–255 (1992).

24. 24.

Lane, W. J. et al. Stromal-derived factor 1-induced megakaryocyte migration and platelet production is dependent on matrix metalloproteinases. *Blood* **96**, 4152–4159 (2000).

25. 25.

Schulz-Knappe, P. et al. HCC-1, a novel chemokine from human plasma. *J. Exp. Med.* **183**, 295–299 (1996).

26. 26.

Butko, E., Pouget, C. & Traver, D. Complex regulation of HSC emergence by the Notch signaling pathway. *Dev. Biol.* **409**, 129–138 (2016).

27. 27.

Mulè, M. P., Martins, A. J. & Tsang, J. S. Normalizing and denoising protein expression data from droplet-based single cell profiling. Preprint at <https://doi.org/10.1101/2020.02.24.96360> (2021).

Acknowledgements

We acknowledge funding from the Wellcome Human Cell Atlas Strategic Science Support (WT211276/Z/18/Z), MRC Human Cell Atlas award and Wellcome Human Developmental Biology Initiative. M.H. is funded by Wellcome (WT107931/Z/15/Z), The Lister Institute for Preventive Medicine and NIHR and Newcastle Biomedical Research Centre; S.A.T. is funded by Wellcome (WT206194), the ERC Consolidator Grant ThDEFINE and EU FET-OPEN MRG-GRAMMAR awards; relevant research in the B.G. group was funded by Wellcome (206328/Z/17/Z) and the MRC (MR/M008975/1 and MR/S036113/1); I.R. is funded by Blood Cancer UK and by the NIHR Oxford Biomedical Centre Research Fund; A.R. is funded by a Wellcome Trust Clinical Research Career Development Fellowship (216632/Z/19/Z) and supported by the NIHR Oxford Biomedical Centre Research Fund; L.J. is funded by an NIHR Academic Clinical Lectureship; S.W. is funded by a Barbour Foundation PhD studentship; M.M. is funded by an Action Medical Research Clinical Fellowship (GN2779); and E.L. is funded by a Sir Henry Dale fellowship from Wellcome and the Royal Society (107630/Z/15/Z), BBSRC (BB/P002293/1) and core support grants to Wellcome and MRC to the Wellcome–MRC Cambridge Stem Cell Institute (203151/Z/16/Z). This research was funded in part by the Wellcome Trust (see above for grant numbers). We thank the Newcastle University Flow Cytometry Core Facility, Bioimaging Core Facility, NovoPath, Genomics Facility and NUIT for technical assistance, the School of Computing for access to the High-Performance Computing Cluster, CellGenIT and A. Farnworth for clinical liaison. We thank the CRUK Cambridge Institute Genomics core for processing all Cambridge libraries and sequencing, and K. Nazor, B. Yeung and T. S. Huang (BioLegend) for discussions to optimize the TotalSeq panel and protocol. The human embryonic and fetal material was provided by the joint MRC–Wellcome (MR/R006237/1) HDBR (<https://www.hdbr.org/>). This publication is part of the Human Cell Atlas (<https://www.humancellatlas.org/publications/>).

Author information

Author notes

1. These authors contributed equally: Laura Jardine, Simone Webb
2. These authors jointly supervised this work: Nicola K. Wilson, Anindita Roy, Berthold Göttgens, Irene Roberts, Sarah A. Teichmann, Muzlifah Haniffa

Affiliations

1. Biosciences Institute, Newcastle University, Newcastle upon Tyne, UK
Laura Jardine, Simone Webb, Issac Goh, Gary Reynolds, Michael Mather, Bayanne Olabi, Emily Stephenson, Rachel A. Botting, Dave Horsfall, Justin Engelbert, Daniel Maunder, Jim McGrath, Rachel Queen, Elizabeth Poyner, Meghan Acres, Steven Lisgo, Deborah Henderson, Jonathan Coxhead, Andrew Filby, Rafiqul Hussain, David Dixon, David McDonald, Dorin-Mirel Popescu & Muzlifah Haniffa
2. Haematology Department, Freeman Hospital, Newcastle-upon-Tyne Hospitals NHS Foundation Trust, Newcastle upon Tyne, UK
Laura Jardine, Caroline Shrubsole, Keir Pickard & Thomas Creasey
3. Department of Haematology, Wellcome–MRC Cambridge Stem Cell Institute, University of Cambridge, Cambridge, UK
Mariana Quiroga Londoño, Nicole Mende, Iwo Kucinski, Myriam L. R. Haltalli, Elisa Laurenti, Nicola K. Wilson & Berthold Göttgens
4. Department of Paediatrics, University of Oxford, Oxford, UK
Caitlin Murnane, Natalina Elliott, Sorcha O’Byrne, Anindita Roy & Irene Roberts
5. Wellcome Sanger Institute, Hinxton, UK

Emma Dann, John E. Lawrence, Petra Balogh, Kerstin B. Meyer, Elena Prigmore, Kirsty Ambridge, Mika Sarkin Jain, Sam Behjati, Sarah A. Teichmann & Muzlifah Haniffa

6. Centre for Immunobiology, Blizard Institute, Queen Mary University of London, London, UK

Hamish King

7. Translational and Clinical Research Institute, Newcastle University, Newcastle upon Tyne, UK

Christopher D. Carey

8. NovoPath, Department of Pathology, Newcastle Hospitals NHS Foundation Trust, Newcastle upon Tyne, UK

Claire Jones, Thomas Ness & Rowen Coulthard

9. Barts Cancer Institute, Queen Mary University of London, London, UK

Mirjana Efremova

10. Wolfson Childhood Cancer Centre, Northern Institute for Cancer Research, Newcastle University, Newcastle upon Tyne, UK

Thomas Creasey

11. School of Computing, Newcastle University, Newcastle upon Tyne, UK

Jaume Bacardit

12. Klarman Cell Observatory, Broad Institute of Harvard and MIT, Cambridge, MA, USA

Monika S. Kowalczyk, Bo Li, Orr Ashenberg, Marcin Tabaka, Danielle Dionne, Timothy L. Tickle, Michal Slyper, Orit

Rozenblatt-Rosen & Aviv Regev

13. Genentech, South San Francisco, CA, USA

Orr Ashenberg

14. Data Sciences Platform, Broad Institute of Harvard and MIT,
Cambridge, MA, USA

Timothy L. Tickle

15. Department of Paediatrics, University of Cambridge, Cambridge, UK

Sam Behjati

16. MRC Molecular Haematology Unit, MRC Weatherall Institute of
Molecular Medicine, University of Oxford, Oxford, UK

Anindita Roy & Irene Roberts

17. Department of Paediatrics, Children's Hospital, John Radcliffe
Hospital, and MRC WIMM, University of Oxford, Oxford, UK

Anindita Roy & Irene Roberts

18. BRC Blood Theme, National Institute for Health Research (NIHR)
Oxford Biomedical Research Centre, Oxford, UK

Anindita Roy & Irene Roberts

19. Theory of Condensed Matter Group, Cavendish Laboratory, University
of Cambridge, Cambridge, UK

Sarah A. Teichmann

20. Department of Dermatology and NIHR Newcastle Biomedical
Research Centre, Newcastle Hospitals NHS Foundation Trust,
Newcastle upon Tyne, UK

Muzlifah Haniffa

Contributions

M.H., S.A.T., I.R. and B.G. conceived and directed the study. M.H., S.A.T., B.G., and N.K.W. designed scRNA-seq and CITEseq experiments and data analysis approaches. L.J. and E.L. designed HSC/MPP culture experiments. I.R. and A. Roy designed experiments on FBM from fetuses with Down syndrome. Samples were isolated by S.L., R.A.B., I.G., J.E., P.B., K.A., S.O. and N.E., libraries were prepared by E.P. and E.S. and sequencing was performed by J.C., R.Q., R.H. and the Wellcome Sanger Institute core facility. Flow cytometry and FACS experiments were performed by R.A.B., L.J. and D. Maunder, supported by D. McDonald and A.F. Cytospins were performed by L.J. and D. Dixon, and in vitro culture differentiation experiments were performed by L.J., C.M. and D. Maunder.

Immunofluorescence microscopy was performed by C.J., T.N., R.C., C.D.C., C.S. and M.A., with analysis performed by M.M., B.O., C.S., E.P. and I.G. M.S.K., B.L., O.A., M.T., D. Dionne, T.L.T., M.S., O.R.-R. and A. Regev generated adult and cord blood scRNA-seq datasets. CITE-seq datasets were generated by E.S., N.M. and N.K.W. Computational analysis was performed by S.W., I.G., M.Q.L., G.R., E.D., I.K., M.M., J.B., M.S.J. and M.E., and web portals were constructed by I.G., D.H. and J.M., with disease information assembled by K.P. and T.C. M.H., L.J., S.W., I.G., G.R., B.O., H.K., K.B.M., T.C., N.M., N.K.W., K.B.M., D.H., D.-M.P., S.B., A. Roy, E.L., B.G., I.R., I.G. and S.A.T. interpreted the data. M.H., L.J., S.W., I.G., G.R., B.G., I.R. and S.A.T. wrote the manuscript, with input from M.L.R.H and J.E.L. All authors read and accepted the manuscript.

Corresponding author

Correspondence to Muzlifah Haniffa.

Ethics declarations

Competing interests

S.O. is now an employee of Becton, Dickinson and Company (BD); the contributions of this author to the work were made before the commencement of employment at BD. O.R.-R. is an employee of Genentech. O.R.-R. is a co-inventor on patent applications filed at the Broad Institute related to single-cell genomics. All other authors declare no competing interests.

Additional information

Peer review information *Nature* thanks Ana Cumano, James Palis and the other, anonymous, reviewer(s) for their contribution to the peer review of this work. Peer reviewer reports are available.

Publisher's note Springer Nature remains neutral with regard to jurisdictional claims in published maps and institutional affiliations.

Extended data figures and tables

Extended Data Fig. 1 A single-cell atlas of human FBM.

1a) Summary of FBM scRNA-seq dataset and reference scRNA-seq datasets used in this study, including published yolk sac and fetal liver data⁴ and publicly available cord blood/ABM data from the Human Cell Atlas Data Coordination Portal. 1b) UMAP of FBM scRNA-seq data (as per Fig. 1a) pre- and post- Harmony batch correction. Sequencing type and sample is represented by colour. 1c) Logistic regression for intersecting cell states annotated in FBM, ABM, cord blood, and FBM with Down syndrome scRNA-seq datasets. Prediction probability indicated by colour scale. 1d) Dotplots for expression of selected cell-state defining genes (left) in FBM CITE-seq data where corresponding protein was available in the ADT panel (right). Genes were selected from DE analysis (two-sided Wilcoxon rank-sum statistical test with Benjamini-Hochberg procedure for multiple testing correction; Supplementary Table 12). Markers used for FACS isolation are shown in bold type. Log-transformed, normalized and scaled gene expression values (upper limit 3) and DSB-normalized protein expression values (upper limit 15) are represented by the colour of the dots. Percentage

of cells in each cell type expressing the marker is shown by the size of the dot. To contextualize dotplots shown in this panel, DE proteins were independently calculated for the FBM CITE-seq data (Supplementary Table 13), with method as described above for genes. 1e) FACS strategy used to isolate cell types for validation based on cell-state defining markers from scRNA-seq data. Representative plots from $n = 2$ samples (17 PCW) are shown. Gating strategy is described in Methods. 1f) UMAP of FBM Smart-seq2 scRNA-seq data ($n = 2$, $k = 486$, 17 PCW; Supplementary Table 15) with a 50-cell per subset sample of predicted 10x scRNA-seq counterparts ($n = 9$, $k = 600$). 10x scRNA-seq data represented by coloured areas and Smart-seq2 data represented by dots of equivalent colour.

Extended Data Fig. 2 A single-cell atlas of human FBM.

2a) Continuous decision tree constructed using the Rpart package to distinguish between the lineage-committed immune cell types in FBM (total) CITE-seq data using the 198 epitopes detected (see [Supplementary Methods](#)). Node splits were labelled ‘lo’ or ‘hi’ for visualization purposes. The branch rules of the tree operate on continuous protein expression values. 2b) Confusion matrix showing the actual cell type labels and the predicted cell type labels for the decision tree (in panel a) when run on the test data (see [Methods](#)). Sensitivity and specificity are illustrated in this heat map, with complete statistics provided in Supplementary Table 14. Overall accuracy computed with 95% CI using a binomial test and checked with a one-sided test (see caret package documentation for *confusionMatrix* function).

Extended Data Fig. 3 Diversification of innate myeloid and lymphoid cells.

3a) UMAP of monocyte, DC, neutrophil and macrophage subsets ($k=34,318$) in the FBM scRNA-seq dataset. 3b) FDG of DC, myeloid progenitor and HSC/MPP subsets ($k=5,702$) in the FBM scRNA-seq dataset. 3c) Left: Illustration displaying role of *SPI1* and *CEBPA* dosage in influencing monocyte and neutrophil differentiation from GMPs. Right: log-transformed, normalized and scaled expression of *CEBPA* and *SPI1* in GMPs from fetal liver and FBM scRNA-seq datasets. 3d) Heat map

showing gene expression (GEX) for early monocyte and neutrophil commitment markers (two-sided Wilcoxon rank-sum statistical test with Benjamini-Hochberg procedure for multiple testing correction; Supplementary Table 30) in FBM scRNA-seq progenitors. Hierarchical clustering of each cell type shown (see [Methods](#)). GEX values are log-transformed, normalized and scaled (upper limit of 3). Sig = signature. 3e) Heat map showing expression of genes implicated in severe congenital neutropenia (Supplementary Table 31) across FBM scRNA-seq Monocle 3-inferred neutrophil pseudotime (DEGs across pseudotime marked with asterisk; one-sided Moran's I statistical test; Supplementary Tables 32, 33). GEX values are log-transformed, normalized and scaled (upper limit of 1.5). 3f) Heat map showing gene enrichment (see [Methods](#)) of blood DC/monocyte signatures¹⁰ in developing and mature haematopoietic tissues (YS, fetal liver⁴, FBM, ABM). 3g) FDG of NK/ILCs (k=915) in the FBM scRNA-seq dataset. Grey ellipse highlights proliferating cells. 3h) Heat map showing NK cytotoxicity gene enrichment in NK cell states in YS, fetal liver and FBM (See [Methods](#)). Relative enrichment is indicated by colour scale. 3i) Heat map of predicted TF activity across inferred FBM DC pseudotime (FBM scRNA-seq DC-lineage cell states as input). TF activity inferred using iRegulon and pseudotime calculated using the Scanpy *sc.tl.dpt* function. GEX normalized to between 0-1 prior to plotting. 3j) Dotplot showing cell state-defining genes for NK and ILCs in the FBM scRNA-seq dataset. Methods/interpretation as in Fig. 1b. 3k) Dotplot showing expression of cell state-defining genes for DC and monocytes in the FBM scRNA-seq dataset. Methods/interpretation as in Fig. 1b. 3l) Dotplot showing expression of cell state-defining genes for myeloid precursors and neutrophils in the FBM scRNA-seq dataset. Methods/interpretation as in Fig. 1b.

[Source data](#)

[**Extended Data Fig. 4 Expanded B-lymphopoiesis in FBM.**](#)

4a) Dotplot of cell state-defining genes for FBM scRNA-seq B-lineage. Methods/interpretation as in Fig. 1b. Abbreviations as in Fig. 2b. 4b) Barplot for mean proportions of B-lineage cell states in fetal liver (n=14), FBM (n=9) and ABM (n=4) scRNA-seq datasets (n=biologically

independent samples; B lineage absent in n=3 YS). *P*-values resulting from quasibinomial regression model (subject to one-sided ANOVA; with correction for sort gates; computed at 95% CI and adjusted for multiple testing using Bonferroni correction) are shown in parentheses; ***p* < 0.01, *****p* < 0.0001; Supplementary Tables 19, 23). 4c) Violin-plot of DEGs (computed using two-sided Wilcoxon rank-sum statistical test with Benjamini-Hochberg procedure for multiple testing correction; ****=*p* < 0.0001; Supplementary Table 34) across FBM scRNA-seq Pre-B progenitor paths as in Fig. 2b; see [Methods](#)). GEX are log-transformed, normalized and scaled. 4d) Barplot showing mean proportion of productive heavy/light chains in FBM B-lineage cells present in both mRNA/BCR-enriched scRNA-seq (n=2, k=5,052). Pie-charts show the proportion of cycling cells (see [Methods](#)) per cell-type. 4e) Heat map of shared clonotypes between FBM B-lineage cell types, as defined by CellRanger. 4f) FDG of B-cell development (k=30,066) in the FBM scRNA-seq dataset. Colour indicates state (left) and Monocle 3 pseudotime value (right). Paths as in Fig. 2b. 4g) FDG of B-lineage (k=28,583) in the FBM scRNA-seq dataset. Colour indicates apoptotic gene enrichment score (see [Methods](#)/legend). 4h) Heat map of B-ALL-implicated genes across Monocle 3-inferred FBM/ABM B cell development pseudotime (see panel F; Supplementary Tables 32, 35–37; DEGs across pseudotime marked with asterisk; one-sided Moran’s I statistical test). Log-transformed, normalized and scaled GEX (upper limit of 2). 4i) Dotplot comparing expression of characteristic T-cell genes in cell states from thymus and FBM scRNA-seq datasets (see [Methods](#)).

Interpretation as in Fig. 1b. Abbreviations: ETP = early thymocyte precursor; DN = double negative; DP = double positive. 4j) Barplot of productively rearranged TRA/B/G/D chains by T-cell state in n=4 biologically independent FBM samples at 14–17 PCW, k=194 cells. Chain rearrangements were as defined by CellRanger. Bars show mean and error bars SD. Mean±SD TCR productivity was 97±7%, 90±14% and 96±8% for CD4-T, CD8-T and Treg.

[Source data](#)

[Extended Data Fig. 5 Tissue-specific properties of HSC/MPPs.](#)

5a) Violin-plots showing GEX for MEM-, myeloid- and lymphoid- lineage genes in FBM scRNA-seq progenitors. GEX are log-transformed, normalized and scaled. Abbreviations: HSC/MPP = haematopoietic stem cell/ multipotent progenitor; CMP = common myeloid progenitor; eo/baso/mast pre. = eosinophil/basophil/mast cell precursor. 5b) FDG visualization of CD34⁺ FBM/fetal liver/cord blood CITE-seq cells on gene expression landscape (total k=35,273; FBM n=3, k=8,829, 14-17 PCW; FL n=4, k=18,904, 14-17 PCW; CB n=4, k=7,540, 40-42 PCW). Cell type is represented by colour, as shown in legend. HSC/MPP groups refer to unsupervised sub-clusters of the most immature compartment rather than functional MPP subpopulations. Abbreviations: MEP = megakaryocyte erythroid progenitor; MkP = megakaryocyte progenitor; EryP = erythroid progenitor; EoBasoMC = eosinophil/basophil/mast cell progenitor; MyP = myeloid progenitor; LyP = lymphoid progenitor. 5c) Logistic Regression for intersecting cell states in CD34⁺ CITE-seq data and FBM scRNA-seq data (see [Methods](#)). Prediction probability is indicated by colour scale. Cell type abbreviations as shown in panel **a** and **b** legend. 5d) Heat map showing cell-cycle gene enrichment in CD34⁺ FBM/fetal liver/cord blood CITE-seq progenitors. Colour indicates relative enrichment. 5e) Dotplot showing expression of genes used for progenitor characterization in the CD34⁺ CITE-seq data. Methods/interpretation as in Fig. [1b](#). 5f) Dotplot showing expression of proteins used for progenitor characterization in CD34⁺ CITE-seq data. Methods/interpretation as in Extended Data Fig. [1d](#) (protein expression upper limit of 4). 5g) Bar-graph showing proportion of progenitor subsets out of total progenitors in fetal liver (n=4), FBM (n=3) and cord blood (n=4) CD34⁺ CITE-seq data (n= biologically independent samples). Proportions are normalized across donors. Bars indicate mean and error bars SD. Cell-type proportions across tissue were tested using a quasibinomial regression model (subject to one-sided ANOVA; with correction for sort gates; computed at 95% CI and adjusted for multiple testing using Bonferroni correction); *= $p < 0.05$ (Supplementary Table [38](#)). 5h) Dotplot showing expression of protein markers significantly differentially expressed between HSC/MPP across tissues (fetal liver, FBM, cord blood) in the CD34⁺ CITE-seq dataset. Top differentially expressed proteins by log(fold change) are shown for each tissue (Supplementary Table [39](#); two-sided Wilcoxon rank-sum statistical test with Benjamini-

Hochberg procedure for multiple testing correction). Methods/interpretation as in Extended Data Fig. [1d](#).

[Source data](#)

[Extended Data Fig. 6 Tissue-specific properties of HSC/MPPs.](#)

6a) Direction of Transition (DoT)-scores computed between CD34⁺ CITE-seq HSC/MPP1 across tissue (using cross-tissue HSC/MPP1 DEGs as input - see Supplementary Table [40](#)). ABM scRNA-seq was used as reference and the origin point was defined as HSC/MPP (see [Methods](#)). Red-coloured cells indicate a shift towards their state (blue colour vice versa). 6b) Sort gates for HSC culture experiments. HSC/MPP, LMPP/MLP and CD34⁺CD38^{mid} cells were index-sorted for single-cell culture on an MS5 stromal layer, as described in Methods. LMPP/MLP and CD34⁺CD38^{mid} cells were analysed as ‘committed progenitors’. Abbreviations: LMPP/MLP = lymphoid-primed multipotent progenitor/ multipotent lymphoid progenitor. Figure was created using BioRender.com. 6c) Examples of single-cell HSC culture outputs showing outputs for: i) MK (CD41⁺), erythroid (CD235a⁺) and myeloid (CD14⁺ monocyte and CD15⁺ neutrophil), ii) NK (CD56⁺) and myeloid (CD14⁺ monocyte and CD15⁺ neutrophil). 6d) Outputs from single-cell culture on MS5 stromal layer for paired fetal liver and FBM HSC/MPPs. Proportion of culture wells producing colonies by cell-type/tissue (assessed by light microscopy under 4x magnification, analysed per plate- k=7 from n=3 biologically independent samples per tissue; lines display mean and error bars SEM). **p* = 0.011 by 2-sided Mann Whitney test of BM HSC/MPP vs. fetal liver HSC/MPP and ****p* = 0.0006 BM committed progenitor vs. fetal liver committed progenitor. 6e) Well contents analysed by flow cytometry and number of lineage outputs per well compared between HSC/MPP and committed progenitors from fetal liver vs. FBM. U=colony present but lineage undefinable by this assay. Statistical comparison (binomial test) for unipotential vs. multipotential colonies: HSC/MPP fetal liver vs. FBM ****p* = 0.0008, 2-sided; committed progenitor fetal liver vs. BM ‘ns’ *p* = 0.27, 2-sided. 6f) Proportion of fetal liver and FBM HSC/MPPs producing myeloid-containing colonies in single-cell culture on MS5 stromal layer (paired FBM and fetal liver from n=2 biologically independent samples).

Statistical comparison is of ‘myeloid-only’ vs. ‘myeloid plus other’ in k=77 wells producing myeloid colonies; *** $p = 0.0001$, 2-sided by binomial test. Abbreviations as follows: M = myeloid; E = erythroid; MK = megakaryocyte; NK = natural killer.

Source data

Extended Data Fig. 7 Perturbed haematopoiesis in Down syndrome.

7a) UMAP of Down syndrome FBM scRNA-seq (n=4, k=16,743, 12-13 PCW) (Supplementary Table 20). Abbreviations as in Fig. 1a. 7b) Top 30 PySCENIC-inferred differentially active TFs in Down syndrome vs. non-Down syndrome FBM scRNA-seq HSC/MPPs, MEMPs and MKs (Supplementary Tables 7, 20). TFs (red) described in text. 7c) Proportions of erythroid lineage cell states in Down syndrome (n=4) and age-matched non-Down syndrome FBM scRNA-seq data (n=2, where n=biologically independent samples). **** $p < 10^{-15}$, 2-sided, by chi-squared test. Abbreviations: eryth = erythroid. 7d) Heat map showing cell-cycle gene enrichment in Down syndrome and age-matched non-Down syndrome FBM erythroid lineage cell states. Colour indicates relative enrichment. 7e) Representative images from single-cell HSC/MPP methylcellulose cultures, showing relative erythrocyte colony size/structure in Down syndrome (top; n=2 biological independent samples; PCW=17, 19; k=246) and non-Down syndrome (bottom; n=3 biologically independent samples; PCW=17, 19, 21; k=365) FBM; scale bar; 400 μ m. 7f) Heat map of erythropoiesis-implicated genes across Monocle 3-inferred erythroid development pseudotime in Down syndrome and non-Down syndrome FBM scRNA-seq datasets (all genes shown are DEGs across both pseudotime trajectories; one-sided Moran’s I statistical test; Supplementary Tables 32, 41, 42). Log-transformed, normalized and scaled GEX (upper limit of 3). 7g) Dotplot showing chromosome 21 TFs differentially expressed in Down syndrome and non-Down syndrome FBM scRNA-seq datasets (two-sided Wilcoxon rank-sum statistical test with Benjamini-Hochberg procedure for multiple testing correction; adjusted- p -value=<0.05; Supplementary Table 21). Dot-size = average log2 fold-change in Down syndrome expression. Colour = log(log(adjusted- p -value)). 7h) Dotplot showing TFs for differentially

active regulons in Down syndrome vs. non-Down syndrome FBM scRNA-seq (see panel **b**). 7i) Top: Heat map showing *TNF* expression in Down syndrome and non-Down syndrome FBM scRNA-seq cell states. Bottom: $\text{TNF}\alpha$ -signalling pathway enrichment (see [Methods](#), Supplementary Table [43](#)). Dot-size = normalized enrichment score (NES) for $\text{TNF}\alpha$ -signalling pathway. Line = $\pm \log_{10}(0.25)$. 7j) Sankey-plot of putative TNF superfamily interactions in Down syndrome FBM scRNA-seq (see [Methods](#); Supplementary Table [44](#)). Fold-change expression in Down syndrome relative to non-Down syndrome (red scale). Combined expression in Down syndrome/non-Down syndrome (blue scale).

[Source data](#)

[**Extended Data Fig. 8 Stromal cell heterogeneity in FBM.**](#)

8a) UMAP of FBM scRNA-seq stromal cells ($k=6,287$). Dotted lines indicate broad lineages. Abbreviations: mac = macrophage; Fb = fibroblast; pre. = precursor. 8b) Dotplot showing cell state-defining genes for osteoclasts and macrophages in the FBM scRNA-seq dataset. Methods/interpretation as in Fig. [1b](#). 8c) Dotplot showing cell state-defining genes for osteochondral-lineage cells in the FBM scRNA-seq dataset. Methods/interpretation as in Fig. [1b](#). 8d) Barplot showing frequency of stromal cell states in FBM scRNA-seq samples. Samples are grouped into 4 developmental stages to facilitate statistical comparison over gestational stage. P -values resulting from quasibinomial regression model (subject to one-sided ANOVA; with correction for sort gates; computed at 95% CI and adjusted for multiple testing using Bonferroni correction) are shown in parentheses; $*p < 0.05$, $**p < 0.01$, $***p < 0.001$, $****p < 0.0001$; Supplementary Tables [19](#), [45](#). 8e) Heat map showing gene enrichment (see [Methods](#)) of postnatal mouse BM stromal cell^{[19](#)} signatures in human FBM scRNA-seq stromal cells (coloured as in panel **a**). 8f) Dotplot showing cell state-defining genes for endothelial cells in the FBM scRNA-seq dataset. Methods/interpretation as in Fig. [1b](#). 8g) Left panel: Violin-plot showing expression of genes with documented role in sinusoidal endothelial cell function^{[4](#)} in sinusoidal endothelial cells from FBM and fetal liver scRNA-seq datasets. Right panel: Equivalent protein dotplot where marker was present in CD34⁺ CITE-seq ADT panel. Asterisks indicate DEGs (two-

sided Wilcoxon rank-sum statistical test with Benjamini-Hochberg procedure for multiple testing correction; $*p < 0.05$, $**p < 0.01$, $***p < 0.001$, $****p < 0.0001$; Supplementary Tables [46](#), [47](#)). Methods/interpretation as in Fig. [3a, c](#) (upper limit of 5.5 for protein dotplot). 8h) Heat map showing expression of mouse BM endothelial cell DEGs from Baryawno et al (see [Supplementary Methods](#)) in FBM scRNA-seq endothelial cells. GEX values are log-transformed, normalized and scaled (upper limit of 3). Hierarchical clustering for each cell type is shown (see [Methods](#)). 8i) Heat map of differentially enriched inflammatory and cytokine production pathways in Down syndrome vs. non-Down syndrome FBM scRNA-seq stroma defined by a two-sided Wilcoxon rank-sum test with Benjamini-Hochberg procedure for multiple testing correction; Supplementary Tables [20](#), [43](#)).

[Source data](#)

[Extended Data Fig. 9 FBM stromal cells in situ.](#)

9a) Expression of IF microscopy markers in the FBM (total) CITE-seq dataset; genes (left) and their protein equivalent (right). Methods/interpretation as in Extended Data Fig. [1d](#) (upper limits of 3/15 applied for gene/protein expression). 9b) Left: Scatterplot of CD34 and CD117 co-expression in FBM leukocytes by flow cytometry and expression of CLEC9A in gated fractions (representative from n=2). Right: Scatterplots of CD34, CD38 and CD117 protein expression in the FBM (total) CITE-seq dataset (Supplementary Table [48](#)). Values are ln(DSB-normalized) and scaled to a lower limit of 0. Quadrants denote manual ‘gating’ thresholds (see [Methods](#)). Kernel density gradient is overlaid. 9c) Longitudinal section of fetal bone stained with hematoxylin and eosin. Left: location of haematopoietic tissue (10x magnification), scale bar; 1mm. Right top: haematopoietic architecture (20x magnification), scale bar; 200 μ m. Right bottom: identification of morphologically distinct cell types (50x magnification), scale bar; 20 μ m. Abbreviations: Eryth. = erythroid Neut. = neutrophil lineage; Eo. = eosinophil. Representative from n=4 samples (14-15 PCW). 9d) Longitudinal section of fetal femur with multiplex IF staining. Yellow boxes = regions of interest. Representative image from n=4 samples (14-15 PCW) at 4x magnification. Scale bar;

3mm. 9e) Sections of fetal femur, each stained with a single primary antibody from the multiplex and co-stained with DAPI. Representative fields of view from n=2 samples (14-15 PCW) at 20x magnification. Scale bars; 100 μ m. 9f) Identification of HSC/MPP and progenitors as cells co-expressing CD34 and CD117 (white arrow): left = all multiplex channels, middle = CD117 only, right = CD34 only. Representative image at 100x magnification. Replicates as per panel g. Scale bars; 50 μ m. 9g) Scatterplot showing proportions of CD34 $^{+}$ CD117 $^{+}$ HSC/MPP and progenitors per nucleated cells in metaphyseal (M) versus diaphyseal (D) regions of interest. Bars display mean and error bars SD of 522 HSC/MPP locations across 127 regions of interest in n=4 biologically independent FBM samples (14-15 PCW). Difference in frequency of CD34 $^{+}$ CD117 $^{+}$ HSC/MPP and progenitors relative to cellular density was assessed by Wald test ($p= 0.431$) (Supplementary Table [28](#)).

Source data

Extended Data Fig. 10 Predicted stromal cell interactions.

10a) Summary of receptor-ligand interactions predicted by CellPhoneDB (see [Methods](#)) between FBM stromal ligands and HSC/MPP receptors (Supplementary Table [49](#)). Significant putative receptor-ligands across FBM neighbourhoods are indicated in Venn diagram overlapping regions. Figure was created using BioRender.com. 10b) GEX dotplot for FBM scRNA-seq stromal ligands and HSC/MPP receptors with role in CellPhoneDB-predicted receptor-ligand interactions shown in panel a. Methods/interpretation as shown in Fig. [1b](#) (upper limit of 2 for both dotplots). Colours represent grouping of stromal cell types, as in panel a. 10c) Protein dotplot for CD34 $^{+}$ CITE-seq HSC/MPPs receptors with role in CellPhoneDB-predicted receptor-ligand interactions as per panels a-b. Methods/interpretation as in Extended Data Fig. [1f](#) (upper limit of 1.5). 10d) Summary of receptor-ligand interactions predicted by CellPhoneDB between FBM HSC/MPP ligands and stromal receptors (Supplementary Table [49](#)). Interpretation as detailed in panel a, and cell-type groupings detailed in Methods. 10e) GEX dotplot for FBM scRNA-seq stromal receptors and HSC/MPP ligands with role in CellPhoneDB-predicted receptor-ligand interactions shown in panel d. Methods/interpretation as

shown in Fig. 1b (upper limit of 20% was placed on the HSC/MPP dotplot and upper limit of 2 was placed on both dotplots).

Supplementary information

Supplementary Information

This file contains Supplementary Methods (additional methodological information for both wet-lab experimental protocols and bioinformatic analysis) and the legends for Supplementary Tables 1–53 (see separate file for the tables).

Reporting Summary

Peer Review File

Supplementary Tables

This file contains Supplementary Tables 1–53 (see Supplementary Information PDF for table legends).

Source data

Source Data Fig. 1

Source Data Fig. 2

Source Data Extended Data Fig. 3

Source Data Extended Data Fig. 4

Source Data Extended Data Fig. 5

Source Data Extended Data Fig. 6

[**Source Data Extended Data Fig. 7**](#)

[**Source Data Extended Data Fig. 8**](#)

[**Source Data Extended Data Fig. 9**](#)

Rights and permissions

[Reprints and Permissions](#)

About this article

Cite this article

Jardine, L., Webb, S., Goh, I. *et al.* Blood and immune development in human fetal bone marrow and Down syndrome. *Nature* **598**, 327–331 (2021). <https://doi.org/10.1038/s41586-021-03929-x>

- Received: 30 July 2020
- Accepted: 18 August 2021
- Published: 29 September 2021
- Issue Date: 14 October 2021
- DOI: <https://doi.org/10.1038/s41586-021-03929-x>

Share this article

Anyone you share the following link with will be able to read this content:

[Get shareable link](#)

Sorry, a shareable link is not currently available for this article.

[Copy to clipboard](#)

Provided by the Springer Nature SharedIt content-sharing initiative

This article was downloaded by **calibre** from <https://www.nature.com/articles/s41586-021-03929-x>

| [Section menu](#) | [Main menu](#) |

- Article
- [Published: 06 October 2021](#)

A single sulfatase is required to access colonic mucin by a gut bacterium

- [Ana S. Luis](#)^{1,2},
- [Chunsheng Jin](#) ORCID: [orcid.org/0000-0002-0229-102X](#)²,
- [Gabriel Vasconcelos Pereira](#) ORCID: [orcid.org/0000-0001-7937-474X](#)¹,
- [Robert W. P. Glowacki](#)¹,
- [Sadie R. Gugel](#)¹,
- [Shaleni Singh](#)¹,
- [Dominic P. Byrne](#)³,
- [Nicholas A. Pudlo](#)¹,
- [James A. London](#)³,
- [Arnaud Baslé](#)⁴,
- [Mark Reihill](#) ORCID: [orcid.org/0000-0003-3896-9346](#)⁵,
- [Stefan Oscarson](#) ORCID: [orcid.org/0000-0002-8273-4918](#)⁵,
- [Patrick A. Eyers](#) ORCID: [orcid.org/0000-0002-9220-2966](#)³,
- [Mirjam Czjzek](#) ORCID: [orcid.org/0000-0002-7483-2841](#)⁶,
- [Gurvan Michel](#)⁶,
- [Tristan Barbeyron](#)⁶,
- [Edwin A. Yates](#)³,
- [Gunnar C. Hansson](#) ORCID: [orcid.org/0000-0002-1900-1869](#)²,
- [Niclas G. Karlsson](#) ORCID: [orcid.org/0000-0002-3045-2628](#)²,
- [Alan Cartmell](#) ORCID: [orcid.org/0000-0002-5512-249X](#)³ &
- [Eric C. Martens](#) ORCID: [orcid.org/0000-0001-6681-2990](#)¹

[Nature](#) volume **598**, pages 332–337 (2021)

- 4242 Accesses
- 107 Altmetric
- [Metrics details](#)

Subjects

- [Bacterial genetics](#)
- [Bacteriology](#)
- [Enzymes](#)
- [Glycobiology](#)
- [X-ray crystallography](#)

Abstract

Humans have co-evolved with a dense community of microbial symbionts that inhabit the lower intestine. In the colon, secreted mucus creates a barrier that separates these microorganisms from the intestinal epithelium¹. Some gut bacteria are able to utilize mucin glycoproteins, the main mucus component, as a nutrient source. However, it remains unclear which bacterial enzymes initiate degradation of the complex *O*-glycans found in mucins. In the distal colon, these glycans are heavily sulfated, but specific sulfatases that are active on colonic mucins have not been identified. Here we show that sulfatases are essential to the utilization of distal colonic mucin *O*-glycans by the human gut symbiont *Bacteroides thetaiotaomicron*. We characterized the activity of 12 different sulfatases produced by this species, showing that they are collectively active on all known sulfate linkages in *O*-glycans. Crystal structures of three enzymes provide mechanistic insight into the molecular basis of substrate specificity. Unexpectedly, we found that a single sulfatase is essential for utilization of sulfated *O*-glycans *in vitro* and also has a major role *in vivo*. Our results provide insight into the mechanisms of mucin degradation by a prominent group of gut bacteria, an important process for both normal microbial gut colonization² and diseases such as inflammatory bowel disease³.

Access options

Subscribe to Journal

Get full journal access for 1 year

\$199.00

only \$3.90 per issue

[Subscribe](#)

All prices are NET prices.

VAT will be added later in the checkout.

Tax calculation will be finalised during checkout.

Rent or Buy article

Get time limited or full article access on ReadCube.

from \$8.99

[Rent or Buy](#)

All prices are NET prices.

Additional access options:

- [Log in](#)
- [Access through your institution](#)
- [Learn about institutional subscriptions](#)

Fig 1: Bacterial growth on colonic mucin and *B. thetaiotaomicron* sulfatase activities.

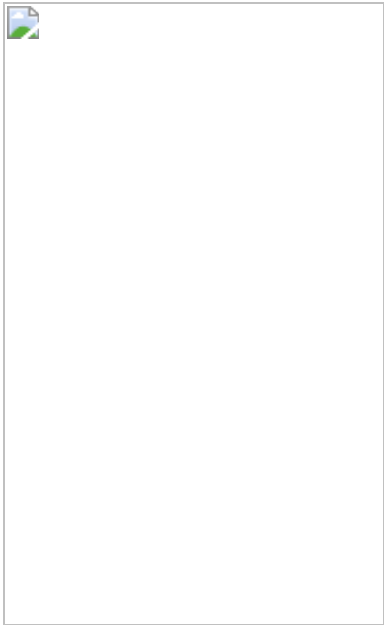


Fig. 2: Activity of *B. thetaiotaomicron* sulfatases on colonic mucin *O*-glycans.

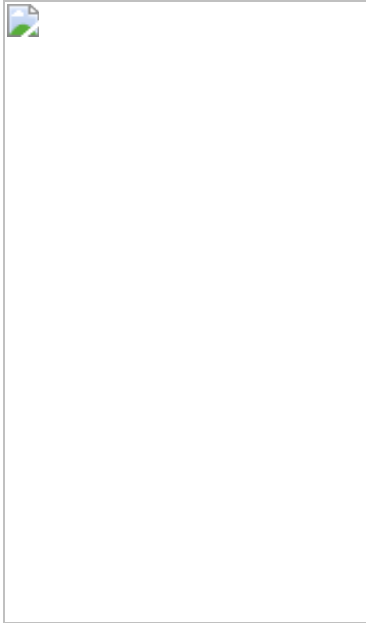


Fig. 3: Crystal structures of 3S-Gal/GalNAc sulfatases.

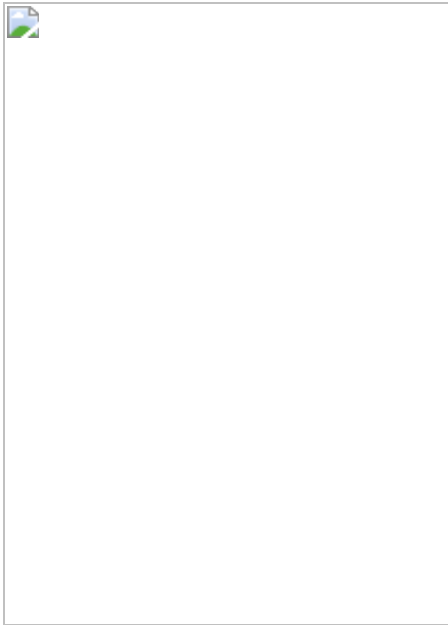
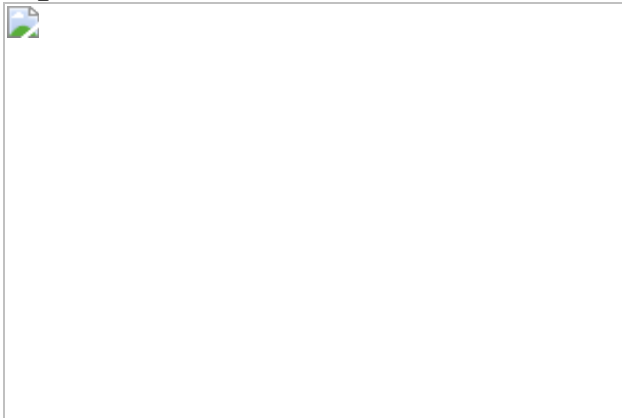


Fig. 4: BT1636^{3S-Gal} activity is required for the use of cMO and competitive fitness in vivo.



Data availability

All data for the experiments, along with corresponding statistical test values, where appropriate, are provided within the paper and in its [Supplementary Information](#). The crystal structure datasets generated have been deposited in the PDB under the following accession numbers: [7ANB](#), [7ANA](#), [7AN1](#), [7OQD](#) and [7ALL](#). The MS raw files have been deposited in the GlycoPOST database under the following IDs: GPST000150 and GPST000196. Glycan structural annotations were deposited to the UniCarb database at <https://unicarb-dr.glycosmos.org/references/462>. There are no restrictions on data or

biological resource availability. Data and biological resources can be obtained by contacting the corresponding authors. [Source data](#) are provided with this paper.

Code availability

No new codes were developed or compiled in this study.

References

1. 1.

Johansson, M. E. et al. The inner of the two Muc2 mucin-dependent mucus layers in colon is devoid of bacteria. *Proc. Natl Acad. Sci. USA* **105**, 15064–15069 (2008).

2. 2.

Benjdia, A., Martens, E. C., Gordon, J. I. & Bertea, O. Sulfatases and a radical S-adenosyl-l-methionine (AdoMet) enzyme are key for mucosal foraging and fitness of the prominent human gut symbiont, *Bacteroides thetaiotaomicron*. *J. Biol. Chem.* **286**, 25973–25982 (2011).

3. 3.

Hickey, C. A. et al. Colitogenic *Bacteroides thetaiotaomicron* antigens access host immune cells in a sulfatase-dependent manner via outer membrane vesicles. *Cell Host Microbe* **17**, 672–680 (2015).

4. 4.

Packey, C. D. & Sartor, R. B. Commensal bacteria, traditional and opportunistic pathogens, dysbiosis and bacterial killing in inflammatory bowel diseases. *Curr. Opin. Infect. Dis.* **22**, 292–301 (2009).

5. 5.

Sears, C. L. & Garrett, W. S. Microbes, microbiota, and colon cancer. *Cell Host Microbe* **15**, 317–328 (2014).

6. 6.

Van der Sluis, M. et al. Muc2-deficient mice spontaneously develop colitis, indicating that Muc2 is critical for colonic protection. *Gastroenterology* **131**, 117–129 (2006).

7. 7.

Velcich, A. et al. Colorectal cancer in mice genetically deficient in the mucin Muc2. *Science* **295**, 1726–1729 (2002).

8. 8.

Bergstrom, K. et al. Core 1- and 3-derived O-glycans collectively maintain the colonic mucus barrier and protect against spontaneous colitis in mice. *Mucosal Immunol.* **10**, 91–103 (2016).

9. 9.

Larsson, J. M. et al. Altered O-glycosylation profile of MUC2 mucin occurs in active ulcerative colitis and is associated with increased inflammation. *Inflamm. Bowel Dis.* **17**, 2299–2307 (2011).

10. 10.

Fu, J. et al. Loss of intestinal core 1-derived O-glycans causes spontaneous colitis in mice. *J. Clin. Invest.* **121**, 1657–1666 (2011).

11. 11.

Kudelka, M. R. et al. *Cosmc* is an X-linked inflammatory bowel disease risk gene that spatially regulates gut microbiota and contributes to sex-specific risk. *Proc. Natl. Acad. Sci. USA* **113**, 14787–14792 (2016).

12. 12.

Larsson, J. M., Karlsson, H., Sjovall, H. & Hansson, G. C. A complex, but uniform *O*-glycosylation of the human MUC2 mucin from colonic biopsies analyzed by nanoLC/MSⁿ. *Glycobiology* **19**, 756–766 (2009).

13. 13.

Holmen Larsson, J. M., Thomsson, K. A., Rodriguez-Pineiro, A. M., Karlsson, H. & Hansson, G. C. Studies of mucus in mouse stomach, small intestine, and colon. III. Gastrointestinal Muc5ac and Muc2 mucin *O*-glycan patterns reveal a regiospecific distribution. *Am. J. Physiol. Gastrointest. Liver Physiol.* **305**, G357–G363 (2013).

14. 14.

Thomsson, K. A. et al. Detailed *O*-glycomics of the Muc2 mucin from colon of wild-type, core 1- and core 3-transferase-deficient mice highlights differences compared with human MUC2. *Glycobiology* **22**, 1128–1139 (2012).

15. 15.

Robbe, C. et al. Evidence of regio-specific glycosylation in human intestinal mucins—presence of an acidic gradient along the intestinal tract. *J. Biol. Chem.* **278**, 46337–46348 (2003).

16. 16.

Katoh, T. et al. Identification and characterization of a sulfoglycosidase from *Bifidobacterium bifidum* implicated in mucin glycan utilization. *Biosci. Biotechnol. Biochem.* **81**, 2018–2027 (2017).

17. 17.

Martens, E. C., Chiang, H. C. & Gordon, J. I. Mucosal glycan foraging enhances fitness and transmission of a saccharolytic human gut bacterial symbiont. *Cell Host Microbe* **4**, 447–457 (2008).

18. 18.

Diez-Roux, G. & Ballabio, A. Sulfatases and human disease. *Annu. Rev. Genomics Hum. Genet.* **6**, 355–379 (2005).

19. 19.

Włodarska, M. et al. Indoleacrylic acid produced by commensal *Peptostreptococcus* species suppresses inflammation. *Cell Host Microbe* **22**, 25–37 (2017).

20. 20.

Tramontano, M. et al. Nutritional preferences of human gut bacteria reveal their metabolic idiosyncrasies. *Nat. Microbiol.* **3**, 514–522 (2018).

21. 21.

Derrien, M., Vaughan, E. E., Plugge, C. M. & de Vos, W. M. *Akkermansia muciniphila* gen. nov., sp. nov., a human intestinal mucin-degrading bacterium. *Int. J. Syst. Evol. Microbiol.* **54**, 1469–1476 (2004).

22. 22.

Pudlo, N. A. et al. Symbiotic human gut bacteria with variable metabolic priorities for host mucosal glycans. *mBio* **6**, e01282 (2015).

23. 23.

Barbeyron, T. et al. Matching the diversity of sulfated biomolecules: creation of a classification database for sulfatases reflecting their substrate specificity. *PLoS ONE* **11**, e0164846 (2016).

24. 24.

Benjdia, A. et al. Anaerobic sulfatase-maturing enzymes, first dual substrate radical S-adenosylmethionine enzymes. *J. Biol. Chem.* **283**,

17815–17826 (2008).

25. 25.

Cartmell, A. et al. How members of the human gut microbiota overcome the sulfation problem posed by glycosaminoglycans. *Proc. Natl Acad. Sci. USA* **114**, 7037–7042 (2017).

26. 26.

Ndeh, D. et al. Metabolism of multiple glycosaminoglycans by *Bacteroides thetaiotaomicron* is orchestrated by a versatile core genetic locus. *Nat. Commun.* **11**, 646 (2020).

27. 27.

Ulmer, J. E. et al. Characterization of glycosaminoglycan (GAG) sulfatases from the human gut symbiont *Bacteroides thetaiotaomicron* reveals the first GAG-specific bacterial endosulfatase. *J. Biol. Chem.* **289**, 24289–24303 (2014).

28. 28.

Tobisawa, Y., Imai, Y., Fukuda, M. & Kawashima, H. Sulfation of colonic mucins by *N*-acetylglucosamine 6-*O*-sulfotransferase-2 and its protective function in experimental colitis in mice. *J. Biol. Chem.* **285**, 6750–6760 (2010).

29. 29.

Neelamegham, S. et al. Updates to the Symbol Nomenclature for Glycans guidelines. *Glycobiology* **29**, 620–624 (2019).

30. 30.

Egan, M., Jiang, H., O'Connell Motherway, M., Oscarson, S. & van Sinderen, D. Glycosulfatase-encoding gene cluster in *Bifidobacterium breve* UCC2003. *Appl. Environ. Microbiol.* **82**, 6611–6623 (2016).

31. 31.

Briliute, J. et al. Complex *N*-glycan breakdown by gut *Bacteroides* involves an extensive enzymatic apparatus encoded by multiple co-regulated genetic loci. *Nat. Microbiol.* **4**, 1571–1581 (2019).

32. 32.

Packer, N. H., Lawson, M. A., Jardine, D. R. & Redmond, J. W. A general approach to desalting oligosaccharides released from glycoproteins. *Glycoconjugate J.* **15**, 737–747 (1998).

33. 33.

Hayes, C. A. et al. UniCarb-DB: a database resource for glycomic discovery. *Bioinformatics* **27**, 1343–1344 (2011).

34. 34.

Everest-Dass, A. V., Abrahams, J. L., Kolarich, D., Packer, N. H. & Campbell, M. P. Structural feature ions for distinguishing *N*- and *O*-linked glycan isomers by LC–ESI–IT MS/MS. *J. Am. Soc. Mass Spectrom.* **24**, 895–906 (2013).

35. 35.

Domon, B. & Costello, C. E. Structure elucidation of glycosphingolipids and gangliosides using high-performance tandem mass spectrometry. *Biochemistry* **27**, 1534–1543 (1988).

36. 36.

Byrne, D. P. et al. New tools for carbohydrate sulfation analysis: heparan sulfate 2-*O*-sulfotransferase (HS2ST) is a target for small-molecule protein kinase inhibitors. *Biochem. J.* **475**, 2417–2433 (2018).

37. 37.

Byrne, D. P. et al. cAMP-dependent protein kinase (PKA) complexes probed by complementary differential scanning fluorimetry and ion mobility–mass spectrometry. *Biochem. J.* **473**, 3159–3175 (2016).

38. 38.

Das, T. M., Rao, C. P. & Kolehmainen, E. Synthesis and characterisation of *N*-glycosyl amines from the reaction between 4,6-*O*-benzylidene-d-glucopyranose and substituted aromatic amines and also between 2-(*O*-aminophenyl) benzimidazole and pentoses or hexoses. *Carbohydr. Res.* **334**, 261–269 (2001).

39. 39.

Kabsch, W. Xds. *Acta Crystallogr. D Biol. Crystallogr.* **66**, 125–132 (2010).

40. 40.

Winter, S. E., Lopez, C. A. & Baumler, A. J. The dynamics of gut-associated microbial communities during inflammation. *EMBO Rep.* **14**, 319–327 (2013).

41. 41.

Evans, P. R. & Murshudov, G. N. How good are my data and what is the resolution? *Acta Crystallogr. D Biol. Crystallogr.* **69**, 1204–1214 (2013).

42. 42.

Long, F., Vagin, A. A., Young, P. & Murshudov, G. N. BALBES: a molecular-replacement pipeline. *Acta Crystallogr. D Biol. Crystallogr.* **64**, 125–132 (2008).

43. 43.

Vagin, A. & Teplyakov, A. Molecular replacement with MOLREP. *Acta Crystallogr. D Biol. Crystallogr.* **66**, 22–25 (2010).

44. 44.

Emsley, P., Lohkamp, B., Scott, W. G. & Cowtan, K. Features and development of Coot. *Acta Crystallogr. D Biol. Crystallogr.* **66**, 486–501 (2010).

45. 45.

Murshudov, G. N. et al. REFMAC5 for the refinement of macromolecular crystal structures. *Acta Crystallogr. D Biol. Crystallogr.* **67**, 355–367 (2011).

46. 46.

Lebedev, A. A. et al. JLigand: a graphical tool for the CCP4 template-restraint library. *Acta Crystallogr. D Biol. Crystallogr.* **68**, 431–440 (2012).

47. 47.

Chen, V. B. et al. MolProbity: all-atom structure validation for macromolecular crystallography. *Acta Crystallogr. D Biol. Crystallogr.* **66**, 12–21 (2010).

48. 48.

Agirre, J. et al. Privateer: software for the conformational validation of carbohydrate structures. *Nat. Struct. Mol. Biol.* **22**, 833–834 (2015).

49. 49.

Terwilliger, T. C. et al. Iterative-build OMIT maps: map improvement by iterative model building and refinement without model bias. *Acta Crystallogr. D Biol. Crystallogr.* **64**, 515–524 (2008).

50. 50.

Collaborative Computational Project, Number 4. The CCP4 suite: programs for protein crystallography. *Acta Crystallogr. D Biol.*

Crystallogr. **50**, 760–763 (1994).

51. 51.

Potterton, L. et al. CCP4i2: the new graphical user interface to the CCP4 program suite. *Acta Crystallogr. D Struct. Biol.* **74**, 68–84 (2018).

52. 52.

Micsonai, A. et al. BeStSel: a web server for accurate protein secondary structure prediction and fold recognition from the circular dichroism spectra. *Nucleic Acids Res.* **46**, W315–W322 (2018).

53. 53.

Desai, M. S. et al. A dietary fiber-deprived gut microbiota degrades the colonic mucus barrier and enhances pathogen susceptibility. *Cell* **167**, 1339–1353 (2016).

54. 54.

Koropatkin, N. M., Martens, E. C., Gordon, J. I. & Smith, T. J. Starch catabolism by a prominent human gut symbiont is directed by the recognition of amylose helices. *Structure* **16**, 1105–1115 (2008).

55. 55.

Degnan, P. H., Barry, N. A., Mok, K. C., Taga, M. E. & Goodman, A. L. Human gut microbes use multiple transporters to distinguish vitamin B₁₂ analogs and compete in the gut. *Cell Host Microbe* **15**, 47–57 (2014).

56. 56.

Katoh, K., Misawa, K., Kuma, K. & Miyata, T. MAFFT: a novel method for rapid multiple sequence alignment based on fast Fourier transform. *Nucleic Acids Res.* **30**, 3059–3066 (2002).

57. 57.

Clamp, M., Cuff, J., Searle, S. M. & Barton, G. J. The Jalview Java alignment editor. *Bioinformatics* **20**, 426–427 (2004).

58. 58.

Stamatakis, A. RAxML version 8: a tool for phylogenetic analysis and post-analysis of large phylogenies. *Bioinformatics* **30**, 1312–1313 (2014).

59. 59.

Felsenstein, J. Evolutionary trees from DNA sequences: a maximum likelihood approach. *J. Mol. Evol.* **17**, 368–376 (1981).

60. 60.

Le, S. Q. & Gascuel, O. An improved general amino acid replacement matrix. *Mol. Biol. Evol.* **25**, 1307–1320 (2008).

61. 61.

Felsenstein, J. Confidence limits on phylogenies: an approach using the bootstrap. *Evolution* **39**, 783–791 (1985).

62. 62.

Kumar, S., Stecher, G. & Tamura, K. MEGA7: Molecular Evolutionary Genetics Analysis version 7.0 for bigger datasets. *Mol. Biol. Evol.* **33**, 1870–1874 (2016).

Acknowledgements

This project has received funding from the European Union’s Horizon 2020 research and innovation programme under Marie Skłodowska-Curie grant agreement no. 748336. This work was supported by National Institutes of Health grants (DK118024 and DK125445 awarded to E.C.M.,

U01AI095473 awarded to G.C.H.), the European Research Council (ERC; 694181), the Knut and Alice Wallenberg Foundation (2017.0028), the Swedish Research Council (2017-00958), Wilhelm och Martina Lundgrens Vetenskapsfond (2020.3597, awarded to A.S.L.) and the Academy of Medical Sciences/Wellcome Trust through Springboard grant SBF005\1065 163470 awarded to A.C. We acknowledge access to the SOLEIL and Diamond Light sources via both University of Liverpool and Newcastle University BAGs (proposal nos mx21970 and mx18598, respectively). We thank the staff of DIAMOND and SOLEIL and members of Liverpool's molecular biophysics group for assistance with data collection. We thank members of the University of Michigan Mouse Facility and acknowledge the University of Michigan Center for Gastrointestinal Research (UMCGR; NIDDK 5P30DK034933) for support. MS analysis of glycans was performed in the Swedish Infrastructure for Biologic Mass Spectrometry (BioMS) supported by the Swedish Research Council. We are also grateful for E. Corre's help regarding bioinformatics analyses (ABIMS platform, Station Biologique de Roscoff, France).

Author information

Affiliations

1. Department of Microbiology and Immunology, University of Michigan, Ann Arbor, MI, USA

Ana S. Luis, Gabriel Vasconcelos Pereira, Robert W. P. Glowacki, Sadie R. Gugel, Shaleni Singh, Nicholas A. Pudlo & Eric C. Martens

2. Department of Medical Biochemistry, Institute for Biomedicine, Sahlgrenska Academy, University of Gothenburg, Gothenburg, Sweden

Ana S. Luis, Chunsheng Jin, Gunnar C. Hansson & Niclas G. Karlsson

3. Department of Biochemistry and Systems Biology, Institute of Systems, Molecular and Integrative Biology, University of Liverpool,

Liverpool, UK

Dominic P. Byrne, James A. London, Patrick A. Eyers, Edwin A. Yates & Alan Cartmell

4. Institute for Cell and Molecular Biosciences, Newcastle University, Newcastle upon Tyne, UK

Arnaud Baslé

5. Centre for Synthesis and Chemical Biology, University College Dublin, Belfield, Dublin, Ireland

Mark Reihill & Stefan Oscarson

6. Sorbonne Université, Univ Paris 06, CNRS, UMR 8227, Integrative Biology of Marine Models, Roscoff, Bretagne, France

Mirjam Czjzek, Gurvan Michel & Tristan Barbeyron

Contributions

A.S.L., A.C. and E.C.M. designed experiments and wrote the manuscript. A.S.L. and A.C. cloned, expressed and purified sulfatases and performed the enzymatic assays. A.C., D.P.B., J.A.L. and P.A.E. carried out and analysed the data from kinetic and binding experiments. E.A.Y., M.R. and S.O. performed chemical syntheses. A.C. and A.B. performed structural biology experiments. C.J., A.S.L., G.C.H. and N.G.K. performed and interpreted data from analytical glycobiology experiments. A.S.L., G.V.P., R.W.P.G., S.G., S.S. and N.A.P. performed bacterial growth experiments and analysed *in vivo* competition data. M.C., G.M. and T.B. performed sulfatase phylogenetic analyses. All authors read and approved the manuscript.

Corresponding authors

Correspondence to Ana S. Luis, Alan Cartmell or Eric C. Martens.

Ethics declarations

Competing interests

The authors declare no competing interests.

Additional information

Peer review information *Nature* thanks B. van den Berg and the other, anonymous, reviewer(s) for their contribution to the peer review of this work. Peer reviewer reports are available.

Publisher's note Springer Nature remains neutral with regard to jurisdictional claims in published maps and institutional affiliations.

Extended data figures and tables

[Extended Data Fig. 1 Growth of *Bacteroides* and *Phocaeicola* type strains and *Akkermansia muciniphila* in different mucin O-glycans.](#)

a, Graphs showing the growth of strains that are able to utilize colonic or gastric O-glycans. Growths were performed in minimal media containing the indicated carbon source. **b**, Growth experiments performed identically to panel **a**, but with two species, *P. massiliensis* and *A. muciniphila*, that grow on gMO but not cMO. A control experiment was performed with *A. muciniphila* grown on cMO plus added GlcNAC to verify that cMO does not contain material that is inhibitory to this species (biological replicates n =3 for both panels, error bars denote the s.e.m. for each time point). Note that gMO were used at 10mg/ml final concentration, while cMO were used at 5mg/ml due to background turbidity. This reduced concentration and the higher amount of sulfate in cMO account for the lower growth on this substrate. cMO, colonic mucin O-glycans; gMO, gastric mucin O-glycans, GlcNAc, N-acetyl-D-glucosamine.

Source data

Extended Data Fig. 2 Schematic representation of polysaccharide utilization loci (PULs) encoding sulfatases (sulf).

Genes are colour coded according to the predicted function of the respective proteins. Glycoside hydrolases (GH) in known families are indicated by GHXX or GH*, where XX and * indicates the respective family number or non-classified, respectively.

Extended Data Fig. 3 Activity and affinity of sulfatases to targeted substrates.

a, Recombinant enzymes (1 μ M) were incubated with 1 mM of substrate in 10 mM MES pH6.5 with 5 mM CaCl₂ for 16h at 37 °C. Sulfated disaccharides were generated by adding 1 μ M of a characterized α 1,3/1,4-fucosidase (BT1625) in the enzymatic reaction. Control reactions without sulfatases were carried in the same conditions. Samples were analysed by mass spectrometry and the intensity of the substrate and reaction products was used for comparison of the relative abundance of these sugars after incubation with the respective enzymes. **b**, Affinity studies looking at the effect of ligand binding on the melting temperature of 3S and 6S-Gal sulfatases. All reactions were performed in 100 mM BTP, pH 7.0 with 150 mM NaCl. For sample melting temperatures see Supplementary Table 11. **c**, Activity of 3S-Gal/GalNAc sulfatases (10 μ M) against 3S-GalNAc (10 mM). Reactions were performed in 10 mM Hepes, pH 7.0, with 150 mM NaCl and 5 mM CaCl₂. The data shown are one representative from the biological replicates conducted (n = 3).

Source data

Extended Data Fig. 4 Enzymatic screen of *Bt* sulfatases using sulfated monosaccharides.

Recombinant enzymes (1 μ M) were incubated with 1 mM of substrate in 10 mM MES pH6.5 with 5 mM CaCl₂ for 16 h at 37 °C. Reactions were analyzed by thin layer chromatography (left side) or HPAEC with pulsed amperometric detection (right side). Control reactions without sulfatases were carried out in the same conditions. The standards in TLC and HPAEC-PAD are labelled on the left side and top, respectively. The different panel represent activities found for sulfatases targeting: (a) 4S-Gal/GalNAc; (b) 3S-GlcNAc (c) 6S-Gal/GalNAc; (d) 6S-GlcNAc. The data shown are representative from biological replicates (n = 3).

[Source data](#)

Extended Data Fig. 5 Activity of *Bt* sulfatases against colonic mucin O-glycans (cMO) analysed by mass spectrometry.

a, Relative abundance of structures detected in different samples organized by sulfate-linkage (top panel) or presence of one or several sugar substitutions such as sulfate, sialic acid and fucose (bottom panel). The colour-coded bars represent the relative abundance and the total number of the structures containing the specific linkage/substitution; **b**, Representation of O-glycans detected by mass spectrometry in cMO batch 2 (control) and after sulfatase treatment from the lower (top) to the higher (bottom) mass range; **c**, Relative abundance and putative structures for the specific m/z shown in panel b. The putative structure for the different mass is shown on the right side of the graphic. The reactions were performed with 1 μ M of enzyme and 0.5% cMO in 10 mM MES pH 6.5 with 5 mM CaCl₂ for 16 h at 37 °C. The complete dataset is provided in Supplementary Table 4 and 5 for cMO batch 1 and 2, respectively.

[Source data](#)

Extended Data Fig. 6 Schematic representation of 3S-Gal/GalNAc sulfatases.

a,(i) Cartoon representation colour ramped from blue ($\alpha/\beta/\alpha$ N-terminal domain) to red (β -sheet C-terminal domain); **(ii)** the final $2mF_{\text{obs}} - DF_{\text{calc}}$

maps contoured at 1σ for GalNAc in BT1622^{3S-Gal/GalNAc} (Top) LacNAc in BT1636^{3S-Gal} (middle) and BT4683^{3S-Gal} (bottom); (iii) represents the simulated annealed composite omit $2mF_{\text{obs}} - DF_{\text{calc}}$ maps contoured at 1σ and (iv) represents the $mF_{\text{obs}} - DF_{\text{calc}}$ maps, prior to building of the ligand contoured at 3σ ; **b**,(i) Overlay of the active site S residues of BT1636^{3S-Gal} (green) BT1622^{3S-Gal/GalNAc} (blue) and BT4683^{3S-Gal} (pink). The putative catalytic residues are shown in bold. The calcium ion is represented as a grey sphere and its polar interactions indicated as dashed lines. The 3S-Gal substrate is from the BT1636^{3S-Gal} 3'S-Lewis-a complex, and BT1622^{3S-Gal/GalNAc} and BT4683^{3S-Gal} structures have been overlaid, (ii) the final $2mF_{\text{obs}} - DF_{\text{calc}}$ maps of the observed 3'S-Lewis-a substrate contoured at 1σ , (iii) represents the simulated annealed composite omit $2mF_{\text{obs}} - DF_{\text{calc}}$ maps contoured at 1σ , and (iv) represents the $mF_{\text{obs}} - DF_{\text{calc}}$ maps of the observed 3'S-Lewis-a substrate, prior to building of the ligand, contoured at 3σ ; **c**, Docking of putative structures of O-glycans targeted by BT4683^{3S-Gal} using the LacNAc as reference point showing that this structure can accommodate a sialic acid in -1 subsite and additional sugars in positive subsites (left hand side). The docking sugars are shown as sticks (middle panel) and a schematic is represented inside the dashed box (right hand side). Using the LacNAc product as an ‘anchor’ additional sugars were built in manually with Coot 0.9 and regularized to low energy conformations.

Extended Data Fig. 7 Phylogenetic tree of S1_20 and S1_4 sulfatases.

The radial trees were constructed using the branched trees shown in Supplementary Figs. 3 and 4. For clarity, all labels and sequence accession codes have been omitted. Red filled circles designate sequences from *B. thetaiotaomicron* sulfatases. The residue is written in black without any attributes if present in the sequence, in grey and italics if the residue is mutated to any type in that sequence, or to a specific residue type if given in brackets. **a**, Radial representation of the phylogenetic tree constructed with representative sequences of the sulfatase S1_20 subfamily. The colour code is given as a pattern of presence or absence of the residues E100, Q173 H177, E334, R353, which are crucial in substrate recognition by BT1636

(acc-code Q8A789, coloured red). A grey X in italics specifically designates that the residue E100 is absent in that sequence, and no obvious orthologous residue can be found from the alignment. **b**, Radial representation of the phylogenetic tree constructed with representative sequences of the sulfatase S1_4 subfamily. The colour code is given as a pattern of presence or absence of the residues R72, E335 and W505, which are crucial in substrate recognition by BT4683 (acc-code Q89YP8, coloured red). A grey X in italics specifically designates that the residue W505 is absent in that sequence, and no obvious orthologous residue can be found from the alignment.

Extended Data Fig. 8 Sulfatase activity is required for growth in cMO and *in vivo* fitness.

a, Growth curves of *Bt* wild-type Δtdk (WT), different sulfatase mutants ($\Delta btXXX$) and complemented strains on glucose, colonic or gastric mucin O-glycans (cMO and gMO, respectively). The curves represent the average of biological replicates ($n = 3$) and the error bars denote s.e.m. **b**, Relative abundance of oligosaccharides detected by mass spectrometry in culture supernatant of WT and $\Delta bt1636^{3S-Gal}$ after growth in cMO for 96h at anaerobic conditions. The control corresponds to cMO incubated in the same conditions without bacterium. The colours represent the relative abundance of structures grouped according to the presence of epitopes (sulfate, fucose and sialic acid) and the numbers represent the total number of structures that contain the respective substitution. **c**, Colonization of gnotobiotic mice fed a fiber-free diet by *Bt* WT and mutants lacking the full ($\Delta anSME$, no S1 sulfatases active) or specific sulfatase activity ($\Delta 6S-GlcNAc$ and $\Delta 6S-GlcNAc + \Delta 6S-Gal/GalNAc$). The fecal relative abundance of each strain was determined at regular intervals until day 42. The relative abundance of time 0 represents the abundance in the gavaged inoculum. At the experimental endpoint the relative abundance was also determined in small intestine and cecum. The graphs represent the average of $n=3-7$ and the error bars denote the s.e.m. The relative abundance in each individual animal is represented in a lighter colour in each of the respective graphics.

[Source data](#)

Supplementary information

Supplementary Information

This file contains Supplementary Discussion and additional references.

Reporting Summary

Supplementary Figure 1

Characterization of negatively charged *O*-glycans from porcine colonic mucins using LC–MS/MS

Supplementary Figure 2

Phylogenetic tree of S1 sulfatases in the genomes of *Bacteroides* and *Phocaeicola* type strains and *A. muciniphila*

Supplementary Figure 3

Phylogenetic tree of representative sulfatases from subfamily S1_20

Supplementary Figure 4

Phylogenetic tree of representative sulfatases from subfamily S1_4

Supplementary Figure 5

Immobilized metal affinity chromatography purification of studied sulfatases

Supplementary Figure 6

Activity profiles of purified sulfatases showing pH optima

Supplementary Figure 7

Biophysical characteristics of inactive sulfatase mutants

Peer Review File

Supplementary Table 1

Family S1 sulfatase subfamilies encoded in the genomes of different *Bacteroides* and *Phocaeicola* type strains and *Akkermansia*.

Supplementary Table 2

List of sulfated saccharides used in the initial sulfatase activity screen.

Supplementary Table 3

Sulfatase kinetics for WT and mutants against different saccharides.

Supplementary Table 4

LC-MS analysis of colonic mucin oligosaccharides (cMO). Biological replicate 1.

Supplementary Table 5

LC-MS analysis of colonic mucin oligosaccharides (cMO). Biological replicate 2.

Supplementary Table 6

Sulfatase signal peptide and localization prediction.

Supplementary Table 7

LC-MS analysis of O-glycans in culture supernatant of bt16363S-Gal mutant by LC-MS/MS.

Supplementary Table 8

Conservation of S1_20 3S-Gal/GalNAc specificity residues in *Bacteroides* and *Phocaeicola* type strains, and *Akkermansia muciniphila*.

Supplementary Table 9

Primers designed to clone *Bt* sulfatases.

Supplementary Table 10

Primers designed to generate the site-directed mutants of *Bt* sulfatases.

Supplementary Table 11

Melting temperatures of galactose targeting sulfatases with and without ligands.

Supplementary Table 12

Analysis of carbohydrate structure ligands.

Supplementary Table 13

X-ray crystallographic and refinement statistics.

Supplementary Table 14

Primers designed to generate the in-frame gene deletions and complementations of *Bt* sulfatases.

Supplementary Table 15

S1_20 homologues of BT1636^{3S-Gal}.

Supplementary Table 16

S1_20 homologues of BT1622^{3S-Gal/GalNAc}.

Source data

[**Source Data Fig. 1**](#)

[**Source Data Fig. 2**](#)

[**Source Data Fig. 4**](#)

[**Source Data Extended Data Fig. 1**](#)

[**Source Data Extended Data Fig. 3**](#)

[**Source Data Extended Data Fig. 4**](#)

[**Source Data Extended Data Fig. 5**](#)

[**Source Data Extended Data Fig. 8**](#)

Rights and permissions

[**Reprints and Permissions**](#)

About this article

Cite this article

Luis, A.S., Jin, C., Pereira, G.V. *et al.* A single sulfatase is required to access colonic mucin by a gut bacterium. *Nature* **598**, 332–337 (2021).

<https://doi.org/10.1038/s41586-021-03967-5>

- Received: 20 November 2020
- Accepted: 26 August 2021
- Published: 06 October 2021
- Issue Date: 14 October 2021
- DOI: <https://doi.org/10.1038/s41586-021-03967-5>

Share this article

Anyone you share the following link with will be able to read this content:

[Get shareable link](#)

Sorry, a shareable link is not currently available for this article.

[Copy to clipboard](#)

Provided by the Springer Nature SharedIt content-sharing initiative

This article was downloaded by **calibre** from <https://www.nature.com/articles/s41586-021-03967-5>

| [Section menu](#) | [Main menu](#) |

- Article
- [Published: 26 August 2021](#)

Burden and characteristics of COVID-19 in the United States during 2020

- [Pei Sen ORCID: orcid.org/0000-0002-7072-2995¹](#),
- [Teresa K. Yamana¹](#),
- [Sasikiran Kandula¹](#),
- [Marta Galanti ORCID: orcid.org/0000-0002-9060-1250¹](#) &
- [Jeffrey Shaman ORCID: orcid.org/0000-0002-7216-7809¹](#)

[Nature](#) volume **598**, pages 338–341 (2021)

- 27k Accesses
- 1070 Altmetric
- [Metrics details](#)

Subjects

- [Computational models](#)
- [SARS-CoV-2](#)
- [Viral infection](#)

Abstract

The COVID-19 pandemic disrupted health systems and economies throughout the world during 2020 and was particularly devastating for the United States, which experienced the highest numbers of reported cases and deaths during 2020^{1,2,3}. Many of the epidemiological features responsible for observed rates of morbidity and mortality have been reported^{4,5,6,7,8}; however, the overall burden and characteristics of COVID-19 in the United States have not been comprehensively quantified. Here we use a data-driven model-inference approach to simulate the pandemic at county-scale in the United States during 2020 and estimate critical, time-varying epidemiological properties underpinning the dynamics of the virus. The pandemic in the United States

during 2020 was characterized by national ascertainment rates that increased from 11.3% (95% credible interval (CI): 8.3–15.9%) in March to 24.5% (18.6–32.3%) during December. Population susceptibility at the end of the year was 69.0% (63.6–75.4%), indicating that about one third of the US population had been infected. Community infectious rates, the percentage of people harbouring a contagious infection, increased above 0.8% (0.6–1.0%) before the end of the year, and were as high as 2.4% in some major metropolitan areas. By contrast, the infection fatality rate fell to 0.3% by year's end.

[Download PDF](#)

Main

During 2020, the United States documented more COVID-19 cases and deaths than any other country in the world¹. The first US COVID-19 case was identified in Washington state on 20 January 2020². Over the course of the year, three pandemic waves took place: (1) a spring outbreak in select, mostly urban areas following the introduction of the virus to the United States; (2) a summer wave that predominantly affected the southern half of the country; and (3) an autumn–winter wave that remained pervasive until the spring of 2021. To understand the transmission of the virus and better control its progression in the future, it is vital that the epidemiological features that have supported these outbreaks are quantified and analysed in both space and time.

Here we use a county-resolved metapopulation model to simulate the transmission of SARS-CoV-2 within and between the 3,142 counties of the United States. The model depicts both documented and undocumented infections and is coupled with an iterative Bayesian inference algorithm—the ensemble adjustment Kalman filter—which assimilates observations of daily cases in each county, as well as population movement between counties^{9,10} ([Supplementary Information](#)). The Bayesian inference supports a fitting of the model to case observations and estimation of unobserved state variables (for example, population susceptibility within a county) and system parameters (for example, the ascertainment rate in each county). Synthetic tests indicate that the inference approach can recover key time-varying parameters across a diversity of simulation scenarios (Extended Data Fig. 1). The model fitting to observed case data captures the three waves of the outbreak as manifest at national scales (Fig. 1a), as well as in major metropolitan areas and at county scales (Extended Data Fig. 2). These inference results are robust to parameter settings and model configurations (Extended Data Figs. 3, 4, [Supplementary Information](#)).

Fig. 1: Model calibration and ascertainment rate.

 **figure1**

a, Model fitting to daily case numbers (blue dots) in the United States and the New York metropolitan area (inset). Solid and dashed lines show the median estimate and 95% CIs, respectively. **b**, Comparison between inferred percentage cumulative infections and seroprevalence in ten locations adjusted for antibody waning. The inset shows residuals of inference (inferred percentage of infected population minus adjusted seroprevalence). Centres and whiskers show medians and 95% CIs, and colour indicates the sample collection date in each location. Distributions are obtained from $n = 100$ ensemble members. Details on the serological survey are provided in [Supplementary Information](#). **c**, Distributions of estimated ascertainment rate in the United States and five metropolitan areas. The centre line shows the median, box bounds represent 25th and 75th percentiles, and whiskers show 2.5th and 97.5th percentiles. Monthly posterior estimates are presented for March to December 2020. Distributions are obtained from $n = 100$ ensemble members.

[Source data](#).

To further validate the fitting, we compared model estimates of cumulative infections to findings from US Centers for Disease Control and Prevention (CDC) seroprevalence surveys conducted at site and state levels³. The seroprevalence data, which provide an out-of-sample corroboration of the model fitting, were adjusted for the waning of antibody levels following adaptive immune response^{11,12} (Extended

Data Fig. 5, [Supplementary Information](#)). Model estimates of cumulative infected percentages are well aligned with adjusted seroprevalence estimates from the CDC 10-site survey across sites and through time (Pearson's $r = 0.97$, mean absolute error (MAE) = 1.31%) (Fig. 1b) and are similarly well matched to adjusted estimates at the state level (Extended Data Fig. 6). In addition, the seroprevalence generated using the estimated daily infections adjusted for seroreversion also matches the observed seroprevalence, and the results are robust to assumed use of a lower-sensitivity seroassay (Extended Data Fig. 6).

A critical feature of SARS-CoV-2 is its ability to infect and transmit largely from individuals who have not been diagnosed with the virus⁴. The model structure and fitting enable estimation of the ascertainment rate, the percentage of infections confirmed diagnostically, at county scales. The national population-weighted ascertainment rate averaged for all of 2020 was 21.8% (95% CI: 15.9–30.3%), similar to an estimate derived from surveys on healthcare-seeking behaviours¹³. This national ascertainment rate increased from 11.3% (8.3–15.9%) during March 2020 to 24.5% (18.6–32.3%) during December 2020 (Fig. 1c). The increase through time is a likely by-product of increasing testing capacity, a relaxation of initial restrictions on test usage, and increasing recognition, concern and care-seeking among the public. We additionally focus on five metropolitan areas in the United States. Small differences in the ascertainment rate manifest across these areas—in particular, ascertainment rates for Phoenix and Miami were higher than the national average for much of the year, whereas those for New York City, Chicago and Los Angeles were consistently below the national average.

At the national level, three pandemic waves were evident during spring, summer and autumn–winter (Fig. 1a); however, the structure differs among the five focus metropolitan areas, with New York and Chicago experiencing strong spring and autumn–winter waves but little activity during summer, Los Angeles and Phoenix undergoing summer and autumn–winter waves, and Miami experiencing all three waves (Extended Data Fig. 2). Los Angeles County, the largest county in the United States, with a population of more than 10 million people, was particularly severely affected during autumn–winter. The differences in virus activity produced different cumulative infection numbers through time (Fig. 2a). Population susceptibility at the end of the year was 69.0% (63.6–75.4%) for the United States, and among the focal metropolitan areas it ranged from 47.6% (37.2–54.8%) in Los Angeles to 73.2% (68.3–77.8%) in Phoenix. Although there is variability among counties, a substantial portion of the US population (69.0%) had not been infected by the end of 2020; however, pockets of lower population susceptibility, which are evident in the southwest and southeast on 1 August 2020 (Fig. 2b), expanded considerably by 31 December 2020 (Fig. 2c). In particular, areas of the upper Midwest and Mississippi

valley, including the Dakotas, Minnesota, Wisconsin and Iowa, are estimated to have population susceptibility below 40% as of 31 December 2020.

Fig. 2: Estimates of population susceptibility.

 figure2



a, Estimated evolution of susceptibility to COVID-19 in the United States and five metropolitan areas. Solid lines show median and the area between the dashed lines is the 95% CI. **b, c**, Estimated susceptibility in 3,142 US counties on 1 August (**b**) and 31 December (**c**) 2020. Colour shows median estimate.

Source data

The structure of the outbreak is evident in both incidence and prevalence estimates (Fig. 3, Extended Data Fig. 7). Incidence indicates the daily number of newly infectious individuals—both confirmed cases of COVID-19 and those whose infections remain undocumented. The majority of infections each month are undocumented (Fig. 3a), as indicated by the low ascertainment rates (Fig. 1c). For all of 2020, an estimated 78.2% of infections in the United States were undocumented. Estimates of daily prevalence provide a measure of the community infectious rate

(CIR), the fraction of the population currently harbouring a contagious infection. The national SARS-CoV-2 CIR was 0.77% (0.60–0.98%) on 31 December 2020, indicating that roughly 1 in 130 people was contagious (a similar percentage, 0.83% (0.52–1.26%), was estimated to be latently infected—that is, infected but not yet contagious) (Fig. 3b). Among the 5 focal metropolitan areas, the CIR varied considerably: in mid-November, Chicago reached a CIR of 1.51% (1.27–1.82%); whereas in Miami CIR increased to 1.25% (1.03–1.53%) during July. Los Angeles was even more burdened at the end of 2020, with a CIR of 2.42% (2.05–2.86%) as of 31 December 2020 (Extended Data Fig. 7).

Fig. 3: Estimated transmission and characteristics of COVID-19 in the United States.

 figure3

a, Estimated monthly total infections (blue bars) and confirmed cases (orange bars) in the United States and the New York metropolitan area (inset). Distributions are obtained from $n = 100$ ensemble members. The blue bars represent the medians and whiskers show 95% CIs. **b**, Daily confirmed cases (blue line, 7-day moving average) and estimated prevalence of contagious infections (red line, median; red dashed lines, 95% CIs) in the United States. Inset, result for the New York metropolitan area. **c**, Estimated CFR (blue lines) and IFR (red lines) in the United States and five metropolitan areas. Solid and dashed lines show median estimate and 95% CIs, respectively.

Source data

The model fitting enables estimation of the case fatality rate (CFR) and the infection fatality rate (IFR). Using public line-list data from the CDC¹⁴, we estimated the distribution of time lag from case confirmation to death for each county and, using these estimates, deconvolved observed deaths to their date of case reporting¹⁵ (Extended Data Figs. 8, 9, [Supplementary Information](#)). CFR and IFR were then generated using these deconvolved death data. Both rates were highest nationally at the beginning of the spring wave: the CFR was 7.1% (4.8–9.8%) and the IFR was 0.77% (0.51–1.25%) during April (Fig. 3c). The national cumulative IFR up to 1 June was 0.69% (0.47–1.04%), in line with previous studies^{5,6,7} (Extended Data Fig. 2, [Supplementary Information](#)). Over the course of the year, with earlier diagnosis and treatment, improved patient care^{16,17,18} and—in the case of CFR—increased reporting of mild infections, the CFR and IFR dropped to 1.29% (0.98–1.68%) and 0.31% (0.22–0.44%) by December 2020, respectively. Both rates varied by location and over time; for instance, intermediate drops of CFR and IFR began for Chicago, Phoenix and Miami during the summer wave, in association with a decrease of the average age of hospitalized patients (Extended Data Fig. 8). During the winter of 2020, the CFR and IFR in most metropolitan areas increased slightly, possibly driven by greater hospitalization rates among older individuals (Extended Data Fig. 8) and strained healthcare resources¹⁹. Overall, these findings delineate the mortality risk associated with infection broadly. The national IFR during the latter half of 2020 hovers around 0.30%, well above estimates for both seasonal influenza²⁰ (<0.08%) and the 2009 influenza pandemic²¹ (0.0076%). As COVID-19 deaths are likely to be under-reported, our estimate of IFR could be biased low.

We further examined the change of the reproduction number R_t , in response to changing local, reported COVID-19 case numbers in five US regions (Northeast, Southeast, Midwest, Southwest and West) during the spring, summer and autumn–winter ([Supplementary Information](#)). Results indicate that communities with increasing cases showed greater reductions of R_t (Extended Data Fig. 10). However, the rate of reduction in R_t decreased over successive waves. These findings are potentially driven by a number of factors modulating the reproduction number, including changing compliance with non-pharmaceutical interventions²² and seasonal modulation of virus transmissibility²³. A more thorough analysis of this preliminary finding is needed.

The United States experienced the highest numbers of confirmed COVID-19 cases and deaths in the world during 2020¹. Our findings provide quantification of the time-evolving epidemiological characteristics associated with successive pandemic waves in the United States, as well as conditions at the end of the year and prospects for

2021. Critically, despite more than 19.6 million reported cases by the end of 2020, an estimated 69% of the population remained susceptible to viral infection. Several factors will considerably alter population susceptibility in the coming months. First, ongoing transmission will infect naive hosts and continue to deplete the susceptible pool. Second, as more vaccine is distributed and administered, more individuals will be protected against symptomatic infection and the IFR will decrease. Finally, our model does not represent reinfection, either through waning immunity or immune escape; however, reinfection has been documented^{[24,25](#)}, evidence of waning antibody levels exists^{[26,27](#)}, and new variants of concern have emerged^{[28,29](#)} and will probably continue to do so. All these processes will affect population susceptibility over time and help to determine when society enters a post-pandemic phase, the pattern of endemicity the virus ultimately assumes and its long-term public health burden^{[30](#)}.

Reporting summary

Further information on research design is available in the [Nature Research Reporting Summary](#) linked to this paper.

Data availability

The human mobility and COVID-19 surveillance data that support the findings of this study are available at GitHub (https://github.com/SenPei-CU/COVID_US_2020). The county-level COVID-19 surveillance data for the United States are available at Johns Hopkins University coronavirus resource center (https://github.com/CSSEGISandData/COVID-19/tree/master/csse_covid_19_data/csse_covid_19_time_series). County-to-county commuting data were downloaded from the US Census Bureau (<https://www.census.gov/data/tables/2015/demo/metro-micro/commuting-flows-2015.html>). Human mobility data in 2020 were provided by SafeGraph (<https://safegraph.com/>), which aggregates anonymized location data from numerous applications to provide insights about physical places, via the SafeGraph Community. To enhance privacy, SafeGraph excludes census block group information if fewer than five devices visited an establishment in a month from a given census block group. We aggregated the mobility data to county level to estimate change of inter-county mobility in 2020. Aggregated and derived data are allowed to be shared publicly by SafeGraph. Seroprevalence data were published by the CDC (<https://www.cdc.gov/coronavirus/2019-ncov/cases-updates/commercial-lab-surveys.html>). The line-list datasets are available at the CDC website (<https://data.cdc.gov/Case-Surveillance/COVID-19-Case-Surveillance-Public-Use-Data/vbim-akqf> and <https://data.cdc.gov/Case-Surveillance/COVID-19-Case->

[Surveillance-Public-Use-Data-with-Ge/n8mc-b4w4](#)). [Source data](#) are provided with this paper.

Code availability

Custom code supporting this study is available at GitHub (https://github.com/SenPei-CU/COVID_US_2020).

References

1. 1.
WHO Coronavirus (COVID-19) Dashboard. *World Health Organization* <https://covid19.who.int> (2021).
2. 2.
Holshue, M. L. et al. First case of 2019 novel coronavirus in the United States. *N. Engl. J. Med.* **382**, 929–936 (2020).
3. 3.
COVID Data Tracker. *US Centers for Disease Control and Prevention* <https://covid.cdc.gov/covid-data-tracker> (2021).
4. 4.
Li, R. et al. Substantial undocumented infection facilitates the rapid dissemination of novel coronavirus (SARS-CoV-2). *Science* **368**, 489–493 (2020).
5. 5.
Brazeau, N. et al. *Report 34: COVID-19 Infection Fatality Ratio: Estimates From Seroprevalence*, <http://spiral.imperial.ac.uk/handle/10044/1/83545> (2020).
6. 6.
O'Driscoll, M. et al. Age-specific mortality and immunity patterns of SARS-CoV-2. *Nature* **590**, 140–145 (2021).
7. 7.

Meyerowitz-Katz, G. & Merone, L. A systematic review and meta-analysis of published research data on COVID-19 infection fatality rates. *Int. J. Infect. Dis.* **101**, 138–148 (2020).

8. 8.

Kalish, H. et al. Undiagnosed SARS-CoV-2 seropositivity during the first six months of the COVID-19 pandemic in the United States. *Sci. Transl. Med.* **13**, abh3826 (2021).

9. 9.

Pei, S., Kandula, S. & Shaman, J. Differential effects of intervention timing on COVID-19 spread in the United States. *Sci. Adv.* **6**, eabd6370 (2020).

10. 10.

Yamana, T., Pei, S., Kandula, S. & Shaman, J. Projection of COVID-19 cases and deaths in the US as individual states re-open May 4, 2020. Preprint at <https://doi.org/10.1101/2020.05.04.20090670> (2020).

11. 11.

Buss, L. F. et al. Three-quarters attack rate of SARS-CoV-2 in the Brazilian Amazon during a largely unmitigated epidemic. *Science* **371**, 288–292 (2021).

12. 12.

Shioda, K. et al. Estimating the cumulative incidence of SARS-CoV-2 infection and the infection fatality ratio in light of waning antibodies. *Epidemiology* **32**, 518–524 (2021).

13. 13.

Estimated Disease Burden of COVID-19. *Centers for Disease Control and Prevention* <https://www.cdc.gov/coronavirus/2019-ncov/cases-updates/burden.html> (2021).

14. 14.

COVID-19 Case Surveillance Public Use Data with Geography. *Centers for Disease Control and Prevention* <https://data.cdc.gov/Case-Surveillance/COVID-19-Case-Surveillance-Public-Use-Data-with-Ge/n8mc-b4w4> (2021).

15. 15.

Goldstein, E. et al. Reconstructing influenza incidence by deconvolution of daily mortality time series. *Proc. Natl Acad. Sci. USA* **106**, 21825–21829 (2009).

16. 16.

RECOVERY Collaborative Group Dexamethasone in hospitalized patients with Covid-19. *N. Engl. J. Med.* **384**, 693–704 (2021).

17. 17.

Horwitz, L. I. et al. Trends in COVID-19 risk-adjusted mortality rates. *J. Hosp. Med.* **16**, 90–92 (2021).

18. 18.

Beigel, J. H. et al. Remdesivir for the treatment of Covid-19—final report. *N. Engl. J. Med.* **383**, 1813–1826 (2020).

19. 19.

Lefrancq, N. et al. Evolution of outcomes for patients hospitalised during the first 9 months of the SARS-CoV-2 pandemic in France: a retrospective national surveillance data analysis. *Lancet Reg. Health Eur.* **5**, 100087 (2021).

20. 20.

Burden of influenza. *Centers for Disease Control and Prevention* <https://www.cdc.gov/flu/about/burden/index.html> (2020).

21. 21.

Riley, S. et al. Epidemiological characteristics of 2009 (H1N1) pandemic influenza based on paired sera from a longitudinal community cohort study. *PLOS Med.* **8**, e1000442 (2011).

22. 22.

Du, Z. et al. Pandemic fatigue impedes mitigation of COVID-19 in Hong Kong. *Res. Sq.* <https://doi.org/10.21203/rs.3.rs-591241/v1> (2021).

23. 23.

Ma, Y., Pei, S., Shaman, J., Dubrow, R. & Chen, K. Role of meteorological factors in the transmission of SARS-CoV-2 in the United States. *Nat. Commun.* **12**, 3602 (2021).

24. 24.

To, K. K.-W. et al. Coronavirus disease 2019 (COVID-19) re-infection by a phylogenetically distinct severe acute respiratory syndrome coronavirus 2 strain confirmed by whole genome sequencing. *Clin. Infect. Dis.* ciaa1275 (2020).

25. 25.

Tillett, R. L. et al. Genomic evidence for reinfection with SARS-CoV-2: a case study. *Lancet Infect. Dis.* **21**, 52–58 (2021).

26. 26.

Self, W. H. Decline in SARS-CoV-2 antibodies after mild infection among frontline health care personnel in a multistate hospital network—12 states, April–August 2020. *Morb. Mortal. Wkly. Rep.* **69**, 1762–1766 (2020).

27. 27.

Choe, P. G. et al. Waning antibody responses in asymptomatic and symptomatic SARS-CoV-2 infection. **27**, 327–329 (2020).

28. 28.

Fiorentini, S. et al. First detection of SARS-CoV-2 spike protein N501 mutation in Italy in August, 2020. *Lancet Infect. Dis.* **21**, s1473-3099 (2021).

29. 29.

Rambaut, A. et al. Preliminary genomic characterization of an emergent SARS-CoV-2 lineage in the UK defined by a novel set of spike mutations. *Virological* <https://virological.org/t/preliminary-genomic-characterisation-of-an-emergent-sars-cov-2-lineage-in-the-uk-defined-by-a-novel-set-of-spike-mutations/563> (2020).

30. 30.

Shaman, J. & Galanti, M. Will SARS-CoV-2 become endemic? *Science* **370**, 527–529 (2020).

Acknowledgements

This study was supported by funding from the National Science Foundation (DMS-2027369) and a gift from the Morris-Singer Foundation. We thank SafeGraph for providing human mobility data and Columbia University Mailman School of Public Health for high-performance computing resources

Author information

Affiliations

1. Department of Environmental Health Sciences, Mailman School of Public Health, Columbia University, New York, NY, USA
Pei Sen, Teresa K. Yamana, Sasikiran Kandula, Marta Galanti & Jeffrey Shaman

Contributions

S.P. and J.S. conceived the study; S.P., T.K.Y., S.K. and M.G. performed the analysis; and S.P. and J.S. drafted the manuscript. All authors revised and reviewed the manuscript.

Corresponding authors

Correspondence to Pei Sen or Jeffrey Shaman.

Ethics declarations

Competing interests

J.S. and Columbia University disclose partial ownership of SK Analytics. J.S. discloses consulting for BNI. All other authors declare no competing interests.

Additional information

Peer review information *Nature* thanks the anonymous reviewer(s) for their contribution to the peer review of this work. Peer reviewer reports are available.

Publisher's note Springer Nature remains neutral with regard to jurisdictional claims in published maps and institutional affiliations.

Extended data figures and tables

Extended Data Fig. 1 Parameter inference for simulated outbreaks.

Results are shown for three major metropolitan areas – New York, Chicago, and Los Angeles. Outbreaks were generated for 60 days using four prescribed scenarios. National daily cases are shown in the top row. Parameter estimates for the last 10 days are not displayed as there is not enough data at the end of the time series to constrain the model. Solid and dashed lines show the median estimate and 95% CIs respectively.

Extended Data Fig. 2 Model fitting and inference results.

(a) Model fitting to daily case numbers (blue dots) in the US and five metropolitan areas. Solid and dashed lines show the median estimate and 95% CIs respectively. (b) Estimated daily ascertainment rates (left column) and transmission rates (right column) for five metropolitan areas. Solid and dashed lines show the median estimate and 95% CIs respectively. (c) Reliability plot for model calibration. Data points show the coverage of the 25%, 50%, 75% and 95% CIs of the posterior fitting at county and national levels. (d) The estimated national cumulative IFR in 2020. The cumulative IFR is computed using the estimated cumulative numbers of death (deconvolved) and infections prior to a given date.

Extended Data Fig. 3 Sensitivity analyses on inference results.

(a) Inference results using fixed parameters (Z, D, μ, θ) estimated from case data prior to April 2 2020. (b) Inference results from a modified version of the transmission model in which the relative infectiousness of undocumented infections, μ , is allowed to vary over time. Fitting to case data (top two rows), estimated monthly ascertainment rate (middle two rows) and population susceptibility (bottom two rows) are shown. Distributions are obtained from $n = 100$ ensemble members. In the top two and bottom two rows, the solid line represents the median, and the dash lines show 95% CIs. In the middle two rows, centre and box bounds represent the median, 25th, and 75th percentiles, and whiskers show 2.5th and 97.5th percentiles.

Extended Data Fig. 4 Inference results from a modified version of the transmission model permitting movement of documented infections among counties.

(a) 25% of documented infections are allowed to move among counties. (b) 50% of documented infections are allowed to move among counties. Fitting to case data (top two rows), estimated monthly ascertainment rate (middle two rows) and population

susceptibility (bottom two rows) are shown. Distributions are obtained from $n = 100$ ensemble members. In the top two and bottom two rows, the solid line represents the median, and the dash lines show 95% CIs. In the middle two rows, the centre and box bounds represent the median, 25th, and 75th percentiles, and the whiskers show 2.5th and 97.5th percentiles.

[Extended Data Fig. 5 The reported \(black\) and adjusted \(red\) seroprevalence.](#)

(a) Results for the 10-site study. (b) and (c) show the results for state-level serological surveys obtained using a maximum monthly attenuation rate of 17.5% and 15%, respectively. Dots and whiskers show the median and 95% CIs respectively. Distributions are obtained from $n = 1,000$ simulated seroprevalence samples.

[Extended Data Fig. 6 Validation of inference using seroprevalence data.](#)

(a) – (b) Comparison between the inferred percentage of cumulative infections and seroprevalence at the state level adjusted for antibody waning. Seroprevalence data adjusted using a maximum monthly attenuation rate of 17.5% (a) and 15% (b) are included in the analysis. (c) – (d) Comparison between the model-generated seroprevalence and observed seroprevalence in 10 locations (c) and at the state level (d). (e) – (f) Comparison between the inferred percentage of cumulative infections and seroprevalence in 10 locations (e) and at the state level (f) adjusted for antibody waning using lower sensitivity and specificity. Distributions are obtained from $n = 100$ ensemble members. Centre and whiskers show median and 95% CIs. Color indicates the sample collection date for each location.

[Extended Data Fig. 7 Inference results in the US and five metropolitan areas.](#)

(a) Estimated monthly total infections (blue bars) and confirmed cases (orange bars) in the US and five metropolitan areas. Distributions are obtained from $n = 100$ ensemble members. The blue bars show medians and whiskers show 95% CIs. (b) Daily confirmed cases (blue line, 7-day moving average) and estimated prevalence of contagious infections (red line, median and 95% CIs) for the US and five metropolitan areas.

[Extended Data Fig. 8 Key statistics obtained from line-list data for the US and five metropolitan areas.](#)

(a) – (b) The crude monthly CFR (**a**) and HFR (**b**) obtained from line-list data for the US and five metropolitan areas. Note that due to incomplete reporting of deaths in the line-list data, these estimates are likely low. (c) – (d) The proportion of confirmed cases (**c**) and hospitalizations (**d**) in four age groups (0-17, 18-49, 50-64, 65+) in the line-list data. Data are shown monthly for the US and five metropolitan areas.

[Extended Data Fig. 9 Estimation of the time-to-event distribution from case confirmation to death for Maricopa County AZ \(a\) and Miami-Dade County FL \(c\).](#)

Deconvolution of daily deaths using the estimated delay distributions for Maricopa County AZ (**b**) and Miami-Dade County FL (**d**).

[Extended Data Fig. 10 Weekly change of \$R_t\$ in response to the change of weekly cases per 100,000 people at county level.](#)

The analysis was performed for five US regions (Northeast, Southeast, Midwest, Southwest, West) during the spring (Feb 21 – May 31), summer (Jun 1 – Sep 15), and fall/winter (Sep 16 – Dec 31) waves. In the five US regions, 116, 162, 126, 45 and 54 counties that reported cumulative cases over 100 per 100,000 people during all three waves and had a population over 100,000 were included in the analysis. A positive/negative change of weekly cases in the x-axis indicates increasing/decreasing community prevalence of COVID-19. The dash lines are the linear fits. The statistical significance of the slope is indicated by asterisks (two-sided t-test. ***: $p < 10^{-5}$, **: $p < 0.001$, *: $p < 0.05$; NS: not significant. P-values are reported in the legends).

Supplementary information

[Supplementary Information](#)

This file contains Supplementary Sections 1–8 including Supplementary Text and Data and Table 1.

[Reporting Summary](#)

[Peer Review File](#)

Source data

[Source Data Fig. 1](#)

[Source Data Fig. 2](#)

[Source Data Fig. 3](#)

Rights and permissions

[Reprints and Permissions](#)

About this article

Cite this article

Sen, P., Yamana, T.K., Kandula, S. *et al.* Burden and characteristics of COVID-19 in the United States during 2020. *Nature* **598**, 338–341 (2021).

<https://doi.org/10.1038/s41586-021-03914-4>

- Received: 15 February 2021
- Accepted: 13 August 2021
- Published: 26 August 2021
- Issue Date: 14 October 2021
- DOI: <https://doi.org/10.1038/s41586-021-03914-4>

Share this article

Anyone you share the following link with will be able to read this content:

[Get shareable link](#)

Sorry, a shareable link is not currently available for this article.

[Copy to clipboard](#)

Provided by the Springer Nature SharedIt content-sharing initiative

This article was downloaded by **calibre** from <https://www.nature.com/articles/s41586-021-03914-4>

- Article
- [Published: 31 August 2021](#)

Lectins enhance SARS-CoV-2 infection and influence neutralizing antibodies

- [Florian A. Lempp](#) [ORCID: orcid.org/0000-0001-6103-8078](#)¹,
- [Leah B. Soriaga](#) [ORCID: orcid.org/0000-0001-5852-741X](#)¹,
- [Martin Montiel-Ruiz](#) [ORCID: orcid.org/0000-0001-6200-9578](#)¹,
- [Fabio Benigni](#)²,
- [Julia Noack](#)¹,
- [Young-Jun Park](#) [ORCID: orcid.org/0000-0003-2901-6949](#)³,
- [Siro Bianchi](#) [ORCID: orcid.org/0000-0002-5100-8905](#)²,
- [Alexandra C. Walls](#) [ORCID: orcid.org/0000-0002-9636-8330](#)³,
- [John E. Bowen](#) [ORCID: orcid.org/0000-0003-3590-9727](#)³,
- [Jiayi Zhou](#) [ORCID: orcid.org/0000-0002-4231-3422](#)¹,
- [Hannah Kaiser](#) [ORCID: orcid.org/0000-0002-3991-7401](#)¹,
- [Anshu Joshi](#)³,
- [Maria Agostini](#)¹,
- [Marcel Meury](#)¹,
- [Exequiel Dellota Jr](#)¹,
- [Stefano Jaconi](#) [ORCID: orcid.org/0000-0001-7527-4434](#)²,
- [Elisabetta Cameroni](#)²,
- [Javier Martinez-Picado](#) [ORCID: orcid.org/0000-0002-4916-2129](#)^{4,5,6},
- [Júlia Vergara-Alert](#)⁷,
- [Nuria Izquierdo-Useros](#)^{4,8},
- [Herbert W. Virgin](#) [ORCID: orcid.org/0000-0001-8580-7628](#)^{1,9,10},
- [Antonio Lanzavecchia](#) [ORCID: orcid.org/0000-0002-3041-7240](#)²,
- [David Veesler](#) [ORCID: orcid.org/0000-0002-6019-8675](#)³,
- [Lisa A. Purcell](#)¹¹,
- [Amalio Telenti](#) [ORCID: orcid.org/0000-0001-6290-7677](#)¹ na1 &
- [Davide Corti](#) [ORCID: orcid.org/0000-0002-5797-1364](#)² na1

[Nature](#) volume **598**, pages 342–347 (2021)

- 29k Accesses

- 159 Altmetric
- [Metrics details](#)

Subjects

- [Antibodies](#)
- [SARS-CoV-2](#)
- [Viral infection](#)

Abstract

SARS-CoV-2 infection—which involves both cell attachment and membrane fusion—relies on the angiotensin-converting enzyme 2 (ACE2) receptor, which is paradoxically found at low levels in the respiratory tract^{1,2,3}, suggesting that there may be additional mechanisms facilitating infection. Here we show that C-type lectin receptors, DC-SIGN, L-SIGN and the sialic acid–binding immunoglobulin-like lectin 1 (SIGLEC1) function as attachment receptors by enhancing ACE2-mediated infection and modulating the neutralizing activity of different classes of spike-specific antibodies. Antibodies to the amino-terminal domain or to the conserved site at the base of the receptor-binding domain, while poorly neutralizing infection of ACE2-overexpressing cells, effectively block lectin-facilitated infection. Conversely, antibodies to the receptor binding motif, while potently neutralizing infection of ACE2-overexpressing cells, poorly neutralize infection of cells expressing DC-SIGN or L-SIGN and trigger fusogenic rearrangement of the spike, promoting cell-to-cell fusion. Collectively, these findings identify a lectin-dependent pathway that enhances ACE2-dependent infection by SARS-CoV-2 and reveal distinct mechanisms of neutralization by different classes of spike-specific antibodies.

[Download PDF](#)

Main

SARS-CoV-2 infects target cells via the spike (S) glycoprotein, which is organized as a homotrimer with each monomer comprising S1 and S2 subunits⁴. The infection process includes binding to cells, triggering of conformational changes in S and then fusion of the viral envelope with the target cell membrane. The S1 subunit of S comprises the N-terminal domain (NTD) and the receptor binding domain (RBD). The RBD interacts with ACE2 through a region defined as the receptor binding motif (RBM). Antibodies against the RBD contribute the majority of the neutralizing activity of polyclonal serum antibodies^{5,6}, potently neutralize SARS-CoV-2 in vitro^{7,8}.

and have shown efficacy in clinical trials for prophylaxis and early therapy of COVID-19^{9,10}.

The search for SARS-CoV-2-neutralizing antibodies has been facilitated by the use of target cells overexpressing the ACE2 receptor¹¹. However, ACE2 expression in the lower respiratory tract is limited, with low levels found in only a small number of type II alveolar basal, goblet and mucous cells^{1,2,3}. The paradox of low ACE2 levels in the lung and infection in other tissues leading to extrapulmonary complications¹² raises the possibility that additional receptors may contribute to viral infection and dissemination, such as DC-SIGN (also known as CD209), L-SIGN (also known as CD209L or CLEC4M), neuropilin-1 (NRP-1), basigin (also known as CD147) or heparan sulfate^{13,14,15,16,17}. It remains to be established whether these molecules act as alternative primary receptors for viral entry, as co-receptors or as attachment receptors that tether viral particles, enhancing their interaction with ACE2.

In this study, we identify DC-SIGN, L-SIGN and SIGLEC1 (also known as CD169, sialoadhesin or Siglec-1) as attachment receptors that enhance ACE2-dependent infection and demonstrate different mechanisms of neutralization by antibodies targeting RBM and non-RBM sites in the presence or absence of lectins.

Lectins are attachment receptors for SARS-CoV-2

To develop an assay for identification of attachment receptors of SARS-CoV-2 infection, we used HEK 293T cells that express low endogenous levels of ACE2. HEK 293T cells were transfected with vectors encoding ACE2 or one of 13 selected lectins and published receptor candidates before infection with vesicular stomatitis virus (VSV) SARS-CoV-2 pseudovirus. Untransfected HEK 293T cells were only weakly permissive to infection, and ACE2 overexpression led to a marked increase in pseudovirus entry. Increased infectivity was also observed in HEK 293T cells following transfection with C-type lectins DC-SIGN and L-SIGN, which were previously reported to be entry receptors^{13,14,18}, as well as with SIGLEC1, which was not previously shown to mediate SARS-CoV-2 entry (Fig. 1a). NRP-1 and CD147 did not enhance SARS-CoV-2 infection in these conditions, although they have been suggested to act as entry receptors^{15,16}. The infection-enhancing activity of the three lectins was also observed with authentic SARS-CoV-2 on cell lines stably expressing these factors (Fig. 1b, Extended Data Fig. 1a-d). A SIGLEC1-blocking antibody inhibited infection of SIGLEC1-expressing HEK 293T cells, supporting a role of this molecule as a SARS-CoV-2 co-factor (Fig. 1c).

Fig. 1: DC-SIGN, L-SIGN and SIGLEC1 function as attachment receptors for SARS-CoV-2 infection.

 **figure1**

a, VSV-SARS-CoV-2 infection of HEK 293T cells transfected to express ACE2 or a panel of selected lectins or candidate receptors ($n = 4$ biologically independent replicates). RLU, relative luminescence units. **b**, Stable cell lines were infected with SARS-CoV-2-Nluc and luciferase levels were quantified at 24 h ($n = 6$). **c**, Inhibition of SARS-CoV-2-Nluc infection with anti-SIGLEC1 monoclonal antibody (clone 7-239) ($n = 3$). **d**, Indicated cell lines were transduced to express lectins or ACE2 and infected with VSV-SARS-CoV-2 ($n = 8$). **e**, Effect of ACE2 siRNA transfection on infection with VSV-SARS-CoV-2 ($n = 8$).

The ectopic expression of DC-SIGN, L-SIGN and SIGLEC1 did not support infection of ACE2-negative cells, such as HeLa or MRC-5 cells (Fig. 1d), indicating that these lectins do not act as primary entry receptors. The requirement of ACE2 for viral infection of lectin-expressing cells was also demonstrated using ACE2-blocking antibodies or ACE2 small interfering RNA (siRNA) (Fig. 1e, Extended Data Fig. 1e).

Collectively, these data reveal a lectin-facilitated pathway of infection that is evident in cells expressing low levels of ACE2, supporting the notion that SARS-CoV-2 may use these lectins as attachment receptors to tether viral particles, thereby facilitating interaction with ACE2.

Attachment receptors facilitate *trans* infection

Interaction with ACE2 could take place in *cis* or in *trans*, as reported for HIV-1¹⁹. To address whether ACE2 and lectins can be found on the same cells (that is, in *cis*), we interrogated the lung cell atlas²⁰ (Extended Data Fig. 2a). DC-SIGN is expressed most prominently on IGSF21⁺ dendritic cells, L-SIGN has a limited expression on vascular structures and SIGLEC1 is broadly expressed at the surface of alveolar macrophages, dendritic cells and monocytes. ACE2 expression is limited to subsets of alveolar epithelial type-2, basal and goblet cells. We then mined single-cell transcriptomic data on 3,085 lung epithelial and immune cells obtained from bronchoalveolar lavage (BAL) fluid or sputum of individuals who suffered from severe COVID-19²¹. The distribution of viral RNA per cell varied across annotated cell types. Specifically, the content of viral RNA in macrophages was greater relative to secretory cells ($P < 2.2 \times 10^{-16}$) (Extended Data Fig. 2b). SIGLEC1 was expressed in 41.4% (459 out of 1,107 cells) of SARS-CoV-2⁺ macrophages, whereas ACE2 expression was negligible in these cells (Fig. 2a). Conversely, ACE2 expression was found in 10.6% (60 out of 565 cells) of SARS-CoV-2⁺ secretory cells, whereas SIGLEC1 expression was negligible. In the full dataset (including cells from BAL or sputum without detectable SARS-CoV-2), 1,037 cells were annotated as dendritic cells (DCs), out of which 349 (34.6%) were SIGLEC1⁺ (34.6%). In total, 19 out of 1,037 DCs (less than 2%) had detectable SARS-CoV-2, of which 47% (9 out of 19) exhibited detectable SIGLEC1 expression. Plotting SIGLEC1, DC-SIGN and L-SIGN expression as a function of SARS-CoV-2 viral load revealed a strong positive correlation for SIGLEC1 in macrophages (Fig. 2a). We confirmed this association in a separate transcriptomic dataset of 1,072 SARS-CoV-2⁺ BAL cells from individuals with severe COVID-19²². We inspected the available sequenced reads from this dataset to assess the nature of viral RNA in SARS-CoV-2⁺ BAL cells. Minimal viral replication was occurring in this cell population comprising largely of macrophages and other non-epithelial cell types.

Fig. 2: Expression of attachment receptors in infected tissues and their role in mediating *trans* infection.

 **figure2**

a, Left, heat map matrix showing counts of cells with detected transcripts for receptor gene(s) (x-axis) by SARS-CoV-2⁺ cell type (y-axis) ($n = 3,085$ cells; total number of each cell type in parentheses). Right, correlation of receptor transcript counts with SARS-CoV-2 RNA counts in macrophages and secretory cells (transcript-positive cells shown as fraction of total number of cells of that type). Two-sided correlation test is based on counts (before log transformation) from Ren et al. [21](#). NK, natural killer cells. CPM, counts per million transcripts; NA, not applicable. **b**, HeLa cells (grey) transduced with lectins (red) were incubated with VSV-SARS-CoV-2 (blue), washed and co-cultured with VeroE6-TMPRSS2 target cells. Infection (RLU) was assayed in the presence or absence of target cells (purple) ($n = 16$ biologically independent replicates). **c**, *Trans* infection performed as in **b**. Viral adsorption was performed in the presence of an anti-SIGLEC1 antibody ($n = 10$). **d**, Transmission of replication-competent SARS-CoV-2 by lipopolysaccharide (LPS)-activated DCs to susceptible target cells. Cells were pre-incubated with the indicated monoclonal antibodies, exposed to SARS-CoV-2, washed and incubated with indicated target HEK 293T cells. *Trans* infection was measured six days later as viral release in the supernatant. GM-CSF, granulocyte-macrophage colony-stimulating factor; hPBMCs, human peripheral blood mononuclear cells. Data are mean \pm s.d. from two independent experiments including cells from five donors. Two-sided paired *t*-test.

The above results suggest limited cooperation of ACE2 and SIGLEC1 in *cis*, because these receptors are rarely expressed in the same cell, suggesting a role for *trans* infection from SIGLEC1⁺ myeloid antigen presenting cells to ACE2⁺ cells. Indeed, lectin-transduced HeLa cells showed enhanced capacity to promote VSV-SARS-CoV-2 *trans* infection of susceptible Vero E6-TMPRSS2 target cells (Fig. [2b](#)), and

SIGLEC1-mediated *trans* infection was inhibited by SIGLEC1-blocking antibodies (Fig. 2c, Extended Data Fig. 2c).

Next, we evaluated viral attachment and *trans* infection in primary myeloid cells using replication-competent SARS-CoV-2. Lectins are expressed mostly on antigen-presenting cells such as macrophages, DCs and monocytes, and their expression can be upregulated by innate inflammatory stimuli such as interferons¹⁹. While both macrophages and DCs are able to take up SARS-CoV-2 via SIGLEC1²³, macrophages mostly release inflammatory cytokines upon viral sensing^{23,24}. Here we demonstrate that SIGLEC1 acts as a key factor in the *trans* infection of susceptible cells from primary DCs. In particular, we found that primary activated DCs cannot be productively infected but can mediate SARS-CoV-2 infection of target cells expressing ACE2 and TMPRSS2, and that this infection was reduced in the presence of an anti-SIGLEC1 antibody (Fig. 2d). In vivo, the *trans* infection mediated by SIGLEC1 could be relevant once inflammatory DCs migrate to pulmonary tissues upon SARS-CoV-2 infection and could help to spread infection in the lung and to distant tissues. These results are consistent with a role of lectins in dissemination of SARS-CoV-2.

Overexpression of ACE2 impairs neutralization

To investigate how ACE2 and attachment receptor expression levels influence neutralizing activity, we compared three monoclonal antibodies targeting distinct sites on the S protein: (1) S2E12, targeting the RBM site Ia/class 1 in the RBD⁷; (2) S309, targeting the conserved N-glycan-containing site IV/class 3 distal from RBM²⁵; and (3) S2X333, targeting site i in the NTD²⁶ (Fig. 3a). These monoclonal antibodies completely neutralize infection of Vero E6 cells with authentic SARS-CoV-2, albeit with different potencies, and their activity was not influenced by the expression of the TMPRSS2 protease (Extended Data Fig. 3a, b). To understand the influence of receptor expression on neutralization, we used cell lines expressing ACE2 and TMPRSS2 (endogenously or upon transduction) at levels varying more than 1,000-fold (Fig. 3b, Extended Data Fig. 3c, d). Whereas the RBM monoclonal antibody S2E12 showed comparable neutralizing activity on all target cells, both S309 and S2X333 showed impaired neutralizing activity when tested on cells overexpressing ACE2, in terms of both maximal neutralization and potency (Fig. 3c, d). Similar results were obtained with both VSV-SARS-CoV-2 and authentic SARS-CoV-2-Nluc, a nanoluciferase-expressing infectious SARS-CoV-2 clone. Overall, a negative correlation was found between ACE2 levels and neutralization potency for non-RBM monoclonal antibodies (Extended Data Fig. 3e).

Fig. 3: ACE2 overexpression influences neutralization by different classes of monoclonal antibodies.

 **figure3**

a, Surface rendering of a composite model of SARS-CoV-2 S bound to S309 (purple), S2E12 (magenta) and S2X333 (orange)^{7,25,26}. The three SARS-CoV-2 S protomers are coloured light blue, gold and pink with *N*-linked glycans rendered dark blue. **b**, SARS-CoV-2 S or RBD binding to the indicated cell lines was quantified by flow cytometry. A, ACE2; T, TMPRSS2. Graph shows mean of two biological replicates. MFI, mean fluorescence intensity. **c**, **d**, A panel of seven cell lines was infected with SARS-CoV-2-Nluc (**c**) or VSV-SARS-CoV-2 pseudovirus (**d**) in the presence of S309, S2E12 or S2X333. Luciferase signals were quantified 24 h after infection ($n = 3$ biologically independent replicates).

Given this uncertainty in the most relevant in vitro correlates of protection, we investigated the capacity of hamsterized S309 and S2E12 monoclonal antibodies to prevent SARS-CoV-2 infection in Syrian hamsters, an animal model that relies on endogenous expression of ACE2²⁷. In a prophylactic setting, S309 was highly effective at doses as low as 0.4 mg kg^{-1} in terms of reduction of viral RNA and infectious virus levels and histopathological score in the lungs (Extended Data Fig. 4a). Furthermore, we did not observe substantial increased efficacy by co-administering S309 with an equal amount of the potent RBM S2E12 monoclonal antibody (Extended Data Fig. 4b). An ‘Fc-silenced’ version of hamsterized S309 monoclonal antibody (GH-S309-N297A) (Extended Data Fig. 5) was similarly protective against SARS-CoV-2 challenge of hamsters, underscoring that the neutralizing activity of S309 was the primary mechanism of action in this condition.

Together, these data indicate that neutralization assays using cells overexpressing ACE2 underestimate the neutralizing activity of non-RBM monoclonal antibodies, which are similarly protective in a relevant animal model of infection to RBM monoclonal antibodies²⁸. The importance of this finding is also supported by the efficacy data of VIR-7831 (a derivative monoclonal antibody of S309) in a phase 3 clinical trial demonstrating 85% protection against hospitalization and death due to COVID-19²⁹.

Antibody-mediated membrane fusion

Infection of permissive cells involves both interactions with ACE2 and attachment receptors as well as fusion of the viral membrane to cellular membranes. We investigated how different classes of S-specific antibodies may interfere with viral fusion events that are involved in viral entry, but also in cell-to-cell fusion, leading to the formation of syncytia in vitro³⁰ and multi nucleate giant cells in human lung from infected individuals³¹. RBM-specific SARS-CoV neutralizing monoclonal antibodies can act as ACE2 mimics, triggering the fusogenic rearrangement of the S protein³². We evaluated monoclonal antibodies of different epitope specificity (Extended Data Table 1) to induce fusogenic rearrangement of soluble S trimers as measured by negative-stain electron microscopy imaging using Fab fragments of the respective monoclonal antibodies (Extended Data Fig. 6a). Five RBM monoclonal antibodies triggered rearrangement to the post-fusion state of a native SARS-CoV-2 S ectodomain trimer, probably owing to conformational selection of open RBDs. Most of these monoclonal antibodies triggered a rapid rearrangement of S, whereas S2D106 did so more slowly. As expected, S2M11, a RBM monoclonal antibody that locks neighbouring RBDs in a closed state⁷, did not induce fusogenic S rearrangements. Antibodies to NTD (S2X333), to site Ib on RBD (REGN10987 and LyCoV555) or to the *N*-glycan-containing site at the base of RBD (S309) also did not trigger rearrangement, owing to the absence of conformational selection for open RBDs.

To investigate whether the antibody-mediated triggering of fusogenic rearrangement could promote membrane fusion, we evaluated a panel of monoclonal antibodies for their capacity to induce cell–cell fusion of CHO cells (which lack ACE2 expression) stably transduced with full-length SARS-CoV-2 S. Syncytia formation was triggered by all monoclonal antibodies recognizing antigenic sites Ia and IIa (Extended Data Table 1), which are accessible only in the open RBD state, with half-maximum effective concentration (EC_{50}) values ranging from 20 ng ml^{−1} for S2E12 to more than 1 µg ml^{−1} for S2D106 (Extended Data Fig. 6b–d). Syncytia were also formed by the three clinical-stage monoclonal antibodies: REGN10933 (casirivimab), Ly-CoV016 (etesevimab) and CT-P59 (regdanvimab). By contrast, syncytia were not formed in the presence of monoclonal antibodies binding to the open and closed RBD states (S2M11, S309, Ly-CoV555 (bamlanivimab) and REGN10987 (imdevimab)), to the NTD (S2X333) or to a conserved site in the S2 subunit stem helix (S2P6)³³. A notable exception is provided by S2X58³⁴, a monoclonal antibody that was structurally defined in this study as binding to site Ib, which is accessible on open and closed RBDs (Extended Data Fig. 7). Of note, syncytia were also formed when using S2E12 Fab, indicating that cell–cell fusion does not result solely from cross-linking of S expressed on opposing cells (Extended Data Fig. 6g). Regarding the possible interaction between fusogenic and non-fusogenic antibodies, we found that syncytia

formation induced by S2E12 could be inhibited by different classes of antibodies comprising S2M11 (which locks RBDs in a closed state), S309 (which targets an *N*-glycan-containing site at the base of RBD) and S2P6 (which destabilizes the stem helix in S2) (Extended Data Fig. [6e](#)). These results highlight that different combinations of antibodies may interfere with each other by promoting or inhibiting membrane fusion.

To address whether antibodies may promote cell-to-cell spread of the infection, we co-cultured S-positive CHO cells with S-negative fluorescently labelled CHO cells. In these conditions, S2E12 promoted unidirectional fusion of S-positive CHO cells with S-negative CHO cells in the absence of ACE2 (defined here as '*trans* fusion') (Extended Data Fig. [6f](#)). To address whether this mechanism may also mediate ACE2-independent infection of tethered virus, we infected HeLa-DC-SIGN cells with live SARS-CoV-2-Nluc virus in the presence of fusion-enhancing monoclonal antibodies at different dilutions. In these conditions, S2E12, S2D106 and S2X58 did not promote infection (Extended Data Fig. [8a](#)). Collectively, these findings indicate that in certain conditions of antibody concentration and cell–cell proximity, a subclass of RBM antibodies selective for the open conformation of RBD may promote cell–cell fusion with ACE2-negative cells. However, the fusogenic activity of these monoclonal antibodies may not be sufficient to promote entry of virions tethered to the cell surface in the absence of ACE2. It remains to be established whether RBM monoclonal antibodies may mediate ACE2-independent SARS-CoV-2 entry under other conditions, as previously observed for anti-MERS-CoV neutralizing monoclonal antibodies captured by Fc γ RIIa-expressing cells *in vitro*[35](#).

Lectin receptors modulate neutralization

Given the dual function of certain RBM antibodies in inhibiting ACE2 binding and triggering fusion and the dependence on attachment receptor expression of neutralization by specific antibodies, we compared the neutralizing activity of a panel of monoclonal antibodies using authentic SARS-CoV-2 and target cells expressing different levels of ACE2 and lectin receptors. When tested on cells overexpressing ACE2, all anti-RBM monoclonal antibodies potently neutralized infection, whereas the non-RBM monoclonal antibodies S309 and S2X333 did not (Figs. [3](#), [4a, d](#)). However, when tested on cells expressing low levels of ACE2 together with SIGLEC1, DC-SIGN or L-SIGN, S309 and S2X333 showed enhanced neutralizing activity, with S309 reaching 100% of neutralization. Of note, while all RBM monoclonal antibodies retained neutralizing activity on SIGLEC1⁺ cells, several RBM monoclonal antibodies (S2D106, S2X58, REGN10987, REGN10933 and LyCoV555) lost neutralizing activity on cells expressing DC-SIGN or L-SIGN, showing only partial neutralization at the highest concentrations tested (Fig. [4b, c, e, f](#), Extended Data Fig. [8c–e](#)). The loss of neutralizing activity of S2X58 and S2D106 monoclonal

antibodies observed on DC-SIGN- and L-SIGN-expressing cells was confirmed with both replication-competent SARS-CoV-2 (wild type), as well as with live SARS-CoV-2-Nluc (Extended Data Fig. 8d). However, all neutralizing monoclonal antibodies blocked *trans* infection of Vero-E6-TMPRSS2 target cells from HeLa cells expressing either DC-SIGN or SIGLEC1 (Extended Data Fig. 9). Together, these data delineate a complex pattern of neutralization of *cis* or *trans* viral infection by different classes of monoclonal antibodies whereby the epitope specificity, valency of binding and the ability to trigger fusogenic rearrangement can result in differential blocking efficiency.

Fig. 4: SIGLEC1, DC-SIGN and L-SIGN modulate neutralization by different classes of antibodies.



a–f, Neutralization of infection with SARS-CoV-2-Nluc pre-incubated with indicated monoclonal antibodies on HEK 293T cell lines stably overexpressing lectins or ACE2. Infection was measured by luciferase signal 24 h after infection ($n = 3$ biologically independent replicates).

Discussion

We have shown that transmembrane lectins act as attachment receptors rather than entry receptors for SARS-CoV-2^{13,14}, thus facilitating infection via the canonical ACE2 pathway. This finding addresses the efficiency of lower respiratory tract infection despite the paradoxically low level of ACE2 expression, even in the presence

of interferon^{36,37}. The attachment role of lectins in SARS-CoV-2 infection is in line with the known biology of these adhesion molecules, which bind *N*-glycans characteristic of cellular membranes and pathogen surfaces to promote *trans* infection³⁸. SIGLEC1 is of particular relevance because it is prominent in lung myeloid cells in association with viral RNA, thus supporting a model of *trans* infection, tissue dissemination and the triggering of immune responses by myeloid cells, rather than these cells being a direct target for productive infection³⁹. Animal models also support a role of attachment receptors in viral pathogenesis^{40,41}.

Expression of lectin receptors influences the neutralizing activity of different classes of S-specific monoclonal antibodies. In addition, we have observed that various monoclonal antibodies have the ability to interfere with fusion events. We have expanded our initial observation on SARS-CoV and MERS-CoV^{32,35} by showing that most RBM monoclonal antibodies can trigger the fusogenic rearrangement of S, albeit with varying efficiency. By stabilizing the RBDs in the open conformations, these antibodies might act as receptor mimics. This finding suggests that premature conformational triggering resulting in loss of the potential of a S protein to engender productive infection—we term this mechanism spike inactivation—may be the prominent mode of viral neutralization for this class of antibodies. However, we have also shown that these antibodies can promote fusion of S-expressing cells with neighbouring cells, even if the neighbouring cells lack ACE2. These data are consistent with a recent study reporting that a subset of RBM monoclonal antibodies can enhance S-mediated membrane fusion and formation of syncytia⁴². Notably, the formation of syncytia has been observed in authoptic samples from severe cases of COVID-19^{31,43,44}. It is tempting to speculate that fusogenic antibodies, although highly effective^{9,10}, may contribute at a later stage to the spread of infection and inflammation.

Overall, our study highlights the finding that ranking of SARS-CoV-2-neutralizing antibodies is highly dependent on the level of ACE2 expression and on the presence of attachment receptors and identifies a mechanism that could result in the creation of multinucleate viral factories, potentially enhanced by specific antibodies.

Methods

Ethics statement

The institutional review board on biomedical research of the Hospital Germans Trias i Pujol (HUGTiP) approved this study. The biologic biosafety committee of the Research Institute Germans Trias i Pujol approved the execution of SARS-CoV-2

experiments at the BSL3 laboratory of the Center of Bioimaging and comparative imaging (CMCIB).

Generation of stable overexpression cell lines

Lentiviruses were generated by co-transfection of Lenti-X 293T cells (Takara) with lentiviral expression plasmids encoding DC-SIGN (CD209), L-SIGN (CLEC4M), SIGLEC1, TMPRSS2 or ACE2 (all obtained from Genecopoeia) and the respective lentiviral helper plasmids. Forty-eight hours after transfection, lentivirus in the supernatant was collected and concentrated by ultracentrifugation for 2 h at 20,000 rpm. Lenti-X 293T (Takara), Vero E6 (ATCC), MRC5 (Sigma-Aldrich), A549 (ATCC) or HeLa (ATCC) cells were transduced in the presence of $6 \mu\text{g ml}^{-1}$ polybrene (Millipore) for 24 h. Cell lines overexpressing two transgenes were transduced subsequently. Selection with puromycin and/or blasticidin (Gibco) was started two days after transduction and selection reagent was kept in the growth medium for all subsequent culturing. Single-cell clones were derived from the A549-ACE2-TMPRSS2 cell line, all other cell lines represent cell pools.

SARS-CoV-2 neutralization

Cells cultured in DMEM supplemented with 10% FBS (VWR) and 1× Penicillin/Streptomycin (Thermo Fisher Scientific) were seeded in black 96-well plates at 20,000 cells per well. Serial 1:4 dilutions of the monoclonal antibodies were incubated with 200 pfu of SARS-CoV-2 (isolate USA-WA1/2020, passage 3, passaged in Vero E6 cells) for 30 min at 37 °C in a BSL-3 facility. Cell supernatant was removed and the virus–antibody mixture was added to the cells. Twenty-four hours after infection, cells were fixed with 4% paraformaldehyde for 30 min, followed by two PBS (pH 7.4) washes and permeabilization with 0.25% Triton X-100 in PBS for 30 min. After blocking in 5% milk powder/PBS for 30 min, cells were incubated with a primary antibody targeting SARS-CoV-2 nucleocapsid protein (Sino Biological, catalogue (cat.) no. 40143-R001) at a 1:2,000 dilution for 1 h. After washing and incubation with a secondary Alexa Fluor 647-labelled antibody mixed with $1 \mu\text{g ml}^{-1}$ Hoechst33342 for 1 h, plates were imaged on an automated cell-imaging reader (Cytation 5, Biotek) and nucleocapsid-positive cells were counted using the manufacturer's supplied software (Gen5 v3.08).

SARS-CoV-2-Nluc neutralization

Neutralization was determined using SARS-CoV-2-Nluc, an infectious clone of SARS-CoV-2 (based on strain 2019-nCoV/USA_WA1/2020) encoding nanoluciferase in place of the viral ORF7, which demonstrates comparable growth kinetics to wild type virus⁴⁵. Cells were seeded into black-walled, clear-bottom 96-well plates at

20,000 cells per well (293T cells were seeded into poly-l-lysine-coated wells at 35,000 cells per well) and cultured overnight at 37 °C. The next day, 9-point fourfold serial dilutions of antibodies were prepared in infection medium (DMEM + 10% FBS). SARS-CoV-2-Nluc was diluted in infection medium at the indicated multiplicity of infection (MOI), added to the antibody dilutions and incubated for 30 min at 37 °C. Medium was removed from the cells, monoclonal antibody–virus complexes were added, and cells were incubated at 37 °C for 24 h. Medium was removed from the cells, Nano-Glo luciferase substrate (Promega) was added according to the manufacturer’s recommendations, incubated for 10 min at room temperature and luciferase signal was quantified on a VICTOR Nivo plate reader using Nivo v3.0.2 software (Perkin Elmer).

SARS-CoV-2 pseudotyped VSV production and neutralization

To generate SARS-CoV-2 pseudotyped VSV, Lenti-X 293T cells (Takara) were seeded in 10-cm dishes for 80% next day confluence. The next day, cells were transfected with a plasmid encoding for SARS-CoV-2 S-glycoprotein (YP_009724390.1) harbouring a C-terminal 19-amino acid truncation using TransIT-Lenti (Mirus Bio) according to the manufacturer’s instructions. One day after transfection, cells were infected with VSV(G*ΔG-luciferase) (Kerafast) at an MOI of 3 infectious units per cell. Viral inoculum was washed off after 1 h and cells were incubated for another day at 37 °C. The cell supernatant containing SARS-CoV-2 pseudotyped VSV was collected at day 2 after transfection, centrifuged at 1,000g for 5 min to remove cellular debris, aliquoted and frozen at –80 °C.

For viral neutralization, cells were seeded into black-walled, clear-bottom 96-well plates at 20,000 cells per well (293T cells were seeded into poly-l-lysine-coated wells at 35,000 cells per well) and cultured overnight at 37 °C. The next day, 9-point fourfold serial dilutions of antibodies were prepared in medium. SARS-CoV-2 pseudotyped VSV was diluted 1:30 in media in the presence of 100 ng ml⁻¹ anti-VSV-G antibody (clone 8G5F11, Absolute Antibody) and added 1:1 to each antibody dilution. Virus:antibody mixtures were incubated for 1 h at 37 °C. Media was removed from the cells and 50 µl of virus:antibody mixtures were added to the cells. One hour post-infection, 100 µl of medium was added to all wells and incubated for 17–20 h at 37 °C. Medium was removed and 50 µl of Bio-Glo reagent (Promega) was added to each well. The plate was shaken on a plate shaker at 300 rpm at room temperature for 15 min and RLU^s were read on an EnSight plate reader using Kaleido v3.0 software (Perkin-Elmer).

Transfection-based attachment receptor screen

Lenti-X 293T cells (Takara) were transfected with plasmids encoding the following receptor candidates (all purchased from Genecopoeia): ACE2 (NM_021804), DC-SIGN (NM_021155), L-SIGN (BC110614), LGALS3 (NM_002306), SIGLEC1 (NM_023068), SIGLEC3 (XM_057602), SIGLEC9 (BC035365), SIGLEC10 (NM_033130), MGL (NM_182906), MINCLE (NM_014358), CD147 (NM_198589), ASGR1 (NM_001671.4), ASGR2 (NM_080913), NRP1 (NM_003873). One day after transfection, cells were infected with SARS-CoV-2 pseudotyped VSV at 1:20 dilution in the presence of 100 ng ml⁻¹ anti-VSV-G antibody (clone 8G5F11, Absolute Antibody) at 37 °C. One hour after infection, 100 µl of medium was added to all wells and incubated for 17–20 h at 37 °C. Medium was removed and 50 µl of Bio-Glo reagent (Promega) was added to each well. The plate was shaken on a plate shaker at 300 rpm at room temperature for 15 min and readings in RLU were taken on an EnSight plate reader (Perkin-Elmer).

siRNA-mediated knockdown of ACE2

For reverse transfection of 293T or HuH7 cells, siRNA pools specific for ACE2 (Dharmacon ON-TARGETplus SMARTpool, L-005755-00-0005, pool of 4 individual siRNAs with target sequences: GACAAGAGCAAACGGUUGA, GCGAGUGGCUAUUUGAAA, GCCAUUAUAUGAAGAGUAU, GGACAAGUUUAACCACGAA) or non-targeting control pool (Dharmacon ON-TARGETplus Non-targeting Pool, D-001810-10-05) were preincubated at 20 nM with Lipofectamine RNAiMAX (Thermo Fisher Scientific) in black-walled clear-bottom 96-well plates according to the manufacturer's instructions. Fifteen-thousand 293T cells or 10,000 HuH7 cells were seeded on top and incubated at 37 °C. After four days, cells were infected with SARS-CoV-2 pseudotyped VSV as described above.

***Trans* infection using HeLa cells**

Parental HeLa cells or HeLa cells stably expressing DC-SIGN, L-SIGN or SIGLEC1 were seeded at 5,000 cells per well in black-walled clear-bottom 96-well plates. One day later, cells reached about 50% confluence and were inoculated with SARS-CoV-2 pseudotyped VSV at 1:10 dilution in the presence of 100 ng/mL anti-VSV-G antibody (clone 8G5F11, Absolute Antibody) at 37 °C for 2 h. For antibody-mediated inhibition of *trans* infection, cells were pre-incubated with 10 µg ml⁻¹ anti-SIGLEC1 antibody (Biologend, clone 7-239) for 30 min. After 2 h inoculation, cells were washed 4 times with complete medium and 10,000 VeroE6-TMPRSS2 cells per well were added and incubated for 17–20 h at 37 °C for *trans* infection. Medium was removed and 50 µl of Bio-Glo reagent (Promega) was added to each well. The plate was shaken on a plate shaker at 300 rpm at room temperature for 15 min and RLU were read on an EnSight plate reader using Kaleido v3.0 software (Perkin-Elmer).

Cell–cell fusion of CHO-S cells

CHO cells stably expressing SARS-CoV-2 S-glycoprotein were seeded in 96-well plates for microscopy (Thermo Fisher Scientific) at 12,500 cells per well and the following day, different concentrations of monoclonal antibodies and nuclei marker Hoechst (final dilution 1:1,000) were added to the cells and incubated for additional 24 h. Fusion degree was established using the Cytation 5 Imager (BioTek) and an object detection protocol was used to detect nuclei as objects and measure their size. The nuclei of fused cells (that is, syncytia) are found aggregated at the centre of the syncytia and are recognized as a unique large object that is gated according to its size. The area of the objects in fused cells divided by the total area of all the object multiplied by 100 provides the percentage of fused cells

Negative-stain electron microscopy imaging the fusogenic rearrangement of soluble S trimers

SARS-CoV-2 S ectodomain trimer was engineered as follow and recombinantly expressed. The SARS-CoV-2 S(D614G) has a mu-phosphatase signal peptide beginning at Q14, a mutated S1/S2 cleavage site (SGAR), ends at residue K1211 and is followed by a TEV cleavage, fold-on trimerization motif, and an 8× His tag in the pCMV vector. Ten micromolar S was incubated with 13 μM Fab protein for 1 or 48 h at room temperature. Samples were diluted to 0.01 mg ml⁻¹ immediately before protein was adsorbed to glow-discharged carbon-coated copper grids for ~30 s before 2% uranyl formate staining. Micrographs were recorded using the Leginon software⁴⁶ on a 100kV FEI Tecnai G2 Spirit with a Gatan Ultrascan 4000 4k × 4k CCD camera at 67,000 nominal magnification. The defocus ranged from 1.0 to 2.0 μm and the pixel size was 1.6 Å.

Cryo-electron microscopy

SARS-CoV-2 HexaPro S⁴⁷ at 1.2 mg ml⁻¹ was incubated with 1.2 fold molar excess of recombinantly purified S2X58 for 10 s at room temperature before application onto a freshly glow discharged 2.0/2.0 UltrAuFoil grid (200 mesh). Plunge freezing used a vitrobot MarkIV (Thermo Fisher Scientific) using a blot force of 0 and 6.5 s blot time at 100% humidity and 23 °C.

Data were acquired using an FEI Titan Krios transmission electron microscope operated at 300 kV and equipped with a Gatan K2 Summit direct detector and Gatan Quantum GIF energy filter, operated in zero-loss mode with a slit width of 20 eV. Automated data collection was carried out using Leginon⁴⁶ at a nominal magnification of 130,000× with a pixel size of 0.525 Å and stage tilt angles up to 35°. The dose rate

was adjusted to 8 counts per pixel s⁻¹, and each movie was acquired in super-resolution mode fractionated in 50 frames of 200 ms. 4,126 micrographs were collected with a defocus range between -0.5 and -3.0 μm. Movie frame alignment, estimation of the microscope contrast-transfer function parameters, particle picking, and extraction were carried out using Warp⁴⁸. Particle images were extracted with a box size of 800 binned to 400 pixels², yielding a pixel size of 1.05 Å.

Two rounds of reference-free 2D classification were performed using CryoSPARC⁴⁹ to select well-defined particle images. These selected particles were subjected to two rounds of 3D classification with 50 iterations each (angular sampling 7.5° for 25 iterations and 1.8° with local search for 25 iterations), using our previously reported closed SARS-CoV-2 S structure as initial model (PDB 6VXX) in Relion⁵⁰. 3D refinements were carried out using non-uniform refinement along with per-particle defocus refinement in CryoSPARC⁵¹. Selected particle images were subjected to the Bayesian polishing procedure implemented in Relion3.0⁵² before performing another round of non-uniform refinement in CryoSPARC followed by per-particle defocus refinement and again non-uniform refinement. Local resolution estimation, filtering, and sharpening were carried out using CryoSPARC. Reported resolutions are based on the gold-standard Fourier shell correlation (FSC) of 0.143 criterion and Fourier shell correlation curves were corrected for the effects of soft masking by high-resolution noise substitution. UCSF ChimeraX⁵³ and Coot⁵⁴ were used to fit atomic models into the cryo-EM maps.

Immunofluorescence analysis

HEK 293T-derived cell lines were seeded onto poly-d-lysine-coated 96-well plates (Sigma-Aldrich) and fixed 24 h after seeding with 4% paraformaldehyde for 30 min, followed by 2 PBS (pH 7.4) washes and permeabilization with 0.25% Triton X-100 in PBS for 30 min. Cells were incubated with primary antibodies anti-DC-SIGN/L-SIGN (Biolegend, cat. no. 845002, 1:500 dilution), anti-DC-SIGN (Cell Signaling, cat. no. 13193S, 1:500 dilution), anti-SIGLEC1 (Biolegend, cat. no. 346002, 1:500 dilution) or anti-ACE2 (R&D Systems, cat. no. AF933, 1:200 dilution) diluted in 3% milk powder/PBS for 2 h at room temperature. After washing and incubation with a secondary Alexa Fluor 647-labeled antibody mixed with 1 μg ml⁻¹ Hoechst33342 for 1 h, plates were imaged on an inverted fluorescence microscope (Echo Revolve).

ACE2 and TMPRSS2 RT-qPCR

RNA was extracted from the cells using the NucleoSpin RNA Plus kit (Macherey-Nagel) according to the manufacturer's protocol. Human airway epithelial (HAE) cells were provided by MatTek Life Sciences (MatTek EpiAirway). RNA was reverse

transcribed using the High Capacity cDNA Reverse Transcription kit (Applied Biosystems) according to the manufacturer's instructions. Intracellular levels of *ACE2* (forward primer: CAAGAGCAAACGGTTAACAC, reverse primer: CCAGAGCCTCTCATTGTAGTCT), *HPRT* (forward primer: CCTGGCGTCGTGATTAGTG, reverse primer: ACACCCTTCCAAATCCTCAG) and *TMPRSS2* (forward primer: CAAGTGCTCCRACACTGGGAT, reverse primer: AACACACCGRTTCTCGTCCTC) were quantified using the Luna Universal qPCR Master Mix (New England Biolabs) according to the manufacturer's protocol. Levels of *ACE2* and *TMPRSS2* were normalized to *HPRT*. Hela cells were used as the reference sample. All quantitative PCRs were run on a QuantStudio 3 Real-Time PCR System (Applied Biosystems).

SARS-CoV-2 S(D614G) production and biotinylation

Prefusion-stabilized SARS-CoV-2 S(D614G) (comprising amino acids Q14 to K1211) with a C-terminal TEV cleavage site, T4 bacteriophage fibritin foldon, 8× His, Avi and EPEA tags was transfected into HEK 293 Freestyle cells, using 293 fectin as a transfection reagent. Cells were left to produce protein for 3 days at 37 °C. Afterwards, supernatant was collected by centrifuging cells for 30 min at 500g, followed by another spin for 30 min at 4,000g. Cell culture supernatant was filtered through a 0.2-μm filter and loaded onto a 5-ml C-tag affinity matrix column, pre-equilibrated with 50 mM Tris pH 8 and 200 mM NaCl. SARS-CoV-2 D614G S was eluted, using 10 column volumes of 100 mM Tris, 200 mM NaCl and 3.8 mM SEPEA peptide. Elution peak was concentrated and injected on a Superose 6 increase 10/300 GL gel filtration column, using 50 mM Tris pH 8 and 200 mM NaCl as a running buffer. Size-exclusion fractions corresponding to monodisperse SARS-CoV-2 S(D614G) were collected and flash frozen in liquid nitrogen for storage at -80 °C. Purified SARS-CoV-2 S(D614G) protein was biotinylated using BirA500 biotinylation kit from Avidity. To 50 μg of S protein, 5 μg of BirA, and 11 μl of BiomixA and BiomixB was added. Final S protein concentration during the biotinylation reaction was ~1 μM. The reaction was left to proceed for 16 h at 4 °C. Then, protein was desalted using two Zeba spin columns pre-equilibrated with 1× PBS pH 7.4.

Flow cytometry analysis for DC-SIGN, L-SIGN, SIGLEC1 and ACE-2

HEK 293T cells expressing DC-SIGN, L-SIGN, SIGLEC1 or ACE2 were resuspended at 4×10^6 cells per ml and 100 μl per well were seeded onto V-bottom 96-well plates (Corning, 3894). The plate was centrifuged at 2,000 rpm for 5 min and washed with PBS (pH 7.4). The cells were resuspended in 200 μl of PBS containing Ghost violet 510 viability dye (Cell Signaling, cat. no. 13-0870-T100, 1:1,000 dilution), incubated for 15 min on ice and then washed. The cells were resuspended in 100 μl of fluorescence-activated cell sorting (FACS) buffer prepared with 0.5% BSA (Sigma-

Aldrich) in PBS containing the primary antibodies at a 1:100 dilution: mouse anti-DC/L-SIGN (Biolegend, cat. no. 845002), rabbit anti-DC-SIGN (Cell Signaling, cat. no. 13193), mouse anti-SIGLEC1 (Biologend, cat. no. 346002) or goat anti-ACE2 (R&D Systems, cat. no. AF933). After 1 h incubation on ice, the cells were washed two times and resuspended in FACS buffer containing the Alexa Fluor 488-labelled secondary antibodies at a 1:200 dilution: goat anti-mouse (Invitrogen cat. no. A11001), goat anti-rabbit (Invitrogen cat. no. A11008) or donkey anti-goat (Invitrogen cat. no. A11055). After incubation for 45 min on ice, the cells were washed 3 times with 200 µl of FACS buffer and fixed with 200 µl of 4% PFA (Alfa Aesar) for 15 min at room temperature. Cells were washed 3 times, resuspended in 200 µl of FACS buffer and analysed by flow cytometry using the CytoFLEX flow cytometer (Beckman Coulter).

Flow cytometry of SARS-CoV-2 S and RBD binding to cells

Biotinylated SARS-CoV-2 S(D614G) protein (Spike_{biotin}, generated in-house) or the biotinylated SARS-CoV-2 S receptor-binding domain (RBD_{biotin}, Sino Biological, 40592-V08B) were incubated with Alexa Fluor 647 streptavidin (AF647-strep, Invitrogen, S21374) at a 1:20 ratio by volume for 20 min at room temperature. The labelled proteins were then stored at 4 °C until further use. Cells were dissociated with TrypLE Express (Gibco, 12605-010) and 10⁵ cells were transferred to each well of a 96-well V bottom plate (Corning, 3894). Cells were washed twice in flow cytometry buffer (2% FBS in PBS (without Ca and Mg)) and stained with Spike_{biotin}-AF647-strep at a final concentration of 20 µg ml⁻¹ or RBD_{biotin}-AF647-strep at a final concentration of 7.5 µg ml⁻¹ for 1 h on ice. Stained cells were washed twice with flow cytometry buffer, resuspended in 1% PFA (Electron Microscopy Sciences, 15714-S) and analysed with the Cytoflex LX (Beckman Coulter).

Recombinant expression of SARS-CoV-2-specific monoclonal antibodies

Human monoclonal antibodies were isolated from plasma cells or memory B cells of SARS-CoV-2-immune donors, as previously described^{25,55,56}. Recombinant antibodies were expressed in ExpiCHO cells at 37 °C and 8% CO₂. Cells were transfected using ExpiFectamine. Transfected cells were supplemented one day after transfection with ExpiCHO Feed and ExpiFectamine CHO Enhancer. Cell culture supernatant was collected 8 days after transfection and filtered through a 0.2-µm filter. Recombinant antibodies were affinity purified on an ÄKTAXpress FPLC device using 5 ml HiTrap MabSelect PrismA columns followed by buffer exchange to Histidine buffer (20 mM histidine, 8% sucrose, pH 6) using HiPrep 26/10 desalting columns.

SARS-CoV-2 trans-infection assay on primary cells

Cell lines used have been described⁵⁷. Isolation and culture of primary cells was performed as described⁵⁸. In brief, peripheral blood mononuclear cells were obtained with a Ficoll–Hypaque gradient (Alere Technologies) from blood donors and monocyte populations (>90% CD14⁺) were isolated with CD14 negative selection magnetic beads (Miltenyi Biotec). Macrophages were obtained by culturing these cells in the presence of 100 ng ml⁻¹ of macrophage colony-stimulating factor (M-CSF) for 7 days and replacing media and cytokines every 2 days. DCs were obtained culturing these cells in the presence of both 1,000 IU ml⁻¹ granulocyte-macrophage colony-stimulating factor (GM-CSF) and interleukin-4 (R&D Systems) for 7 days and replacing medium and cytokines every 2 days. Activated cells were differentiated by culturing myeloid cells at day 5 for 2 more days in the presence of 1,000 IU ml⁻¹ of interferon- α (IFN α) (Sigma-Aldrich) or 100 ng ml⁻¹ LPS (Sigma-Aldrich). The SARS-CoV-2 viral strain used on primary cells was isolated in March 2020 from a nasopharyngeal swab as described⁵⁷. The virus was propagated for two passages and a virus stock was prepared by collecting the supernatant from Vero E6 cells. The genomic sequence was deposited at the GISAID repository (<http://gisaid.org>) with accession ID EPI_ISL_510689. For *trans* infection, cells were pre-incubated for 15 min at room temperature with 10 μ g ml⁻¹ anti-SIGLEC1 7–239 (Abcam) or IgG1 isotype control (BD Biosciences), or left untreated before viral exposure. Uptake experiments with SARS-CoV-2 were performed by pulsing 0.1×10^6 DCs with 200 μ l SARS-CoV-2 with $10^{6.15}$ median tissue culture infectious dose (TCID₅₀) per ml for 3 h at 37 °C. After extensive washing, cells were co-cultured at a ratio 3:1 with HEK 293T cells expressing or not expressing ACE2 and TMPRSS-2. Six days later, the amount of viral release to the supernatant was measured with a SARS-CoV-2 nucleocapsid protein High-sensitivity Quantitative ELISA (Immuno Diagnostics).

SIGLEC1 surface expression analysis by FACS

A total of 2.5×10^5 myeloid cells was blocked with 1 mg ml⁻¹ of human IgGs and stained with anti-SIGLEC1–PE or matched isotype–PE control (BioLegend) at 4 °C for 30 min. The mean number of SIGLEC1 monoclonal antibody binding sites per cell was obtained with a Quantibrite kit (Becton Dickinson), subtracting values obtained for isotype control. Samples were analysed with a Canto Flow Cytometer using Flow Jo software to evaluate collected data.

SARS-CoV-2 infection model in hamster

Virus preparation

The SARS-CoV-2 strain used in this study, BetaCov/Belgium/GHB-03021/2020 (EPI ISL 109 407976|2020-02-03), was recovered from a nasopharyngeal swab taken from an asymptomatic patient infected with SARS-CoV-2—confirmed by quantitative PCR with reverse transcription (RT–qPCR)—who returned from Wuhan, China in February 2020. A close relation with the prototypic Wuhan-Hu-1 2019-nCoV (GenBank accession 112 number MN908947.3) strain was confirmed by phylogenetic analysis. Infectious virus was isolated by serial passaging on HuH7 and Vero E6 cells;⁵⁹ passage 6 virus was used for the study described here. The titre of the virus stock was determined by end-point dilution on Vero E6 cells by the Reed and Muench method⁶⁰. Live virus-related work was conducted in the high-containment ABSL3 and BSL3+ facilities of the KU Leuven Rega Institute (3CAPS) under licenses AMV 30112018 SBB 219 2018 0892 and AMV 23102017 SBB 219 20170589 according to institutional guidelines.

Cells

Vero E6 cells (African green monkey kidney, ATCC CRL-1586) were cultured in minimal essential medium (Gibco) supplemented with 10% fetal bovine serum (Integro), 1% l- glutamine (Gibco) and 1% bicarbonate (Gibco). End-point titrations were performed with medium containing 2% fetal bovine serum instead of 10%.

SARS-CoV-2 infection model in hamsters. The hamster infection model of SARS-CoV-2 has been described^{59,61}. The specific study design is shown in the schematic below. In brief, wild-type Syrian Golden hamsters (*Mesocricetus auratus*) were purchased from Janvier Laboratories and were housed per two in ventilated isolator cages (IsoCage N Biocontainment System, Tecniplast) with ad libitum access to food and water and cage enrichment (wood block). The animals were acclimatized for four days before the start of the study. Housing conditions and experimental procedures were approved by the ethics committee of animal experimentation of KU Leuven (license P065- 2020). Sample size was dimensioned in order to have a significant difference of at least 1 log viral RNA (effect size $d = 2.004$) between control and treated groups, by using a two-tailed *t*-test with 80% power and an α error of 0.05, calculated with G*Power 3.1 software. Female 6- to 8-week-old hamsters were anaesthetized with ketamine/xylazine/atropine and inoculated intranasally with 50 μ l containing 2×10^6 TCID₅₀ SARS-CoV-2 (day 0).

Treatment regimen

Hamsters were allocated into different monoclonal antibody or dosing groups at random. Animals were prophylactically treated 48 h before infection by intraperitoneal administration and monitored for appearance, behaviour and weight. At day 4 after

infection, hamsters were euthanized by intraperitoneal injection of 500 µl Dolethal (200 mg ml⁻¹ sodium pentobarbital) (Vétoquinol). Lungs were collected and viral RNA and infectious virus were quantified by RT-qPCR and end-point virus titration, respectively. Blood samples were collected before infection for PK analysis. The circulating antibody levels were measured by mesoscale bridging ELISA using an anti-human LS mutation monoclonal antibody for capture and anti-human CH2 monoclonal antibody for detection³⁴.

SARS-CoV-2 RT-qPCR. Collected lung tissues were homogenized using bead disruption (Precellys) in 350µl RLT buffer (RNeasyMinikit,Qiagen) and centrifuged (10,000 rpm, 5 min) to pellet the cell debris. RNA was extracted according to the manufacturer's instructions. Of 50 µl eluate, 4 µl was used as a template in RT-qPCR reactions. RT-qPCR was performed on a LightCycler96 platform (Roche) using the iTaq Universal Probes One-Step RT-qPCR kit (BioRad) with N2 primers and probes targeting the nucleocapsid⁵⁹. Standards of SARS-CoV-2 cDNA (IDT) were used to express viral genome copies per mg tissue or per ml serum.

End-point virus titrations

Lung tissues were homogenized using bead disruption (Precellys) in 350 µL minimal essential medium and centrifuged (10,000 rpm, 5 min, 4 °C) to pellet the cell debris. To quantify infectious SARS-CoV-2 particles, end-point titrations were performed on confluent Vero E6 cells in 96-well plates. Viral titres were calculated by the Reed and Muench method⁶⁰ using the Lindenbach calculator and were expressed as TCID₅₀ per mg tissue. The samples for RNA and virus titration were run by the technicians in a blinded manner, without knowing the treatment group.

Histology

For histological examination, lungs were fixed overnight in 4% formaldehyde and embedded in paraffin. Tissue sections (5 µm) were analysed after staining with haematoxylin and eosin and scored blindly for lung damage by an expert pathologist. The scored parameters, to which a cumulative score of 1 to 3 was attributed, were the following: congestion, intra-alveolar haemorrhagic, apoptotic bodies in bronchus wall, necrotizing bronchiolitis, perivascular oedema, bronchopneumonia, perivascular inflammation, peribronchial inflammation and vasculitis.

Binding of immunocomplexes to hamster monocytes

Immunocomplexes were generated by complexing S309 monoclonal antibody (hamster IgG, either wt or N297A) with a biotinylated anti-idiotype Fab fragment and

Alexa Fluor 488-streptavidin, using a precise molar ratio (4:8:1, respectively). Pre-generated fluorescent immunocomplexes were serially diluted and incubated at 4 °C for 3 h with freshly revitalized hamster splenocytes, obtained from a naive animal. Cellular binding was then evaluated by cytometry upon exclusion of dead cells and physical gating on monocyte population. Results are expressed as Alexa Fluor 488 mean fluorescent intensity of the entire monocyte population.

Binding of immunocomplexes to hamster FcgRIV and human FcgRIIIA by biolayer interferometry

Antibody immunocomplexes were first generated by cross-linking hamster S309 and S309-N297A with a specific F(ab)2 anti-S309 idiotype monoclonal antibodies (2:1 $\mu\text{g ml}^{-1}$ ratio) for 40 min at room temperature. Recombinant golden hamster (GH) Fc γ RIV and biotinylated human Fc γ RIIIA (Acro Biosystems) were diluted to 0.25 and 0.5 $\mu\text{g ml}^{-1}$ respectively in kinetic buffer (PBS + BSA 0.01%, pH 7.1) and immobilized on anti-His-Penta or streptavidin SAX Biosensors (FortéBio) for 10 min. Fc γ Rs-coated biosensors were incubated for 5 min with immunocomplexes mixture (4.5 $\mu\text{g ml}^{-1}$), to allow association, followed by a 5-min dissociation step. The shift in the biolayer interferometry signal generated by change in molecular binding was recorded in real time using an Octet RED96 system (FortéBio). Binding raw data were exported and plotted using GraphPad Prism software (V9).

Bioinformatic analyses

Processed Human Lung Cell Atlas (HLCA) data and cell-type annotations²⁰ were downloaded from Github (<https://github.com/krasnowlab/HLCA>). Processed single-cell transcriptome data and annotation of lung epithelial and immune cells from individuals infected with SARS-CoV-2^{21,22} were downloaded from the NCBI GEO database (ID: GSE158055) and Github (https://github.com/zhangzlab/covid_balf). Available sequence data from the second single-cell transcriptomics study by Liao et al.²² were downloaded from NCBI SRA (ID: PRJNA608742) for inspection of reads corresponding to viral RNA using NCBI MagicBlast and SAMtools. Reads that supported a junction between the 5' leader sequence and the transcription regulatory sequence (TRS) preceding open reading frames for viral genes were counted as evidence of subgenomic mRNA, a surrogate readout for viral replication. Such reads constituted a small fraction of TRS-containing viral reads, ranging from undetectable to 3.4%. The proportion of single guide RNA relative to genomic RNA was estimated by counting TRS-containing reads supporting a leader–TRS junction. Criteria and methods for detection of leader-TRS junction reads were adapted from Andersen et al.⁶². The viral genome reference and TRS annotation were based on Wuhan-Hu-1 NC_045512.2/MN908947⁶³. Only two samples from individuals with severe COVID-

19 had detectable leader–TRS junction reads (SRR11181958 and SRR11181959). Summary visualizations and analyses for the datasets above were performed using R and the following R packages: `data.table`, `ggplot2`, `cowplot`, `scales`, `RColorBrewer`, `viridis`, `scater`, and `SingleCellExperiment`.

Statistics and reproducibility

If not stated otherwise, all experiments were performed with at least three biological replicates for each condition. Experiments were independently repeated at least two times, and one representative dataset is shown. All error bars throughout the study represent the s.d. Statistical tests are detailed in the respective figure legends.

Reporting summary

Further information on research design is available in the [Nature Research Reporting Summary](#) linked to this paper.

Data availability

FACS gating strategies are provided as [Supplementary Information](#). The cryo-EM maps have been deposited to the Electron Microscopy Data Bank with accession numbers [EMD-24607](#) (two RBDs open) and [EMD-24608](#) (three RBDs open). Single-cell transcriptome datasets used in this study had been published previously: NCBI Gene Expression Omnibus (ID: [GSE158055](#)), NCBI Sequence Read Archive (ID: [PRJNA608742](#)). All further relevant source data that support the findings of this study are available from the corresponding author upon reasonable request. [Source data](#) are provided with this paper.

References

1. 1.

Hikmet, F. et al. The protein expression profile of ACE2 in human tissues. *Mol. Syst. Biol.* **16**, e9610 (2020).

2. 2.

Hou, Y. J. et al. SARS-CoV-2 reverse genetics reveals a variable infection gradient in the respiratory tract. *Cell* **182**, 429–446.e14 (2020).

3. 3.

Zou, X. et al. Single-cell RNA-seq data analysis on the receptor ACE2 expression reveals the potential risk of different human organs vulnerable to 2019-nCoV infection. *Front. Med.* **14**, 185–192 (2020).

4. 4.

Walls, A. C. et al. Structure, function, and antigenicity of the SARS-CoV-2 spike glycoprotein. *Cell* **181**, 281–292.e6 (2020).

5. 5.

Piccoli, L. et al. Mapping neutralizing and immunodominant sites on the SARS-CoV-2 spike receptor-binding domain by structure-guided high-resolution serology. *Cell* **183**, 1024–1042.e21 (2020).

6. 6.

Greaney, A. J. et al. Comprehensive mapping of mutations to the SARS-CoV-2 receptor-binding domain that affect recognition by polyclonal human serum antibodies. *Cell Host Microbe* **29**, 463–476 (2021).

7. 7.

Tortorici, M. A. et al. Ultrapotent human antibodies protect against SARS-CoV-2 challenge via multiple mechanisms. *Science* **370**, 950–957 (2020).

8. 8.

Hansen, J. et al. Studies in humanized mice and convalescent humans yield a SARS-CoV-2 antibody cocktail. *Science* **369**, 1010–1014 (2020).

9. 9.

Chen, P. et al. SARS-CoV-2 neutralizing antibody LY-CoV555 in outpatients with Covid-19. *N. Engl. J. Med.* **384**, 229–237 (2021).

10. 10.

Weinreich, D. M. et al. REGN-COV2, a neutralizing antibody cocktail, in outpatients with Covid-19. *N. Engl. J. Med.* **384**, 238–251 (2021).

11. 11.

Crawford, K. H. D. et al. Protocol and reagents for pseudotyping lentiviral particles with SARS-CoV-2 spike protein for neutralization assays. *Viruses* **12**, 238 (2020).

12. 12.

Gustine, J. N. & Jones, D. Immunopathology of hyperinflammation in COVID-19. *Am. J. Pathol.* **191**, 4–17 (2021).

13. 13.

Amraie, R. et al. CD209L/L-SIGN and CD209/DC-SIGN act as receptors for SARS-CoV-2. Preprint at *bioRxiv* <https://doi.org/10.1101/2020.06.22.165803> (2020).

14. 14.

Soh, W. T. et al. The N-terminal domain of spike glycoprotein mediates SARS-CoV-2 infection by associating with L-SIGN and DC-SIGN. Preprint at *bioRxiv* <https://doi.org/10.1101/2020.11.05.369264> (2020).

15. 15.

Wang, K. et al. CD147-spike protein is a novel route for SARS-CoV-2 infection to host cells. *Signal Transduct. Target. Ther.* **5**, 283 (2020).

16. 16.

Cantuti-Castelvetro, L. et al. Neuropilin-1 facilitates SARS-CoV-2 cell entry and infectivity. *Science* **370**, 856–860 (2020).

17. 17.

Clausen, T. M. et al. SARS-CoV-2 infection depends on cellular heparan sulfate and ACE2. *Cell* **183**, 1043–1057 (2020).

18. 18.

Thépaut, M. et al. DC/L-SIGN recognition of spike glycoprotein promotes SARS-CoV-2 trans-infection and can be inhibited by a glycomimetic antagonist. *PLoS Pathog.* **17**, e1009576 (2021).

19. 19.

Izquierdo-Useros, N. et al. Siglec-1 is a novel dendritic cell receptor that mediates HIV-1 *trans*-infection through recognition of viral membrane gangliosides. *PLoS Biol.* **10**, e1001448 (2012).

20. 20.

Travaglini, K. J. et al. A molecular cell atlas of the human lung from single-cell RNA sequencing. *Nature* **587**, 619–625 (2020).

21. 21.

Ren, X. et al. COVID-19 immune features revealed by a large-scale single cell transcriptome atlas. *Cell* **184**, 1895–1913.e19 (2021).

22. 22.

Liao, M. et al. Single-cell landscape of bronchoalveolar immune cells in patients with COVID-19. *Nat. Med.* **26**, 842–844 (2020).

23. 23.

Perez-Zsolt, D. et al. Siglec-1 on dendritic cells mediates SARS-CoV-2 *trans*-infection of target cells while on macrophages triggers proinflammatory responses. Preprint at *bioRxiv* <https://doi.org/10.1101/2021.05.11.443572> (2021).

24. 24.

Lu, Q. et al. SARS-CoV-2 exacerbates proinflammatory responses in myeloid cells through C-type lectin receptors and Tweety family member 2. *Immunity* **54**, 1304–1319.e9 (2021).

25. 25.

Pinto, D. et al. Cross-neutralization of SARS-CoV-2 by a human monoclonal SARS-CoV antibody. *Nature* **583**, 290–295 (2020).

26. 26.

McCallum, M. et al. N-terminal domain antigenic mapping reveals a site of vulnerability for SARS-CoV-2. *Cell* **184**, 2332–2347.e16 (2021).

27. 27.

Chan, J. F. et al. Simulation of the clinical and pathological manifestations of coronavirus disease 2019 (COVID-19) in a golden Syrian hamster model: implications for disease pathogenesis and transmissibility. *Clin. Infect. Dis.* **71**, 2428–2446 (2020).

28. 28.

Baum, A. et al. REGN-COV2 antibodies prevent and treat SARS-CoV-2 infection in rhesus macaques and hamsters. *Science* **370**, 1110–1115 (2020).

29. 29.

Gupta, A. et al. Early Covid-19 treatment with SARS-CoV-2 neutralizing antibody sotrovimab. Preprint at *medRxiv* <https://doi.org/10.1101/2021.05.27.21257096> (2021).

30. 30.

Buchrieser, J. et al. Syncytia formation by SARS-CoV-2-infected cells. *EMBO J.* **40**, e107405 (2021).

31. 31.

Bussani, R. et al. Persistence of viral RNA, pneumocyte syncytia and thrombosis are hallmarks of advanced COVID-19 pathology. *EBioMed.* **61**, 103104 (2020).

32. 32.

Walls, A. C. et al. Unexpected receptor functional mimicry elucidates activation of coronavirus fusion. *Cell* **176**, 1026–1039.e15 (2019).

33. 33.

Pinto, D. et al. Broad betacoronavirus neutralization by a stem helix-specific human antibody. *Science* **373**, 1109–1116 (2021).

34. 34.

Starr, T. N. et al. SARS-CoV-2 RBD antibodies that maximize breadth and resistance to escape. *Nature* **597**, 97–102 (2021).

35. 35.

Wan, Y. et al. Molecular mechanism for antibody-dependent enhancement of coronavirus entry. *J. Virol.* **94**, 69–15 (2020).

36. 36.

Blanco-Melo, D. et al. Imbalanced host response to SARS-CoV-2 drives development of COVID-19. *Cell* **181**, 1036–1045.e9 (2020).

37. 37.

Ziegler, C. G. K. et al. SARS-CoV-2 receptor ACE2 is an interferon-stimulated gene in human airway epithelial cells and is detected in specific cell subsets across tissues. *Cell* **181**, 1016–1035.e19 (2020).

38. 38.

Chang, Y. C. & Nizet, V. Siglecs at the host–pathogen interface. *Adv. Exp. Med. Biol.* **1204**, 197–214 (2020).

39. 39.

Cathcart, A. L. et al. The dual function monoclonal antibodies VIR-7831 and VIR-7832 demonstrate potent in vitro and in vivo activity against SARS-CoV-2. Preprint at *bioRxiv* <https://doi.org/10.1101/2021.03.09.434607> (2021).

40. 40.

Sewald, X. et al. Retroviruses use CD169-mediated trans-infection of permissive lymphocytes to establish infection. *Science* **350**, 563–567 (2015).

41. 41.

Uchil, P. D. et al. A protective role for the lectin CD169/Siglec-1 against a pathogenic murine retrovirus. *Cell Host Microbe* **25**, 87–100.e10 (2019).

42. 42.

Asarnow, D. et al. Structural insight into SARS-CoV-2 neutralizing antibodies and modulation of syncytia. *Cell* **184**, 3192–3204.e16 (2021).

43. 43.

Xu, Z. et al. Pathological findings of COVID-19 associated with acute respiratory distress syndrome. *Lancet Respir. Med.* **8**, 420–422 (2020).

44. 44.

Tian, S. et al. Pulmonary pathology of early-phase 2019 novel coronavirus (COVID-19) pneumonia in two patients with lung cancer. *J. Thorac. Oncol.* **15**, 700–704 (2020).

45. 45.

Xie, X. et al. A nanoluciferase SARS-CoV-2 for rapid neutralization testing and screening of anti-infective drugs for COVID-19. *Nat. Commun.* **11**, 5214 (2020).

46. 46.

Suloway, C. et al. Automated molecular microscopy: the new Leginon system. *J. Struct. Biol.* **151**, 41–60 (2005).

47. 47.

Hsieh, C. L. et al. Structure-based design of prefusion-stabilized SARS-CoV-2 spikes. *Science* **369**, 1501–1505 (2020).

48. 48.

Tegunov, D. & Cramer, P. Real-time cryo-electron microscopy data preprocessing with Warp. *Nat. Methods* **16**, 1146–1152 (2019).

49. 49.

Punjani, A., Rubinstein, J. L., Fleet, D. J. & Brubaker, M. A. cryoSPARC: algorithms for rapid unsupervised cryo-EM structure determination. *Nat. Methods* **14**, 290–296 (2017).

50. 50.

Zivanov, J. et al. New tools for automated high-resolution cryo-EM structure determination in RELION-3. *Elife* **7**, e42166 (2018).

51. 51.

Punjani, A., Zhang, H. & Fleet, D. J. Non-uniform refinement: adaptive regularization improves single-particle cryo-EM reconstruction. *Nat. Methods* **17**, 1214–1221 (2020).

52. 52.

Zivanov, J., Nakane, T. & Scheres, S. H. W. A Bayesian approach to beam-induced motion correction in cryo-EM single-particle analysis. *IUCrJ* **6**, 5–17 (2019).

53. 53.

Pettersen, E. F. et al. UCSF ChimeraX: structure visualization for researchers, educators, and developers. *Protein Sci.* **30**, 70–82 (2021).

54. 54.

Casanal, A., Lohkamp, B. & Emsley, P. Current developments in Coot for macromolecular model building of electron cryo-microscopy and crystallographic data. *Protein Sci.* **29**, 1069–1078 (2020).

55. 55.

Corti, D. et al. A neutralizing antibody selected from plasma cells that binds to group 1 and group 2 influenza A hemagglutinins. *Science* **333**, 850–856 (2011).

56. 56.

Tortorici, M. A. et al. Ultrapotent human antibodies protect against SARS-CoV-2 challenge via multiple mechanisms. *Science* **370**, 950–957 (2020).

57. 57.

Rodon, J. et al. Identification of plitidepsin as potent inhibitor of SARS-CoV-2-induced cytopathic effect after a drug repurposing screen. *Front. Pharmacol.* **12**, 646676 (2021).

58. 58.

Perez-Zsolt, D. et al. Anti-Siglec-1 antibodies block Ebola viral uptake and decrease cytoplasmic viral entry. *Nat. Microbiol.* **4**, 1558–1570 (2019).

59. 59.

Boudewijns, R. et al. STAT2 signaling restricts viral dissemination but drives severe pneumonia in SARS-CoV-2 infected hamsters. *Nat. Commun.* **11**, 5838 (2020).

60. 60.

Reed, L. J. & Muench, H. A simple method of estimating fifty per cent endpoints. *Am. J. Epidemiol.* **27**, 493–497 (1938).

61. 61.

Sanchez-Felipe, L. et al. A single-dose live-attenuated YF17D-vectored SARS-CoV-2 vaccine candidate. *Nature* **590**, 320–325 (2021).

62. 62.

Alexandersen, S., Chamings, A. & Bhatta, T. R. SARS-CoV-2 genomic and subgenomic RNAs in diagnostic samples are not an indicator of active replication. *Nat. Commun.* **11**, 6059 (2020).

63. 63.

Wu, F. et al. A new coronavirus associated with human respiratory disease in China. *Nature* **579**, 265–269 (2020).

64. 64.

Chua, R. L. et al. COVID-19 severity correlates with airway epithelium–immune cell interactions identified by single-cell analysis. *Nat. Biotechnol.* **38**, 970–979 (2020).

65. 65.

Bost, P. et al. Host–viral infection maps reveal signatures of severe COVID-19 patients. *Cell* **181**, 1475–1488.e12 (2020).

66. 66.

Tortorici, M. A. et al. Broad sarbecovirus neutralization by a human monoclonal antibody. *Nature* **597**, 103–108 (2021).

67. 67.

Shi, R. et al. A human neutralizing antibody targets the receptor-binding site of SARS-CoV-2. *Nature* **584**, 120–124 (2020).

68. 68.

Jones, B. E. et al. The neutralizing antibody, LY-CoV555, protects against SARS-CoV-2 infection in nonhuman primates. *Sci. Transl. Med.* **13**, abf1906 (2021).

69. 69.

ACTIV-3/TICO LY-CoV555 Study Group A neutralizing monoclonal antibody for hospitalized patients with Covid-19. *N. Engl. J. Med.* **384**, 905–914 (2021).

70. 70.

Kim, C. et al. A therapeutic neutralizing antibody targeting receptor binding domain of SARS-CoV-2 spike protein. *Nat. Commun.* **12**, 288 (2021).

Acknowledgements

We thank D.R.-R., J.M.-B., D.P.-Z., I.E. and X.M.-T. from IrsiCaixa for their contribution to *trans*-infection experiments. J.V.-A. and N.I.-U. are part of the CBIG consortium (constituted by IRTA-CReSA, BSC and IrsiCaixa) and are supported by Grifols. N.I.-U. is supported by grant PID2020-117145RB-I00 from the Spanish Ministry of Science and Innovation. J.M.-P. is supported by grant PID2019-109870RB-I00 from the Spanish Ministry of Science and Innovation and in part by Grifols. The authors acknowledge the crowdfunding initiative #Yomecorono (<https://www.yomecorono.com>). This study was supported by the National Institute of Allergy and Infectious Diseases (DP1AI158186 and HHSN272201700059C to D.V.), a Pew Biomedical Scholars Award (D.V.), Investigators in the Pathogenesis of Infectious Disease Awards from the Burroughs Wellcome Fund (D.V.) and Fast Grants (D.V.). The funders had no role in study design, data collection and analysis, decision to publish, or preparation of the manuscript. The following reagent was deposited by the Centers for Disease Control and Prevention and obtained through BEI Resources, NIAID, NIH: SARS-Related Coronavirus 2, Isolate USA-WA1/2020, NR-52281.

Author information

Author notes

1. These authors contributed equally: Amilio Telenti, Davide Corti

Affiliations

1. Vir Biotechnology, San Francisco, CA, USA

Florian A. Lempp, Leah B. Soriaga, Martin Montiel-Ruiz, Julia Noack, Jiayi Zhou, Hannah Kaiser, Maria Agostini, Marcel Meury, Exequiel Dellota Jr, Herbert W. Virgin & Amilio Telenti

2. Humabs Biomed SA, a subsidiary of Vir Biotechnology, Bellinzona, Switzerland

Fabio Benigni, Siro Bianchi, Stefano Jaconi, Elisabetta Cameroni, Antonio Lanzavecchia & Davide Corti

3. Department of Biochemistry, University of Washington, Seattle, WA, USA

Young-Jun Park, Alexandra C. Walls, John E. Bowen, Anshu Joshi & David Veesler

4. IrsiCaixa AIDS Research Institute, Badalona, Spain

Javier Martinez-Picado & Nuria Izquierdo-Useros

5. University of Vic–Central University of Catalonia (UVic-UCC), Vic, Spain

Javier Martinez-Picado

6. Catalan Institution for Research and Advanced Studies (ICREA), Barcelona, Spain

Javier Martinez-Picado

7. IRTA, Centre de Recerca en Sanitat Animal (CReSA, IRTA-UAB), Campus de la UAB, Bellaterra (Cerdanyola del Vallès), Spain

Júlia Vergara-Alert

8. Germans Trias i Pujol Research Institute (IGTP), Can Ruti Campus, Badalona, Spain

Nuria Izquierdo-Useros

9. Department of Pathology and Immunology, Washington University School of Medicine, Saint Louis, MO, USA

Herbert W. Virgin

10. Department of Internal Medicine, UT Southwestern Medical Center, Dallas, TX, USA

Herbert W. Virgin

11. Vir Biotechnology, St Louis, MO, USA

Lisa A. Purcell

Contributions

Conceived the study: F.A.L., L.S., A.L., L.P., D.V., A.T. and D.C. Designed the study and experiments: F.A.L., L.S., M.M.-R., J.N., F.B. and D.C. Performed in vitro virological experiments: F.A.L., F.B., Y.-J.P., S.B., M.M.-R., J.N., A.C.W., J.E.B., J.Z., H.K. and M.A. Electron microscopy data collection and analysis: Y.-J.P., A.C.W. and J.E.B. Produced antibodies for in vitro and in vivo studies: S.J. and E.C. Primary cell analyses: J.V.-A., J.M.-P. and N.I.-U. Recombinant glycoproteins production: J.E.B., M.M., A.J. and E.D. Hamster model and data analysis: F.B. Bioinformatic analysis: L.S. and A.T. Manuscript writing: F.A.L, F.B., L.P., D.V., A.L., A.T. and D.C. Supervision: L.P., D.V., H.W.V., A.T. and D.C.

Corresponding authors

Correspondence to Amalio Telenti or Davide Corti.

Ethics declarations

Competing interests

F.A.L., L.S., F.B., S.B., M.M.-R., J.N., J.Z., H.K., M.A., M.M., E.D., S.J., E.C., H.W.V., A.L., L.P., A.T. and D.C. are employees of Vir Biotechnology and may hold shares in Vir Biotechnology. H.W.V. is a founder of PierianDx and Casma Therapeutics. L.P. is a former employee and shareholder in Regeneron Pharmaceuticals. Neither company provided funding for this work or is performing related work. D.V. is a consultant for Vir Biotechnology. The laboratory of D.V. has received a sponsored research agreement from Vir Biotechnology. A patent application related to SIGLEC1 and SARS-CoV-2 recognition has been filed by IrsiCaixa (US 63/152,346). J.M.-P. reports institutional grants and educational and consultancy fees from AbiVax, Astra-Zeneca, Gilead Sciences, Grifols, Janssen, Merck and ViiV Healthcare. N.I.-U. reports institutional grants from Pharma Mar, Dentaid and Palobiofarma. The remaining authors declare no competing interests.

Additional information

Peer review information *Nature* thanks Stanley Perlman and the other, anonymous, reviewer(s) for their contribution to the peer review of this work.

Publisher's note Springer Nature remains neutral with regard to jurisdictional claims in published maps and institutional affiliations.

Extended data figures and tables

Extended Data Fig. 1 Characterization of DC-SIGN, L-SIGN and SIGLEC-1 as SARS-CoV-2 attachment factors.

a–b, Binding of antibodies targeting DC/-L-SIGN, DC-SIGN, SIGLEC1 or ACE2 on HEK293T stably over-expressing the respective attachment receptors was analyzed by flow cytometry (a) and immunofluorescence analysis (b) (scale bar: 50 μm). **c**, Stable HEK293T cell lines overexpressing lectins or ACE2 were infected with authentic SARS-CoV-2 (MOI 0.1) and immunostained at 24 h for nucleocapsid protein (red) (scale bar: 100 μm). **d**, HEK293T cells over-expressing the respective attachment receptors were infected with VSV-SARS-CoV-2 wildtype spike (grey bars) or spike bearing mutations of the B.1.1.7 variant (red bars). Luminescence was analyzed one day post infection ($n=4$ biologically independent replicates). **e**, Stable cell lines were incubated with anti-ACE2 polyclonal antibodies and infected with VSV-SARS-CoV-2 ($n=3$ biologically independent replicates).

Extended Data Fig. 2 Expression of attachment receptors in infected tissues.

a, Distribution and expression of ACE2, DC-SIGN, L-SIGN, and SIGLEC1 in the human lung cell atlas. **b**, Major cell types with detectable SARS-CoV-2 genome in bronchoalveolar lavage fluid and sputum of severe COVID-19 patients. Left panel shows a t-SNE embedding of single-cell gene expression profiles coloured by cell type and sized by viral load (logCPM); right panel, distribution plots by annotated cell type denote the cumulative fraction of cells (y-axis) with detected viral RNA per cell up to the corresponding logCPM value (x-axis). Viral RNA is also found in neutrophils, plasma and T cells – an observation that has been reported previously^{21,64,65,66,67,68,69,70} **c**, SIGLEC1 surface expression comparison. Mean number of SIGLEC1 antibody binding sites per cell displayed by SIGLEC1 stably transduced cell lines and different myeloid cells left untreated or exposed to IFNα or LPS for 48 h and assessed by quantitative FACS analysis. Data show mean values and SEM from one experiment including cells from 3 donors.

Extended Data Fig. 3 Characterization of SARS-CoV-2-susceptible cell lines.

a, SARS-CoV-2 neutralization with S309, S2E12 and S2X333 on Vero E6 or Vero E6-TMPRSS2 cells. Cells were infected with SARS-CoV-2 (isolate USA-WA1/2020) at MOI 0.01 in the presence of the respective mAbs. Cells were fixed 24h post infection, viral nucleocapsid protein was immunostained and quantified ($n = 3$ biologically independent replicates). **b**, IFA images of experiment in (a): SARS-CoV-2 neutralization with 10 µg/ml of S309, S2E12 and S2X333 on Vero E6 or Vero E6-TMPRSS2 cells (scale bar: 100 µm). **c**, Purified, fluorescently-labelled SARS-CoV-2 spike protein or RBD protein was incubated with the indicated cell lines and protein binding was quantified by flow cytometry. **d**, Cellular ACE2 and TMPRSS2 transcripts were quantified by RT-qPCR. Expression levels were adjusted by HPRT levels and are presented as normalized to HeLa cell levels, showing the mean of technical triplicates. **e**, Correlation analysis between ACE2 transcript levels and maximum antibody neutralization in all SARS-CoV-2-susceptible cell lines. Nonparametric, two-tailed Spearman correlation was calculated using GraphPad Prism.

Extended Data Fig. 4 S309 or a cocktail of S309 and S2E12 provide robust in vivo protection against SARS-CoV-2 challenge.

Syrian hamsters ($n = 4$ –19) were injected with the indicated amount of mAb(s) 48 h before intra-nasal challenge with SARS-CoV-2. **a–b**, Quantification of viral RNA in the lungs 4 days post-infection. *** $p < 0.0001$ vs C; $\circ\circ p = 0.0023$ 4 vs 0.1, $p = 0.0096$ 1.5 vs 0.1. **c–d**, Quantification of replicating virus in lung homogenates harvested 4 days post infection using a TCID50 assay. *** $p < 0.0001$ vs C; *** $p = 0.0002$ 1.5 vs C; * $p = 0.0146$ 0.4 vs C; $\circ\circ p = 0.0056$ 4 vs 0.1; $\circ p = 0.0236$ 1.5 vs 0.1. **e–f**, Histopathological score of the lung tissue was assessed 4 days post infection. *** $p = 0.0005$ vs C; * $p = 0.0369$ vs C. Nonparametric one-way ANOVA, Kruskal-Wallis test with Dunn's multiple comparisons test (alpha threshold 0.05). Data are from at least 2 independent experiments, except the group dosed with 0.1 mg/kg ($n = 4$) that was tested once. **g–h**, Efficacy plots based on the correlation between the level of serum antibody measured at the time of infection and the level of SARS-CoV2 (viral RNA) measured in lungs on day 4 after infection. The dotted lines represents EC50 and EC90 for viral reduction (EC90 of S309 alone vs S309 + S2E12: 9 vs 11 µg/ml, respectively).

[Source data](#)

Extended Data Fig. 5 Binding of immunocomplexes to hamster splenocytes/FcgR and role of host effector function in SARS-CoV-2 challenge.

Alexa-488 fluorescent IC were titrated (0–200 nM range) and incubated with total naïve hamster splenocytes. Binding was revealed with a cytometer upon exclusion of dead/apoptotic cells and physical gating on bona fide monocyte population. **a**, fluorescent intensity associated to hamster cells of immune-complex (IC) made with either hamster (GH-S309, dark grey and GH-S309-N297A, blue) or human (Hu-S309, green) Fc antibodies. A single replicate of two is shown. **b**, relative Alexa-488 mean fluorescent intensity of the replicates measured on the entire monocyte population. Data are from a single representative experiment repeated three times with similar results. **c–d**, kinetics of binding of the same hamster and human ICs to hamster FcgRIV (panel C) and human FcgRIIIA (panel D) by Octet BLI analysis. **e–g**, Syrian hamsters ($n = 6$) were injected with the indicated amount (mg/kg) of hamster IgG2a S309 either wt or Fc silenced (S309-N297A). **e**, Quantification of viral RNA in the lung 4 days post infection. ** p = 0.0022 vs control. **f**, Quantification of replicating virus in the lung 4 days post infection. ** p = 0.0022 vs control **g**, Histopathological score in the lung 4 days post infection. ** p = 0.0022 vs C; * p = 0.0411 1.5 (N297A) vs C, p = 0.0130 4 (N297A) vs control. Control animals (white symbols) were injected with 4 mg/kg unrelated control isotype mAb. 2-tailed nonparametric Mann-Whitney t test (alpha threshold 0.05). Data are from a single experiment.

Source data

Extended Data Fig. 6 RBM mAbs trigger the fusogenic rearrangement of the S protein and promote membrane fusion.

a, MAbs or soluble ACE2 were incubated for 1 h with native-like soluble prefusion S trimer of SARS-CoV-2 to track by negative stain EM imaging the fusogenic rearrangement of soluble S trimers visible as rosettes (scale bar: 20 nm). 100 micrographs per sample were analyzed. **b**, Cell-cell fusion of CHO cells expressing SARS-CoV-2 S (CHO-S) on the plasma membrane in the absence (upper panel) or presence of 5 µg/ml of S2E12 mAb (lower panel) as detected by immunofluorescence. Nuclei stained with Hoechst dye; cytoplasm stained with CellTracker Green (scale bar: 100 µm). **c**, CHO-S cell-cell fusion mediated by different spike-specific MAbs quantified as described in Methods. **d**, Structures of 11 Fab-RBD complexes related to MAbs used in (c) (RBD orientation is fixed) and of ACE2-RBD as determined by a combination of X-ray crystallography and cryo-EM analysis (PDBs, Extended Data Table 1). Shown in parentheses the RBD antigenic site as defined according to Piccoli et al.⁵. **e**, Inhibition of S2E12-induced cell-cell fusion performed as in (c) by a fixed amount (15 µg/ml) of indicated MAbs. **f**, Trans-fusion of S-positive CHO cells with S-negative fluorescently-labelled CHO cells. Staining as in (b) (scale bar: 300 µm, inset 50 µm). **g**, CHO-S cells were seeded in 96-well plates and incubated with S2E12 IgG or Fab. Cell-Cell fusion was quantified by imaging as described in methods.

Extended Data Fig. 7 Data collection and processing of the S/S2X58 complex cryoEM datasets.

a-b, Representative electron micrograph and 2D class averages of SARS-CoV-2 S in complex with the S2X58 Fab embedded in vitreous ice. Scale bar: 400 Å. **c**, Gold-standard Fourier shell correlation curves for the S2X58-bound SARS-CoV-2 S trimer in one RBD closed (black line) and three RBDs open conformations (gray line). The 0.143 cutoff is indicated by a horizontal dashed line. Due to steric clashes between the S2X58 Fab and the NTD of a neighboring monomer in the closed S state, this mAb appears to conformationally select the open RBDs, thus explaining its fusogenic activity. **d**, Local resolution maps calculated using cryoSPARC for the SARS-CoV-2 S/S2X58 Fab complex structure with one RBD closed and three RBDs open shown in two orthogonal orientations. **e**, Cryo-EM data collection statistics.

Extended Data Fig. 8 SARS-CoV-2 live virus neutralization.

a, HeLa cells expressing DC-SIGN are refractory to SARS-CoV-2 infection. HEK293T or HeLa cells stably expressing DC-SIGN were infected with SARS-CoV-2-Nluc at MOI 0.04 in the presence of the indicated antibodies. Infection was analyzed by quantification of luminescent signal at 24 h post infection ($n=2$ biologically independent replicates). **b**, Neutralization of infection by SARS-CoV-2-Nluc pre-incubated with the stem helix antibody S2P6 on HEK293T cell lines stably overexpressing lectins or ACE2. Infection was measured by luciferase signal 24h post infection ($n = 3$ biologically independent replicates) **c**, Infection neutralization by authentic SARS-CoV-2-Nluc pre-incubated with indicated mAbs on HEK293T cell lines stably overexpressing L-SIGN ($n=3$ biologically independent replicates). Infection was measured by luciferase signal 24h post infection ($n = 3$ biologically independent replicates). **d**, HEK293T cells stably expressing ACE2 or lectins were infected with SARS-CoV-2 at MOI 0.02 in the presence of the indicated mAbs. Cells were fixed 24h post infection, viral nucleocapsid protein was immunostained and positive cells were quantified ($n = 3$ biologically independent replicates). **e**, Summary of the mechanisms of action of different classes of spike-specific mAbs based on this and previous studies. *, mAb-mediated inhibition of fusion between CHO-spike cells and ACE2⁺ Vero-E6 cells; **, based on mAb-dependent activation of human Fcgrs performed with a bioluminescent reporter assay as in ref. ²⁵ ^a, S2X58 binds to open RBD due to a conformational clash with neighboring NTD.

Extended Data Fig. 9 Trans-infection neutralization.

HeLa cells transduced with DC-SIGN (a) or SIGLEC1 (b) were incubated with VSV-SARS-CoV-2, extensively washed and incubated with serial dilutions of anti-spike

antibodies. After 30 min, susceptible target cells (Vero-E6-TMPRSS2) were added for co-culture. Luminescence signal was quantified 24h post co-culturing to determine trans-infection levels ($n=3$ biologically independent replicates).

Extended Data Table 1 mAbs used in this study

Supplementary information

Supplementary Information

Flow cytometry gating strategies.

Reporting Summary

Source data

Source Data Extended Data Fig. 4

Source Data Extended Data Fig. 5

Rights and permissions

Reprints and Permissions

About this article

Cite this article

Lempp, F.A., Soriaga, L.B., Montiel-Ruiz, M. *et al.* Lectins enhance SARS-CoV-2 infection and influence neutralizing antibodies. *Nature* **598**, 342–347 (2021).
<https://doi.org/10.1038/s41586-021-03925-1>

- Received: 03 April 2021
- Accepted: 18 August 2021
- Published: 31 August 2021
- Issue Date: 14 October 2021

- DOI: <https://doi.org/10.1038/s41586-021-03925-1>

Share this article

Anyone you share the following link with will be able to read this content:

[Get shareable link](#)

Sorry, a shareable link is not currently available for this article.

[Copy to clipboard](#)

Provided by the Springer Nature SharedIt content-sharing initiative

This article was downloaded by **calibre** from <https://www.nature.com/articles/s41586-021-03925-1>

| [Section menu](#) | [Main menu](#) |

- Article
- Open Access
- [Published: 22 September 2021](#)

Biologically informed deep neural network for prostate cancer discovery

- [Haitham A. Elmarakeby](#) [ORCID: orcid.org/0000-0002-4315-4347^{1,2,3}](#),
- [Justin Hwang](#) [ORCID: orcid.org/0000-0003-1686-7103⁴](#),
- [Rand Arafeh^{1,2}](#),
- [Jett Crowdus^{1,2}](#),
- [Sydney Gang¹](#),
- [David Liu^{1,2}](#),
- [Saud H. AlDubayan^{1,2}](#),
- [Keyan Salari^{1,2,5}](#),
- [Steven Kregel⁶](#),
- [Camden Richter¹](#),
- [Taylor E. Arnoff^{1,2}](#),
- [Jihye Park^{1,2}](#),
- [William C. Hahn](#) [ORCID: orcid.org/0000-0003-2840-9791^{1,2}](#) &
- [Eliezer M. Van Allen](#) [ORCID: orcid.org/0000-0002-0201-4444^{1,2}](#)

Nature volume **598**, pages 348–352 (2021)

- 25k Accesses
- 200 Altmetric
- [Metrics details](#)

Subjects

- [Cancer genomics](#)
- [Computer science](#)

Abstract

The determination of molecular features that mediate clinically aggressive phenotypes in prostate cancer remains a major biological and clinical challenge^{1,2}. Recent advances in interpretability of machine learning models as applied to biomedical problems may enable discovery and prediction in clinical cancer genomics^{3,4,5}. Here we developed P-NET—a biologically informed deep learning model—to stratify patients with prostate cancer by treatment-resistance state and evaluate molecular drivers of treatment resistance for therapeutic targeting through complete model interpretability. We demonstrate that P-NET can predict cancer state using molecular data with a performance that is superior to other modelling approaches. Moreover, the biological interpretability within P-NET revealed established and novel molecularly altered candidates, such as *MDM4* and *FGFR1*, which were implicated in predicting advanced disease and validated in vitro. Broadly, biologically informed fully interpretable neural networks enable preclinical discovery and clinical prediction in prostate cancer and may have general applicability across cancer types.

[Download PDF](#)

Main

With the advancement of molecular profiling technologies, the ability to observe millions of genomic, transcriptional and additional features from patients with cancer and their tumours has grown markedly over the past decade. Specifically, in prostate cancer, the availability of rich molecular profiling data linked to clinical annotation has enabled discovery of many individual genes, pathways, and complexes that promote lethal castration-resistant prostate cancer (CRPC), which has led to both biological investigations and clinical evaluations of these individual features for predictive utility^{1,2,6,7,8,9,10,11,12}. However, the relationships between these molecular features and their combined predictive and biological contributions to disease progression, drug resistance and lethal outcomes remain largely uncharacterized.

There is a wide range of potential approaches when developing a predictive model, although each comes with trade-offs of accuracy and interpretability. In translational cancer genomics, interpretability of predictive models is critical, as properties that contribute to the predictive capabilities of the model may not only inform patient care, but also provide insights into the underlying biological processes to prompt functional investigation and therapeutic targeting. Linear models such as logistic regression tend to have high interpretability with less accurate predictive performance, whereas deep learning models often have less interpretability but higher predictive performance^{13,14}. Using a typical fully connected dense deep learning approach for building predictive models may also result in overfitting unless the network is well regularized, and such models have a tendency to be computationally expensive and less interpretable¹⁵.

Efforts to search for slimmer architecture and sparse networks given a full model demonstrated that sparse models can decrease storage requirements and improve computational performance^{16,17,18}. However, finding such a sparse model may be challenging, since the typical training–pruning–retraining cycle is usually computationally expensive, and recent studies indicate that building a sparse model de novo may be easier¹⁹. In addition, efforts to enhance the interpretability of deep learning models and the need to explain model decisions led to the development of multiple attribution methods, including LIME²⁰, DeepLIFT¹³, DeepExplain²¹ and SHAP²², that can be used to enhance the deep learning explainability and understand how the model is processing information and making decisions.

Together, the advances in sparse model development and attribution methods have informed the development of deep learning models to solve biological problems using customized neural network architectures that are inspired by biological systems. For example, visible neural networks were developed to model the effect of gene interaction on cell growth in yeast (DCell) and cancer cell line interactions with therapies (DrugCell)^{3,5}. A pathway-associated sparse deep neural network (PASNet) used a flattened version of pathways to predict patient prognosis in Glioblastoma multiforme²³. However, whether biologically informed neural networks can accelerate biological discovery with translational potential and simultaneously enable clinical predictive modelling is largely unknown. Here we hypothesized that a biologically informed deep learning model built on advances in sparse deep learning architectures, encoding of biological information and incorporation of explainability algorithms would achieve superior predictive performance compared with established models and reveal novel patterns of treatment resistance in prostate cancer, with translational implications.

Results

We developed a deep-learning predictive model that incorporates previous biologically established hierarchical knowledge in a neural network language to predict cancer state in patients with prostate cancer on the basis of their genomic profiles. A set of 3,007 curated biological pathways were used to build a pathway-aware multi-layered hierarchical network (P-NET) (Methods). In P-NET, the molecular profile of the individual is fed into the model and distributed over a layer of nodes representing a set of genes using weighted links (Fig. 1, Extended Data Fig. 1). Later layers of the network encode a set of pathways with increasing levels of abstraction, whereby lower layers represent fine pathways and later layers represent more complex biological pathways and biological processes. The connections between different layers are constrained to follow known child–parent relationships among encoded features, genes and pathways, and as a result the network is geared toward interpretability by design.

Fig. 1: Interpretable biologically informed deep learning.

 figure1

P-NET is a neural network architecture that encodes different biological entities into a neural network language with customized connections between consecutive layers (that is, features from patient profile, genes, pathways, biological processes and outcome). In this study, we focus primarily on processing mutations and copy-number alterations. The trained P-NET provides a relative ranking of nodes in each layer to inform generation of biological hypotheses. Solid lines show the flow of information from the inputs to generate the outcome and dashed lines show the direction of calculating the importance score of different nodes. Candidate genes are validated to understand their function and mechanism of action.

We trained and tested P-NET with a set of 1,013 prostate cancers (333 CRPCs and 680 primary cancers) (Methods; Supplementary Tables 1–5), divided into 80% training, 10% validation and 10% testing, to predict disease state (primary or metastatic disease) using somatic mutation and copy number data (Methods). The trained P-NET outperformed typical machine learning models, including linear and radial basis function support vector machine, logistic regression, and decision trees (area under the receiver operating characteristic (ROC) curve (AUC) = 0.93, area under the precision-recall curve (AUPRC) = 0.88, accuracy = 0.83) (Fig. 2, Extended Data Fig. 2, Supplementary Tables 6, 7, Methods). Incorporation of additional molecular features was feasible in P-NET (for example, fusions) but did not impact the performance of the model in this specific prediction task (Extended Data Figs. 3, 4). Furthermore, we evaluated whether the sparse model had characteristics distinct from a dense fully connected deep learning model. We trained a dense model with the same number of parameters as in the P-NET model on training sets with a logarithmically increasing number of samples from 100 to 811 (80% of the total number of samples). The mean performance (determined by AUC) of the P-NET model was higher than the dense model over all sample sizes, and this difference was statistically significant in smaller sample sizes (up to 500) (for example, mean AUC of fivefold cross-validation was significantly higher for P-NET compared with a dense network trained on 155

samples, $P = 0.004$) (Fig. 2c, Extended Data Fig. 5a–e; statistical test results are listed in Supplementary Table 8). Furthermore, a dense network that had the same number of neurons and layers as P-NET but a much larger number of parameters (14 million) also achieved inferior performance (Extended Data Fig. 5f).

Fig. 2: Prediction performance of P-NET.



a, P-NET outperforms other models in terms of the AUPRC, values shown in brackets, when tested on the testing set ($n = 204$ from the Armenia et al. dataset⁸). RBF, radial basis function. **b**, When evaluated using two independent external validation cohorts^{24,25}, P-NET achieves 73% true-negative rate (TN) and 80% true-positive rate (TP), showing that it can generalize to classify unseen samples. FN, false-negative rate; FP, false-positive rate. **c**, P-NET achieves better performance (measured as the average AUC over five cross-validation splits) with smaller numbers of samples compared to a dense fully connected network with the same number of parameters. The solid line represents the mean AUC and the bands represent mean \pm s.d. ($n = 5$ experiments). The difference in performance is statistically significant for all sample

sizes up to 500 ($*P < 0.05$, one-sided t -test) (Methods). **d**, Patients with primary prostate cancer and high P-NET scores, HPS, (wrongly classified by P-NET to be resistant samples) have a greater tendency to exhibit biochemical recurrence (BCR) compared with patients with lower P-NET scores, LPS, who tend to exhibit progression-free survival ($P = 8 \times 10^{-5}$; log-rank test, two sided). This shows that the P-NET model may be useful in stratifying patients in the clinic and predicting potential BCR (raw data are included in Supplementary Table 9). LPS, low P-NET score; HPS, high P-NET score.

We next performed external validation of the predictive aspects of the model using two additional prostate cancer validation cohorts, one primary²⁴ and one metastatic²⁵ (sample identifiers are listed in Supplementary Tables 4, 5; Methods). The trained P-NET model correctly classified 73% of the primary tumours and 80% of the metastatic tumours, indicating that the model can generalize to unseen samples with an adequate predictive performance (Fig. 2b). We hypothesized that patients with primary tumour samples incorrectly classified by P-NET as castration-resistant metastatic tumours may in fact have worse clinical outcomes. Patients with high P-NET scores misclassified as resistant disease were significantly more likely to have biochemical recurrence than patients with low P-NET scores ($P = 8 \times 10^{-5}$; log-rank test), indicating that for patients with primary prostate cancer, the P-NET score may be used to predict potential biochemical recurrence (Fig. 2d, Supplementary Table 9).

To understand the interactions between different features, genes, pathways and biological processes that contributed to the predictive performance and to study the paths of impact from the input to the outcome, we visualized the whole structure of P-NET with the fully interpretable layers after training (Fig. 3). Among aggregate molecular alterations, copy number variation was more informative compared with mutations, consistent with previous reports²⁶. In addition, P-NET selected a hierarchy of pathways (out of 3,007 pathways on which P-NET was trained) as relevant to classification, including cell cycle checkpoints, post-translational modification (including ubiquitination and SUMOylation) and transcriptional regulation by *RUNX2* and *TP53*. Multiple members of the cell cycle pathway have been functionally implicated in metastatic prostate cancer, and specifically functionally interrogated in treatment-resistant contexts^{27,28}. Ubiquitination and SUMOylation pathways contribute to the regulation of multiple tumour suppressors and oncogenes, including *AR*²⁹, and dysregulation of these pathways has been linked to prostate cancer initiation and progression in preclinical models³⁰. *RUNX2* is an osteogenic transcription factor that regulates cell proliferation and is associated with metastatic disease in patients with prostate cancer³¹.

Fig. 3: Inspecting and interpreting P-NET.

 **figure3**

Visualization of inner layers of P-NET shows the estimated relative importance of different nodes in each layer. Nodes on the far left represent feature types; the nodes in the second layer represent genes; the next layers represent higher-level biological entities; and the final layer represents the model outcome. Nodes with darker colours are more important, while transparent nodes represent the residual importance of undisplayed nodes in each layer. The contribution of a certain data type to the importance of each gene is depicted using the Sankey diagram—for example, the importance of the *AR* gene is driven mainly by gene amplification, the importance of *TP53* is driven by mutation, and the importance of *PTEN* is driven by deletion. NR, nuclear receptor; SHR, steroid hormone receptors; transc., transcription; transl., translation.

To evaluate the relative importance of specific genes contributing to the model prediction, we inspected the genes layer and used the DeepLIFT attribution method to obtain the total importance score of genes (Methods)¹³. Highly ranked genes included *AR*, *PTEN*, *RBI* and *TP53*, which are known prostate cancer drivers previously associated with metastatic disease^{1,2,9,32}. In addition, alterations in less expected genes, such as *MDM4*, *FGFRI*, *NOTCH1*³³ and *PDGFA*, strongly contributed to predictive performance (Extended Data Fig. 6, 7). To understand the behaviour of trained P-NET, we checked the activation of each node in the network, where activation here represents the signed outcome of a certain node given its inputs, and tested whether this activation changed with the change of the input sample class (primary versus metastatic) (Methods). We observed that the difference in the node activation was higher in higher layers and more concentrated in highly ranked nodes in each layer (Extended Data Fig. 8). For example, the activation distribution of the nodes of layer H3 was different when P-NET was given a primary sample compared with a resistant sample (Extended Data Fig. 8c). Thus, the interpretable architecture of P-NET can be interrogated to understand how the input information is transformed through layers and nodes, enabling further understanding of the state and importance of the involved biological entities.

Through evaluation of multiple layers in the P-NET trained model, we observed convergence in *TP53*-associated biology contributing to CRPC. Tracing the relevance of *TP53*-related pathways to the gene levels, roles for *TP53* and *MDM2* have been previously established in prostate cancer disease progression^{32,34,35,36,37,38,39,40}, we also observed alterations in *MDM4* that contributed substantially to this network convergence. *MDM4* can inhibit wild-type *TP53* expression by binding to and masking the transcriptional activation domain⁴⁰, although its role in prostate cancer treatment resistance is incompletely characterized⁴¹.

We further studied the *MDM4* profile both in clinical samples and in functional models. High amplification of *MDM4* was more prevalent in resistant samples compared with primary samples (χ^2 Yates correction = 40.8251, $P < 0.00001$). Alterations in *AR*, *TP53*, and *MDM4* genes are depicted in Fig. 4a. In a genome-wide gain-of-function preclinical screen using 17,255 open reading frames (ORFs) in LNCaP cells, *MDM4* overexpression was significantly associated with resistance to enzalutamide, a second-generation antiandrogen medication which is used for patients with CRPC⁴² (Fig. 4b). We then used CRISPR–Cas9 to target *MDM4* in multiple prostate cancer cell lines (Methods). Compared with a negative control, proliferation of prostate cancer cells was significantly reduced ($P < 0.0001$; *t*-test) (Fig. 4c; Supplementary Data 1) in response to *MDM4* depletion using two distinct single-guide RNAs (sgRNAs) (Extended Data Fig. 9, Supplementary Data 2). This indicated that selective therapeutic targeting of *MDM4* may be viable in patients with *TP53*-wild-type advanced prostate cancer. We thus sought to study the effect of inhibiting *MDM4* in prostate cell lines with mutant and wild-type *TP53*. Prostate cells with wild-type *TP53* were more sensitive to the *MDM4* selective inhibitor RO-5963 (which also inhibits *MDM2*) compared with *TP53*-mutant cell lines⁴³ (Fig. 4d; Methods). Overall, convergence of p53 pathway dysregulation across multiple layers of the trained P-NET model identified specific vulnerabilities involving *MDM4*, which can be therapeutically targeted with *MDM4*-selective inhibition in a genetically stratified prostate cancer patient population.

Fig. 4: Clinical and functional evaluation of P-NET.

 **figure4**

a, Joint distribution of *AR*, *TP53* and *MDM4* alterations across 1,013 prostate cancer samples using an UpSetPlot⁵⁵. A gene is defined as altered if it has a mutation, deep deletion or high amplification. **b**, Analysis of enzalutamide (enza)-resistant genes in LNCaP cells based on a genome-scale screen including 17,255 ORFs⁴². The relative enzalutamide resistance of each ORF (*x*-axis) is plotted as a Z-score (*y*-axis), with higher Z-scores representing more resistance (Supplementary Table 10). *MDM4* and other gene hits are highlighted on the graph, with *MDM4* scoring as the strongest hit among these genes. CSS, low androgen medium. **c**, Relative viability of C4-2, LNCaP, LNCaP Abl and LNCaP 95 cells after transduction of CRISPR–Cas9 and sgRNAs targeting *MDM4* (2 guides) or control GFP (2 guides). Data are mean \pm s.e.m. of three replicates (the experiment was repeated three times with three replicates; Supplementary Data 1). **d**, Sensitivity of different prostate cancer cell lines to RO-5963. Relative viability is shown at each indicated dosage of RO5963. Data are mean \pm s.d. of three replicates (the experiment was repeated three times; Supplementary Data 4). DU145, PC-3 and LAPC-4 are *TP53*-mutant prostate cancer cells; the other cells are *TP53* wild type.

Discussion

Broadly, P-NET leveraged a biologically informed, rather than arbitrarily overparameterized, architecture for prediction. As a result, P-NET markedly reduced the number of parameters for learning, which led to enhanced interpretability. The sparse architecture in P-NET has better predictive performance when compared to other machine learning models, including dense networks, and may be applicable to other similar tasks. Application of P-NET to a molecular cohort of patients with prostate cancer demonstrated (1) model performance that may enable prediction of clinically aggressive disease in populations of patients with primary prostate cancer, and (2) convergent biological processes that contribute to a metastatic prostate cancer clinical phenotype that harbour novel therapeutic strategies in molecularly stratified populations.

Furthermore, P-NET provided a simple way for integrating multiple molecular features (for example, mutations, copy number variations and fusions, among others) weighted differently to reflect their importance in predicting the final outcome, which previously required different statistical approaches for each feature to enable cancer gene discovery^{44,45}. Even more, P-NET provided a framework for encoding hierarchical prior knowledge using neural network languages and turning these hierarchies into a computational model that can be used both for prediction and for biological discovery in clinicogenomic contexts. Specifically, P-NET accurately predicted advanced prostate disease based on patients' genomic profiles and had the ability to predict potential biochemical recurrence. Visualization of the architecture of P-NET enabled a multilevel view of the involved biological pathways and processes, which may guide researchers to develop hypotheses regarding the underlying biological processes involved in cancer progression and translate these discoveries into therapeutic opportunities. Specifically, P-NET rediscovered known genes implicated in CRPC, such as *AR*, *PTEN*, *TP53* and *RBL*. Moreover, P-NET identified *MDM4* as a relevant gene in this clinical context, which was experimentally validated and may inform use of *MDM4*-selective inhibitors for genetically stratified (*TP53*-wild-type) patients with metastatic prostate cancer.

Whereas P-NET provides a framework for outcome prediction and hypothesis generation, the model still requires tuning and training before being used. As with all deep learning models, the final trained model heavily depends on the hyperparameters used to train the model. In addition, P-NET encodes biological pathways inside the network in a hardcoded way, which makes the model dependent on the quality of the annotations used to build the model. Use of models that leverage other hardcoded biological priors (such as KEGG and Gene Ontology) or user-specified specific biological modules may further guide model development and functional evaluation. Finally, advances in computation may enable use of this approach in a patient-specific

precision oncology schematic, paired with patient-specific model systems for directly comparable experimental assessments. Thus, the portability of this approach across different histological and clinical contexts requires further evaluation.

In conclusion, P-NET, a biologically informed deep neural network, accurately classified castration-resistant metastatic versus primary prostate cancers. Visualizing the trained model generated novel hypotheses for mechanisms of metastasis in prostate cancer and provided insights with direct potential for clinical translation in molecularly stratified prostate cancer patient populations. Biologically guided neural networks represent a novel approach to integrating cancer biology with machine learning by building mechanistic predictive models, providing a platform for biological discovery that may be broadly applicable across cancer prediction and discovery tasks.

Methods

P-NET design

We introduce P-NET, an artificial neural network with biologically informed, parsimonious architecture that accurately predicts metastasis in patients with prostate cancer on the basis of their genomic profiles. P-NET is a feedforward neural network with constraints on the nodes and edges. In P-NET, each node encodes some biological entity (for example, genes and pathways) and each edge represents a known relationship between the corresponding entities. The constraints on the nodes allow for better understanding of the state of different biological components. The constraints on the edges allow us to use a large number of nodes without increasing the number of edges, which leads to a smaller number of parameters compared to fully connected networks with the same number of nodes, and thus potentially fewer computations. The architecture was built using the Reactome pathway datasets⁴⁶. The whole Reactome dataset was downloaded and processed to form a layered network of five layers of pathways, one layer of genes, and one layer for features. This sparse model had slightly over 71,000 weights with the number of nodes per layer distributed as shown in Extended Data Fig. 1e. A dense network with the same number of nodes would have more than 270 million weights with the first layer containing more than 94% of the weights. A hybrid model which contains a sparse layer followed by dense layers still contains over 14 million weights. The number of dense weights is calculated as $w_l = n_l \times (n_{l-1} + 1)$, where w_l is the number of weights per layer l and n_l is the number of nodes of the same layer. Note that the P-NET model is not bound to a certain architecture, as the model architecture is automatically built by reading model specifications provided by the user via a gene matrix transposed file format (.gmt) file,

and custom pathways, gene sets and modules with custom hierarchies can be provided by the user.

The meaning of the nodes, layers and connection of P-NET is encoded through a carefully engineered architecture and a set of restrictions on the connections of the network. The input layer is meant to represent features that can be measured and fed into the network. The second layer represents a set of genes of interest. The higher layers represent a hierarchy of pathways and biological processes that are manually curated. The first layer of P-NET is connected to the next layer via a set of one-to-one connections, and each node in the next layer is connected to exactly three nodes of the input layer representing mutations, copy number amplification and copy number deletions. This scheme results in a much smaller number of weights in the first layer compared with a fully connected network and the special pattern of the connection matrix results in more efficient training. The second layer is restricted to have connections reflecting the gene-pathway relationships as curated by the Reactome pathway dataset. The connections are encoded by a mask matrix M that is multiplied by the weights matrix W to zero-out all the connections that do not exist in the Reactome pathway dataset. For the next layers, a similar scheme is devised to control the connection between consecutive layers to reflect the real parent-child relationships that exist in the Reactome dataset. The output of each layer is calculated as

$y = f[(M * W)^T x + b]$, where f is the activation function, M is the mask matrix, W is the weights matrix, x is the input matrix, b is the bias vector, and $*$ is the Hadamard product (see Extended Data Fig. 1a–c). The activation of each node is kept into the range of $[-1, 1]$ by applying the tanh function $\{f = \tanh\} = \{\{(\{rm\}\{e\})\}^{2x} - 1\} / \{\{(\{rm\}\{e\})\}^{2x} + 1\}$ to the weighted inputs of the node. The activation of the outcome layers is calculated by the sigmoid function $\{\sigma = 1 / (1 + \{(\{rm\}\{e\})\}^{-x})\}$.

To allow each layer to be useful by itself, we added a predictive layer with sigmoid activation after each hidden layer. P-NET has a smaller number of nodes per layer in the later layers compared to the first layers Extended Data Fig. 1e. Since it is more challenging to fit the data using a smaller number of weights in the later layers, we used a higher loss weight for later layer outcomes during the optimization process. The final prediction of the network was calculated by taking the average of all the layer outcomes, Extended Data Fig. 1d. The learning rate was initialized to be 0.001 and actively reduced after every 50 epochs to allow for smooth convergence. Since we have an unbalanced dataset, we weighted the classes differently to reduce the network bias toward one class based on the bias in the training set. The model was trained using Adam optimizer⁴⁷ to reduce the binary cross-entropy loss functions $H = \frac{1}{N} \sum_i \{y_i \log(p(y_i)) + (1-y_i) \log(1-p(y_i))\}$, where y_i is the label for sample i , $p(y_i)$ is the probability that sample i has a metastatic cancer as calculated using the sigmoid

function $\backslash(\sigma \backslash)$, and N is the total number of samples. Empirically we found that using adaptive learning rate besides Adam led to smoother convergence and improved prediction performance. We checked different gradient-based attribution methods to rank the features in all the layers, and we chose to use the DeepLIFT scheme as implemented in the DeepExplain library¹³.

DeepLIFT is a backpropagation-based attribution approach for assigning a sample-level importance score for each feature. In this work, we are interested in assigning scores for each node in each layer. Given a certain sample, a specific target t , and a set of layer nodes $\{(x_1^s, x_2^s, \dots, x_i^s, \dots, x_{n_l}^s)\}$, where n_l is the number of nodes in a certain layer l , DeepLIFT calculates an importance score $(C_i^{l,s})$ for each node on the basis of the difference in the target activation $t - t_0$ such that the difference equals the aggregation of the calculated scores for all the nodes. That is, the difference in target activation is given by:

$$\$ \$ \triangle t = t - \{t\}_0 \$ \$$$

Which equals the sum of all node scores when fed by a certain sample $\langle S \rangle$. That is,

$$\$ \$ \triangle t = \mathop{\sum} \limits_{i=1}^{n_l} \{C_i^{l,s}\} \$ \$$$

We used the ‘Rescale rule’ of DeepLIFT as implemented by DeepExplain to calculate the sample-level importance of all nodes in all layers. Further details are available in ref. [13](#). To calculate the total node-level importance (C_i^l) we aggregated the sample-level importance scores over all the n_s testing-set samples.

$$\$ \$ C_i^l = \mathop{\rm rm \{ \}} \mathop{\sum} \limits_{s=1}^{n_s} \{C_i^{l,s}\} \$ \$$$

Note that this is an absolute score (always positive) that measures the impact of a certain node on the outcome. The activation of the corresponding node i , however, could be positive or negative.

To reduce the bias introduced by over-annotation of certain nodes (nodes that are member of too many pathways), we adjusted the DeepLIFT scores using a graph informed function f that considers the connectivity of each node. The importance score (C_i^l) is divided by the node degree (d_i^l) if the node degree is larger than the mean of node degrees plus 5σ where σ is the standard deviation of node degrees.

$$\$ \$ d_i^l = \{fan\} \mathop{\rm rm \{ \}} \{in\}_i + \{fan\} \mathop{\rm rm \{ \}} \{out\}_i \$ \$$$

$$\begin{aligned}
 \text{\$\$} & \{\{\text{adjusted}\} \{\text{\rm}_}\} C\}_{\{i\}}^{\{l\}} = f(x) = \begin{cases} \frac{C_{\{i\}}^{\{l\}}}{\mu + \sigma} & \{d\}_{\{i\}}^{\{l\}} > \mu + \sigma \\ \text{otherwise} \end{cases} \\
 & \end{aligned}
 \text{\$\$}$$

P-NET training and evaluation

To check the utility of the developed model, we trained P-NET to predict cancer state (primary/metastatic) of patients with prostate cancer on the basis of their genomic profiles. We used tumour or germline-matched whole-exome sequencing of 1,013 patients along with the corresponding somatic mutations and copy number alterations that were prepared using a unified computational pipeline for harmonized somatic alteration derivation⁸ (annotated in this study as the ‘Armenia et al.’ cohort). The mutations were aggregated on the gene level with focus on nonsynonymous mutations to align with prior work on mutational significance in prostate cancer whole-exome datasets, excluding silent, intron, 3’ untranslated region (UTR), 5’ UTR, RNA and long intergenic non-coding RNA (lincRNA) mutations. The copy number alterations for each gene were assigned on the basis of the called segment-level copy number emphasizing high gains and deep deletions and excluding single-copy amplification and deletions, as defined by GISTIC2.0 and generated from the source data type. For secondary analyses involving RNA data (fusions, expression), bulk whole transcriptomes from the subset of the Armenia et al. cohort, where such data were available, were secured from their source studies ($n = 455$ from TCGA, $n = 204$ from SU2C-PCF consortia) for uniform alignment and quantification of RNA sequences. Reads were downloaded as FASTQs from TCGA (ISB-CGC; <https://isb-cgc.appspot.com/>) and as CRAMs from SU2C (from Amazon S3 bucket, dbGaP accession code, phs000915.v2.p2) and then converted to FASTQs using samtools fastq. In cases where an SU2C sample had both transcriptome capture and polyA sequencing, transcriptome capture was used to optimize for fusion detection as the primary use of these data. Adapters were trimmed with cutadapt v2.2 and reads were aligned using STAR aligner v2.7.2b^{48,49}. STAR-aligned bam files were passed into RSEM to generate gene-level transcript counts and transcript per million (TPM) quantifications using the GENCODE release 30 gene annotation lifted over to GRCh37. STAR chimeric junctions were supplied to STAR-Fusion v1.7.0 in kickstart mode to call fusions⁵⁰. Fusion calls were filtered down to those that included genes classified as oncogene or fusion in the Cancer Gene Census⁵¹. To test model flexibility for RNA-based fusion inputs, as a secondary analysis we also developed P-NET models trained to predict cancer state incorporating fusions or different definitions of copy number states (Extended Data Fig. 3, 4).

The prediction performance was measured using the average AUC, the AUPRC and the F1 score. The corresponding measures were reported for the testing split and also for the cross-validation setup. The input data were divided into a testing set (10%) and

a development set (90%). The development set was further divided into a validation set that has the same size as the testing set and the remaining samples are reserved for training. For the cross-validation experiments, the development dataset was divided into five folds stratified by the label classes to account for the bias in the dataset. The external validation results are produced by a model that is trained on the main dataset and tested on two independent external validation datasets. To mitigate the bias issue in the main dataset, we trained two models on two balanced subsamples drawn from the main dataset. The prediction scores of the two models are averaged to produce the final predictions on the two external validation datasets. The implementation of the proposed system along with the reproducible results are available on GitHub (https://github.com/marakeby/pnet_prostate_paper).

Statistical analysis

The change in the area under the ROC curve between P-NET and other models is tested using DeLong test⁵². The *P*-values are corrected for multiple hypothesis testing using FDR. For other scores including AUPRC, accuracy, F1 and recall, bootstrapping statistical test with 2,000 sampling is used and the difference in score median was tested for significance. The resulting *P* value was corrected using the false-discovery rate (FDR) method. The AUC of five-fold cross-validation resulting from training and testing P-NET and dense models over multiple sample sizes is compared using a *t*-test of the means for the null hypothesis that two samples (P-NET scores and dense scores) have identical average (expected) values with the assumption that the populations have identical variances. The same test is applied to other scores including recall, precision, AUPRC, F1 and accuracy. For the survival analysis (Fig. 2d), a nonparametric log-rank test is used to compare estimates of the hazard functions of the two groups at each observed event time. A *t*-test of means is used to compare the reduction of prostate cancer cells proliferation in comparison to negative control in response to *MDM4* depletion. Chi-squared test with Yates correction is used to compare the expected and observed frequencies of *MDM4* high amplifications in two groups (patients with primary and metastatic tumours).

Analysis of a genome-scale ORF screen

A genome-scale ORF screen was previously performed in LNCaP cells⁴². In brief, cells were infected with a pooled ORF library, subject to puromycin selection to isolate cells containing the respective ORFs, and then seeded in low androgen medium (CSS) with enzalutamide. The relative effect of each ORF on cell proliferation was determined after 25 days in culture and is represented as Z-scores. Raw results of the ORF screen were obtained from the Hwang et al. source study. We postulated that amplified genes identified by P-NET regulate oncogenic functions in metastatic CRPC. To validate this hypothesis, we analysed this previously published genome-

scale ORF screen performed in LNCaP cells, which identified genes that, when overexpressed, promoted resistance to the *AR* inhibitor, enzalutamide⁴² (Fig. 4b). LNCaP cells are dependent on *AR* and treatment with enzalutamide attenuates cell proliferation. On the basis of this analysis, *MDM4* scored as a robust enzalutamide-resistant gene relative to other hits, including cell cycle regulators (*CDK4* and *CDK6*) or those with roles in FGF signalling (*FGFR2*, *FGFR3* and *FGF6*); these are two pathways implicated in driving resistance to anti-androgen therapies in clinical prostate cancers^{27,53}.

Sensitivity to RO-5963

LNCaP, LNCaP Abl, LNCaP 95, DU145, LAPC-4, LNCaP enzalutamide resistant, C4-2 and PC3 cells were seeded in 96-well plates at a density of 3,000 cells per well. After 24 h, cells were treated with increasing concentrations of RO-5963 for 4 days. Cell proliferation was determined using CellTiter-Glo assay. IC₅₀ values were determined using GraphPad Prism. Data are represented as the mean ± s.d. of three replicates. The experiment was repeated three times (raw data and analysis files in Supplementary Data 4). All cell lines tested negative for mycoplasma contamination. Authentication was performed using STR profiles and/or obtained directly from ATCC for all publicly available cell lines.

MDM4 gene-depletion experiments

Blasticidin-resistant Cas9-positive prostate cancer cells were cultured in 150 µg ml⁻¹ blasticidin (Thermo Fisher Scientific, NC9016621) for 72 h to enrich cells with optimal Cas9 activity. One million cells were seeded in parallel in 12-well plates and infected with lentiviruses expressing puromycin-resistant sgRNAs targeting *MDM4* or GFP control. Cells were then subjected to puromycin selection for 3 days and then the cells were counted using a Vi-Cell and seeded for a proliferation assay. 7 days later, cells were counted again with a Vi-Cell to assess viability, representing a total of 12 days. The target sequence against GFP was CACCGGCCACAAGTTCAGCGTGTGCG (sgGFP). The target sequences against *MDM4* were AGATGTTAACACTGAGCAG (sgMDM4-1) and CTCTCCTGGACAAATCAATC (sgMDM4-2).

Immunoblotting

Cells were lysed using 2× sample buffer (62.5 mM Tris pH 6.8, 2% SDS, 10% glycerol, Coomassie dye) and freshly added 4% β-mercaptoethanol. Lysed cells were scraped, transferred into a 1.5 ml microcentrifuge tube, sonicated for 15 s and boiled at 95 °C for 10 min.

Proteins were resolved in NuPAGE 4–12% Bis-Tris Protein gels (Thermo Fisher Scientific) and run with NuPAGE MOPS SDS Running Buffer (Thermo Fisher Scientific, NP0001). Proteins were transferred to nitrocellulose membranes using an iBlot apparatus (Thermo Fisher Scientific). Membranes were blocked in Odyssey Blocking Buffer (LI-COR Biosciences, 927-70010) for 1 h at room temperature, and membranes were then cut and incubated in primary antibodies diluted in Odyssey Blocking Buffer at 4 °C overnight. The following morning, membranes were washed with phosphate-buffered saline with 0.1% Tween (PBST) and incubated with fluorescent anti-rabbit or anti-mouse secondary antibodies at a dilution of 1:5,000 (Thermo Fisher Scientific, NC9401842 (rabbit) and NC0046410 (mouse)) for 1 h at room temperature. Membranes were again washed with PBST and then imaged using an Odyssey Imaging System (LI-COR Biosciences). Primary antibodies used include *MDM4* (Abcam, ab16058) at a dilution of 1:500 and α-tubulin (Sigma, T9026) at a dilution of 1:1,000.

Gene depletion of *MDM4* reduces prostate cancer cell viability

To determine how prostate cancer cells would respond to precision tools that target *MDM4* at the gene level, we used CRISPR-Cas9 and two sgRNAs targeting distinct sequences of *MDM4* in prostate cancer cell lines. Compared with a negative-control sgRNA (GFP), viability of 4 different prostate cancer cells was reduced by about 50–80% (Fig. 4c) in response to *MDM4* depletion (Extended Data Fig. 9) after 12 days in culture. Altogether, we concluded that *MDM4* regulates enzalutamide resistance, and that targeting *MDM4* through either chemical or genetic approaches significantly attenuated the viability of prostate cancer cell lines. Our observations indicate that antagonizing *MDM4* in metastatic CRPCs that harbour wild-type p53 is an attractive precision strategy. *MDM4* antibodies (A300-287A) and (ab16058) were used together for immunoblotting experiments done in Extended Data Fig. 9.

Chemical inhibition of *MDM4* reduces prostate cancer cell viability

Given the proposed role of *MDM4* in driving enzalutamide resistance in prostate cancer cells, we sought to determine the response of prostate cancer cells to chemical inhibition of *MDM4*. We evaluated RO-5963, a small molecule *MDM2/4* dual inhibitor with the greatest selectivity towards *MDM4* in its class⁴³. This drug has previously demonstrated robust efficacy against *MDM4* dependent cancer cell lines⁵⁴. We evaluated the effects of increasing concentrations of RO-5963 on prostate cancer cell proliferation.

Reporting summary

Further information on research design is available in the [Nature Research Reporting Summary](#) linked to this paper.

Data availability

All data used and generated from this study are deposited in <https://doi.org/10.5281/zenodo.5163213>. These datasets were derived from the following public domain resources^{8,24,25,46}. The main dataset⁸ was downloaded from https://static-content.springer.com/esm/art%3A10.1038%2Fs41588-018-0078-z/MediaObjects/41588_2018_78_MOESM6_ESM.xlsx; https://static-content.springer.com/esm/art%3A10.1038%2Fs41588-018-0078-z/MediaObjects/41588_2018_78_MOESM4_ESM.txt; https://static-content.springer.com/esm/art%3A10.1038%2Fs41588-018-0078-z/MediaObjects/41588_2018_78_MOESM10_ESM.txt; https://static-content.springer.com/esm/art%3A10.1038%2Fs41588-018-0078-z/MediaObjects/41588_2018_78_MOESM10_ESM.txt; and https://static-content.springer.com/esm/art%3A10.1038%2Fs41588-018-0078-z/MediaObjects/41588_2018_78_MOESM5_ESM.xlsx. The external validation dataset^{24,25} was downloaded from https://met500.path.med.umich.edu/met500_download_datasets/somatic_v4.csv; https://static-content.springer.com/esm/art%3A10.1038%2Fnature20788/MediaObjects/41586_2017_BFnature20788_MOESM324_ESM.zip; and https://static-content.springer.com/esm/art%3A10.1038%2Fnature20788/MediaObjects/41586_2017_BFnature20788_MOESM325_ESM.zip.

Code availability

Custom code was developed as part of the analysis reported here, and has been deposited on GitHub: https://github.com/marakeby/pnet_prostate_paper. The library names and versions used in the implementation are provided in https://github.com/marakeby/pnet_prostate_paper/blob/master/environment.yml. The final version of the code will be permanently available, after publication acceptance, on <https://doi.org/10.5281/zenodo.5163855>.

References

1. 1.

Robinson, D., et al. Integrative clinical genomics of advanced prostate cancer. *Cell* **161**, 1215–1228 (2015).

2. 2.

Abida, W., et al. Genomic correlates of clinical outcome in advanced prostate cancer. *Proc. Natl Acad. Sci. USA* **116**, 11428–11436 (2019).

3. 3.

Ma, J., et al. Using deep learning to model the hierarchical structure and function of a cell. *Nat Methods* **15**, 290–298 (2018).

4. 4.

Yang, J. H., et al. A white-box machine learning approach for revealing antibiotic mechanisms of action. *Cell* **177**, 1649–1661.e9 (2019).

5. 5.

Kuenzi, B. M., et al. Predicting drug response and synergy using a deep learning model of human cancer cells. *Cancer Cell* **38**, 672–684.e6 (2020).

6. 6.

Gundem, G., et al. The evolutionary history of lethal metastatic prostate cancer. *Nature* **520**, 353–357 (2015).

7. 7.

Aggarwal, R., et al. Clinical and genomic characterization of treatment-emergent small-cell neuroendocrine prostate cancer: a multi-institutional prospective study. *J. Clin. Oncol.* **36**, 2492–2503 (2018).

8. 8.

Armenia, J., et al. The long tail of oncogenic drivers in prostate cancer. *Nat. Genet.* **50**, 645–651 (2018).

9. 9.

Quigley, D. A., et al. Genomic hallmarks and structural variation in metastatic prostate cancer. *Cell* **175**, 758–769.e9 (2018).

10. 10.

Rodrigues, D. N., et al. Immunogenomic analyses associate immunological alterations with mismatch repair defects in prostate cancer. *J. Clin. Invest.* **128**, 5185 (2018).

11. 11.

Chen, W. S., et al. Genomic drivers of poor prognosis and enzalutamide resistance in metastatic castration-resistant prostate cancer. *Eur. Urol.* **76**, 562–571 (2019).

12. 12.

Zhao, S. G., et al. The DNA methylation landscape of advanced prostate cancer. *Nat. Genet.* **52**, 778–789 (2020).

13. 13.

Shrikumar A., Greenside P., Kundaje A. Learning important features through propagating activation differences. Preprint at <https://arxiv.org/abs/1704.02685> (2017).

14. 14.

Murdoch, W. J., Singh, C., Kumbier, K., Abbasi-Asl, R., Yu, B. Definitions, methods, and applications in interpretable machine learning. *Proc. Natl Acad. Sci. USA* **116**, 22071–22080 (2019).

15. 15.

Xu, Q., Zhang, M., Gu, Z., Pan, G. Overfitting remedy by sparsifying regularization on fully-connected layers of CNNs. *Neurocomputing* **328**, 69–74 (2019).

16. 16.

Han S., Pool J., Tran J., Dally W. in *Advances in Neural Information Processing Systems* (eds Cortes C. et al.) 1135–1143 (Curran Associates, 2015).

17. 17.

Li H., Kadav A., Durdanovic I., Samet H., Graf H. P. Pruning filters for efficient ConvNets. Preprint at <http://arxiv.org/abs/1608.08710> (2016).

18. 18.

Frankle J., Carbin M. The lottery ticket hypothesis: finding sparse, trainable neural networks. In *International Conference on Learning Representations 2019* <https://openreview.net/forum?id=rJl-b3RcF7> (OpenReview, 2018).

19. 19.

Dettmers T., Zettlemoyer L. Sparse networks from scratch: faster training without losing performance. Preprint at <http://arxiv.org/abs/1907.04840> (2019).

20. 20.

Ribeiro M. T., Singh S. & Guestrin C. Why should I trust you?: Explaining the predictions of any classifier. In *Proc. 22nd ACM SIGKDD International Conference on Knowledge Discovery and Data Mining* 1135–1144 (ACM, 2016).

21. 21.

Ancona M., Ceolini E., Öztireli C., Gross M. Towards better understanding of gradient-based attribution methods for deep neural networks. Preprint at <http://arxiv.org/abs/1711.06104> (2017).

22. 22.

Lundberg S. M., Lee S.-I. in *Advances in Neural Information Processing Systems* 30 (eds Guyon I. et al.) 4765–4774 (Curran Associates, 2017).

23. 23.

Hao, J., Kim, Y., Kim, T.-K., Kang, M. PASNet: pathway-associated sparse deep neural network for prognosis prediction from high-throughput data. *BMC Bioinformatics* **19**, 510 (2018).

24. 24.

Fraser, M., et al. Genomic hallmarks of localized, non-indolent prostate cancer. *Nature* **541**, 359–364 (2017).

25. 25.

Robinson, D. R., et al. Integrative clinical genomics of metastatic cancer. *Nature* **548**, 297–303 (2017).

26. 26.

Hieronymus, H., et al. Copy number alteration burden predicts prostate cancer relapse. *Proc. Natl Acad. Sci. USA* **111**, 11139–11144 (2014).

27. 27.

Han, G. C., et al. Genomic resistance patterns to second-generation androgen blockade in paired tumor biopsies of metastatic castration-resistant prostate cancer. *JCO Precis. Oncol.* **1**, PO.17.00140 (2017).

28. 28.

Sharma, A., et al. The retinoblastoma tumor suppressor controls androgen signaling and human prostate cancer progression. *J. Clin. Invest.* **120**, 4478–4492 (2010).

29. 29.

Sutinen, P., Malinen, M., Heikkinen, S., Palvimo, J. J. SUMOylation modulates the transcriptional activity of androgen receptor in a target gene and pathway selective manner. *Nucleic Acids Res.* **42**, 8310–8319 (2014).

30. 30.

Chen, Z., Lu, W. Roles of ubiquitination and SUMOylation on prostate cancer: mechanisms and clinical implications. *Int. J. Mol. Sci.* **16**, 4560–4580 (2015).

31. 31.

Ge, C., et al. Role of Runx2 phosphorylation in prostate cancer and association with metastatic disease. *Oncogene* **35**, 366–376 (2016).

32. 32.

Levine, A. J. p53: 800 million years of evolution and 40 years of discovery. *Nat. Rev. Cancer* **20**, 471–480 (2020).

33. 33.

Farah, E., et al. NOTCH signaling is activated in and contributes to resistance in enzalutamide-resistant prostate cancer cells. *J. Biol. Chem.* **294**, 8543–8554 (2019).

34. 34.

Navone, N. M., et al. p53 protein accumulation and gene mutation in the progression of human prostate carcinoma. *J. Natl Cancer Inst.* **85**, 1657–1669 (1993).

35. 35.

Leite, K. R., et al. Abnormal expression of MDM2 in prostate carcinoma. *Mod. Pathol.* **14**, 428–436 (2001).

36. 36.

Zhang, Z., Li, M., Wang, H., Agrawal, S., Zhang, R. Antisense therapy targeting *MDM2* oncogene in prostate cancer: Effects on proliferation, apoptosis, multiple gene expression, and chemotherapy. *Proc. Natl Acad. Sci. USA* **100**, 11636–11641 (2003).

37. 37.

Schlomm, T., et al. Clinical significance of p53 alterations in surgically treated prostate cancers. *Mod Pathol.* **21**, 1371–1378 (2008).

38. 38.

Tovar, C., et al. MDM2 antagonists boost antitumor effect of androgen withdrawal: implications for therapy of prostate cancer. *Mol. Cancer* **10**, 49 (2011).

39. 39.

Feng, F. Y., et al. MDM2 inhibition sensitizes prostate cancer cells to androgen ablation and radiotherapy in a p53-dependent manner. *Neoplasia* **18**, 213–222 (2016).

40. 40.

Chopra, H., et al. Activation of p53 and destabilization of androgen receptor by combinatorial inhibition of MDM2 and MDMX in prostate cancer cells. *Oncotarget* **9**, 6270–6281 (2018).

41. 41.

Pei, D., Zhang, Y., Zheng, J. Regulation of p53: a collaboration between Mdm2 and Mdmx. *Oncotarget* **3**, 228–235 (2012).

42. 42.
Hwang, J. H., et al. CREB5 promotes resistance to androgen-receptor antagonists and androgen deprivation in prostate cancer. *Cell Rep.* **29**, 2355–2370.e6 (2019).
43. 43.
Graves, B., et al. Activation of the p53 pathway by small-molecule-induced MDM2 and MDMX dimerization. *Proc. Natl Acad. Sci. USA* **109**, 11788–11793 (2012).
44. 44.
Mermel, C. H., et al. GISTIC2.0 facilitates sensitive and confident localization of the targets of focal somatic copy-number alteration in human cancers. *Genome Biol.* **12**, R41 (2011).
45. 45.
Lawrence, M. S., et al. Discovery and saturation analysis of cancer genes across 21 tumour types. *Nature* **505**, 495–501 (2014).
46. 46.
Fabregat, A., et al. The Reactome pathway knowledgebase. *Nucleic Acids Res.* **46**, D649–D655 (2018).
47. 47.
Kingma D. P., Ba J. Adam: a method for stochastic optimization. Preprint at <http://arxiv.org/abs/1412.6980> (2014).
48. 48.
Martin, M. Cutadapt removes adapter sequences from high-throughput sequencing reads. *EMBnet.journal* **17**, 10–12 (2011).
49. 49.
Dobin, A., et al. STAR: ultrafast universal RNA-seq aligner. *Bioinformatics* **29**, 15–21 (2013).
50. 50.

Haas, B. J., et al. Accuracy assessment of fusion transcript detection via read-mapping and de novo fusion transcript assembly-based methods. *Genome Biol.* **20**, 213 (2019).

51. 51.

Sondka, Z., et al. The COSMIC Cancer Gene Census: describing genetic dysfunction across all human cancers. *Nat. Rev. Cancer* **18**, 696–705 (2018).

52. 52.

DeLong, E. R., DeLong, D. M., Clarke-Pearson, D. L. Comparing the areas under two or more correlated receiver operating characteristic curves: a nonparametric approach. *Biometrics* **44**, 837–845 (1988).

53. 53.

Bluemn, E. G., et al. Androgen receptor pathway-independent prostate cancer is sustained through FGF signaling. *Cancer Cell* **32**, 474–489.e6 (2017).

54. 54.

Howard, T. P., et al. MDM2 and MDM4 are therapeutic vulnerabilities in malignant rhabdoid tumors. *Cancer Res.* **79**, 2404–2414 (2019).

55. 55.

Lex, A., Gehlenborg, N., Strobelt, H., Vuillemot, R., Pfister, H. UpSet: visualization of intersecting sets. *IEEE Trans. Vis. Comput. Graph.* **20**, 1983–1992 (2014).

Acknowledgements

This work was supported by Fund for Innovation in Cancer Informatics (H.A.E. and E.M.V.A.), Mark Foundation Emerging Leader Award (E.M.V.), PCF-Movember Challenge Award (H.A.E. and E.M.V.A.), Physician Research Award (PC200150) of the US Department of Defense (S.H.A.), NIH U01 CA233100 (E.M.V.A.) and U01 CA176058 (W.C.H.)

Author information

Affiliations

1. Dana-Farber Cancer Institute, Boston, MA, USA

Haitham A. Elmarakeby, Rand Arafah, Jett Crowdus, Sydney Gang, David Liu, Saud H. AlDubayan, Keyan Salari, Camden Richter, Taylor E. Arnoff, Jihye Park, William C. Hahn & Eliezer M. Van Allen

2. Broad Institute of MIT and Harvard, Cambridge, MA, USA

Haitham A. Elmarakeby, Rand Arafah, Jett Crowdus, David Liu, Saud H. AlDubayan, Keyan Salari, Taylor E. Arnoff, Jihye Park, William C. Hahn & Eliezer M. Van Allen

3. Al-Azhar University, Cairo, Egypt

Haitham A. Elmarakeby

4. University of Minnesota, Division of Hematology, Oncology and Transplantation, Minneapolis, MN, USA

Justin Hwang

5. Department of Urology, Massachusetts General Hospital, Harvard Medical School, Boston, MA, USA

Keyan Salari

6. Department of Pathology, University of Illinois at Chicago, Chicago, IL, USA

Steven Kregel

Contributions

Conceptualization: H.A.E. and E.M.V. Methodology: H.A.E. and E.M.V. Software: H.A.E. Formal analysis: H.A.E., J.C., D.L., S.H.A., K.S., J.P. and E.M.V.A.

Investigation: J.H., R.A., S.G., S.K., C.R., T.E.A., H.A.E., W.C.H. and E.M.V.

Writing, original draft: H.A.E., J.H., C.R., T.E.A. and E.M.V. Writing, review and editing: H.A.E., J.H., D.L., S.H.A., K.S., C.R., T.E.A., J.P., W.C.H. and E.M.V.

Visualization: H.A.E., J.H., C.R., T.E.A. and E.M.V. Supervision: W.C.H. and E.M.V.

Funding acquisition: H.A.E., W.C.H. and E.M.V.

Corresponding author

Correspondence to Eliezer M. Van Allen.

Ethics declarations

Competing interests

W.C.H. is a consultant for Thermo Fisher, Solasta Ventures, iTeos, Frontier Medicines, Tyra Biosciences, MPM Capital, KSQ Therapeutics and Parexel and is a founder of KSQ Therapeutics. E.M.V. is a consultant/advisor for Tango Therapeutics, Genome Medical, Invitae, Enara Bio, Janssen, Manifold Bio and Monte Rosa Therapeutics. E.M.V. receives research support from Novartis and BMS. The other authors declare no competing interests.

Additional information

Peer review information *Nature* thanks Trey Ideker, Michal Rosen-Zvi and the other, anonymous, reviewer(s) for their contribution to the peer review of this work.

Publisher's note Springer Nature remains neutral with regard to jurisdictional claims in published maps and institutional affiliations.

Extended data figures and tables

Extended Data Fig. 1 P-NET architecture and characteristics.

a, Dense layer with inputs $(x \in \{R\}^{\{dx\}})$ and output $(y \in \{R\}^{\{dy\}})$ vectors. The matrix $(W \in \{R\}^{\{dx\} \times \{dy\}})$ is a trainable weights matrix and $(b \in \{R\}^{\{dy\}})$ is the bias vector. (f) is the layer activation function. **b**, Arbitrary sparse layers are flexible to encode any connection scheme with the added $(M \in \{\{0,1\}\}^{\{dx\} \times \{dy\}})$ binary mask matrix that controls the connectivity of the layer imposing sparsity on the weights matrix. **c**, A patterned sparse matrix with mask matrix (M) that follows a certain pattern. This pattern can be used to make computations more efficient. **d**, Predictive node is connected to each hidden layer in P-NET, and the final prediction is calculated by taking the average of all the predictive elements in the network. **e**, The number of parameters per layer of P-NET.

Extended Data Fig. 2 Computational performance of P-NET as compared to other models.

a, Original confusion matrix calculated by using a typical 0.5 threshold of the prediction scores to generate binary predictions. **b**, Adjusted confusion matrix calculated using an adaptive threshold that is used to maximize F1 score. **c**, The ROC

curve of P-NET compared to other models showing that P-NET outperforms other models in terms of the area under curve (AUC) when tested on the testing set ($n=204$ of Armenia et al dataset). The models are compared by repeatedly training and testing each model in a cross-validation setup ($n = 5$ experiments) with testing sample sizes of 188, 182, 182, 182, and 181 respectively. Performance metrics reported here include; accuracy (**d**), area under ROC curve (**e**), area under precision recall curve AUPRC (**f**), F1 measure (**g**), precision (**h**), and recall (**i**). P-NET outperforms other models on average using all the metrics except Precision. Data in **d-i** are represented as boxplots where the middle line is the median, the lower and upper hinges correspond to the 1st and 3rd quartiles, the whisker corresponds to the minimum or maximum values no further than $1.5 \times \text{IQR}$ from the hinge (where IQR is the inter-quartile range). Data beyond the end of the whiskers are outlying points that are plotted individually.

Extended Data Fig. 3 The effects of incorporating fusions in the P-NET model training.

The effect of incorporating fusions in the P-NET model training. Three models are reported here to study the effect of fusion on the P-NET performance i) ‘no-Fusion’ model incorporating only copy number and mutations for each gene ii) ‘Fusion’ model where fusion is added to the model as one binary variable to indicate whether a certain sample has fusion or not (restricted to ETS fusions and oncogene fusions). ‘Fusion (genes)’ model where fusions are included as binary variables for each gene indicating whether a certain gene was involved in a fusion or not (restricted to ETS fusions and oncogene fusions). **a**, The AUC curve of the three trained models showing similar performance when tested on the testing set. **b**, A bootstrapped version of the AUC comparison (2000 bootstrap samplings) showing similar performance of the three models. **c**, The importance score of all features showing that the fusion indicator has a non-zero score even when it is added to the 27k features fed into the model. **d**) The overall contributions of different data types (calculated as the aggregation of the importance scores of all corresponding features) showing minor contributions of the fusion features. The signal from the fusion features goes smaller when distributed over genes (‘Fusions (genes)’ model) compared to the single feature encoding (‘Fusion’ model). **e**, The effect of adding fusion on the top ranked nodes in each layer as compared to the baseline ‘no-Fusion’ model rankings. Adding the fusion has a small effect on the top ranked nodes in higher layers, e.g. more than %80 of the top ranked nodes in h5 has not been affected by the fusion addition (‘Fusion’ model) compared to the baseline ‘no-Fusion’ model. The effect of the fusion addition is more prominent in the earlier layers, especially h0.

Extended Data Fig. 4 The effects of CNV definition on the P-NET model performance and stability.

Two different models are trained on (i) mutations plus only high amplifications and deep deletions, referred to by ‘two copies’ in the legend and (ii) mutations plus all GISTIC2.0 states (deep deletion, deletion, neutral, amplification, high amplification) referred to by ‘single copy’ in the legends. **a)** AUC comparison between the two models showing slight increase in the performance when including all the copy number levels. **b)** The stability of top features is studied by comparing the overlap between features picked by the model over 5-fold data splits. The stability index is calculated for five data splits (D1-D5) where the cells show the overlap between top 10 features picked by the model for each pair of the data splits. **c)** comparing the stability index of the two models shows that restricting the copy number levels (‘two copies’ model) has a positive effect on stabilizing the features picked by the model when trained on different data splits.

[Extended Data Fig. 5 Performance comparison of sparse P-NET to dense models.](#)

Comparing the performance of P-NET to a dense network with the same number of trainable parameters using different sizes of training sets (**a**: Recall, **b**: Precision, **c**: AUPRC, **d**: F1, **e**: Accuracy). Sample sizes marked by (*) indicate statistically significant differences (p -value <0.05 , one-sided t -test) while those marked by (n.s.) are not. The solid line represents the mean and the bands represent mean \pm SD ($n=5$ experiments). **f**, Comparison of P-NET to a dense model with the same architecture (same number of nodes) but with large number of trainable parameters (14 M) shows that sparse P-NET is still better than a dense model in terms of the area under ROC curve, AUC.

[Extended Data Fig. 6 Relative ranking of nodes in each layer.](#)

Relative ranking of nodes in each layer based on P-NET total importance score. The height of the bar represents the estimated total importance score calculated as the summation of all sample-level importance scores over the testing set ($n = 204$). The error bar represents the 95-confidence interval around the estimated score calculated using 1000 bootstrap cycles over the testing set.

[Extended Data Fig. 7 Relationship between P-NET importance scores and copy number enrichment of important genes.](#)

a, Copy number enrichment of genes on chr1p (containing *MDM4*) relative to their model importance score. The y-axis shows the enrichment of the amplification in metastatic samples relative to primary samples, using -log (signed p) from Fisher’s exact test. There is evidence of high amplification enrichment around *MDM4* specifically, but the higher model coefficient (importance score) is also partially

informed by its relevance in biological pathways relative to neighboring genes (e.g. *PKP1*). **b)** There is less evidence for copy number focality being enriched around *EIF3E* on chr8q, which suggests that the model coefficient may be largely driven by the biological “bias” and less so by copy number focality. **c**, *PDGFA* on chr7p is a representative example where there is a mix of signal between modest focality at the peak where *PDGFA* is observed and biological “bias”.

Extended Data Fig. 8 Activation distribution of important nodes in each layer.

The activation distribution of top ranked nodes in each layer. Nodes in each layer are ordered based on their total importance score. The shown distribution is estimated using kernel density estimation to estimate the underlying distribution of node activations calculated for the testing set ($n = 204$). The current implementation of P-NET uses *tanh* activation function so the activation values are in the range -1 to 1 . The figure shows better discrimination between sample classes (Primary- blue vs. Metastatic-orange) in higher layers compared to lower layers and in top ranked nodes compared to lower ranked ones. This shows that the total importance score of the nodes is manifested locally through the differential activation of nodes (nodes process different samples differently).

Extended Data Fig. 9 Immunoblot confirming *MDM4* gene deletion.

Immunoblot confirming *MDM4* gene deletion in all cell lines used in Fig. 4-c. Tubulin is a loading control. Quantification of *MDM4* depletion is given under the *MDM4* blots. ImageStudioLite was used for quantification (Quantification numbers are included in Supplementary Data 3). The experiment was repeated 3 times with similar results.

Supplementary information

Reporting Summary

Supplementary Tables 1–10

Supplementary Table 1 IDs of samples used in training. Supplementary Table 2 IDs of samples used in testing. Supplementary Table 3 IDs of samples used in validation. Supplementary Table 4 External validation (Robinson et al. (2017)). Supplementary Table 5 External validation (primary). Supplementary Table 6 FDR-adjusted table for comparing P-NET to other models. Supplementary Table 7 P-NET compared to other models. Supplementary Table 8 *P*-values of comparing P-NET to dense models when

trained on different sample size. Supplementary Table 9 Survival data. Supplementary Table 10 functional ORF screen z-score list in all conditions from Hwang et al. (2019) used in Fig. 4

Supplementary Data 1

KD MDM4 proliferation raw data of 3 experiments in 4 cell lines in triplicates

Supplementary Data 2

MDM4 gene depletion experiments

Supplementary Data 3

Quantification of MDM4 of 3 western blot experiments

Supplementary Data 4

MDM4 inhibitor raw data, analysis files, figures and IC50

Rights and permissions

Open Access This article is licensed under a Creative Commons Attribution 4.0 International License, which permits use, sharing, adaptation, distribution and reproduction in any medium or format, as long as you give appropriate credit to the original author(s) and the source, provide a link to the Creative Commons license, and indicate if changes were made. The images or other third party material in this article are included in the article's Creative Commons license, unless indicated otherwise in a credit line to the material. If material is not included in the article's Creative Commons license and your intended use is not permitted by statutory regulation or exceeds the permitted use, you will need to obtain permission directly from the copyright holder. To view a copy of this license, visit <http://creativecommons.org/licenses/by/4.0/>.

Reprints and Permissions

About this article

Cite this article

Elmarakeby, H.A., Hwang, J., Arafeh, R. *et al.* Biologically informed deep neural network for prostate cancer discovery. *Nature* **598**, 348–352 (2021).

<https://doi.org/10.1038/s41586-021-03922-4>

- Received: 06 November 2020
- Accepted: 17 August 2021
- Published: 22 September 2021
- Issue Date: 14 October 2021
- DOI: <https://doi.org/10.1038/s41586-021-03922-4>

Share this article

Anyone you share the following link with will be able to read this content:

[Get shareable link](#)

Sorry, a shareable link is not currently available for this article.

[Copy to clipboard](#)

Provided by the Springer Nature SharedIt content-sharing initiative

This article was downloaded by **calibre** from <https://www.nature.com/articles/s41586-021-03922-4>

| [Section menu](#) | [Main menu](#) |

- Article
- [Published: 29 September 2021](#)

Circadian autophagy drives iTRF-mediated longevity

- [Matt Ulgherait](#)¹,
- [Adil M. Midoun](#)²,
- [Scarlet J. Park](#) [ORCID: orcid.org/0000-0002-1545-6284](#)^{3,4},
- [Jared A. Gatto](#)¹,
- [Samantha J. Tener](#) [ORCID: orcid.org/0000-0003-4367-7372](#)¹,
- [Julia Siewert](#)¹,
- [Naomi Klickstein](#)⁵,
- [Julie C. Canman](#)⁶,
- [William W. Ja](#) [ORCID: orcid.org/0000-0002-4003-7356](#)^{3,4} &
- [Mimi Shirasu-Hiza](#) [ORCID: orcid.org/0000-0002-2730-1765](#)¹

[Nature](#) volume **598**, pages 353–358 (2021)

- 9046 Accesses
- 220 Altmetric
- [Metrics details](#)

Subjects

- [Ageing](#)
- [Metabolism](#)

Abstract

Time-restricted feeding (TRF) has recently gained interest as a potential anti-ageing treatment for organisms from *Drosophila* to humans^{1,2,3,4,5}. TRF restricts food intake to specific hours of the day. Because TRF controls the timing of feeding, rather than nutrient or caloric content, TRF has been hypothesized to depend on circadian-regulated functions; the underlying molecular mechanisms of its effects remain unclear. Here, to exploit the genetic tools and well-characterized ageing markers of *Drosophila*, we developed an intermittent TRF (iTRF) dietary regimen that robustly extended fly lifespan and delayed the onset of ageing markers in the muscles and gut. We found that iTRF enhanced circadian-regulated transcription and that iTRF-mediated lifespan extension required both circadian regulation and autophagy, a conserved longevity pathway. Night-specific induction of autophagy was both necessary and sufficient to extend lifespan on an ad libitum diet and also prevented further iTRF-mediated lifespan extension. By contrast, day-specific induction of autophagy did not extend lifespan. Thus, these results identify circadian-regulated autophagy as a critical contributor to iTRF-mediated health benefits in *Drosophila*. Because both circadian regulation and autophagy are highly conserved processes in human ageing, this work highlights the possibility that behavioural or pharmaceutical interventions that stimulate circadian-regulated autophagy might provide people with similar health benefits, such as delayed ageing and lifespan extension.

Access options

Subscribe to Journal

Get full journal access for 1 year

\$199.00

only \$3.90 per issue

[Subscribe](#)

All prices are NET prices.
VAT will be added later in the checkout.

Tax calculation will be finalised during checkout.

Rent or Buy article

Get time limited or full article access on ReadCube.

from \$8.99

[Rent or Buy](#)

All prices are NET prices.

Additional access options:

- [Log in](#)
- [Access through your institution](#)
- [Learn about institutional subscriptions](#)

Fig. 1: iTRF extends lifespan and healthspan without dietary restriction.

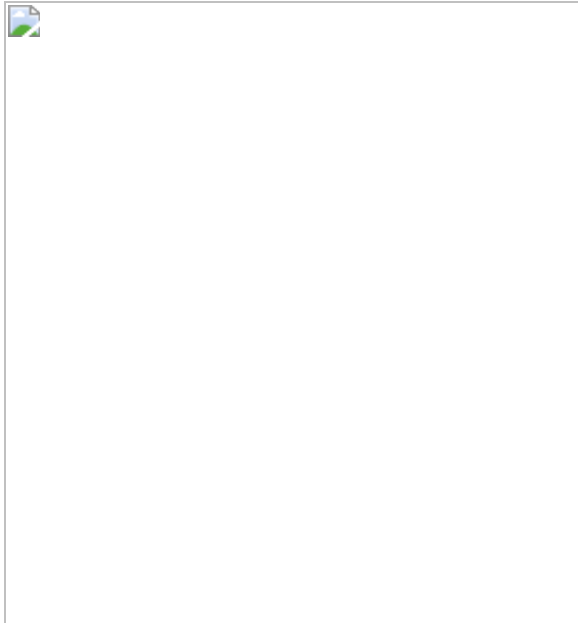


Fig. 2: Core circadian clock components are required for iTRF-mediated lifespan and healthspan extension.

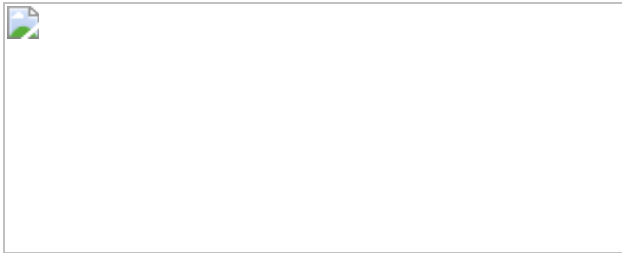


Fig. 3: Autophagy mediators are required for iTRF-mediated lifespan extension.

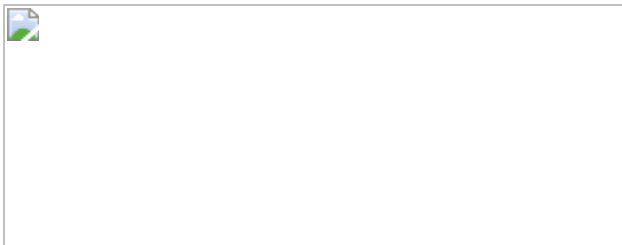
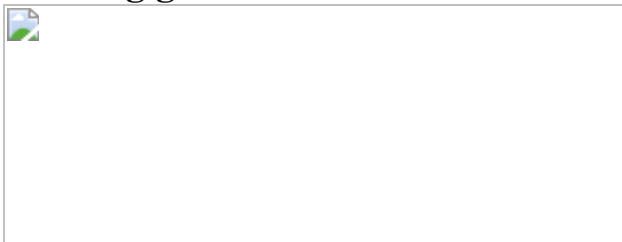


Fig. 4: Increasing circadian-regulated expression of autophagy-promoting genes is sufficient for the health benefits of iTRF.



Data availability

The authors declare that all data supporting the findings of this study are available, including replicate experiments, and will be made available on reasonable request from the corresponding author.

References

1. 1.

Longo, V. D. & Panda, S. Fasting, circadian rhythms, and time-restricted feeding in healthy lifespan. *Cell Metab.* **23**, 1048–1059 (2016).

2. 2.

Villanueva, J. E. et al. Time-restricted feeding restores muscle function in *Drosophila* models of obesity and circadian-rhythm disruption. *Nat. Commun.* **10**, 2700 (2019).

3. 3.

Chaix, A., Zarrinpar, A., Miu, P. & Panda, S. Time-restricted feeding is a preventative and therapeutic intervention against diverse nutritional challenges. *Cell Metab.* **20**, 991–1005 (2014).

4. 4.

Gill, S., Le, H. D., Melkani, G. C. & Panda, S. Time-restricted feeding attenuates age-related cardiac decline in *Drosophila*. *Science* **347**, 1265–1269 (2015).

5. 5.

de Cabo, R. & Mattson, M. P. Effects of intermittent fasting on health, aging, and disease. *N. Engl. J. Med.* **381**, 2541–2551 (2019).

6. 6.

Catterson, J. H. et al. Short-term, intermittent fasting induces long-lasting gut health and TOR-independent lifespan extension. *Curr. Biol.* **28**, 1714-1724.e4 (2018).

7. 7.

Manoogian, E. N. C. & Panda, S. Circadian rhythms, time-restricted feeding, and healthy aging. *Ageing Res. Rev.* **39**, 59–67 (2017).

8. 8.

Ja, W. W. et al. Prandiology of *Drosophila* and the CAFE assay. *Proc. Natl Acad. Sci. USA* **104**, 8253–8256 (2007).

9. 9.

Murphy, K. R., Park, J. H., Huber, R. & Ja, W. W. Simultaneous measurement of sleep and feeding in individual *Drosophila*. *Nat. Protoc.* **12**, 2355–2366 (2017).

10. 10.

Partridge, L., Alic, N., Bjedov, I. & Piper, M. D. W. Ageing in *Drosophila*: the role of the insulin/Igf and TOR signalling network. *Exp. Gerontol.* **46**, 376–381 (2011).

11. 11.

Cox, K. H. & Takahashi, J. S. Circadian clock genes and the transcriptional architecture of the clock mechanism. *J. Mol. Endocrinol.* **63**, R93–R102 (2019).

12. 12.

Dunlap, J. C. & Loros, J. J. Making time: conservation of biological clocks from fungi to animals. *Microbiol Spectr.* **5**, FUNK-0039-2016 (2017).

13. 13.

Allada, R. & Chung, B. Y. Circadian organization of behavior and physiology in *Drosophila*. *Annu. Rev. Physiol.* **72**, 605–624 (2010).

14. 14.

Panda, S. Circadian physiology of metabolism. *Science* **354**, 1008–1015 (2016).

15. 15.

Duong, H. A., Robles, M. S., Knutti, D. & Weitz, C. J. A molecular mechanism for circadian clock negative feedback. *Science* **332**, 1436–1439 (2011).

16. 16.

Xu, K., Zheng, X. & Sehgal, A. Regulation of feeding and metabolism by neuronal and peripheral clocks in *Drosophila*. *Cell Metab.* **8**, 289–300 (2008).

17. 17.

García-Gaytán, A. C. et al. Synchronization of the circadian clock by time-restricted feeding with progressive increasing calorie intake. Resemblances and differences regarding a sustained hypocaloric restriction. *Sci. Rep.* **10**, 10036 (2020).

18. 18.

Kinouchi, K. et al. Fasting imparts a switch to alternative daily pathways in liver and muscle. *Cell Rep.* **25**, 3299–3314.e6 (2018).

19. 19.

Wang, H. et al. Time-restricted feeding shifts the skin circadian clock and alters UVB-induced DNA damage. *Cell Rep.* **20**, 1061–1072 (2017).

20. 20.

Yamamoto, D. et al. Peripheral circadian rhythms in the liver and white adipose tissue of mice are attenuated by constant light and restored by time-restricted feeding. *PLoS ONE* **15**, e0234439 (2020).

21. 21.

Delventhal, R. et al. Dissection of central clock function in *Drosophila* through cell-specific CRISPR-mediated clock gene disruption. *eLife* **8**, e48308 (2019).

22. 22.

Ulgherait, M. et al. Circadian regulation of mitochondrial uncoupling and lifespan. *Nat. Commun.* **11**, 1927 (2020).

23. 23.

Ulgherait, M. et al. Dietary restriction extends the lifespan of circadian mutants tim and per. *Cell Metab.* **24**, 763–764 (2016).

24. 24.

Hansen, M., Rubinsztein, D. C. & Walker, D. W. Autophagy as a promoter of longevity: insights from model organisms. *Nat. Rev. Mol. Cell Biol.* **19**, 579–593 (2018).

25. 25.

Scott, R. C., Schuldiner, O. & Neufeld, T. P. Role and regulation of starvation-induced autophagy in the *Drosophila* fat body. *Dev. Cell* **7**, 167–178 (2004).

26. 26.

Kalfalah, F. et al. Crosstalk of clock gene expression and autophagy in aging. *Aging* **8**, 1876–1895 (2016).

27. 27.

Ma, D., Li, S., Molusky, M. M. & Lin, J. D. Circadian autophagy rhythm: a link between clock and metabolism? *Trends Endocrinol. Metab.* **23**, 319–325 (2012).

28. 28.

Rubinsztein, D. C., Mariño, G. & Kroemer, G. Autophagy and aging. *Cell* **146**, 682–695 (2011).

29. 29.

Chang, J. T., Kumsta, C., Hellman, A. B., Adams, L. M. & Hansen, M. Spatiotemporal regulation of autophagy during *Caenorhabditis elegans* aging. *eLife* **6**, e18459 (2017).

30. 30.

DeVorkin, L. & Gorski, S. M. Monitoring autophagy in *Drosophila* using fluorescent reporters in the UAS-GAL4 system. *Cold Spring Harb. Protoc.* **2014**, 967–972 (2014).

31. 31.

Ulgherait, M., Rana, A., Rera, M., Graniel, J. & Walker, D. W. AMPK modulates tissue and organismal aging in a non-cell-autonomous manner. *Cell Rep.* **8**, 1767–1780 (2014).

32. 32.

Mirouse, V., Swick, L. L., Kazgan, N., St Johnston, D. & Brenman, J. E. LKB1 and AMPK maintain epithelial cell polarity under energetic stress. *J. Cell Biol.* **177**, 387–392 (2007).

33. 33.

Barcelo, H. & Stewart, M. J. Altering *Drosophila* S6 kinase activity is consistent with a role for S6 kinase in growth. *Genesis* **34**, 83–85 (2002).

34. 34.

Tricoire, H. et al. The steroid hormone receptor EcR finely modulates *Drosophila* lifespan during adulthood in a sex-specific manner. *Mech. Ageing Dev.* **130**, 547–552 (2009).

35. 35.

Kaneko, M., Park, J. H., Cheng, Y., Hardin, P. E. & Hall, J. C. Disruption of synaptic transmission or clock-gene-product oscillations in circadian pacemaker cells of *Drosophila* cause abnormal behavioral rhythms. *J. Neurobiol.* **43**, 207–233 (2000).

36. 36.

Plautz, J. D., Kaneko, M., Hall, J. C. & Kay, S. A. Independent photoreceptive circadian clocks throughout *Drosophila*. *Science* **278**, 1632–1635 (1997).

37. 37.

Duffy, J. F., Zitting, K.-M. & Chinoy, E. D. Aging and circadian rhythms. *Sleep Med. Clin.* **10**, 423–434 (2015).

38. 38.

Cabrera, D., Young, M. W. & Axelrod, S. Time-restricted feeding prolongs lifespan in *Drosophila* in a peripheral clock-dependent manner. Preprint at *bioRxiv* <https://doi.org/10.1101/2020.09.14.296368> (2020).

39. 39.

Delventhal, R. et al. Dissection of central clock function in *Drosophila* through cell-specific CRISPR-mediated clock gene disruption. *eLife* **8**, e48308 (2019).

40. 40.

Murphy, K. R. et al. Postprandial sleep mechanics in *Drosophila*. *eLife* **5**, e19334 (2016).

41. 41.

Rera, M., Clark, R. I. & Walker, D. W. Intestinal barrier dysfunction links metabolic and inflammatory markers of aging to death in *Drosophila*. *Proc. Natl Acad. Sci. USA* **109**, 21528-21533 (2012).

42. 42.

Rera, M. et al. Modulation of longevity and tissue homeostasis by the *Drosophila* PGC-1 homolog. *Cell Metab.* **14**, 623-634 (2011).

43. 43.

Hughes, M. E., Hogenesch, J. B. & Kornacker, K. JTK_CYCLE: an efficient nonparametric algorithm for detecting rhythmic components in genome-scale data sets. *J. Biol. Rhythms* **25**, 372-380 (2010).

44. 44.

Claesson, M. J. et al. Comparison of two next-generation sequencing technologies for resolving highly complex microbiota composition using tandem variable 16S rRNA gene regions. *Nucleic Acids Res.* **38**, e200 (2010).

45. 45.

Rana, A., Rera, M. & Walker, D. W. Parkin overexpression during aging reduces proteotoxicity, alters mitochondrial dynamics, and extends lifespan. *Proc. Natl Acad. Sci. USA* **110**, 8638-8643 (2013).

46. 46.

Schneider, C. A., Rasband, W. S. & Eliceiri, K. W. NIH Image to ImageJ: 25 years of image analysis. *Nat. Methods* **9**, 671-675 (2012).

47. 47.

Copeland, J. M. et al. Extension of *Drosophila* life span by RNAi of the mitochondrial respiratory chain. *Curr. Biol.* **19**, 1591-1598 (2009).

Acknowledgements

We thank all members of the Shirasu-Hiza and Canman laboratories for support, discussions and feedback. We also thank D. W. Walker and J. Giebultowicz for fly lines. Other stocks were obtained from the Bloomington *Drosophila* Stock Center (NIH P40OD018537). Work was supported by Charles H. Revson Foundation (to M.U.), AFAR Glenn Foundation Postdoctoral Fellowship for Aging Research (to M.U.), Celia Lipton Farris and Victor W. Farris Foundation Graduate Student Fellowship (to S.J.P.), NIH T32GM007088 (to J.G.), NIH R01GM117407 (to J.C.C.), NIH R01GM130764 (to J.C.C.), Joe W. and Dorothy Dorsett Brown

Foundation (to W.W.J.), NIH R56AG065986 (to W.W.J.), NIH R35GM127049 (to M.S.-H.) and NIH R01AG045842 (to M.S.-H.).

Author information

Affiliations

1. Department of Genetics and Development, Columbia University Vagelos College of Physicians and Surgeons, New York, NY, USA

Matt Ulgherait, Jared A. Gatto, Samantha J. Tener, Julia Siewert & Mimi Shirasu-Hiza

2. Department of Biology, École Normale Supérieure, PSL Research University, Paris, France

Adil M. Midoun

3. Skaggs Graduate School, The Scripps Research Institute, Jupiter, FL, USA

Scarlet J. Park & William W. Ja

4. Department of Neuroscience, The Scripps Research Institute, Jupiter, FL, USA

Scarlet J. Park & William W. Ja

5. Department of Biological Sciences, Columbia University, New York, NY, USA

Naomi Klickstein

6. Department of Pathology and Cell Biology, Columbia University Vagelos College of Physicians and Surgeons, New York, NY, USA

Julie C. Canman

Contributions

M.U. and M.S.-H. conceived the experiments. Experiments were performed and analysed by M.U. (all), A.M.M. (lifespan experiments), S.J.P. and W.W.J. (feeding analysis), J.G. (western blots and lifespan experiments), S.J.T. (qRT–PCR and lifespan experiments), J.S. (lifespan experiments) and N.K. (biochemical and imaging experiments, and western blots). M.U., J.C.C. and M.S.-H. made intellectual contributions, designed the figures and wrote the manuscript.

Corresponding author

Correspondence to Mimi Shirasu-Hiza.

Ethics declarations

Competing interests

The authors declare no competing interests.

Additional information

Peer review information *Nature* thanks Tor Erik Rusten and the other, anonymous, reviewer(s) for their contribution to the peer review of this work.

Publisher's note Springer Nature remains neutral with regard to jurisdictional claims in published maps and institutional affiliations.

Extended data figures and tables

[**Extended Data Fig. 1 Lifespan changes in response to different feeding and fasting regimens.**](#)

Light blue boxes on graphs indicate duration of TRF (aqua), IF (medium blue), or iTRF (sky blue) during lifespan. **a**, Schematic of different feeding regimens utilized in *Drosophila* lifespan screen. **b**, 12-hour time-restricted feeding (TRF) from day 10 until death shortened female lifespan (top; *ad lib*, solid gray, n=292; TRF, dashed gray, n=142) and minimally extended male lifespan (bottom; *ad lib*, solid, n=241; TRF, dashed, n=314). **c**, In contrast, TRF from days 10-40 extended female (top; *ad lib*, solid gray, n=292; TRF, dashed gray, n=150) and male (bottom; *ad lib*, solid gray, n=241; TRF, dashed gray, n=406) lifespan. **d**, 24-hour intermittent fasting (IF) from day 10-death shortened both female (top; *ad lib*, solid gray, n=145; IF, dashed gray, n=149) and male (bottom top; *ad lib*, solid gray, n=241; IF, dashed gray, n=276) lifespan. **e**, Intermittent time-restricted feeding (iTRF) from day 10-death did not extend lifespan (*ad lib*, solid gray, n=142; TRF, dashed gray, n=157). **f**, iTRF regimen from days 10-40 extended male lifespan (*ad lib*, solid gray, n=323; TRF, dashed gray, n=382). (See [Methods](#) and SI for trials, statistics, and source data; n=number of individual flies; p-values were obtained by log-rank analysis (**b–f**).

[Extended Data Fig. 2 Characterization of iTRF windows and effect on feeding and dietary restriction.](#)

Light blue boxes on graphs indicate duration of iTRF during lifespan; solid and dashed lines represent flies on *ad lib* and iTRF diets, respectively. **a–e**, 10-day periods of iTRF in early to mid-life (days 10-40 of adulthood) can extend lifespan but not later in life (days 40-50): (**a**) days 10-20 with females (*ad lib* n=311; iTRF n=319); days 20-30 with (**b**) females (iTRF n=337) and (**c**) males (*ad lib* n=323; iTRF n=366); days 30-40 with (**d**) females (iTRF n=355) and (**e**) males (iTRF n=293) all extend lifespan. **f, g**, iTRF days 40-50 of adulthood did not extend male (iTRF n=302) or female (iTRF n=349) lifespan. **h**, Relative to flies on *ad lib* diet (dark gray dots, n=13), flies on iTRF (shown as blue or green dots depending on diet phase, n=14) starve during the fasting phase (n.a., no food available) and eat more during the feeding phase (green dots). **i**, iTRF extended mean lifespan regardless of dietary protein concentration (n=98-347 for each sample of *ad lib* or iTRF flies at each protein concentration). **j**, After partial genetic ablation of insulin producing cells, iTRF still extended lifespan (dashed

brown, n=424) relative to *ad lib* diet (solid brown, n=310), to a similar extent as in genetic controls (*ad lib*, solid gray, n=161; iTRF, dashed gray, n=180). (See [Methods](#) and SI for trials, statistics, and source data; n=number of individual flies; ***= $p<0.0001$; p-values were obtained by log-rank analysis (a-g, and j) and unpaired two-tailed t-test (h-i). Center values=averages; error bars=SEM.).

[Extended Data Fig. 3 iTRF delays aging markers \(protein aggregation and intestinal dysfunction\) and extends lifespan independent of microbiota.](#)

a, Representative western blot of Triton-insoluble protein accumulation of p62/ref(2)P (each sample=30 flies/condition/timepoint; see also Supplementary Fig. 1). **b**, Quantification of triton insoluble protein levels showed that iTRF flies (light gray) exhibited reduced accumulation of p62/ref(2)P with age, relative to *ad lib* flies (dark gray) (average of 4 biological repeats). **c**, Representative images of 40-day old indirect flight muscle stained for polyubiquitin protein aggregates (green), p62/ref(2)P (magenta), and filamentous actin (F-actin, blue); scale bar=50 μ m. **d, e**, iTRF significantly reduced (d) polyubiquitin aggregates and (e) accumulation of p62 aggregates (*ad lib* n=10 thoraces, iTRF n=11 thoraces). **f**, iTRF also reduced age-related intestinal over-proliferation, as marked by phospho-histone H3 staining (p-HH3) (*ad lib* n=8 guts; iTRF n=9 guts); scale bar=50 μ m. **g**, Light blue boxes on graphs indicate duration of iTRF during lifespan. iTRF (dashed line) delayed age-related intestinal barrier dysfunction relative to *ad lib* (solid line), as marked by decreased numbers of smurf flies (n=8-12 cohorts of 20-31 flies). **h-j**, Light colored boxes on graphs indicate duration of antibiotic treatment (AB, green) or antibiotic treatment plus iTRF diet (blue/green striped) during lifespan. iTRF flies showed delayed age-related growth in microbiome load with age (n=30 flies/condition/timepoint, 4 biological replicates) (**h**). iTRF extended lifespan upon microbiome clearance via antibiotics treatment during either (**i**) total lifespan (*ad lib* n=227, iTRF n=268) or (**j**) only days 10-40 of adulthood (*ad lib* n=144, iTRF n=190). (See [Methods](#) and SI for trials, statistics, and source data; n=number of flies unless otherwise indicated; n.s.= $p>0.05$, *= $p<0.05$, **= $p<0.01$, ***= $p<0.001$, ****= $p<0.0001$; p-values were obtained by ANOVA followed by Tukey's post-hoc test (**b, g**,

h), unpaired two-tailed student's t-test (**d–f**), and log-rank analysis (**i, j**). Center values=averages; error bars=SEM.).

Extended Data Fig. 4 Circadian mutants show a normal lifespan response to dietary protein restriction but do not respond to iTRF.

a, Gene expression of *timeless*, similar to *period* and *Clock*, was enhanced by iTRF during the fasting phase (each n=4 biological replicates of 30 female flies/genotype/condition/timepoint; unmarked=n.s.). **b, c**, Light blue boxes on graphs indicate duration of iTRF during lifespan. Circadian mutants did not respond to iTRF with extended lifespan relative to controls (*ad lib* n=187-288; iTRF n=290-311): **(b)** *cycle*⁰¹ (*ad lib* n=65, iTRF n=121) and **(c)** *timeless*⁰¹ (*ad lib* n=120, iTRF n=152) and *period*⁰¹ (*ad lib* n=215, iTRF n=184) null mutant females did not respond to iTRF with extended lifespan. **d, e, (d)** *cycle*⁰¹ and **(e)** *period*⁰¹ mutant females showed a normal “tent-curve” lifespan response to dietary protein titration (n=61-272 flies/genotype/condition/timepoint). **f**, *period*⁰¹ mutant females did not starve significantly faster than controls whether they have been on iTRF or *ad lib* diet (controls: *ad lib* n=31, iTRF n=35; *per*: *ad lib* n=27, iTRF n=42). **g**, Similar to controls (gray, *ad lib* n=30; light gray, iTRF, n=29), *period*⁰¹ mutant females (orange, *ad lib* n=27; light orange, iTRF, n=27) ate more on iTRF relative to on *ad lib* diet. **h**, Unlike control iTRF flies (light gray), which had reduced accumulation of p62/ref(2)P with age relative to *ad lib* flies (dark gray), *per* mutants had similar levels on *ad lib* (orange) or iTRF (light orange) diets (each dot=1 sample=30 flies; each bar=average of 4 biological repeats). Actin blot is repeated from Fig. [2h](#) because the same western blot was used to quantify Ubiquitin, p62/ref(2)P, and actin (loading control); see also Supplementary Fig. [1](#). **i**, Representative images of indirect flight muscle from 40-day-old flies stained for filamentous actin (F-actin, blue), ubiquitin (green), and p62/ref(2)P (magenta) showed that, unlike genetic controls (*ad lib* n=10, iTRF n=11 thoraces), *period* mutants did not have decreased polyubiquitin, or p62/ref(2)P aggregate accumulation in response to iTRF (*ad lib* n=10, iTRF n=10 thoraces); scale bar=50 μm. (See [Methods](#) and SI for trials, statistics, and source data; n=number of flies unless otherwise indicated; n.s.=p>0.05, * =p<0.05, **=p<0.01,

=p<0.001, *=p<0.0001; p-values were obtained by ANOVA followed by Tukey's post-hoc test (**a**, **g–i**) and log-rank analysis (**b**, **c**, **f**). Center values=averages; error bars=SEM.).

Extended Data Fig. 5 *period* mutants are defective in autophagy regulation and autophagy induction in response to fasting.

a, b, Similar to circadian genes, iTRF increased the peak amplitude of (**a**) *atg1* and (**b**) *atg8a* mRNA expression during the fasting period in wild-type flies (gray) but not *period*⁰¹ mutants (orange) (each dot=1 sample of 30 flies; each bar=average of 4 biological repeats). **c, d**, *period*⁰¹ mutants (orange) had (**c**) reduced activation of AMPK and (**d**) high levels of TORC1 activity as marked by S6K phosphorylation, both in response to fasting during iTRF, compared to controls (gray) (each dot=1 sample of 30 flies; each bar=average of 4 biological repeats); see also Extended Data Fig. 10. **e**, Representative images of posterior midgut cells during fasting phase of iTRF of 35-day-old flies labeled with LysoTracker™ (magenta), GFP-Atg8a (green), and DAPI to label the DNA (blue), showed that control animals (n=8 guts; each dot represents 2-3 Z-stacks of the posterior midgut of 1 animal) had high levels of LysoTracker™ and GFP-Atg8a puncta compared to *period* mutants (n=8 guts); scale bar=20 μm; white dashed boxes on images represent inset area presented in Fig. 3g. (See [Methods](#) and SI for trials, statistics, and source data; n=number of flies unless otherwise indicated; n.s.=p>0.05, * =p<0.05, ** =p<0.01, *** =p<0.001, **** =p<0.0001; p-values were obtained by ANOVA followed by Tukey's post-hoc test (a-d) and unpaired, two-tailed t-test (e). Center values=averages; error bars=SEM.).

Extended Data Fig. 6 Circadian manipulation of upstream metabolic and autophagy regulators partially determines lifespan response to iTRF.

Light blue boxes on graphs indicate duration of iTRF during lifespan. **a–d**, Relative to controls (gray: ad lib, solid, n=161; iTRF, dashed, n=164), which had an ~20% increase in mean lifespan in response to iTRF, circadian overexpression of: (**a**) dominant-negative (DN) AMPK (K57A,

sage green) shortened the lifespan of animals on *ad lib* diets (solid, n=184) and caused a 13% increase in mean lifespan in response to iTRF (dashed, n=170); **(b)** constitutively active (CA) AMPK (T184D, dark green) extended lifespan on *ad lib* diet (solid, n=156) and caused an 8% increase in mean lifespan in response to iTRF (dashed, n=134); **(c)** dominant-negative (DN) S6K (KQ, light blue) extended lifespan on *ad lib* diet (solid, n=292) and caused a 12% increase in mean lifespan in response to iTRF (dashed, n=180); **(d)** constitutively active CA-S6K (STDETE, medium blue) minimally shortened lifespan on *ad lib* diets (solid, n=237) and caused an 8% increase in mean lifespan in response to iTRF (dashed, n=282). **e, f**, RU486 feeding did not influence control (**e**) or *per⁰¹* (**f**) lifespan in flies lacking UAS transgenes (control: *ad lib* n=136-146, iTRF n=129-142; *per⁰¹*: *ad lib* n=294-501, iTRF n=238-415). (See [Methods](#) and SI for trials, statistics, and source data; n=number of flies; p-values were obtained by log-rank analysis (**a-f**)).

Extended Data Fig. 7 Circadian regulation of Atg8a is necessary for iTRF and sufficient to extend lifespan.

a, Using *tim*-GAL4 to drive expression of *mCherry-atg8a*, we confirmed oscillating mCherry-Atg8a and free mCherry protein expression by western blot analysis (see also Supplementary Fig. 1), which demonstrated circadian autophagic flux in controls on *ad lib* diet (each lane=30 flies; each time point of quantification=average of 3 biological repeats). **b-d**, Solid lines represent *ad lib* flies; dashed lines represent iTRF flies; light blue boxes on graphs indicate duration of iTRF during lifespan. RNAi-mediated circadian knockdown of **(b)** *atg1* (pink: *ad lib* n=217, iTRF n=166) and **(c)** *atg8a* (purple: *ad lib* n=196, iTRF n=139) was necessary for iTRF-mediated lifespan extension (controls, gray: *ad lib* n=194-316, iTRF n=196-409). **(d)** Circadian overexpression of mCherry-Atg8a was sufficient to extend lifespan on *ad lib* diet (solid lines: gray, control n=185; purple, mCh-*atg8a* n=422) and responded minimally to iTRF (dashed lines: gray, control n=421, purple, mCh-*atg8a* n=437). (See [Methods](#) and SI for trials, statistics, and source data; n=number of flies unless otherwise indicated; p-values were obtained by log-rank analysis (**b-d**). Center values=averages; error bars=SEM.).

Extended Data Fig. 8 *atg1* is necessary and sufficient for iTRF-mediated delays in aging-associated climbing defects and protein aggregation.

a, c, Light blue boxes on graphs indicate duration of iTRF during lifespan. **a, b**, Relative to controls (gray), circadian knockdown of *atg1* (pink) increased aging markers of (**a**) climbing defects (n=10 vials of 10 flies/condition/genotype/timepoint) and (**b**) protein aggregation (each lane=30 flies; each time point of quantification=average of 4 biological repeats) and made flies resistant to the effects of iTRF (dashed lines, lighter shades), relative to *ad lib* diets (solid lines, darker shades). **c, d**, In contrast, relative to controls (gray), circadian overexpression of *atg1* (magenta) decreased aging markers of (**c**) climbing defects (n=10 vials of 10 flies/condition/genotype/timepoint) and (**d**) protein aggregation (each lane=30 flies; each time point of quantification=average of 4 biological repeats; see also Supplementary Fig. 1) and also made flies resistant to the effects of iTRF (dashed lines), relative to *ad lib* diets (solid lines). (See [Methods](#) and SI for trials, statistics, and source data; n=number of flies unless otherwise indicated; n.s.=p>0.05, ***=p<0.001, ****=p<0.0001; p-values were obtained by ANOVA followed by Tukey's post-hoc test (**a-d**). Center values=averages; error bars=SEM.).

Extended Data Fig. 9 Enhanced autophagy specifically during the night phase is necessary and sufficient for TRF-mediated lifespan extension.

a, RU-induced overexpression of *atg1* during iTRF-like phases of the circadian cycle causes circadian enhanced, night-specific expression of *atg1* (n=4 biological replicates of 30 flies/timepoint/condition; unmarked=n.s.). **b, c**, Light aqua boxes on graphs indicate duration of shifted-TRF during lifespan. **b**, Relative to *ad lib* diet (*period⁰¹* mutants *ad lib*, solid orange, n=225), neither night-biased 12:12 treatment of shifted TRF (dashed orange, n=228) or RU-induced *atg1* expression (solid magenta, n=319) alone extended the lifespan of *per⁰¹* mutants. Combined, night-biased 12:12 shifted TRF and RU-induced *atg1* expression modestly increased lifespan of *per⁰¹* mutants (dashed magenta, n=239). **c**, Replotted here are *per⁰¹*

mutants on *ad lib* diet (solid orange, n=225) and on night-biased 12:12 shifted TRF (dashed orange, n=228). Day-biased 12:12 RU-induced exogenous *atg1* expression decreased the lifespan of *per⁰¹* mutants (solid magenta, n=206); this lifespan was increased by night-biased shifted TRF (dashed magenta, n=192). Also shown below are re-plots comparing control and *per⁰¹* mutant backgrounds with night (**b**) and day (**c**) biased RU-induced *atg1* expression on *ad lib* diet (second row) or shifted TRF (third row). **d**, Graphic schematic illustrating endogenous rhythms of *atg1* expression (gray) and the predicted effects of RU treatment and 12:12 TRF, either night biased and day-biased, on exogenous *atg1* expression.

(See [Methods](#) and SI for trials, statistics, and source data; n=number of flies unless otherwise indicated; n.s.=p>0.05, ***=p<0.001, ****=p<0.0001; p-values were obtained by ANOVA followed by Tukey's post-hoc test (**a**) and log-rank analysis (**b, c**). Center values=averages; error bars=SEM.).

Supplementary information

(a)

This file contains the Western blots used in this article. Dashed orange boxes indicate region of blot shown in each figure. Blots in Figure 1f and Extended Data Figure 3a showing anti-Ubiquitin (Ub, top), anti-p62 (ref(2)P; center), and anti-Actin (bottom) western blot staining of *ad lib* or iTRF fed-flies at days 7 or 40 post-eclosion. **(b)** Blots in Figure 2h and Extended Data Figure 4h showing anti-Ubiquitin (Ub, top), anti-p62 (ref(2)P; center), and anti-Actin (bottom) western blot staining of control and *period* mutant flies fed *ad lib* or iTRF diets at days 7 or 40 post-eclosion. **(c)** Blots in Figure 3e showing anti-mCherry (top) and anti-Actin (bottom) western blot staining of control and *period* mutant flies. **(d)** Blots in Extended Data Figure 7a showing anti-mCherry (top) and anti-Actin (bottom) western blot staining of control and *timeless-GAL4* driven *mCherry-atg8a* expressing flies. **(e)** Blots in Extended Data Figure 8b showing anti-Ubiquitin (Ub, top), anti-p62 (ref(2)P; center), and anti-Actin (bottom) western blot staining of control and *atg1-RNAi* flies fed *ad lib* or iTRF diets at days 7 or 40 post-eclosion. **(f)** Blots in Extended Data Figure 8d showing anti-Ubiquitin (Ub, top), anti-p62 (ref(2)P; center), and anti-

Actin (bottom) western blot staining of control and Atg1-overexpressing flies fed *ad lib* or iTRF diets at days 7 or 40 post-eclosion.

Reporting Summary

Supplementary Table 1

Supplementary Table 1 contains exact n, mean and medians, number of trials, and statistics for all lifespan experiments (Figures 1-4, Extended Data Figures 1-4 and 6-9), as well as climbing assays (Figures 2g, 8a, and 8c). Repeats are listed as “rep” in the “Figure” column; LS = lifespan; n=number of individual flies; p-values were obtained by log-rank analysis.

Supplementary Table 2

Supplementary Table 2 is the raw data source file, composed of a spreadsheet with 13 tabs; each tab contains the source data for a figure (Fig. 1-4) or extended data figure (ED1-9). Source data include tables of subjects at risk for lifespans, average food intake as measured by CaFe assay, percent flies past the marker for climbing assays, calculated mRNA levels using standard qRT-PCR methods, and blot quantitations.

Rights and permissions

Reprints and Permissions

About this article

Cite this article

Ulgherait, M., Midoun, A.M., Park, S.J. *et al.* Circadian autophagy drives iTRF-mediated longevity. *Nature* **598**, 353–358 (2021).
<https://doi.org/10.1038/s41586-021-03934-0>

- Received: 09 June 2020

- Accepted: 19 August 2021
- Published: 29 September 2021
- Issue Date: 14 October 2021
- DOI: <https://doi.org/10.1038/s41586-021-03934-0>

Share this article

Anyone you share the following link with will be able to read this content:

[Get shareable link](#)

Sorry, a shareable link is not currently available for this article.

[Copy to clipboard](#)

Provided by the Springer Nature SharedIt content-sharing initiative

[**Evidence that overnight fasting could extend healthy lifespan**](#)

- Stephen L. Helfand
- Rafael de Cabo

News & Views 29 Sept 2021

This article was downloaded by **calibre** from <https://www.nature.com/articles/s41586-021-03934-0>

- Article
- [Published: 29 September 2021](#)

Structure-based classification of tauopathies

- [Yang Shi](#) ORCID: [orcid.org/0000-0003-1579-7561¹](https://orcid.org/0000-0003-1579-7561),
- [Wenjuan Zhang](#)¹,
- [Yang Yang](#)¹,
- [Alexey G. Murzin](#)¹,
- [Benjamin Falcon](#)¹,
- [Abhay Kotecha](#) ORCID: [orcid.org/0000-0002-4480-5439²](https://orcid.org/0000-0002-4480-5439),
- [Mike van Beers](#)²,
- [Airi Tarutani](#)³,
- [Fuyuki Kametani](#) ORCID: [orcid.org/0000-0001-9125-7001³](https://orcid.org/0000-0001-9125-7001),
- [Holly J. Garringer](#) ORCID: [orcid.org/0000-0002-1899-7676⁴](https://orcid.org/0000-0002-1899-7676),
- [Ruben Vidal](#)⁴,
- [Grace I. Hallinan](#)⁴,
- [Tammaryn Lashley](#)⁵,
- [Yuko Saito](#)⁶,
- [Shigeo Murayama](#)⁷,
- [Mari Yoshida](#)⁸,
- [Hidetomo Tanaka](#) ORCID: [orcid.org/0000-0002-8490-3877⁹](https://orcid.org/0000-0002-8490-3877),
- [Akiyoshi Kakita](#)⁹,
- [Takeshi Ikeuchi](#) ORCID: [orcid.org/0000-0001-8828-8085¹⁰](https://orcid.org/0000-0001-8828-8085),
- [Andrew C. Robinson](#) ORCID: [orcid.org/0000-0003-2208-7728¹¹](https://orcid.org/0000-0003-2208-7728),
- [David M. A. Mann](#)¹¹,
- [Gabor G. Kovacs](#) ORCID: [orcid.org/0000-0003-3841-5511^{12,13}](https://orcid.org/0000-0003-3841-5511),
- [Tamas Revesz](#)⁵,
- [Bernardino Ghetti](#) ORCID: [orcid.org/0000-0002-1842-8019⁴](https://orcid.org/0000-0002-1842-8019),

- [Masato Hasegawa](#) ORCID: [orcid.org/0000-0001-7415-8159³](https://orcid.org/0000-0001-7415-8159),
- [Michel Goedert](#) ORCID: [orcid.org/0000-0002-5214-7886^{1 na2}](https://orcid.org/0000-0002-5214-7886) &
- [Sjors H. W. Scheres](#) ORCID: [orcid.org/0000-0002-0462-6540^{1 na2}](https://orcid.org/0000-0002-0462-6540)

[Nature](#) volume **598**, pages 359–363 (2021)

- 8584 Accesses
- 104 Altmetric
- [Metrics details](#)

Subjects

- [Cryoelectron microscopy](#)
- [Neurodegeneration](#)

Abstract

The ordered assembly of tau protein into filaments characterizes several neurodegenerative diseases, which are called tauopathies. It was previously reported that, by cryo-electron microscopy, the structures of tau filaments from Alzheimer's disease^{1,2}, Pick's disease³, chronic traumatic encephalopathy⁴ and corticobasal degeneration⁵ are distinct. Here we show that the structures of tau filaments from progressive supranuclear palsy (PSP) define a new three-layered fold. Moreover, the structures of tau filaments from globular glial tauopathy are similar to those from PSP. The tau filament fold of argyrophilic grain disease (AGD) differs, instead resembling the four-layered fold of corticobasal degeneration. The AGD fold is also observed in ageing-related tau astrogliopathy. Tau protofilament structures from inherited cases of mutations at positions +3 or +16 in intron 10 of *MAPT* (the microtubule-associated protein tau gene) are also identical to those from AGD, suggesting that relative overproduction of four-repeat tau can give rise to the AGD fold. Finally, the structures of tau filaments from cases of familial British dementia and familial Danish dementia are the same as those from cases of Alzheimer's disease and primary age-related tauopathy. These findings suggest a hierarchical classification of

tauopathies on the basis of their filament folds, which complements clinical diagnosis and neuropathology and also allows the identification of new entities—as we show for a case diagnosed as PSP, but with filament structures that are intermediate between those of globular glial tauopathy and PSP.

Access options

Subscribe to Journal

Get full journal access for 1 year

\$199.00

only \$3.90 per issue

[Subscribe](#)

All prices are NET prices.

VAT will be added later in the checkout.

Tax calculation will be finalised during checkout.

Rent or Buy article

Get time limited or full article access on ReadCube.

from \$8.99

[Rent or Buy](#)

All prices are NET prices.

Additional access options:

- [Log in](#)
- [Access through your institution](#)
- [Learn about institutional subscriptions](#)

Fig. 1: Three-layered 4R tau filament structures.

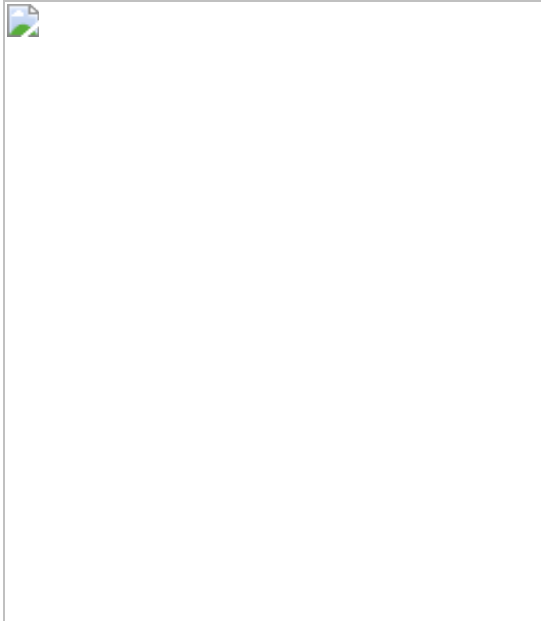


Fig. 2: Four-layered 4R tau filament structures.

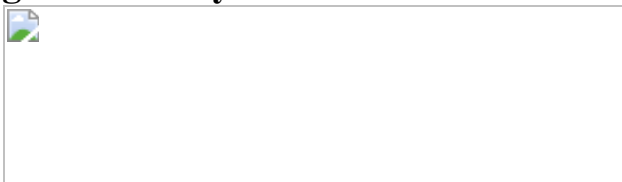


Fig. 3: Structure-based classification of tauopathies.



Data availability

Cryo-EM maps have been deposited in the Electron Microscopy Data Bank (EMDB) under accession numbers [EMD-13218](#) for PSP, [EMD-13219](#) for GGT-I, [EMD-13220](#) for GGT-II, [EMD-13221](#) for GGT-III, [EMD-13223](#) for GPT type 1a, [EMD-13224](#) for GPT type 1b, [EMD-13225](#) for GPT type 2, [EMD-13226](#) for AGD type 1 and [EMD-13227](#) for AGD type 2.

Corresponding refined atomic models have been deposited in the Protein Data Bank (PDB) under accession numbers [7P65](#) for PSP, [7P66](#) for GGT type 1, [7P67](#) for GGT type 2, [7P68](#) for GGT type 3, [7P6A](#) for GPT type 1a, [7P6B](#) for GPT type 1b, [7P6C](#) for GPT type 2, [7P6D](#) for AGD type 1 and [7P6E](#) for AGD type 2. Cryo-EM datasets have been deposited in the Electron Microscopy Public Image Archive (EMPIAR) under accession numbers 10765 for PSP-RS case 1, 10766 for the GGT-I case, 10767 for PSP-F case 2, 10768 for AGD case 1, and 10769 for the +16 case. Any other relevant data are available from the corresponding authors upon request.

References

1. 1.

Fitzpatrick, A. W. P. et al. Cryo-EM structures of tau filaments from Alzheimer's disease. *Nature* **547**, 185–190 (2017).

2. 2.

Falcon, B. et al. Tau filaments from multiple cases of sporadic and inherited Alzheimer's disease adopt a common fold. *Acta Neuropathol.* **126**, 699–708

3. 3.

Falcon, B. et al. Structures of filaments from Pick's disease reveal a novel tau protein fold. *Nature* **561**, 137–140 (2018).

4. 4.

Falcon, B. et al. Novel tau filament fold in chronic traumatic encephalopathy encloses hydrophobic molecules. *Nature* **568**, 420–423 (2019).

5. 5.

Zhang, W. et al. Novel tau filament fold in corticobasal degeneration. *Nature* **580**, 283–287 (2020).

6. 6.

Goedert, M., Spillantini, M. G., Jakes, R., Rutherford, D. & Crowther, R. A. Multiple isoforms of human microtubule-associated protein tau: sequences and localization in neurofibrillary tangles of Alzheimer's disease. *Neuron* **3**, 519–526 (1989).

7. 7.

Ghetti, B. et al. Frontotemporal dementia caused by microtubule-associated protein tau gene (*MAPT*) mutations: a chameleon for neuropathology and neuroimaging. *Neuropathol. Appl. Neurobiol.* **41**, 24–46 (2015).

8. 8.

Shi, Y. et al. Cryo-EM structures of tau filaments from Alzheimer's disease with PET ligand APN-1607. *Acta Neuropathol.* **141**, 697–708 (2021).

9. 9.

Steele, J. C., Richardson, J. C. & Olszewski, J. Progressive supranuclear palsy. a heterogeneous degeneration involving the brainstem, basal ganglia and cerebellum with vertical gaze and pseudobulbar palsy, nuchal dystonia and dementia. *Arch. Neurol.* **10**, 333–359 (1964).

10. 10.

Williams, D. R. et al. Characteristics of two distinct clinical phenotypes in pathologically proven progressive supranuclear palsy: Richardson's syndrome and PSP-parkinsonism. *Brain* **128**, 1247–1258 (2005).

11. 11.

Höglinger, G. U. et al. Clinical diagnosis of progressive supranuclear palsy: the Movement Disorder Society criteria. *Mov. Disord.* **32**, 853–864 (2017).

12. 12.

Kovacs, G. G. et al. Distribution patterns of tau pathology in progressive supranuclear palsy. *Acta Neuropathol.* **140**, 99–119 (2020).

13. 13.

Sanders, D. W. et al. Distinct tau prion strains propagate in cells and mice and define different tauopathies. *Neuron* **82**, 1271–1288 (2014).

14. 14.

Molina, J. A. et al. Primary progressive aphasia with glial cytoplasmic inclusions. *Eur. Neurol.* **40**, 71–77 (1998).

15. 15.

Ahmed, Z. et al. Globular glial tauopathies (GGT) presenting with motor neuron disease or frontotemporal dementia: an emerging group of 4-repeat tauopathies. *Acta Neuropathol.* **122**, 415–428 (2011).

16. 16.

Ahmed, Z. et al. Globular glial tauopathies (GGT): consensus recommendations. *Acta Neuropathol.* **126**, 537–544 (2013).

17. 17.

Clark, C. N. et al. Temporal variant frontotemporal dementia is associated with globular glial tauopathy. *Cogn. Behav. Neurol.* **28**, 92–97 (2015).

18. 18.

Tanaka, H. et al. Globular glial tauopathy type II: clinicopathological study of two autopsy cases. *Neuropathology* **39**, 111–119 (2019).

19. 19.

Fu, Y. J. et al. Sporadic, four-repeat tauopathy with frontotemporal lobar degeneration, Parkinsonism, and motor neuron disease: a distinct clinicopathological and biochemical disease entity. *Acta Neuropathol.* **120**, 21–32 (2010).

20. 20.

Miki, Y., Mori, F., Hori, E., Kaimori, M. & Wakabayashi, K. Hippocampal sclerosis with four repeat tau-positive round inclusions in the dentate gyrus: a new type of four-repeat tauopathy. *Acta Neuropathol.* **117**, 713–718 (2009).

21. 21.

Kovacs, G. G. et al. Tauopathy with hippocampal 4-repeat tau immunoreactive spherical inclusions: a report of three cases. *Brain Pathol.* **28**, 274–283 (2018).

22. 22.

Borrego-Écija, S. et al. Tauopathy with hippocampal 4-repeat tau immunoreactive spherical inclusions in a patient with PSP. *Brain Pathol.* **28**, 284–286 (2018).

23. 23.

Nakane, T. et al. Single-particle cryo-EM at atomic resolution. *Nature* **587**, 152–156 (2020).

24. 24.

Braak, H. & Braak, E. Argyrophilic grains: characteristic pathology of cerebral cortex in cases of adult-onset dementia without Alzheimer changes. *Neurosci. Lett.* **76**, 124–127 (1987).

25. 25.

Braak, H. & Braak, E. Cortical and subcortical argyrophilic grains characterize a disease associated with adult-onset dementia. *Neuropathol. Appl. Neurobiol.* **15**, 13–26 (1989).

26. 26.

Tolnay, M. & Clavaguera, F. Argyrophilic grain disease: a late-onset dementia with distinctive features among tauopathies. *Neuropathology* **24**, 269–283 (2004).

27. 27.

Saito, Y. et al. Staging of argyrophilic grains: an age-associated tauopathy. *J. Neuropathol. Exp. Neurol.* **63**, 911–918 (2004).

28. 28.

Ferrer, I., Santpere, G. & Van Leeuwen, F. W. Argyrophilic grain disease. *Brain* **131**, 1416–1432 (2008).

29. 29.

Kovacs, G. G. et al. Aging-related tau astrogliopathy (ARTAG): harmonized evaluation strategy. *Acta Neuropathol.* **131**, 87–102 (2016).

30. 30.

Klotz, S. et al. Multiple system aging-related tau astrogliopathy with complex proteinopathy in an oligosymptomatic octogenarian. *Neuropathology* **41**, 72–83 (2021).

31. 31.

Spillantini, M. G. et al. Familial multiple system tauopathy with presenile dementia: a disease with abundant neuronal and glial tau filaments. *Proc. Natl Acad. Sci. USA* **94**, 4113–4118 (1997).

32. 32.

Hutton, M. et al. Association of missense and 5'-splice-site mutations in tau with the inherited dementia FTDP-17. *Nature* **393**, 702–705 (1998).

33. 33.

Spillantini, M. G. et al. Mutation in the tau gene in familial multiple system tauopathy with presenile dementia. *Proc. Natl Acad. Sci. USA* **95**, 7737–7741 (1998).

34. 34.

Forrest, S. L. et al. Retiring the term FTDP-17 as MAPT mutations are genetic forms of sporadic frontotemporal tauopathies. *Brain* **141**, 521–534 (2018).

35. 35.

Arai, T. et al. Identification of amino-terminally cleaved tau fragments that distinguish progressive supranuclear palsy from corticobasal degeneration. *Ann. Neurol.* **55**, 72–79 (2004).

36. 36.

Taniguchi-Watanabe, S. et al. Biochemical classification of tauopathies by immunoblot, protein sequence and mass spectrometric analyses of sarkosyl-insoluble and trypsin-resistant tau. *Acta Neuropathol.* **131**, 267–280 (2016).

37. 37.

Miki, T. et al. Factors associated with development and distribution of granular/fuzzy astrocytes in neurodegenerative diseases. *Brain Pathol.* **30**, 811–830 (2020).

38. 38.

Vidal, R. et al. A stop-codon mutation in the *BRI* gene associated with familial British dementia. *Nature* **399**, 776–781 (1999).

39. 39.

Vidal, R. et al. A decamer duplication in the 3' region of the *BRI* gene originates an amyloid peptide that is associated with dementia in a Danish kindred. *Proc. Natl Acad. Sci. USA* **97**, 4920–4925 (2000).

40. 40.

Holton, J. L. et al. Regional distribution of amyloid-Bri deposition and its association with neurofibrillary degeneration in familial British dementia. *Am. J. Pathol.* **158**, 515–526 (2001).

41. 41.

Holton, J. L. et al. Familial Danish dementia: a novel form of cerebral amyloidosis associated with deposition of both amyloid-Dan and amyloid-beta. *J. Neuropathol. Exp. Neurol.* **61**, 254–267 (2002).

42. 42.

Dan, A. et al. Extensive deamidation at asparagine residue 279 accounts for weak immunoreactivity of tau with RD4 antibody in Alzheimer's disease brain. *Acta Neuropathol. Commun.* **1**, 54 (2013).

43. 43.

Duyckaerts, C. et al. PART is part of Alzheimer disease. *Acta Neuropathol.* **129**, 749–756 (2015).

44. 44.

Hallihan, G. I. et al. Structure of tau filaments in prion protein amyloidoses. *Acta Neuropathol.* **142**, 227–241 (2021).

45. 45.

Kametani, F. et al. Comparison of common and disease-specific post-translational modifications of pathological tau associated with a wide range of tauopathies. *Front. Neurosci.* **14**, 581936.

46. 46.

Grinberg, L. T. et al. Argyrophilic grain disease differs from other tauopathies by lacking tau acetylation. *Acta Neuropathol.* **125**, 581–593 (2013).

47. 47.

Kovacs, G. G. et al. *MAPT* S305I mutation: implications for argyrophilic grain disease. *Acta Neuropathol.* **116**, 103–118 (2008).

48. 48.

Rönnbäck, A. et al. Neuropathological characterization of two siblings carrying the *MAPT* S305S mutation demonstrates features resembling argyrophilic grain disease. *Acta Neuropathol.* **127**, 297–298 (2014).

49. 49.

Varani, L. et al. Structure of tau exon 10 splicing regulatory element RNA and destabilization by mutations of frontotemporal dementia and parkinsonism linked to chromosome 17. *Proc. Natl Acad. Sci. USA* **96**, 8229–8234 (1999).

50. 50.

Poorkaj, P. et al. Tau is a candidate gene for chromosome 17 frontotemporal dementia. *Ann. Neurol.* **43**, 815–825 (1998).

51. 51.

Bugiani, O. et al. Frontotemporal dementia and corticobasal degeneration in a family with a P301S mutation in tau. *J. Neuropathol. Exp. Neurol.* **58**, 667–677 (1999).

52. 52.

Lladó, A. et al. A novel *MAPT* mutation (P301T) associated with familial frontotemporal dementia. *Eur. J. Neurol.* **14**, e9–e10 (2007).

53. 53.

Lewis, J. et al. Neurofibrillary tangles, amyotrophy and progressive motor disturbance in mice expressing mutant (P301L) tau protein. *Nat. Genet.* **25**, 402–405 (2000).

54. 54.

Allen, B. et al. Abundant tau filaments and nonapoptotic neurodegeneration in transgenic mice expressing human P301S tau protein. *J. Neurosci.* **22**, 9340–9351 (2002).

55. 55.

Coughlin, D. G., Dickson, D. W., Josephs, K. A. & Litvan, I. Progressive supranuclear palsy and corticobasal degeneration. *Adv. Exp. Med. Biol.* **1281**, 151–176 (2021)

56. 56.

Josephs, K. A. et al. Atypical progressive supranuclear palsy with corticospinal tract degeneration. *J. Neuropathol. Exp. Neurol.* **65**, 396–405 (2006).

57. 57.

Clavaguera, F. et al. Brain homogenates from human tauopathies induce tau inclusions in mouse brain. *Proc. Natl Acad. Sci. USA* **110**, 9535–9540 (2013).

58. 58.

Evans, W. et al. The tau *H2* haplotype is almost exclusively Caucasian in origin. *Neurosci. Lett.* **369**, 183–185 (2004).

59. 59.

Farlow, J. L. et al. Whole-exome sequencing in familial Parkinson’s disease. *JAMA Neurol.* **73**, 68–75 (2016).

60. 60.

Spina, S. et al. The tauopathy associated with mutation +3 in intron 10 of *Tau*: characterization of the MSTD family. *Brain* **131**, 72–89 (2008).

61. 61.

Braak, H., Braak, E., Ohm, T. & Bohl, J. Silver impregnation of Alzheimer’s neurofibrillary changes counterstained for basophilic material and lipofuscin pigment. *Stain Technol.* **69**, 197–200 (1988).

62. 62.

Guo, H. et al. Electron-event representation data enable efficient cryoEM file storage with full preservation of spatial and temporal resolution. *IUCrJ* **7**, 860–869 (2020).

63. 63.

Zivanov, J. et al. A Bayesian approach to beam-induced motion correction in cryo-EM single-particle analysis. *IUCrJ* **6**, 5–17 (2020).

64. 64.

Rohou, A. & Grigorieff, N. CTFFIND4: fast and accurate defocus estimation from electron micrographs. *J. Struct. Biol.* **192**, 216–221.

65. 65.

He, S. & Scheres, S. H. W. Helical reconstruction in RELION. *J. Struct. Biol.* **198**, 163–176 (2017).

66. 66.

Zivanov, J. et al. New tools for automated high-resolution cryo-EM structure determination in RELION-3. *Elife* **7**, e42166 (2018).

67. 67.

Wagner, T. et al. SPHIRE-crYOLO is a fast and accurate fully automated particle picker for cryo-EM. *Commun. Biol.* **2**, 218 (2019).

68. 68.

Scheres, S. H. W. Amyloid structure determination in RELION-3.1. *Acta Crystallogr. D* **76**, 94–101 (2020).

69. 69.

Zivanov, J. et al. Estimation of high-order aberrations and anisotropic magnification from cryo-EM data sets in RELION-3.1. *IUCrJ* **7**, 253–267 (2020).

70. 70.

Chen, S. et al. High-resolution noise substitution to measure overfitting and validate resolution in 3D structure determination by single particle electron cryomicroscopy. *Ultramicroscopy* **135**, 24–35 (2013).

71. 71.

Casañal, A. et al. Current developments in Coot for macromolecular model building of electron cryo-microscopy and crystallographic data. *Protein Sci.* **29**, 1069–1078 (2020).

72. 72.

Williams, C. J. et al. MolProbity: more and better reference data for improved all-atom structure validation. *Protein Sci.* **27**, 293–315 (2018).

73. 73.

Brown, A. et al. Tools for macromolecular model building and refinement into electron cryo-microscopy reconstructions. *Acta Crystallogr. D* **71**, 136–153 (2015).

74. 74.

Afonine, P. V. et al. Real-space refinement in PHENIX for cryo-EM and crystallography. *Acta Crystallogr. D* **74**, 531–544 (2018).

75. 75.

Pettersen, E. F. et al. UCSF ChimeraX: structure visualization for researchers, educators, and developers. *Protein Sci.* **30**, 70–82 (2021).

Acknowledgements

We thank the families of the patients for donating brain tissues; U. Kuederli, M. Jacobsen, F. Epperson and R. M. Richardson for human brain collection and technical support; E. Gelpi for preparing brain samples from the ARTAG case; E. de Jong, B. van Knippenberg, L. Yu and E. Ioannou for support with the Krios G4 microscope; T. Darling and J. Grimmett for help with high-performance computing; and S. Lövestam, T. Nakane, R. A. Crowther, F. Clavaguera, K. Del Tredici, H. Braak, Z. Ahmed and M. G. Spillantini for helpful discussions. We acknowledge Diamond Light Source for access to and support with the cryo-EM facilities at the UK's national Electron Bio-imaging Centre (eBIC) (under proposals BI23268-49 and BI23268-19), funded by the Wellcome Trust, Medical Research Council (MRC) and Biotechnology and Biological Sciences Research Council (BBSRC). This study was supported by the MRC Laboratory of Molecular Biology Electron Microscopy facility. W.Z. was supported by a foundation that prefers to remain anonymous. M.G. is an Honorary

Professor in the Department of Clinical Neurosciences of the University of Cambridge. This work was supported by the UK MRC (MC_U105184291 to M.G. and MC_UP_A025_1013 to S.H.W.S.); the EU/EFPIA/Innovative Medicines Initiative (2) Joint Undertaking IMPRiND project 116060 to M.G.; the Japan Agency for Science and Technology (CREST) (JPMJCR18H3 to M.H.); the Japan Agency for Medical Research and Development (AMED) (JP20dm0207072 to M.H. and JP21dk0207045 and JP21ek0109545 to T.I.); JP20ek0109392, JP20ek0109391 and an Intramural Research Grant (number 30–8) for Neurological and Psychiatric Disorders of NCNP to M.Y.; the US National Institutes of Health (P30-AG010133, UO1-NS110437 and RF1-AG071177) to R.V., B.G. R.V. and B.G. were supported by the Department of Pathology and Laboratory Medicine, Indiana University School of Medicine. G.G.K. was supported by the Safra Foundation and the Rossy Foundation. T.R. is supported by the National Institute for Health Research Queen Square Biomedical Research Unit in Dementia. T.L. holds an Alzheimer’s Research UK Senior Fellowship. The Queen Square Brain Bank is supported by the Reta Lila Weston Institute for Neurological Studies.

Author information

Author notes

1. These authors contributed equally: Yang Shi, Wenjuan Zhang
2. These authors jointly supervised this work: Michel Goedert, Sjors H. W. Scheres

Affiliations

1. MRC Laboratory of Molecular Biology, Cambridge, UK

Yang Shi, Wenjuan Zhang, Yang Yang, Alexey G. Murzin, Benjamin Falcon, Michel Goedert & Sjors H. W. Scheres

2. Thermo Fisher Scientific, Eindhoven, The Netherlands

Abhay Kotecha & Mike van Beers

3. Department of Brain and Neurosciences, Tokyo Metropolitan Institute of Medical Science, Tokyo, Japan

Airi Tarutani, Fuyuki Kametani & Masato Hasegawa

4. Department of Pathology and Laboratory Medicine, Indiana University School of Medicine, Indianapolis, IN, USA

Holly J. Garringer, Ruben Vidal, Grace I. Hallinan & Bernardino Ghetti

5. Department of Neurodegenerative Disease and Queen Square Brain Bank for Neurological Disorders, UCL Queen Square Institute of Neurology, London, UK

Tammaryn Lashley & Tamas Revesz

6. Department of Neuropathology, Tokyo Metropolitan Geriatric Hospital and Institute of Gerontology, Tokyo, Japan

Yuko Saito

7. Molecular Research Center for Children's Mental Development, United Graduate School of Child Development, University of Osaka, Osaka, Japan

Shigeo Murayama

8. Institute for Medical Science of Aging, Aichi Medical University, Nagakute, Japan

Mari Yoshida

9. Department of Pathology, Brain Research Institute, Niigata University, Niigata, Japan

Hidetomo Tanaka & Akiyoshi Kakita

10. Department of Molecular Genetics, Brain Research Institute, Niigata University, Niigata, Japan

Takeshi Ikeuchi

11. Clinical Sciences Building, University of Manchester, Salford Royal Foundation Trust, Salford, UK

Andrew C. Robinson & David M. A. Mann

12. Department of Laboratory Medicine and Pathobiology and Tanz Centre for Research in Neurodegenerative Diseases, University of Toronto, Toronto, Ontario, Canada

Gabor G. Kovacs

13. Institute of Neurology, Medical University of Vienna, Vienna, Austria

Gabor G. Kovacs

Contributions

T.L., Y. Saito, S.M., M.Y., H.T., A.K., A.C.R., D.M.A.M., G.G.K., T.R. and B.G. identified patients and performed neuropathology. R.V., H.J.G., G.I.H. and T.I. performed genetic analysis. A.T., F.K., M.H., Y. Shi, W.Z., Y.Y. and B.F. prepared tau filament samples and performed biochemical analyses. Y. Shi, W.Z., Y.Y., B.F., A.K. and M.v.B. performed cryo-EM data acquisition. Y. Shi, W.Z., Y.Y., A.G.M. and S.H.W.S. performed cryo-EM structure determination. M.G. and S.H.W.S. supervised the project. All authors contributed to writing the manuscript.

Corresponding authors

Correspondence to Michel Goedert or Sjors H. W. Scheres.

Ethics declarations

Competing interests

The authors declare no competing interests.

Additional information

Peer review information *Nature* thanks Gil Rabinovici, Henning Stahlberg and the other, anonymous, reviewer(s) for their contribution to the peer review of this work. Peer reviewer reports are available.

Publisher's note Springer Nature remains neutral with regard to jurisdictional claims in published maps and institutional affiliations.

Extended data figures and tables

Extended Data Fig. 1 Tau immunohistochemistry.

Representative tau staining of the brain regions used for cryo-EM structure determination (see [Methods](#)), using antibody AT8 (pS202/pT205 tau). Scale bars are 50 µm, except for GGT Type I, FBD and FDD, for which they are 25 µm. For PSP-RS case 3, both the thalamus (Tha) and the entorhinal cortex (EC) are shown. Similar results were obtained using a minimum of six additional stained sections for each case.

Extended Data Fig. 2 Cryo-EM reconstructions.

a, Cryo-EM maps for tau filaments from six cases of PSP. For each map, a sum of the reconstructed density for several XY-slices is shown, corresponding to approximately 4.7 Å. The disease cases are referenced at the bottom of each image, the filament types at the top left and the percentages of a given filament type among the tau filaments in the dataset at the top right. Scale bar 5 nm. The same scale applies to all panels, except **d–g**. **b–h**, As in **a**, but a case of GGT-I and a case of GGT-II (**b**); a case diagnosed as PSP-F, but that contains filaments with the PGT fold (**c**); two cases of AGD (**d**); scale bar 5nm, the same scale applies to panels **d–g**; entorhinal cortex of PSP-RS case 3 (**e**); a case of ARTAG (**f**); three cases

with mutations +16 or +3 in intron 10 of *MAPT* (**g**); a case of FBD and a case of FDD (**h**). Panels **d–f** contain blank squares to indicate the absence of AGD type I filaments in some cases. The inset with dashed lines shows 2D class average images of tau filaments from a case of GGT-III without apparent twist.

Extended Data Fig. 3 Cryo-EM resolution estimates.

Fourier Shell Correlation (FSC) curves for cryo-EM maps and atomic structures of PSP filaments (from PSP-RS case 1); GGT filament types 1-3 (from GGT-I); GPT filament types 1a, 1b and 2 (from PSP-F case 2); and AGD filament types 1 and 2 (from AGD case 1 and the +16 case, repectively). FSC curves are shown for two independently refined cryo-EM half-maps (black); for the final refined atomic model against the final cryo-EM map (red); for the atomic model refined in the first half-map against that half-map (blue); and for the refined atomic model in the first half-map against the other half-map (yellow).

Extended Data Fig. 4 Schematics of tau filament folds.

a–d, Schematics of the tau folds for PSP (**a**), GGT (**b**), GPT (**c**) and AGD (**d**). Negatively charged residues are shown in red, positively charged residues in blue, polar residues in green, apolar residues in white, sulfur-containing residues in yellow, prolines in purple and glycines in pink. Thick connecting lines with arrow heads are used to indicate β -strands; additional densities are shown in grey.

Extended Data Fig. 5 Tau pathology in limbic-predominant neuronal inclusion body 4R tauopathy (LNT, PSP-F case 2).

a, Low power view of hippocampus stained with antibody AT8 (pS202/pT205tau). **b**, Low power view of frontal cortex stained with AT8. **c**, Higher power view of hippocampus stained with AT8. **d**, AT8-positive globular astrocyte in hippocampus. **e**, AT8-positive neurons in hippocampus. **f**, Hippocampus stained with antibody RD4 (specific for 4R tau). **g**, Gallyas-Braak silver-positive neurons and glial cells in hippocampus. **h**, Hippocampus stained with antibody RD3 (specific for 3R

tau). **i**, Higher-power view of frontal cortex stained with AT8. **j**, AT8-positive globular astrocyte in frontal cortex. **k**, AT8-positive neurons in frontal cortex. **l**, Frontal cortex stained with RD4. **m**, Gallyas-Braak silver-positive neurons and glial cells in frontal cortex. **n**, Frontal cortex stained with RD3. Representative images are shown. Similar results were obtained using a minimum of six additional stained sections for each panel. Scale bars: 400 µm in (**a**); 200 µm in (**b**), 50 µm in (**c, f, g, h, i, l, m, n**); 10 µm in (**d, e, j, k**).

Extended Data Fig. 6 Structural comparisons.

a, Comparison of two different main-chain conformations for GPT type 1 filaments (type 1a in purple; type 1b in green) and the main-chain conformation of GPT type 2 filaments (red). **b**, Comparison of the PSP (orange), GGT (blue) and GPT (purple) folds. **c**, Comparison of the interprotofilament interfaces of GGT type 3 and GPT type 2 filaments. **d**, Comparison of the AGD type 1 (light blue), AGD type 2 (pink) and CBD (grey) folds.

Extended Data Fig. 7 Argyrophilic grains in the entorhinal cortex.

Representative tau staining with antibodies RD4 (4R tau), RD3 (3R tau), AT8 (pS202/pT205 tau), as well as Gallyas-Braak silver, of the entorhinal cortex from cases 1 and 2 with mutation +3 in intron 10 of *MAPT* and from case 3 of PSP-RS. Similar results were obtained using a minimum of six additional stained sections for each case. Scale bar, 50 µm.

Extended Data Fig. 8 Immunoblot analysis of 4R tauopathies.

Hyperphosphorylated full-length tau (64 and 68 kDa) and C-terminal fragments (33 kDa and 37 kDa) were detected in sarkosyl-insoluble fractions from the brain regions used for cryo-EM by anti-tau antibody T46. A prominent 33-kDa band was characteristic of PSP and GGT; strong 37-kDa bands were in evidence in AGD, ARTAG, cases with intron 10 mutations in *MAPT* (+3 and +16) and in CBD. PSP-RS case 3 had a strong 33-kDa band in thalamus (Tha) and strong 37-kDa bands in entorhinal

cortex (EC), consistent with AGD co-pathology. Similar results were obtained in three independent experiments. The original, uncropped image is available in Supplementary Fig. 1.

Extended Data Table 1 Cryo-EM data collection, refinement and validation statistics

Extended Data Table 2 Cases of tauopathy used for cryo-EM

Supplementary information

Supplementary Information

This file contains Supplementary Tables 1–3 and Supplementary Figure 1.

Reporting Summary

Peer Review File

Rights and permissions

Reprints and Permissions

About this article

Cite this article

Shi, Y., Zhang, W., Yang, Y. *et al.* Structure-based classification of tauopathies. *Nature* **598**, 359–363 (2021). <https://doi.org/10.1038/s41586-021-03911-7>

- Received: 01 June 2021
- Accepted: 13 August 2021
- Published: 29 September 2021

- Issue Date: 14 October 2021
- DOI: <https://doi.org/10.1038/s41586-021-03911-7>

Share this article

Anyone you share the following link with will be able to read this content:

[Get shareable link](#)

Sorry, a shareable link is not currently available for this article.

[Copy to clipboard](#)

Provided by the Springer Nature SharedIt content-sharing initiative

[**Structural strains of misfolded tau protein define different diseases**](#)

- Henning Stahlberg
- Roland Riek

News & Views 29 Sept 2021

This article was downloaded by **calibre** from <https://www.nature.com/articles/s41586-021-03911-7>

| [Section menu](#) | [Main menu](#) |

- Article
- [Published: 06 October 2021](#)

Structure and assembly of the mammalian mitochondrial supercomplex CIII₂CIV

- [Irene Vercellino](#) ORCID: [orcid.org/0000-0001-5618-3449¹](https://orcid.org/0000-0001-5618-3449) &
- [Leonid A. Sazanov](#) ORCID: [orcid.org/0000-0002-0977-7989¹](https://orcid.org/0000-0002-0977-7989)

[Nature](#) volume **598**, pages 364–367 (2021)

- 4077 Accesses
- 143 Altmetric
- [Metrics details](#)

Subjects

- [Bioenergetics](#)
- [Cryoelectron microscopy](#)
- [Energy metabolism](#)
- [Supramolecular assembly](#)

Abstract

The enzymes of the mitochondrial electron transport chain are key players of cell metabolism. Despite being active when isolated, *in vivo* they associate into supercomplexes¹, whose precise role is debated.

Supercomplexes CIII₂CIV₁₋₂ (refs. ^{2,3}), CICIII₂ (ref. ⁴) and CICIII₂CIV

(respirasome)^{5,6,7,8,9,10} exist in mammals, but in contrast to CICIII₂ and the respirasome, to date the only known eukaryotic structures of CIII₂CIV₁₋₂ come from *Saccharomyces cerevisiae*^{11,12} and plants¹³, which have different organization. Here we present the first, to our knowledge, structures of mammalian (mouse and ovine) CIII₂CIV and its assembly intermediates, in different conformations. We describe the assembly of CIII₂CIV from the CIII₂ precursor to the final CIII₂CIV conformation, driven by the insertion of the N terminus of the assembly factor SCAF1 (ref. ¹⁴) deep into CIII₂, while its C terminus is integrated into CIV. Our structures (which include CICIII₂ and the respirasome) also confirm that SCAF1 is exclusively required for the assembly of CIII₂CIV and has no role in the assembly of the respirasome. We show that CIII₂ is asymmetric due to the presence of only one copy of subunit 9, which straddles both monomers and prevents the attachment of a second copy of SCAF1 to CIII₂, explaining the presence of one copy of CIV in CIII₂CIV in mammals. Finally, we show that CIII₂ and CIV gain catalytic advantage when assembled into the supercomplex and propose a role for CIII₂CIV in fine tuning the efficiency of electron transfer in the electron transport chain.

Access options

Subscribe to Journal

Get full journal access for 1 year

\$199.00

only \$3.90 per issue

[Subscribe](#)

All prices are NET prices.

VAT will be added later in the checkout.

Tax calculation will be finalised during checkout.

Rent or Buy article

Get time limited or full article access on ReadCube.

from \$8.99

[Rent or Buy](#)

All prices are NET prices.

Additional access options:

- [Log in](#)
- [Access through your institution](#)
- [Learn about institutional subscriptions](#)

Fig. 1: Structures of the mammalian supercomplex CIII₂CIV.

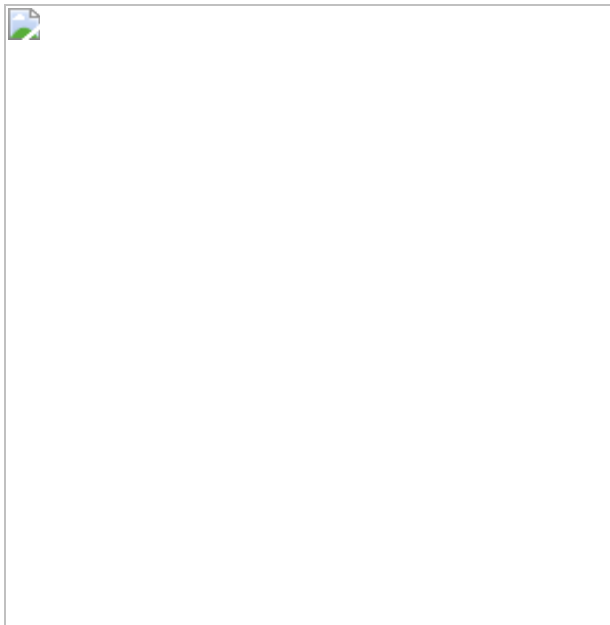


Fig. 2: Interaction interfaces in CIII₂CIV.

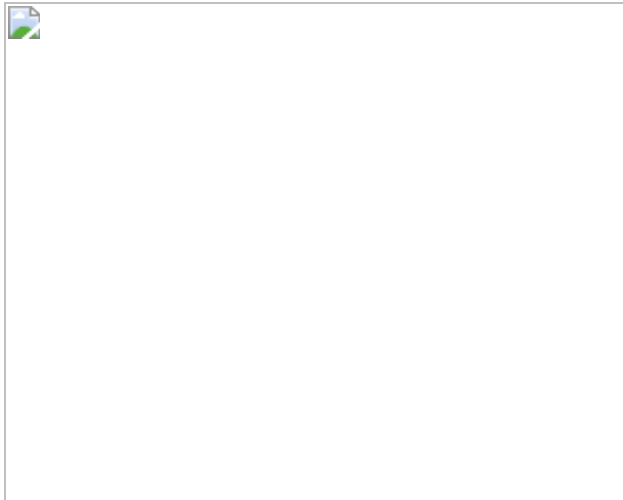
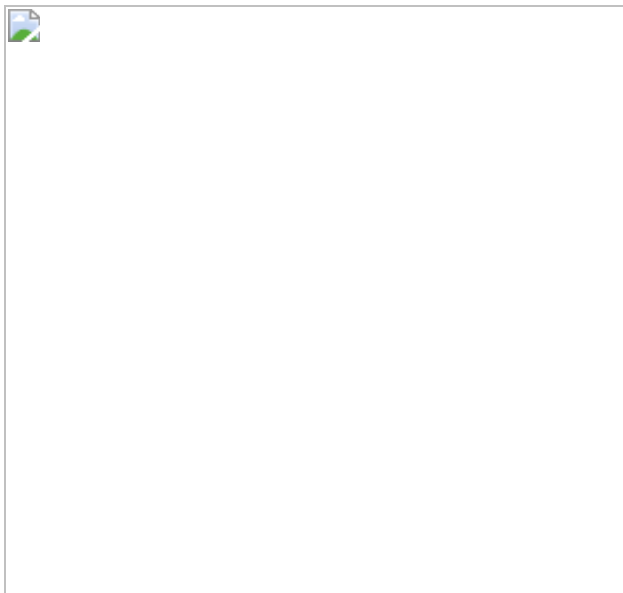


Fig. 3: The assembly and functional role of CIII₂CIV.



Data availability

Structures of the CIII₂CIV intermediate, assembled locked, mature unlocked and CIII₂ from CICIII₂ were deposited in the PDB (access IDs [7O3E](#), [7O37](#), [7O3C](#) and [7O3H](#), respectively) and corresponding cryo-electron microscopy density maps in the EMDB (IDs [12705](#), [12702](#), [12703](#) and [12706](#), respectively). Any other relevant data and information are available from the corresponding author on request. The following models, deposited in the PDB (<https://www.rcsb.org>), have been cited throughout

the paper: 1NTZ, 3CX5, 3L75, 5IY5, 5J4Z, 5Z62, 6HWH, 6HU9, 6QBX and 7JRP.

References

1. 1.
Schägger, H. & Pfeiffer, K. Supercomplexes in the respiratory chains of yeast and mammalian mitochondria. *EMBO J.* **19**, 1777–1783 (2000).
2. 2.
Calvo, E. et al. Functional role of respiratory supercomplexes in mice: SCAF1 relevance and segmentation of the Qpool. *Sci. Adv.* **6**, eaba7509 (2020).
3. 3.
Lobo-Jarne, T. et al. Human COX7A2L regulates complex III biogenesis and promotes supercomplex organization remodeling without affecting mitochondrial bioenergetics. *Cell Rep.* **25**, 1786–1799.e4 (2018).
4. 4.
Letts, J. A., Fiedorczuk, K., Degliesposti, G., Skehel, M. & Sazanov, L. A. Structures of respiratory supercomplex I+III₂ reveal functional and conformational crosstalk. *Mol. Cell* **75**, 1131–1146.e6 (2019).
5. 5.
Lobo-Jarne, T. & Ugalde, C. Respiratory chain supercomplexes: structures, function and biogenesis. *Semin. Cell Dev. Biol.* **76**, 179–190 (2018).
6. 6.

Davies, K. M., Blum, T. B. & Kühlbrandt, W. Conserved in situ arrangement of complex I and III2 in mitochondrial respiratory chain supercomplexes of mammals, yeast, and plants. *Proc. Natl Acad. Sci. USA* **115**, 3024–3029 (2018).

7. 7.

Letts, J. A., Fiedorczuk, K. & Sazanov, L. A. The architecture of respiratory supercomplexes. *Nature* **537**, 644–648 (2016).

8. 8.

Sousa, J. S., Mills, D. J., Vonck, J. & Kühlbrandt, W. Functional asymmetry and electron flow in the bovine respirasome. *eLife* **5**, e21290 (2016).

9. 9.

Gu, J. et al. The architecture of the mammalian respirasome. *Nature* **537**, 639–643 (2016).

10. 10.

Guo, R., Zong, S., Wu, M., Gu, J. & Yang, M. Architecture of human mitochondrial respiratory megacomplex I 2 III 2 IV 2. *Cell* **170**, 1247–1257 (2017).

11. 11.

Hartley, A. M. et al. Structure of yeast cytochrome c oxidase in a supercomplex with cytochrome bc 1. *Nat. Struct. Mol. Biol.* **26**, 78–83 (2019).

12. 12.

Rathore, S. et al. Cryo-EM structure of the yeast respiratory supercomplex. *Nat. Struct. Mol. Biol.* **26**, 50–57 (2019).

13. 13.

Maldonado, M., Guo, F. & Letts, J. A. Atomic structures of respiratory complex III2, complex IV, and supercomplex III2-IV from vascular plants. *eLife* **10**, e62047 (2021).

14. 14.

Cogliati, S. et al. Mechanism of super-assembly of respiratory complexes III and IV. *Nature* **539**, 579–582 (2016).

15. 15.

Spikes, T. E., Montgomery, M. G. & Walker, J. E. Structure of the dimeric ATP synthase from bovine mitochondria. *Proc. Natl Acad. Sci. USA* **117**, 23519–23526 (2020).

16. 16.

Pinke, G., Zhou, L. & Sazanov, L. A. Cryo-EM structure of the entire mammalian F-type ATP synthase. *Nat. Struct. Mol. Biol.* **27**, 1077–1085 (2020).

17. 17.

Wiseman, B. et al. Structure of a functional obligate complex III2IV2 respiratory supercomplex from *Mycobacterium smegmatis*. *Nat. Struct. Mol. Biol.* **25**, 1128–1136 (2018).

18. 18.

García-Poyatos, C. et al. Scaf1 promotes respiratory supercomplexes and metabolic efficiency in zebrafish. *EMBO Rep.* **21**, e50287 (2020).

19. 19.

Lopez-Fabuel, I. et al. Complex I assembly into supercomplexes determines differential mitochondrial ROS production in neurons and astrocytes. *Proc. Natl Acad. Sci. USA* **113**, 13063–13068 (2016).

20. 20.

Xia, D. et al. Structural analysis of cytochrome bc₁ complexes: implications to the mechanism of function. *Biochim. Biophys. Acta* **1827**, 1278–1294 (2013).

21. 21.

Pérez-Pérez, R. et al. COX7A2L is a mitochondrial complex III binding protein that stabilizes the III₂+IV supercomplex without affecting respirasome formation. *Cell Rep.* **16**, 2387–2398 (2016).

22. 22.

Zong, S. et al. Structure of the intact 14-subunit human cytochrome c oxidase. *Cell Res.* **28**, 1026–1034 (2018).

23. 23.

Zong, S. et al. UQCRCFS1N assembles mitochondrial respiratory complex-III into an asymmetric 21-subunit dimer. *Protein Cell* **9**, 586–591 (2018).

24. 24.

Hunte, C., Koepke, J., Lange, C., Roßmanith, T. & Michel, H. Structure at 2.3 Å resolution of the cytochrome bc₁ complex from the yeast *Saccharomyces cerevisiae* co-crystallized with an antibody Fv fragment. *Structure* **8**, 669–684 (2000).

25. 25.

Stuchebrukhov, A., Schäfer, J., Berg, J. & Brzezinski, P. Kinetic advantage of forming respiratory supercomplexes. *Biochim. Biophys. Acta Bioenerg.* **1861**, 148193 (2020).

26. 26.

Berndtsson, J. et al. Respiratory supercomplexes enhance electron transport by decreasing cytochrome c diffusion distance. *EMBO Rep.* **21**, e51015 (2020).

27. 27.

Blanchi, C., Genova, M. L., Castelli, G. P. & Lenaz, G. The mitochondrial respiratory chain is partially organized in a supercomplex assembly: kinetic evidence using flux control analysis. *J. Biol. Chem.* **279**, 36562–36569 (2004).

28. 28.

Lapuente-Brun, E. et al. Supercomplex assembly determines electron flux in the mitochondrial electron transport chain. *Science* **340**, 1567–1570 (2013).

29. 29.

Moe, A., Di Trani, J., Rubinstein, J. L. & Brzezinski, P. Cryo-EM structure and kinetics reveal electron transfer by 2D diffusion of cytochrome *c* in the yeast III–IV respiratory supercomplex. *Proc. Natl Acad. Sci. USA* **118**, e2021157118 (2021).

30. 30.

Fedor, J. G. & Hirst, J. Mitochondrial supercomplexes do not enhance catalysis by quinone channeling. *Cell Metab.* **28**, 525–531.e4 (2018).

31. 31.

Letts, J. A., Degliesposti, G., Fiedorczuk, K., Skehel, M. & Sazanov, L. A. Purification of ovine respiratory complex i results in a highly active and stable preparation. *J. Biol. Chem.* **291**, 24657–24675 (2016).

32. 32.

Kampjut, D., Steiner, J. & Sazanov, L. A. Cryo-EM grid optimisation for membrane proteins. *iScience* **24**, 102139 (2021).

33. 33.

Cheng, A. et al. High resolution single particle cryo-electron microscopy using beam-image shift. *J. Struct. Biol.* **204**, 270–275 (2018).

34. 34.

Zivanov, J., Nakane, T. & Scheres, S. H. W. Estimation of high-order aberrations and anisotropic magnification from cryo-EM data sets in RELION-3.1. *IUCrJ* **7**, 253–267 (2020).

35. 35.

Zheng, S. Q. et al. MotionCor2: anisotropic correction of beam-induced motion for improved cryo-electron microscopy. *Nat. Methods* **14**, 331–332 (2017).

36. 36.

Rohou, A. & Grigorieff, N. CTFFIND4: fast and accurate defocus estimation from electron micrographs. *J. Struct. Biol.* **192**, 216–221 (2015).

37. 37.

Zhang, K. Gctf: real-time CTF determination and correction. *J. Struct. Biol.* **193**, 1–12 (2016).

38. 38.

Bepler, T. et al. Positive-unlabeled convolutional neural networks for particle picking in cryo-electron micrographs. *Nat. Methods* **16**, 1153–1160 (2019).

39. 39.

Kelley, L. A., Mezulis, S., Yates, C. M., Wass, M. N. & Sternberg, M. J. E. The Phyre2 web portal for protein modeling, prediction and analysis. *Nat. Protoc.* **10**, 845–858 (2015).

40. 40.

Emsley, P., Lohkamp, B., Scott, W. G. & Cowtan, K. Features and development of Coot. *Acta Crystallogr. D* **66**, 486–501 (2010).

41. 41.

Sherwood, S. & Hirst, J. Investigation of the mechanism of proton translocation by NADH:ubiquinone oxidoreductase (complex I) from bovine heart mitochondria: does the enzyme operate by a Q-cycle mechanism? *Biochem. J.* **400**, 541–550 (2006).

42. 42.

Kubota, T., Yoshikawa, S. & Matsubara, H. Kinetic mechanism of beef heart ubiquinol: cytochrome c oxidoreductasel. *J. Biochem.* **111**, 91–98 (1992).

43. 43.

Rieske, J. S. [44] Preparation and properties of reduced coenzyme Q-cytochrome c reductase (complex III of the respiratory chain). *Methods Enzymol.* **10**, 239–245 (1967).

44. 44.

Trumpower, B. L. & Edwards, C. A. Purification of a reconstitutively active iron-sulfur protein (oxidation factor) from succinate•cytochrome c reductase complex of bovine heart mitochondria. *J. Biol. Chem.* **254**, 8697–8706 (1979).

45. 45.

[No authors listed] Reduced cytochrome c solution. *Cold Spring Harb. Protoc.* **2015**, pdb.rec084475 (2015).

Acknowledgements

We thank the pre-clinical facility of the IST Austria and A. Venturino for assistance with the animals; and V.-V. Hodirnau for assistance during the Titan Krios data collection, performed at the IST Austria. The data processing was performed at the IST high-performance computing cluster. This project has received funding from the European Union’s Horizon 2020 research and innovation program under the Marie Skłodowska-Curie grant agreement no. 754411.

Author information

Affiliations

1. IV & LAS: IST Austria, Klosterneuburg, Austria

Irene Vercellino & Leonid A. Sazanov

Contributions

I.V. purified the sample, prepared cryo-electron microscopy grids, acquired and processed EM data, built and analysed the atomic models and wrote the initial draft of the manuscript. L.A.S. designed and supervised the project, analysed data and models and revised the manuscript. I.V. and L.A.S. acquired funding.

Corresponding author

Correspondence to Leonid A. Sazanov.

Ethics declarations

Competing interests

The authors declare no competing interests.

Additional information

Peer review information *Nature* thanks Werner Kühlbrandt and the other, anonymous, reviewer(s) for their contribution to the peer review of this work. Peer reviewer reports are available.

Publisher's note Springer Nature remains neutral with regard to jurisdictional claims in published maps and institutional affiliations.

Extended data figures and tables

Extended Data Fig. 1 Sample preparation overview.

a, Purification of the mouse sample: on top, chromatograms of the MonoQ (left), the first SEC (middle) and the second SEC (right). The pooled fractions are highlighted in blue. At the bottom, native PAGE and western blot of the purification steps: from left to right, Coomassie-stained solubilised material (SM), then Coomassie staining, complex I in-gel activity assay, complex IV in-gel activity assay, western blot for Core2, western blot for SCAF1 of the purification steps. **b**, Purification of the ovine sample: the same steps as shown in **a**. For Gel source data, please see Supplementary Fig. 1. The mouse purification was repeated at least 5 times, the ovine preparation was repeated at least 10 times, all attempts of replication were successful, and one representative preparation per sample type is shown in the figure.

Extended Data Fig. 2 Processing pipeline for the mouse CIII₂CIV dataset.

Scheme of the processing pipeline, with representative micrograph, pre-processing, classification steps and final maps, coloured by local resolution, with relative angular distribution plot.

Extended Data Fig. 3 Processing pipeline for the mouse CICIII₂ data, FSC curves of the mouse maps and representative densities from the cryo-EM maps.

a, Processing pipeline as in Extended Data Fig. 2: the same set of micrographs was used, but the classification focused on CICIII₂. **b**, Gold-standard half-map and model-map FSC curves for the mouse dataset. **c–h**, Representative densities of CIII₂ (**c–e**) and CIV (**f–i**) for α -helices - contoured at 2.7σ - (**c** and **f**), β -sheets -contoured at 2.7σ - (**d** and **g**), cofactors -contoured at 1.9σ - (**e** and **i**) and lipids -contoured at 1.8σ - (**h**, from CIII₂).

Extended Data Fig. 4 Processing pipeline and maps of the ovine CIII₂CIV dataset.

a, Processing pipeline of the ovine CIII₂CIV dataset, as in Extended Data Figs. 2, 3. **b**, Final maps of the ovine CIII₂CIV locked (left, 2.8σ contour) and unlocked (right, 3σ contour for CIII and 6σ for CIV), shown from the side (top) and from the matrix (bottom). The respective mouse models, coloured as in Figs. 1, 3, were superimposed on CIII₂, to show the conservation of the conformations across mammalian species.

Extended Data Fig. 5 Processing pipelines for CICIII₂CIV.

Processing scheme as in Extended Data Figs. 2–4, for the ovine (**a, b**) and mouse (**c**) respirasomes.

Extended Data Fig. 6 MPP cavity in different supercomplexes.

a, Cryo-EM map density (grey mesh) carved around Sub9 (orange cartoon) and SCAF1 (blue) positions in supercomplexes CIII₂CIV, CICIII₂ and CICIII₂CIV. For CIII₂CIV and the mouse CICIII₂, the unique positions of a single copy each of Sub9 and SCAF1 were used, while for respirasomes, where the limited resolution prevented Sub9-focused classification and so CIII₂ adopts a random orientation, two-fold symmetry-related positions of these proteins were also added. Contour levels are 2, 1.9 and 2.1σ for mouse CIII₂CIV mature unlocked, assembled locked and intermediate locked respectively; 8σ for ovine CIII₂CIV mature unlocked; 2.9σ for

mouse CICIII₂; 6.7 σ for mouse CICIII₂CIV; 6.7 and 5.3 σ for ovine CICIII₂CIV tight and loose respectively. **b**, Sub9 (orange) integration into the MPP walls: UQCRC1 (Core1) and UQCRC2 (Core2) are shown in grey (Core1 light and Core2 dark), except for the strands of Core2 forming continuous sheets with Sub9, which are shown in yellow. **c**, SCAF1 (blue), Sub7 (yellow) and ISP (red) arrangement in the intermediate (left) and assembled locked (right) classes. The rest of CIII is depicted in grey. The density for Sub7 is carved in grey, to show the ordering of the loop in the assembled versus intermediate class. In the insets at the bottom, the densities for SCAF1 and ISP are shown in the two classes. 2.9 σ contour for CIII₂CIV intermediate and 2.3 σ for assembled.

Extended Data Fig. 7 SCAF1 in CIII and CIV and functional implications.

a, Surface charge representation (as in Fig. 3) of Core1 and SCAF1 in the unlocked class (full model is grey with a sketched eye indicating the perspective). SCAF1 cartoon is green. A white asterisk indicates the MPP "mouth". **b**, SCAF1 (cyan) and COX7A1 (blue) models fitted to the locked (left, 2.5 σ contour) and unlocked class (right, 2.7 σ contour) CIV maps. The arrows in **b** and **c** indicate bulky residues used to identify the subunit based on the map density. SCAF1 model, but not COX7A1, fits the density in both classes. **c**, Ovine SCAF1 (cyan) and COX7A1 (blue) models fitted to CIV map from respirasome (7.3 σ contour): contrary to CIII₂CIV, COX7A1 model fits the density, unlike SCAF1. **d**, Sequence alignment of mammalian COX7A isoforms. The SCAF1 portions interacting with CIII₂ are indicated above the alignment. The black arrows indicate the positions highlighted in **b** and **c**. **e**, Activity measurements (described in the Methods) of CIII₂+CIV (light grey) and supercomplex CIII₂CIV (dark grey). The electron transfer rates (in e-/s) are calculated from the CIII₂-driven oxidation of DQH₂ or from the CIV-driven oxidation of reduced cyt c, as indicated. The bars represent the mean, the dots depict the single measurements. The 5-10 nM ox cyt c represents 2.5-5:1 cyt c/CIII₂CIV ratio (two independent experiments). All other measurements come from 3 independent experiments (two values in the CIII₂+CIV sample with 50 μ M red cyt c

overlap, therefore only two dots are visible). **f**, Cofactor distances within and between CIII₂ and CIV, in the unlocked conformation. Cyt c is bound to CIII₂ and CIV as in Fig. 3b. The transparent cartoon represents the protein subunits, the cofactors are sticks (hemes) and spheres (FeS clusters and Cu centers), in orange for CIII₂, cyan for CIV and black for cyt c. The dashed lines represent the IMM.

Extended Data Fig. 8 Structural differences among supercomplexes and comparison between CIII₂ movements in CICIII₂ and intermediate vs assembled CIII₂CIV.

a, Top left, CIII₂CIV and respirasome (ovine, PDB 5j4z) aligned by CIII₂: CI of respirasome is grey, CIV of respirasome is blue, CIII₂ is yellow and CIV of CIII₂CIV is cyan (the colour scheme for mammalian CIII₂CIV is consistent throughout the panel). CIII₂CIV locked is shown on the left, unlocked on the right. The two possible orientations of CIII₂CIV based on CIII₂ are shown at the top and at the bottom. Top right, plant CIII₂CIV (PDB 7jrp) and mammalian CIII₂CIV aligned by CIII₂ in the locked (top) and unlocked (bottom) conformations. The plant CIV is blue. Bottom left, yeast CIII₂CIV₂ (PDB 6hu9) and mammalian CIII₂CIV aligned by CIII₂ in the locked (left) and unlocked (right) conformations. The yeast CIV is blue. Bottom right, *M. smegmatis* CIII₂CIV₂ (PDB 6hwh) and mammalian CIII₂CIV aligned by CIII₂ in the locked (left) and unlocked (right) conformations. The bacterial CIV is blue. The straight arrows indicate the shift of CIV towards mammalian CIV, and the curved arrows indicate the 90 or 180° flip of CIV around its vertical axis. **b**, Side (top) and IMS (bottom) views of the extreme frames of CIII₂ 3DVA mode 0 (open on the left and closed in the middle, 5σ contour). Ovals indicate the position of the ISP Fe-S domains, only visible in the closed state. On the right, overlay of the two extremes, with closed in dark grey and open in light grey. Arrows indicate the “breathing” movement of the TM and IMS domains. **c**, Same as **b**, but with CIII₂ intermediate (left) and assembled (right) models from CIII₂CIV fitted to the densities and coloured as in Figs. 1, 3.

Extended Data Table 1 Cryo-EM data collection, refinement and validation statistics

Extended Data Table 2 Subunit composition of the deposited models

Supplementary information

Supplementary Information

This file contains additional discussion relevant for the main text.

Reporting Summary

Peer Review File

Uncropped gels

Supplementary Fig. 1 . All the original, uncropped scans of the native gels and western blots shown in Extended Data Fig. 1 are shown.

Overview of the structural features of CIII

Supplementary Video 1 C_{IV} .The mature unlocked state map and model are shown, followed by a transition through the three different conformations, viewed from the side and from the top. Finally, the cytochrome c binding sites, inferred from the crystal structures cited in the manuscript, are shown. The colour scheme is the same as in the rest of the manuscript.

“Breathing” movement of CIII

Supplementary Video 2 $\text{C}_{\text{IIICII}}_2$. The result of the 3DVA analysis on CIII_2 is shown, viewed from the side first, then from the IMS. The fluctuating movements between a closed state, with the two ISP C-terminal domains visible, and an open state, with no density corresponding to ISP, are depicted.

Rights and permissions

[Reprints and Permissions](#)

About this article

Cite this article

Vercellino, I., Sazanov, L.A. Structure and assembly of the mammalian mitochondrial supercomplex CIII₂CIV. *Nature* **598**, 364–367 (2021).
<https://doi.org/10.1038/s41586-021-03927-z>

- Received: 02 April 2021
- Accepted: 12 August 2021
- Published: 06 October 2021
- Issue Date: 14 October 2021
- DOI: <https://doi.org/10.1038/s41586-021-03927-z>

Share this article

Anyone you share the following link with will be able to read this content:

[Get shareable link](#)

Sorry, a shareable link is not currently available for this article.

[Copy to clipboard](#)

Provided by the Springer Nature SharedIt content-sharing initiative

| [Section menu](#) | [Main menu](#) |

- Article
- Open Access
- [Published: 15 September 2021](#)

Structural basis of human transcription–DNA repair coupling

- [Goran Kokic](#) [ORCID: orcid.org/0000-0001-8912-7099¹](#),
- [Felix R. Wagner¹](#),
- [Aleksandar Chernev²](#),
- [Henning Urlaub](#) [ORCID: orcid.org/0000-0003-1837-5233^{2,3}](#) &
- [Patrick Cramer](#) [ORCID: orcid.org/0000-0001-5454-7755¹](#)

Nature volume **598**, pages 368–372 (2021)

- 15k Accesses
- 143 Altmetric
- [Metrics details](#)

Subjects

- [Cryoelectron microscopy](#)
- [DNA damage and repair](#)
- [Transcription](#)

Abstract

Transcription-coupled DNA repair removes bulky DNA lesions from the genome^{1,2} and protects cells against ultraviolet (UV) irradiation³. Transcription-coupled DNA repair begins when RNA polymerase II (Pol II) stalls at a DNA lesion and recruits the Cockayne syndrome protein CSB, the E3 ubiquitin ligase, CRL4^{CSA} and UV-stimulated scaffold protein A (UVSSA)³. Here we provide five high-resolution structures of Pol II transcription complexes containing human transcription-coupled DNA repair factors and the elongation factors PAF1 complex (PAF) and SPT6. Together with biochemical and published^{3,4} data, the structures provide a model for

transcription–repair coupling. Stalling of Pol II at a DNA lesion triggers replacement of the elongation factor DSIF by CSB, which binds to PAF and moves upstream DNA to SPT6. The resulting elongation complex, EC^{TCR}, uses the CSA-stimulated translocase activity of CSB to pull on upstream DNA and push Pol II forward. If the lesion cannot be bypassed, CRL4^{CSA} spans over the Pol II clamp and ubiquitylates the RPB1 residue K1268, enabling recruitment of TFIIH to UVSSA and DNA repair. Conformational changes in CRL4^{CSA} lead to ubiquitylation of CSB and to release of transcription-coupled DNA repair factors before transcription may continue over repaired DNA.

[Download PDF](#)

Main

Eukaryotic cells use transcription-coupled DNA repair (TCR) to eliminate bulky DNA lesions, such as UV light-induced pyrimidine dimers^{1,2}. When Pol II encounters a bulky lesion in the template strand, transcription elongation stalls and this triggers TCR⁵. TCR requires the Cockayne syndrome proteins, CSB and CSA, and UVSSA^{3,4}. CSB, CSA and UVSSA bind to arrested Pol II in vivo^{4,6,7} and recruit the DNA nucleotide excision repair machinery³. CSB binds to the Pol II elongation complex^{8,9,10} and to CSA^{11,12}, which in turn binds to UVSSA⁴. CSA also associates with DNA damage-binding protein 1 (DDB1), cullin-4A (CUL4A) and RING box protein 1 (RBX1) to form CRL4^{CSA}, an E3 ubiquitin ligase^{13,14}. CRL4^{CSA} may be responsible for ubiquitylation of damage-stalled Pol II at RPB1 residue K1268, which is required for TCR and transcription restart^{4,7,15,16}. Following ubiquitylation of Pol II, UVSSA recruits TFIIH and other factors that are required for nucleotide excision repair^{4,7,17}.

As a first step towards understanding the molecular mechanism of TCR, the structural basis for Pol II stalling at a pyrimidine dimer lesion was previously reported¹⁸. Another study has localized the yeast counterpart of CSB (Rad26) on the Pol II elongation complex and suggested that its translocase activity pulls on upstream DNA to push Pol II onto the lesion¹⁹. However, yeast lacks counterparts of CSA and UVSSA, prompting us to study the human TCR mechanism. This is feasible based on the structure of the Pol II elongation complex EC*, which contains the elongation factors DSIF²⁰, PAF, RTF1 and SPT6 (ref. ²¹). Using cryo-electron microscopy (cryo-EM), we resolved five different Pol II elongation complex structures containing CSB, the CSA–DDB1 complex or the complete CRL4^{CSA}, and UVSSA. Together with biochemical probing, our results provide the structural basis for coupling transcription to DNA repair in human cells.

Structure of Pol II–TCR complex

We prepared recombinant human CSB, the CSA–DDB1 complex and UVSSA and tested the effect of these factors on Pol II transcription over an arrest sequence (Extended Data Fig. 1a). CSB facilitated Pol II passage over the arrest sequence, as previously described^{8,19}. UVSSA also facilitated Pol II passage to some extent, whereas CSA–DDB1 did not. When all three factors were present, a more than additive effect of stimulation by CSB and UVSSA was observed, indicating that TCR factors cooperatively stimulate Pol II elongation. This effect was largely due to stimulation of the ATPase activity of CSB by CSA (Extended Data Fig. 1b,c).

Consistent with these results, our recombinant TCR factors bound a Pol II elongation complex containing a large DNA bubble¹⁹ (Extended Data Fig. 1e). We solved the structure of the resulting Pol II–CSB–CSA–DDB1–UVSSA elongation complex (referred to here as the Pol II–TCR complex) by cryo-EM at an overall resolution of 2.8 Å (structure 1; Fig. 1a, Extended Data Figs. 3, 10). UVSSA was more flexible, but helical density features and crosslinking mass spectrometry data enabled unambiguous placement of a homology model for the N-terminal Vsp27–Hrs–STAM (VHS) domain^{4,22,23} (Extended Data Figs. 2a, 10i,j; Methods). This resulted in a nearly complete atomic model of the Pol II–TCR complex with very good stereochemistry (Extended Data Table 1).

Fig. 1: Structure of the Pol II–TCR complex.

 figure1

a, Cryo-EM density (left) and ribbon model (right) of the Pol II–CSB–CSA–DDB1–UVSSA complex. The scheme depicts the domain composition and colour code for proteins. The solid black lines mark residues included in the model. UBD, ubiquitin-binding domain; WHD, winged-helix domain; DUF, domain of unknown function. **b**, Zoom-in on the upstream DNA fork bound to the pulling hook of CSB in the pre-translocated state. **c**, Same as in **b** but in the post-translocated state.

The structure of the TCR complex shows that CSB contacts upstream DNA, UVSSA lies near downstream DNA, and CSA forms a bridge between them (Fig. 1, Supplementary Video 1). The binding of CSB alters the trajectory of upstream DNA by approximately 50°, essentially as observed for Rad26 (ref. 19) (Fig. 1a). CSB contacts the Pol II clamp and protrusion that form opposite sides of the active centre cleft (Fig. 1a). CSA and UVSSA do not bind to Pol II, consistent with their recruitment by CSB in vivo⁴. CSB binds to the CSA β-propeller domain with its ATPase lobe 1 and with its helical CSA-interacting motif (Fig. 1a, Extended Data Fig. 2d), which is essential for CSA binding and TCR in vivo⁴. The binding of the CSA-interacting motif to CSA might restrict the mobile ATPase lobe 2 of CSB to an active conformation, explaining the stimulation of CSB ATPase activity by CSA (Extended Data Fig. 6e). UVSSA contacts the opposite face of the CSA β-propeller via its VHS domain (Fig. 1a, Extended Data Fig. 10i,j), which explains why recruitment of UVSSA to stalled Pol II depends on CSA in vivo^{4,23,24}.

The structure rationalizes known mutations associated with Cockayne syndrome²⁵ (Extended Data Fig. 4). Many mutations in CSB and CSA cluster in the CSB–CSA interface, including three CSB mutations (R670W, W686C and S687L) that lead to severe type II Cockayne syndrome. Other mutations in CSB are found in the ATP-binding site and in the interface with upstream DNA and probably impair CSB function. By contrast, the CSA mutation W361C, which causes UV-sensitive syndrome²⁵, maps to the CSA–UVSSA interface and is predicted to impair recruitment of UVSSA. This supports the view that recruitment of UVSSA is critical for transcription–repair coupling, whereas loss of CSB and CSA might additionally impair transcription elongation or processing of stalled Pol II, perhaps explaining the more-severe clinical manifestations of Cockayne syndrome than of UV-sensitive syndrome^{3,25}.

CSB translocase and elongation stimulation

Our structure suggests how the translocase activity of CSB pushes Pol II forward. The two ATPase lobes hold upstream DNA, and a helix–loop–helix element ('pulling hook') protrudes from lobe 2 and inserts into the upstream fork of the DNA bubble (Fig. 1b, Extended Data Fig. 6a,c,d). The pulling hook contains a conserved phenylalanine residue (F796) that stacks with its aromatic side chain against the first base of the non-template strand at position –14 (Fig 1b, Extended Data Fig. 6a). Substitution of F796 by alanine impairs CSB activity, showing that the pulling hook is required for CSB function (Extended Data Fig. 1f,g). Rad26 contains an element corresponding to the pulling hook¹⁹ (Extended Data Fig. 6d).

To better understand the translocase mechanism of CSB, we also solved the Pol II–TCR structure in the presence of ADP•BeF₃ at 2.7 Å resolution (structure 2; Extended Data Figs. 5, 10). The CSB translocase adopts the pre-translocated and post-translocated states in structures 1 and 2, respectively, elucidating the mechanism of the translocase (Fig. 1c, Extended Data Fig. 6c, Supplementary Video 2). Upon ATP binding, the ATPase lobe 2 of CSB closes and pulls on the template strand of the upstream DNA, whereas the pulling hook pulls on the non-template strand in the same direction. As lobe 1 of CSB is anchored to the Pol II clamp, pulling on the upstream DNA template will push Pol II forward.

Switching from elongation to TCR

Comparison of the Pol II–TCR structure with the structure of the Pol II EC* (ref. 21) reveals a clash between CSB and DSIF, which comprises the subunits SPT4 and SPT5 (ref. 20). We therefore tested whether the binding of CSB to Pol II displaces DSIF. We labelled DNA, CSB and DSIF with different fluorescent dyes and monitored the composition of Pol II complexes by electrophoretic mobility shift assay (Methods). The addition of increasing amounts of CSB indeed displaced DSIF from Pol II (Fig. 2a). To investigate whether CSB could replace DSIF during transcription, we conducted RNA elongation assays (Fig. 2b). Whereas the Pol II–DSIF complex could not transcribe over an arrest sequence, the addition of CSB stimulated the passage of Pol II, indicating that CSB replaced DSIF on transcribing Pol II. Competition between DSIF and CSB for Pol II binding explains the observation that SPT5 can repress TCR²⁶. In summary, these results indicate that the switch from active Pol II elongation to TCR involves replacement of DSIF by CSB on the surface of Pol II.

Fig. 2: Formation and structure of EC^{TCR}.



a, Electrophoretic mobility shift assay monitors replacement of DSIF by CSB on the Pol II elongation complex. The gel was scanned in three different channels to reveal the elongation complex (via DNA), DSIF and CSB through different fluorescent labels. The experiment was repeated three times. Asterisks indicate the attachment of the fluorescent label. For gel source data, see Supplementary Fig. 1. **b**, CSB can

replace DSIF during elongation and stimulate Pol II progression over an arrest site. The experiment was repeated three times. For gel source data, see Supplementary Fig. 1. **c**, Differences between EC* (left; PDB code: 6TED²¹) and the new EC^{TCR} (right).

To further investigate the switch from elongation to TCR, we extended our Pol II–TCR complex preparation by adding SPT6, PAF and RTF1, and analysed the resulting complex by cryo-EM (Extended Data Fig. 7). The overall resolution of the structure was 2.9 Å and it revealed all factors except RTF1, which probably dissociated after loss of DSIF (structure 3; Fig. 2c, Extended Data Fig. 8a). This 22-subunit Pol II–CSB–CSA–DDB1–UVSSA–SPT6–PAF complex represents an alternative elongation complex that we call EC^{TCR}.

The conversion of EC* to EC^{TCR} involves three structural changes (Supplementary Video 3). First, TCR factors replace DSIF and displace RTF1, which interacts with DSIF^{21,27}. Second, upstream DNA moves and contacts the helix–hairpin–helix domain of SPT6 (Fig. 2c). Helix–hairpin–helix domains are found in several DNA-binding proteins²⁸ and yeast Spt6 binds to DNA²⁹. Modelling shows that extension of upstream DNA leads to a clash with parts of SPT6, and thus changes in the position of DNA or SPT6 are required to accommodate longer DNA (Extended Data Fig 8b). Third, the C-terminal linker of the PAF subunit, LEO1, that contacts upstream DNA in EC* (ref. 30) moves by up to approximately 30 Å and forms a helix that binds to lobe 2 of the CSB ATPase (Fig. 2c). This contact accounts for the known PAF–CSB interaction that is induced by UV light *in vivo*^{31,32} and for our observation that PAF stimulates CSB ATPase activity (Extended Data Fig. 1d, h).

Ubiquitylation by CRL4^{CSA}

The cellular response to UV irradiation not only involves recruitment of TCR factors but also ubiquitylation events^{7,12,16,32}. Ubiquitylation of the largest Pol II subunit, RPB1, on K1268 regulates transcription shutdown and recovery^{7,16}. In addition, the E3 ligase CRL4^{CSA} polyubiquitylates CSB, leading to degradation of CSB¹². To investigate these events *in vitro*, we performed ubiquitylation assays with the complete Pol II–TCR complex containing CRL4^{CSA} (Fig. 3a). We observed ubiquitylation of CSA and CUL4A and polyubiquitylation of CSB, as previously described¹⁴. We also detected ubiquitylation of UVSSA and identified 11 ubiquitylation sites on RPB1, including residue K1268 as the highest-scoring site (Fig. 3b). Ubiquitylation of Pol II was dependent on CSB and occurred in the absence of UVSSA (Extended Data Fig 9a), as shown *in vivo*³³. These results indicate that CRL4^{CSA} is the E3 ligase that ubiquitylates K1268.

Fig. 3: Complete Pol II–TCR complex and ubiquitylation by CRL4^{CSA}.

 **figure3**

a, In vitro ubiquitylation of the complete Pol II–TCR complex by CRL4^{CSA}. The experiment was repeated two times. For gel source data, see Supplementary Fig. 1. **b**, Tandem mass spectrometry fragment spectrum of the RPB1 peptide 1261–IMNSDENK(Gly-Gly)MQEEEE VVDKMDDVFLR-1286. **c**, Structure of the EC^{TCR} containing CRL4^{CSA}. Two conformations related to targeting of the Pol II jaw domain (left) or CSB (right) for ubiquitylation are shown. RBX1 and the E2 enzyme–donor ubiquitin complex were modelled as described in the Methods.

We then solved the structure of the complete Pol II–TCR complex including CRL4^{CSA} at an overall resolution of 3.0 Å (Fig. 3c, Extended Data Figs. 9, 10). Focused classification revealed two distinct states that differed in the conformation of CRL4^{CSA} (Extended Data Figs. 9, 10). In the first state (structure 4), UVSSA positions the C-terminal domain of CUL4A such that RBX1 faces a loop in the RPB1 jaw domain that contains the ubiquitylated residue K1268. RBX1 binds to an E2 enzyme–ubiquitin complex³⁴, which we modelled onto our structure (Fig. 3c). In this model, the activated C terminus of ubiquitin is positioned at the K1268-containing loop, which explains how CRL4^{CSA} directs site-specific Pol II ubiquitylation.

In the second state of the complete Pol II–TCR complex structure (structure 5), CUL4A and RBX1 have moved over a large distance to reach the C-terminal region of CSB (Fig. 3c). This CSB region is targeted by ubiquitylation³⁵ and is essential for TCR³⁶. Conversion of the first state to the second state of the complete EC^{TCR} complex requires extensive rearrangements within CRL4^{CSA}, including an approximately 70° rotation of the DDB1 β-propeller B and a roughly 100 Å displacement and approximately 20° rotation of CUL4A (Supplementary Video 4). Modelling an E2 enzyme–ubiquitin complex onto structure 5 reveals minor clashes with Pol II, showing that some adjustments are required for E2 binding. The conversion to the second state may occur when nucleotide excision repair factors are recruited to downstream DNA. Thus, stable conversion of the complete EC^{TCR} complex to the state observed in structure 5 is predicted to enable ubiquitylation of CSB and to complete transcription–repair coupling.

TCR model

Our work converges with published data³ on a molecular model that explains how the complete TCR complex, consisting of CSB, CRL4^{CSA} and UVSSA, mechanistically couples transcription to DNA repair (Fig. 4). When Pol II encounters an obstacle that cannot be overcome with the elongation factor TFIIS, Pol II stalls and the TCR complex binds. This requires displacement of DSIF and converts EC* to EC^{TCR}, which then uses the ATPase activity of CSB to push Pol II forward. If the obstacle can be bypassed, Pol II resumes elongation and EC* is re-established. If the obstacle cannot be overcome, CRL4^{CSA} ubiquitylates Pol II at K1268, leading to recruitment of TFIIH near UVSSA⁴ and downstream DNA. TFIIH may then use ATPase activity¹⁷ to push Pol II backwards³⁷ and enable DNA repair. Finally, rearrangement of CRL4^{CSA} leads to polyubiquitylation of CSB and degradation by the proteasome, which releases TCR factors that are all anchored via CSB. Release of TCR factors liberates the Pol II sites for DSIF and RTF1, and EC* is re-established. Pol II may resume transcription after DNA repair. Interconversion between EC* and EC^{TCR} may facilitate both bypass of small DNA lesions and repair of large lesions. Alternatively, Pol II becomes persistently stalled and is degraded³⁸.

Fig. 4: Model for human transcription–DNA repair coupling.

 figure4

The cycle starts from EC* (left) and involves several intermediate states of EC^{TCR} that we structurally define here. The question marks denote uncertain parts of the model, such as exposure of the DNA lesion and resumption of transcription following DNA repair.

Methods

No statistical methods were used to predetermine sample size. The experiments were not randomized, and the investigators were not blinded to allocation during

experiments and outcome assessment.

Cloning and protein expression

Vectors encoding full-length human CSA, DDB1, CSB, UVSSA, CUL4A and mouse RBX1 were obtained from Harvard Medical School PlasmID Repository. Genes were amplified by PCR and cloned into respective vectors by ligation-independent cloning³⁹. CSA and RBX1 were cloned into the 438A vector (addgene no. 55218), and CSB, DDB1, UVSSA and CUL4A were cloned into the 438B vector (addgene no. 55219), resulting in no tag or 6×His tag, respectively. CSA and DDB1, and CSA, DDB1, CUL4A and RBX1 were combined into single vectors by ligation-independent cloning³⁹. The CSB ATPase-deficient mutant (CSB K538R)⁴⁰ and the pulling hook mutant (CSB F796A) were produced by around-the-horn-mutagenesis and expressed and purified as their wild-type counterparts. For fluorescent labelling of CSB, the gene was cloned into the 438-SNAP-V1 vector (addgene no. 55222), which resulted in a SNAPf tag at the N terminus. For fluorescent labelling of DSIF, a ybbR tag⁴¹ preceded by a GGGG linker was introduced to the C terminus of Spt4 by around-the-horn mutagenesis.

Proteins were expressed in insect cells. Sf9 (ThermoFisher), Sf21 (Expression Systems) and Hi5 (Expression Systems) cell lines were not tested for mycoplasma contamination and were not authenticated in-house. Preparation of bacmids and baculoviruses has previously been described in detail⁴². In brief, 600 ml of Hi5 cells grown in ESF-921 medium were infected with V1 virus and grown for 2–3 days. Cells were collected by centrifugation (30 min, 4 °C, 500g) and resuspended in lysis buffer (400 mM NaCl, 20 mM Tris-HCl pH 7.9, 10% glycerol (v/v), 1 mM DTT, 30 mM imidazole pH 8.0, 0.284 µg ml⁻¹ leupeptin, 1.37 µg ml⁻¹ pepstatin A, 0.17 mg ml⁻¹ PMSF and 0.33 mg ml⁻¹ benzamidine). Cell suspension was frozen in liquid nitrogen and stored at –80 °C until protein purification.

Protein purification

Pol II was purified from the pig thymus as previously described^{30,43}. Human transcription elongation factors (DSIF, PAF, SPT6, RTF1 and P-TEFb) were prepared as previously described^{20,21,30}. All protein purification steps were performed at 4 °C, unless stated otherwise. The purity of protein preparations was monitored by SDS-PAGE using NuPAGE 4–12% Bis-Tris protein gels (Invitrogen), followed by Coomassie staining. Initial purification steps were the same for all TCR proteins. Cells were thawed in a water bath at 30 °C. Cells were opened by sonication and the lysate was clarified by centrifugation and ultracentrifugation. Clarified lysate was further filtrated through 0.8-µm syringe filters and applied onto a HisTrap HP 5-ml column

(GE Healthcare) equilibrated in lysis buffer. The column was washed with 5 CV of lysis buffer, 20 CV of high-salt buffer (800 mM NaCl, 20 mM Tris-HCl pH 7.9, 10% glycerol (v/v), 1 mM DTT, 30 mM imidazole pH 8.0, 0.284 µg ml⁻¹ leupeptin, 1.37 µg ml⁻¹ pepstatin A, 0.17 mg ml⁻¹ PMSF and 0.33 mg ml⁻¹ benzamidine) and again 5 CV lysis buffer. Proteins were eluted with a 0–80% gradient of elution buffer (400 mM NaCl, 20 mM Tris-HCl pH 7.9, 10% glycerol (v/v), 1 mM DTT, 500 mM imidazole pH 8.0, 0.284 µg ml⁻¹ leupeptin, 1.37 µg ml⁻¹ pepstatin A, 0.17 mg ml⁻¹ PMSF and 0.33 mg ml⁻¹ benzamidine). In the case of the CSA–DDB1 complex, an additional step was introduced at this point to separate the CSA–DDB1 complex from excess of DDB1. After a high-salt wash, the column was washed with a low-salt buffer (150 mM NaCl, 20 mM Tris-HCl pH 7.9, 10% glycerol (v/v), 1 mM DTT, 30 mM imidazole pH 8.0, 0.284 µg ml⁻¹ leupeptin, 1.37 µg ml⁻¹ pepstatin A, 0.17 mg ml⁻¹ PMSF and 0.33 mg ml⁻¹ benzamidine) and protein was eluted directly onto a 5-ml HiTrapQ HP column (GE Healthcare) in a low-salt elution buffer (150 mM NaCl, 20 mM Tris-HCl pH 7.9, 10% glycerol (v/v), 1 mM DTT, 500 mM imidazole pH 8.0, 0.284 µg ml⁻¹ leupeptin, 1.37 µg ml⁻¹ pepstatin A, 0.17 mg ml⁻¹ PMSF and 0.33 mg ml⁻¹ benzamidine). The HiTrapQ column was washed with 5 CV of low-salt buffer and proteins were eluted with a 0–100% of monoQ elution buffer (1 M NaCl, 20 mM Tris-HCl pH 7.9, 10% glycerol (v/v), 1 mM DTT, 500 mM imidazole pH 8.0, 0.284 µg ml⁻¹ leupeptin, 1.37 µg ml⁻¹ pepstatin A, 0.17 mg ml⁻¹ PMSF and 0.33 mg ml⁻¹ benzamidine).

For all TCR proteins, appropriate protein fractions were pulled, mixed with 2 mg of TEV protease and dialysed overnight against the dialysis buffer (400 mM NaCl, 20 mM Tris-HCl pH 7.9, 10% glycerol (v/v) and 1 mM DTT). After, dialysis protein solution was passed through a 5-ml HisTrap column equilibrated in dialysis buffer. Flow-through containing the protein was collected, concentrated and loaded onto Superdex 200 10/300 increase column (GE Healthcare) equilibrated in storage buffer (400 mM NaCl, 20 mM NaOH:HEPES pH 7.5, 10% glycerol (v/v) and 1 mM DTT). Peak fractions were pulled, concentrated, flash frozen and stored at –80 °C.

CSB containing N-terminal SNAPf and TwinStrepII tag was purified as follows. The clarified lysate was incubated with 1 ml of Strep-TactinXT 4Flow high-capacity resin (IBA) pre-equilibrated in lysis buffer and washed extensively with lysis buffer. Protein was eluted with BXT buffer (IBA), concentrated and loaded onto Superdex 200 10/300 increase column (GE Healthcare) equilibrated in storage buffer (400 mM NaCl, 20 mM NaOH:HEPES pH 7.5, 10% glycerol (v/v) and 1 mM DTT). Peak fractions were pulled, concentrated, flash frozen and stored at –80 °C.

RNA extension assays

DNA and RNA oligonucleotides were ordered from Integrated DNA Technologies. Sequences¹⁹ used in the assay are: CTA CAT ACA CCA CAC ACC ACA CCG AGA AAA AAA AAT TAC CCC TTC ACC CTC ACT GCC CCA CAT TCT AAC CAC ACA TCA CTT ACC TGG ATA CAC CCT TAC TCC TCT CGA TAC CTC ACC ACC TTA CCT ACC ACC CAC (template strand); GTG GGT GGT AGG TAA GGT GGT GAG GTA TCG AGA GGA GTA AGG GTG TAT CCA GGT AAG TGA TGT GTG GTT AGA ATG TGG GGC AGT GAG GGT GAA GGG GTA ATT TTT TTT TCT CGG TGT GGT GTG TGG TGT ATG TAG (non-template strand); and /5Cy5/rUrUrA rUrArU rUrUrU rArUrU rCrUrU rArUrC rGrA rGrArG rGrA (RNA). Template-strand DNA and RNA were mixed in equimolar ratio and annealed in water by heating to solution to 95 °C followed by slow cooling (1 °C per min) to 4 °C. Pol II was mixed with DNA–RNA scaffold in equimolar ratio and incubated at 30 °C for 10 min. Next, 1.5 M excess of non-template DNA was added and the solution was incubated for 10 min more at 30 °C. A typical RNA extension reaction contained Pol II (200 nM) in the final buffer containing 100 mM NaCl, 20 mM HEPES pH 7.5, 5% (v/v) glycerol, 5 mM MgCl₂ and 1 mM DTT. When proteins were titrated, the highest protein concentration was 2 μM (in case of a protein mixture, concentration of each factor was 2 μM), followed by a half-log dilution series. In the case of the DSIF–CSB competition assay, Pol II was pre-incubated with 1.5× excess of DSIF before addition of TCR factors. Reactions were pre-incubated at 37 °C for 5 min and started with the addition of NTPs (0.5 mM GTP, UTP and CTP, 1 mM ATP and 0.5 mM dATP). Reactions were quenched with 2× quenching buffer (7 M urea in TBE buffer, 20 mM EDTA and 10 μg ml⁻¹ proteinase K (Thermo Scientific)). Proteins were digested for 30 min at 37 °C. RNA products were separated on a sequencing gel and visualized with a Typhoon FLA 9500 (GE Healthcare Life Sciences). Gel quantification was performed with ImageJ software and data were plotted with Prism 9 software.

Three-colour electrophoretic mobility shift assay

DNA and RNA oligonucleotides were ordered from Integrated DNA Technologies. Sequences¹⁹ used in the assay are: /56-FAM/CGC TCT GCT CCT TCT CCC ATC CTC TCG ATG GCT ATG AGA TCA ACT AG (template strand); CTA GTT GAT CTC ATA GCC ATC GAG AGG ATG GGA GAA GGA GCA GAG CG (non-template strand); and rArCrA rUrCrA rUrArA rCrArU rUrUrG rArArC rArArG rArArU rArUrA rUrArU rArCrA rArArA rUrCrG rArGrA rGrGrA (RNA). For this assay, CSB and DSIF were fluorescently labelled. SNAPf–CSB (50 μM) was incubated with 10× molar excess of SNAP-Surface 546 substrate (New England BioLabs) overnight at 4 °C in CSB storage buffer. Labelled CSB was purified from the excess dye by Superdex 200 10/300 increase column (GE Healthcare) equilibrated in storage buffer (400 mM NaCl, 20 mM NaOH:HEPES pH 7.5, 10% glycerol (v/v) and 1 mM DTT). Labelling efficiency was around 100%. DSIF subunit SPT4 contained a ybbR tag on the C terminus and the protein was labelled by using Sfp

phosphopantetheinyl transferase, as previously described in detail⁴¹. Substrate for the labelling reaction was LD666-CoA (Lumidyne Technologies) and the labelling efficiency was around 85%. The Pol II elongation complex was assembled by incubating Pol II with 1.3× excess of template strand:RNA for 10 min at 30 °C, followed by the addition of 1.5× excess of non-template strand and further incubation for 10 min at 30 °C. Next, the Pol II elongation complex was supplemented with 1.2× excess of DSIF and incubated for 10 min at 30 °C. Finally, CSB was titrated in the reaction and the reaction was further incubated for 10 min at 30 °C. Final reaction contained Pol II (100 nM), DSIF (120 nM) and CSB (400 nM, 200 nM, 150 nM, 100 nM, 50 nM and 25 nM) in final buffer containing 100 mM NaCl, 20 mM HEPES pH 7.5, 10% glycerol, 2 mM MgCl₂ and 1 mM DTT. Reactions were loaded on a NativePAGE 3–12% Bis-Tris gels (Thermo Scientific) and ran at 150 V for 1.5 h. The gels were scanned in Typhoon FLA 9500 (GE Healthcare Life Sciences) in three different channels for the visualization of template-strand DNA, CSB and DSIF.

Analytical size-exclusion chromatography

Analytical size-exclusion chromatography was used to monitor association of TCR factors with Pol II (Extended Data Fig. 1e) and to monitor RTF1 association with EC* and EC^{TCR} (Extended Data Fig. 8a). In the case of TCR factors, the proteins were mixed in equimolar ratios in the final size-exclusion buffer (100 mM NaCl, 20 mM HEPES 7.5, 5% glycerol, 1 mM MgCl₂ and 1 mM DTT) and ran over a Superose 6 Increase 3.2/300 column. The Pol II elongation complex was formed as for structure 1. In the case of RTF1 binding, all factors were added to the pre-formed Pol II elongation complex in 1.5× excess in the final size-exclusion buffer and incubated for 1 h at 30 °C in the presence of 1 mM ATP and P-TEFb. The complexes were injected onto a Superose 6 Increase 3.2/300 column and the fractions were analysed by SDS-PAGE. The template strand and RNA used for the EC* and EC^{TCR} formation were the same (template strand: CGC TCT GCT CCT TCT CCC ATC CTC TCG ATG GCT ATG AGA TCA ACT AG; RNA: rArCrA rUrCrA rUrArA rCrArU rUrUrG rArArC rArArG rArArU rArUrA rUrArU rArCrA rArArA rUrCrG rArGrA rGrGrA) but differed in the non-template strand, which was fully complementary to the template strand in the case of EC* (non-template strand: CTA GTT GAT CTC ATA GCC ATC GAG AGG ATG GGA GAA GGA GCA GAG CG) or formed a large bubble with the template strand in the case of EC^{TCR} (non-template strand: CTA GTT GAT CTC ATA TTT CAT TCC TAC TCA GGA GAA GGA GCA GAG CG).

In vitro ubiquitylation assay

Ubiquitin, UBE1 and UbcH5b were purchased from Boston Biochem. The Pol II elongation complex was formed as for structural analysis of structure 1. The

ubiquitylation reaction contained Pol II ECs (0.8 μ M), CSB (0.8 μ M), UVSSA (0.8 μ M), CSA–DDB1–CUL4A–RBX1 (0.8 μ M), UBE1 (150 nM), UbcH5b (0.5 μ M) and ubiquitin (300 μ M) in 100 mM NaCl, 50 mM Tris pH 7.9, 10 mM MgCl₂, 0.2 mM CaCl₂, 5% glycerol and 1 mM DTT. Reactions were started by the addition of ATP (3 mM) and stopped with EDTA (15 mM). Proteins were separated on NuPAGE 4–12% Bis-Tris protein gels (Invitrogen) and stained with Coomassie. In the case of the ubiquitylation assay in the absence of CSB or UVSSA, the assay was performed as described above, but with lower concentrations of Pol II, CRL4^{CSA} and CSB or UVSSA (0.4 μ M). The proteins were separated on 3–8% Tris-acetate gel (Invitrogen) and transferred onto a PVDF membrane with a Trans-Blot Turbo Transfer System (Bio-Rad) for immunoblotting. The membrane was blocked with 5% (w/v) milk powder in PBS containing 0.1% Tween-20 (PBST) for 1 h at room temperature. The membrane was then incubated with F-12 anti-RPB1 antibody (1:100 dilution; Santa Cruz Biotechnology) in PBST supplemented with 2.5% (w/v) milk powder. After washing the membrane with PBST, the membrane was incubated with an anti-mouse HRP conjugate (1:3,000 dilution; ab5870, Abcam) in PBST supplemented with 1% (w/v) milk powder for 1 h at room temperature. The membrane was developed with SuperSignal West Pico Chemiluminescent Substrate (Thermo Fisher) and scanned with a ChemoCam Advanced Fluorescence imaging system (Intas Science Imaging).

ATPase assay

The enzyme-coupled ATPase assay uses two separate fast enzymatic reactions to couple ATP regeneration to NADH oxidation. The typical reaction contained 100 nM protein in buffer containing 50 mM potassium acetate, 20 mM KOH-HEPES pH 7, 5 mM magnesium acetate, 5% glycerol (v/v), 0.2 mg ml⁻¹ BSA, 3 mM phosphoenolpyruvate (PEP), 0.3 mM NADH and excess pyruvate kinase and lactate dehydrogenase enzyme mix (Sigma). The reaction mixture was incubated for 10 min at 30 °C and the reaction was started by addition of ATP (1.5 mM final). The rate of ATP hydrolysis was monitored by measuring a decrease in the absorption at 340 nm using the Infinite M1000Pro reader (Tecan). Resulting curves were fit to a linear model using GraphPad Prism version 9.

Crosslinking mass spectrometry

The Pol II elongation complex was formed as described in the RNA extension assay. DNA and RNA sequences used for elongation complex formation are the following¹⁹: CGC TCT GCT CCT CCC ATC CTC TCG ATG GCT ATG AGA TCA ACT AG (template strand); CTA GTT GAT CTC ATA TTT CAT TCC TAC TCA GGA GAA GGA GCA GAG CG (non-template strand); and rArUrC rGrAr GrArG rGrA (RNA). Equimolar amounts of elongation complex, CSB, CSA–DDB1 and UVSSA

were mixed in the final complex formation buffer of 100 mM NaCl, 20 mM HEPES pH 7.5, 1 mM DTT, 1 mM MgCl₂ and 5% glycerol. The complex was incubated at 30 °C for 10 min and subsequently purified over a Superose 6 Increase 3.2/300 column equilibrated in complex formation buffer. For BS3 crosslinking, the protein solution was supplemented with 1 mM BS3 and incubated at 30 °C for 30 min. The crosslinking was quenched with 50 mM ammonium bicarbonate. For EDC crosslinking, the complex formation buffer contained HEPES pH 6.7 instead of pH 7.5. The protein solution was supplemented with 2 mM EDC and 5 mM sulfo-NHS and incubated at 30 °C for 30 min. The crosslinking reaction was quenched with 50 mM 2-mercaptoethanol and 20 mM Tris pH 7.9.

Analysis of crosslinked peptides was performed as previously described¹⁷. The crosslinked proteins were reduced with 10 mM DTT for 30 min at 37 °C and alkylated with 40 mM iodoacetamide for 30 min at 25 °C. Protein digestion was performed overnight in denaturing conditions (1 M urea) with 5 µg trypsin (Promega) at 37 °C. Formic acid (FA) and acetonitrile (ACN) were added to the digested samples to 0.1% (v/v) and 5% (v/v) final concentrations. Samples were purified with Sep-Pak C18 1cc 50 mg sorbent cartridge (Waters) by washing away salts and contaminants with 5% (v/v) ACN, 0.1% (v/v) FA and eluting bound peptides with 80% (v/v) ACN and 0.1% (v/v) FA. The extracted peptides were dried under vacuum and resuspended in 30 µl 30% (v/v) ACN and 0.1% (v/v) trifluoroacetic acid (TFA). Size separation of peptides was performed with a Superdex Peptide PC3.2/30 column (GE Healthcare) at flow rate of 50 µl min⁻¹ 30% (v/v) ACN and 0.1% (v/v) TFA. Fractions (100 µl) corresponding to elution volume 1.1–2 ml were collected, dried under vacuum and resuspended in 20 µl 2% (v/v) ACN and 0.05% (v/v) TFA.

Mass spectrometry analysis was performed on the Q Exactive HF-X Mass Spectrometer (Thermo Fisher Scientific) coupled with the Dionex UltiMate 3000 UHPLC system (Thermo Fisher Scientific). Online chromatographical separation was achieved with an in-house packed C18 column (ReproSil-Pur 120 C18-AQ, 1.9-µm pore size, 75-µm inner diameter and 30 cm in length; Dr. Maisch). Samples were analysed as three 5-µl injections, separated on a 75-min gradient: flow rate of 300 nl min⁻¹; mobile phase A was 0.1% (v/v) FA; mobile phase B was 80% (v/v) ACN and 0.08% (v/v) ACN. The gradient was formed with an increase from 8%/12%/18% mobile phase B to 38%/42%/48% (depending on the fraction). MS1 acquisition was achieved with the following settings: resolution of 120,000; mass range of 380–1,580 *m/z*; injection time of 50 ms; and automatic gain control target of 1×10^6 . MS2 fragment spectra were collected with dynamic exclusion of 10 s and varying normalized collision energy for the different injection replicates (28%/30%/28–32%) and the following settings: isolation window of 1.4 *m/z*; resolution of 30,000; injection time of 128 ms; and automatic gain control target of 2×10^5 .

Result raw files were converted to the mgf format with ProteomeDiscoverer 2.1.0.81 (Thermo Fisher Scientific): signal-to-noise ratio of 1.5, and precursor mass of 350–7,000 Da. Crosslinked peptides were identified with pLink v2.3.9 (pFind group⁴⁴) and the following parameters: missed cleavage sites was 3; fixed modification was carbamidomethylation of cysteines; variable modification was oxidation of methionines; peptide tolerance was 10 p.p.m.; fragment tolerance was 20 p.p.m.; peptide length was 5–60 amino acids; and the spectral false discovery rate was 1%. The sequence database was assembled from all proteins within the complex. Crosslink sites were visualized with XiNet⁴⁵ and the Xlink Analyzer⁴⁶ plugin in Chimera.

The samples for the ubiquitylation analysis were produced by an in vitro ubiquitylation assay as described above. Control sample was prepared in the same way but without the addition of ubiquitin to make sure that endogenously purified Pol II was not already ubiquitylated. In addition to site-specific Pol II ubiquitylation, promiscuous ubiquitylation of free CSB and UVSSA was observed that probably resulted from a population of TCR factors not bound to Pol II.

For mass spectrometry, the samples were reduced with 5 mM DTT for 30 min at 37 °C and alkylated with 20 mM chloroacetamide for 30 min at room temperature. Unreacted chloroacetamide was quenched by supplementing an additional 5 mM DTT.

Proteolytic digestion was performed overnight in denaturing conditions (1 M urea) with trypsin (Promega) in a 1:20 (w/w) protein ratio. The digestion mixtures were acidified with FA to 1% (v/v) end concentration and ACN was added to 5% (v/v) final concentration. Reversed-phase chromatographical purification for mass spectrometric analysis was performed with Harvard Apparatus Micro SpinColumns C18 by washing away salts and contaminants with 5% (v/v) ACN and 0.1% (v/v) FA. Purified peptides were eluted with 50% (v/v) ACN and 0.1% (v/v) FA. The peptide mixture was dried under vacuum and resuspended in 2% (v/v) ACN and 0.05% (v/v) TFA (5 µl for 1 µg of estimated protein amount before digestion).

Liquid chromatography with tandem mass spectrometry analysis was performed by injecting 4 µl of the samples in the Dionex UltiMate 3000 UHPLC system (Thermo Fisher Scientific) coupled with the Orbitrap Fusion Tribrid Mass Spectrometer (Thermo Fisher Scientific). Peptides were separated on an in-house packed C18 column (ReproSil-Pur 120 C18-AQ, 1.9-µm pore size, 75-µm inner diameter and 31 cm in length; Dr. Maisch). Chromatographical separation was achieved with 0.1% (v/v) FA (mobile phase A) and 80% (v/v) ACN and 0.08% (v/v) ACN (mobile phase B). A gradient was formed by the increase of mobile phase B from 5% to 42% in 43 min. Eluting peptides were analysed by data-dependent acquisition with the following MS1 parameters: resolution of 60,000; scan range of 350–1,500 *m/z*; injection time of 50 ms; and automatic gain control target of 4×10^5 . Analytes with charge states 2–7 were selected for higher-energy collisional dissociation with 30% normalized collision

energy. Dynamic exclusion was set to 10 s. Fragment MS2 spectra were acquired with the following settings: isolation window of 1.6 *m/z*; detector type was orbitrap; resolution of 15,000; injection time of 120 ms; and automatic gain control target of 5×10^4 .

The resulting acquisition files were analysed with MaxQuant⁴⁷ (v1.6.17.0). Fragment peptide spectra were searched against a database containing all proteins of the complex and common protein contaminants. Oxidation of methionines, acetylation of protein N terminus and ubiquitylation residue on lysines were set as variable modifications. Carbamidomethylation of cysteines was set as a fixed modification. Default settings were used with the following exceptions: main search peptide tolerance was set to 6 p.p.m.; trypsin was selected for digestion enzyme; and maximum missed cleavages were increased to 3.

Cryo-EM sample preparation and image processing

The same DNA scaffolds were used for all structures¹⁹: CGC TCT GCT CCT TCT CCC ATC CTC TCG ATG GCT ATG AGA TCA ACT AG (template strand) and CTA GTT GAT CTC ATA TTT CAT TCC TAC TCA GGA GAA GGA GCA GAG CG (non-template strand). In the case of Pol II complex formation with TCR factors only, the shorter RNA was used: rArUrC rGrArG rArGrG rA. If SPT6, PAF and RTF1 were also present, longer RNA was used: rArCrA rUrCrA rUrArA rCrArU rUrUrG rArArC rArArG rArArU rArUrA rUrArU rArCrA rArArA rUrCrG rArGrA rGrGrA. The elongation complex was formed as in the RNA extension assays. For the Pol II–CSB–CSA–DDB1–UVSSA structure, the pre-formed elongation complex was mixed with twofold excess of TCR factors in complex formation buffer containing 100 mM NaCl, 20 mM HEPES pH 7.5, 1 mM MgCl₂, 4% glycerol and 1 mM DTT. The protein solution was incubated at room temperature for 10 min and purified by the Superose 6 Increase 3.2/300 column equilibrated in complex formation buffer. Peak fractions were crosslinked with 0.1% glutaraldehyde on ice for 10 min and quenched with a mixture of lysine (50 mM final) and aspartate (20 mM final). The quenched protein solution was dialysed in Slide-A-Lyzer MINI Dialysis Device of 20K MWCO (Thermo Fisher Scientific) for 6 h against the complex formation buffer without glycerol. For the Pol II–CSB–CSA–DDB1–UVSSA–ADP•BeF₃ structure, the complex was supplemented with 0.5 mM ADP•BeF₃ before complex purification by size-exclusion chromatography. In the case of complex formation between Pol II, TCR factors, PAF, SPT6 and RTF1, the pre-formed elongation complex was mixed with twofold excess of all proteins in complex formation buffer. In addition, the reaction was supplemented with P-TEFb and ATP (1 mM final), as previously described³⁰. Because ATP was present, we used a CSB ATPase-deficient mutant for complex formation. The complex was incubated at 30 °C for 1 h and purified by a Superose 6 Increase 3.2/300 column

equilibrated in complex formation buffer. Downstream steps including crosslinking and dialysis were the same as for the previous samples. Dialysed samples were immediately used for the preparation of cryo-EM grids. Of the sample, 4 µl was applied to glow-discharged R2/1 carbon grids (Quantifoil), which were blotted for 5 s and plunge-frozen in liquid ethane with a Vitrobot Mark IV (FEI) operated at 4 °C and 100% humidity.

Micrographs were acquired on a FEI Titan Krios transmission electron microscope with a K3 summit direct electron detector (Gatan) and a GIF quantum energy filter (Gatan) operated with a slit width of 20 eV. Data collection was automated using SerialEM⁴⁸ and micrographs were taken at a magnification of ×81,000 (1.05 Å per pixel) with a dose of 1–1.05 e/Å² per frame over 40 frames. For Pol II–CSA–DDB1–CSB–UVSSA, a total of 10,300 micrographs were acquired; for Pol II–CSA–DDB1–CSB–UVSSA–ADP•BeF₃, 10,940 micrographs were acquired; for Pol II–CSA–DDB1–CSB–UVSSA–SPT6–PAF, 8,365 micrographs were acquired; and for Pol II–CRL4^{CSA}–CSB–UVSSA–Spt6–PAF, 19,472 micrographs were acquired. Estimation of the contrast-transfer function, motion correction and particle picking was done on-the-fly using Warp⁴⁹. Initial 2D classification and 3D classification steps were done in CryoSPARC⁵⁰, followed by further processing in RELION 3.0 (refs ^{51,52,53}). Owing to the flexibility of proteins on the Pol II surface, many rounds of signal subtraction and focused classifications were performed, as detailed for every dataset in Extended Data Figs. ^{3, 5, 7, 9}. As a result, the focused classified maps were assembled into a final composite map for each structure. Masks were created with UCSF Chimera⁵⁴. The final composite maps were created from focused refined maps and denoised in Warp⁴⁹.

Model building and refinement

The focused refined maps and the final composite maps were used for model building. For the Pol II–CSB–CSA–DDB1–UVSSA structure, we first docked existing structures into the density. An initial CSB model was produced with SWISS-MODEL^{55,56} using the Rad26 structure (Protein Data Bank (PDB) code: 5VVR¹⁹) as the template. The model was fitted into the CSB focused refined map in Chimera⁵⁴ and rebuilt in Coot⁵⁷, followed by real-space refinement in PHENIX⁵⁸. The CSA–DDB1 crystal structure (PDB code: 4A11 (ref. ¹⁴)) was fitted into the CSA–DDB1 focused refined map and real-space refinement in PHENIX⁵⁸. During 3D classifications, the β-propeller B of DDB1 was found to adopt many different conformations, apparently rotating around the junction with the rest of the protein, and the final model reflects the most commonly observed conformation. The N-terminal VHS domain of UVSSA was predicted with SWISS-MODEL^{55,56} using the GGA3 VHS domain as a template (PDB code: 1JPL⁵⁹). Guided by the crosslinking mass spectrometry data and EM density, the model was fitted into the CSA–UVSSA

focused refined map, followed by several rounds of flexible fitting in Namdinator⁶⁰ and real-space refinement in PHENIX⁵⁸. The Pol II model (PDB code: 7B0Y⁶¹) was fitted into the final map and nucleic acids were modified and built in Coot. All protein models were combined in Coot and real-space refined in PHENIX into the final composite map using secondary structure, base-pairing and base-stacking restraints. For the Pol II–CSB–CSA–DDB1–UVSSA–ADP•BeF₃ model, ADP•BeF₃ was fitted into the density together with the Pol II–CSB–CSA–DDB1–UVSSA model and real-space refined in PHENIX into the final composite map using secondary structure, base-pairing and base-stacking restraints.

For the Pol II–CSB–CSA–DDB1–UVSSA–SPT6–PAF structure, the SPT6 and PAF models (PDB code: 6TED²¹) were fitted into corresponding focused refined maps, adjusted in Coot and real-space refined in PHENIX. Owing to the improved resolution of the SPT6 core, we built an atomic model for it (the SPT6 core was previously modelled on the backbone level). The C-terminal part of LEO1 was displaced in our structure, and therefore these elements were manually built in Coot and deposited as polyalanine because the register could not be determined with certainty. RNA outside Pol II was poorly resolved, presumably due to the absence of DSIF, so we modelled it on the basis of the previous structure (PDB code: 6TED²¹). All models were combined in Coot and real-space refined in PHENIX in the final composite map. In the case of the Pol II–CSB–CRL4^{CSA}–UVSSA–SPT6–PAF complex, 3D classification of the stably bound CSA–DDB1–CSB complex revealed two distinct conformations of CUL4A–RBX1. In the first conformation (state 1), CUL4A interacts with UVSSA; in the second conformation (state 2), CUL4A interacts with CSB. Owing to increased flexibility of CUL4A–RBX1, only a smaller subset of particles was used for the final focused refinement of this region. Both focused refinement rounds yielded reconstructions with well-resolved CSA–DDB1, which was then used to resample maps on the map of CSA–DDB1–CSB reconstructed from all particles with stably bound TCR proteins. The crystal structure of the CUL4A–RBX1 (PDB code: 4A0K¹⁴) complex was fitted into the corresponding focused refined maps, followed by several rounds of flexible fitting in Namdinator⁶⁰ and real-space refinement in PHENIX⁵⁸. The β-propeller B of DDB1 was manually adjusted in Chimera and Coot for both CRL4^{CSA} conformations. The model of Pol II–CSB–CSA–DDB1–UVSSA–SPT6–PAF was combined with CUL4A–RBX1 in Coot and the complete models were real-space refined in corresponding composite maps in PHENIX using secondary structure, base-pairing and base-stacking restraints. For Fig. 3, full RBX1 was modelled on the basis of a CUL4A–RBX1 structure (PDB code: 2HYE)⁶² due to lower map quality in this region, and the E2 enzyme–donor ubiquitin complex was not present in the complex and was modelled on the basis of a RNF4 RING–UbcH5a–ubiquitin structure (PDB code: 4AP4)⁶³. In the case of structures containing a CSB ATPase-deficient mutant, the ATPase lobe 2 of CSB is very flexible. Since the complex was incubated

with ATP, it is likely that the structure contains a mixture of empty and ATP-bound CSB molecules, resulting in both pre-translocated and post-translocated states of CSB. Final models were validated in Molprobity⁶⁴ and the figures were generated with Chimera⁵⁴ and ChimeraX⁶⁵.

Reporting summary

Further information on research design is available in the [Nature Research Reporting Summary](#) linked to this paper.

Data availability

The electron density reconstructions and structure coordinates were deposited to the Electron Microscopy Database (EMDB) and to the PDB under the following accession codes: [EMDB-13004](#) and PDB [7OO3](#) for structure 1, [EMDB-13009](#) and PDB [7OOB](#) for structure 2, [EMDB-13010](#) and PDB [7OOP](#) for structure 3, [EMDB-13015](#) and PDB [7OPC](#) for structure 4, and [EMDB-13016](#) and PBD [7OPD](#) for structure 5. The crosslinking mass spectrometry data and the ubiquitin mapping data have been deposited to the ProteomeXchange Consortium via PRIDE with the dataset identifier [PXD025328](#).

References

1. 1.

Bohr, V. A., Smith, C. A., Okumoto, D. S. & Hanawalt, P. C. DNA repair in an active gene: removal of pyrimidine dimers from the DHFR gene of CHO cells is much more efficient than in the genome overall. *Cell* **40**, 359–369 (1985).

2. 2.

Mellon, I., Spivak, G. & Hanawalt, P. C. Selective removal of transcription-blocking DNA damage from the transcribed strand of the mammalian DHFR gene. *Cell* **51**, 241–249 (1987).

3. 3.

van den Heuvel, D., van der Weegen, Y., Boer, D. E. C., Ogi, T. & Luijsterburg, M. S. Transcription-coupled DNA repair: from mechanism to human disorder. *Trends Cell Biol.* **31**, 359–371 (2021).

4. 4.

van der Weegen, Y. et al. The cooperative action of CSB, CSA, and UVSSA target TFIIH to DNA damage-stalled RNA polymerase II. *Nat. Commun.* **11**, 2104 (2020).

5. 5.

Lainé, J.-P. & Egly, J. M. Initiation of DNA repair mediated by a stalled RNA polymerase IIO. *EMBO J.* **25**, 387–397 (2006).

6. 6.

van den Boom, V. et al. DNA damage stabilizes interaction of CSB with the transcription elongation machinery. *J. Cell Biol.* **166**, 27–36 (2004).

7. 7.

Nakazawa, Y. et al. Ubiquitination of DNA damage-stalled RNAPII promotes transcription-coupled repair. *Cell* **180**, 1228–244.e24 (2020).

8. 8.

Selby, C. P. & Sancar, A. Cockayne syndrome group B protein enhances elongation by RNA polymerase II. *Proc. Natl Acad. Sci. USA* **94**, 11205–11209 (1997).

9. 9.

Tantin, D., Kansal, A. & Carey, M. Recruitment of the putative transcription-repair coupling factor CSB/ERCC6 to RNA polymerase II elongation complexes. *Mol. Cell. Biol.* **17**, 6803–6814 (1997).

10. 10.

van Gool, A. J. et al. The Cockayne syndrome B protein, involved in transcription-coupled DNA repair, resides in an RNA polymerase II-containing complex. *EMBO J.* **16**, 5955–5965 (1997).

11. 11.

Henning, K. A. et al. The Cockayne syndrome group A gene encodes a WD repeat protein that interacts with CSB protein and a subunit of RNA polymerase II TFIIH. *Cell* **82**, 555–564 (1995).

12. 12.

Groisman, R. et al. CSA-dependent degradation of CSB by the ubiquitin-proteasome pathway establishes a link between complementation factors of the Cockayne syndrome. *Genes Dev.* **20**, 1429–1434 (2006).

13. 13.

Groisman, R. et al. The ubiquitin ligase activity in the DDB2 and CSA complexes is differentially regulated by the COP9 signalosome in response to DNA damage. *Cell* **113**, 357–367 (2003).

14. 14.

Fischer, E. S. et al. The molecular basis of CRL4DDB2/CSA ubiquitin ligase architecture, targeting, and activation. *Cell* **147**, 1024–1039 (2011).

15. 15.

Bregman, D. B. et al. UV-induced ubiquitination of RNA polymerase II: a novel modification deficient in Cockayne syndrome cells. *Proc. Natl Acad. Sci. USA* **93**, 11586–11590 (1996).

16. 16.

Tufegdžić Vidaković, A. et al. Regulation of the RNAPII pool is integral to the DNA damage response. *Cell* **180**, 1245–1261.e21 (2020).

17. 17.

Kokic, G. et al. Structural basis of TFIIH activation for nucleotide excision repair. *Nat. Commun.* **10**, 2885 (2019).

18. 18.

Brueckner, F., Hennecke, U., Carell, T. & Cramer, P. CPD damage recognition by transcribing RNA polymerase II. *Science* **315**, 859–862 (2007).

19. 19.

Xu, J. et al. Structural basis for the initiation of eukaryotic transcription-coupled DNA repair. *Nature* **551**, 653–657 (2017).

20. 20.

Bernecky, C., Plitzko, J. M. & Cramer, P. Structure of a transcribing RNA polymerase II–DSIF complex reveals a multidentate DNA–RNA clamp. *Nat. Struct. Mol. Biol.* **24**, 809–815 (2017).

21. 21.

Vos, S. M., Farnung, L., Linden, A., Urlaub, H. & Cramer, P. Structure of complete Pol II–DSIF–PAF–SPT6 transcription complex reveals RTF1 allosteric activation. *Nat. Struct. Mol. Biol.* **27**, 668–677 (2020).

22. 22.

Schwertman, P. et al. UV-sensitive syndrome protein UVSSA recruits USP7 to regulate transcription-coupled repair. *Nat. Genet.* **44**, 598–602 (2012).

23. 23.

Zhang, X. et al. Mutations in UVSSA cause UV-sensitive syndrome and destabilize ERCC6 in transcription-coupled DNA repair. *Nat. Genet.* **44**, 593–597 (2012).

24. 24.

Fei, J. & Chen, J. KIAA1530 protein is recruited by Cockayne syndrome complementation group protein A (CSA) to participate in transcription-coupled repair (TCR). *J. Biol. Chem.* **287**, 35118–35126 (2012).

25. 25.

Vessoni, A. T., Guerra, C. C. C., Kajitani, G. S., Nascimento, L. L. S. & Garcia, C. C. M. Cockayne syndrome: the many challenges and approaches to understand a multifaceted disease. *Genet. Mol. Biol.* **43**, e20190085 (2020).

26. 26.

Li, W., Giles, C. & Li, S. Insights into how Spt5 functions in transcription elongation and repressing transcription coupled DNA repair. *Nucleic Acids Res.* **42**, 7069–7083 (2014).

27. 27.

Wier, A. D., Mayekar, M. K., Heroux, A., Arndt, K. M. & VanDemark, A. P. Structural basis for Spt5-mediated recruitment of the Pafl complex to chromatin. *Proc. Natl Acad. Sci. USA* **110**, 17290–17295 (2013).

28. 28.
Doherty, A. J., Serpell, L. C. & Ponting, C. P. The helix-hairpin-helix DNA-binding motif: a structural basis for non-sequence-specific recognition of DNA. *Nucleic Acids Res.* **24**, 2488–2497 (1996).
29. 29.
Close, D. et al. Crystal structures of the *S. cerevisiae* Spt6 core and C-terminal tandem SH2 domain. *J. Mol. Biol.* **408**, 697–713 (2011).
30. 30.
Vos, S. M. et al. Structure of activated transcription complex Pol II–DSIF–PAF–SPT6. *Nature* **560**, 607–612 (2018).
31. 31.
van den Heuvel, D. et al. A CSB–PAF1C axis restores processive transcription elongation after DNA damage repair. *Nat. Commun.* **12**, 1342 (2021).
32. 32.
Boeing, S. et al. Multiomic analysis of the UV-induced dna damage response. *Cell Rep.* **15**, 1597–1610 (2016).
33. 33.
Nakazawa, Y. et al. Mutations in UVSSA cause UV-sensitive syndrome and impair RNA polymerase IIo processing in transcription-coupled nucleotide-excision repair. *Nat. Genet.* **44**, 586–592 (2012).
34. 34.
Baek, K., Scott, D. C. & Schulman, B. A. NEDD8 and ubiquitin ligation by cullin-RING E3 ligases. *Curr. Opin. Struct. Biol.* **67**, 101–109 (2021).
35. 35.
Ranes, M. et al. A ubiquitylation site in Cockayne syndrome B required for repair of oxidative DNA damage, but not for transcription-coupled nucleotide excision repair. *Nucleic Acids Res.* **44**, 5246–5255 (2016).
36. 36.

Anindya, R. et al. A ubiquitin-binding domain in Cockayne syndrome B required for transcription-coupled nucleotide excision repair. *Mol. Cell* **38**, 637–648 (2010).

37. 37.

Gregersen, L. H. & Svejstrup, J. Q. The cellular response to transcription-blocking DNA damage. *Trends Biochem. Sci* **43**, 327–341 (2018).

38. 38.

Wilson, M. D., Harreman, M. & Svejstrup, J. Q. Ubiquitylation and degradation of elongating RNA polymerase II: the last resort. *Biochim. Biophys. Acta* **1829**, 151–157 (2013).

39. 39.

Gradia, S. D. et al. MacroBac: new technologies for robust and efficient large-scale production of recombinant multiprotein complexes. *Methods Enzymol.* **592**, 1-26 (2017).

40. 40.

Citterio, E. et al. Biochemical and biological characterization of wild-type and ATPase-deficient Cockayne syndrome B repair protein. *J. Biol. Chem.* **273**, 11844-11851 (1998).

41. 41.

Yin, J., Lin, A. J., Golan, D. E. & Walsh, C. T. Site-specific protein labeling by Sfp phosphopantetheinyl transferase. *Nat. Protoc.* **1**, 280-285 (2006).

42. 42.

Vos, S. M. et al. Architecture and RNA binding of the human negative elongation factor. *eLife* **5**, e14981 (2016).

43. 43.

Bernecky, C., Herzog, F., Baumeister, W., Plitzko, J. M. & Cramer, P. Structure of transcribing mammalian RNA polymerase II. *Nature* **529**, 551-554 (2016).

44. 44.

Yang, B. et al. Identification of cross-linked peptides from complex samples. *Nat. Methods* **9**, 904-906 (2012).

45. 45.

Combe, C. W., Fischer, L. & Rappsilber, J. xiNET: cross-link network maps with residue resolution. *Mol. Cell. Proteomics* **14**, 1137-1147 (2015).

46. 46.

Kosinski, J. et al. Xlink Analyzer: software for analysis and visualization of cross-linking data in the context of three-dimensional structures. *J. Struct. Biol.* **189**, 177-183 (2015).

47. 47.

Cox, J. & Mann, M. MaxQuant enables high peptide identification rates, individualized p.p.b.-range mass accuracies and proteome-wide protein quantification. *Nat. Biotechnol.* **26**, 1367-1372 (2008).

48. 48.

Mastronarde, D. N. Automated electron microscope tomography using robust prediction of specimen movements. *J. Struct. Biol.* **152**, 36-51 (2005).

49. 49.

Tegunov, D. & Cramer, P. Real-time cryo-electron microscopy data preprocessing with Warp. *Nat. Methods* **16**, 1146-1152 (2019).

50. 50.

Punjani, A., Rubinstein, J. L., Fleet, D. J. & Brubaker, M. A. cryoSPARC: algorithms for rapid unsupervised cryo-EM structure determination. *Nat. Methods* **14**, 290-296 (2017).

51. 51.

Scheres, S. H. W. Processing of structurally heterogeneous cryo-EM data in RELION. *Nature* **579**, 125-157 (2016).

52. 52.

Scheres, S. H. W. A Bayesian view on cryo-EM structure determination. *J. Mol. Biol.* **415**, 406-418 (2012).

53. 53.

Scheres, S. H. W. RELION: implementation of a Bayesian approach to cryo-EM structure determination. *J. Struct. Biol.* **180**, 519-530 (2012).

54. 54.

Pettersen, E. F. et al. UCSF Chimera — visualization system for exploratory research and analysis. *J. Comput. Chem.* **25**, 1605-1612 (2004).

55. 55.

Biasini, M. et al. SWISS-MODEL: modelling protein tertiary and quaternary structure using evolutionary information. *Nucleic Acids Res.* **42**, W252-W258 (2014).

56. 56.

Bordoli, L. et al. Protein structure homology modeling using SWISS-MODEL workspace. *Nat. Protoc.* **4**, 1-13 (2008).

57. 57.

Emsley, P., Lohkamp, B., Scott, W. G. & Cowtan, K. Features and development of Coot. *Acta Crystallogr. D* **66**, 486-501 (2010).

58. 58.

Adams, P. D. et al. PHENIX: a comprehensive Python-based system for macromolecular structure solution. *Acta Crystallogr. D* **66**, 213-221 (2010).

59. 59.

Misra, S., Puertollano, R., Kato, Y., Bonifacino, J. S. & Hurley, J. H. Structural basis for acidic-cluster-dileucine sorting-signal recognition by VHS domains. *Nature* **415**, 933-937 (2002).

60. 60.

Kidmose, R. T. et al. Namdinator — automatic molecular dynamics flexible fitting of structural models into cryo-EM and crystallography experimental maps.

IUCrJ **6**, 526-531 (2019).

61. 61.

Zhang, S. et al. Structure of a transcribing RNA polymerase II–U1 snRNP complex. *Science* **371**, 305-309 (2021).

62. 62.

Angers, S. et al. Molecular architecture and assembly of the DDB1–CUL4A ubiquitin ligase machinery. *Nature* **443**, 590-593 (2006).

63. 63.

Plechanovová, A., Jaffray, E. G., Tatham, M. H., Naismith, J. H. & Hay, R. T. Structure of a RING E3 ligase and ubiquitin-loaded E2 primed for catalysis. *Nature* **489**, 115-120 (2012).

64. 64.

Chen, V. B. et al. MolProbity: all-atom structure validation for macromolecular crystallography. *Acta Crystallogr. D* **66**, 12-21 (2009).

65. 65.

Goddard, T. D. et al. UCSF ChimeraX: meeting modern challenges in visualization and analysis. *Protein Sci.* **27**, 14-25 (2018).

Acknowledgements

We thank current and former members of the Cramer laboratory, in particular, C. Dienemann for assistance with cryo-EM data collection, S. Vos and Y. Chen for assistance with protein purification, Y. Chen for providing P-TEFb, and C. Diederich and S. Dodonova for insightful discussions; M. Ninov for assistance with mass spectrometry; S. Lorenz for discussions about ubiquitylation; and B. Safaric and M. Scherr for advice on protein labelling. G.K. was supported by a Boehringer Ingelheim Fonds PhD fellowship. H.U. is supported by the Deutsche Forschungsgemeinschaft (SFB860). P.C. was supported by the Deutsche Forschungsgemeinschaft (EXC 2067/1 39072994, SFB860 and SPP2191) and the European Research Council Advanced Investigator Grant CHROMATRANS (grant agreement no. 882357).

Funding

Open access funding provided by Max Planck Society.

Author information

Affiliations

1. Department of Molecular Biology, Max Planck Institute for Biophysical Chemistry, Göttingen, Germany

Goran Kokic, Felix R. Wagner & Patrick Cramer

2. Max Planck Institute for Biophysical Chemistry, Bioanalytical Mass Spectrometry, Göttingen, Germany

Aleksandar Chernev & Henning Urlaub

3. University Medical Center Göttingen, Institute of Clinical Chemistry, Bioanalytics Group, Göttingen, Germany

Henning Urlaub

Contributions

G.K. designed and carried out all of the experiments except for the crosslinking mass spectrometry, which was carried out by A.C. F.R.W. assisted with cryo-EM data processing. H.U. supervised the mass spectrometry. P.C. supervised the research. G.K. and P.C. wrote the manuscript, with input from all authors.

Corresponding author

Correspondence to Patrick Cramer.

Ethics declarations

Competing interests

The authors declare no competing interests.

Additional information

Peer review information *Nature* thanks Martijn Luijsterburg and the other, anonymous, reviewer(s) for their contribution to the peer review of this work. Peer review reports are available.

Publisher's note Springer Nature remains neutral with regard to jurisdictional claims in published maps and institutional affiliations.

Extended data figures and tables

Extended Data Fig. 1 Biochemical characterisation of TCR factors.

a, *In vitro* transcription over an arrest sequence in the presence of TCR factors. The ratio of band intensity for bypass and arrest products was plotted for triplicate measurement. Data are presented as mean values \pm SD. **b**, *In vitro* transcription over an arrest sequence in the presence of CSB or CSB-CSA-DDB1 complex. The experiment was repeated two times independently with similar results. Bar graph shows an average value for duplicate measurement. **c**, ATPase assay monitoring CSB activity in the presence of increasing amounts of CSA-DDB1. The experiment was repeated two times independently with similar results. **d**, ATPase assay monitoring stimulation of CSB activity in the presence of Pol II elongation complex, TCR factors and PAF. Analysis shown in **h**. **e**, Analytical size exclusion chromatography of CSA-DDB1, CSB, UVSSA, CSA-DDB1-CSB-UVSSA and Pol II-CSA-DDB1-CSB-UVSSA complexes. The two latter samples were analysed by SDS-PAGE, which confirmed complex composition and purity. The experiment was performed once for individual factors and at least three times for the complexes. **f**, *In vitro* transcription over an arrest sequence in the presence of CSB or CSB mutant F796A. The experiment was repeated two times independently with similar results. Bar graph shows an average value for duplicate measurement. **g**, ATPase assay monitoring the activity of CSB mutant F796A alone, in the presence of bubble DNA and in the presence of a Pol II elongation complex (EC). Analysis shown in **h**. **h**, Summary of ATPase assay results. The rate of ATP hydrolysis was plotted for triplicate measurement. The colour code as in panels **d** and **g**. Data are presented as mean values \pm SD. For original gel scans and graph data associated with the Extended Data Fig. 1 see Supplementary Fig. 1 and Supplementary Table 1, respectively.

Extended Data Fig. 2 Cross-linking mass-spectrometry interaction networks.

a, Cross-linking mass-spectrometry interaction network within the Pol II-CSA-DDB1-CSB-UVSSA complex after crosslinking with BS3. (right) Crosslinks with the score above 3 that were detected at least twice are shown. (left) Crosslinks were mapped

onto the Pol II-CSA-DDB1-CSB structure. Coloured rods connecting crosslinked residues represent permitted (blue) or non-permitted (red) crosslinking distances. 89% of mapped crosslink sites fall within the permitted crosslinking distance of 30 Å. 11% of crosslinks in violation of crosslinking distance are likely a result of complex flexibility or technical errors. Histogram shows the number of crosslinks detected at a particular crosslinking distance. **b**, Cross-linking mass-spectrometry interaction network within the Pol II-CSA-DDB1-CSB-UVSSA complex after crosslinking with EDC. (left) Crosslinks with the score above 3 that were detected at least twice are shown. (right) Crosslinks were mapped onto the Pol II-CSA-DDB1-CSB structure. 83% of mapped crosslink sites fall within the permitted crosslinking distance of 20 Å. 17% of crosslinks in violation of crosslinking distance are likely a result of complex flexibility or technical errors. Histogram shows the number of crosslinks detected at a particular crosslinking distance. **c**, BS3 crosslinks with a score above 3 that were detected at least twice and mapped onto Pol II. The Pol II surface area within the 30 Å radius of the crosslink site was colored as a protein footprint. **d**, BS3 and EDC crosslinks used to identify the CSA-interacting motif (CIM) in CSB.

[Extended Data Fig. 3 Cryo-EM analysis of the Pol II-CSB-CSA-DDB1-UVSSA complex \(Structure 1\).](#)

a, Processing tree. The number of particles in a particular class is reported above the density. Densities used for further processing are coloured as in Fig. [1a](#). **b**, Final composite map created from the focused refined maps. **c**, Local resolution estimate for the composite map. **d**, Fourier shell correlation plots for all focused refined maps and the composite map. **e**, Angular distribution plot for the high-resolution Pol II class used as a starting point for focused classifications.

[Extended Data Fig. 4 Mapping of human disease mutations onto structure 2.](#)

Cockayne syndrome and UV-sensitive syndrome mutations^{[25](#)} were mapped onto our Pol II-TCR structure and clustered based on their location. A UVSSA mutation that cannot reverse TCR defect was also included^{[33](#)}.

[Extended Data Fig. 5 Cryo-EM analysis of the Pol II-CSB-CSA-DDB1-UVSSA-ADP:BeF₃ complex \(Structure 2\).](#)

a, Processing tree. Number of particles in a particular class is reported above the density. Densities used for further processing are coloured as in Fig. [1a](#). **b**, Final composite map created from the focused refined maps. **c**, Local resolution estimate for the composite map. **d**, Fourier shell correlation plots for all focused refined maps and

the composite map. **e**, Angular distribution plot for the high-resolution Pol II class used as a starting point for focused classifications.

Extended Data Fig. 6 DNA binding by CSB and transcription stimulation.

a, CSB interactions with upstream DNA in pre-translocated state (structure 1). **b**, CSB interactions with upstream DNA in post-translocated state (structure 2). **c**, Scheme illustrating the movement of DNA during CSB-dependent ATPase activity. **d**, Comparison of models and cryo-EM densities for the pulling pin in the structure reported here and the yeast Pol II-Rad26 structure reported previously (PDB code 5VVR)¹⁹. **e**, Structure-based model for CSB stimulation by CSA due to restricting lobe 2 motion via CIM binding to CSA.

Extended Data Fig. 7 Cryo-EM analysis of the Pol II-CSB-CSA-DDB1-UVSSA-SPT6-PAF complex (Structure 3).

a, Processing tree. Number of particles in a particular class is reported above the density. Densities used for further processing are coloured as in Fig. [2c](#). **b**, Final composite map created from the focused refined maps. **c**, Local resolution estimate for the composite map. **d**, Fourier shell correlation plots for all focused refined maps and the composite map. **e**, Angular distribution plot for the high-resolution Pol II class used as a starting point for focused classifications.

Extended Data Fig. 8 Additional analysis of EC^{TCR}.

a, Analytical size-exclusion chromatography of EC* (left) and EC^{TCR} (right) in the presence of RTF1. Peak fractions were analysed by SDS PAGE. While RTF1 elutes with EC* in stoichiometric amounts, it elutes with EC^{TCR} sub-stoichiometrically, which is indicative of weaker association of RTF1 with EC^{TCR} compared to EC*. The experiment with EC*-RTF1 was performed once and with EC^{TCR}-RTF1 twice. For gel source data, see Supplementary Fig. [1](#). **b**, Modelling shows clashes between UVSSA and extended downstream DNA, and between SPT6 and extended upstream DNA, suggesting that some repositioning of DNA and/or SPT6 and UVSSA occurs when DNA is longer.

Extended Data Fig. 9 Biochemical and cryo-EM analysis of the Pol II-CSB-CRL4^{CSA}-UVSSA-SPT6-PAF complex (Structures 4 and 5).

a, Pol II ubiquitination in the absence of UVSSA or CSB. The experiment was repeated two times independently with similar results. For Western blot source data, see Supplementary Fig. 1. **b**, Processing tree. Number of particles in a particular class is reported above the density. Densities used for further processing are coloured as in Fig. 3c. **c**, Final composite map created from the focused refined maps. **d–f**, Local resolution estimate for the composite map and focused refined maps containing CRL4^{CSA}. **g**, Fourier shell correlation plots for all focused refined maps and the composite map. **h**, Angular distribution plot for the high-resolution Pol II class used as a starting point for focused classifications.

Extended Data Fig. 10 Quality of cryo-EM densities.

Cryo-EM density of the pulling hook (**a**), pulling hook wedging into the upstream fork of the transcription bubble (**b**), CSA-interacting motif (CIM) in CSB (**c**), ADP:BeF₃ (**d**), beta-propellers in CSA-DDB1 (**e–h**), CSA-UVSSA (**i**) together with crosslinks used to position the VHS-domain of UVSSA (**j**), SPT6 and a zoom-in on the SPT6-Pol II stalk contacts (**k**), CTR9 and WDR61 (**l**), LEO1 C-terminal helix (**m**), CRL4^{CSA} conformation targeting Pol II (**n**), CRL4^{CSA} conformation targeting CSB (**o**). For each density we indicated from which structure the density was taken, Structure 1, 2, 3, 4 or 5.

Extended Data Table 1 Cryo-EM data collection, refinement and validation statistics

Supplementary information

Supplementary Information

The file contains Supplementary Fig. 1 and Supplementary Table 1. Supplementary Fig. 1 contains uncropped gel scans for Figs. 2a, b and 3a, and Extended Data Figs. 1a, b, f, 8a and 9a. Supplementary Table 1 contains source data associated with graphs for Extended Data Fig. 1a, b, f, h.

Reporting Summary

Supplementary Video 1

| Pol II-CSB-CSA-DDB1-UVSSA structure rotating around a vertical axis.

Supplementary Video 2

| Mechanism of CSB translocation that pulls on upstream DNA and pushes elongating Pol II forward.

Supplementary Video 3

| Conversion of EC* to EC^{TCR} involves three major structural changes.

Supplementary Video 4

| Conformational rearrangements in CRL4^{CSA} to target either Pol II or CSB for ubiquitination.

Peer Review File

Rights and permissions

Open Access This article is licensed under a Creative Commons Attribution 4.0 International License, which permits use, sharing, adaptation, distribution and reproduction in any medium or format, as long as you give appropriate credit to the original author(s) and the source, provide a link to the Creative Commons license, and indicate if changes were made. The images or other third party material in this article are included in the article's Creative Commons license, unless indicated otherwise in a credit line to the material. If material is not included in the article's Creative Commons license and your intended use is not permitted by statutory regulation or exceeds the permitted use, you will need to obtain permission directly from the copyright holder. To view a copy of this license, visit <http://creativecommons.org/licenses/by/4.0/>.

Reprints and Permissions

About this article

Cite this article

Kokic, G., Wagner, F.R., Chernev, A. *et al.* Structural basis of human transcription–DNA repair coupling. *Nature* **598**, 368–372 (2021). <https://doi.org/10.1038/s41586-021-03906-4>

- Received: 12 April 2021
- Accepted: 12 August 2021

- Published: 15 September 2021
- Issue Date: 14 October 2021
- DOI: <https://doi.org/10.1038/s41586-021-03906-4>

Share this article

Anyone you share the following link with will be able to read this content:

[Get shareable link](#)

Sorry, a shareable link is not currently available for this article.

[Copy to clipboard](#)

Provided by the Springer Nature SharedIt content-sharing initiative

This article was downloaded by **calibre** from <https://www.nature.com/articles/s41586-021-03906-4>

| [Section menu](#) | [Main menu](#) |

Career Guide